Massachusetts Institute of Technology
Department of Civil and Environmental Engineering

Final Technical Report

to

U.S. Army Research Office

Funding Number: DAAD 19-00-1-0436
Agency Report Number: 40368EV

FRACTURE FLOW RESEARCH

Volume 2

Modeling Joint Patterns Using Combinations of Mechanical and Probabilistic Concepts

by

Jean Louis Z. Locsin

Herbert H. Einstein

DISTRIBUTION STATEMENT A
Approved for Public Release
Distribution Unlimited

August 2005

20050824 147

REPORT DOCUMENTATION PAGE

Form Approved
OMB NO. 0704-0188

Public Reporting burden for this collection of information is estimated to average 1 hour per response, including the time for reviewing instructions, searching existing data sources, gathering and maintaining the data needed, and completing and reviewing the collection of information. Send comment regarding this burden estimates or any other aspect of this collection of information, including suggestions for reducing this burden, to Washington Headquarters Services, Directorate for information Operations and Reports, 1215 Jefferson Davis Highway, Suite 1204, Arlington, VA 22202-4302, and to the Office of Management and Budget, Paperwork Reduction Project (0704-0188,) Washington, DC 20503.

1. AGENCY USE ONLY (Leave Blank)	2. REPORT DATE August 4, 2005	3. REPORT TYPE AND DATES COVERED Final Report July 1, 2000 – Dec. 31, 2004

4. TITLE AND SUBTITLE
Fracture Flow Research
~~Volume 1: Modeling Rock Fracture Intersections – Application in the Boston Area and Evaluation of the Well Test Flow Dimension~~
Volume 2: Modeling Joint Patterns Using Combinations of Mechanical and Probabilistic Concepts

5. FUNDING NUMBERS
DAAD19-00-1-0436

6. AUTHOR(S)
Herbert H. Einstein, Jean-Louis Locsin

7. PERFORMING ORGANIZATION NAME(S) AND ADDRESS(ES)
Massachusetts Institute of Technology
Department of Civil and Environmental Engineering
77 Massachusetts Avenue, 1-342
Cambridge, MA 02139

8. PERFORMING ORGANIZATION REPORT NUMBER

9. SPONSORING / MONITORING AGENCY NAME(S) AND ADDRESS(ES)
U. S. Army Research Office
P.O. Box 12211
Research Triangle Park, NC 27709-2211

10. SPONSORING / MONITORING AGENCY REPORT NUMBER
40368-EV

40368.1-EV

11. SUPPLEMENTARY NOTES
The views, opinions and/or findings contained in this report are those of the author(s) and should not be construed as an official Department of the Army position, policy or decision, unless so designated by other documentation.

12 a. DISTRIBUTION / AVAILABILITY STATEMENT
Approved for public release; distribution unlimited.

12 b. DISTRIBUTION CODE

13. ABSTRACT (Maximum 200 words)
Fractures govern flow, deformation and strength of rock masses. Fracture flow is important with regard to resource extraction (water, gas, oil) as well as groundwater contamination. Fractures through their effect on deformability and strength goven stability of tunnels and slopes in rock and the behavior of building,-, bridge – and dam foundations. Very importantly, they also strongly affect penetration resistance.

The research consisted of two components, modeling of joint (fracture) intersections and fracture pattern modeling. The two volumes of the final report correspond to these two components.

Fracture intersections govern connectivity of fracture patterns and fracture flow (deformability, strength). The research developed an algorithm with which orientation and length of fracture intersections can be represented. The algorithm was applied and tested with a synthetic case and the fracture pattern in the Boston area. Also, an attempt at simplified flow dimension models was undertaken. The results show that complete numerical modeling is better than simplified modeling.

Fracture pattern modeling so far was limited to geometric models or simple mechanical models. The research developed a new model to represent fracture (joint) patterns in sedimentary rock specifically, layer perpendicular joints. One model is mechanically based (flaw model) the other one (rejection model) is quasi-mechanical. Both models have probabilistic aspects. The models' predictions were compared to fracture patterns observed in the field. The models, particularly the flaw model perform satisfactorily. Issues requiring further study are joint spacing smaller than saturation and joints which cross more than one layer.

14. SUBJECT TERMS	15. NUMBER OF PAGES
Rock Fracture, Fracture Flow, Joint Patterns, Fracture Intersections	[redacted]529
	16. PRICE CODE

17. SECURITY CLASSIFICATION OR REPORT	18. SECURITY CLASSIFICATION ON THIS PAGE	19. SECURITY CLASSIFICATION OF ABSTRACT	20. LIMITATION OF ABSTRACT
UNCLASSIFIED	UNCLASSIFIED	UNCLASSIFIED	UL

Table of Contents

1 Introduction 35

2 Field and Laboratory Observations 40

2.1 Field Observations 40

2.1.1 Joint Spacing-Layer Thickness Relationship 40

2.1.2 Joint Spacing Probability Distributions 53

2.2 Laboratory Observations 63

2.3 Summary 73

3 Stress Distribution Models 75

3.1 Hobbs' (1967) Simplified Model 75

3.1.1 Tensile Stress Distribution: Single Joint 75

3.1.2 Tensile Stress Distribution: Two Joints 84

3.2 Ji and Saruwatari's (1998) Simplified Model 92

3.2.1 Tensile Stress Distribution: Two Joints 92

4 Saturation Mechanisms 101

4.1 Tensile Stress Distributions: Simplified Models vs. Finite Element Models . 101

4.2 Compressive Stress Saturation Mechanism 109

4.3 Interface Slippage Saturation Mechanism 118

5 Joint Spacing Distribution Models 125

5.1 Probabilistic Approach 127

5.2 Numerical Approach 131

6 New Models 155

6.1 Introduction and Overview 155
6.2 Flaw Model 156
6.2.1 Flaw Model without Saturation Mechanisms 160
6.2.2 Flaw Model with Saturation Mechanisms 162
6.2.3 Saturation Mean Spacing Parametric Study 179
6.2.4 Simulated Joint Spacing Distributions for Flaw Model 211
6.3 Rejection Procedure 261
6.3.1 Rejection Procedure without Saturation Mechanisms 263
6.3.2 Rejection Procedure with Saturation Mechanisms 264
6.3.3 Saturation Mean Spacing Parametric Study 267
6.3.4 Simulated Joint Spacing Distributions 272
7 Comparison: New Models vs. Field Data 287
7.1 Introduction 287
7.2 Case 1: Becker & Gross (1996) 290
7.2.1 General Observations 290
7.2.2 Joint Spacing Data 295
7.2.3 Model Parameter Values 299
7.2.4 Simulation Results and Discussion 301
7.3 Case 2: Saltzman (2001) 338
7.3.1 General Observations 338
7.3.2 Joint Spacing Data 340
7.3.3 Model Parameter Values 345
7.3.4 Simulation Results and Discussion 346

7.4 Case 3: Gross et al. (1997) 374
7.4.1 General Observations 374
7.4.2 Joint Spacing Data 376
7.4.3 Model Parameter Values 383
7.4.4 Simulation Results and Discussion 384
7.5 Case 4: Baudo (2001) 411
7.5.1 General Observations 411
7.5.2 Joint Spacing Data 413
7.5.3 Model Parameter Values 419
7.5.4 Simulation Results and Discussion 422
8 Summary and Conclusions 443
9 References 471
10 Appendix 475
10.1 Flaw Model Code 475
10.2 Rejection Procedure Code 510

List of Figures

Figure 1 – Diagram of a typical fracture modeling process using probabilistic and geometric approaches 38
Figure 2 – Competent jointing layer bounded at the top and bottom by incompetent non-jointing layers. Layers are subjected to a far-field extensional strain (ε) 39
Figure 3 – Diagram of modeling process for spacing of layer-perpendicular joints in sedimentary rock based on a combination of mechanical and probabilistic concepts. 39
Figure 4 – Possible mechanism for the formation of layer-perpendicular joints in layered sedimentary rock. 40
Figure 5 – Definition of FSI and FSR. Points are not from real data and serve as examples only. 42
Figure 6 – Mechanical layers defined by the J_1 joints and the occurrence of cross-joints (J_2) between them. Sketched from descriptions of J_1 and J_2 joints given in Gross (1993). 43
Figure 7 – A case where the mechanical layer thickness can be defined by lithology in one direction and previous jointing (J_1) in another. 44
Figure 8 – A borehole intersecting a portion of a fractured bed. β is the angle between the core and the fractures, θ is the angle between the core axis and the bedding, D is the core diameter and T is the thickness of the bed. Sketched from Fig. 5 in Narr and Lerche (1984). 45
Figure 9 – Illustration of intersected beds vs. intersected jointed beds. Sketched from descriptions of intersected beds and intersected jointed beds in Narr and Lerche (1984). 46
Figure 10 – General shape of curves used to fit bed thickness-spacing data in Ladeira and Price (1981). Sketched from Fig. 2 in Ladeira and Price (1981). 48
Figure 11 – Suggested fit to bed thickness-spacing data with relationships of the nature shown in Figure 10. There is an initial linear relationship followed by a constant value of joint spacing beyond a certain value of bed thickness. A bilinear fit is also shown (C). A and B are sketched from Fig. 3 (a) of Ladeira and Price (1981). C is sketched from Fig. 1 (d) in Wu and Pollard (1995) 48
Figure 12 – Bed thickness and joint spacing curves for the three locations in the Asmari Formation in Iran. Converted into bed thickness vs. joint spacing from plots in McQuillan (1973) 50
Figure 13 – Schematic of the limestone/dolostone layer studied by Becker and Gross (1996). Sketched from Fig. 7 in Becker and Gross (1996) but without the vertical scale 51
Figure 14 – Histogram of the spacing data (in cm) from the Gerofit Formation. Plotted from data in Becker and Gross (1996). 55
Figure 15 – Histogram of the natural logarithms of spacing. Plotted from data in Becker and Gross (1996). 55
Figure 16 – Histogram of spacing values (cm) in section I. Plotted from data in Becker and Gross (1996). 56

Figure 17 – Histogram of spacing values (cm) in section II. Plotted from data in Becker and Gross (1996). 57
Figure 18 – Histogram of spacing values (cm) in section III. Plotted from data in Becker and Gross (1996). 57
Figure 19 – Histogram of spacing values (cm) in section IV. Plotted from data in Becker and Gross (1996). 58
Figure 20 – Joint spacing distribution from Huang and Angelier (1989). Gamma distribution with $\alpha = 3.2$ and $\beta = 19.5$. Reproduced from information in Fig. 3 in Huang and Angelier (1989). 59
Figure 21 – Fitted exponential distributions for discontinuity data from the Lower Chalk in the Chinnor shaft and the Chinnor tunnel (Chinnor, Oxfordshire). Reproduced from data in Fig. 5 and Fig. 6 in Priest and Hudson (1976). 60
Figure 22 – Fitted exponential distributions for discontinuity data from the Kielder experimental tunnel at Rogerley Quarry, Durham from Priest and Hudson (1976). Reproduced from data in Fig. 9 and Fig. 10 in Priest and Hudson (1976). 61
Figure 23 – Fitted exponential distribution for discontinuity data in the Lower Chalk of the Channel Tunnel from Priest and Hudson (1976). Reproduced from data in Fig. 12 in Priest and Hudson (1976). 62
Figure 24 – Example of jointing layer with the faces exposed as well as its surface exposed. The top figure is the top surface of the ouctrop. The bottom figure is the exposed face of the outcrop. 65
Figure 25 – Components for the calculation of the area mean spacing (Wu and Pollard, 1995). 65
Figure 26 – Sketch of the experimental set-up for four-point bending in Wu and Pollard (1995). A constant radius of curvature is maintained so that uniform extension strain is applied to the brittle coating. Sketched from Fig. 3 (b) and Fig. 10 in Wu and Pollard (1995) 66
Figure 27 – Comparison between area mean joint spacing and scanline mean joint spacing at two levels of strain. The distance from one side of the measurement area (see Figure 25) to the scanline is varied. Sketched from Fig. 5 in Wu and Pollard (1995). 66
Figure 28 – Schematic of a poorly developed joint set and a well developed joint set relative to the area mean spacing measurement area *A*. Sketched from Fig. 5 in Wu and Pollard (1995) 66
Figure 29 – Schematic of how the strain level affects the area mean spacing as observed in the experiments by Wu and Pollard (1995). Sketched from curves in Fig. 12 in Wu and Pollard (1995). 68
Figure 30 – A schematic of the curves Wu and Pollard (1995) used to fit their experimental data. Sketched from Fig. 12 (h) in Wu and Pollard (1995) 69
Figure 31 – Polystyrene plate subjected to four-point bending. Sketched from Fig. 5 in Rives et al. (1992). 71
Figure 32 – Top view of the brittle coating and the location of the scanline. Sketched from Fig. 5 in Rives et al. (1992) 71
Figure 33 – A schematic of the evolution of the joint spacing distribution according to Rives et al. (1992). This figure follows Fig. 7 in Rives et al. (1992). 72

Figure 34 – Illustration of an idealized stress reduction shadow. Inside the shadow, the stresses are perturbed by the presence of the joint. 75
Figure 35 – Jointing layer sandwiched between two non-jointing layers. All layers are subjected to an equal amount of strain, ε. 76
Figure 36 – Formation of joint in jointing layer induces stress change in the vicinity of the joint. Note that v is the displacement at a point that is far enough from the jointing layer such that it has not been affected by the formation of the joint. 77
Figure 37 – Forces acting on a slice of the jointing layer. 80
Figure 38 – Variation of normalized stress ($\frac{\sigma_{local}}{\sigma_{farfield}}$) with distance away from a joint using different E_J/G_n ratios. Curves were constructed using Equation 21b 82
Figure 39 – Variation of normalized shear stress ($\frac{\tau_d}{\sigma_{farfield}}$) with distance away from a joint using different E_J/G_n ratios 83
Figure 40 – Variation and direction of interface shear stress away from segment midpoint. 84
Figure 41 – Definition of variables for Hobbs' model of the stress reduction shadow interaction of adjacent joints. 85
Figure 42 – Stress ratio distribution between adjacent joints according to Hobbs' (1967) model with $l = 1.0$ for $E_J/G_n = 2$, 5 and 10. 86
Figure 43 – Normalized shear stress along an interface in Hobbs' (1967) model for $l = 1.0$ for $E_J/G_n = 2$, 5 and 10. 88
Figure 44 – Stress ratio distribution between two joints with different spacings ($l = 1$, 2 and 4) using a single value of $E_J/G_n = 5.0$. 89
Figure 45 – Normalized shear distribution for two segments of different length but the same properties ($E_J/G_n = 5.0$) and applied strain 90
Figure 46 – Relationship between applied strain (ε_2) and normalized spacing according to Hobbs' (1967) model for different E_J/G_n ratios. Note that t is the jointing layer thickness. The normalized spacing here is the smallest normalized length a segment formed by two adjacent joints should have in order to produce a normal stress at its midpoint equal to the tensile strength of the rock given the corresponding applied strain 92
Figure 47 – Definition of variables for Ji and Saruwatari (1998). 93
Figure 48 – Relationship between M and d for different values of n. 94
Figure 49 – Stress ratio variation between adjacent joints according to Ji and Saruwatari's (1998) model. 95
Figure 50 – Normalized shear stress along the interface according to Ji and Saruwatari's (1998) model. 96
Figure 51 – Variation of normalized local stress with distance from the segment midpoint for various segment lengths. 97
Figure 52 – Relationship between applied strain and normalized spacing according to Ji and Saruwatari's (1998) model for different E_J/G_n ratios. Note that t is the jointing layer thickness 99

Figure 53 – Stress reduction shadow due to a single joint in a layer subjected to uniform extensional strain (by FEM, FRANC2D program). The color yellow represents the far field stress. 102
Figure 54 – Comparison between the analytical stress reduction shadow by Hobbs (1967) and finite element simulations using FRANC2D. Region of compressive stress of small magnitude in the FE simulation encircled. 103
Figure 55 – Finite element mesh used to model two medium spaced joints. 104
Figure 56 – Contours of σ_{xx}. Note: the color red represents compressive stress, all other colors denote tensile stresses with values between zero and the far field stress value (denoted by the color blue). 105
Figure 57 – Comparison of finite element results with both stress distribution models for the medium-spaced joints. 106
Figure 58 – Finite element mesh for two closely-spaced joints 107
Figure 59 – Contours of σ_{xx}. Note: the color red represents compressive stress, all other colors denote tensile stresses with values between zero and the far field stress value (denoted by the color blue). 107
Figure 60 – Comparison of finite element results with both stress distribution models for the closely-spaced joints. 108
Figure 61 – Set-up of the finite element model used by Bai and Pollard (2000). The jointing and non-jointing layers have Poisson's ratios of ν_f and ν_n, respectively. Note that U_y can be zero (i.e., no overburden). This figure is a sketch of Fig. 1 (a) in Bai and Pollard (2000). 110
Figure 62 – Illustration of the effect of the ratio between the jointing layer Young's modulus (E_f) and the bounding layer Young's modulus (E_n) to the critical spacing-to-thickness ratio. The curve is a fit of the finite element simulation results. This plot is the same as Fig. 4 (b) in Bai and Pollard (2000) 112
Figure 63 – Contours of the parameter D as a function of the jointing layer and bounding layer Poisson's ratios (ν_f and ν_n, respectively). Plotted from Equation 44. 113
Figure 64 – Illustration of the effect of D (Equation 44) on the critical spacing-to-thickness ratio. This plot is simular to Fig. 5 (b) in Bai and Pollard (2000) 114
Figure 65 – Illustration of the effect of overburden on the critical spacing-to-thickness ratio. This plot is the same as Fig. 7 in Bai and Pollard (2000). 115
Figure 66 – Laboratory set-up used by Bai and Pollard (2000) to study critical spacing-to-thickness ratio. This figure is sketched from Fig. 8 in Bai and Pollard (2000). 118
Figure 67 – Modified interface shear stress distribution to account for interfacial slip. The modified shear stress distribution allows for a maximum absolute shear stress value of τ_0. 119
Figure 68 – Example of the local normal stress and interface shear stress distribution when interface slippage is considered. The solid curve represents the local normal stress and the dashed curve the interface shear stress. Plotted from Equation 56. 123
Figure 69 – Local normal stress (solid line) and interface shear stress (dashed line) distribution at full slippage. Plotted from Equation 56. 124

Figure 70 – Illustration of the predicted joint spacing distribution from the simplified stress distribution models. 126
Figure 71 – Plots of $q(x)$ with parameters $\lambda = 0.1$ (cm^{-1}), $\mu = 5$ cm for $\alpha = 0$, 1, 2 and 3. 129
Figure 72 – Resulting probability density functions of x all with $B = 100$, $\lambda = 0.2$ (cm^{-1}), $\mu = 5$ cm for $\alpha = 1$, 3 and 10. 130
Figure 73 – Jointing layer sandwiched between two non-jointing layers. All layers are subjected to an equal amount of strain, ε_1 132
Figure 74 – Variation of normalized stress with distance away from a joint using different E_f/G_n ratios. 133
Figure 75 – Normalized distance from the joint to a particular percentage of the remote stress as a function of the E_f/G_n ratio. 135
Figure 76 – Illustration of the stress reduction shadow. 136
Figure 77 – Schematic of the stress reduction shadow. 137
Figure 78 – Completely overlapping stress reduction shadows. The second joint forms just at the edge of the stress reduction shadow of the existing joint. 137
Figure 79 – Touching stress reduction shadows. 138
Figure 80 – Change in the standard deviation as the number of segments increases. In this algorithm, the longest segment is halved. 139
Figure 81 – Change in the standard deviation as the number of segments increases. In this algorithm, a randomly selected segment is halved. 140
Figure 82 – Change in the standard deviation as the number of segments increases. In this algorithm, the longest segment is divided randomly. 141
Figure 83 – Change in the standard deviation as the number of segments increases. In this algorithm, a randomly selected segment is divided randomly. 142
Figure 84 – The skewness values of the different joint spacing distributions approach zero for the quasi-normal distribution. This figure follows Fig. 7 in Rives et al. (1992). 144
Figure 85 – Skewness with increasing number of segments. In this algorithm, the longest segment is halved. 145
Figure 86 – Relationship among the mean, minimum and maximum joint spacing values for longest segment halving. 146
Figure 87 – Skewness with increasing number of segments. In this algorithm, a randomly selected segment is halved. 147
Figure 88 – Relationship among the mean, minimum and maximum joint spacing values for halving a randomly selected segment. 148
Figure 89 – Skewness with increasing number of segments. In this algorithm, the longest segment is divided randomly. 149
Figure 90 – Relationship among the mean, minimum and maximum joint spacing values for randomly dividing the longest segment. 150
Figure 91 – Skewness with increasing number of segments. In this algorithm, a randomly selected segment is divided randomly. 151
Figure 92 – Relationship among the mean, minimum and maximum joint spacing values for randomly dividing a randomly selected segment. 152

Figure 93 – Skewness versus number of segments for the longest segment halving algorithm (additional results). 153
Figure 94 – Spacing distribution after the initial pattern is generated. 154
Figure 95 – Geometry of the problem. 158
Figure 96 – Schematic of the local tensile stress profile along the y-direction at different distances from an existing joint. 158
Figure 97 – Schematic of the average tensile stress at different distances from an existing joint. 159
Figure 98 – Uniform probability distribution of tensile strength. 159
Figure 99 – Example of the initial unjointed layer containing flaws (there are 14 in this case). The unjointed layer is basically one big segment containing all the flaws. The strain required to form a joint at each flaw is calculated (shown). These strains will differ for each flaw based on the tensile strength at the flaw as well as the location of the flaw with respect to the midpoint of the layer. A new joint is located at the flaw that requires the lowest strain to form a joint. 160
Figure 100 – Jointing layer after the formation of a single joint. There are now two segments and all the flaws are no longer contained within a single segment as in Figure 99. 161
Figure 101 – Shear stress distribution allowing for interface slippage. 163
Figure 102 – Forces acting on a slice of jointing layer. 164
Figure 103 – Example of the plot of shear stress distribution considering slippage and the corresponding tensile stress distribution. 167
Figure 104 – Tensile stress distribution at impending slippage. The stress distributions for both models (considering and disregarding interface slippage) are identical. .. 169
Figure 105 – Tensile stress distributions when the extensional strain is increased to 0.02. Model with slippage predicts lower stresses compared to model without slippage. 170
Figure 106 – Tensile stress distributions when the extensional strain reaches about 0.039. At this stage, the model considering slippage predicts stresses way below those from the model without slippage. 171
Figure 107 – Progression of the tensile stress distribution until the limiting condition (i.e., full slippage). 172
Figure 108 – Illustration of the possible scenarios for the (x, σ_{t-flaw}) pairs with respect to the limiting stress distribution in the initial step of the new algorithm. Point A is right on the limiting stress distribution triangle (jointing is possible). Slippage has to occur up to point A for jointing at A to occur. Point B is inside the triangle (jointing is possible). Point C is outside the triangle and point D is right at the tip (jointing not possible in both cases). 175
Figure 109 – Illustration of the effect of the non-jointing (bounding) layer thickness (d) on the relationship between saturation mean spacing and jointing layer thickness. 180
Figure 110 – Contours of saturation mean spacing (SMS) as a function of the jointing layer thickness and non-jointing layer thickness for the interface slippage model. 181
Figure 111 – Mean joint spacing as the applied strain increases for different bounding layer thickness (d) values. Note: t is the jointing layer thickness. 181
Figure 112 – Illustration of the effect of the ratio between the jointing layer modulus of elasticity and the bounding layer shear modulus. 182

Figure 113 – Contours of saturation mean spacing (SMS) as a function of both the jointing layer thickness and the $\frac{E_f}{G_n}$ ratio for the interface slippage model. 183
Figure 114 – Mean joint spacing as the applied strain increases for different values of the $\frac{E_f}{G_n}$ ratio. 183
Figure 115 – Illustration of the effect of interface shear strength (in MPa) on the relationship between jointing layer thickness (t) and the saturation mean spacing. 184
Figure 116 – Contours of saturation mean spacing (SMS) as a function of the jointing layer thickness and interface shear strength for the interface slippage model. 185
Figure 117 – Illustration of the effect of flaw density on the relationship between jointing layer thickness and the saturation mean spacing. 186
Figure 118 – Effect of the non-jointing layer thickness on the relationship between saturation mean spacing and jointing layer thickness. 187
Figure 119 – Contours of saturation mean spacing (SMS) as a function of jointing layer thickness and non-jointing layer thickness for the compressive stress model. 188
Figure 120 – Effect of the $\frac{E_f}{G_n}$ ratio on the relationship between saturation mean spacing and jointing layer thickness. 189
Figure 121 – Contours of saturation mean spacing (SMS) as a function of jointing layer thickness and the $\frac{E_f}{G_n}$ ratio for the compressive stress model. 190
Figure 122 – Effect of the flaw density in the jointing layer on the relationship between saturation mean spacing and jointing layer thickness. 191
Figure 123 – Tensile stress vs. tensile strength for the interface slippage saturation mechanism for the case with and without flaws. New joint formation is only possible with the existence of flaws because there is a limit to the tensile stress that can be achieved. 192
Figure 124 – Tensile stress vs. tensile strength for the compressive stress saturation mechanism for the case with and without flaws. The existing joints are spaced above the critical spacing, $t \cdot \left(\frac{s}{t}\right)_{cr}$. A new joint can form with or without the flaws (the two dropdown lines) because there is no limit to the tensile stress as long as the spacing is above critical. 192
Figure 125 – Example of the relationship between saturation mean spacing and jointing layer thickness for the three different models. 194
Figure 126 – The three saturation mechanisms at an interface shear strength of 20MPa. Note that the interface slip and combined mechanism data coincide almost perfectly. 195
Figure 127 – The three saturation mechanisms at an interface shear strength of 30MPa. 196
Figure 128 – The three saturation mechanisms at an interface shear strength of 40MPa. 196
Figure 129 – Contours of the saturation mean spacing (SMS) as a function of the jointing layer thickness and the interface shear strength in the model considering only interface slippage as the saturation mechanism (same as Figure 116). 197

Figure 130 – Contours of saturation mean spacing (SMS) as a function of the jointing layer thickness and the interface shear strength in the model considering only the compressive stress as the saturation mechanism. 197
Figure 131 – Contours of saturation mean spacing (SMS) as a function of the jointing layer thickness and the interface shear strength in the model considering both interface slippage and compressive stress as saturation mechanisms..... 198
Figure 132 – Saturation mean spacing results from the three different models for a $\frac{E_f}{G_n}$ ratio of 5.0..... 199
Figure 133 – Saturation mean spacing results from the three different models for a $\frac{E_f}{G_n}$ ratio of 10..... 200
Figure 134 – Saturation mean spacing results from the three different models for a $\frac{E_f}{G_n}$ ratio of 40..... 200
Figure 135 – Contours of saturation mean spacing (SMS) as a function of the jointing layer thickness and the $\frac{E_f}{G_n}$ ratio in the model considering only interface slippage as the saturation mechanism..... 201
Figure 136 – Contours of saturation mean spacing (SMS) as a function of the jointing layer thickness and the $\frac{E_f}{G_n}$ ratio in the model considering only compressive stress as the saturation mechanism..... 201
Figure 137 – Contours of saturation mean spacing (SMS) as a function of the jointing layer thickness and the $\frac{E_f}{G_n}$ ratio in the combined mechanism model. 202
Figure 138 - Saturation mean spacing results from the three different models for D = 0.17..... 203
Figure 139 - Saturation mean spacing results from the three different models for D = 0.0. 203
Figure 140 - Saturation mean spacing results from the three different models for D = -0.17..... 204
Figure 141 – Contours of saturation mean spacing (SMS) as a function of the jointing layer thickness and the parameter D in the model considering only compressive stress as the saturation mechanism. 204
Figure 142 – Contours of saturation mean spacing (SMS) as a function of the jointing layer thickness and the parameter D in the combined mechanism model. 205
Figure 143 - Saturation mean spacing results from the three different models for a non-jointing layer thickness value of 0.01 m. 206
Figure 144 - Saturation mean spacing results from the three different models for a non-jointing layer thickness value of 0.1 m. 206
Figure 145 - Saturation mean spacing results from the three different models for a non-jointing layer thickness value of 0.5 m. 207
Figure 146 – Contours of saturation mean spacing (SMS) as a function of the jointing layer thickness and the non-jointing layer thickness in the model considering only interface slippage as the saturation mechanism. 207

Figure 147 – Contours of saturation mean spacing (SMS) as a function of the jointing layer thickness and the non-jointing layer thickness in the model considering only the compressive stress as the saturation mechanism 208
Figure 148 – Contours of saturation mean spacing (SMS) as a function of the jointing layer thickness and the non-jointing layer thickness in the combined mechanism model 208
Figure 149 - Saturation mean spacing results from the three different models for a jointing layer with 500 flaws. 209
Figure 150 - Saturation mean spacing results from the three different models for a jointing layer with 1000 flaws. 210
Figure 151 - Saturation mean spacing results from the three different models for a jointing layer with 2000 flaws. 210
Figure 152 – Cumulative probability distribution comparison between a simulated joint pattern of low intensity (0.125 joints/m) and two known cumulative distribution forms (exponential and log-normal). The flaw model with saturation mechanism is used. 214
Figure 153 – Cumulative probability distribution comparison between a simulated joint pattern of medium-high intensity (2.5 joints/m) and two known cumulative distribution forms (exponential and log-normal). The flaw model with saturation mechanism is used. 215
Figure 154 – Cumulative probability distribution comparison between a simulated joint pattern at saturation (~8.3 joints/m in this case) and known cumulative distribution forms (log-normal and normal). The flaw model with saturation mechanism is used. 216
Figure 155 – Cumulative probability distribution comparison between a simulated joint pattern of low intensity (0.125 joints/m) and two known cumulative distribution forms (exponential and log-normal). The flaw model WITHOUT saturation mechanism is used. 217
Figure 156 – Cumulative probability distribution comparison between a simulated joint pattern of medium-high intensity (2.5 joints/m) and two known cumulative distribution forms (exponential and log-normal). The flaw model WITHOUT saturation mechanism is used 218
Figure 157 – Cumulative probability distribution comparison between a simulated joint pattern of high intensity (~8.3 joints/m) and known cumulative distribution forms (log-normal and normal). The flaw model WITHOUT saturation mechanism is used. 219
Figure 158 – Comparison between the simulated joint spacing CDFs at high joint intensity (0.125 joints/m) from the flaw model using the saturation mechanism and the flaw model that does not. 220
Figure 159 – Comparison between the simulated joint spacing CDFs at medium-high joint intensity (2.5 joints/m) from the flaw model using the saturation mechanism and the flaw model that does not. 220
Figure 160 – Comparison between the simulated joint spacing CDFs at high joint intensity (~8.3 joints/m) from the flaw model using the saturation mechanism and the flaw model that does not. 221

Figure 161 – Effect of $\frac{E_f}{G_n}$ ratio on the joint spacing CDF or the joint spacing distribution in the flaw model with saturation mechanism. Joint intensity is fixed at ~4.2 joints/m. 223
Figure 162 – Effect of $\frac{E_f}{G_n}$ ratio on the standard deviation of spacing for a fixed joint intensity (~4.2 joints/m). 223
Figure 163 – Tensile stress distribution with distance from a joint (x/t) according to Hobbs' (1967) model. 224
Figure 164 – Simulated cumulative distribution for $\frac{E_f}{G_n} = 2.0$ and the corresponding exponential and and log-normal CDFs. Flaw model with saturation is used. 225
Figure 165 – Simulated cumulative distribution for $\frac{E_f}{G_n} = 8.0$ and the corresponding log-normal CDF. Flaw model with saturation is used 225
Figure 166 – Simulated cumulative distribution for $\frac{E_f}{G_n} = 8.0$ (same data as Figure 165) and the corresponding normal CDF. Flaw model with saturation is used. 226
Figure 167 – Simulated cumulative distribution for $\frac{E_f}{G_n} = 15.0$ and the corresponding log-normal CDF. Flaw model with saturation is used 226
Figure 168 – Simulated cumulative distribution for $\frac{E_f}{G_n} = 15.0$ (same data as Figure 167) and the corresponding normal CDF. Flaw model with saturation is used. 227
Figure 169 – Effect of the non-jointing layer thickness (d) on the standard deviation of joint spacing holding all other parameters fixed. 228
Figure 170 – Effect of the non-jointing layer thickness (d) on the joint spacing CDF or the joint spacing distribution in the flaw model using a saturation mechanism. 229
Figure 171 – Joint spacing CDF for a non-jointing layer thickness of 0.01 m (jointing layer thickness = 0.18 m) and the corresponding exponential and log-normal distributions. Flaw model using saturation mechanism is used. 229
Figure 172 – Joint spacing CDF for a non-jointing layer thickness of 0.05 m (jointing layer thickness = 0.18 m) and the corresponding exponential and log-normal distributions. Flaw model using saturation mechanism is used. 230
Figure 173 – Joint spacing CDF for a non-jointing layer thickness of 0.2 m (jointing layer thickness = 0.18 m) and the corresponding log-normal distribution. Flaw model using saturation mechanism is used. 230
Figure 174 – Joint spacing CDF for a non-jointing layer thickness of 0.2 m (jointing layer thickness = 0.18 m) and the corresponding normal distribution. The simulated spacing data here is the same as in Figure 173. Flaw model using saturation mechanism is used. 231
Figure 175 – Standard deviation of spacing as a function of the $\frac{E_f}{G_n}$ ratio for two different sets of minimum and maximum tensile strengths with the same max-to-min ratio (= 2.0). Flaw model with saturation. 234
Figure 176 – Standard deviation of spacing as a function of the $\frac{E_f}{G_n}$ ratio for two different sets of minimum and maximum tensile strengths with the same max-to-min ratio (= 8.0). Flaw model with saturation. 235

Figure 177 – Standard deviation of spacing as a function of the $\frac{E_f}{G_n}$ ratio for two different sets of minimum and maximum tensile strengths with the same max-to-min ratio (= 20.0). Flaw model with saturation. 236
Figure 178 – Simulated joint spacing CDFs at different joint intensities for different choices of the minimum and maximum tensile strength values but with constant max-to-min ratio = 2.0. Flaw model with saturation is used. 237
Figure 179 – Effect of the ratio between the maximum and minimum tensile strength on the standard deviation of simulated joint spacing for different values of $\frac{E_f}{G_n}$ at a fixed joint intensity (~4.2 joints/m). Flaw model with saturation mechanism is used. Minimum tensile strength = 1.0 MPa. 238
Figure 180 – Effect of the ratio between the maximum and minimum tensile strength on the simulated joint spacing CDF. Flaw model with saturation mechanism is used. 239
Figure 181 – Joint spacing CDF for a maximum to minimum tensile strength ratio of 2.0 and the corresponding log-normal CDF. Flaw model with saturation is used..... 239
Figure 182 – Joint spacing CDF for a maximum to minimum tensile strength ratio of 8.0 and the corresponding log-normal CDF. Flaw model with saturation is used..... 240
Figure 183 – Joint spacing CDF for a maximum to minimum tensile strength ratio of 100.0 and the corresponding log-normal CDF. Flaw model with saturation is used. 240
Figure 184 – Effect of the standard deviation of tensile strength using the flaw model WITH the compressive stress saturation mechanism at joint intensity below saturation (~4.2 joints/m). Tensile strength is NORMALLY distributed. Mean tensile strength is 7.0 MPa. 241
Figure 185 – Variation of tensile strength along the jointing layer for the uncorrelated strength model. The tensile strength has a uniform probability distribution between 4.0 and 10.0 MPa. The strength is defined at 1000 points along the layer. 243
Figure 186 – Variation of tensile strength along the jointing layer for a correlated strength model. Parameter values: $\phi = 0.1$, $\sigma_\varepsilon = 0.05$ and $\mu_{\sigma_t} = 7.0$ MPa..... 244
Figure 187 – Variation of tensile strength along the jointing layer for a correlated strength model. Parameter values: $\phi = 0.1$, $\sigma_\varepsilon = 0.1$ and $\mu_{\sigma_t} = 7.0$ MPa..... 244
Figure 188 – Variation of tensile strength along the jointing layer for a correlated strength model. Parameter values: $\phi = 0.9$, $\sigma_\varepsilon = 0.05$ and $\mu_{\sigma_t} = 7.0$ MPa. 245
Figure 189 – Variation of tensile strength along the jointing layer for a correlated strength model. Parameter values: $\phi = 0.9$, $\sigma_\varepsilon = 0.1$ and $\mu_{\sigma_t} = 7.0$ MPa. 245
Figure 190 – Ratio between adjacent strength values for a minimum of 4.0 MPa and a maximum of 10.0 MPa using a uniform probability distribution of tensile strength in an uncorrelated strength model. 246
Figure 191 – Ratio between adjacent strength values for the correlated strength model with parameters $\phi = 0.1$, $\sigma_\varepsilon = 0.1$ and $\mu_{\sigma_t} = 7.0$ MPa..... 247
Figure 192 – Ratio between adjacent strength values for the correlated strength model with parameters $\phi = 0.9$, $\sigma_\varepsilon = 0.1$ and $\mu_{\sigma_t} = 7.0$ MPa. 247

Figure 193 – Ratio between adjacent strength values for the correlated strength model with parameters $\phi = 0.1$, $\sigma_\varepsilon = 0.01$ and $\mu_{\sigma_t} = 7.0$ MPa..... 248
Figure 194 – Ratio between adjacent strength values for the correlated strength model with parameters $\phi = 0.9$, $\sigma_\varepsilon = 0.01$ and $\mu_{\sigma_t} = 7.0$ MPa..... 248
Figure 195 – Variation of tensile strength along the jointing layer for two different mean strength values. For both cases, $\phi = 0.1$, and $\sigma_\varepsilon = 0.05$..... 249
Figure 196 – Effect of the correlation factor, ϕ, on the standard deviation of joint spacing for different $\frac{E_J}{G_n}$ values. The joint intensity is fixed (~4.2 /m), jointing layer thickness is 0.18 m, non-jointing layer thickness is 0.05 m, $\mu_s = 7.0$ MPa and $\sigma_\varepsilon = 0.1$..... 250
Figure 197 – Effect of the parameter σ_ε (shown as SD epsilon) on the standard deviation of spacing for different $\frac{E_J}{G_n}$ values. The joint intensity is fixed (~4.2 /m), jointing layer thickness is 0.18 m, non-jointing layer thickness is 0.05 m, $\mu_{\sigma_t} = 7.0$ MPa and $\phi = 0.5$..... 251
Figure 198 – Effect of the correlation factor on the resulting joint spacing CDF. The joint intensity is fixed (~4.2 /m), jointing layer thickness is 0.18 m, non-jointing layer thickness is 0.05 m, $\sigma_\varepsilon = 0.1$ and $\mu_{\sigma_t} = 7.0$ MPa..... 251
Figure 199 – Effect of the parameter σ_ε (noted as SD epsilon) on the resulting joint spacing CDF. The joint intensity is fixed (~4.2 /m), jointing layer thickness is 0.18 m, non-jointing layer thickness is 0.05 m, $\phi = 0.5$ and $\mu_{\sigma_t} = 7.0$ MPa..... 252
Figure 200 – Comparison between the simulated joint spacing CDF and those of known probability distribution forms at a joint intensity of ~0.125 joints/m. The parameter values are $\phi = 0.1$, $\mu_{\sigma_t} = 7.0$ MPa and $\sigma_\varepsilon = 0.1$..... 253
Figure 201 – Comparison between the simulated joint spacing CDF and those of known probability distribution forms at a joint intensity of ~2.5 joints/m. The parameter values are $\phi = 0.1$, $\mu_{\sigma_t} = 7.0$ MPa and $\sigma_\varepsilon = 0.1$..... 253
Figure 202 – Comparison between the simulated joint spacing CDF and those of known probability distribution forms at a joint intensity of ~8.3 joints/m. The parameter values are $\phi = 0.1$, $\mu_{\sigma_t} = 7.0$ MPa and $\sigma_\varepsilon = 0.1$..... 254
Figure 203 – Comparison between the simulated joint spacing CDF and those of known probability distribution forms at a joint intensity of ~0.125 joints/m. The parameter values are $\phi = 0.5$, $\mu_{\sigma_t} = 7.0$ MPa and $\sigma_\varepsilon = 0.1$..... 255
Figure 204 – Comparison between the simulated joint spacing CDF and those of known probability distribution forms at a joint intensity of ~2.5 joints/m. The parameter values are $\phi = 0.5$, $\mu_{\sigma_t} = 7.0$ MPa and $\sigma_\varepsilon = 0.1$..... 255
Figure 205 – Comparison between the simulated joint spacing CDF and those of known probability distribution forms at a joint intensity of ~8.3 joints/m. The parameter values are $\phi = 0.5$, $\mu_{\sigma_t} = 7.0$ MPa and $\sigma_\varepsilon = 0.1$..... 256

Figure 206 – Comparison between the simulated joint spacing CDF and those of known probability distribution forms at a joint intensity of ~0.125 joints/m. The parameter values are $\phi = 0.9$, $\mu_{\sigma_t} = 7.0$ MPa and $\sigma_\varepsilon = 0.1$ 257
Figure 207 – Comparison between the simulated joint spacing CDF and those of known probability distribution forms at a joint intensity of ~2.5 joints/m. The parameter values are $\phi = 0.9$, $\mu_{\sigma_t} = 7.0$ MPa and $\sigma_\varepsilon = 0.1$ 257
Figure 208 – Comparison between the simulated joint spacing CDF and those of known probability distribution forms at a joint intensity of ~8.3 joints/m. The parameter values are $\phi = 0.9$, $\mu_{\sigma_t} = 7.0$ MPa and $\sigma_\varepsilon = 0.1$ 258
Figure 209 – Comparison between the simulated joint spacing CDF and those of known probability distribution forms at a joint intensity of ~0.125 joints/m. The parameter values are $\phi = 0.9$, $\mu_{\sigma_t} = 7.0$ MPa and $\sigma_\varepsilon = 0.5$. 259
Figure 210 – Comparison between the simulated joint spacing CDF and those of known probability distribution forms at a joint intensity of ~2.5 joints/m. The parameter values are $\phi = 0.9$, $\mu_{\sigma_t} = 7.0$ MPa and $\sigma_\varepsilon = 0.5$. 259
Figure 211 – Comparison between the simulated joint spacing CDF and those of known probability distribution forms at a joint intensity of ~8.3 joints/m. The parameter values are $\phi = 0.9$, $\mu_{\sigma_t} = 7.0$ MPa and $\sigma_\varepsilon = 0.5$. 260
Figure 212 – Single joint and schematic of its stress reduction shadow. 261
Figure 213 – Two joints with overlapping stress-reduction shadows..... 261
Figure 214 – Illustration of the variation of normalized tensile stress along a jointed layer. The maximum tensile stress occurs within the longest segment. 263
Figure 215 – Illustration of the variation of normalized tensile stress along a jointed layer when saturation mechanism is included. The third segment from the left has a spacing below critical. 265
Figure 216 – Effect of the $\frac{E_f}{G_n}$ ratio on the saturation mean spacing in the rejection procedure with saturation mechanism. The non-jointing layer thickness is 0.04 m, ν_f is 0.25, and ν_n is 0.30. 268
Figure 217 – Effect of the $\frac{E_f}{G_n}$ ratio on the saturation standard deviation of spacing. Rejection procedure with saturation mechanism. The non-jointing layer thickness is 0.04 m, ν_f is 0.25, and ν_n is 0.30. 269
Figure 218 – Effect of the $\frac{E_f}{G_n}$ ratio on the ratio between the standard deviation and mean spacing at saturation (SSD/SMS). Rejection procedure with saturation mechanism. The non-jointing layer thickness is 0.04 m, ν_f is 0.25, and ν_n is 0.30. 270
Figure 219 – Effect of the non-jointing layer thickness (d) on the saturation mean spacing in the rejection procedure. $\frac{E_f}{G_n}$ is 4.0, ν_f is 0.25, and ν_n is 0.30. 271
Figure 220 – Effect of the non-jointing layer thickness (d) on the saturation standard deviation of spacing in the rejection procedure. $\frac{E_f}{G_n}$ is 4.0, ν_f is 0.25, and ν_n is 0.30 271

Figure 221 – Effect of the non-jointing layer thickness on the ratio between the standard deviation and mean spacing at saturation (SSD/SMS). Rejection procedure with saturation mechanism. The $\frac{E_f}{G_n}$ is 4.0, ν_f is 0.25, and ν_n is 0.30. 272
Figure 222 – Cumulative probability distribution comparison between a simulated joint pattern at low joint intensity (0.125 joints/m) and two known cumulative distribution forms (exponential and log-normal). Rejection procedure with saturation mechanism is used. 273
Figure 223 – Cumulative probability distribution comparison between a simulated joint pattern at medium-high joint intensity (2.5 joints/m) and two known cumulative distribution forms (exponential and log-normal). Rejection procedure with saturation mechanism is used. 274
Figure 224 – Cumulative probability distribution comparison between a simulated joint pattern at saturation (10 joints/m) and known cumulative distribution forms (log-normal and normal). Rejection procedure with saturation mechanism is used. 275
Figure 225 – Cumulative probability distribution comparison between a simulated joint pattern at low intensity (0.125 joints/m) and two known cumulative distribution forms (exponential and log-normal). Rejection procedure WITHOUT saturation mechanism is used. 276
Figure 226 – Cumulative probability distribution comparison between a simulated joint pattern at medium-high joint intensity (2.5 joints/m) and two known cumulative distribution forms (exponential and log-normal). Rejection procedure WITHOUT saturation mechanism is used. 277
Figure 227 – Cumulative probability distribution comparison between a simulated joint pattern at high intensity (10 joints/m) and known cumulative distribution forms (log-normal and normal). Rejection procedure WITHOUT saturation mechanism is used. 278
Figure 228 – Effect of the $\frac{E_f}{G_n}$ ratio on the standard deviation of spacing. All other parameters held constant and joint intensity is ~4.2 joints/m. 280
Figure 229 – Effect of $\frac{E_f}{G_n}$ ratio on the joint spacing CDF for the rejection procedure with saturation mechanism. All other parameters are fixed. Joint intensity is fixed at ~4.2 joints/m. 280
Figure 230 – Comparison between the joint CDF at $\frac{E_f}{G_n}$ = 2.0 in Figure 229 and the corresponding log-normal distribution obtained via maximum likelihood. 281
Figure 231 – Comparison between the joint CDF at $\frac{E_f}{G_n}$ = 6.0 in Figure 229 and the corresponding log-normal distribution obtained via maximum likelihood. 281
Figure 232 – Comparison between the joint CDF at $\frac{E_f}{G_n}$ = 10.0 in Figure 229 and the corresponding log-normal distribution obtained via maximum likelihood. 282
Figure 233 – Comparison between the joint CDF at $\frac{E_f}{G_n}$ = 40.0 in Figure 229 and the corresponding log-normal distribution obtained via maximum likelihood. 282
Figure 234 – Effect of the non-jointing layer thickness on the standard deviation of spacing. All other parameters held constant and joint intensity is ~4.2 joints/m. . 284

Figure 235 – Effect of the non-jointing layer thickness (d) on the joint spacing CDF for the rejection procedure with saturation mechanism. All other parameters fixed. Joint intensity is fixed at ~4.2 joints/m. 284
Figure 236 – Comparison between the joint CDF at $d = 0.02$ m in Figure 235 and the corresponding log-normal distribution obtained via maximum likelihood. 285
Figure 237 – Comparison between the joint CDF at $d = 0.04$ m in Figure 235 and the corresponding log-normal distribution obtained via maximum likelihood. 285
Figure 238 – Comparison between the joint CDF at $d = 0.18$ m in Figure 235 and the corresponding log-normal distribution obtained via maximum likelihood. 286
Figure 239 – Comparison between the joint CDF at $d = 0.20$ m in Figure 235 and the corresponding log-normal distribution obtained via maximum likelihood. 286
Figure 240 – Schematic of the two joint sets (~293° and ~345° or ~165°) superimposed. This figure is does not depict the actual abutting relationship between the two joint sets in layers where both are present. Sketched from information in Fig. 12 in Eyal et al. (2001). 292
Figure 241 – Schematic of the relationship among the maximum horizontal (compressive) stress direction, the maximum extensional strain direction and the ~293° joint set orientation. Sketched from information in Fig. 12 in Eyal et al. (2001). 293
Figure 242 – Jointing layer with an illustration of joint height vs. joint length. 294
Figure 243 – Schematic of the joint and faults zones as well as the four different sections along the 190-m long scanline laid on the limestone/dolostone jointing layer in Becker and Gross (1996). Horizontal axis is shown to scale, vertical axis is not. For fault zones, relative displacement is also shown (magnitudes of these displacements are not to scale). Sketched from Fig. 7 in Becker and Gross (1996) but without the vertical scale. 294
Figure 244 – Histogram of joint spacing data for the entire 190 m scanline (constructed from joint spacing data in Becker and Gross, 1996). Spacing is in cm. 296
Figure 245 – Joint spacing histogram for section I (constructed from joint spacing data in Becker and Gross, 1996). Spacing is in cm. 296
Figure 246 – Joint spacing histogram for section II (constructed from joint spacing data in Becker and Gross, 1996). Spacing is in cm. 297
Figure 247 – Joint spacing histogram for section III (constructed from joint spacing data in Becker and Gross, 1996). Spacing is in cm. 297
Figure 248 – Joint spacing histogram for section IV (constructed from joint spacing data in Becker and Gross, 1996). Spacing is in cm. 298
Figure 249 – Histogram of dynamic Young's Modulus (constructed from data in Saltzman, 2001). 300
Figure 250 – Histogram of tensile strength (constructed from data in Saltzman, 2001). 301
Figure 251 – Shape of the tensile stress distribution for small and large $\frac{E_f}{G_n}$ or d values. 303
Figure 252 – Standard deviation vs. $\frac{E_f}{G_n}$ ratio for section I (two tensile strength ranges). Actual standard deviation of joint spacing ~ 0.15 m. 307

Figure 253 – Comparison between actual and simulated joint spacing CDFs for section I using four different $\frac{E_f}{G_n}$ ratios for a minimum tensile strength of 4.0 MPa and a maximum of 10.0 MPa. 308
Figure 254 – Comparison between actual and simulated joint spacing CDFs for section I using four different $\frac{E_f}{G_n}$ ratios for a minimum tensile strength of 2.0 MPa and a maximum of 12.0 MPa. 308
Figure 255 – Comparison between actual and simulated joint spacing CDFs for section I using four different $\frac{E_f}{G_n}$ ratios for a minimum tensile strength << the maximum... 309
Figure 256 – Standard deviation vs. $\frac{E_f}{G_n}$ ratio for section II (two tensile strength ranges). Actual standard deviation of joint spacing ~ 0.08 m. 311
Figure 257 – Comparison between actual and simulated joint spacing CDFs for section II using four different $\frac{E_f}{G_n}$ ratios for a minimum tensile strength of 4.0 MPa and a maximum of 10.0 MPa. 311
Figure 258 – Comparison between actual and simulated joint spacing CDFs for section II using four different $\frac{E_f}{G_n}$ ratios for a minimum tensile strength of 2.0 MPa and a maximum of 12.0 MPa. 312
Figure 259 – Comparison between actual and simulated joint spacing CDFs for section II using four different $\frac{E_f}{G_n}$ ratios for a minimum tensile strength << the maximum... 312
Figure 260 – Standard deviation vs. $\frac{E_f}{G_n}$ ratio for section III (two tensile strength ranges). Actual standard deviation of joint spacing ~ 0.09 m. 313
Figure 261 – Comparison between actual and simulated joint spacing CDFs for section III using four different $\frac{E_f}{G_n}$ ratios for a minimum tensile strength of 4.0 MPa and a maximum of 10.0 MPa. 314
Figure 262 – Comparison between actual and simulated joint spacing CDFs for section III using four different $\frac{E_f}{G_n}$ ratios for a minimum tensile strength of 2.0 MPa and a maximum of 12.0 MPa. 314
Figure 263 – Comparison between actual and simulated joint spacing CDFs for section III using four different $\frac{E_f}{G_n}$ ratios for a minimum tensile strength << the maximum. 315
Figure 264 – Standard deviation vs. $\frac{E_f}{G_n}$ ratio for section IV (two tensile strength ranges). Actual standard deviation of joint spacing ~ 0.13 m. 316
Figure 265 – Comparison between actual and simulated joint spacing CDFs for section IV using four different $\frac{E_f}{G_n}$ ratios for a minimum tensile strength of 4.0 MPa and a maximum of 10.0 MPa. 317
Figure 266 – Comparison between actual and simulated joint spacing CDFs for section IV using four different $\frac{E_f}{G_n}$ ratios for a minimum tensile strength of 2.0 MPa and a maximum of 12.0 MPa. 317

Figure 267 – Comparison between actual and simulated joint spacing CDFs for section IV using four different $\frac{E_f}{G_n}$ ratios for a minimum tensile strength << the maximum. 318

Figure 268 – Standard deviation of joint spacing vs. $\frac{E_f}{G_n}$ for section I using different values of the correlation factor, ϕ. Other parameter values are $\mu_{\sigma_t} = 7.0$ and $\sigma_\varepsilon = 0.2$ 321

Figure 269 – Simulated joint spacing CDFs for different values of the correlation factor (≥ 0.7) together with the actual joint spacing CDF for section I. The simulation parameter values are: $\frac{E_f}{G_n} = 3.0$, $\sigma_\varepsilon = 0.2$ and $\mu_{\sigma_t} = 7.0$ 321

Figure 270 – Simulated joint spacing CDFs for different values of the correlation factor (≥ 0.7) together with the actual joint spacing CDF for section I. The simulation parameter values are: $\frac{E_f}{G_n} = 3.0$, $\sigma_\varepsilon = 0.5$ and $\mu_{\sigma_t} = 7.0$ 322

Figure 271 – Standard deviation of joint spacing vs. $\frac{E_f}{G_n}$ for section II using different values of the correlation factor, ϕ. Other parameter values are $\mu_{\sigma_t} = 7.0$ and $\sigma_\varepsilon = 0.2$ 323

Figure 272 – Simulated joint spacing CDFs for different values of the correlation factor (≥ 0.7) together with the actual joint spacing CDF for section II. The simulation parameter values are: $\frac{E_f}{G_n} = 3.0$, $\sigma_\varepsilon = 0.2$ and $\mu_{\sigma_t} = 7.0$ 324

Figure 273 – Simulated joint spacing CDFs for different values of the correlation factor (≥ 0.7) together with the actual joint spacing CDF for section II. The simulation parameter values are: $\frac{E_f}{G_n} = 3.0$, $\sigma_\varepsilon = 0.5$ and $\mu_{\sigma_t} = 7.0$ 324

Figure 274 – Standard deviation of joint spacing vs. $\frac{E_f}{G_n}$ for section III using different values of the correlation factor, ϕ. Other parameter values are $\mu_{\sigma_t} = 7.0$ and $\sigma_\varepsilon = 0.2$ 325

Figure 275 – Simulated joint spacing CDFs for different values of the correlation factor (≥ 0.7) together with the actual joint spacing CDF for section III. The simulation parameter values are: $\frac{E_f}{G_n} = 3.0$, $\sigma_\varepsilon = 0.2$ and $\mu_{\sigma_t} = 7.0$ 326

Figure 276 – Simulated joint spacing CDFs for different values of the correlation factor (≥ 0.7) together with the actual joint spacing CDF for section III. The simulation parameter values are: $\frac{E_f}{G_n} = 3.0$, $\sigma_\varepsilon = 0.5$ and $\mu_{\sigma_t} = 7.0$ 326

Figure 277 – Standard deviation of joint spacing vs. $\frac{E_f}{G_n}$ for section IV using different values of the correlation factor, ϕ. Other parameter values are $\mu_{\sigma_t} = 7.0$ and $\sigma_\varepsilon = 0.2$ 327

Figure 278 – Simulated joint spacing CDFs for different values of the correlation factor (≥ 0.7) together with the actual joint spacing CDF for section IV. The simulation parameter values are: $\frac{E_f}{G_n} = 3.0$, $\sigma_\varepsilon = 0.2$ and $\mu_{\sigma_t} = 7.0$ 328

Figure 279 – Simulated joint spacing CDFs for different values of the correlation factor (≥ 0.7) together with the actual joint spacing CDF for section IV. The simulation parameter values are: $\frac{E_f}{G_n} = 3.0$, $\sigma_\varepsilon = 0.5$ and $\mu_{\sigma_t} = 7.0$ 328
Figure 280 – Standard deviation vs. $\frac{E_f}{G_n}$ ratio for section I. Actual standard deviation of joint spacing ~ 0.15 m..... 330
Figure 281 – Comparison between actual and simulated joint spacing CDFs for section I using four different $\frac{E_f}{G_n}$ ratios..... 331
Figure 282 – Standard deviation vs. $\frac{E_f}{G_n}$ ratio for section II. Actual standard deviation of joint spacing ~ 0.08 m..... 332
Figure 283 – Comparison between actual and simulated joint spacing CDFs for section II using four different $\frac{E_f}{G_n}$ ratios..... 333
Figure 284 – Standard deviation vs. $\frac{E_f}{G_n}$ ratio for section III. Actual standard deviation of joint spacing ~ 0.09 m..... 334
Figure 285 – Comparison between actual and simulated joint spacing CDFs for section III using four different $\frac{E_f}{G_n}$ ratios..... 335
Figure 286 – Standard deviation vs. $\frac{E_f}{G_n}$ ratio for section IV. Actual standard deviation of joint spacing ~ 0.13 m..... 336
Figure 287 – Comparison between actual and simulated joint spacing CDFs for section IV using four different $\frac{E_f}{G_n}$ ratios..... 337
Figure 288 – Schematic of the limestone/dolostone layers studied by Saltzman (2001) (sketched from a photgraph in Saltzman, 2001). The layers are bounded by marlstone (represented by dark solid lines)..... 339
Figure 289 – Schematic of the relationship among the maximum horizontal stress, the maximum and minimum extensional strains and the ~165° joint set orientation. Sketched from information in Fig. 12 in Eyal et al. (2001)..... 339
Figure 290 – Spacing histogram for layer 1 (GN1). Constructed from data in Saltzman (2001)..... 341
Figure 291 – Spacing histogram for layer 2 (GN2). Constructed from data in Saltzman (2001)..... 341
Figure 292 - Spacing histogram for layer 3 (GN3). Constructed from data in Saltzman (2001)..... 342
Figure 293 - Spacing histogram for layer 4 (GN4). Constructed from data in Saltzman (2001)..... 342
Figure 294 – Joint spacing CDF for layer 1 and a log-normal distribution. Chi-squared goodness-of-fit accepted at the 0.05 and 0.01 levels..... 343
Figure 295 – Joint spacing CDF for layer 2 and a log-normal distribution. Chi-squared goodness-of-fit accepted at the 0.05 and 0.01 levels..... 343
Figure 296 – Joint spacing CDF for layer 3 and a log-normal distribution. Chi-squared goodness-of-fit accepted at the 0.05 and 0.01 levels..... 344

Figure 297 – Joint spacing CDF for layer 4 and a log-normal distribution. Chi-squared goodness-of-fit accepted at the 0.05 and 0.01 levels. 344
Figure 298 – Actual vs. simulated joint spacing CDFs using the flaw model with saturation for different values of $\frac{E_f}{G_n}$ for layer 1 (GN1). The minimum tensile strength is 4.0 MPa and the maximum 10.0 MPa. 347
Figure 299 – Actual vs. simulated joint spacing CDFs using the flaw model without saturation for different values of $\frac{E_f}{G_n}$ for layer 1 (GN1). The minimum tensile strength is 4.0 MPa and the maximum 10.0 MPa. 348
Figure 300 – Actual vs. simulated joint spacing CDFs using the flaw model without saturation for different values of $\frac{E_f}{G_n}$ for layer 1 (GN1). The minimum tensile strength is 2.0 MPa and the maximum 12.0 MPa. 348
Figure 301 – Actual vs. simulated joint spacing CDFs using the flaw model without saturation for different values of $\frac{E_f}{G_n}$ for layer 1 (GN1). The minimum tensile strength is 1.0 MPa and the maximum 1.0e7 MPa. 349
Figure 302 – Actual vs. simulated joint spacing CDFs using the flaw model with saturation for different values of $\frac{E_f}{G_n}$ for layer 2 (GN2). The minimum tensile strength is 4.0 MPa and the maximum 10.0 MPa. 350
Figure 303 – Actual vs. simulated joint spacing CDFs using the flaw model with saturation for different values of $\frac{E_f}{G_n}$ for layer 2 (GN2). The minimum tensile strength is 2.0 MPa and the maximum 12.0 MPa. 351
Figure 304 - Actual vs. simulated joint spacing CDFs using the flaw model with saturation for different values of $\frac{E_f}{G_n}$ for layer 2 (GN2). The minimum tensile strength is 1.0 MPa and the maximum 1.0e7 MPa. 351
Figure 305 – Actual vs. simulated joint spacing CDFs using the flaw model with saturation for different values of $\frac{E_f}{G_n}$ for layer 3 (GN3). The minimum tensile strength is 4.0 MPa and the maximum 10.0 MPa. 352
Figure 306 – Actual vs. simulated joint spacing CDFs using the flaw model without saturation for different values of $\frac{E_f}{G_n}$ for layer 3 (GN3). The minimum tensile strength is 4.0 MPa and the maximum 10.0 MPa. 353
Figure 307 – Actual vs. simulated joint spacing CDFs using the flaw model without saturation for different values of $\frac{E_f}{G_n}$ for layer 3 (GN3). The minimum tensile strength is 2.0 MPa and the maximum 12.0 MPa. 353
Figure 308 – Actual vs. simulated joint spacing CDFs using the flaw model without saturation for different values of $\frac{E_f}{G_n}$ for layer 3 (GN3). The minimum tensile strength is 1.0 MPa and the maximum 1.0e7 MPa. 354
Figure 309 – Actual vs. simulated joint spacing CDFs using the flaw model with saturation for different values of $\frac{E_f}{G_n}$ for layer 4 (GN4). The minimum tensile strength is 4.0 MPa and the maximum 10.0 MPa. 355

Figure 310 – Actual vs. simulated joint spacing CDFs using the flaw model without saturation for different values of $\frac{E_f}{G_n}$ for layer 4 (GN4). The minimum tensile strength is 4.0 MPa and the maximum 10.0 MPa. 355
Figure 311 - Actual vs. simulated joint spacing CDFs using the flaw model without saturation for different values of $\frac{E_f}{G_n}$ for layer 4 (GN4). The minimum tensile strength is 2.0 MPa and the maximum 12.0 MPa. 356
Figure 312 - Actual vs. simulated joint spacing CDFs using the flaw model without saturation for different values of $\frac{E_f}{G_n}$ for layer 4 (GN4). The minimum tensile strength is 1.0 MPa and the maximum 1.0e7 MPa. 356
Figure 313 - Variation of tensile strength along the jointing layer for the uncorrelated strength model. The tensile strength has a uniform probability distribution between 4.0 and 10.0 MPa. The strength is defined at 1000 points along the layer. 358
Figure 314 - Variation of tensile strength along the jointing layer for a correlated strength model. Parameter values: $\phi = 0.9$, $\sigma_\varepsilon = 0.05$ and $\mu_{\sigma_t} = 7.0$ MPa. The strength is defined at 1000 points along the layer. 359
Figure 315 – Actual vs. simulated joint spacing CDFs using the flaw model with correlation without saturation for different values of ϕ for layer 1 (GN1). The minimum tensile strength is 4.0 MPa and the maximum 10.0 MPa. The $\frac{E_f}{G_n}$ ratio is fixed at 3.0. 361
Figure 316 – Actual vs. simulated joint spacing CDFs using the flaw model with correlation without saturation for different values of ϕ for layer 1 (GN1). The minimum tensile strength is 2.0 MPa and the maximum 12.0 MPa. The $\frac{E_f}{G_n}$ ratio is fixed at 3.0. 361
Figure 317 – Actual vs. simulated joint spacing CDFs using the flaw model with correlation and saturation for different values of ϕ for layer 2 (GN2). The minimum tensile strength is 4.0 MPa and the maximum 10.0 MPa. The $\frac{E_f}{G_n}$ ratio is fixed at 3.0. 362
Figure 318 – Actual vs. simulated joint spacing CDFs using the flaw model with correlation and saturation for different values of ϕ for layer 2 (GN2). The minimum tensile strength is 2.0 MPa and the maximum 12.0 MPa. The $\frac{E_f}{G_n}$ ratio is fixed at 3.0. 363
Figure 319 - Actual vs. simulated joint spacing CDFs using the flaw model with correlation without saturation for different values of ϕ for layer 3 (GN3). The minimum tensile strength is 4.0 MPa and the maximum 10.0 MPa. The $\frac{E_f}{G_n}$ ratio is fixed at 3.0. 364
Figure 320 – Actual vs. simulated joint spacing CDFs using the flaw model with correlation without saturation for different values of ϕ for layer 3 (GN3). The minimum tensile strength is 2.0 MPa and the maximum 12.0 MPa. The $\frac{E_f}{G_n}$ ratio is fixed at 3.0. 365

Figure 321 – Actual vs. simulated joint spacing CDFs using the flaw model with correlation without saturation for different values of ϕ for layer 4 (GN4). The minimum tensile strength is 4.0 MPa and the maximum 10.0 MPa. The $\frac{E_f}{G_n}$ ratio is fixed at 3.0. 366
Figure 322 – Actual vs. simulated joint spacing CDFs using the flaw model with correlation without saturation for different values of ϕ for layer 4 (GN4). The minimum tensile strength is 2.0 MPa and the maximum 12.0 MPa. The $\frac{E_f}{G_n}$ ratio is fixed at 3.0. 367
Figure 323 – Actual vs. simulated joint spacing CDFs using the rejection procedure with saturation for different values of $\frac{E_f}{G_n}$ for layer 1 (GN1)..... 368
Figure 324 – Actual vs. simulated joint spacing CDFs using the rejection procedure without saturation for different values of $\frac{E_f}{G_n}$ for layer 1 (GN1). 369
Figure 325 – Actual vs. simulated joint spacing CDFs using the rejection procedure with saturation for different values of $\frac{E_f}{G_n}$ for layer 2 (GN2)..... 370
Figure 326 – Actual vs. simulated joint spacing CDFs using the rejection procedure without saturation for different values of $\frac{E_f}{G_n}$ for layer 3 (GN3). 371
Figure 327 – Actual vs. simulated joint spacing CDFs using the rejection procedure without saturation for different values of $\frac{E_f}{G_n}$ for layer 4 (GN4). 372
Figure 328 – Schematic of the outcrop from Gross et al. (1997). Chert layers are represented as thick solid lines. The normal fault is made up of three segments (F1, F2, and F3). The strike of the outcrop face is approximately 350°. Sketched from Fig. 2 in Gross et al. (1997). 375
Figure 329 – Schematic of the orientations of the fault, outcrop and the 055° set. Sketched from descriptions in Gross et al. (1997). 376
Figure 330 – Normalized spacing histogram for set A. 378
Figure 331 – Normalized spacing histogram for set B. 379
Figure 332 – Comparison between dataset A and a log-normal probability distribution. Mean normalized spacing is 1.12..... 379
Figure 333 – Comparison between dataset A and a normal probability distribution. Mean normalized spacing is 1.12..... 380
Figure 334 – Comparison between dataset B and a log-normal probability distribution. Mean normalized spacing is 0.74..... 380
Figure 335 – Comparison between dataset B and a normal probability distribution. Mean normalized spacing is 0.74..... 381
Figure 336 – Joint spacing CDF comparison for layer 2. Mean spacing-to-thickness ratio is 0.76. Chert layer thickness is 0.05 m. Spacings are not normalized..... 385
Figure 337 – Joint spacing CDF comparison for layer 2. Mean spacing-to-thickness ratio is 0.76. Chert layer thickness is 0.1 m. Spacings are not normalized..... 385
Figure 338 – Joint spacing CDF comparison for layer 5. Mean spacing-to-thickness ratio is 1.13. Chert layer thickness is 0.05 m. Spacings are not normalized..... 386

Figure 339 – Joint spacing CDF comparison for layer 5. Mean spacing-to-thickness ratio is 1.13. Chert layer thickness is 0.1 m. Spacings are not normalized. 386
Figure 340 – Joint spacing CDF comparison for layer 2. Mean spacing-to-thickness ratio is 0.76. Chert layer thickness is 0.05 m. The $\frac{E_f}{G_n}$ values are allowed to exceed unity. Spacings are not normalized. 387
Figure 341 – Joint spacing CDF comparison for layer 2. Mean spacing-to-thickness ratio is 0.76. Chert layer thickness is 0.1 m. The $\frac{E_f}{G_n}$ values are allowed to exceed unity. Spacings are not normalized. 388
Figure 342 – Joint spacing CDF comparison for layer 5. Mean spacing-to-thickness ratio is 1.13. Chert layer thickness is 0.05 m. The $\frac{E_f}{G_n}$ values are allowed to exceed unity. Spacings are not normalized. 388
Figure 343 – Joint spacing CDF comparison for layer 5. Mean spacing-to-thickness ratio is 1.13. Chert layer thickness is 0.1 m. The $\frac{E_f}{G_n}$ values are allowed to exceed unity. Spacings are not normalized. 389
Figure 344 – Comparison between simulated and actual joint spacing CDFs for dataset A using various chert layer thickness values. The $\frac{E_f}{G_n}$ ratio is 0.05. H_0 is rejected for all values of d. 390
Figure 345 – Comparison between simulated and actual joint spacing CDFs for dataset A using various chert layer thickness values. The $\frac{E_f}{G_n}$ ratio is 0.5. H_0 is accepted only for d = 0.8 and 1.0 m. 391
Figure 346 – Comparison between simulated and actual joint spacing CDFs for dataset A using various chert layer thickness values. The $\frac{E_f}{G_n}$ ratio is 0.75. H_0 is rejected only for d = 0.2 m. 391
Figure 347 – Detail of d = 1.0 from Figure 346. 392
Figure 348 – Comparison between simulated and actual joint spacing CDFs for dataset A using various chert layer thickness values. The $\frac{E_f}{G_n}$ ratio is 1.0. H_0 is rejected only for d = 0.2 m. 392
Figure 349 – Detail of d = 1.0 from Figure 348. 393
Figure 350 – Comparison between simulated and actual joint spacing CDFs for dataset B using various chert layer thickness values. The $\frac{E_f}{G_n}$ ratio is 0.05. H_0 is rejected for all values of d. 393
Figure 351 – Comparison between simulated and actual joint spacing CDFs for dataset B using various chert layer thickness values. The $\frac{E_f}{G_n}$ ratio is 0.5. H_0 is accepted only for d = 1.0 m. 394
Figure 352 – Comparison between simulated and actual joint spacing CDFs for dataset B using various chert layer thickness values. The $\frac{E_f}{G_n}$ ratio is 0.75. H_0 is rejected only for d = 0.2 m. 394
Figure 353 – Detail of d = 1.0 from Figure 352. 395

Figure 354 – Comparison between simulated and actual joint spacing CDFs for dataset B using various chert layer thickness values. The $\frac{E_f}{G_n}$ ratio is 1.0. H_0 is rejected only for d = 0.2 m. 395
Figure 355 – Detail of d = 1.0 from Figure 354. 396
Figure 356 – Comparison between simulated and actual joint spacing CDFs for layer 5. Joint spacing is not normalized A thick chert layer is used here (d=1.0 m) . Compare this comparison with Figure 338 and Figure 339. H_0 is accepted for all values of $\frac{E_f}{G_n}$. Note the change in vertical scale as the value of cumulative probability increases: near the tail differences in cumulative probability are less than 0.01 (or 1 percentage point). 396
Figure 357 – Comparison of joint spacing CDFs for dataset A for a chert layer thickness of 0.05 m and $\frac{E_f}{G_n}$ values exceeding unity. 397
Figure 358 – Comparison of joint spacing CDFs for dataset A for a chert layer thickness of 0.1 m and $\frac{E_f}{G_n}$ values exceeding unity. 398
Figure 359 - Comparison of joint spacing CDFs for dataset B for a chert layer thickness of 0.05 m and $\frac{E_f}{G_n}$ values exceeding unity. 398
Figure 360 – Comparison of joint spacing CDFs for dataset B for a chert layer thickness of 0.1 m and $\frac{E_f}{G_n}$ values exceeding unity. 399
Figure 361 – Comparison between simulated and actual joint spacing CDFs using the flaw model with correlated strength model for dataset A. The chert layer thickness is d = 0 .1 and $\frac{E_f}{G_n}$ is 0.05. H_0 is rejected for all values of ϕ. 400
Figure 362 - Comparison between simulated and actual joint spacing CDFs using the flaw model with correlated strength model for dataset A. The chert layer thickness is d = 0 .1 and $\frac{E_f}{G_n}$ is 0.75. H_0 is rejected for all values of ϕ. 401
Figure 363 – Comparison between simulated and actual joint spacing CDFs using the flaw model with correlated strength model for dataset A. The chert layer thickness is d = 0 .1 and $\frac{E_f}{G_n}$ is 2.0. H_0 is rejected for all values of ϕ. 401
Figure 364 – Comparison between simulated and actual joint spacing CDFs using the flaw model with correlated strength model for dataset A. The chert layer thickness is d = 0 .1 and $\frac{E_f}{G_n}$ is 6.0. H_0 is rejected for ϕ=0.6 – 0.9. 402
Figure 365 - Comparison between simulated and actual joint spacing CDFs using the flaw model with correlated strength model for dataset A. The chert layer thickness is d = 0 .1 and $\frac{E_f}{G_n}$ is 10.0. H_0 is rejected for ϕ=0.8 – 0.9. 402
Figure 366 - Comparison between simulated and actual joint spacing CDFs using the flaw model with correlated strength model for dataset B. The chert layer thickness is d = 0 .1 and $\frac{E_f}{G_n}$ is 0.05. H_0 is rejected for all values of ϕ. 403

Figure 367 - Comparison between simulated and actual joint spacing CDFs using the flaw model with correlated strength model for dataset B. The chert layer thickness is d = 0 .1 and $\frac{E_f}{G_n}$ is 0.75. H_0 is rejected for all values of ϕ. 403
Figure 368 – Comparison between simulated and actual joint spacing CDFs using the flaw model with correlated strength model for dataset B. The chert layer thickness is d = 0 .1 and $\frac{E_f}{G_n}$ is 2.0. H_0 is rejected for ϕ=0.4 – 0.9..... 404
Figure 369 – Comparison between simulated and actual joint spacing CDFs using the flaw model with correlated strength model for dataset B. The chert layer thickness is d = 0 .1 and $\frac{E_f}{G_n}$ is 6.0. H_0 is accepted for all values of ϕ..... 404
Figure 370 - Comparison between simulated and actual joint spacing CDFs using the flaw model with correlated strength model for dataset B. The chert layer thickness is d = 0 .1 and $\frac{E_f}{G_n}$ is 10.0. H_0 is accepted for all values of ϕ..... 405
Figure 371 – Comparison between simulated and actual joint spacing CDFs for dataset A using the rejection procedure. The $\frac{E_f}{G_n}$ ratio is 0.05..... 406
Figure 372 - Comparison between simulated and actual joint spacing CDFs for dataset A using the rejection procedure. The $\frac{E_f}{G_n}$ ratio is 1.0..... 406
Figure 373 - Comparison between simulated and actual joint spacing CDFs for dataset B using the rejection procedure. The $\frac{E_f}{G_n}$ ratio is 0.05..... 407
Figure 374 - Comparison between simulated and actual joint spacing CDFs for dataset B using the rejection procedure. The $\frac{E_f}{G_n}$ ratio is 1.0..... 407
Figure 375 – Comparison between simulated and actual joint spacing CDFs for dataset A using the rejection procedure for a chert layer thickness of 0.05 m. The $\frac{E_f}{G_n}$ is allowed to exceed unity. 408
Figure 376 – Comparison between simulated and actual joint spacing CDFs for dataset A using the rejection procedure for a chert layer thickness of 0.1 m. The $\frac{E_f}{G_n}$ is allowed to exceed unity. 408
Figure 377 - Comparison between simulated and actual joint spacing CDFs for dataset B using the rejection procedure for a chert layer thickness of 0.05 m. The $\frac{E_f}{G_n}$ is allowed to exceed unity. 409
Figure 378 – Comparison between simulated and actual joint spacing CDFs for dataset B using the rejection procedure for a chert layer thickness of 0.1 m. The $\frac{E_f}{G_n}$ is allowed to exceed unity. 409
Figure 379 – The 4-km-long scanline tracing the path of the Cattaraugus Creek (from Baudo, 2001)..... 412
Figure 380 – Spacing histogram form layer 1. Constructed from data in Baudo (2001). 415
Figure 381 – Spacing histogram form layer 2. Constructed from data in Baudo (2001). 416

Figure 382 – Spacing histogram form layer 2. Constructed from data in Baudo (2001). 416
Figure 383 – Comparison of layer 1 joint spacing (set II, northeast-striking) CDF with exponential and log-normal CDFs. Chi-square accepted at 0.05 level for log-normal probability distribution..... 417
Figure 384 – Comparison of layer 2 joint spacing (set II, northeast-striking) CDF with exponential and log-normal CDFs. Chi-square rejected at 0.05 level for log-normal probability distribution..... 418
Figure 385 – Comparison of layer 3 joint spacing (set II, northeast-striking) CDF with exponential and log-normal CDFs. Chi-square accepted at 0.05 level for log-normal probability distribution..... 418
Figure 386 – Demonstration of the effect of the tensile strength ratio. Tensile strength ratio is the maximum tensile strength divided by the minimum tensile strength. .. 420
Figure 387 – Effect of the jointing layer Poisson's ratio (ν_f) on the simulated joint spacing CDF for layer 1. Note that D is a function of ν_f and ν_n (the bounding layer Poisson's ratio)..... 421
Figure 388 – Effect of the bounding layer Poisson's ratio (ν_n) on the simulated joint spacing CDF for layer 1. Note that D is a function of ν_f (the jointing layer Poisson's ratio) and ν_n. 421
Figure 389 – Demonstration of the effect of the bounding layer thickness on the joint spacing CDF for layer 1..... 422
Figure 390 – Comparison between actual and simulated joint spacing CDFs for layer 1. The bounding layer thickness is 0.03 m..... 423
Figure 391 – Comparison between actual and simulated joint spacing CDFs for layer 1. The bounding layer thickness is 0.10 m..... 424
Figure 392 - Comparison between actual and simulated joint spacing CDFs for layer 2. The bounding layer thickness is 0.03 m..... 425
Figure 393 - Comparison between actual and simulated joint spacing CDFs for layer 2. The bounding layer thickness is 0.10 m..... 425
Figure 394 - Comparison between actual and simulated joint spacing CDFs for layer 3. The bounding layer thickness is 0.03 m..... 426
Figure 395 - Comparison between actual and simulated joint spacing CDFs for layer 3. The bounding layer thickness is 0.05 m..... 426
Figure 396 – Effect of the tensile strength ratio on the simulated joint spacing CDF.... 428
Figure 397 – Effect of σ_ε (SDe in figure) on the joint spacing CDF for $\phi = 0.1$. 428
Figure 398 – Effect of σ_ε (SDe in figure) on the joint spacing CDF for $\phi = 0.8$. 429
Figure 399 – Comparison between actual and simulated joint spacing CDFs for layer 1 using $\sigma_\varepsilon = 0.1$. 430
Figure 400 – Comparison between actual and simulated joint spacing CDFs for layer 1 using $\sigma_\varepsilon = 0.8$ 430
Figure 401 – Comparison between actual and simulated joint spacing CDFs for layer 2 using $\sigma_\varepsilon = 0.1$. 431

Figure 402 – Comparison between actual and simulated joint spacing CDFs for layer 2 using $\sigma_\varepsilon = 0.8$ 431
Figure 403 – Comparison between actual and simulated joint spacing CDFs for layer 3 using $\sigma_\varepsilon = 0.1$. 432
Figure 404 – Comparison between actual and simulated joint spacing CDFs for layer 3 using $\sigma_\varepsilon = 0.8$ 433
Figure 405 – Effect of the bounding layer thickness on the simulated joint spacing CDF for layer 1. 434
Figure 406 - Effect of the jointing layer Poisson's ratio on the simulated joint spacing CDF for layer 1. 434
Figure 407 - Effect of the bounding layer Poisson's ratio on the simulated joint spacing CDF for layer 1. 435
Figure 408 – Comparison between the actual and simulated joint spacing CDFs for layer 1 using the rejection procedure. 436
Figure 409 - Comparison between the actual and simulated joint spacing CDFs for layer 2 using the rejection procedure. 436
Figure 410 - Comparison between the actual and simulated joint spacing CDFs for layer 3 using the rejection procedure. 437
Figure 411 – Effect of $\frac{E_f}{G_n}$ ratio and bounding layer thickness, d, on the length of segment exposed to maximum tensile stress. 439
Figure 412 – Strike histogram for set II joints in layer 1 441
Figure 413 – Strike histogram for set II joints in layer 2 442
Figure 414 – Strike histogram for set II joints in layer 3 442
Figure 415 – Tensile stress vs. tensile strength for the interface slippage saturation mechanism for the case with and without flaws. New joint formation is only possible with the existence of flaws because there is a limit to the tensile stress that can be achieved. 448
Figure 416 – Tensile stress vs. tensile strength for the compressive stress saturation mechanism for the case with and without flaws. The existing joints are spaced above the critical spacing. A new joint can form with or without the flaws (the two dropdown lines) because there is no limit to the tensile stress as long as the spacing is above critical. 448
Figure 417 – Shape of the tensile stress distribution for different values of $\frac{E_f}{G_n}$ or d values. 450
Figure 418 – Illustration of the (insignificant) effect of the tensile strength ratio in the flaw model with uncorrelated strength on the joint spacing CDF. Tensile strength ratio is the maximum tensile strength divided by the minimum tensile strength. .. 467

List of Tables

Table 1 – Summary of field-observed layer thickness-to-spacing ratios. ♦ - Non-linear relationship observed between layer thickness and spacing. 53

Table 2 – Summary of data statistics for each section in Becker and Gross (1996). Entries are from Table 2 in Becker and Gross (1996). Spacings are in cm. 56

Table 3 – Summary of stress distribution and spacing for both the Hobbs (1967) and Ji and Saruwatari (1998) models. 100

Table 4 – The normalized distance from a joint to specific percentages of the remote stress as a function of the E_f/G_n ratio. 135

Table 5 – Known probability distribution forms, their parameters and the corresponding maximum likelihood (ML) parameter estimates. Note: n is the number of joint spacing data. 213

Table 6 – Summary of the effect of the $\frac{E_f}{G_n}$ on the variance of spacing. 222

Table 7 – Summary of the effect of the non-jointing layer thicknes, d, on the variance of spacing. 228

Table 8 – Summary of the effect of $\frac{E_f}{G_n}$ on the resulting joint spacing. 279

Table 9 – Summary of the effect of the non-jointing layer thickness on the resulting joint spacing. 283

Table 10 – Summary of joint spacing data and statistics for each section (Becker and Gross, 1996). Measurements are in m. 295

Table 11 – Field observations by Becker and Gross (1996) and their corresponding implications in the model. 299

Table 12 – Actual mean spacing values from Becker and Gross (1996) data. Measurements are in m. 305

Table 13 – Summary of joint spacing statistics for each layer. Measurements are in cm. 340

Table 14 – Field observations with their corresponding model implications for the spacing data from Saltzman (2001). 345

Table 15 – Summary of simulation parameters for the case of Saltzman (2001). 346

Table 16 – Mean and median normalized spacing for each of the six chalk layers. Layer 4 is divided into North and South parts due to large difference in joint intensity. Note that joints in layer 6 were not included in the dataset. 377

Table 17 – Statistics of normalized spacing for the combined datasets. 377

Table 18 – Summary of possible probability distribution functions for spacing datasets A and B based on a visual comparison with known probability distributions. 381

Table 19 – Summary of possible probability distribution functions for spacing data from each layer based on a visual comparison with known probability distributions. 382

Table 20 – Summary of field observations and their corresponding model implications. 383

Table 21 – Summary of lithologies of the layers intersected by the three scanlines considered (from data by Baudo, 2001). 414

Table 22 – Spacing statistics for case 4. Calculated from data in Baudo (2001). 415

Table 23 – Field observations and their corresponding model implications for case 4. 419

Table 24 – Results of visual and statistical comparisons for joint spacing data from the three layers using the flaw model with uncorrelated strength. 438
Table 25 – Results of visual and statistical comparisons for joint spacing data from the three layers using the flaw model with correlated strength. 438
Table 26 – Results of visual and statistical comparisons for joint spacing data from the three layers using the rejection procedure 438
Table 27 – Effects of parameters that limit tensile stress on the mean joint spacing-layer thickness relationship. 449
Table 28 – Effect of $\frac{E_f}{G_n}$ and d on the mean joint spacing when using the compressive stress saturation mechanism in both the flaw model and rejection procedure. f – flaw model. r – rejection procedure. 451
Table 29 – Effect of $\frac{E_f}{G_n}$ and d on joint spacing distribution in the flaw model and rejection procedure. f – flaw model. r – rejection procedure. 451
Table 30 – Effect of ratio of maximum to minimum tensile strength on joint spacing distribution in the flaw model with uncorrelated strength. 452
Table 31 – Effects of correlated strength parameters♣ on joint spacing distribution in the flaw model. ♣ - varying one, keeping others constant 453
Table 32 – Summary of joint spacing statistics from data by Becker and Gross (1996) 454
Table 33 – Parameter values for uncorrelated strength submodel in flaw model. The same values are used in the rejection procedure except for the tensile strength ranges. 454
Table 34 – Parameter values for correlated strength submodel. 455
Table 35 – Summary of results for the case of Becker and Gross, 1996. 455
Table 36 – Summary of spacing statistics from data by Saltzman (2001) 457
Table 37 - Parameter values for uncorrelated strength submodel in flaw model. The same values are used in the rejection procedure except for the tensile strength ranges. . 457
Table 38 - Parameter values for correlated strength submodel 458
Table 39 – Summary of comparison results for the joint spacing data in Saltzman (2001). ♠ - without saturation mechanism. * - with saturation mechanism. 459
Table 40 – Summary of spacing statistics for the data by Gross et al. (1997) 461
Table 41 – Summary of spacing statistics for datasets A and B. 461
Table 42 - Parameter values for uncorrelated strength submodel in flaw model. The same values are used in the rejection procedure except for the tensile strength range. Note that $\frac{E_f}{G_n}$>1.0 (i.e., chert is brecciated) 462
Table 43 - Parameter values for correlated strength submodel 462
Table 44 - Summary of comparison results for the data by Gross et al. (1997). 463
Table 45 – Summary of layer lithologies and thicknesses for the data by Baudo (2001). 465
Table 46 – Important field observations and corresponding assumptions for the case of Baudo (2001). 466
Table 47 - Parameter values for uncorrelated strength submodel in flaw model. The same values are used in the rejection procedure. 467
Table 48 - Parameter values for correlated strength submodel 468
Table 49 – Summary of comparison results for the data by Baudo (2001). 468

1 Introduction

Rock fracture pattern description is important in civil engineering, engineering geology, and petroleum engineering. Fracture patterns influence the deformability, strength, and stability of a rock mass as well as the fluid flow through it. In petroleum engineering, access to hydrocarbon deposits in rock is generally through fractures. In rock slopes and tunnels in rock, fractures can form blocks that may slide or fall, posing serious danger and thus requiring artificial support. Furthermore, the existence of fractures often leads to a more deformable and weaker rock mass as fractures are usually planes of weakness.

Several approaches have been used to model or describe rock fracture patterns. Geometric-deterministic models, for example, simply describe the geometry of the fracture pattern based on the actual measurements and observations at a particular site. Geometric-statistical models describe fracture patterns in terms of the best-fitting probability distributions of the measured fracture characteristics (e.g., orientation, size, and spacing). Such models are often simplified in that the fracture characteristics are not associated with specific locations. This problem is remedied in geometric-stochastic models. The statistical models and particularly the stochastic models are often used in an iterative process (**Figure 1**). An initial pattern is created and the statistics of the initial fracture pattern are compared to those of the actual pattern. Based on this comparison, a new pattern is generated (**Figure 1**). The process is repeated until the statistics of the generated fracture pattern match those of the actual fracture pattern.

Although the existing models may adequately describe fracture patterns in rock, they rely mainly on the geometry of the observed fracture pattern, not on the mechanisms behind them. The probabilistic concepts used to generate fracture patterns in geometric-stochastic models, for example, are not or are only indirectly linked to mechanical reasoning. A full mechanical model, on the other hand, appears impractical at this stage because the information required to mechanically model fracture patterns is difficult to obtain. Hence, a fracture pattern modeling approach that uses a combination of probabilistic and mechanical concepts should be explored.

Using such an approach, it is unreasonable to expect that a single model applicable to all possible fracture patterns can be formulated. For this reason, a specific type of fracture pattern must be considered. Layer-perpendicular joints are considered here because they often occur in sedimentary rocks, which predominate near the Earth's surface, but also occur in other types of rock. The study of jointing in sedimentary rock has also been partly motivated by potential economic gains in the petroleum industry. Sedimentary rocks are often found in alternating competent and incompetent layers with the former usually jointed and the latter remaining largely intact (**Figure 2**). As a result, the joints are limited in height to the thickness of the competent layer. The formation of these layer-confined, layer-perpendicular joints in sedimentary rock is often attributed to a net extension of the layer in the direction perpendicular to the joints (**Figure 2**).

Given the importance of rock joint patterns, numerous approaches to represent or predict their geometry exist. For layer-perpendicular joints in sedimentary rock, in particular,

approaches range from statistical or empirical relations based on field observations to laboratory experiments to theoretical models. Discussing and evaluating these approaches will be a major part of this report. A brief introductory review will be given now:

Field observations in the literature indicate that the spacing of layer-perpendicular joints in sedimentary rock is often linearly-related to layer thickness. Thicker layers often contain more widely-spaced joints than do thinner layers. Ladeira and Price (1981) find evidence that non-jointing layer thickness also affects joint spacing. Specifically, thinner non-jointing layers lead to smaller joint spacing and vice-versa. Joint spacing is also observed to follow some probability distribution (e.g., Rives et al., 1992; Becker and Gross, 1996; Huang and Angelier, 1989). In the literature, various probability distribution forms have been used to describe joint spacing. The probability distributions that best describe joint spacing are usually unimodal and skewed towards smaller spacing.

Laboratory experiments in the literature indicate a similar relationship between joint spacing and layer thickness (e.g., Wu and Pollard, 1995). Additionally, laboratory experiments by some researchers suggest that the form of joint spacing probability distribution changes with increasing joint intensity (e.g., Rives et al., 1992). Specifically, joint spacing follows a shifted-exponential probability distribution at low joint intensity, a log-normal probability distribution at intermediate joint intensity, and a quasi-normal probability distribution at high joint intensity (Rives et al., 1992). However, in field data, a quasi-normal probability distribution of joint spacing is never observed. The phenomenon of joint saturation is also observed in the laboratory experiments (Rives et al., 1992; Wu and Pollard, 1995). Joint saturation is the state at which the joint spacing no longer changes with increasing applied strain.

Theoretical models are mainly used to describe the stresses in the rock when joints are present. A joint perturbs the stresses around it because it is composed of two stress-free surfaces. In jointed layered sedimentary rock, even though tensile stresses cannot be transmitted across the joints they can still develop in the area between two joints through shear forces at the interface with the bounding non-jointing layers. Stresses in layered sedimentary rock with existing joints can be described using finite-element methods (e.g., FRANC2D by Wawrzynek and Ingraffea, 1991). Simplified methods have also been used for the same purpose (e.g., Hobbs, 1967; Ji and Saruwatari, 1998; Ji et al., 1998). Also, these simplified methods rely mainly on the shear-lag method (Cox, 1952) and are usually one-dimensional models of stress. They show that the tensile stress distribution is influenced mainly by the elastic contrast between the jointing and non-jointing layers denoted by $\frac{E_f}{G_n}$, where E_f and G_n are the Young's modulus and shear modulus of the jointing and non-jointing layers, respectively. From the simplified tensile stress distributions, joint spacing-layer thickness relationships have been derived. Hobbs' (1967) model for the tensile stress distribution suggests a linear spacing-thickness relationship while Ji and Saruwatari's (1998)

model suggests a non-linear relationship. These simplified tensile stress distribution models (Hobbs, 1967; Ji and Saruwatari, 1998) generally suggest a bimodal joint spacing probability distribution, a shape that differs from those in field and laboratory observations for layer-perpendicular joint spacing. To address this issue, Narr and Suppe (1991) combined the Hobbs (1967) tensile stress distribution model with an assumed tensile strength distribution of the rock layer to simulate layer-perpendicular joint patterns. This resulted in positively-skewed joint spacing probability distributions. Rabinovitch and Bahat (1999) used a different approach that relies more on probability than Narr and Suppe's (1991) model. Their model uses a hazard function that defines the "jointing hazard" with increasing distance from a single existing joint. The jointing hazard increases to a maximum value with distance from the joint. From this hazard function, the probability distribution of spacing between a single existing joint and one new joint is derived.

Based on the information found in the literature, one can conclude that the following factors affect the probability distribution of layer-perpendicular joint spacing in sedimentary rock: jointing layer thickness, non-jointing layer thickness, applied strain, joint intensity, material properties of the layers, joint saturation effects, and tensile strength of the jointing layer. However, none of the field or laboratory observations and none of the models consider all these factors.

In order to improve modeling capabilities, the deficiencies of previous models need to be addressed in the new proposed models. A diagram describing the proposed models is shown in **Figure 3**. The proposed models need to have the following capabilities in addition to those already implemented in the early models:

1. Include saturation effects: compressive stress development and interface slippage.

2. Include the effect of non-jointing layer thickness.

3. Include the effect of a correlated strength model for the jointing layer.

Using the proposed models, one will be able to study the possible effects of material properties, layer geometries, joint intensity, and saturation mechanisms on the joint spacing probability distribution and also on the relationship between joint spacing and layer thickness. Comparing the results from the proposed models to actual data will help determine their effectiveness and at the same time, establish their limitations. This exercise will also help gain insight on how an approach using a combination of probabilistic and mechanical concepts could be used for other more complex fracture patterns.

The outline of the report is as follows: First, information on field and laboratory observations regarding layer-perpendicular joint spacing in sedimentary rock from the literature is presented in **Chapter 2**. This is followed by a presentation of the stress distribution models in the literature that have been used to describe the stresses in the

jointed layer (**Chapter 3**). Two possible joint saturation mechanisms are then discussed in **Chapter 4**. These are the compressive stress development and interface slippage saturation mechanisms. **Chapter 5** outlines some joint spacing distribution models in the literature that have been used to describe layer-perpendicular joints in sedimentary rock and discusses their limitations. **Chapter 6** presents the two proposed models for joint spacing. The first model depends on a stress distribution model and a tensile strength model to simulate the jointing process. The second model relies on a stress distribution model and a probabilistic process. In **Chapter 7**, the proposed jointing models are evaluated comparing the joint spacing probability distributions observed in the field to simulated joint spacing data. **Chapter 8** contains conclusions of the study as well as some recommendations for future work.

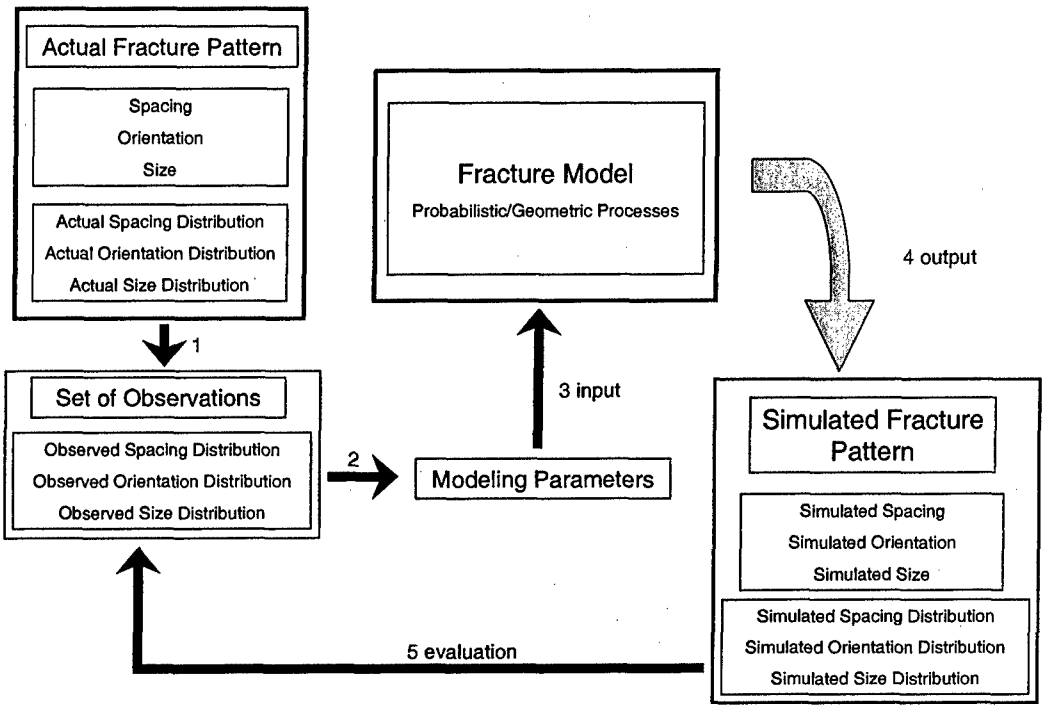


Figure 1 – Diagram of a typical fracture modeling process using probabilistic and geometric approaches.

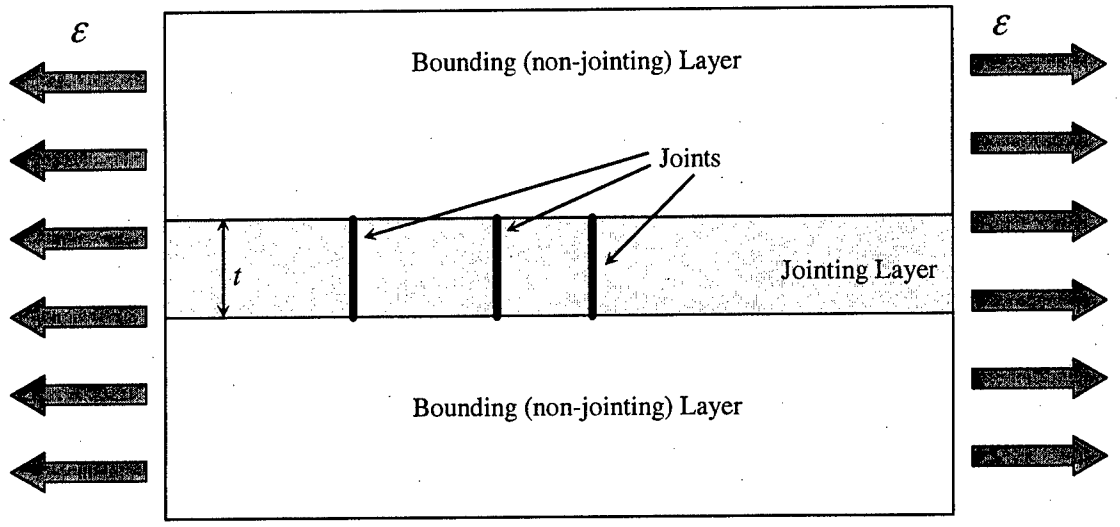


Figure 2 – Competent jointing layer bounded at the top and bottom by incompetent non-jointing layers. Layers are subjected to a far-field extensional strain (ε).

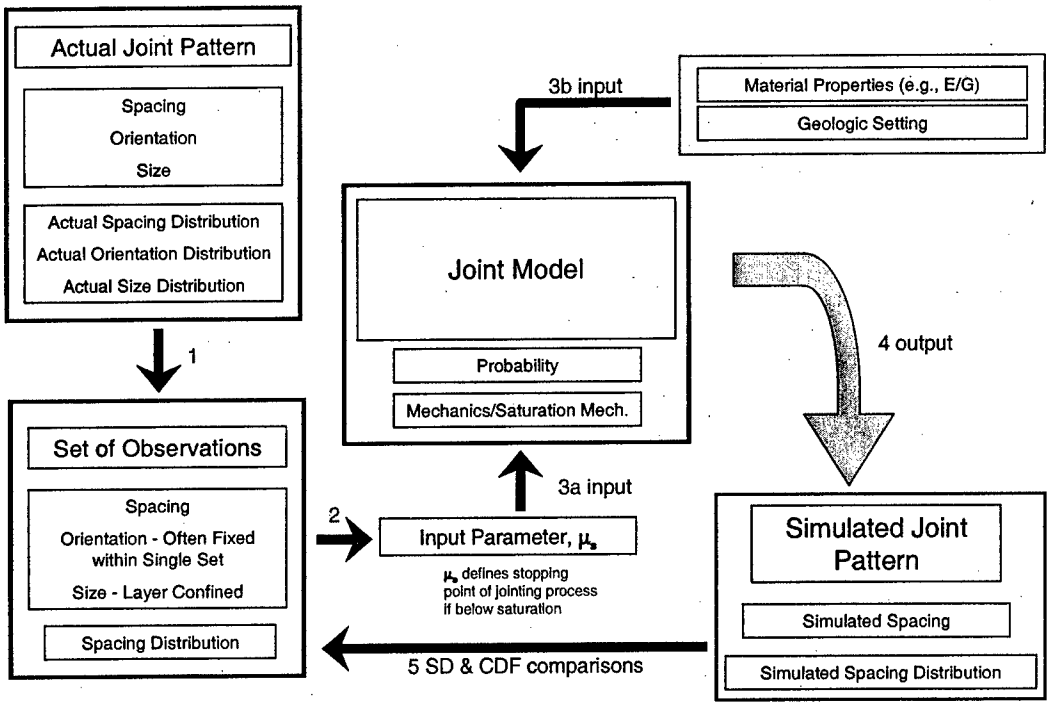


Figure 3 – Diagram of modeling process for spacing of layer-perpendicular joints in sedimentary rock based on a combination of mechanical and probabilistic concepts.

2 Field and Laboratory Observations

The prevalent joints in sedimentary rock are often perpendicular to the layer and usually confined within the layer (i.e., the joint height is equal to the layer thickness, t in **Figure 4**). This report focuses on this type of jointing. Before proceeding to model the patterns of these layer-confined, layer-perpendicular joints in sedimentary rock, one must look at the various observations made about these patterns in order to aid in their modeling. As for the joint length (i.e., in three dimensions, the dimension perpendicular to joint height and aperture), these are, where observable, typically much greater than the joint height. The joint length is not necessarily perpendicular to the exposed face of the outcrop as the joint set may not strike perpendicular to the direction of the outcrop. Being joints, they are the result of tensile stresses in the layer (mode I). The mechanism responsible for this type of jointing is often represented as a far-field extensional strain (ε in **Figure 4**) applied to a system of layers typically composed of a stiff jointing layer bounded by ductile non-jointing layers. The spacing between the resulting joints (shown in **Figure 4**) is often controlled by the layer thickness. Other factors such as grain size and composition also influence joint spacing but these are not considered in this report. This chapter presents previous field and laboratory work found in the literature. Section **2.1** presents previous field work whereas section **2.2** details previous laboratory work. These are followed by a brief summary (section **2.3**).

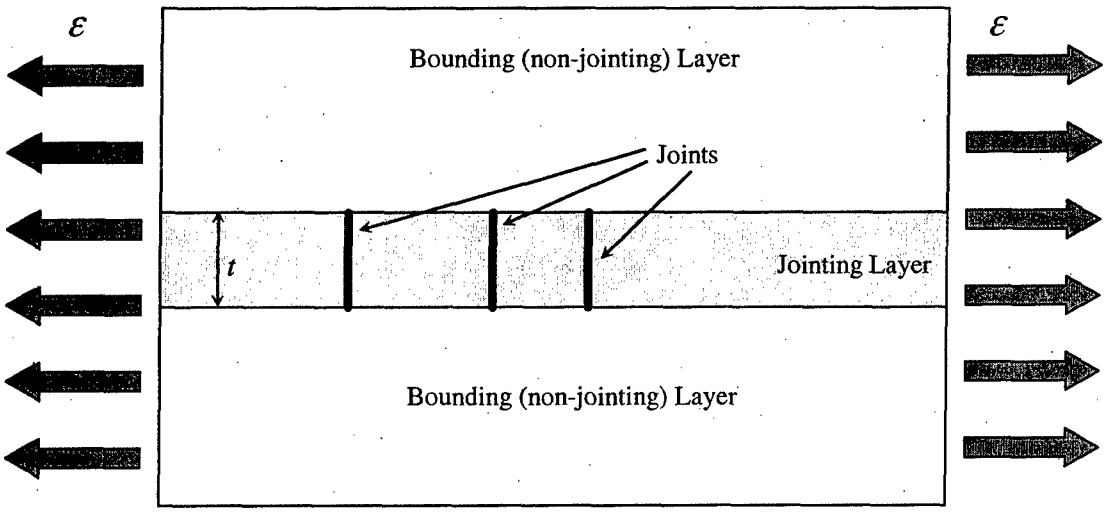


Figure 4 – Possible mechanism for the formation of layer-perpendicular joints in layered sedimentary rock.

2.1 Field Observations

2.1.1 Joint Spacing-Layer Thickness Relationship

In this section, a summary of observations found in the literature regarding the relationship between joint spacing and layer thickness is presented. A linear relationship between the mean (or median) spacing of layer-perpendicular joints and layer thickness

in sedimentary rock has been widely accepted by geologists. Thick layers contain more widely-spaced joints than do thin layers. Ladeira and Price (1981) observed that such a linear relationship between joint spacing and layer thickness is true only up to a certain value of thickness (< 1 to 2 meters) depending on the rock type. The spacing remains constant when the layer thickness equals or exceeds this value. Other researchers such as McQuillan (1973) gathered fracture density data suggesting a non-linear relationship between mean spacing and layer thickness.

Such relationships between spacing and layer thickness have been observed largely in sedimentary rocks since it is in these rocks that layers are well-defined and more easily recognized. Layer thickness in this report refers to mechanical layer thickness (MLT). In this report, Gross' (1993) definition of MLT is used: mechanical layer thickness is the distance between two mechanical layer boundaries. Mechanical layering commonly develops as a consequence of change in lithology (Gross, 1993). For a limestone bed bounded above and below by un-jointed mudstone, the contacts between these beds act as mechanical layer boundaries. Gross (1993) also suggested that pre-existing systematic joints can also act as mechanical layer boundaries so that the spacing between two of these joints can be considered a mechanical layer thickness. In this report, layer thickness refers to lithology-controlled MLT.

A summary of the available data on fracture spacing in sedimentary rocks in the literature would prove helpful in consolidating all these observations. This would also provide insight on the different techniques that were used to explain these observations. The three parameters that are typically used to describe the relationship between spacing and layer thickness are the Fracture Spacing Index (FSI), Fracture Spacing Ratio (FSR) and to a lesser extent the Fracture Index. These are defined below for convenience.

1. Fracture Spacing Index (FSI) – slope of the best-fit line in a plot of layer thickness versus median joint spacing. The layer thickness intercept may or may not be zero (**Figure 5**).

2. Fracture Spacing Ratio (FSR) – layer thickness divided by the median joint spacing for an individual layer (**Figure 5**).

3. Fracture Index – ratio between layer thickness and the mean joint spacing for a single layer.

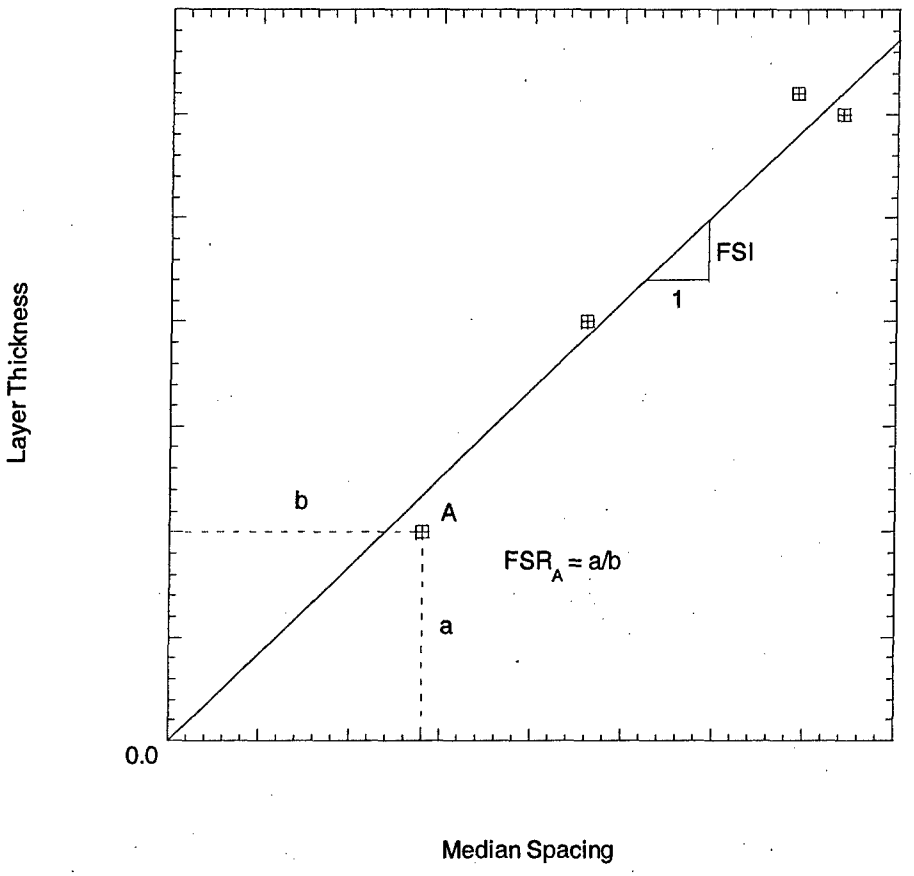


Figure 5 – Definition of FSI and FSR. Points are not from real data and serve as examples only.

Narr and Suppe (1991) gathered joint spacing data in the Monterey formation of California (Santa Maria Basin). The measurements were made in the following types of rock: chert, dolostone, porcelanite and siliceous shale. They plotted the layer thickness versus the median joint spacing first according to lithology (i.e., chert, dolostone, porcelanite and siliceous shale) and found that the slopes of the regression lines (the fracture spacing index, FSI) in these plots do not deviate much from a value of 1.29. Narr and Suppe (1991) then plotted the same data according to study site location and re-calculated the fracture spacing indices. These new FSI's also did not deviate much from a value of 1.29. This suggests that the relationship is independent of lithology or location for the hard rocks of the Monterey Formation. Inferred spacings from borehole data (Narr, 1991) from a nearby offshore oil field (Point Arguello) have fracture spacing indices ranging from 0.08 to 0.45 suggesting that such independence is quite limited.

Gross (1993) studied joints that were formed within layers defined by jointing rather than lithology. The joints that define the layer thickness are shown as J_1 joints in **Figure 6**. In essence, the spacing between two J_1 joints serves as a layer thickness. Within the joint-defined layers, another set of joints is present. The author called them cross-joints (also shown as J_2 joints in **Figure 6**). The cross-joint (J_2) orientations exhibit some scatter around the direction perpendicular to the J_1 joints. Two localities in the Monterey Formation exhibited such a jointing pattern: the Alegria and Gaviota stations (clay

siliceous members of the Monterey Formation). A strong linear relationship was observed between the median cross-joint (J_2) spacing and the layer thicknesses defined by the J_1 joints. The Alegria cross-joint (J_2) spacing gives an FSI of 1.23 while the Gaviota cross-joint spacing (J_2) 1.26. When the spacing data from both sites were combined, the FSI is 1.26. This paper shows that a linear thickness-spacing relationship like that for joints in lithology-defined mechanical layers may also be exhibited by joints formed in mechanical layers whose thickness is defined by jointing (e.g., by the J_1 joints).

Gross (1993) also provided FSI values from other locations with lithology-defined mechanical layers.

1. Santa Barbara Channel, Monterey Formation – FSI = 1.32
2. Huntington, Pennsylvania – FSI = 1.79
3. Watkins Glen, New York – FSI = 0.68

The rock types for these three locations were not given.

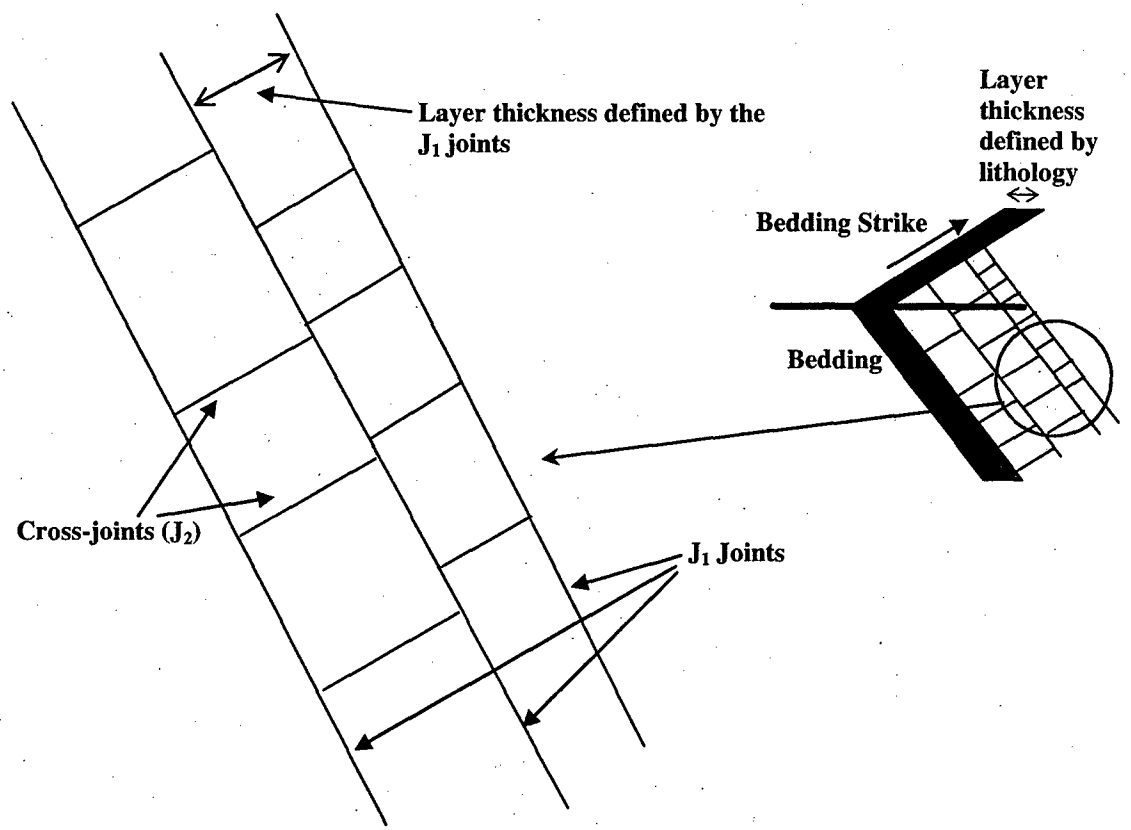


Figure 6 – Mechanical layers defined by the J_1 joints and the occurrence of cross-joints (J_2) between them. Sketched from descriptions of J_1 and J_2 joints given in Gross (1993).

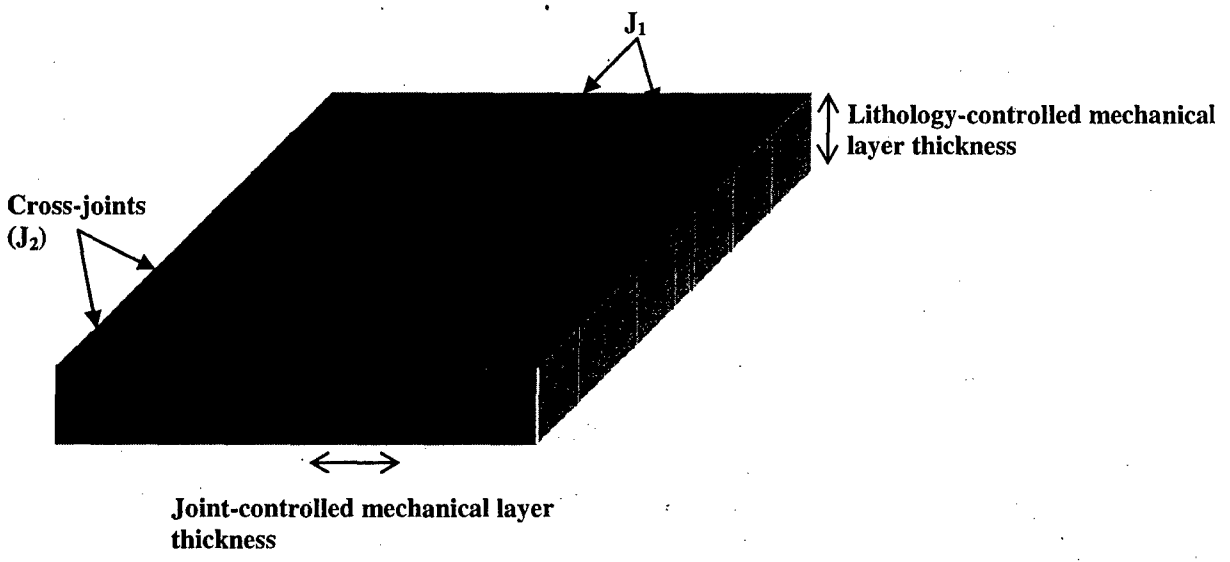


Figure 7 – A case where the mechanical layer thickness can be defined by lithology in one direction and previous jointing (J_1) in another.

Ruf et al. (1998) studied cross-joints (J_2 in **Figure 7**) in a large outcrop of the Devonian Brallier Formation near Huntington, Pennsylvania. The joints were formed between two types of mechanical layer boundaries: those defined by earlier joints (J_1 in **Figure 7**) and those defined by lithology (**Figure 7**). These earlier J_1 joints were controlled by lithology. The plot of lithology-controlled layer thickness versus the median J_1 joint spacing gives an FSI of 0.91 with a coefficient of determination, $r^2 = 0.86$. For the cross-joints (J_2) that were formed, two FSI plots were constructed based on how the mechanical layer thickness is defined: lithology-controlled and jointing-controlled. Ruf et al. (1998) obtained the following FSI and coefficient of determination values:

1. Lithology-controlled layer thickness – FSI = 0.97 and $r^2 = 0.69$
2. Jointing-controlled layer thickness – FSI = 1.02 and $r^2 = 0.78$

These results show that, in this case, cross-joint spacing may correlate better with the jointing-controlled layer thickness than with the lithology-controlled layer thickness. However, the difference in the values of r^2 is small.

In an effort to determine probabilistically the ratio of layer thickness to average joint spacing from core data in layered rock, Narr and Lerche (1984) compiled spacing data from two limestone outcrops to test their proposed method. The method involves constructing a curve relating the ratio of layer thickness to average joint spacing (Fracture Index) to the number of intersected jointed layers (i.e., layers containing joints) given the core diameter, the thicknesses of the layers intersected, the angle between the core axis and the joints and the bedding planes or layers (**Figure 8**). The number of intersected jointed layers pertains to the number of layers with at least one of its joints intersected by the borehole. If the borehole is perpendicular to the bedding planes, it may not encounter

a joint in every layer. However, if the borehole is drilled parallel to bedding, the bedding perpendicular joints will be sampled better. To test the method, joint spacing measurements were made on two limestone outcrops. No actual boreholes were used but hypothetical boreholes represented by lines were superimposed on the images of the outcrops. These lines were drawn perpendicular to the bedding and parallel to the joint planes. The number of intersected beds (the number of all the layers that are intersected, layers 1 to 4 in **Figure 9**) and intersected jointed beds (the number of layers among all the layers intersected where the borehole itself intersects a joint, layers 1 and 4 in **Figure 9**) could then be counted from the image. Actual measured fracture index values from the five beds observed on Outcrop 1 range from 0.67 to 1.55 with an average of 0.98. On Outcrop 2, six beds were observed and measured fracture indices ranged from 0.54 to 0.92 with an average of 0.71. The paper is mainly geared towards testing the method that the authors have developed rather than providing additional insight into what other factors may affect the bed thickness-joint spacing relationship. However, it is valuable in terms of the data it provides.

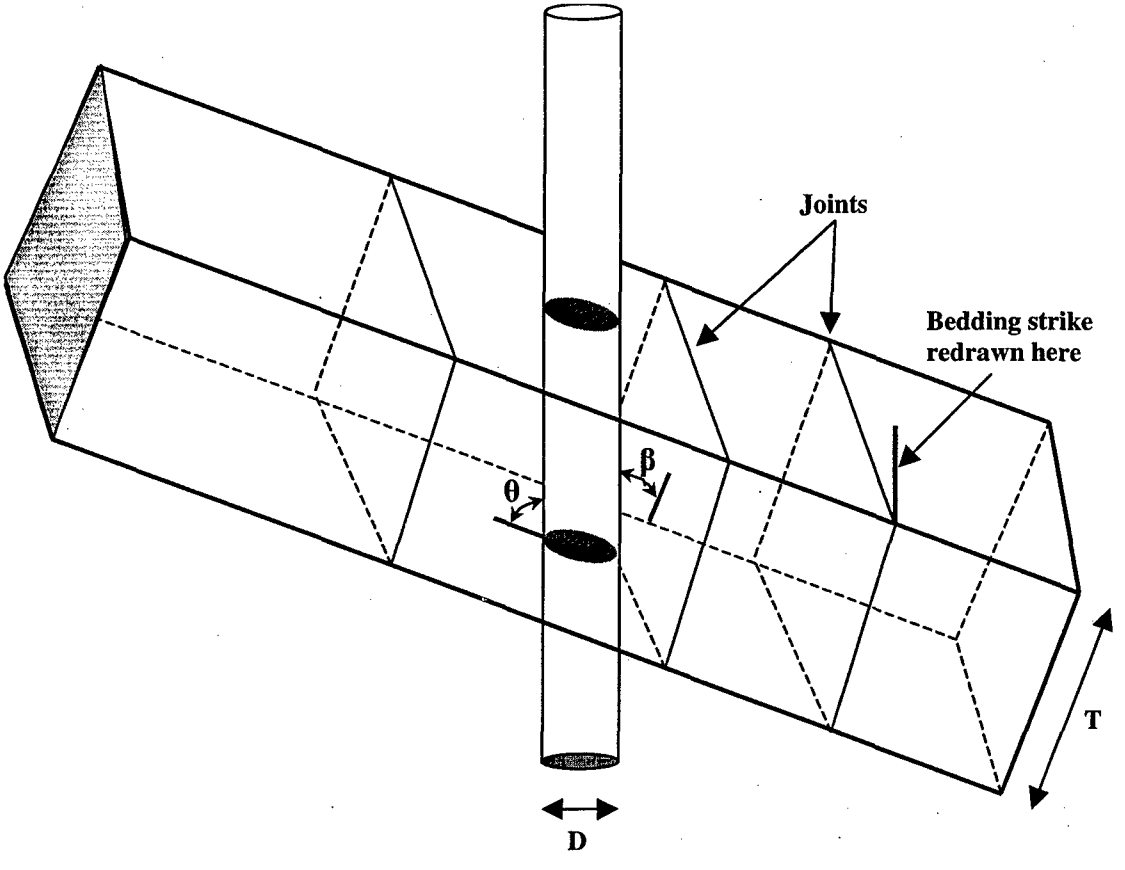


Figure 8 – A borehole intersecting a portion of a fractured bed. β is the angle between the core and the fractures, θ is the angle between the core axis and the bedding, D is the core diameter and T is the thickness of the bed. Sketched from Fig. 5 in Narr and Lerche (1984).

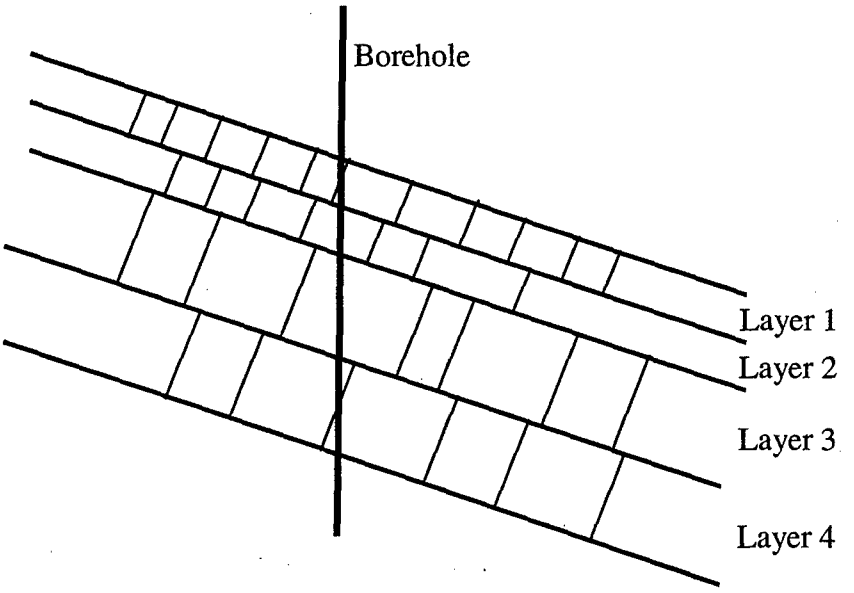


Figure 9 – Illustration of intersected beds vs. intersected jointed beds. Sketched from descriptions of intersected beds and intersected jointed beds in Narr and Lerche (1984).

Narr (1991) proposed a method of determining the fracture spacing index from borehole data. This method is similar to that proposed by Narr and Lerche (1984) except that the FSI is plotted against the expected number of fractured layers (i.e., expected number of layers encountered by boreholes that have a fracture/s intersecting the borehole) rather than the fracture index. Borehole data were obtained from four wells drilled in an oil field. Dolostone, siliceous shale, porcelanite and mudstone are the main lithologies present in the cores although chert beds are present in one of them. Considering all lithologies, the calculated fracture spacing index values from each of the four core data sets are 0.27, 0.12, 0.08 and 0.45 for the wells named A, D, F and G, respectively. The paper also gives the fracture spacing indices for some cases where not all of the lithologies in each core are considered. For example, if only porcelanite and siliceous shale are considered, the fracture spacing indices would be 0.29, 0.16, 0.23 and 0.70, respectively. If only dolostone is considered, the fracture spacing indices become 0.42, 0.10, 0.00 and 0.44. Again, these indices are inferred from core data (using a method similar to Narr and Lerche, 1984) and not from actual joint spacing data. If anything, this information may serve as an indication of the variability of the joint spacing even for rock beds in the same area.

Huang and Angelier (1989) compiled spacing data from limestone beds in southeastern France. The joint measurements were taken from two layers of different ages (Neocomian and Apto-Albian). The mean joint spacing was plotted with layer thickness and the results show that the slope of the relationship is different for the two limestones. An attempt to extract FSR numbers from the plots in the paper gave the following values:

1. Apto-Albian limestones – FSR = 0.93
2. Neocomian limestones – FSR = 1.67

Observed layer thickness values in the Neocomian limestones were greater than those in the Apto-Albian limestones. In both cases, the limestone layers are interbedded with thick shale layers (10 cm to 1.0 m). Huang and Angelier (1989) attributed the difference in FSR values to the degree of compaction. However, it is not clear on what basis this claim is made and whether or not the relative ages of the limestones has an effect on the FSR values.

Ladeira and Price (1981) studied the effect of the thicknesses of the adjacent incompetent layers on the joint spacing in the competent layer. Data for the study came specifically from greywacke (greenish fine-grained sandstone) formations in the United Kingdom. The data were divided into two groups according to adjacent layer thickness: > 5 cm and <5 cm. They observed that thicker adjacent incompetent beds lead to wider joint spacing in the competent bed. The authors also observed, for each type of rock, a threshold value for bed thickness beyond which the joint spacing either remains constant (i.e., the linear relationship between joint spacing and bed thickness no longer applies) or very nearly so. This threshold value is about 1.0 m for the United Kingdom greywackes and about 2.0 m for the Portuguese greywackes. They suspect that the mechanism for hydraulic fracturing governs in the thicker layers as opposed to bedding plane traction in the thinner layers. In hydraulic fracturing, the appearance of a fracture relieves the hydraulic pressure at the fracture and in the vicinity of the fracture. The amount of pressure relief depends on the permeability of the unfractured rock and is a function of distance from the joint. This means that at a certain distance from the fracture, the hydraulic pressure is still not relieved and fracturing may occur. If the permeability is constant, the joint spacing will also be constant. This behavior was observed in the greywackes from the UK and Portugal and also in limestone from Portugal. The authors fitted continuous curves to the data and these types of curves are drawn schematically in **Figure 10** (curves **A**, **B** and **C**). Also suggested is a fit consisting of two parts: a linear part and a portion where joint spacing remains constant (shown schematically in **Figure 11** lines **A** and **B**). **Figure 11** also shows what some authors call a bilinear fit for curve **C** in **Figure 10**.

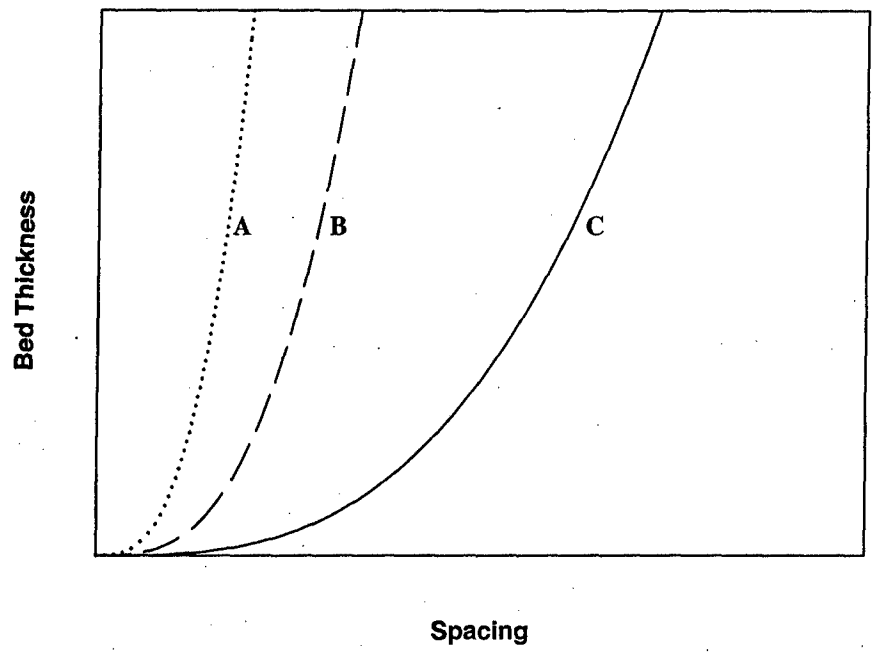


Figure 10 – General shape of curves used to fit bed thickness-spacing data in Ladeira and Price (1981). Sketched from Fig. 2 in Ladeira and Price (1981).

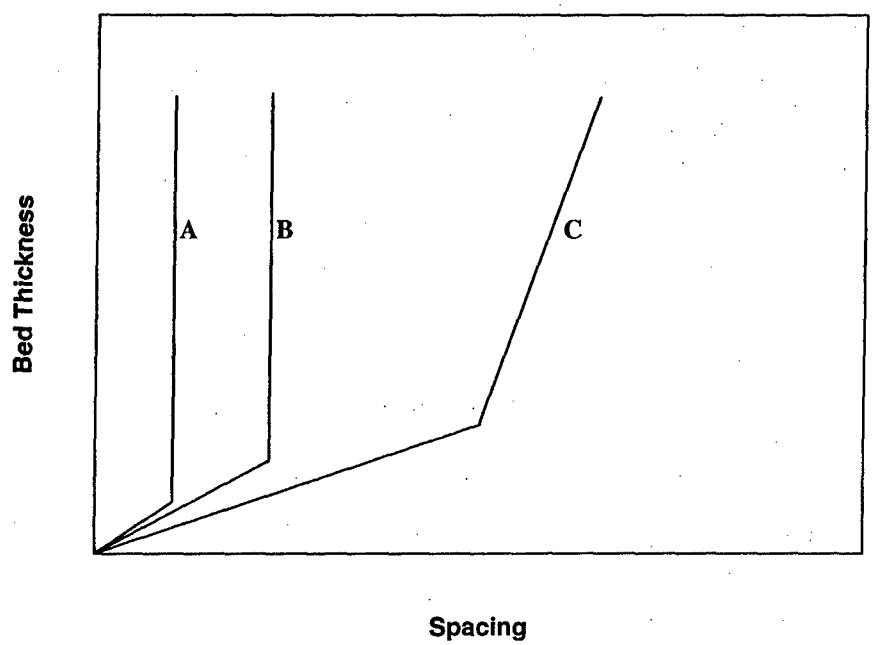


Figure 11 – Suggested fit to bed thickness-spacing data with relationships of the nature shown in Figure 10. There is an initial linear relationship followed by a constant value of joint spacing beyond

a certain value of bed thickness. A bilinear fit is also shown (C). A and B are sketched from Fig. 3 (a) of Ladeira and Price (1981). C is sketched from Fig. 1 (d) in Wu and Pollard (1995)

McQuillan (1973) collected fracture spacing data from the Asmari Formation in Iran. An overall view of one of the sites (a gorge) showed the variation of the layer thicknesses. Layer thicknesses ranged from thin near the top of the gorge to massive towards the bottom. Most of the data were collected from the upper portions of the formation (thickness between 15 to 365 cm or 0.49 to 12 ft.). Since the layer thickness values observed at the site were numerous, the author divided the thicknesses into seven groups. Also, the measurements were grouped according to which part of the structure (anticlines) in which they were measured. For example, the Kuh-e Asmari anticline was divided into northwest plunge, southeast plunge, northeast flank, southwest flank and center. Observations show that for a given layer thickness, the fracture densities (or spacing values) in the different parts of the structure are not much different from the density value for the entire structure. This suggests an invariance of the density with respect to structure. Putting together the data for the entire range of bed thicknesses revealed that thicker limestone beds have lower fracture densities (large spacing) than thin ones as is expected. For example, in the Kuh-e Asmari anticline, the average fracture density for a layer thickness of about 0.778 feet was observed to be 42 fractures/100ft whereas the observed density for a layer thickness of 21 feet is 14 fractures/100ft. A linear relationship was observed between the fracture density and the logarithm of layer thickness. This means that the relationship between average fracture spacing (which can be calculated in feet as the inverse of the fracture density) and layer thickness is non-linear (an attempt to obtain this relationship is shown in **Figure 12**). Therefore, the relationship between average fracture spacing and layer thickness cannot be described strictly by a parameter similar to the FSI or FSR. These curves look similar to the ones observed by Ladeira and Price (1981) where the slope of the relationship increases with the layer thickness.

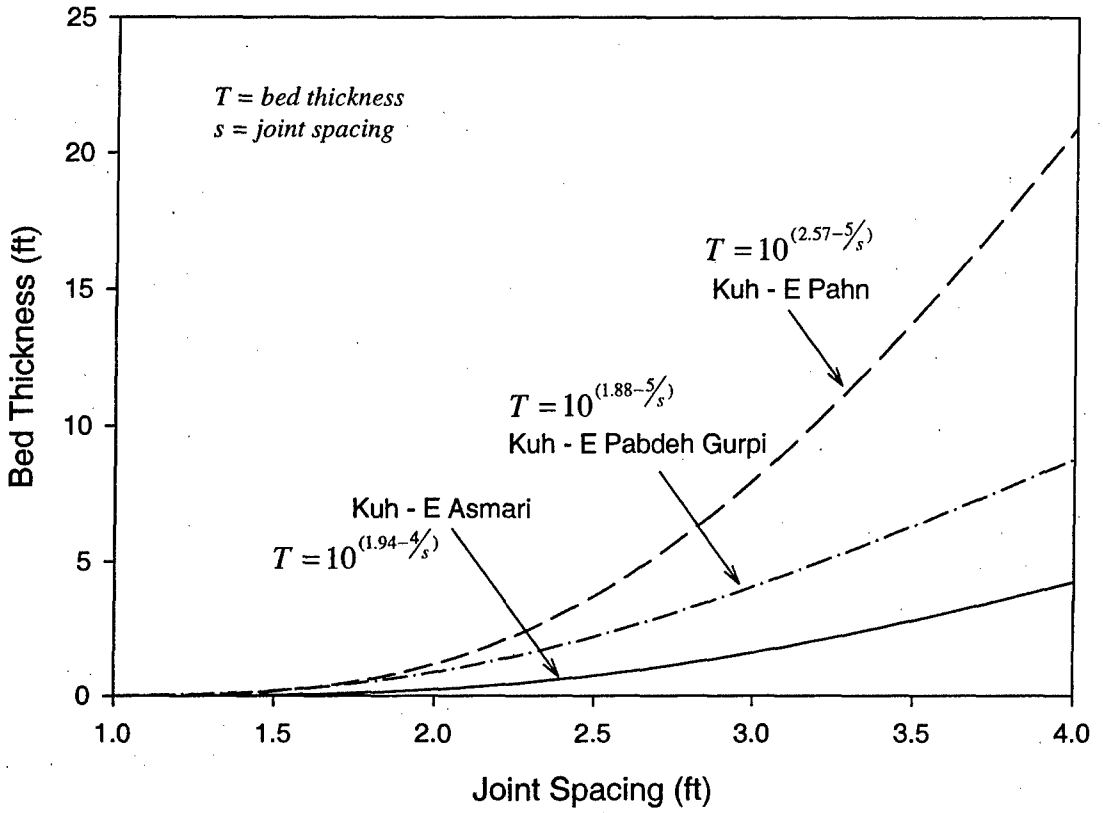


Figure 12 – Bed thickness and joint spacing curves for the three locations in the Asmari Formation in Iran. Converted into bed thickness vs. joint spacing from plots in McQuillan (1973).

Engelder et al. (1997) studied the joints in sandstone layers in the Elk Basin Anticline near the Montana-Wyoming border. They observed that in this formation, the FSI is a function of structural position. The FSI in the forelimb of the anticline is 0.96 and 0.79 in the backlimb. The authors attributed this difference to the larger amount of strain to which the forelimb has been subjected. It has to be added that this observation seems to apply only to the strike joints in the formation. Limited data on dip joints suggest that the layer thickness-joint spacing relationship is independent of structural position, unlike for the strike joints. Also, the results seem contrary to the observation by a number of other researchers that the linear relationship between layer thickness and joint spacing breaks down for layer thicknesses greater than about 2 m. Some of the beds studied in this formation have thicknesses between 2 and 10 m. This paper provides a good set of data where measurements from individual beds (thickness, joint spacing, type of joint measured: strike or dip joint, etc.) are given in tabular form.

Becker and Gross (1996) studied joint spacing in a single layer of limestone/dolostone in the Gerofit formation in southern Israel. The layer is cut by several fault and joint zones (**Figure 13**). They purposely focused on spacing measurements in this single layer in an effort to determine how spacing changes along the bed, which has a relatively constant

thickness (18±1.2 cm) along the scanline. The bed was divided into four sections (**Figure 13**). They found that the ratio of layer thickness to median joint spacing varied along the scanline and that the central portion of the layer had a higher ratio than the two ends (i.e., central portion has more joints). The authors suspect that a possible explanation for this is that the central portion has been subjected to higher strains than the ends (suggested by the presence of the fault and joint zones). The FSR values for the four sections are 0.76, 1.30, 1.25 and 0.87. An additional factor (amount of strain) figuring in the relationship between bed thickness and joint spacing is investigated in Becker and Gross (1996).

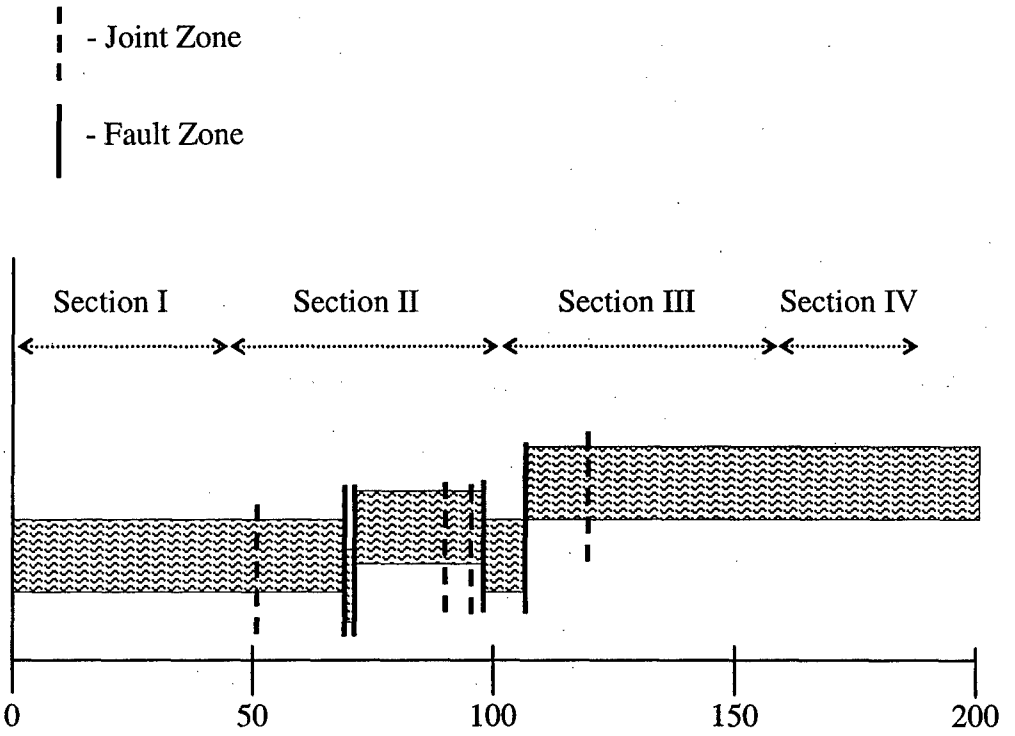


Figure 13 – Schematic of the limestone/dolostone layer studied by Becker and Gross (1996). Sketched from Fig. 7 in Becker and Gross (1996) but without the vertical scale.

Pascal et al. (1997) tried to model fractures that occur in horizontally layered rocks. Specifically, they attempted to model joints that nucleate from limestone beds in order to find the probability that these joints propagate to mudstone layers bounding them. To test their model, they gathered spacing data from limestone/mudstone layers at Llantwit Major in Wales, UK. Measurements were made on nine limestone beds interbedded with four mudstone layers. The length of the outcrop is 11 m. The ratio between limestone layer thickness and mean joint spacing (FSR) ranges from 0.47 to 1.60 with a mean of 0.92 and a standard deviation of 0.33. This example shows that even for limestone beds in a single formation, FSR can vary.

Ji and Saruwatari (1998) gathered spacing data from 42 sandstone layers in the St. Roch Formation 112 km northeast of Quebec City. The fracture spacing index for the 42 layers was found to be 1.20. The paper also quoted FSI values from other studies:

1. Aydan and Kawamoto (1990) – sandstone, FSI = 0.79
2. Price (1960) – sandstone, FSI = 0.82
3. Angelier et al. (1989) – sandstone, FSI = 1.67

The general trend in the papers that study the relationship between layer thickness and fracture spacing is that the data is processed in a way that might reveal other factors affecting the relationship. For example: plotting the data from a single formation by location to see if the relationship is invariant with respect to location (Narr and Suppe, 1991). A number of researchers also found that the linear relationship between layer thickness and joint spacing in layered sedimentary rock is not observed in all cases. **Table 1** shows a summary of the observed layer thickness-to-spacing ratios that were presented earlier.

Table 1 – Summary of field-observed layer thickness-to-spacing ratios. ♦ - Non-linear relationship observed between layer thickness and spacing.

Source	FSR	FSI	Fracture Index
Narr and Lerche (1984)	-	-	0.67 to 1.55 (from five different layers)
Huang and Angelier (1989)	0.93 and 1.67 for two different limestones	-	-
Narr (1991)	-	0.08, 0.12, 0.27 and 0.45 (calculated)	-
Narr and Suppe (1991)	-	1.29	-
Gross (1993)	-	1.23	-
Gross (1993)	-	1.32	-
Gross (1993)	-	1.79	-
Gross (1993)	-	0.68	-
Becker and Gross (1996)	0.76, 0.87, 1.23 and 1.31	-	-
Engelder et al. (1997)	-	0.79 and 0.96	-
Pascal et al. (1997)	0.47 to 1.60	-	-
Ji and Saruwatari (1998)	-	1.20	-
Ji and Saruwatari (1998) from secondary sources	-	0.79, 0.82 and 1.67	-
Ruf et al. (1998)	-	0.97	-
McQuillan (1973)	♦	-	-
Ladeira and Price (1981)	♦	-	-

2.1.2 Joint Spacing Probability Distributions

The joint spacing probability distribution is another aspect of jointing that has often been included in field studies. In the following paragraphs, the different types of joint spacing probability distributions observed in the field are presented.

Rives et al. (1992) gathered joint spacing data from three locations: Scarborough and Whitby on the coast of North Yorkshire, UK and Nash Point on the coast of South Wales,

UK. In both the Scarborough and Whitby locations, rock platforms have been exposed by coastal erosion. This allows one to measure not only joint spacing but trace length as well. At Scarborough, layers of mudstone, siltstone and sandstone were exposed whereas at Whitby, there are layers of shale. Trace lengths at Scarborough commonly exceeded 50 m. At Nash Point, low tides expose single beds of limestone and shale. Trace lengths typically exceeded the width of the exposure (100 to 200 m). Rives et al. (1992) included the mode-to-mean joint spacing ratio as a parameter to aid in the characterization of the appropriate probability distribution. They then compared the mode to mean joint spacing ratio from the three locations. The Whitby joint spacing data produced the lowest mode/mean ratio and the Nash Point joint spacing data produced the highest mode/mean ratio. An exponential distribution fit the Whitby joint spacing data well whereas log-normal distributions fit both the Scarborough and Nash Point data.

Narr and Suppe (1991) gathered joint spacing data from the Monterey formation in California. Joint spacing measurements were taken from layers of dolostone, chert, porcelanite and siliceous shale. The ratio of layer thickness to joint spacing was observed to be independent of lithology with a value of 1.3. The authors also observed that mean joint spacing in individual layers is consistently greater than median joint spacing. Also, the standard deviation for spacing is typically 0.56 times the mean spacing. This indicates that an exponential distribution may not be fit to describe the joint spacing distribution in the studied layers. Since the authors did not feel confident that the joint spacing data from any individual layer were sufficient to describe a joint spacing distribution, they combined all the data from the different lithological layers. This was done by normalizing each joint spacing value by dividing it by the thickness of the layer from which it was obtained. The combined data was best described by a log-normal distribution.

Becker and Gross (1996) studied joint spacing data from a 190-m-long scanline along a single limestone/dolostone bed of approximately uniform thickness (about 18 cm). Among the four observed systematic joint sets in the study area (vertical joints trending approximately 340, 293, 230 and 195), the 293 ± 3 set was chosen for study by the authors. The spacing values range from 0.3 cm to 75 cm. **Figure 14** shows the histogram for all spacing data from the single bed. The shape of the histogram appears to be log-normal. If the distribution is indeed log-normal, then the histogram of the logarithms of the spacing values should appear to be normal. **Figure 15** shows that this is somewhat the case.

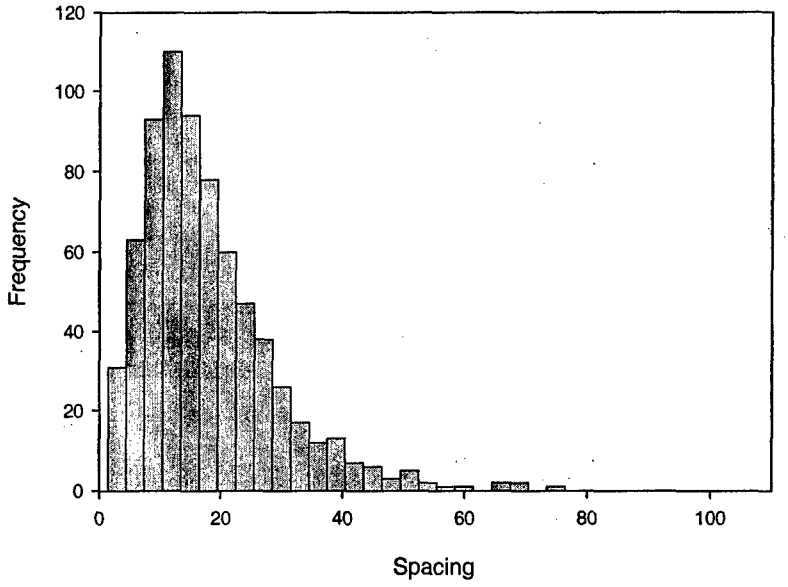


Figure 14 – Histogram of the spacing data (in cm) from the Gerofit Formation. Plotted from data in Becker and Gross (1996).

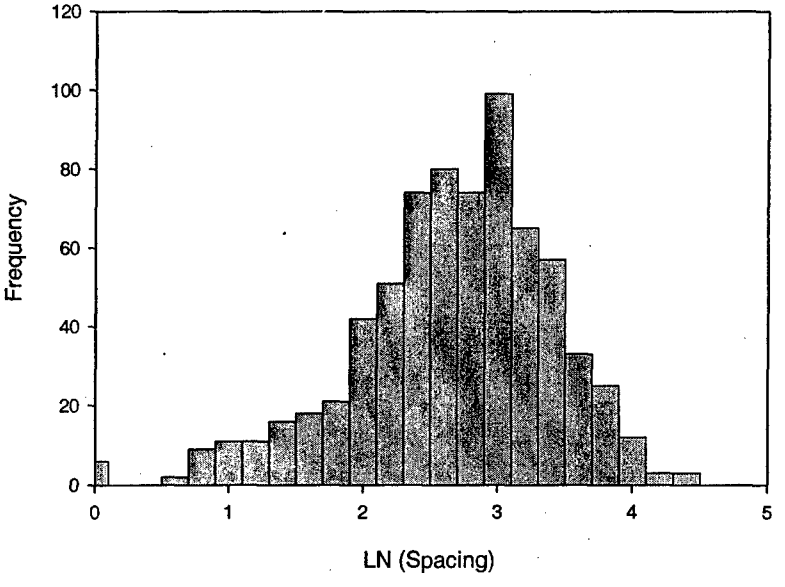


Figure 15 – Histogram of the natural logarithms of spacing. Plotted from data in Becker and Gross (1996).

Suspecting that the middle section of the limestone bed may be more strained due to the existence of fracture zones, the authors divided the entire length into four sections (I, II, III, and IV), with sections II and III seemingly more strained than section I and IV. The

spacing histogram for each section is shown in **Figure 16** to **Figure 19**. Although sections II and III appear to be best described by log-normal distributions, it was found that they cannot be. On the other hand, sections I and IV are likely to be log-normal. **Table 2** below shows some important statistics for the spacing data in each section. The mean spacing is observed to be lower in the two middle sections as is the standard deviation and supports the suspicion that the middle of the layer has been subjected to a higher level of strain than the ends.

Table 2 – Summary of data statistics for each section in Becker and Gross (1996). Entries are from Table 2 in Becker and Gross (1996). Spacings are in cm.

	Section I	Section II	Section III	Section IV
Number of Spacing Data	110	237	271	94
Sum of Spacing Data	2602.6	3276.2	3901.4	1943.2
Mean	23.66	13.82	14.40	20.67
Standard Deviation	14.96	7.76	9.31	12.85
Minimum	2.00	2.00	0.30	2.30
Maximum	75.00	39.70	67.00	64.00

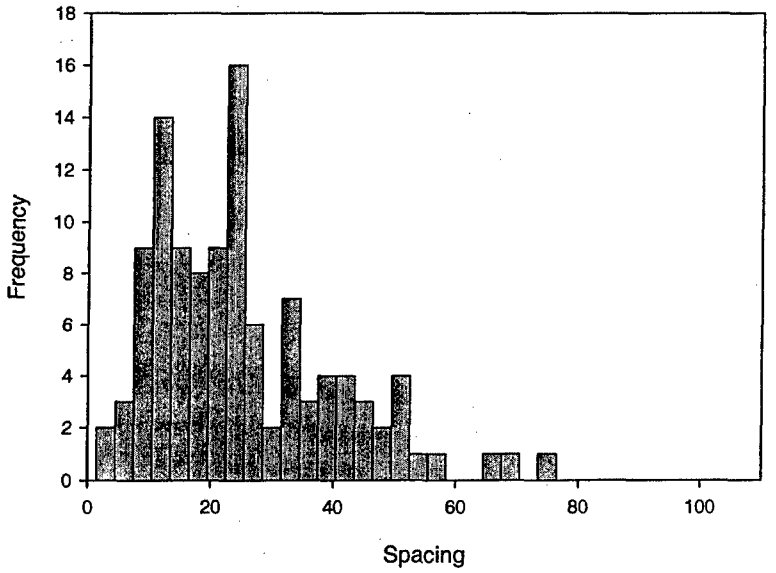


Figure 16 – Histogram of spacing values (cm) in section I. Plotted from data in Becker and Gross (1996).

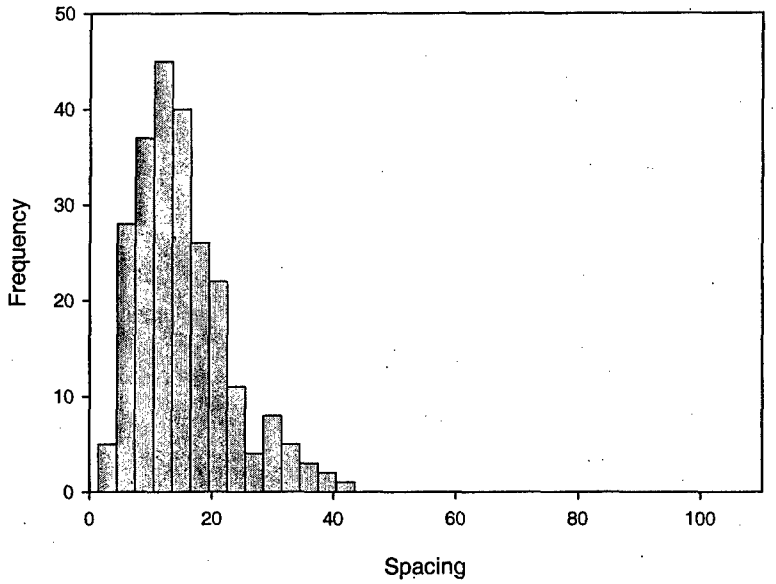


Figure 17 – Histogram of spacing values (cm) in section II. Plotted from data in Becker and Gross (1996).

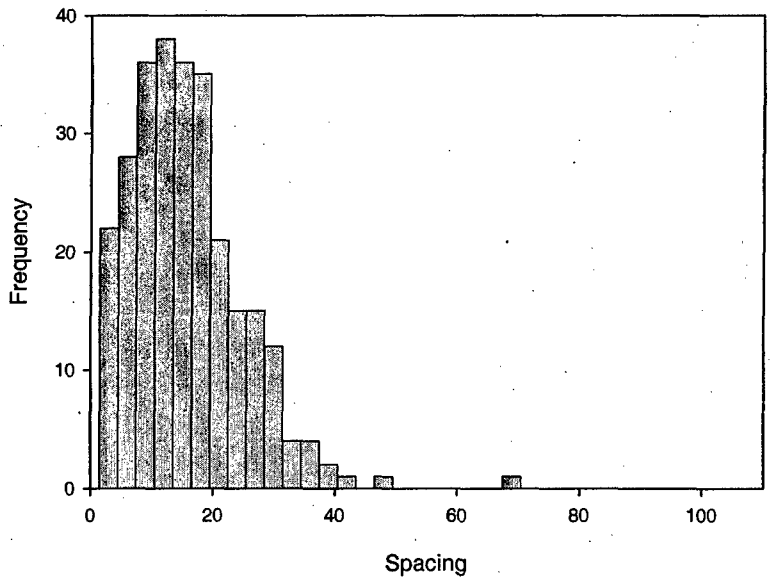


Figure 18 – Histogram of spacing values (cm) in section III. Plotted from data in Becker and Gross (1996).

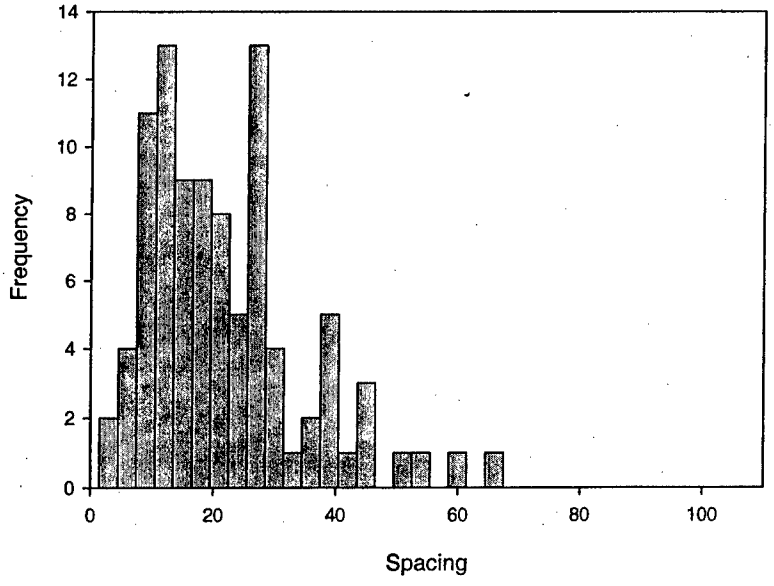


Figure 19 – Histogram of spacing values (cm) in section IV. Plotted from data in Becker and Gross (1996).

Huang and Angelier (1989) gathered joint spacing data from locations in two countries: The Sisteron area in southern France and the Zeit-Mellaha area in Egypt. In the Sisteron area, the authors studied a series of shale and limestone. Two sets of bedding perpendicular joints trending N-S and ENE-WSW were found mainly in the limestone layers. The ENE-WSW set is dominant. Most of the joints in both sets were found to be conjugate shear fractures. In the Zeit-Mellaha area, joint spacings in a horizontal layer of calcareous sandstone were measured. This set of joints strikes N20°E and is vertical. In this case, the joints were found to be related to several extensional tectonic events (Gauthier, 1986). The authors also noted that all small and large spacing values were measured and joints belonging to other sets were omitted from the measurements. It was found that neither an exponential distribution nor a log-normal distribution adequately described these data. They found that the Gamma distribution fit the joint spacing data well. The Gamma distribution has parameters α and β and the equation is shown below:

$$f(L) = \frac{1}{\Gamma(\alpha+1)\beta^{\alpha+1}} L^{\alpha} \exp\left(-\frac{L}{\beta}\right) \qquad L > 0$$

The parameter values are obtained by the maximum likelihood method using the arithmetic and geometric mean of the data. Given an arithmetic mean of 62.5 cm and a geometric mean of 53 cm, α and β are found to be 3.2 and 19.5, respectively. The plot of the Gamma distribution that best fits the joint spacing data is shown in **Figure 20**.

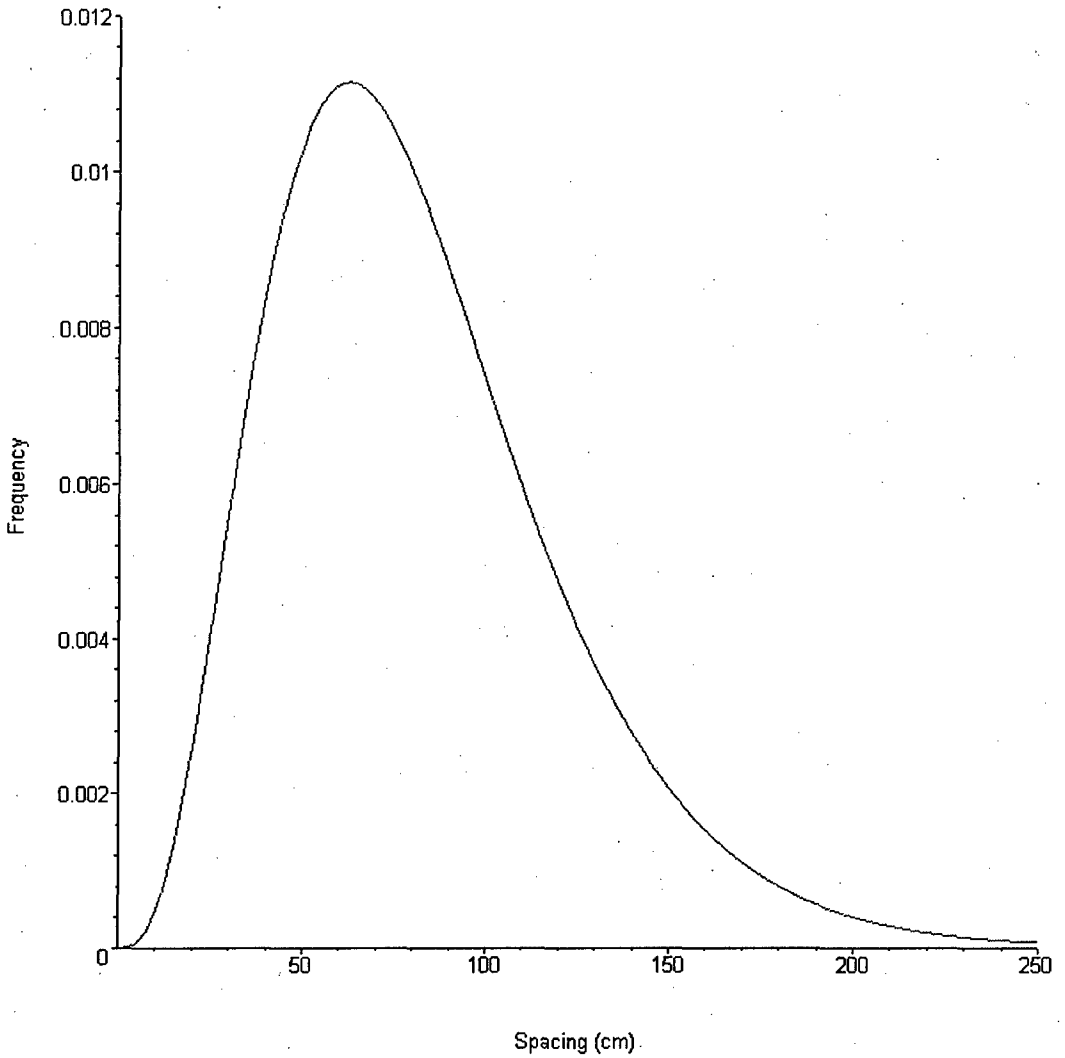


Figure 20 – Joint spacing distribution from Huang and Angelier (1989). Gamma distribution with $\alpha = 3.2$ and $\beta = 19.5$. Reproduced from information in Fig. 3 in Huang and Angelier (1989).

Priest and Hudson (1976) suggested that a negative exponential distribution should be adequate to describe discontinuity (i.e., all, including joints) spacing. They gathered spacing data along various scanlines in three different tunnels. They found in all three tunnels that the discontinuity mean spacing and standard deviation are approximately equal, an indication that the exponential distribution may be used to fit the data (**Figure 21** to **Figure 23**). It must be noted, however, that no distinction was made among the different types of discontinuities that were encountered. In other words, it is likely that the spacing for all discontinuities intersecting the scanlines were measured discounting the possibility that some of these discontinuities may occur in sets.

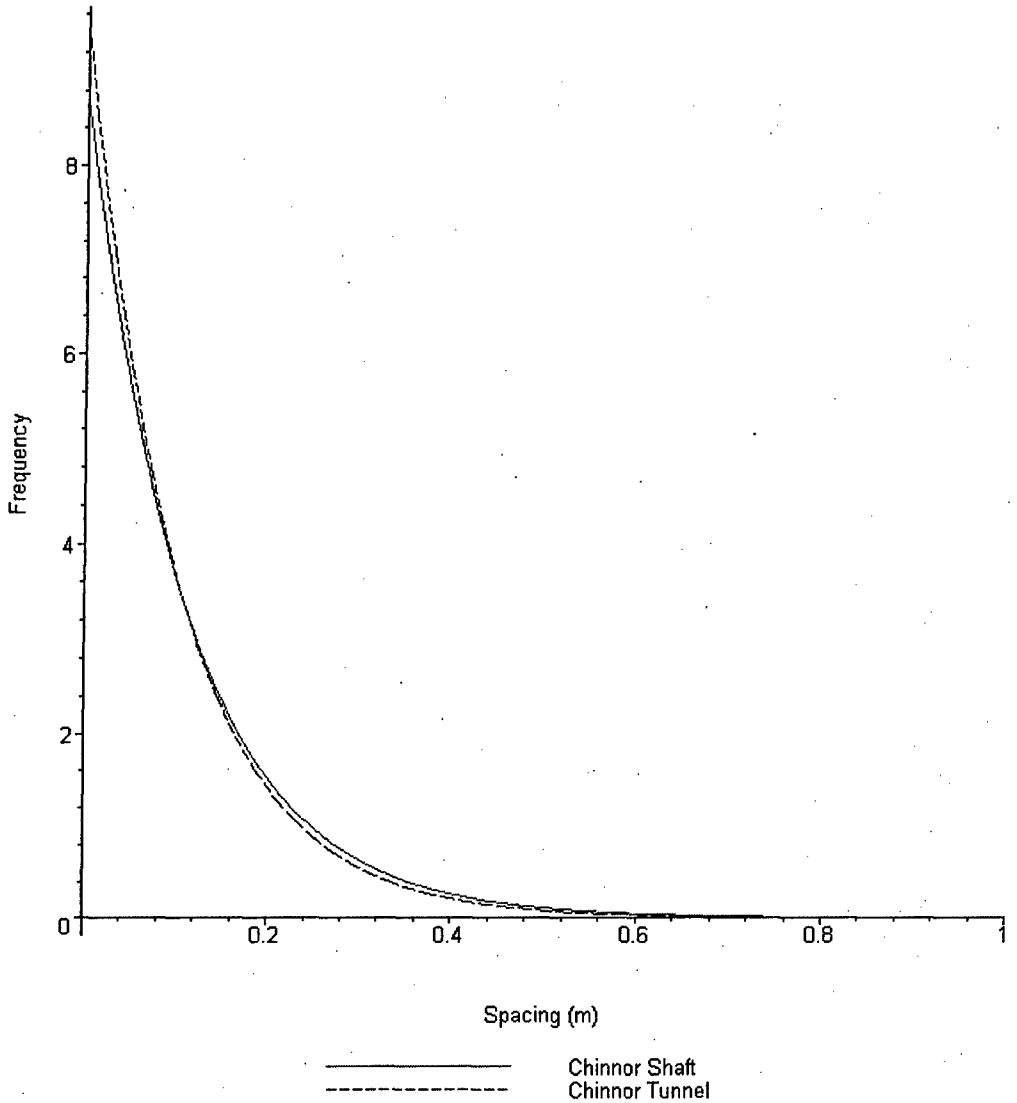


Figure 21 – Fitted exponential distributions for discontinuity data from the Lower Chalk in the Chinnor shaft and the Chinnor tunnel (Chinnor, Oxfordshire). Reproduced from data in Fig. 5 and Fig. 6 in Priest and Hudson (1976).

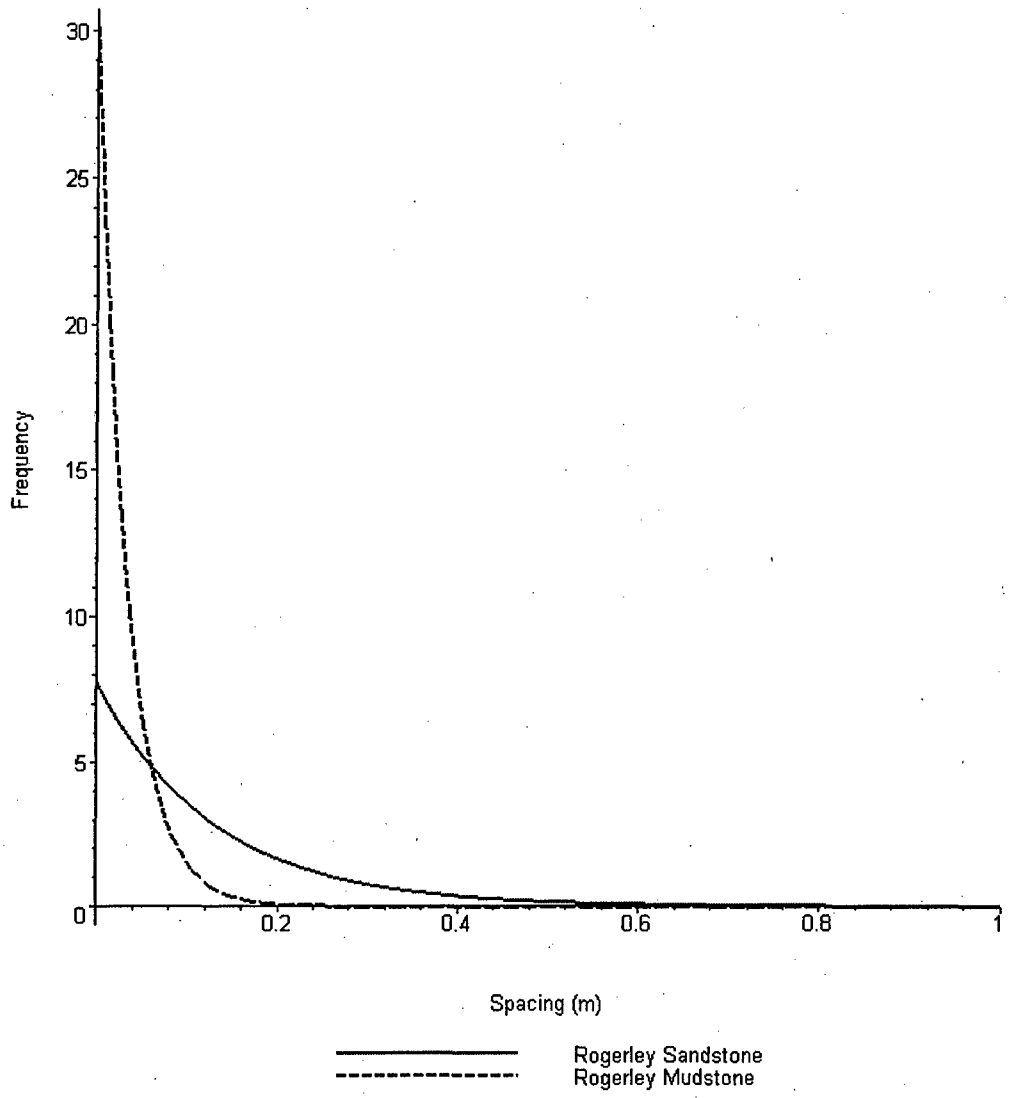


Figure 22 – Fitted exponential distributions for discontinuity data from the Kielder experimental tunnel at Rogerley Quarry, Durham from Priest and Hudson (1976). Reproduced from data in Fig. 9 and Fig. 10 in Priest and Hudson (1976).

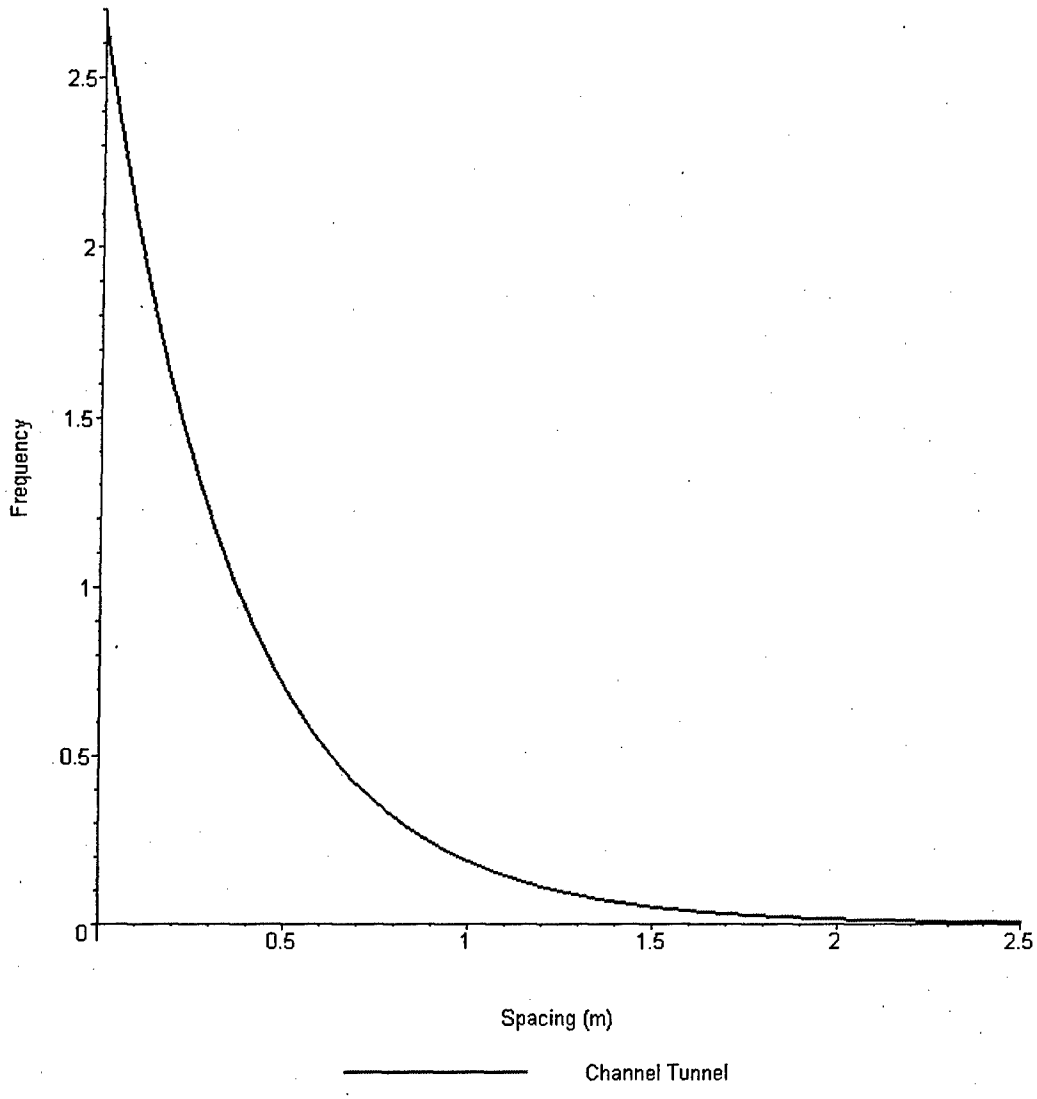


Figure 23 – Fitted exponential distribution for discontinuity data in the Lower Chalk of the Channel Tunnel from Priest and Hudson (1976). Reproduced from data in Fig. 12 in Priest and Hudson (1976).

From the preceding paragraphs it can be seen that no single form of probability distribution can be used to describe joint spacing. However, joint spacing appears to consistently exhibit positive skewness (i.e., skewed towards the small values).

2.2 Laboratory Observations

In this section, a summary of laboratory experiments found in the literature is presented. Laboratory experiments aimed at reproducing the jointing process in layered sedimentary rock have also been performed (e.g., Rives et al., 1992; Wu and Pollard, 1995). The laboratory set-up typically consists of a brittle jointing layer glued to a ductile layer subjected to extensional strain (e.g., Rives et al., 1992; Wu and Pollard, 1995). Tensile stresses in the brittle layer are developed to balance the shear stresses at the interface with the ductile layer. These tensile stresses cause jointing in the brittle layer. Researchers have found from these experiments that once the strain surpasses a certain value for a given set of conditions (e.g., rock mechanical properties, thickness, etc.) the joint spacing ceases to decrease. At and beyond this level of strain the rock is said to be at joint "saturation" with respect to the extensional mechanism of jointing. In these experiments, observations regarding the mean joint spacing and the probability distribution of joint spacing were made as the number of joints increased.

Wu and Pollard (1995) proposed a joint spacing measurement that takes into account the lengths of the layer-perpendicular joints. Recall that the length of the joint is defined as the distance that it extends into the layer (**Figure 24**), this is different from the height of the joint which is usually equal to the thickness of the layer. The spacing of these joints is usually measured using a scanline on the face of an exposed layer or bed (scanline 1 in **Figure 24**) and the length of the joint into the layer or bed is usually neglected. The measured spacing along such a scanline could be different if it were placed at a different location (e.g., scanline 2 in **Figure 24**). Joints that were exposed on the outcrop face may no longer extend to the new location of the scanline or other joints may be exposed there that do not appear on the outcrop face (**Figure 24**). According to the authors, an area measurement of joint spacing takes care of this problem. However, Wu and Pollard's (1995) measurement requires that the surface of the bed be exposed since it is on this surface that the area measurement of joint spacing is conducted (**Figure 24**). While the scanline measurement of spacing only takes into account the distances between individual joints that cross the scanline, the area measurement of spacing also considers the lengths of the joints.

The area mean spacing is calculated using the expression:

$$S_{area} = \frac{A}{l_0 + L} = \frac{A}{l_0 + \sum_{i=1}^{n} l_i}$$

where l_0 is the length of the side of the square measuring region shown in **Figure 25**, with an area $A = l_0^2$, l_i is the that part of the length of each individual joint (of which there are n) that is in the area A (**Figure 25**). Recall that the mean spacing along a scanline is given by:

$$S_{scanline} = \frac{l}{n+1}$$

where l is the length of the scanline and n is the number of joints intersecting the scanline.

Wu and Pollard (1995) also conducted jointing experiments on a square (100 mm by 100 mm) layer of brittle coating material (methylene chloride) that has been painted on the surface of a layer of polymethyl methacrylate (PMMA; **Figure 26**). This layer of PMMA is then subjected to four-point bending which applies a uniform extension strain on the brittle material. Area and scanline measurements of joint spacing in the layer of brittle material were made at different levels of strain. **Figure 25** could be thought of as the plan view of the entire area of the brittle coating with the smaller measurement area, A, inside it. Since the scanline mean spacing depends on the location of the scanline, this type of spacing was measured at different distances of the scanline from one side of a square area on the brittle coating. In **Figure 24** or **Figure 25**, for example, the scanlines would be located at increasing values of x. On the other hand, there is only one measurement of area joint mean spacing at each level of strain. However, the entire square area of brittle material is not used in the measurement of the area mean joint spacing because of edge effects (i.e., joints tend to be more concentrated at the edges). The authors found that an 80mm by 80mm square that neglected the edges was appropriate in their experiments.

At various levels of applied strain, both the area mean spacing and scanline mean spacing (at different scanline locations) were measured and compared (**Figure 27**). At low strains, when the joint set is still poorly developed (**Figure 28**), the scanline mean joint spacing fluctuates about the area mean joint spacing (recall that the scanline mean joint spacing varies with the location of the scanline). At high strains, when the joint set is well developed (**Figure 28**), both the scanline mean joint spacing and the area mean joint spacing decrease and become almost equal for the different scanline locations.

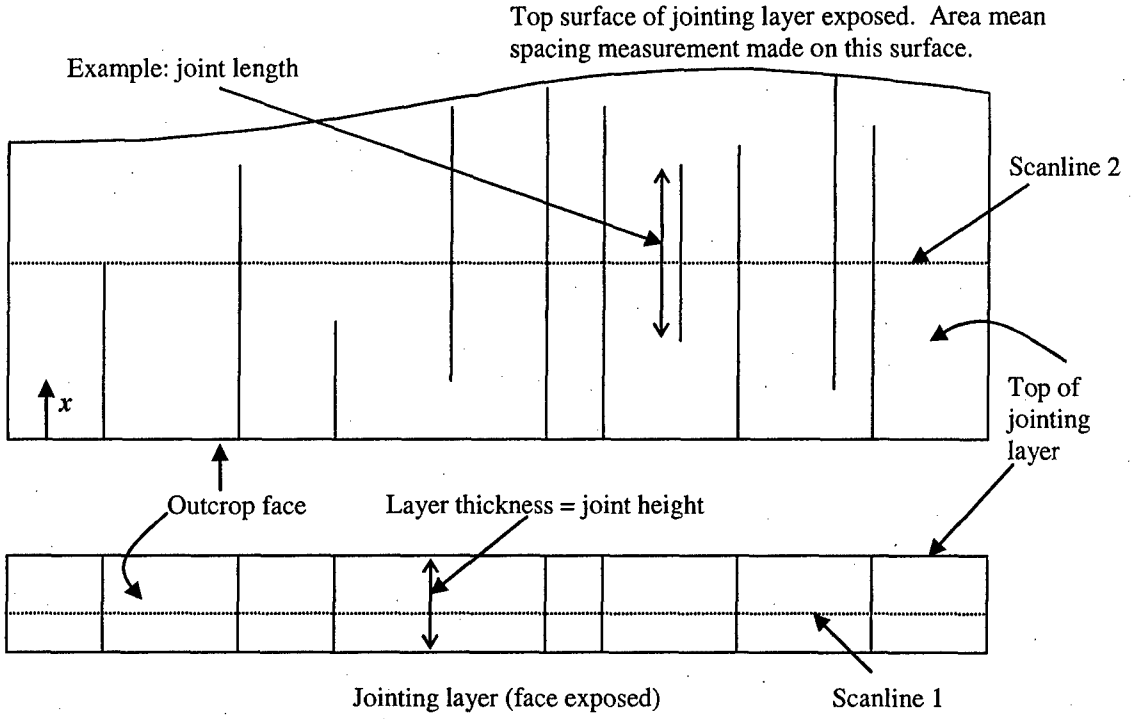


Figure 24 – Example of jointing layer with the faces exposed as well as its surface exposed. The top figure is the top surface of the ouctrop. The bottom figure is the exposed face of the outcrop.

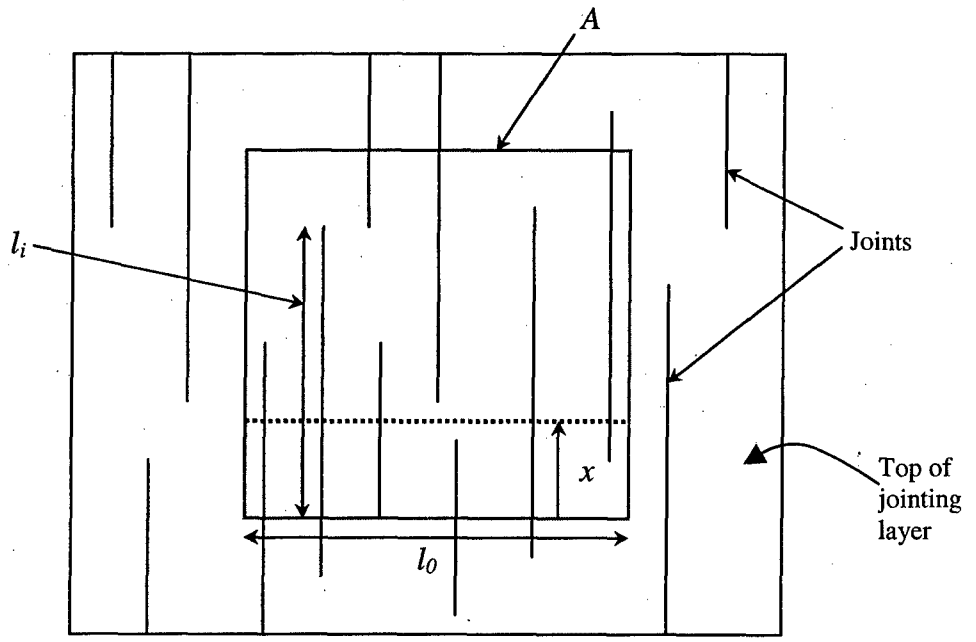


Figure 25 – Components for the calculation of the area mean spacing (Wu and Pollard, 1995).

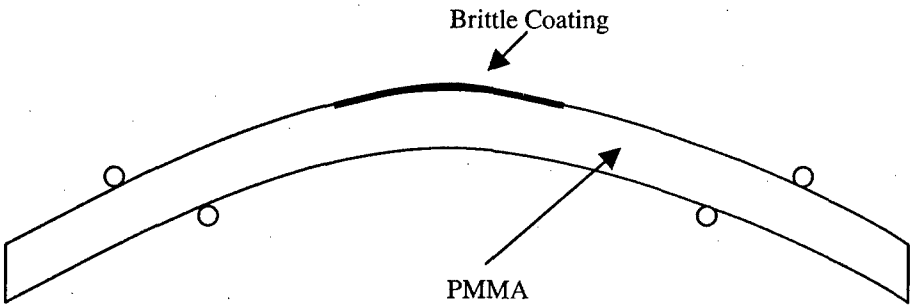


Figure 26 – Sketch of the experimental set-up for four-point bending in Wu and Pollard (1995). A constant radius of curvature is maintained so that uniform extension strain is applied to the brittle coating. Sketched from Fig. 3 (b) and Fig. 10 in Wu and Pollard (1995).

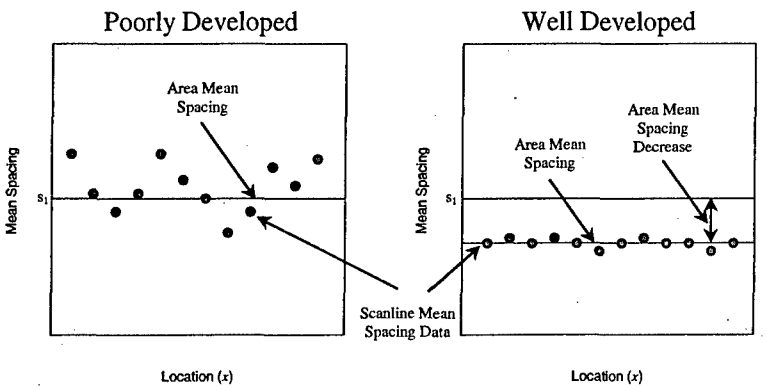


Figure 27 – Comparison between area mean joint spacing and scanline mean joint spacing at two levels of strain. The distance from one side of the measurement area (see Figure 25) to the scanline is varied. Sketched from Fig. 5 in Wu and Pollard (1995).

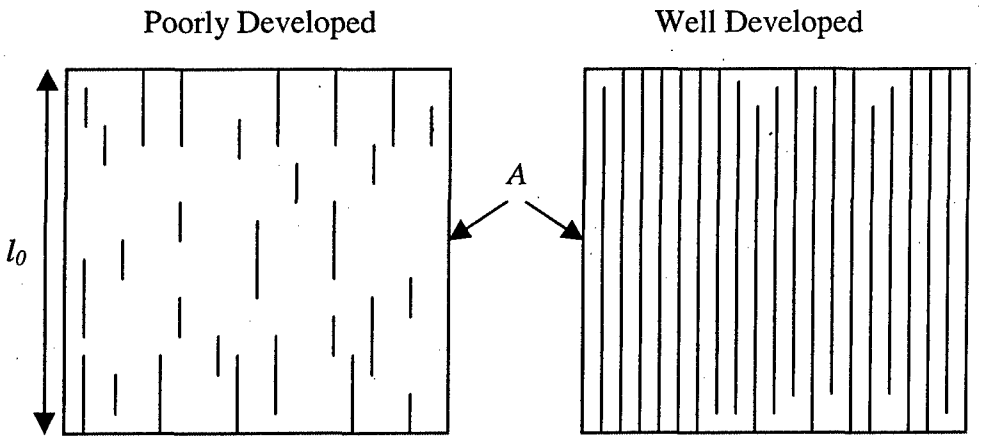


Figure 28 – Schematic of a poorly developed joint set and a well developed joint set relative to the area mean spacing measurement area *A*. Sketched from Fig. 5 in Wu and Pollard (1995).

In order to see why the scanline mean spacing values approach the area mean spacing measurement as the joint set develops, consider the equation for the area mean spacing.

As more and more strain is applied to the brittle coating, joint spacing decreases and the joints increase in length. At high strains, the joints approximately span the entire brittle layer (and the area of measurement, A). This means that the each l_i approaches l_0 (**Figure 28**) and the area mean spacing becomes

$$S_{area-sat} = \frac{A}{l_0 + \sum_{i=1}^{n} l_i} = \frac{l_0^2}{l_0 + nl_0} = \frac{l_0}{n+1}$$

When a scanline mean joint spacing measurement is taken on the area, A, its length will be l_0 and the above expression is exactly the scanline mean spacing.

The area mean joint spacing was plotted against strain level in order to see the mean joint spacing evolution (a schematic is shown in **Figure 29**). Wu and Pollard's (1995) results show that at strain levels below the saturation level, the mean joint spacing (area method) decreases rapidly as the strain is increased. This rapid decrease is followed by a sudden flattening of the curve (approximately constant mean spacing with increasing strain) suggesting that the saturation strain level has been reached (**Figure 29**). This constant spacing is then called the saturated mean spacing (scanline or area, it doesn't matter because they are almost equal at joint saturation as demonstrated above). Using different thickness values of the brittle coating (0.016 mm to 0.373 mm), the authors were able to construct a saturated mean spacing versus layer thickness relationship that showed what was expected: as thickness increases mean spacing also increases. However, one cannot make the brittle coating too thick since the assumption of uniform extensional strain over the thickness of the brittle coating would cease to apply.

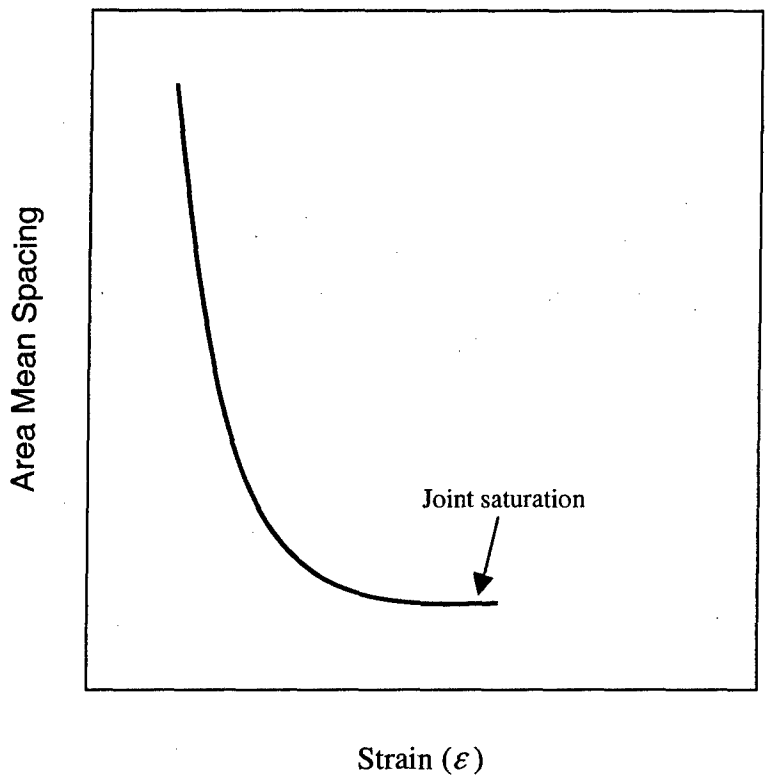


Figure 29 – Schematic of how the strain level affects the area mean spacing as observed in the experiments by Wu and Pollard (1995). Sketched from curves in Fig. 12 in Wu and Pollard (1995).

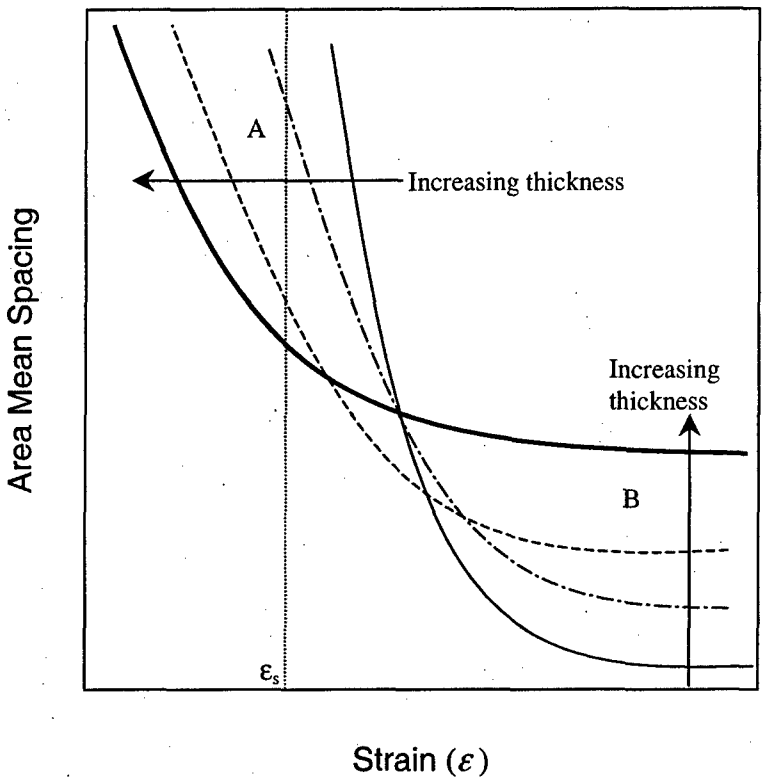


Figure 30 – A schematic of the curves Wu and Pollard (1995) used to fit their experimental data. Sketched from Fig. 12 (h) in Wu and Pollard (1995).

Figure 30 shows a schematic of the plot of area mean spacing versus applied strain obtained by Wu and Pollard (1995). The data points that the authors used to make the observation that the spacing increases as the layer thickness increases were taken from part B of the curves in **Figure 30** (i.e., at saturation). However, the authors did not mention that at lower strains (e.g., ε_s in **Figure 30**), the observation would be the reverse: spacing increases as layer thickness decreases for a given strain. This may have been a coincidence for this experiment but it is worth noting since no one has reported such an observation in the field data.

It must also be noted that the experimental set-up that Wu and Pollard (1995) used is quite different from what would result from an idealization of what is found in the field. In the field, the jointing layer is subjected to tractions on both the bottom and top surfaces. The authors' set-up has the layer's top surface free of tractions.

Based on their findings, the authors noted the following:

1. The area method of calculating the mean joint spacing is more desirable because it takes individual joint lengths into account in the calculation. However, this type of measurement also requires that the surface of the jointed layer be exposed. Also, for

a chosen size l_0 and location of the area A, this method gives a single value for mean spacing at each level of strain unlike the scanline mean spacing which is dependent on the scanline location at lower strain values.

2. The experiments show that at low strain levels, mean joint spacing decreases rapidly with increasing level of applied strain. This makes it unreasonable to compare mechanical properties between jointed layers because the amount of strain is difficult to quantify and the mean spacing is very sensitive to strain so that one is likely comparing two layers under different strain levels.

3. As the joint set develops, the decrease in joint spacing is accompanied by an increase in joint lengths.

4. At joint saturation, it is also difficult to quantify the amount of strain based on the mean joint spacing because beyond the saturation strain, mean spacing ceases to change. In other words, for a given layer, a wide range of strains can result in the same mean joint spacing.

5. If possible, an assessment of the level of strain should accompany joint spacing measurements.

From a practical point of view, one gets the impression that a comparison between the area mean joint spacing in an area A and the mean scanline spacing at various scanline locations in A can be used to determine the stage of joint set development. The more stable the scanline mean spacing values are (i.e., mean spacing does not vary much with location of the scanline) and the closer they are to the area mean spacing, the more developed the joint set is. Wu and Pollard's (1995) approach requires that the surface of the bed be exposed. If only the mean scanline spacing on the exposed face of the layer can be measured, their approach cannot be applied. Other authors proposed that the level of joint set development can also be determined from the type of joint spacing distribution.

Rives et al. (1992) observed how joint spacing distribution changes as the applied strain is increased (or as joint density increases) in laboratory experiments. These experiments subjected polystyrene plates, whose surfaces were treated with alcohol in order to form a brittle coating (the jointing layer), to four-point bending (**Figure 31**). A scanline was then used to measure joint spacing values (**Figure 32**) as the applied strain or the joint density increased.

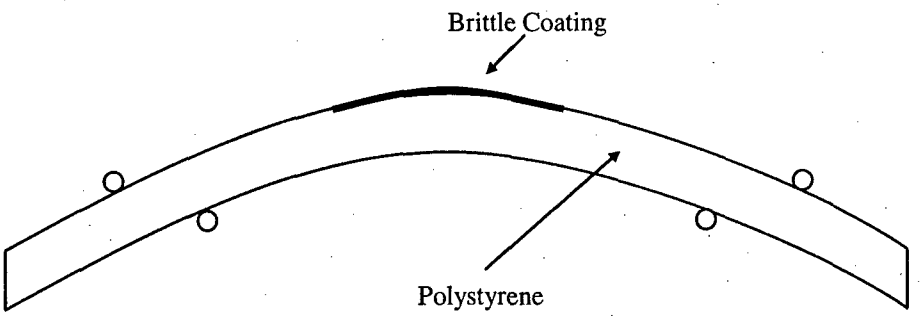


Figure 31 – Polystyrene plate subjected to four-point bending. Sketched from Fig. 5 in Rives et al. (1992).

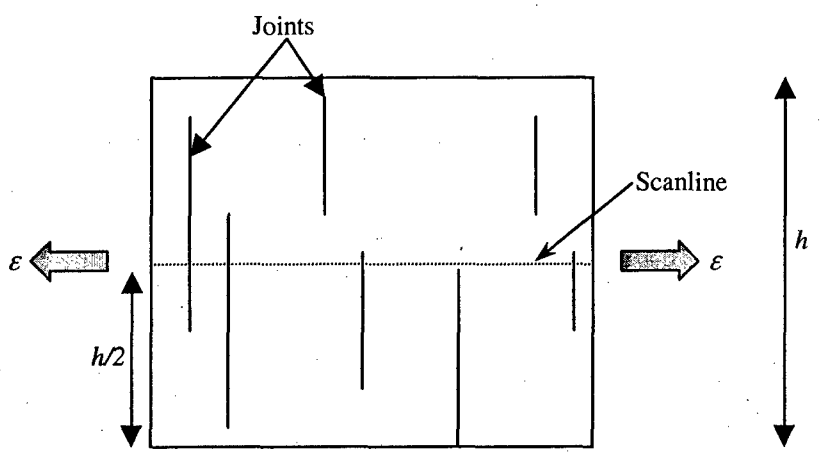


Figure 32 – Top view of the brittle coating and the location of the scanline. Sketched from Fig. 5 in Rives et al. (1992).

At low joint densities, they observed a shifted exponential distribution (terminology from Kottegoda and Rosso, 1998) for spacing; at intermediate joint densities log-normal distribution; and at high joint densities quasi-normal distribution (**Figure 33**). At low densities the locations of joints probably coincide with the locations of flaws or points of weakness in the rock. If these flaws are distributed randomly (i.e., Poisson points on a line), then it is easy to understand that the joint spacing would have a shifted exponential distribution. On the other hand, at high joint densities, the spacing values become more clustered and the distribution of spacing approaches a quasi-normal distribution. The authors suggested that the mode to mean joint spacing ratio be used to assess the level of joint set development (i.e., the level of applied strain). For an exponential distribution, this ratio would be low. Log-normal distributions would have intermediate mode/mean ratios while normal distributions would have mode/mean ratios close to one.

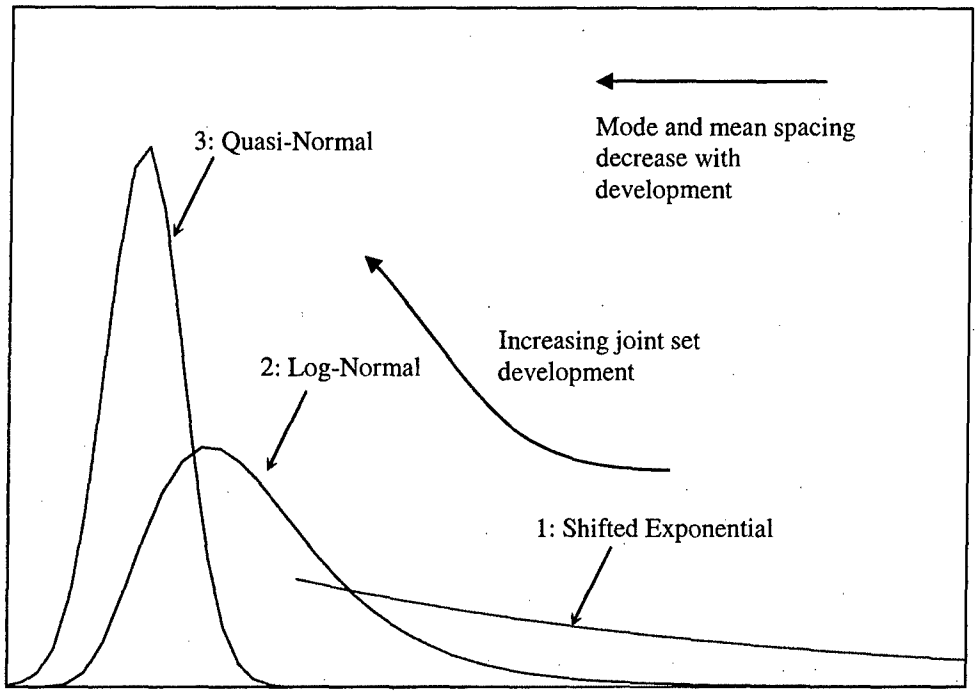


Figure 33 – A schematic of the evolution of the joint spacing distribution according to Rives et al. (1992). This figure follows Fig. 7 in Rives et al. (1992).

The main points that can be obtained from the laboratory experiments by Rives et al. (1992) and Wu and Pollard (1995) are the following:

1. Joint saturation can occur in brittle layers on a ductile substrate subjected to remote extension applied through bending. Sedimentary rock formations are deposited in a similar fashion: competent layers alternating with incompetent layers. It must be noted, however, that the application of tensile strain through bending of layers may not always occur in nature. Remote tension may also be caused by unloading (e.g., when the layers above are eroded). Net tensile strains may also occur in a direction perpendicular to maximum compressive stress.

2. The form of the joint spacing distribution may be linked to joint intensity. At low joint intensity, the joint spacing is shifted-exponential, log-normal at intermediate joint intensity and quasi-normal at high joint intensity.

2.3 Summary

From the field and laboratory observations found in the literature, the following points can be gleaned:

1. Joint spacing is related to layer thickness. Joint spacing is wider in thicker layers than it is in thinner layers. The relationship between layer thickness and joint spacing is widely accepted to be linear even though some researchers observed a non-linear relationship. Such a relationship appears to become invalid for very thick layers.

2. The bounding layer thickness may also affect joint spacing (Ladeira and Price, 1981). Ji et al. (1998) show that the tensile stress in the jointing layer is affected by the thickness of the non-jointing bounding layers. Thin non-jointing bounding layers lead to higher tensile stresses in the jointing layer than do thick non-jointing bounding layers given the same applied extensional strain. Higher stresses lead to more jointing and closer joint spacing.

3. The differing FSR, FSI or Fracture Index values for different rock types suggest that material properties also affect the relationship between layer thickness and joint spacing.

4. There is no single form of probability distribution that can describe the joint spacing distribution in layered sedimentary rock. This is evident from field data.

5. The form of the joint spacing distribution appears to depend on the level of joint set development. From laboratory experiments, the joint spacing distribution changes from a shifted exponential at low joint intensity, to log-normal at intermediate joint intensity, to quasi-normal distribution at high joint intensity.

6. The quasi-normal distribution of joint spacing observed in laboratory experiments (Rives et al., 1992) is never observed in the field. Practically speaking, this cannot be used to assess the level of joint set development.

7. Joint lengths are seldom fully observable in the field so the area mean spacing method for determining the level of joint set development is also of limited use (Wu and Pollard, 1995).

8. The FSI can only be used to describe the relationship between layer thickness and joint spacing in multiple "saturated" layers. At saturation, joint spacing does not change with increasing strain (see **Figure 29** and **Figure 30**). Below saturation, joint spacing is sensitive to strain (see **Figure 29** and **Figure 30**) so there is a greater chance that strains are different in different layers. It would be incorrect to obtain the FSI from combined mean or median spacing data from layers at different strain. The FSR or Fracture Index may be used to describe the relationship at any joint intensity since it considers only the median or mean spacing from a single layer.

The question now becomes how the jointing patterns from the observations described above could have been produced mechanically. In order to answer this question, focus must now turn towards models that could be used to describe the stresses in such a geologic setting. The stress distribution could help in the development of a jointing process which, in turn, may lead to an explanation for the observations (especially about the joint spacing distribution) made above.

3 Stress Distribution Models

A joint, by definition, has two stress-free surfaces. The stress field is altered by the formation of a joint and it is important to determine the physical extent of such an alteration because it may determine where subsequent joints can form. Such a stress field alteration is termed a "stress reduction shadow" after Gross et al. (1995) (**Figure 34**). Particularly in sedimentary rock layers subjected to extensional strain in the direction parallel to bedding, the normal stress (initially tensile) at the location of a joint is reduced to zero. It seems reasonable to assume that a non-cohesive joint will be unable to transmit tensile stresses. In this chapter, two tensile stress distribution models found in the literature are presented: Hobbs' (1967) model in section **3.1**; Ji and Saruwatari's (1998) model in section **3.2**. These sections mostly detail the derivation of the tensile stress distribution in each model. A brief analysis is included in each section after the derivation. All the graphs in this chapter are not from the references and were produced independently for the purpose of the analyses.

3.1 Hobbs' (1967) Simplified Model

3.1.1 Tensile Stress Distribution: Single Joint

The simplest and most cited theoretical derivation of the extent of the stress shadow is that by Hobbs (1967). Essentially, Hobbs' model consists of a 'jointing layer' sandwiched between two 'non-jointing layers' (**Figure 35**). The jointing layer usually has higher stiffness than the bounding non-jointing layers (i.e., $E_f = E_{jointing} > E_n = E_{non\text{-}jointing}$). Perfect bonding is assumed at the interfaces (i.e., no relative displacement at the interfaces). The entire system is then subjected to an extensional strain, ε. The layers are assumed to be linear elastic and, furthermore, it is also assumed that $\sigma = E\varepsilon$.

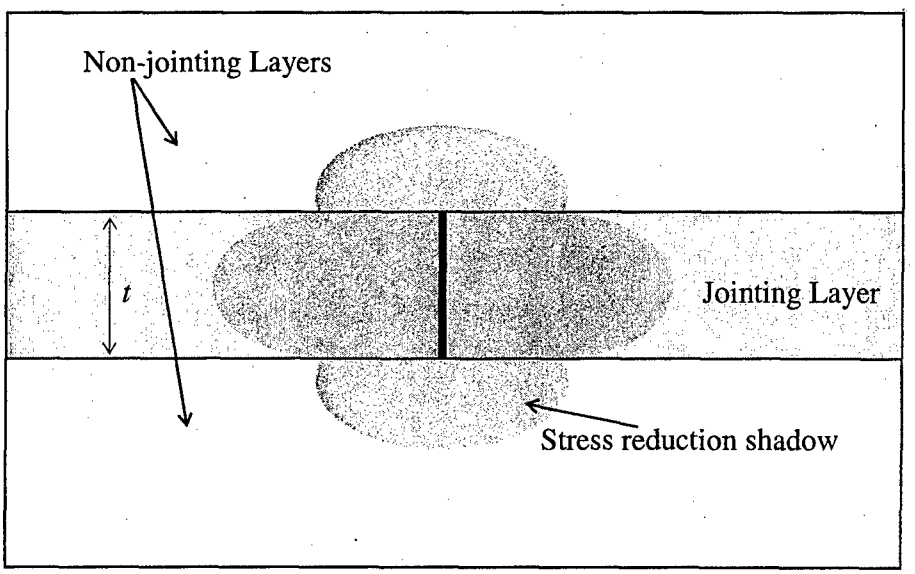


Figure 34 – Illustration of an idealized stress reduction shadow. Inside the shadow, the stresses are perturbed by the presence of the joint.

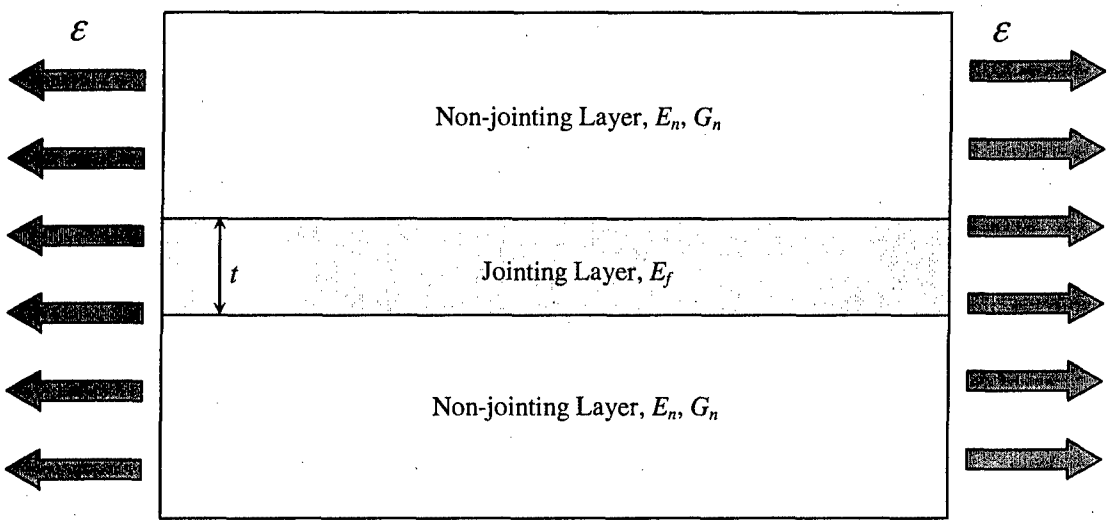


Figure 35 – Jointing layer sandwiched between two non-jointing layers. All layers are subjected to an equal amount of strain, ε.

The jointing layer has a thickness t and Young's modulus E_f and the non-jointing layers have a shear modulus of G_n. An additional assumption is that the thicknesses of the non-jointing beds are greater than that of the jointing bed. This requirement has to do with the shear stress distribution in the system when the joint is formed. When the strain reaches ε_l (the strain that causes the normal stress in the jointing layer to exceed the tensile strength of the rock), a joint is formed (**Figure 36**). Shear stresses are produced within the bounding beds as a direct result of differences in elastic displacement between the jointing bed and bounding beds (Gross et al., 1995). This means that due to the presence of the joint, the displacement of the non-jointing layer at the interface would be different from the displacement a distance away from the interface. Hobbs (1967) assumed that the shear stress is a maximum at the layer interface and decreases linearly to zero in the non-jointing beds, a distance equal to the thickness of the jointing layer (thus the requirement that the non-jointing layer has to be at least as thick as the jointing layer). The layer parallel stress now becomes a function of the distance, x, away from the joint because at the joint there has to be a reduction to zero stress and an infinite distance away from the joint the far field stress must exist.

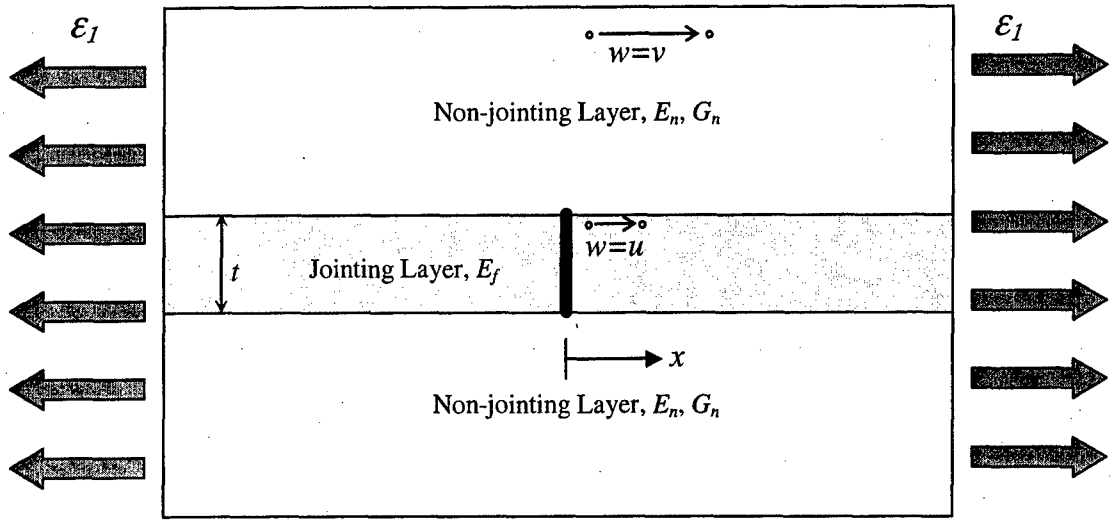


Figure 36 – Formation of joint in jointing layer induces stress change in the vicinity of the joint. Note that v is the displacement at a point that is far enough from the jointing layer such that it has not been affected by the formation of the joint.

In order to calculate the force in the jointed layer, Hobbs (1967) employs the "shear-lag" model by Cox (1952):

$$\frac{dP}{dx} = 2C(u - v) \qquad \textbf{Equation 1}$$

where P is the load or force in the layer in the direction parallel to the strain direction, u is the displacement in the bed with a single joint, v is the displacement in the neighboring beds prior to the formation of the single joint (**Figure 36**), w is the variable that represents the displacement as it varies away from the interface and C is a constant. Differentiating the above expression once gives

$$\frac{d^2P}{dx^2} = 2C\left(\frac{du}{dx} - \frac{dv}{dx}\right) \qquad \textbf{Equation 2}$$

Since v is the displacement in the neighboring beds just before the formation of a single joint, $\frac{dv}{dx}$ must be equal to ε_1, the strain in all the layers just before joint formation. Substitution yields

$$\frac{d^2P}{dx^2} = 2C\left(\frac{du}{dx} - \varepsilon_1\right) \qquad \textbf{Equation 3}$$

In terms of the normal strain, the load can be expressed as:

$$P = E_f t \frac{du}{dx}$$ **Equation 4**

Combining **Equation 3** and **Equation 4** gives

$$\frac{d^2P}{dx^2} = \frac{2C}{E_f t}\left(P - E_f t \varepsilon_1\right)$$ **Equation 5**

The solution to the above differential equation is

$$P = E_f t \varepsilon_1 + A \sinh Dx + B \cosh Dx$$ **Equation 6**

where

$$D = \sqrt{\frac{2C}{E_f t}}$$ **Equation 7**

In order to work with stresses, the load P must be divided by the thickness of the layer, t.

$$\sigma_{local} = E_f \varepsilon_1 + \frac{A}{t} \sinh Dx + \frac{B}{t} \cosh Dx$$ **Equation 8**

where σ_{local} is the normal stress at some distance x away from the joint. For the case of a single joint, the stress distribution a distance away from the joint can be determined. One only needs to find the constants A, B and D. The first two can be found by applying the boundary conditions: at $x = 0$, $\sigma_{local} = 0$ and $x \to \infty$, $\sigma_{local} = \sigma_{farfield} = E_f \varepsilon_1$. The first boundary condition leads to the equation below:

$$0 = E_f \varepsilon_1 + \frac{A}{t} \sinh(0) + \frac{B}{t} \cosh(0) = E_f \varepsilon_1 + \frac{B}{t}$$ **Equation 9**

For the second boundary condition, both sides of the equation are divided by $\cosh Dx$ to obtain the following:

$$\frac{\sigma_{local}}{\cosh Dx} = \frac{E_f \varepsilon_1}{\cosh Dx} + \frac{A}{t} \frac{\sinh Dx}{\cosh Dx} + \frac{B}{t}$$ **Equation 10**

Applying the second boundary condition and realizing that $\sigma_{local} = \sigma_{farfield} = E_f \varepsilon_1$ as $x \to \infty$ and $\lim_{x \to \infty} \frac{\sinh Dx}{\cosh Dx} = 1$, **Equation 10** becomes

$$\frac{A}{t}+\frac{B}{t}=0$$

or

$$\frac{A}{t}=-\frac{B}{t} \qquad \textbf{Equation 11}$$

These equations (**Equation 9** and **Equation 11**) give the following:

$$\frac{A}{t}=E_f\varepsilon_1 \qquad \textbf{Equation 12}$$

and

$$\frac{B}{t}=-E_f\varepsilon_1 \qquad \textbf{Equation 13}$$

Substituting these back into the expression for the local stress yields

$$\sigma_{local}=E_f\varepsilon_1(1+\sinh Dx-\cosh Dx) \qquad \textbf{Equation 14}$$

The constant D must also be found. Using equilibrium of forces for the loads acting on a slice of the jointing layer shown in **Figure 37**, one obtains

$$\frac{dP}{dx}=-2\tau_d \qquad \textbf{Equation 15}$$

where τ_d is the shear stress acting along the interface.

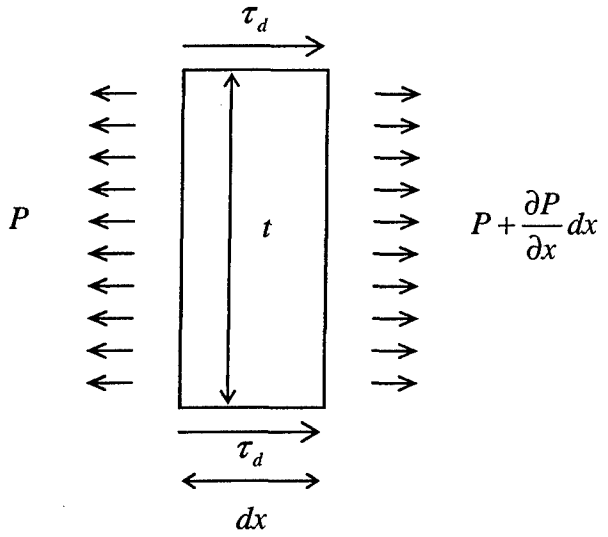


Figure 37 – Forces acting on a slice of the jointing layer.

Recalling Cox's (1952) shear-lag model,

$$\frac{dP}{dx} = 2C(u-v) \qquad \textbf{Equation 1}$$

and combining the two expressions for $\frac{dP}{dx}$ (**Equation 1** and **Equation 15**) yields

$$C = \frac{-\tau_d}{(u-v)} \qquad \textbf{Equation 16}$$

An assumption must now be made regarding the variation of the shear stress in the non-jointing layers. Hobbs assumed a linear variation with a maximum value of τ_d at the interface ($y=0$) and zero at a distance t from the interface ($y=t$) or

$$\tau = \tau_d\left(\frac{t-y}{t}\right) \qquad \textbf{Equation 17}$$

Let w be the displacement in the non-jointing layers due to the extension. At the interface ($y=0$) w is equal to u. At a distance t from the interface ($y=t$), w is equal to v (**Figure 36**). Using the definition of shear strain, the following is obtained:

$$\frac{dw}{dy} = \frac{\tau}{G_n} = \frac{\tau_d}{G_n}\left(\frac{t-y}{t}\right) \qquad \textbf{Equation 18}$$

The quantity $v-u$ can then be calculated from **Equation 18**.

$$v-u=\Delta w=\int_0^t \frac{\tau_d}{G_n}\left(\frac{t-y}{t}\right)dy=\frac{\tau_d}{G_n}\frac{t}{2}$$

Substituting the above result into $C=\frac{-\tau_d}{(u-v)}$ **(Equation 16)** yields

$$C=\frac{2G_n}{t} \qquad \textbf{Equation 19}$$

and since $D=\sqrt{\frac{2C}{E_f t}}$ **(Equation 7)**, the following equation results

$$D=\frac{2}{t}\sqrt{\frac{G_n}{E_f}} \qquad \textbf{Equation 20}$$

Substituting **Equation 20** into **Equation 14** gives the expression for the local tensile stress.

$$\sigma_{local}=E_f\varepsilon_1\left(1+\sinh\sqrt{\frac{G_n}{E_f}}\frac{2x}{t}-\cosh\sqrt{\frac{G_n}{E_f}}\frac{2x}{t}\right) \qquad \textbf{Equation 21a}$$

or

$$\frac{\sigma_{local}}{\sigma_{farfield}}=1+\sinh\sqrt{\frac{G_n}{E_f}}\frac{2x}{t}-\cosh\sqrt{\frac{G_n}{E_f}}\frac{2x}{t} \qquad \textbf{Equation 21b}$$

Figure 38 shows how the normalized stress **(Equation 21b)** varies with normalized distance away from a joint. It can be observed that with this model, the extent of the stress reduction shadow increases with increasing $\frac{E_f}{G_n}$ ratio or increasing relative stiffness of the jointing layer to the non-jointing layers.

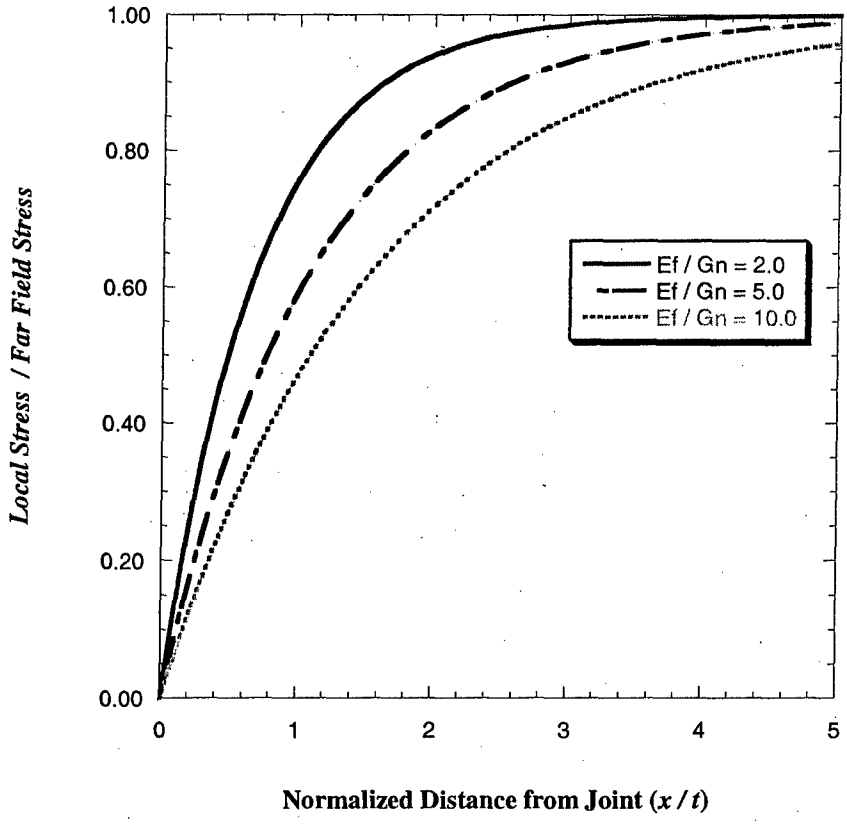


Figure 38 – Variation of normalized stress ($\frac{\sigma_{local}}{\sigma_{farfield}}$) with distance away from a joint using different $^{E_f}/_{G_n}$ ratios. Curves were constructed using Equation 21b.

Figure 39 shows how the shear stress at the interface (i.e., $\tau_d = \tau_d(x)$) varies with distance from the joint (**Figure 40** shows a schematic of the interface shear stress) in the cases shown in **Figure 38**. Larger $^{E_f}/_{G_n}$ ratios result in lower normalized shear stresses at the interface (**Figure 39**).

In **Figure 38**, the normalized local (tensile) stress at some distance $\frac{x}{t}$ is given by $\frac{\sigma_{local}}{\sigma_{farfield}} = \frac{P}{\sigma_{farfield} t} = -\int 2 \cdot \frac{\tau_d}{\sigma_{farfield}} \cdot d\left(\frac{x}{t}\right)$ (from equilibrium of forces in **Figure 37**, see also **Equation 15**) and is smaller for high $^{E_f}/_{G_n}$ ratios than for low $^{E_f}/_{G_n}$ ratios. Although it is not readily apparent in **Figure 39**, it follows that the area, $-\int \frac{\tau_d}{\sigma_{farfield}} \cdot d\left(\frac{x}{t}\right)$, between $\frac{x}{t} = 0$ and some $\frac{x}{t} > 0$ is always smaller for high $^{E_f}/_{G_n}$ ratios than for low $^{E_f}/_{G_n}$ ratios (note that $\frac{\tau_d}{\sigma_{farfield}} = \frac{\tau_d(x)}{\sigma_{farfield}}$ is negative in **Figure 39**).

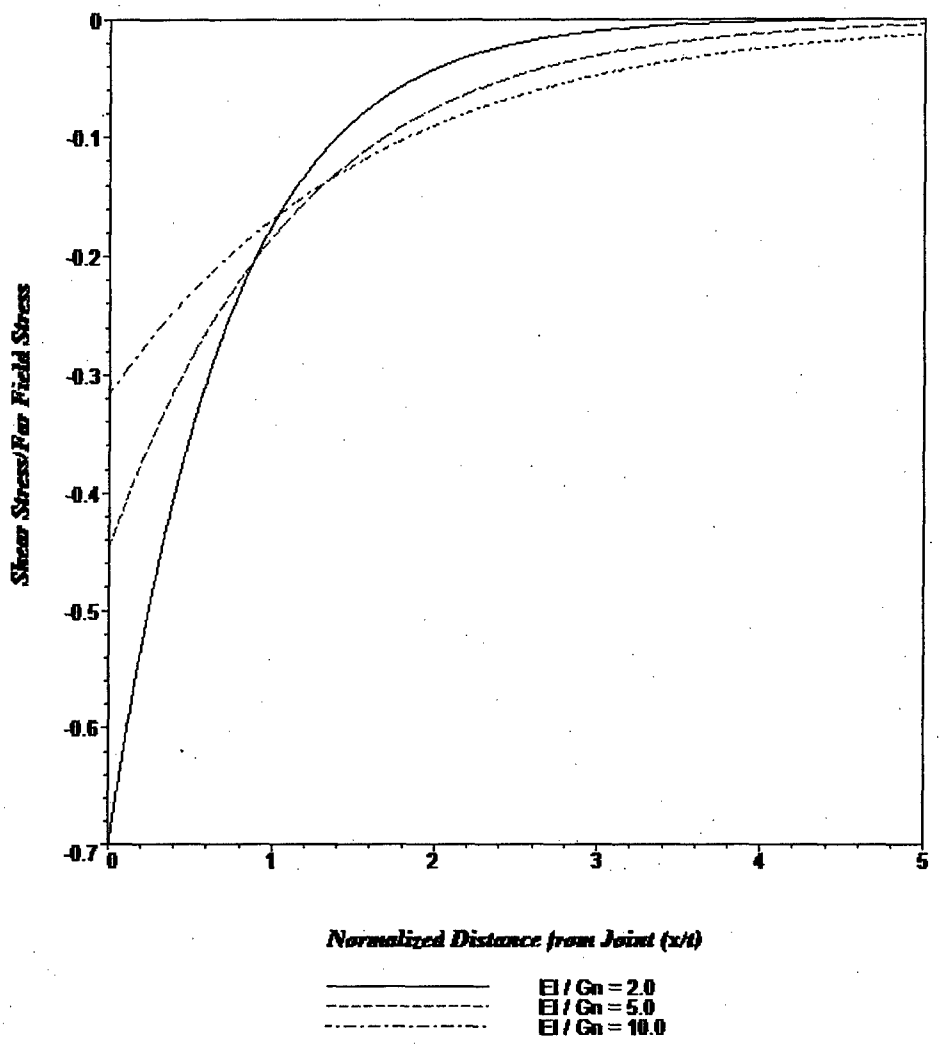


Figure 39 – Variation of normalized shear stress ($\frac{\tau_d}{\sigma_{farfield}}$) with distance away from a joint using different E_f/G_n ratios.

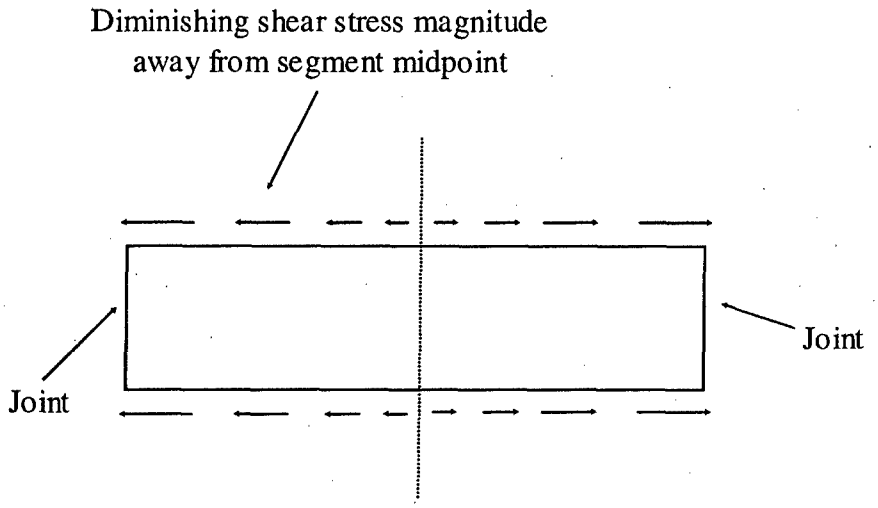


Figure 40 – Variation and direction of interface shear stress away from segment midpoint.

3.1.2 Tensile Stress Distribution: Two Joints

It is also important to look at the stress distribution that exists in the region between two adjacent joints a distance (or spacing) L apart when the applied strain reaches ε_2 ($> \varepsilon_1$). The same solution as the single joint case is applicable (**Equation 8**):

$$\sigma_{local} = E_f \varepsilon_2 + \frac{A}{t}\sinh Dx + \frac{B}{t}\cosh Dx$$

However, different boundary conditions must be applied to solve for the constants A and B. The origin is now taken to be the midpoint of the segment that is L units long formed by two adjacent joints (**Figure 41**). Specifically, the boundary conditions are

$$\sigma_{local} = 0 \text{ at } x = -\frac{L}{2} \text{ and } x = \frac{L}{2}$$

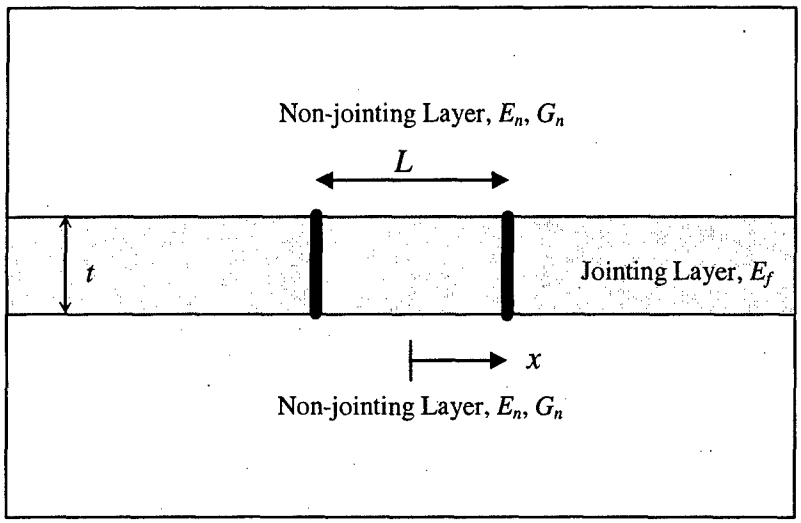


Figure 41 – Definition of variables for Hobbs' model of the stress reduction shadow interaction of adjacent joints.

Applying the boundary conditions yields the following equations

$$0 = E_f \varepsilon_2 - \frac{A}{t}\sinh D\frac{L}{2} + \frac{B}{t}\cosh D\frac{L}{2} \qquad \textbf{Equation 22}$$

$$0 = E_f \varepsilon_2 + \frac{A}{t}\sinh D\frac{L}{2} + \frac{B}{t}\cosh D\frac{L}{2} \qquad \textbf{Equation 23}$$

Adding the two equations above gives

$$\frac{B}{t} = -\frac{E_f \varepsilon_2}{\cosh\frac{DL}{2}} \qquad \textbf{Equation 24}$$

and $\frac{A}{t}$ is found to be zero. With the constant D the same as before, substitution yields

$$\sigma_{local} = E_f \varepsilon_2 \left[1 - \frac{\cosh\left(2\frac{x}{t}\sqrt{\frac{G_n}{E_f}}\right)}{\cosh\left(\frac{2}{t}\sqrt{\frac{G_n}{E_f}}\frac{L}{2}\right)}\right] \qquad \textbf{Equation 25}$$

With $m = \frac{x}{t}$, $l = \frac{L}{t}$ and $\sigma_{farfield} = E_f \varepsilon_2$, the above equation becomes

$$\frac{\sigma_{local}}{\sigma_{farfield}} = 1 - \frac{\cosh\left(2m\sqrt{\frac{G_n}{E_f}}\right)}{\cosh\left(\sqrt{\frac{G_n}{E_f}}l\right)}$$

Equation 26

The variable $m = \frac{x}{t}$ varies from $-\frac{l}{2}$ to $+\frac{l}{2}$ where $l = \frac{L}{t}$.

Figure 42 shows how the normal stress varies between two joints according to Hobbs' (1967) model. Three different values of $^{E_f}/_{G_n}$ ratios are used and $l = \frac{L}{t} = 1.0$. **Figure 42** reveals that higher values of $^{E_f}/_{G_n}$ lead to lower peaks in the stress distribution.

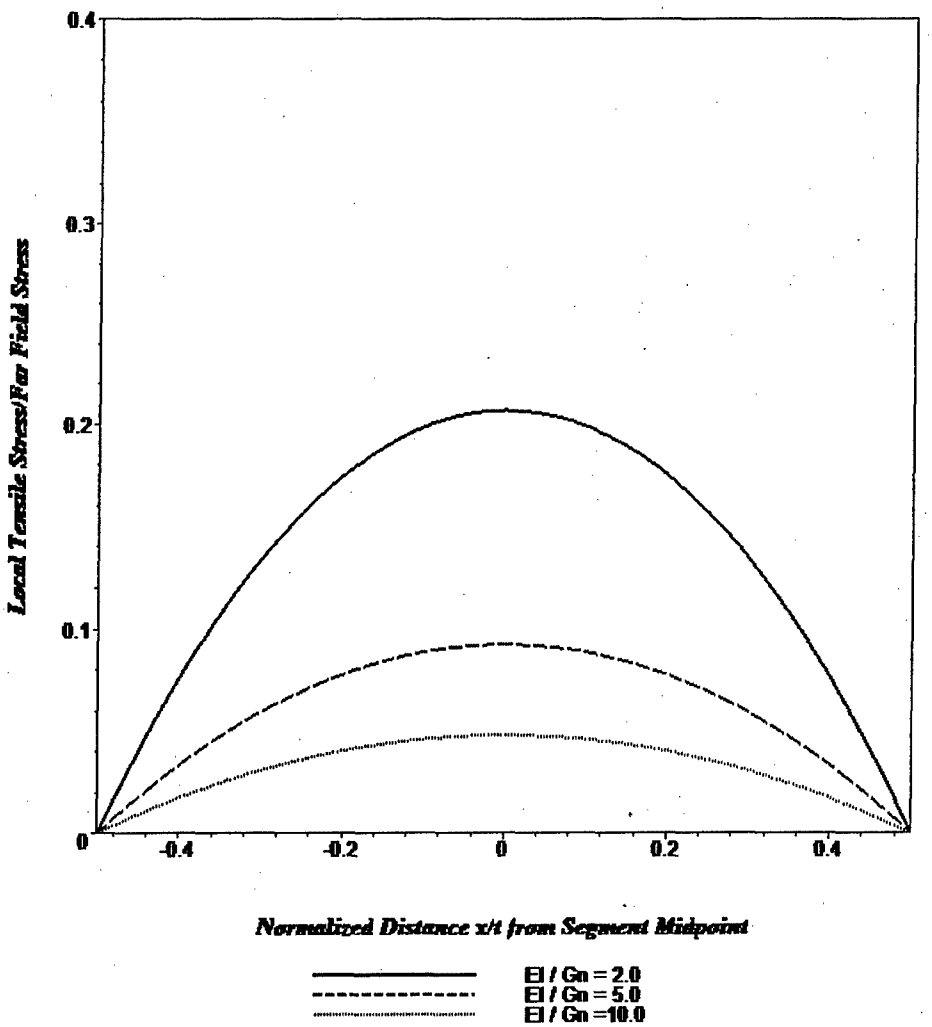


Figure 42 – Stress ratio distribution between adjacent joints according to Hobbs' (1967) model with $l = 1.0$ for $^{E_f}/_{G_n} = 2, 5$ and 10.

In order to understand this trend, consider the shear stress distribution along the interface between the jointing layer and one of the non-jointing layers. Recall the equation relating the load to the shear stress (see **Equation 15** and **Figure 37**):

$$\frac{dP}{dx} = -2\tau_d \qquad \textbf{Equation 15}$$

Making the substitution $P = t \cdot \sigma_{local}$ and solving for τ_d leads to

$$\tau_d = -\frac{t}{2} \cdot \frac{d\sigma_{local}}{dx} \qquad \textbf{Equation 27}$$

Substituting the expression for σ_{local} (**Equation 25**), the shear stress distribution is obtained as

$$\tau_d = -\frac{t}{2} E_f \varepsilon_2 \left[-\frac{2}{t}\sqrt{\frac{G_n}{E_f}} \frac{\sinh\left(2\frac{x}{t}\sqrt{\frac{G_n}{E_f}}\right)}{\cosh\left(\frac{2}{t}\sqrt{\frac{G_n}{E_f}}\frac{L}{2}\right)} \right] = E_f \varepsilon_2 \left[\sqrt{\frac{G_n}{E_f}} \frac{\sinh\left(2\frac{x}{t}\sqrt{\frac{G_n}{E_f}}\right)}{\cosh\left(\frac{2}{t}\sqrt{\frac{G_n}{E_f}}\frac{L}{2}\right)} \right] \qquad \textbf{Equation 28}$$

With $m = \frac{x}{t}$, $l = \frac{L}{t}$ and $\sigma_{farfield} = E_f \varepsilon_2$, the normalized shear stress is given by

$$\frac{\tau_d}{E_f \varepsilon_2} = \frac{\tau_d}{\sigma_{farfield}} = \left[\sqrt{\frac{G_n}{E_f}} \frac{\sinh\left(2m\sqrt{\frac{G_n}{E_f}}\right)}{\cosh\left(\sqrt{\frac{G_n}{E_f}}l\right)} \right] \qquad \textbf{Equation 29}$$

Figure 43 shows how the shear stress varies with distance from the segment midpoint for three different values of E_f/G_n and $l = 1.0$. The maximum absolute shear stresses occur near the locations of the joints (the shear stress should be zero at the joint locations because it needs to shift to the opposite direction once it crosses the joint). It can be seen that as E_f/G_n increases, the maximum absolute shear stresses decrease. This makes sense because larger E_f/G_n ratios mean relatively smaller G_n values which, given some value of strain, would lead to smaller shear stresses. Consequently, since the normal stress σ_{local} at a point is related to the area under the shear stress distribution up to that point (i.e.,

$\sigma_{local} = -\int \frac{2}{t} \tau_d \cdot dx$), lower shear stresses (caused by lower G_n) lead to lower peaks in the normal stress distribution as observed in **Figure 42**.

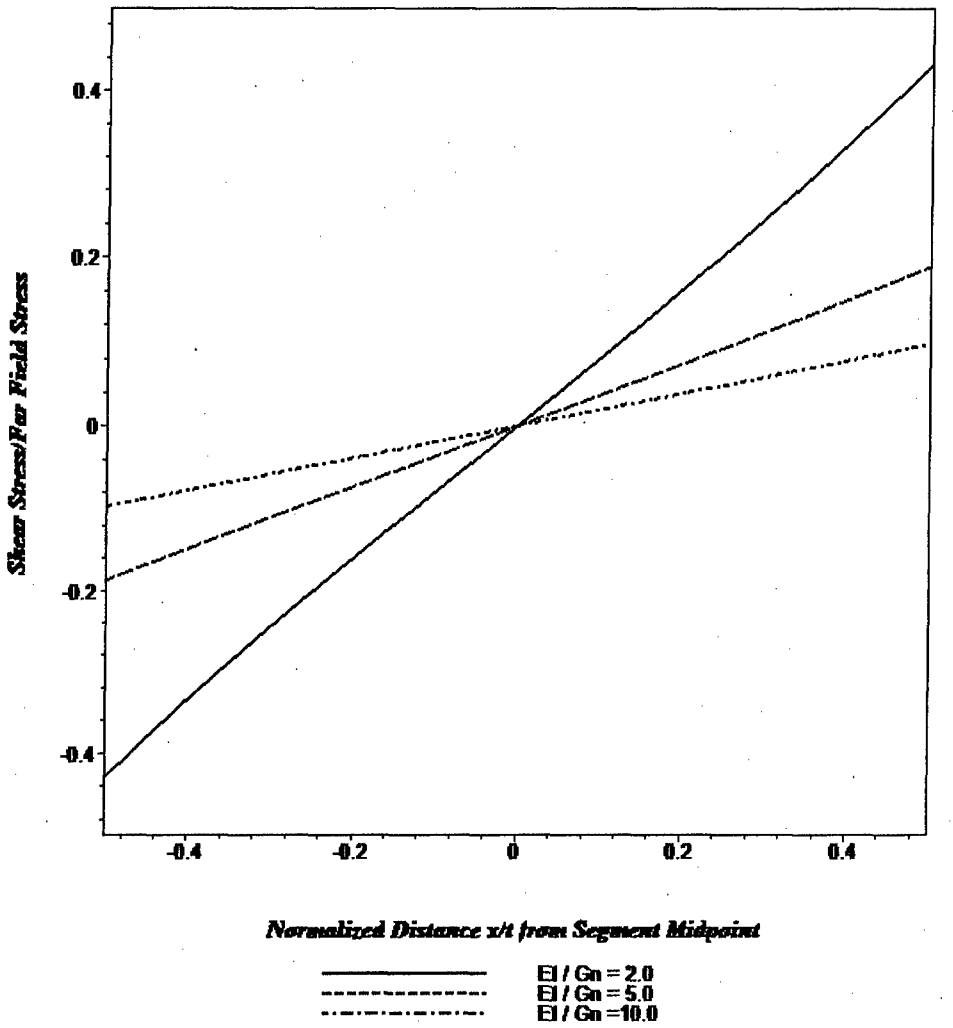


Figure 43 – Normalized shear stress along an interface in Hobbs' (1967) model for $l = 1.0$ for E_f/G_n =2, 5 and 10.

Figure 44 shows how the spacing between joints (or the length of a segment, *L*) affects the stress distribution. The longer segments develop stresses nearer to the remote stress value than do the shorter segments simply because a larger total shear force acts on the interfaces of longer segments given the same applied strain and rock properties (area under the curves in **Figure 45**).

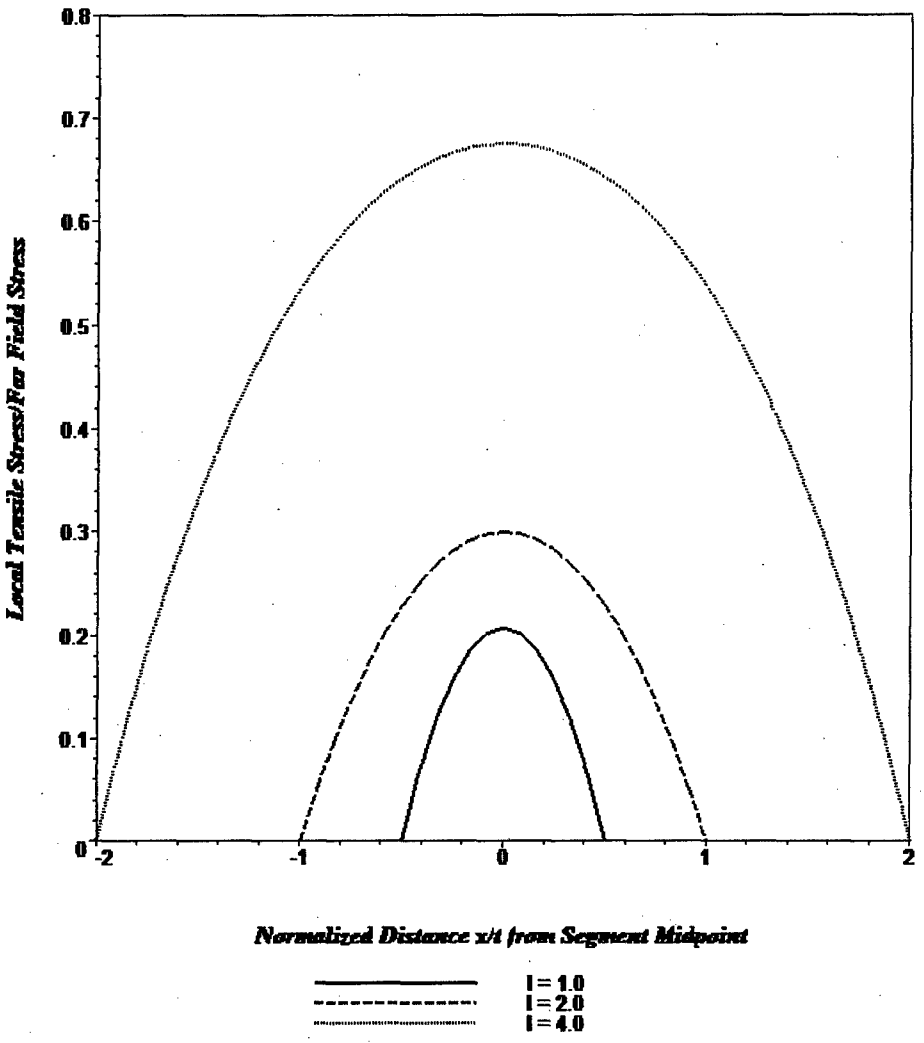


Figure 44 – Stress ratio distribution between two joints with different spacings (l = 1, 2 and 4) using a single value of E_f/G_n = 5.0.

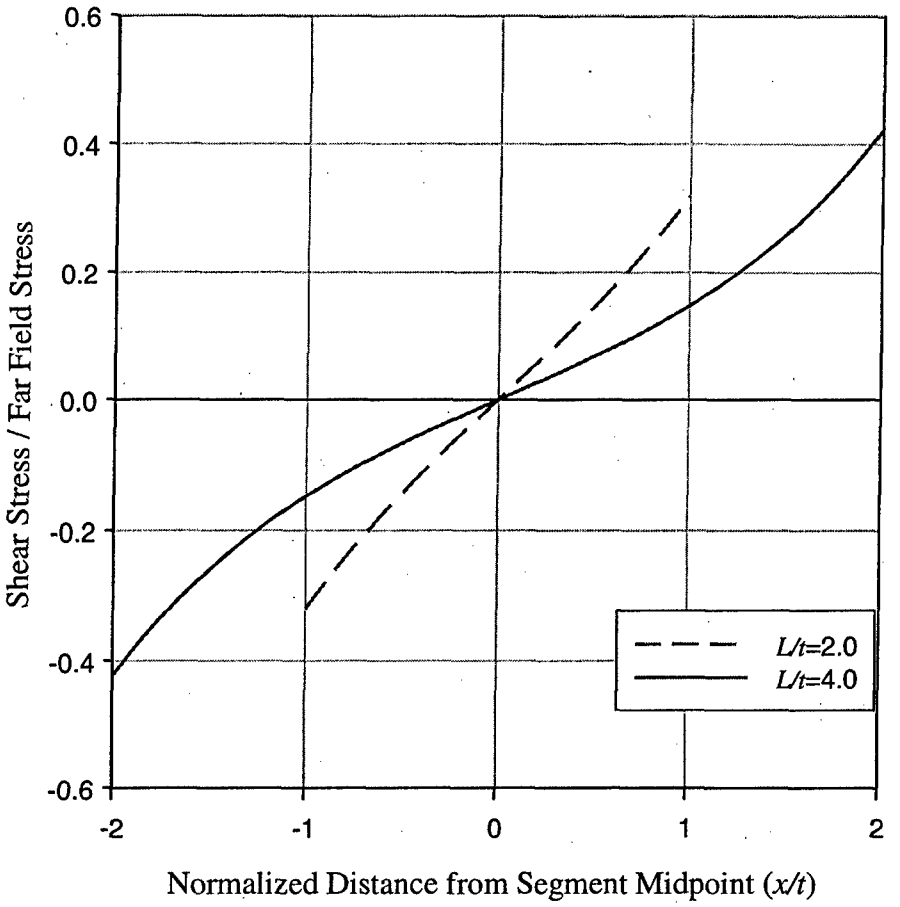


Figure 45 – Normalized shear distribution for two segments of different length but the same properties ($E_f/G_n = 5.0$) and applied strain.

Using the stress distribution (**Equation 25**), Hobbs (1967) also calculated the joint spacing corresponding to a specific amount of applied strain (e.g., some $\varepsilon_2 > \varepsilon_1$). The maximum local stress occurs at the midpoint of the segment (i.e., $m = \frac{x}{t} = 0$) and is given by:

$$\sigma_{local}(m=0) = \sigma_{local-\max} = E_f \varepsilon_2 \left(1 - \frac{1}{\cosh\left(\sqrt{\frac{G_n}{E_f}} l \right)} \right) \qquad \textbf{Equation 30}$$

Jointing occurs at $m = \frac{x}{t} = 0$ when $\sigma_{local-\max} = E_f \varepsilon_1$ (i.e., the tensile strength of the layer) so that

$$E_f \varepsilon_1 = E_f \varepsilon_2 \left(1 - \frac{1}{\cosh\left(\sqrt{\frac{G_n}{E_f}} l \right)} \right) \qquad \textbf{Equation 31}$$

Solving for l yields the following

$$l = \frac{L}{t} = \sqrt{\frac{E_f}{G_n}} \cosh^{-1}\left(\frac{\varepsilon_2}{\varepsilon_2 - \varepsilon_1} \right) \qquad \textbf{Equation 32}$$

or

$$L = t\sqrt{\frac{E_f}{G_n}} \cosh^{-1}\left(\frac{\varepsilon_2}{\varepsilon_2 - \varepsilon_1} \right) \qquad \textbf{Equation 33}$$

This means that at an applied strain equal to ε_2, segments formed by joints that are exactly L units apart will develop a normal stress that approaches the cracking stress at their midpoints. It follows that the spacing at this level of strain could either be L (if segments do not break) or $\frac{L}{2}$ units long (if segments do break). **Figure 46** shows the relationship between normalized spacing ($\frac{L}{t}$) and applied strain. Three values of E_f/G_n are used. The normalized spacing in **Figure 46** indicates the smallest length a segment formed by two adjacent joints should have in order to produce a normal stress at its midpoint that is equal to the tensile strength of the rock at a given applied strain according to Hobbs' (1967) model.

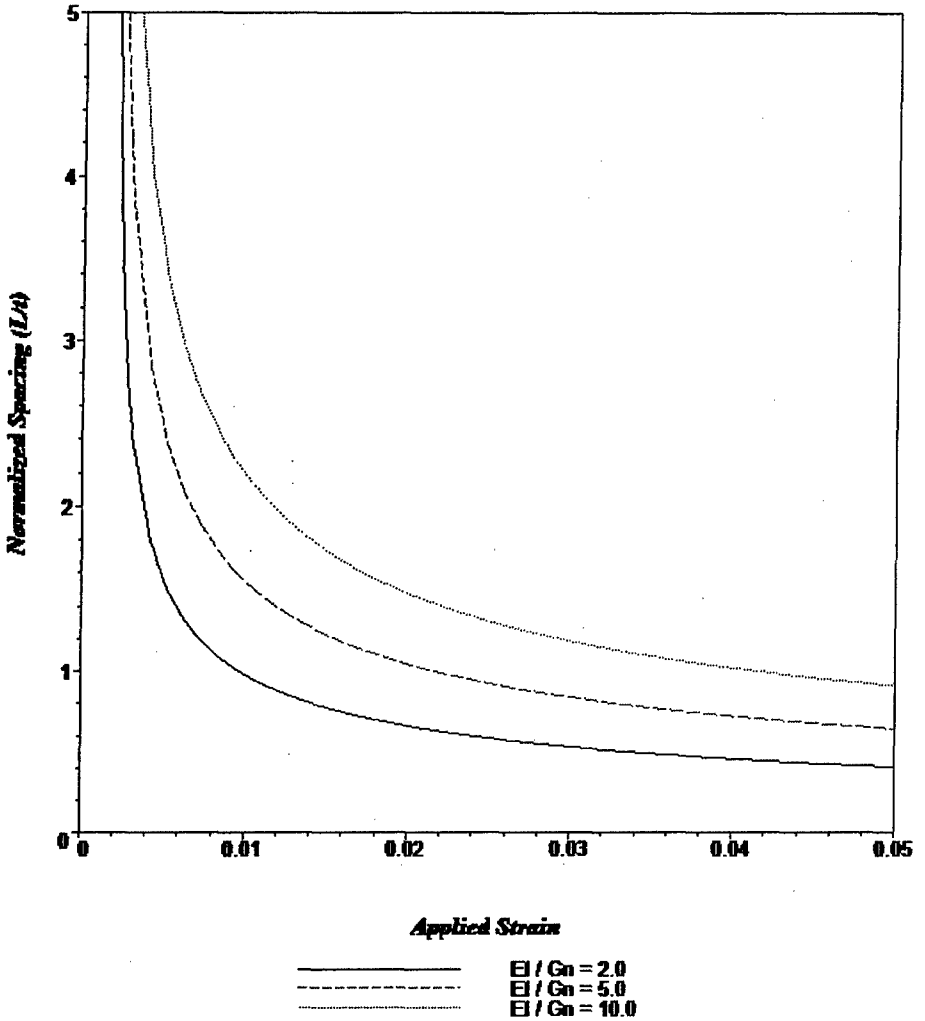


Figure 46 – Relationship between applied strain (ε_2) and normalized spacing according to Hobbs' (1967) model for different $^{E_l}/_{G_n}$ ratios. Note that t is the jointing layer thickness. The normalized spacing here is the smallest normalized length a segment formed by two adjacent joints should have in order to produce a normal stress at its midpoint equal to the tensile strength of the rock given the corresponding applied strain.

3.2 Ji and Saruwatari's (1998) Simplified Model

3.2.1 Tensile Stress Distribution: Two Joints

Ji and Saruwatari (1998) used a modified Hobbs' (1967) model to describe the stress distribution in the region between two joints. The main modification involves the assumption of a different shear stress distribution in the non-jointing layers. Recall that Hobbs (1967) assumed a linear decay in the shear stress away from the interface into the non-jointing layers. Also, Hobbs (1967) assumed that the bounding non-jointing layers are at least as thick as the jointing layer. For convenience, the expression by Hobbs (1967) is repeated here.

$$\frac{\sigma_{local}}{\sigma_{farfield}} = \left[1 - \frac{\cosh(Dx)}{\cosh\left(D\frac{L}{2}\right)}\right]$$ **Equation 26**

where $D = \frac{2}{t}\sqrt{\frac{G_n}{E_f}}$. Recall also that the constant D was derived from the shear stress distribution in the non-jointing layer (see **Equation 16** to **Equation 20**).

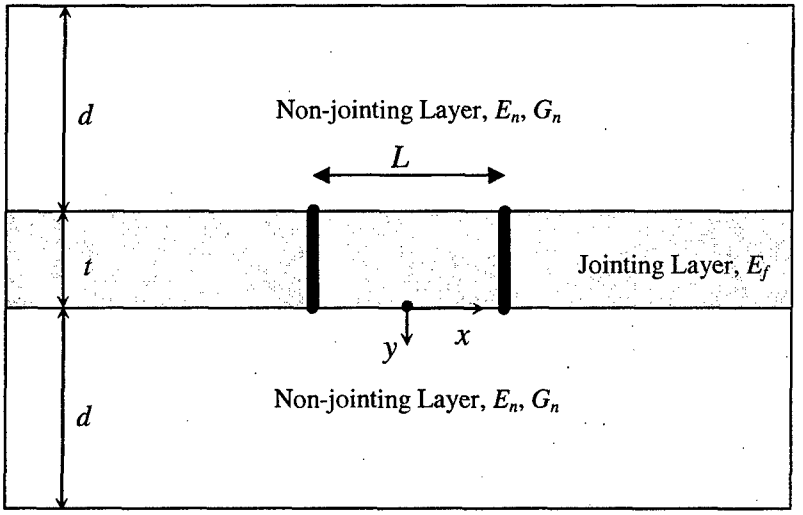


Figure 47 – Definition of variables for Ji and Saruwatari (1998).

Note that Ji and Saruwatari (1998) introduce the non-jointing layer thickness (d) into the stress distribution. **Figure 47** shows the geometry of the problem now with the non-jointing layer thickness, d, included. Ji and Saruwatari (1998) use a parameter, β, instead of D in their stress distribution equation below.

$$\frac{\sigma_{local}}{\sigma_{farfield}} = 1 - \frac{\cosh(\beta x)}{\cosh\left(\frac{\beta L}{2}\right)}$$ **Equation 34**

where x starts from the midpoint of the segment of length L and the parameter β is given by

$$\beta = \frac{1}{\sqrt{\frac{(1+\nu_n)tE_f}{E_n}M}} = \frac{1}{\sqrt{\frac{tE_f}{2G_n}M}} = \sqrt{\frac{G_n}{E_f}}\sqrt{\frac{2}{Mt}}$$ **Equation 35**

and the parameter M reflects the distribution of the shear stress in the non-jointing layer:

$$M = \int_0^{\frac{d}{2}} \left(\frac{d-2y}{d+2y} \right)^n dy = h(d)$$

The variable y is the distance from an interface (**Figure 47**). The parameters D in Hobbs' (1967) model and β in Ji and Saruwatari's (1998) model are analogous and only reflect the different types of assumed shear stress distribution in the non-jointing layers. The parameter n indicates how the shear stress varies with distance away from the interface. Note that the parameter M is a function of d only (i.e., the non-jointing layer thickness). For example, for $n=1$, $M=[\ln(2)-\frac{1}{2}]d$ and for $n=3$, $M=[3\ln(2)-2]d$ (**Figure 48**).

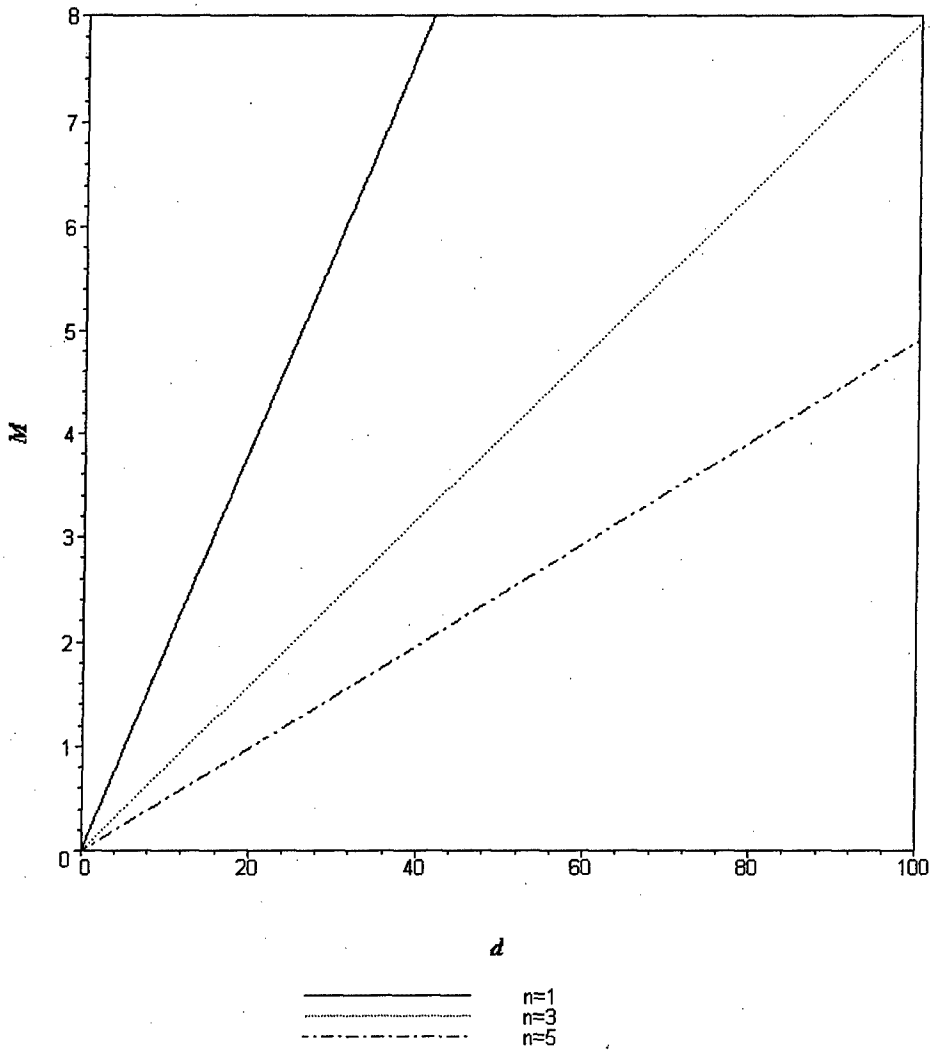


Figure 48 – Relationship between M and d for different values of n.

Letting $m = \frac{x}{t}$ and $l = \frac{L}{t}$ and making the substitutions $x = tm$, $L = lt$ and $M = h(d)$, the equation for the normalized stress (**Equation 34**) becomes

$$\frac{\sigma_{local}}{\sigma_{farfield}} = 1 - \frac{\cosh\left(\sqrt{\frac{G_n}{E_f}}\sqrt{\frac{2t}{h(d)}}m\right)}{\cosh\left(\sqrt{\frac{G_n}{E_f}}\sqrt{\frac{1}{2h(d)t}}lt\right)} \qquad \textbf{Equation 36}$$

Figure 49 shows how the normalized stress varies with distance from the segment midpoint for different values of E_f/G_n and $l = 1.0$. It can be observed that a larger E_f/G_n ratio leads to a lower peak value of normalized stress compared to smaller E_f/G_n values for a given segment length or joint spacing.

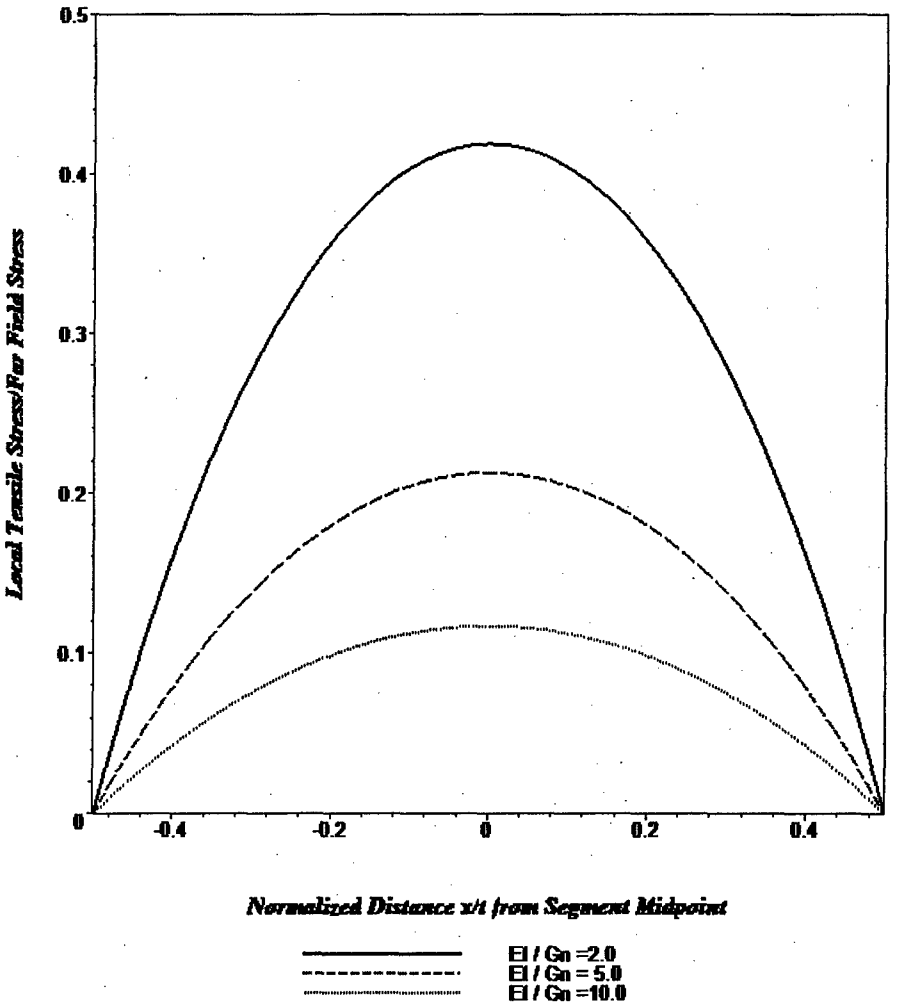


Figure 49 – Stress ratio variation between adjacent joints according to Ji and Saruwatari's (1998) model.

Using the same approach in obtaining the normalized shear stress in the Hobbs' (1967) model, the normalized shear stress in the Ji and Saruwatari (1998) model is given by

$$\frac{\tau_d}{\sigma_{farfield}} = \frac{t}{2}\left[\sqrt{\frac{G_n}{E_f}}\sqrt{\frac{2t}{h(d)}}\frac{\sinh\left(\sqrt{\frac{G_n}{E_f}}\sqrt{\frac{2t}{h(d)}}m\right)}{\cosh\left(\sqrt{\frac{G_n}{E_f}}\sqrt{\frac{1}{2h(d)t}}lt\right)}\right] \qquad \textbf{Equation 37}$$

Figure 50 shows the normalized shear stress variation with distance from the segment midpoint for the Ji and Saruwatari (1998) model. The same trend in the Hobbs (1967) model can be observed here. As the E_f/G_n ratio increases, lower shear stresses are observed. This subsequently leads to lower peaks in the normal stress distribution as observed in **Figure 49**.

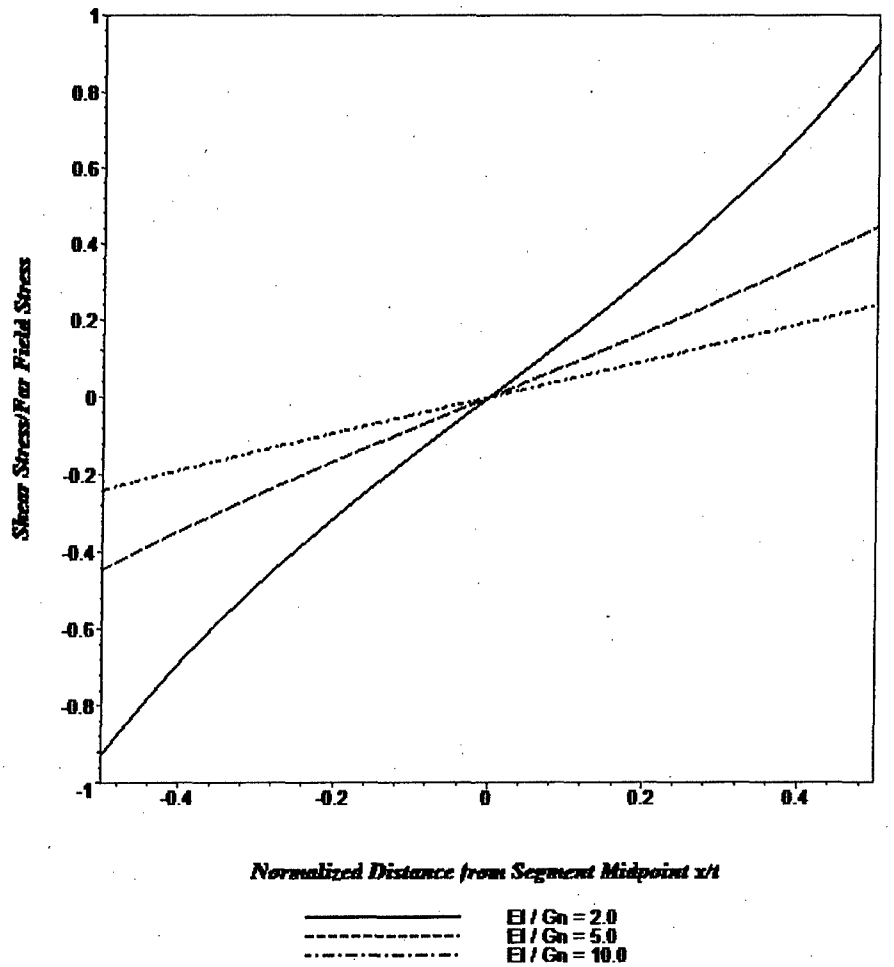


Figure 50 – Normalized shear stress along the interface according to Ji and Saruwatari's (1998) model.

Figure 51 shows how the normalized stress distribution changes with segment length or joint spacing (i.e., L). As expected, longer segments develop peak normal stresses nearer the far field value.

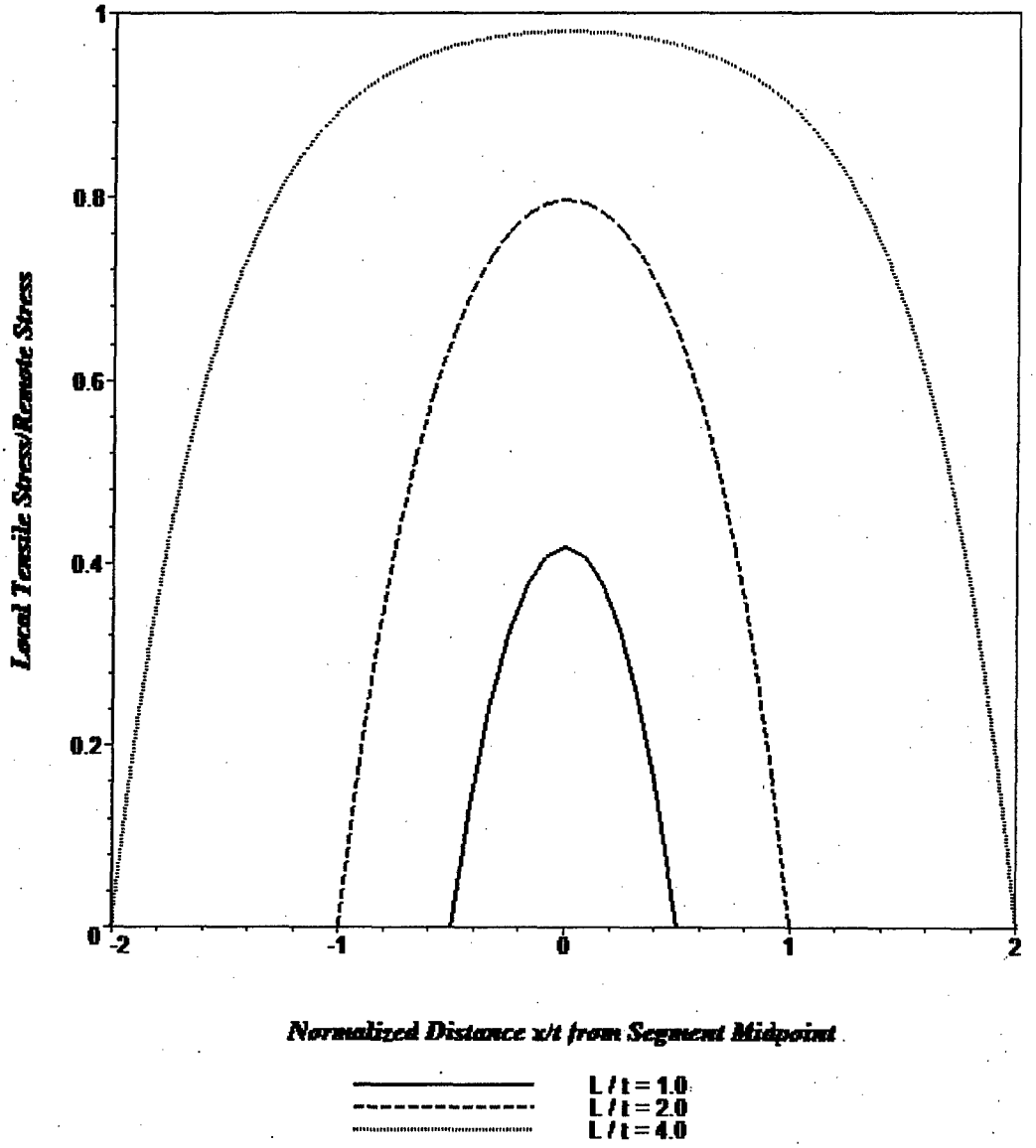


Figure 51 – Variation of normalized local stress with distance from the segment midpoint for various segment lengths.

Like Hobbs (1967), Ji and Saruwatari (1998) also derived joint spacing for a given value of applied strain. In **Equation 36**, the far field stress is simply $E_f \varepsilon_2$ so that

$$\sigma_{local} = E_f \varepsilon_2 \left(1 - \frac{\cosh\left(\sqrt{\frac{G_n}{E_f}} \sqrt{\frac{2t}{h(d)}} m \right)}{\cosh\left(\sqrt{\frac{G_n}{E_f}} \sqrt{\frac{1}{2h(d)t}} lt \right)} \right)$$ **Equation 38**

The maximum local stress occurs at the midpoint of the segment (i.e., $m = 0$) and is given by:

$$\sigma_{local-\max} = E_f \varepsilon_2 \left(1 - \frac{1}{\cosh\left(\sqrt{\frac{G_n}{E_f}} \sqrt{\frac{1}{2h(d)t}} lt \right)} \right)$$ **Equation 39**

Again, as in Hobbs' (1967) model, jointing occurs when the local stress reaches the tensile strength ($\sigma_{local} = E_f \varepsilon_1$).

$$E_f \varepsilon_1 = E_f \varepsilon_2 \left(1 - \frac{1}{\cosh\left(\sqrt{\frac{G_n}{E_f}} \sqrt{\frac{1}{2h(d)t}} lt \right)} \right)$$ **Equation 40**

Solving for the quantity $l = \frac{L}{t}$ in **Equation 40** yields

$$l = \frac{L}{t} = \sqrt{\frac{E_f}{G_n}} \sqrt{2th(d)} \frac{1}{t} \cosh^{-1}\left(\frac{\varepsilon_2}{\varepsilon_2 - \varepsilon_1} \right)$$ **Equation 41**

Since the function $h(d)$ is simply the quantity d multiplied by some constant, let $\sqrt{h(d)} = g(\sqrt{d})$

$$L = g(\sqrt{d}) \sqrt{\frac{E_f}{G_n}} \sqrt{2t} \cosh^{-1}\left(\frac{\varepsilon_2}{\varepsilon_2 - \varepsilon_1} \right)$$ **Equation 42**

Equation 41 and **Equation 42** are analogous to **Equation 32** and **Equation 33**. Hence, using Ji and Saruwatari's (1998) model, the joint spacing depends on both the square root of the jointing layer thickness (t) as well as the square root of the non-jointing layer

thickness (d). **Figure 52** shows the relationship between normalized spacing required to reach the cracking stress at midpoint and the applied strain.

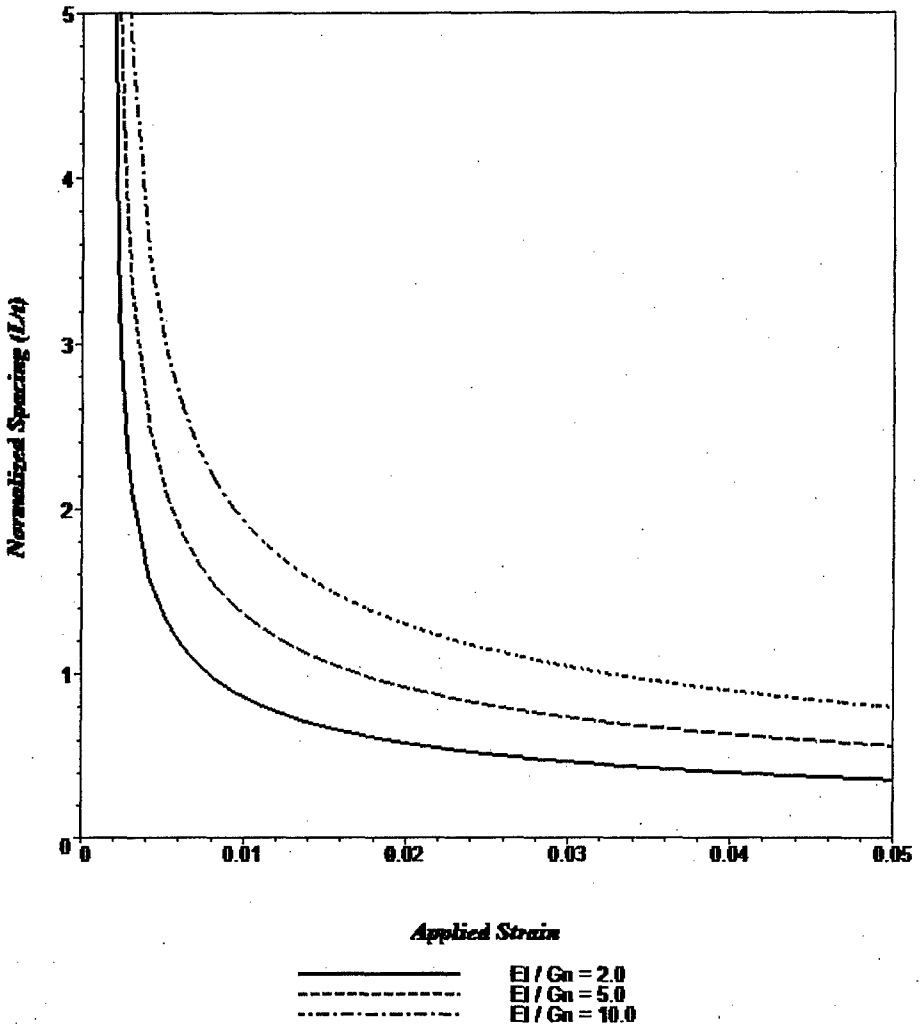


Figure 52 – Relationship between applied strain and normalized spacing according to Ji and Saruwatari's (1998) model for different E_f/G_n ratios. Note that t is the jointing layer thickness.

A summary of both stress distribution models is presented in **Table 3**.

Table 3 – Summary of stress distribution and spacing for both the Hobbs (1967) and Ji and Saruwatari (1998) models.

Model	Stress Distribution	Spacing
Hobbs (1967)	$\frac{\sigma_{local}}{\sigma_{farfield}} = 1 - \frac{\cosh\left(2m\sqrt{\frac{G_n}{E_f}}\right)}{\cosh\left(\sqrt{\frac{G_n}{E_f}}l\right)}$ $m = \frac{x}{t},\ l = \frac{L}{t}$	$L = t\sqrt{\frac{E_f}{G_n}}\cosh^{-1}\left(\frac{\varepsilon_2}{\varepsilon_2 - \varepsilon_1}\right)$ Linear in t
Ji and Saruwatari (1998)	$\frac{\sigma_{local}}{\sigma_{farfield}} = 1 - \frac{\cosh\left(\sqrt{\frac{G_n}{E_f}}\sqrt{\frac{2t}{h(d)}}m\right)}{\cosh\left(\sqrt{\frac{G_n}{E_f}}\sqrt{\frac{1}{2h(d)t}}lt\right)}$ $m = \frac{x}{t},\ l = \frac{L}{t}$	$L = \sqrt{\frac{E_f}{G_n}}\sqrt{2th(d)}\cosh^{-1}\left(\frac{\varepsilon_2}{\varepsilon_2 - \varepsilon_1}\right)$ Non-linear in t

The simplified models above show how the stress distribution depends on the material properties of the rock and the layer geometries (i.e., the jointing layer for Hobbs, 1967; the jointing and bounding layers for Ji and Saruwatari, 1998). They also describe the relationship between spacing and layer thickness at different levels of strain. Hobbs (1967) proposes a linear relationship between thickness and spacing whereas Ji and Saruwatari (1998) propose a non-linear relationship. Ji and Saruwatari (1998) also include the effect of the non-jointing layer thickness. The difference in the models lies in the assumption of the shear stress distribution in the bounding non-jointing layers. Hobbs (1967) assumes a linear shear stress distribution whereas Ji and Saruwatari (1998) assume non-linear forms of the shear stress distribution. Also, Hobbs (1967) requires that the bounding layers be as thick as the jointing layer. This may not be true in the real world. The simplified models do not take into account the issue of joint saturation. This behavior is discussed in the next section.

4 Saturation Mechanisms

In the previous section, simplified methods for describing the tensile stress distribution were presented. However, the jointing behavior suggested by these simplified models is not consistent with the observations made in laboratory tests, i.e., that the spacing does not change after the strain reaches a certain magnitude (saturation). To this author's knowledge, saturation, so far, has not been observed in the field. In this chapter, a comparison between tensile stress distributions from simplified models and finite element models is presented (section **4.1**). Two saturation mechanisms suggested in the literature are then explored: compressive stress development (section **4.2**) and interface slippage (section **4.3**). The analysis in section **4.1** is the result of new work whereas sections **4.2** and **4.3** are an elaboration of what is found in the literature. Figures (including plots) in section **4.1** are not from references and were produced independently. Some plots in section **4.3** were also produced independently, these are indicated in the captions.

4.1 Tensile Stress Distributions: Simplified Models vs. Finite Element Models

In the simplified models, the normal stresses are always tensile so the formation of new joints is possible as the strain increases. This is possibly a product of the assumed one-dimensional nature of the stress in the simplified models. Finite element simulations were carried out so that a comparison with the simplified models could be made. The program FRANC2D (Wawrzynek and Ingraffea, 1991) was used for this purpose. First, a single joint is modeled in a layer that has the same properties as its bounding layers. The entire system is subjected to a uniform extensional strain in the direction perpendicular to the plane of the joint. The horizontal normal stress (σ_{xx}) contours are shown in **Figure 53**. The far field stress is represented by the color yellow. The color red represents zero to negative normal stresses (compressive stress in FRANC2D convention). **Figure 53** shows that zero or compressive stresses occur near the joint mid-length. At a short distance from the joint, a transition from compressive to tensile stresses occurs (i.e., red to brown). However, tensile stresses greater than the far field tensile stresses (in blue) occur at or near the joint tips.

Figure 54 shows the normalized horizontal stress ($\frac{\sigma_{xx}}{\sigma_{farfield}}$) with horizontal distance away from the joint midpoint for two different situations together with the stress distribution derived by Hobbs (1967) using the same rock properties. It includes the situation shown in **Figure 53**. The stresses near the joint (encircled in **Figure 54**) are actually compressive according to the finite-element calculations but are not really that large and can probably be considered equal to zero in this case. These compressive stresses are possibly a result of some numerical errors in the finite element simulation. Hobbs' (1967) model predicts larger stresses than the finite element simulations.

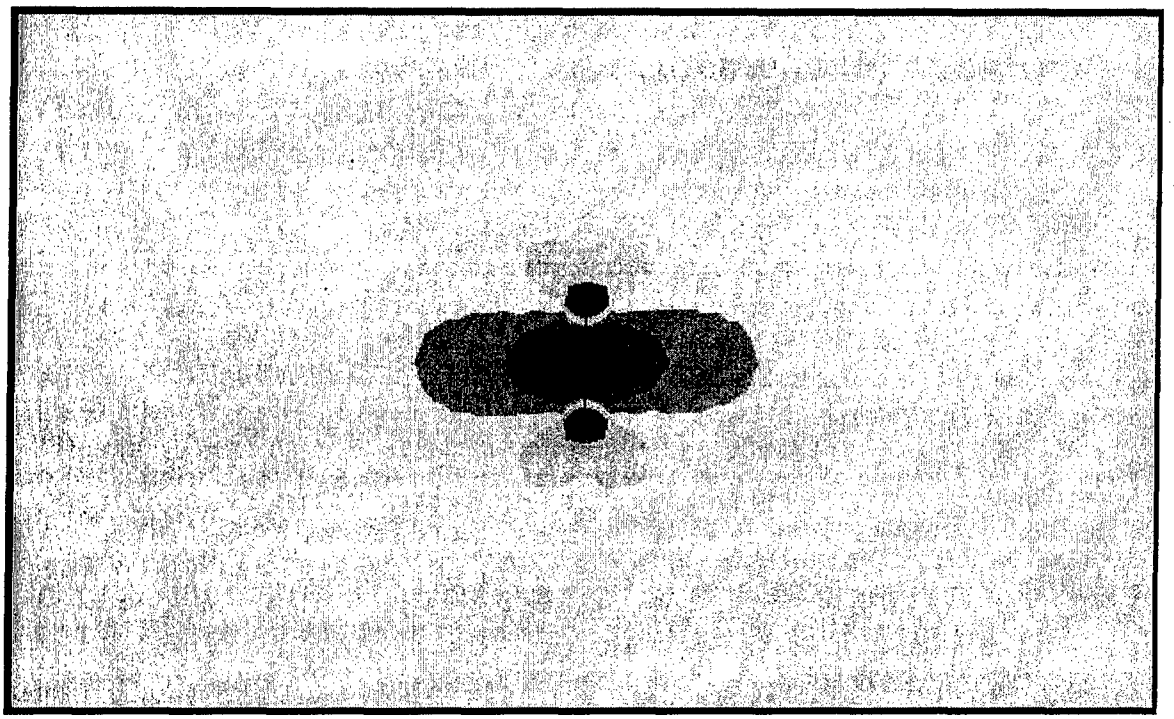


Figure 53 – Stress reduction shadow due to a single joint in a layer subjected to uniform extensional strain (by FEM, FRANC2D program). The color yellow represents the far field stress.

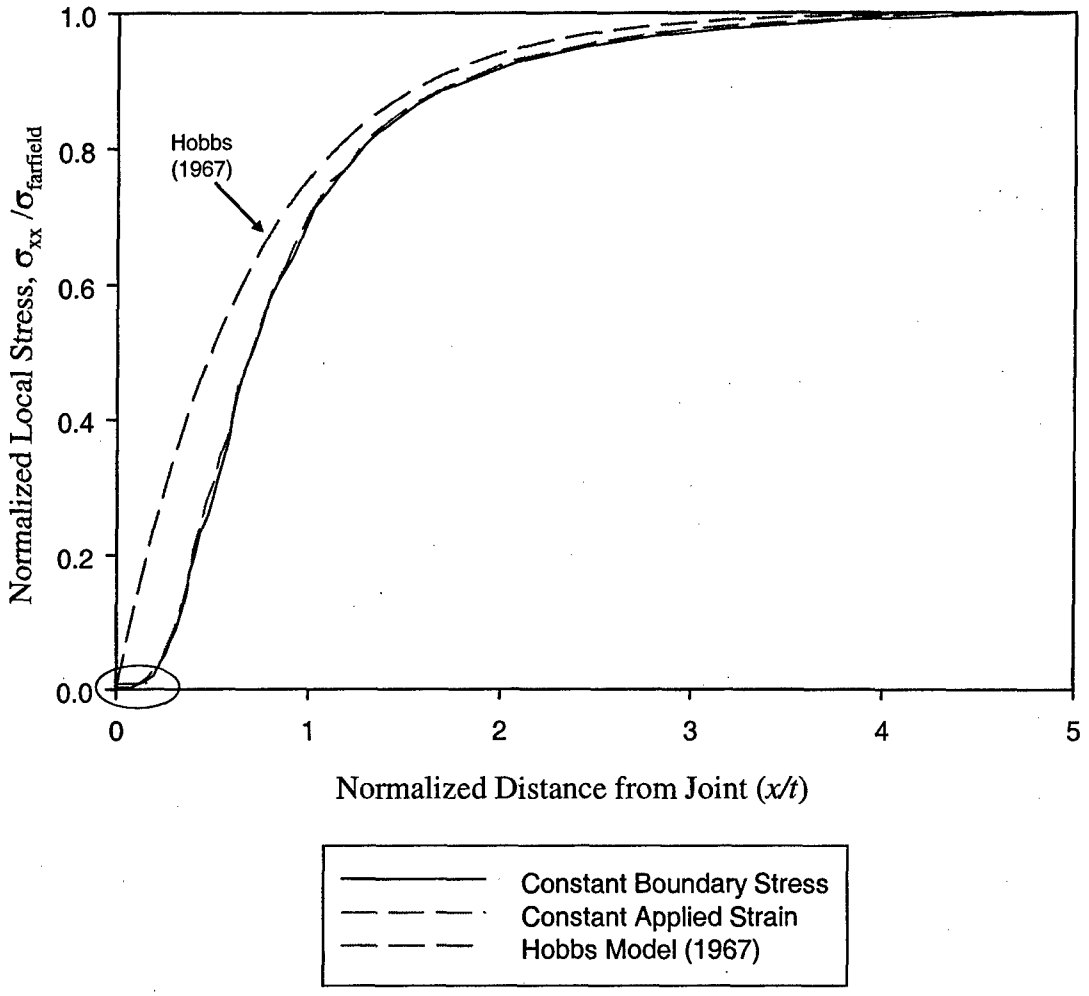


Figure 54 – Comparison between the analytical stress reduction shadow by Hobbs (1967) and finite element simulations using FRANC2D. Region of compressive stress of small magnitude in the FE simulation encircled.

Finite element simulations were also performed in order to find out how the stress reduction shadows of two adjacent joints interact. **Figure 55** shows the finite element mesh for two joints that are 2 units long and spaced 4 units apart. This translates to a spacing-to-thickness ratio of 2.0. As before, the entire system is subjected to extensional strain.

Figure 56 shows the horizontal stress (σ_{xx}) contours for **Figure 55**. Compressive stresses are presented in red (could also be zero stress). These occur in a very small zone near the joints. In **Figure 57**, $\frac{\sigma_{xx}}{\sigma_{farfield}}$ is plotted along the line connecting the midpoints of the two joints. It can be seen that both the Hobbs (1967) and Ji and Saruwatari (1998)

models predict larger stresses than the finite-element solution at every point along the line. However, one must keep in mind that the simplified models represent the average tensile stress at a location between the two joints and the finite element results do not.

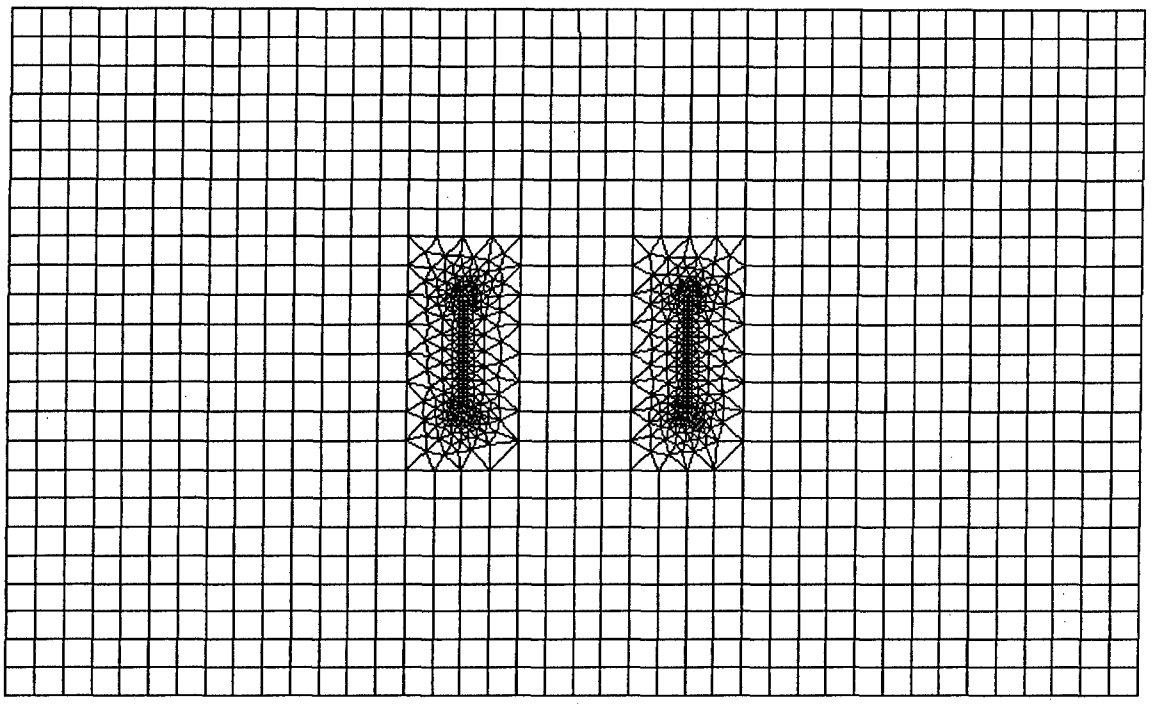


Figure 55 – Finite element mesh used to model two medium spaced joints.

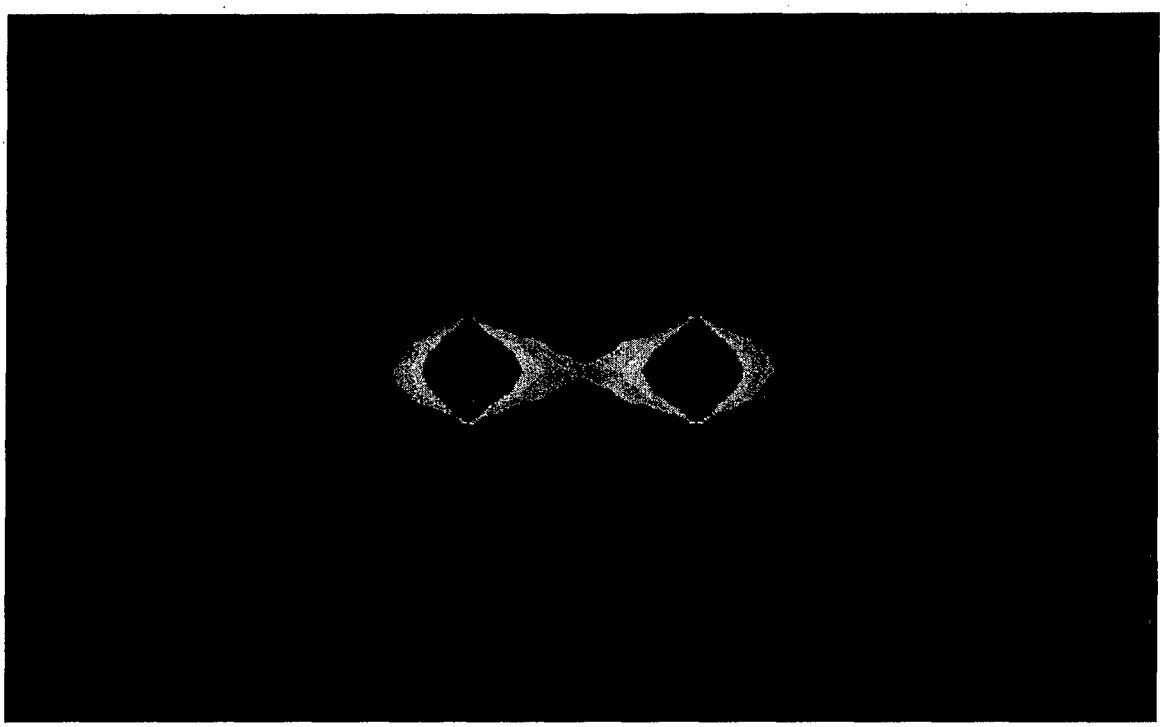


Figure 56 – Contours of σ_{xx}. Note: the color red represents compressive stress, all other colors denote tensile stresses with values between zero and the far field stress value (denoted by the color blue).

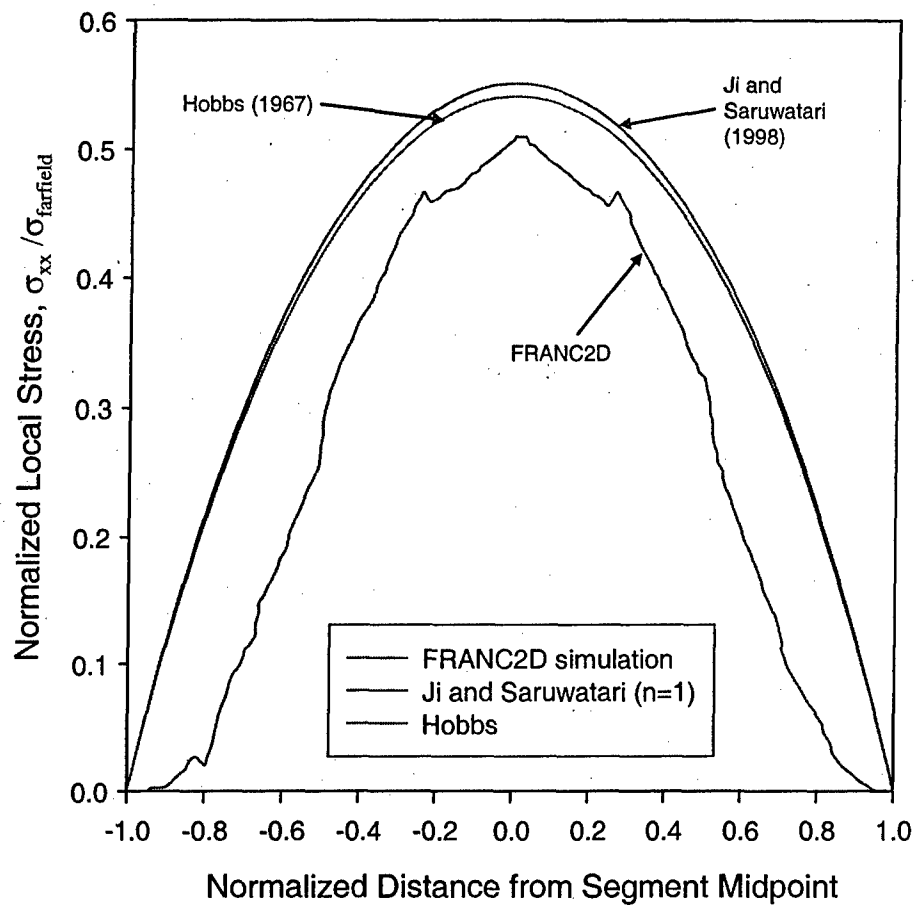


Figure 57 – Comparison of finite element results with both stress distribution models for the medium-spaced joints.

The second case involving stress reduction shadow interaction involves two closely-spaced joints. The joints are 2 units long and are spaced 2 units from each other for a spacing-to-thickness ratio of 1.0. The finite element mesh for this case is shown in **Figure 58**. As in the previous case, the entire system is subjected to extensional strain.

Contours of σ_{xx} are shown in **Figure 59**. As before, compressive stresses are rendered in red. The far field stress is presented in blue. It is apparent from **Figure 59** that only compressive horizontal stresses exist along the line connecting the midpoints of the joints. The values of $\frac{\sigma_{xx}}{\sigma_{farfield}}$ along this line are plotted in **Figure 60** together with the stresses predicted by the Hobbs (1967) and Ji and Saruwatari (1998) models. The stresses from the finite element simulation all fall below zero and those predicted by the models do not. This is where the simplified models break down because they do not take into account the two-dimensional nature of the problem.

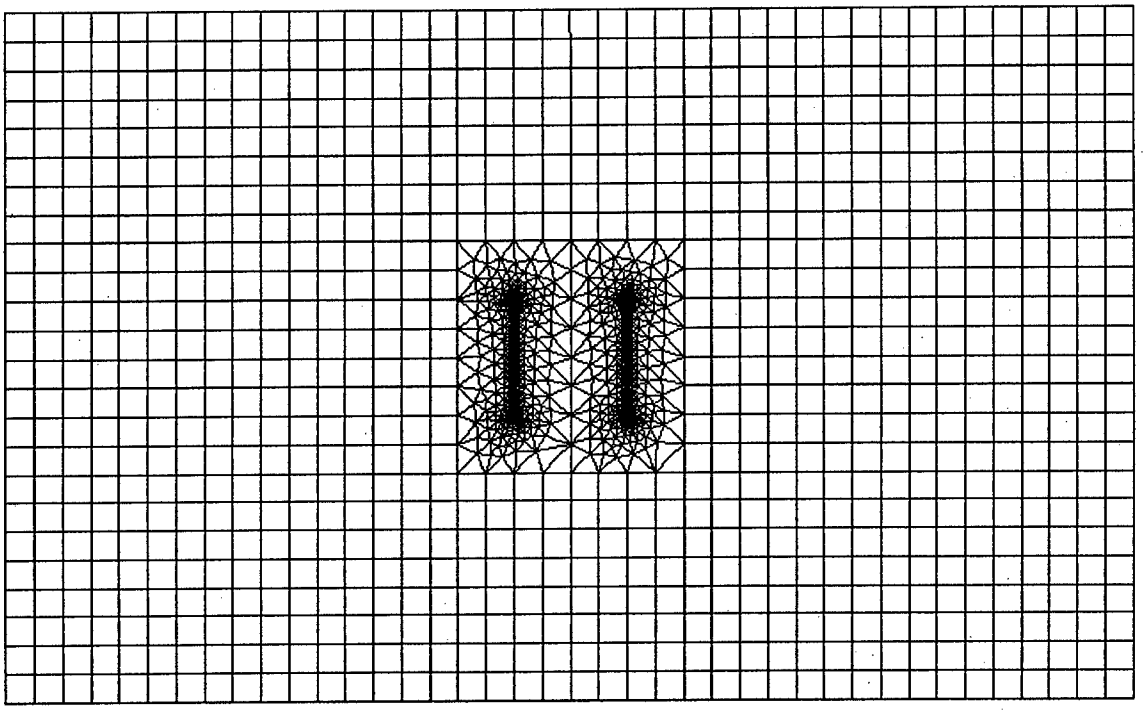


Figure 58 – Finite element mesh for two closely-spaced joints.

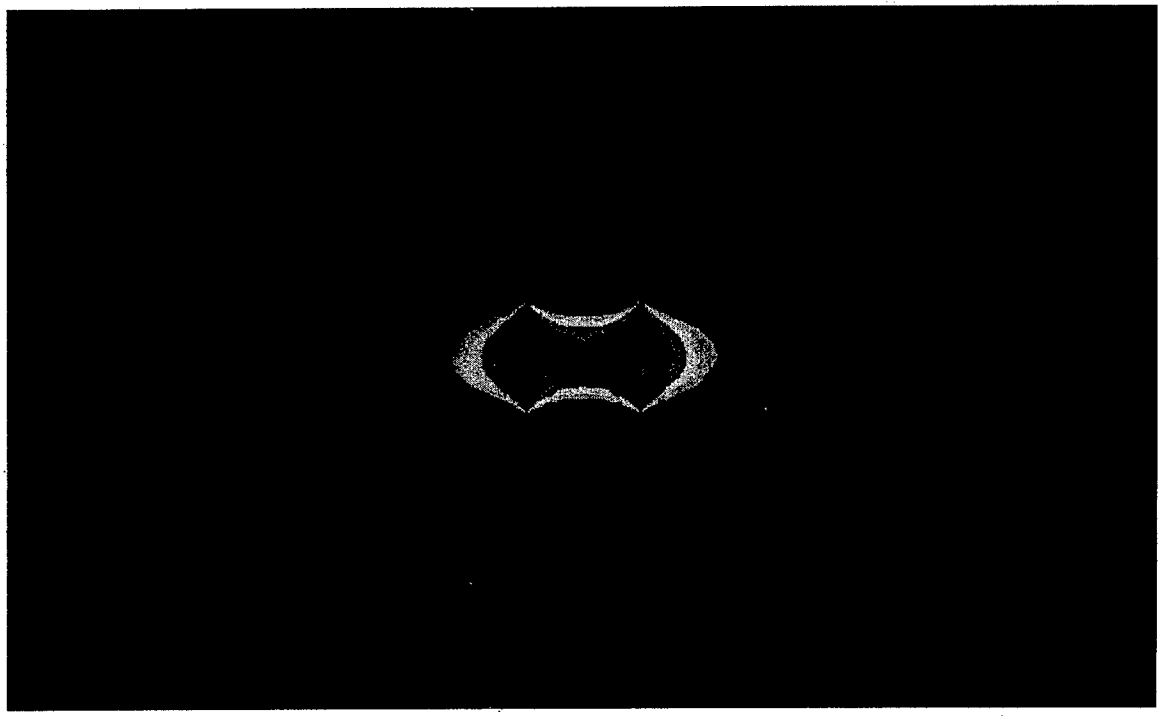


Figure 59 – Contours of σ_{xx}. Note: the color red represents compressive stress, all other colors denote tensile stresses with values between zero and the far field stress value (denoted by the color blue).

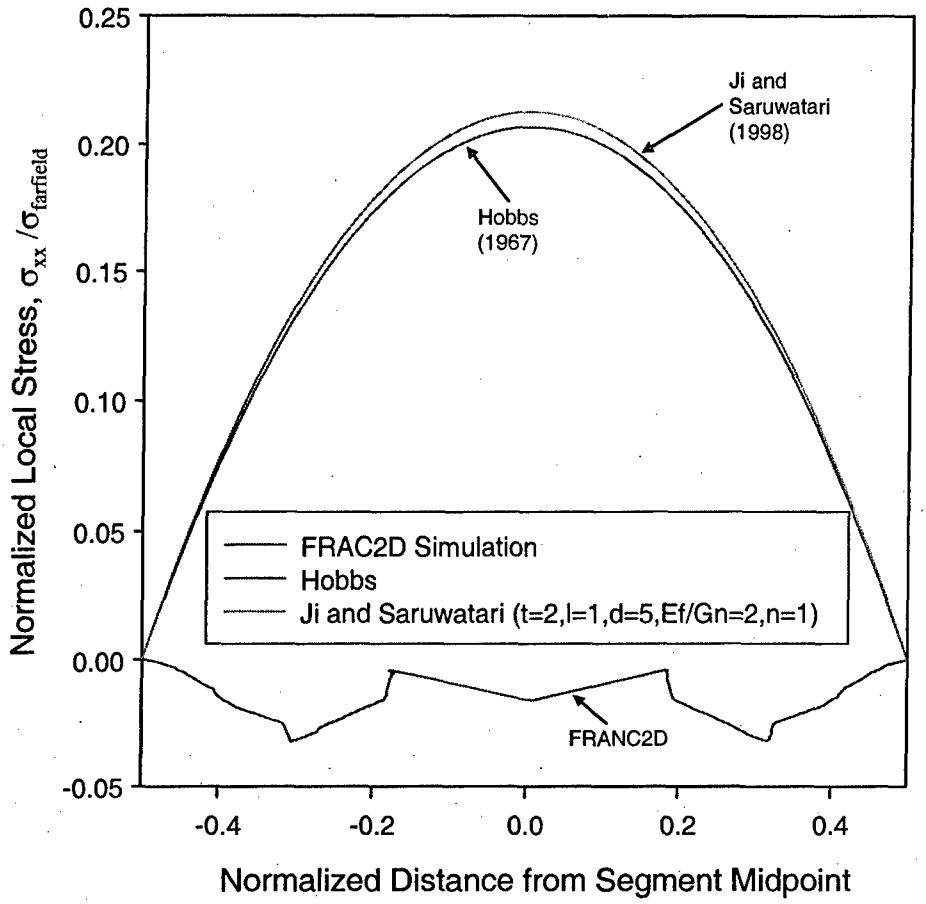


Figure 60 – Comparison of finite element results with both stress distribution models for the closely-spaced joints.

Two important observations can be obtained from this section:

1. The peak normal stress (tensile) occurs at the midpoint of a segment (e.g., **Figure 42** and **Figure 49**). Also, longer segments attain larger normal stresses than do shorter segments when the non-jointing (bounding) layers are subjected to the same amount of strain (e.g., **Figure 44** and **Figure 51**). Therefore, a joint is more likely to occur first at the midpoints of the longest segments than at the midpoints of shorter segments.

2. There is a zone of compressive normal stress in the vicinity of a joint even when the non-jointing (bounding) layers are subjected to extensional strain (**Figure 53** and **Figure 56**). This is apparent in the finite element simulations but cannot be reproduced by the simplified models. If two joints are spaced sufficiently close, compressive stresses may occur all along the line connecting their midpoints (**Figure 59**). This may preclude the further formation of layer-perpendicular joints.

4.2 Compressive Stress Saturation Mechanism

Bai and Pollard (2000) performed a study to determine the effects of applied strain, overburden and difference in elastic constants between the jointing and non-jointing layers on the spacing-to-thickness ratio at which compressive stresses occur. Using finite elements (FE), they calculated the stress field that would result between joints in a layer sandwiched between two non-jointing layers all subjected to a uniform extensional displacement (**Figure 61**). Specifically, the stress in the direction normal to the joint planes along the line PP' is calculated. They found that there exists a critical spacing-to-thickness ratio, $(\frac{s}{t})_{cr}$, below which the joint perpendicular normal stress at point o (σ_{xx-o}) in **Figure 61** is compressive rather than tensile. Note that point o is located halfway between the two middle joints and at the jointing layer mid-height (see **Figure 61**). Based on this finding, the authors conclude that $(\frac{s}{t})_{cr}$ represents the smallest possible spacing-to-thickness ratio for layer perpendicular joints that can be achieved through such a jointing mechanism. Further jointing between joints spaced below the critical level cannot occur due to the compressive stress that exists there. This can therefore be considered a saturation mechanism. However, this does not discount the possibility of further jointing under a different stress state. For example, compressive stresses applied in the vertical direction may also cause jointing with the same orientation. Note that the convention for stresses and strains is positive for tension and negative for compression (e.g., the average applied strain in the x-direction is positive or $\varepsilon_{xx-ave} = {}^{2U_x}/_{W}$).

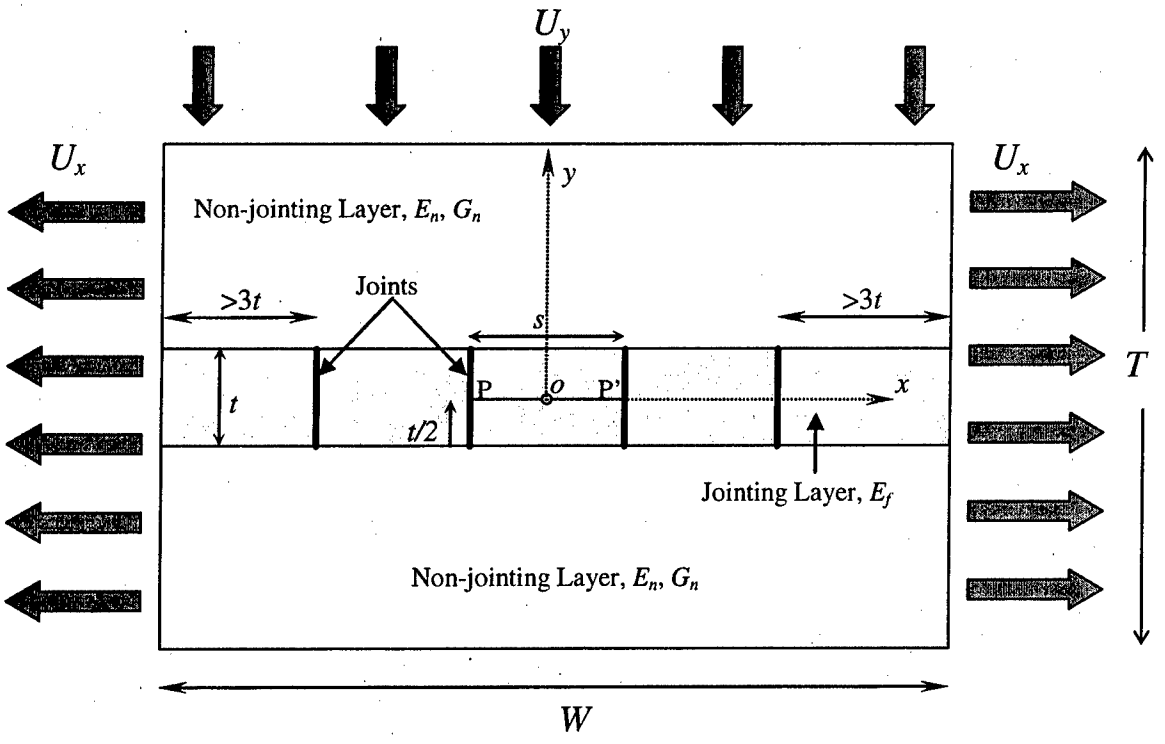


Figure 61 – Set-up of the finite element model used by Bai and Pollard (2000). The jointing and non-jointing layers have Poisson's ratios of ν_f and ν_n, respectively. Note that U_y can be zero (i.e., no overburden). This figure is a sketch of Fig. 1 (a) in Bai and Pollard (2000).

In their finite element model (FEM), the authors assumed the following:

1. There is no slip at the interfaces between the jointing and non-jointing layers (i.e., layers are welded together).

2. Plane strain conditions exist.

3. The bottom boundary in **Figure 61** is fixed in the y – direction but free to move in the x – direction.

4. The top boundary in **Figure 61** is free to move in both x and y directions.

5. To represent overburden stresses, the top boundary can also be subjected to a uniform downward displacement (U_y, **Figure 61**). This was done instead of applying a uniform stress because the finite element program used (Fracture Analysis Code or FRANC, Wawrzynek and Ingraffea, 1987) does not allow mixed stress-displacement boundary conditions as input.

6. To represent the uniform extension, a uniform displacement boundary condition is applied to the left and right ends of the model (U_x in **Figure 61**). The average strain in the x – direction is calculated as $\varepsilon_{xx-ave} = {}^{2U_x}/_{W}$.

7. The stresses between the two middle joints in a set-up of four equally spaced joints are sufficient to model the stresses between two adjacent joints in a long series of regularly spaced joints with the same spacing. The authors found that adding more equally-spaced joints does not affect the calculated stress field in the region between the two middle joints.

Bai and Pollard (2000) performed a number of simulations to determine the effect of combinations of specific modeling parameters on $(\frac{s}{t})_{cr}$. Particularly, the effects of the following parameters were investigated:

1. The average applied strain (calculated as $\varepsilon_{xx-ave} = {}^{2U_x}/_{W}$). The simulation results show that $(\frac{s}{t})_{cr}$ is independent of ε_{xx-ave}. Specifically, ε_{xx-ave} affects the magnitude of σ_{xx} but not its sign (i.e., whether tensile or compressive). Moreover, there is a linear relationship between σ_{xx-o} and ε_{xx-ave}. The slope of the σ_{xx-o} vs. ε_{xx-ave} relationship is positive when the $\frac{s}{t}$ ratio is greater than $(\frac{s}{t})_{cr}$ and negative if it is less than $(\frac{s}{t})_{cr}$. In other words, if a segment length is found to be at or below the critical spacing (i.e., $\leq t \cdot (\frac{s}{t})_{cr}$), there is absolutely no possibility that it can develop tensile stresses even if the applied extensional strain is increased. Consequently, in the program, there is no longer a need to check these segments for the possibility of jointing every time the strain is increased if they have been deemed critical at a lower strain. This saves computation time.

2. The ratio of Young's moduli, ${}^{E_f}/_{E_n}$. Bai and Pollard's (2000) finite element simulations were performed at constant Poisson's ratio values ($\nu_f = \nu_n = 0.2$). The results revealed that as the ratio ${}^{E_f}/_{E_n}$ increases, $(\frac{s}{t})_{cr}$ also increases. The best-fit curve to the simulated data is shown in **Figure 62**: $(\frac{s}{t})_{cr}$ varies from about 0.8 for ${}^{E_f}/_{E_n} = 0.0$ to about 1.12 for large ${}^{E_f}/_{E_n}$ ratios. Realistically, however, the ratio ${}^{E_f}/_{E_n}$ is rarely reported in the literature to be less than 1.0 because the jointing layers are usually stiffer than the non-jointing layers. If only $(\frac{s}{t})_{cr}$ values for ${}^{E_f}/_{E_n} \geq 1.0$ are included, the ratio would vary from approximately 0.976 to 1.12. The best-fit curve is given by **Equation 43**:

$$\left(\frac{s}{t}\right)_{cr} = 0.792 + 0.328\left(1 - \exp\left[-0.824\left(\frac{E_f}{E_n} - 0.0025\right)^{0.824}\right]\right) \qquad \textbf{Equation 43}$$

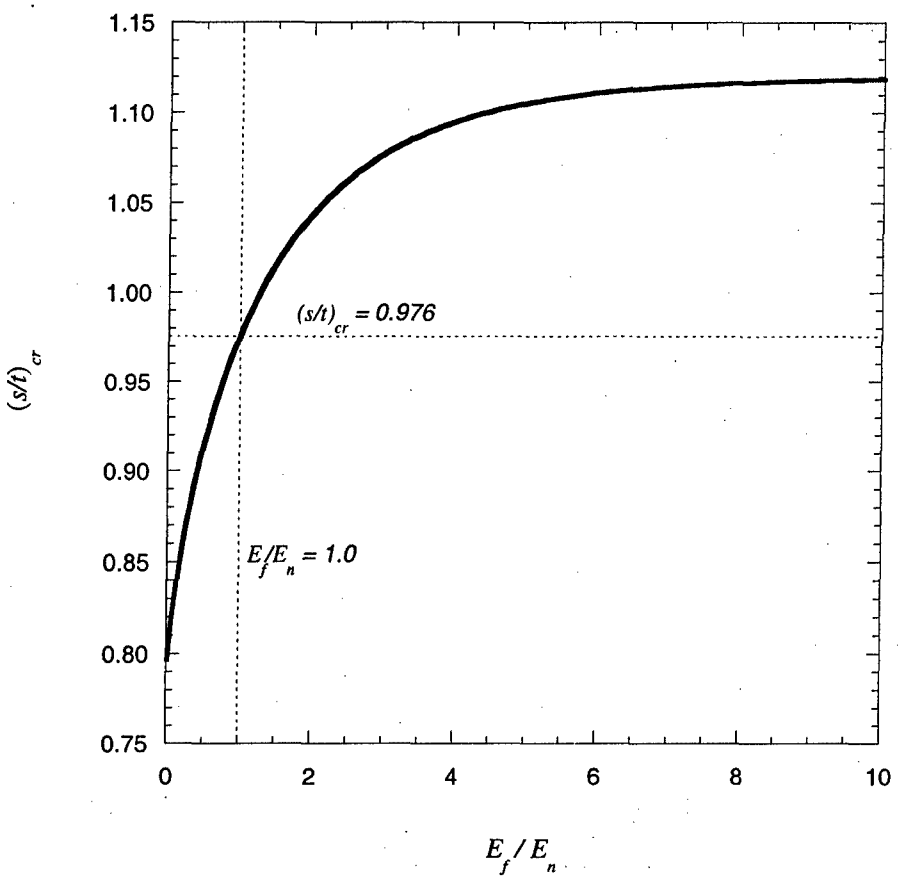


Figure 62 – Illustration of the effect of the ratio between the jointing layer Young's modulus (E_f) and the bounding layer Young's modulus (E_n) to the critical spacing-to-thickness ratio. The curve is a fit of the finite element simulation results. This plot is the same as Fig. 4 (b) in Bai and Pollard (2000).

3. The effect of the Poisson's ratios of the jointing and non-jointing layers (ν_f and ν_n, respectively). These Poisson's ratios are represented as a single parameter, D, which is defined by the following equation:

$$D = \frac{(1-2\nu_f)(1+\nu_f)-(1-2\nu_n)(1+\nu_n)}{(1-\nu_f^2)+(1-\nu_n^2)} \qquad \textbf{Equation 44}$$

Figure 63 shows how D varies with ν_f and ν_n to better visualize the relationship (the contours are the values of D): for a given value of ν_f, D increases as ν_n increases. On the other hand, for a given value of ν_n, D decreases as ν_f increases. It is also worthwhile to note that a positive value of D indicates that $\nu_f < \nu_n$ and a negative value of D means $\nu_f > \nu_n$. In the simulations, D is varied while keeping $E_f = E_n = 40$ GPa.

The results show that as D increases, $(\frac{s}{t})_{cr}$ decreases (**Figure 64**). The best-fit curve in **Figure 64** is given by the equation

$$\left(\frac{s}{t}\right)_{cr} = 0.976 - 0.302D - 0.129D^2 + 0.117D^3 \qquad \textbf{Equation 45}$$

The ratio 0.976 in **Equation 45** is the critical spacing-to-thickness ratio at $\frac{E_f}{E_n} = 1.0$ (see **Figure 62**).

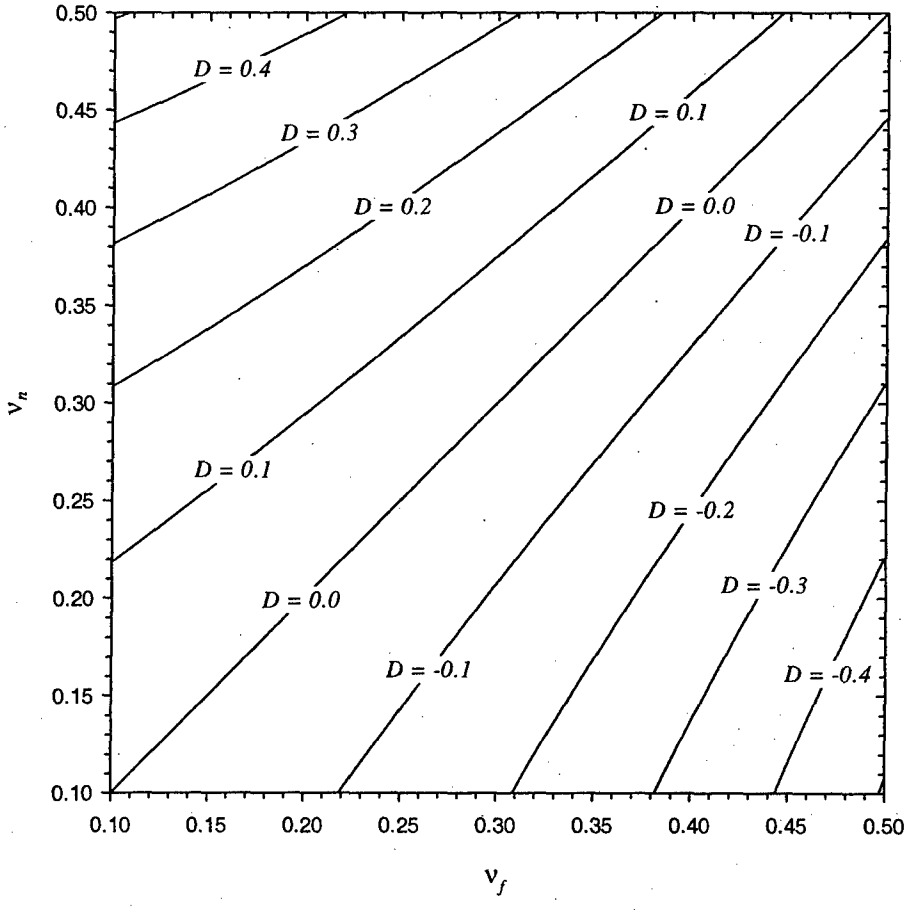


Figure 63 – Contours of the parameter D as a function of the jointing layer and bounding layer Poisson's ratios (ν_f and ν_n, respectively). Plotted from Equation 44.

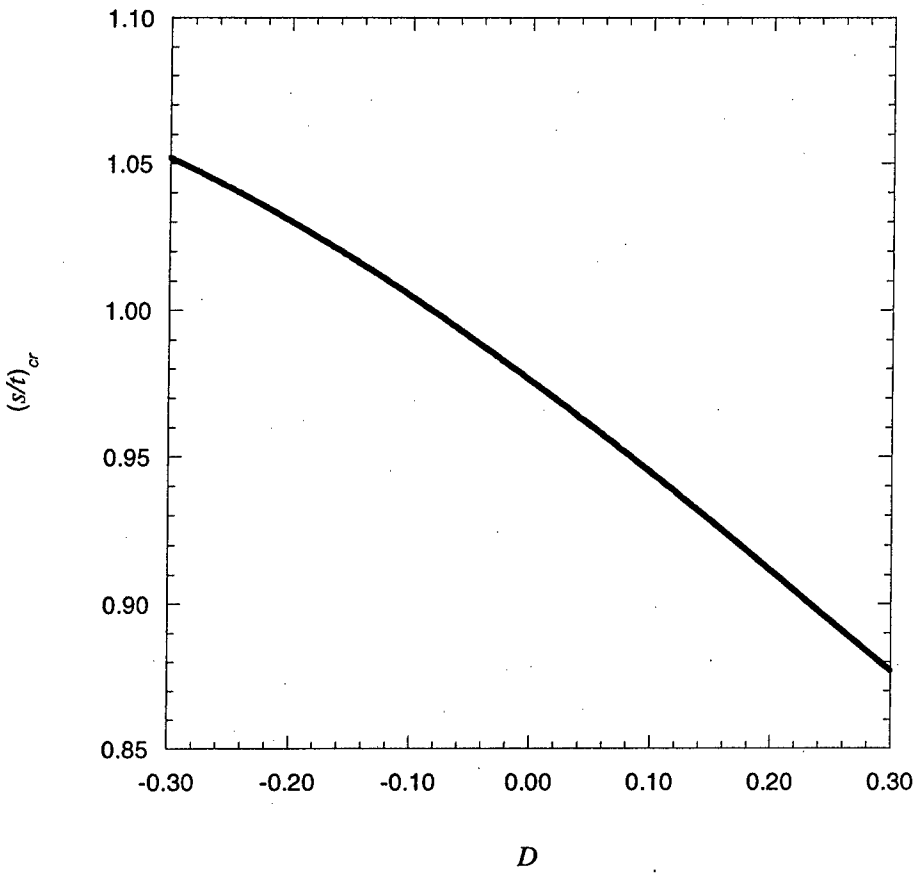


Figure 64 – Illustration of the effect of D (Equation 44) on the critical spacing-to-thickness ratio. This plot is simular to Fig. 5 (b) in Bai and Pollard (2000).

4. The effect of overburden stress (S_v). To determine the effect of overburden stress on $(\frac{s}{t})_{cr}$, the magnitude of the applied displacement, U_y in **Figure 61**, is varied. The Young's moduli E_f and E_n are kept constant at 40 GPa as are the Poisson's ratios ν_f and ν_n at 0.2. Also, an average applied strain $\varepsilon_{xx-ave} = 0.002$ is applied in all cases. Recall that ε_{xx-ave} does not affect $(\frac{s}{t})_{cr}$ and only affects the magnitude of σ_{xx-o}, not its sign. The overburden stress, S_v, is calculated using the expression for the stress σ_{yy} under plane strain conditions or:

$$S_v = \frac{E_f}{(1+\nu_f)(1-2\nu_f)}[\nu_f \varepsilon_{xx-ave} - (1-\nu_f)\frac{|U_y|}{T}]$$

Note that T is the total thickness of the jointing and non-jointing layers in **Figure 61**. When $\nu_f = 0.2$, $\varepsilon_{xx-ave} = 0.002$, and $|U_y|/T = 5\times10^{-4}$ in the above equation, the overburden stress S_v is zero. Also, as U_y increases, S_v increases (which makes sense). The maximum S_v applied is 200 MPa. The resulting range of values for $(\frac{s}{t})_{cr}$ is between 0.976 and

1.018. The best-fit curve for the simulation $(\frac{s}{t})_{cr}$ vs. S_v data points is shown in **Figure 65**. It shows that for a given set of elastic constants, a larger overburden stress leads to a larger $(\frac{s}{t})_{cr}$. The best-fit curve is given by:

$$\left(\frac{s}{t}\right)_{cr} = 0.976 + 1.118\times10^{-4} S_v - 7.562\times10^{-8} S_v^2 + 2.806\times10^{-9} S_v^2 \qquad \textbf{Equation 46}$$

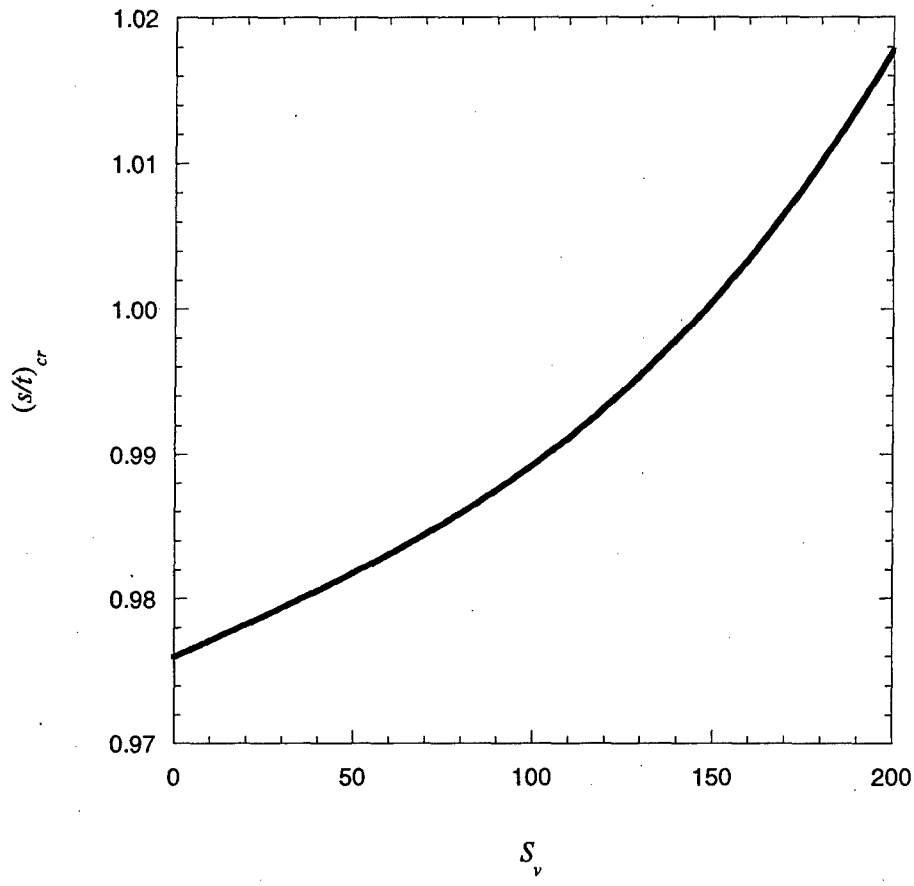


Figure 65 – Illustration of the effect of overburden on the critical spacing-to-thickness ratio. This plot is the same as Fig. 7 in Bai and Pollard (2000).

To summarize, the $(\frac{s}{t})_{cr}$ ratio increases with:

- Increasing E_f/E_n ratio
- Increasing overburden stress, S_v

and decreases with

- Increasing D. Note that D increases when ν_f decreases (for a fixed value of ν_n) or when ν_n increases (for a fixed value of ν_f (see **Figure 63**). Also, D is positive if $\nu_f < \nu_n$ and negative if $\nu_f > \nu_n$.

The combined effect of these three factors can be expressed in the following equation:

$$\left(\frac{s}{t}\right)_{cr} = \beta\gamma\left[0.792 + 0.328\left(1 - \exp\left[-0.824\left(\frac{E_f}{E_n} - 0.0025\right)^{0.824}\right]\right)\right] \qquad \textbf{Equation 47}$$

where

$$\beta = \frac{0.976 - 0.302D - 0.129D^2 + 0.117D^3}{0.976}$$

from **Figure 64** and

$$\gamma = \frac{0.976 + 1.118\times10^{-4}S_v - 7.562\times10^{-8}S_v^2 + 2.806\times10^{-9}S_v^2}{0.976}$$

from **Figure 65**. **Equation 47** is obtained by taking **Equation 43** and multiplying it by **Equation 45** and **Equation 46** each normalized by 0.976. If the jointing and non-jointing layers have the same elastic properties and there is no overburden (i.e., $\frac{E_f}{E_n} = 1.0$ in **Equation 43**, $D = 0$ in **Equation 45** and $S_v = 0$ in **Equation 46**), $(\frac{s}{t})_{cr} = 0.976$.

Based on their study, Bai and Pollard (2000) suggest that $\frac{s}{t}$ values between 0.8 and 1.2 (i.e., 0.833<FSR<1.25) indicate that the layer perpendicular joints have reached a state of saturation or very nearly so. The reason being that at these values of $\frac{s}{t}$, compressive stresses instead of tensile stresses are acting in the area between the joints. They also suggest that further jointing could have been achieved through other mechanisms. One example would be that suggested by Gross (personal communication) where the filling of existing joints with mineral deposit changes its mechanical behavior and allows new closely spaced joints to form. On the other hand, $\frac{s}{t}$ values greater than 1.2 (i.e., FSR <0.833) suggest that the layer is not yet saturated with respect to layer perpendicular joints.

Laboratory experiments were also performed by Bai and Pollard (2000) using Plexiglass plates ($E = 31.0$ GPa and $\nu = 0.36$) with various $\frac{s}{t}$ ratios (0.4, 0.6, 1.0, 1.4). These plates are 0.005 m thick and extensional displacement is applied through holes at the ends of the plate (**Figure 66**). Strain gauges are placed at point o (**Figure 66**) in order to measure the horizontal and vertical strains (ε_{xx} and ε_{yy}). Plane stress condition is

assumed to apply to the experiment and the stress, σ_{xx-o}, can be calculated using the following equation:

$$\sigma_{xx-o} = \frac{E}{1-\nu}(\varepsilon_{xx} + \nu\varepsilon_{yy}) \qquad \textbf{Equation 48}$$

Bai and Pollard's (2000) measurements showed that ε_{xx} at point o is positive (tensile) for the $\frac{s}{t}$ ratios used in their experiments and is approximately linearly related to the applied extensional strain ($\varepsilon_{xx-ave} = {}^{2U_x}/_{W}$ where W is the width of the plexiglass plate, 0.57 m in **Figure 66**). According to Bai and Pollard (2000), if the measured vertical strain, ε_{yy}, at point o has a large enough magnitude then σ_{xx-o} in **Equation 48** could become compressive (negative). In such a set-up, one can expect shortening (-) in the vertical direction because of the stretching (+) in the horizontal direction. Stretching (+) in the horizontal direction does not guarantee tensile stresses in the x-direction everywhere because the strain ε_{xx} will be lower at points between two joints (say point b in **Figure 66**) than at points outside (say point a in **Figure 66**) and as **Equation 48** suggests, the measured vertical strain, ε_{yy}, which will likely be compressive (-), may control the sign of the normal stress in the x-direction.

However, in this author's opinion, ε_{xx} and ε_{yy} at point o should both be zero due to symmetry. This author also expects that ε_{yy} is negative (compressive or shortening) at all points except where $y = 0$ (where $\varepsilon_{yy} = 0$) regardless of the $\frac{s}{t}$ ratio. For Bai and Pollard (2000) to measure non-zero values of ε_{xx}, the strain gauge must be located at some $x \neq 0$. Also, in order to measure non-zero values of ε_{yy}, the strain gauge must be located at some point where $y \neq 0$. Bai and Pollard (2000) must have placed the strain gauges slightly away from point o. In that case, it would be possible for them to measure positive ε_{xx} values. Coupled with the fact that vertical shortening will surely be measured at that same point (ε_{yy}<0), **Equation 48** can give negative (compressive) values of σ_{xx-o}. This is true for the $\frac{s}{t}$ ratios of 0.4 and 0.6. For $\frac{s}{t}$ ratios of 1.0 and 1.4, the calculated σ_{xx-o} is tensile (positive).

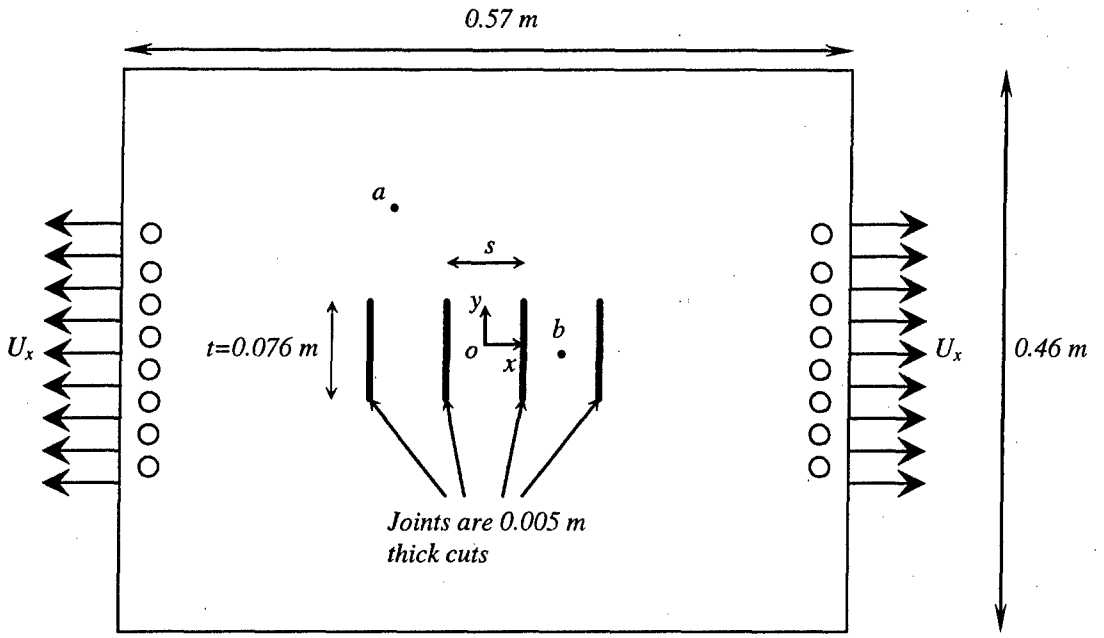


Figure 66 – Laboratory set-up used by Bai and Pollard (2000) to study critical spacing-to-thickness ratio. This figure is sketched from Fig. 8 in Bai and Pollard (2000).

Bai and Pollard (2000) also used finite element models of the same set-up to calculate σ_{xx-o}. However, this finite element model did not include the holes that were used in the laboratory set-up (**Figure 66**). The finite element simulations predicted the same behavior as the laboratory experiments for the different $\frac{s}{t}$ ratios. There were small discrepancies between the experimental and FE simulation ε_{xx-ave} and ε_{xx} values. The authors attributed the discrepancy partly to the fact that the displacement is applied through the holes in the Plexiglass plate in the experimental set-up. Bai and Pollard (2000) surmised that the plate deforms more close to the holes and less further away from them. This causes the average strain in the experiments to be less than that in the FEM. At any rate, the FE simulations predicted essentially the same σ_{xx-o} as those observed in the experiments for the different $\frac{s}{t}$ ratios used; compressive σ_{xx-o} for $\frac{s}{t}$ of 0.4 and 0.6, tensile for 1.0 and 1.4. Note that the set-up in **Figure 66** and its corresponding finite-element set-up differ from that used to obtain **Equation 47**. There will be differences between the critical $\frac{s}{t}$ ratios from each set-up because one assumes plane strain conditions while the other plane stress.

4.3 Interface Slippage Saturation Mechanism

Another saturation mechanism that needs to be investigated is that which is brought about by interface slippage. One can imagine that the interface between the jointing and bounding layers has some finite strength. It is, therefore, possible that in the process of jointing, this interface strength may be exceeded. The following model discusses this possibility and how the tensile stress distribution can be modeled.

A paper by Ji et al. (1998) contends that new joints may also occur near the ends of a segment rather than at its midpoint if the interface is allowed to have a finite strength (i.e., interbed slip is allowed). Allowing for interfacial slip changes the shape of the shear stress distribution along the interface (**Figure 67**). In this case, the interface shear stress is limited to some value, τ_0.

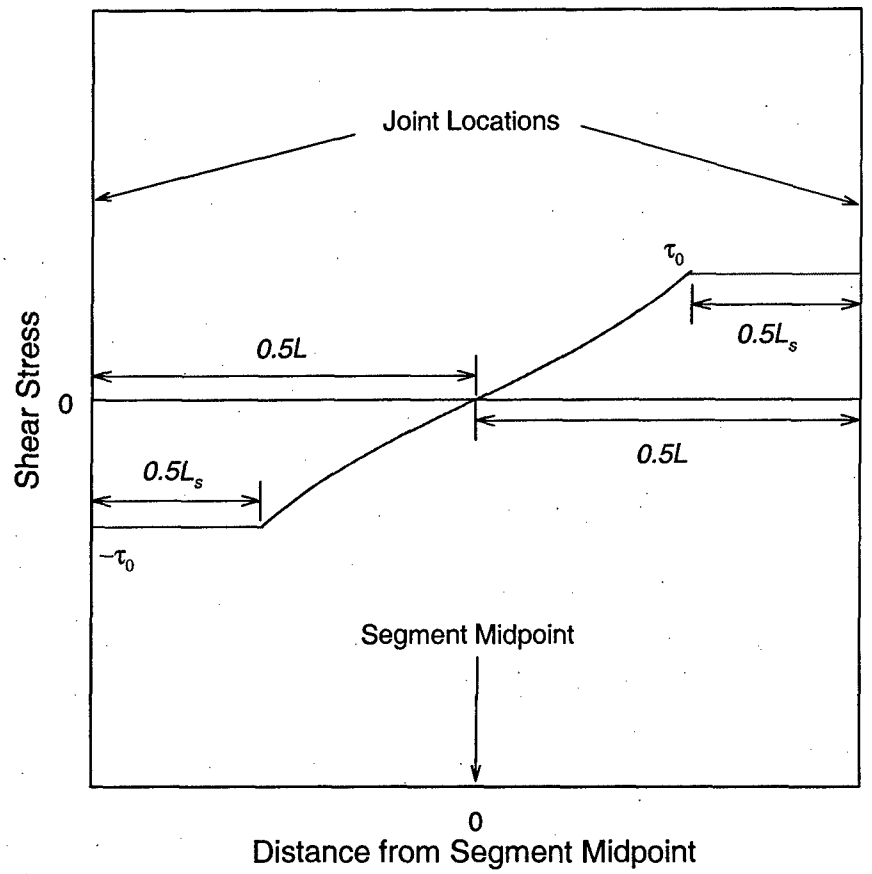


Figure 67 – Modified interface shear stress distribution to account for interfacial slip. The modified shear stress distribution allows for a maximum absolute shear stress value of τ_0.

Ji et al. (1998) used the same approach as Hobbs (1967) and Ji and Saruwatari (1998) (i.e., the shear-lag approach) in deriving the stress distributions. Also, Ji et al. (1998) use the same variable names as Ji and Saruwatari (1998) (see **Figure 47**). The solution is still of the form:

$$\sigma_{local} = E_f \varepsilon + \frac{A}{t}\sinh \beta x + \frac{B}{t}\cosh \beta x \qquad \textbf{Equation 49}$$

However, the boundary conditions are different. These are given by:

$$\sigma_{local} = \sigma_{fc} \text{ at } x = \pm\frac{(L - L_s)}{2}$$

where L is the length of the segment (or the spacing between two adjacent joints), L_s is that part of L that is experiencing interfacial slippage and σ_{fc} is the local normal stress at a distance $\frac{L - L_s}{2}$ from the segment midpoint. Applying the boundary conditions, **Equation 49** becomes

$$\sigma_{local} = E_f\varepsilon + (\sigma_{fc} - E_f\varepsilon)\frac{\cosh \beta x}{\cosh\left(\beta\frac{(L - L_s)}{2}\right)} \qquad \textbf{Equation 50}$$

where $\beta = \left[\frac{8G_n}{E_f t d}\right]^{\frac{1}{2}}$ (see also **Equation 35**). The magnitude of the local normal stress can be calculated directly from the shear stress distribution at the interface, τ_d (i.e., $\sigma_{local} = -\int\frac{2}{t}\tau_d \cdot dx$, see also **Equation 15** and **Figure 37**). Using this relationship between τ_d and σ_{local}, the shear stress can be derived from **Equation 50** as:

$$\tau_d = -\frac{t}{2}\cdot\frac{d\sigma_{local}}{dx} = -\frac{t}{2}\cdot\beta(\sigma_{fc} - E_f\varepsilon)\frac{\sinh \beta x}{\cosh\left(\beta\frac{(L - L_s)}{2}\right)} \qquad \textbf{Equation 51}$$

Substituting $x = \pm\frac{L - L_s}{2}$ and $\tau_d = \tau_0$ (the limit shear stress at the interface) in **Equation 51** and solving for σ_{fc}

$$\left|\sigma_{fc}\right| = \left|E_f\varepsilon - \frac{2\tau_0}{t\beta}\cdot\frac{1}{\tanh\left(\beta\frac{(L - L_s)}{2}\right)}\right| \qquad \textbf{Equation 52}$$

Using the relationship between the local stress in the jointing layer and the shear stress at the interface (i.e., $\sigma_{local} = -\int\frac{2}{t}\tau_d \cdot dx$ with $\tau_d = \tau_0$ and $\sigma_{local} = \sigma_{fc}$), σ_{fc} can also be expressed as

$$\left|\sigma_{fc}\right| = \left|-\int \frac{2}{t}\tau_0 \cdot dx\right| = \left|-\frac{2}{t}\tau_0 \frac{L_s}{2}\right| = \left|\tau_0 \frac{L_s}{t}\right| \qquad \textbf{Equation 53}$$

These two equations (**Equation 52** and **Equation 53**) are then combined to calculate L_s or

$$L_s = \frac{E_f \varepsilon t}{\tau_0} - \frac{2}{\beta} \cdot \frac{1}{\tanh\left(\beta \frac{(L - L_s)}{2}\right)} \qquad \textbf{Equation 54}$$

The quantity L_s cannot be isolated in the above equation. The value of L_s can be solved for numerically. This then completely defines the local normal stress distribution:

$$\sigma_{local} = E_f \varepsilon - (E_f \varepsilon - \tau_0 \frac{L_s}{t}) \frac{\cosh \beta x}{\cosh\left(\beta \frac{(L - L_s)}{2}\right)} \qquad \textbf{Equation 55}$$

The quantity $(E_f \varepsilon - \tau_0 \frac{L_s}{t})$ is always greater than zero because without the presence of jointing, $E_f \varepsilon$ is the stress due to the applied strain if there were no jointing (i.e., the maximum attainable local normal stress in the x-direction). The quantity $\tau_0 \frac{L_s}{t}$ is the normal tensile stress in the jointing layer at a distance $\frac{L_s}{2}$ from a joint (or σ_{fc} in **Equation 53**) which should be less than $E_f \varepsilon$. The minimum value of $\cosh(\beta x)$ occurs at $x = 0$ so that the maximum local normal stress also occurs at $x = 0$. The shape of the σ_{local} curve is linear with x in the intervals $\frac{L - L_s}{2} \le x \le \frac{L}{2}$ and $-\frac{L}{2} \le x \le -\frac{L - L_s}{2}$ because the interface shear stress in these intervals is constant (τ_0). In the interval $-\frac{L - L_s}{2} \le x \le \frac{L - L_s}{2}$, σ_{local} is non-linear in x as described by the equation above. **Equation 56** gives the complete definition of σ_{local} considering interface slippage.

$$\sigma_{local} = \begin{cases} \frac{2}{t}\tau_0(x+\frac{L}{2}) & , \quad -\frac{L}{2} \le x \le -\frac{L-L_s}{2} \\ E_f\varepsilon - (E_f\varepsilon - \tau_0\frac{L_s}{t})\frac{\cosh\beta x}{\cosh\left(\beta\frac{(L-L_s)}{2}\right)} & , \quad -\frac{L-L_s}{2} \le x \le \frac{L-L_s}{2} \\ \frac{2}{t}\tau_0(-x+\frac{L}{2}) & , \quad \frac{L-L_s}{2} \le x \le \frac{L}{2} \end{cases} \quad \textbf{Equation 56}$$

Figure 68 shows an example of the distribution of the interface shear stress and the corresponding σ_{local} when slippage has already occurred. The interface shear stress is limited to τ_0 and the normal stress distribution is linear where slippage has taken place. Where there is no slippage, the normal stress is defined by hyperbolic functions (middle part of above equation).

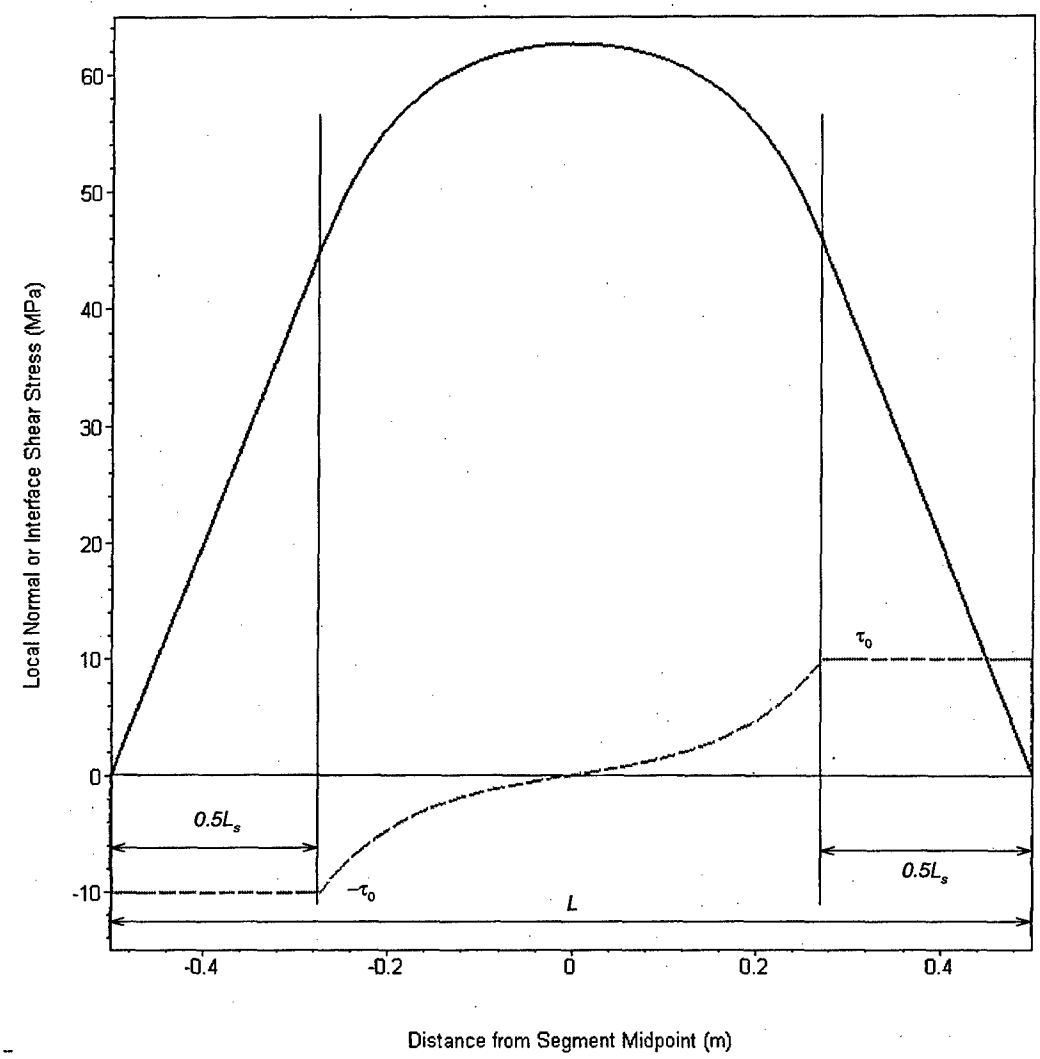


Figure 68 – Example of the local normal stress and interface shear stress distribution when interface slippage is considered. The solid curve represents the local normal stress and the dashed curve the interface shear stress. Plotted from Equation 56.

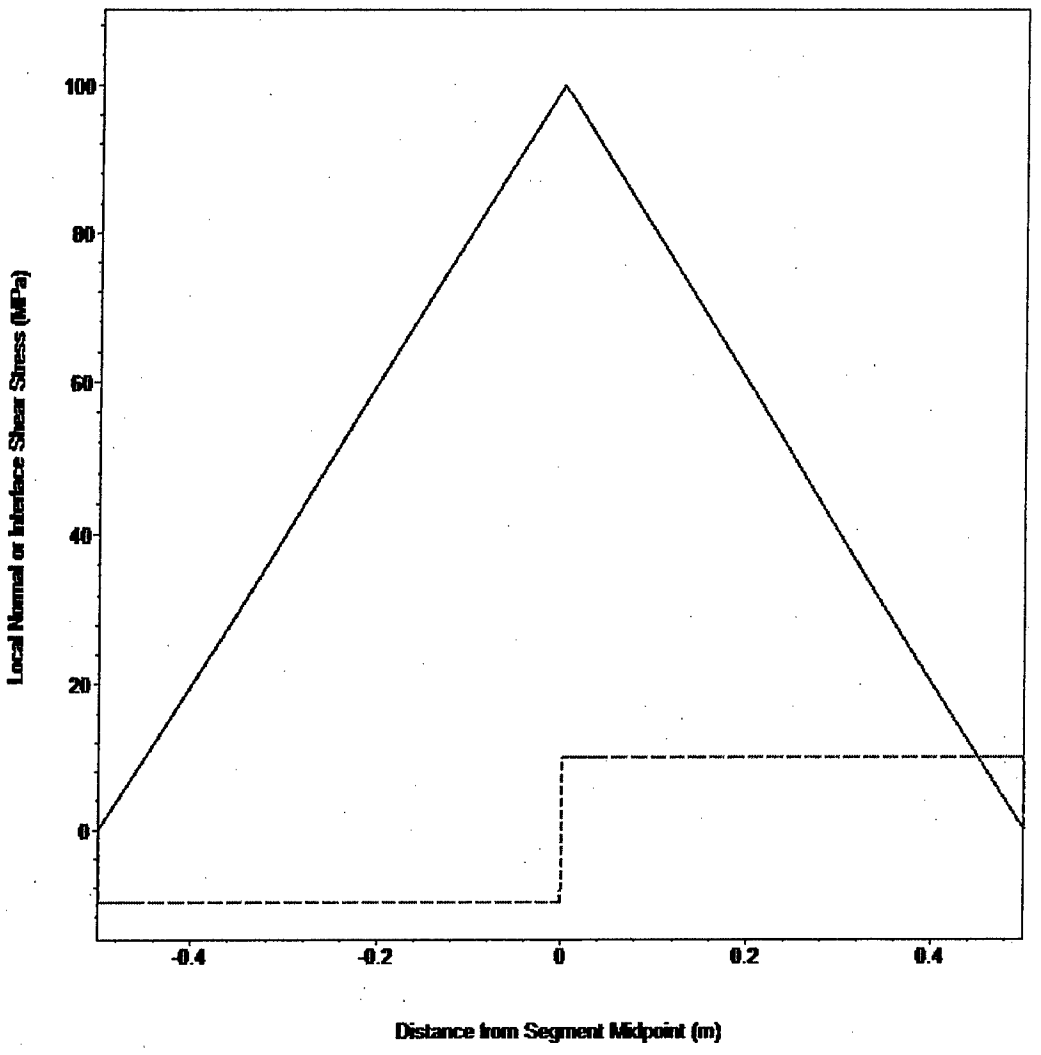


Figure 69 – Local normal stress (solid line) and interface shear stress (dashed line) distribution at full slippage. Plotted from Equation 56.

Interface slippage also limits the magnitude of the normal (tensile) stress in the jointing layer. Looking at **Figure 68**, it is easy to see that if the strain is increased to a level such that $L_s = L$ (full slippage, **Figure 69**), the local normal stress distribution will become triangular (the shear stress distribution rectangular on both sides of the segment midpoint) and cannot increase beyond that. If the magnitude of the triangular stress distribution is not enough to cause further jointing, then no more joints can form inside the segment no matter how much the strain is increased. Interface slippage can, therefore, be considered a saturation mechanism.

5 Joint Spacing Distribution Models

So far, stress distribution models (simplified one-dimensional and two-dimensional models) and saturation mechanisms have been presented. The simplified stress distribution models have been used to explain the observed relationships between joint spacing and layer thickness (i.e., **Table 3** , repeated below). The saturation mechanisms, on the other hand, appear to explain the existence of a physical limit to the density of layer-perpendicular joints that a layer can support. Another aspect of the layer-perpendicular joints in sedimentary rock is the probability distribution of their spacing. Laboratory observations have indicated that shifted-exponential, log-normal and quasi-normal joint spacing distributions can be observed at different jointing intensities (Rives et al., 1992). Field observations indicate that a quasi-normal probability distribution is rare. Log-normal joint spacing distributions are most often observed although the gamma distribution (e.g., Huang and Angelier, 1989) and the exponential distribution (Priest and Hudson, 1976) have also been used to describe the spacing of discontinuities. Laboratory and field evidence point to the fact that no single form of probability distribution can be used to describe all of the observed sets of joint spacing data. The question now is how the characteristics of the joint spacing distribution may be related to the possible mechanisms of jointing. How can one go from the geologic setting to the stress distribution models and finally, to the joint spacing distribution?

Table 3 – Summary of stress distribution and spacing for both the Hobbs (1967) and Ji and Saruwatari (1998) models.

Model	Stress Distribution	Spacing
Hobbs (1967)	$\frac{\sigma_{local}}{\sigma_{farfield}} = 1 - \frac{\cosh\left(2m\sqrt{\frac{G_n}{E_f}}\right)}{\cosh\left(\sqrt{\frac{G_n}{E_f}}l\right)}$ $m = \frac{x}{t}, l = \frac{L}{t}$	$L = t\sqrt{\frac{E_f}{G_n}}\cosh^{-1}\left(\frac{\varepsilon_2}{\varepsilon_2 - \varepsilon_1}\right)$ Linear in t
Ji and Saruwatari (1998)	$\frac{\sigma_{local}}{\sigma_{farfield}} = 1 - \frac{\cosh\left(\sqrt{\frac{G_n}{E_f}}\sqrt{\frac{2t}{h(d)}}m\right)}{\cosh\left(\sqrt{\frac{G_n}{E_f}}\sqrt{\frac{1}{2h(d)t}}lt\right)}$ $m = \frac{x}{t}, l = \frac{L}{t}$	$L = \sqrt{\frac{E_f}{G_n}}\sqrt{2th(d)}\cosh^{-1}\left(\frac{\varepsilon_2}{\varepsilon_2 - \varepsilon_1}\right)$ Non-linear in t

As an example, consider how the simplified stress distributions would lead to some form of joint spacing distribution. The simplified stress distributions can describe the relationship between layer thickness and joint spacing as a function of the bounding layer thickness and the mechanical properties of the layers at different levels of strain (i.e., **Table 3**). According to these simplified models, at any given strain, the joint spacing is

either L or $\frac{L}{2}$. This leads to a joint spacing distribution similar to that shown in **Figure 70**. Field data (e.g., Huang and Angelier, 1989; Narr and Suppe, 1991; Becker and Gross, 1996; Saltzman, 2001) indicate that actual joint spacing distributions in layered sedimentary rock are quite unlike that in **Figure 70**. Laboratory data (e.g., Rives et al., 1992) also do not appear to possess a form of joint spacing distribution similar to that shown in **Figure 70**. Thus, the stress distribution models alone are not sufficient to explain the different joint spacing distribution forms that have been observed in field and laboratory data.

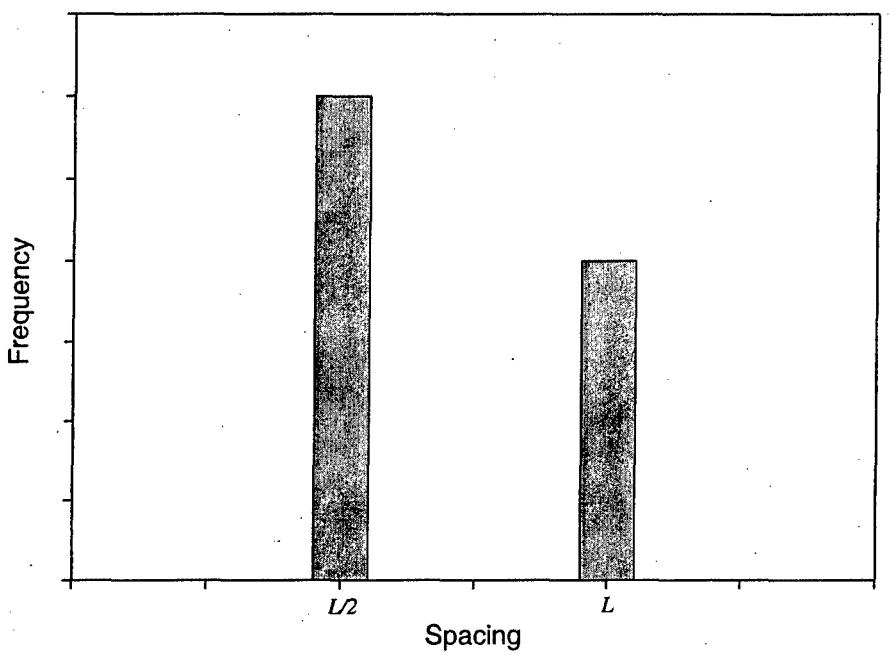


Figure 70 – Illustration of the predicted joint spacing distribution from the simplified stress distribution models.

Researchers have attempted to reproduce or explain the joint spacing distributions that have been observed in the field. Some have used a probabilistic approach (e.g., Rabinovitch and Bahat, 1999; section **5.1**) whereas others have used numerical jointing processes based on plausible mechanisms of jointing (e.g., Rives et al. , 1992; section **5.2**).

5.1 Probabilistic Approach

Rabinovitch and Bahat (1999) formulated a probability distribution for the location of a new joint relative to an existing joint with the use of a function, $q(x)$. This function is defined in the following manner: if the random variable X is the distance from a single existing joint, the probability that a new joint forms between x and $x+dx$ given that no joint formed between 0 and x is $q(x)dx$. Therefore, by definition, $q(x)$ is a "hazard function." The probability density function ($f(x)$) of X can be obtained by first expressing $q(x)dx$ in the following manner:

$$q(x)dx = P[\text{ new joint forms in } (x, x+dx) \mid \text{no new joint formed between 0 and } x]$$

or

$$q(x)dx = P[x < X \le x+dx \mid X > x]$$

Using the definition of conditional probability, the above expression becomes

$$q(x)dx = \frac{P[(x < X \le x+dx) \cap (X > x)]}{P[X > x]}$$

but $P[(x < X \le x+dx) \cap (X > x)] = P[x < X \le x+dx]$ so that

$$q(x)dx = \frac{P[(x < X \le x+dx)]}{P[X > x]} = \frac{f(x)dx}{1-F(x)}$$

or simply

$$q(x) = \frac{f(x)}{1-F(x)}$$

where $F(x)$ is the cumulative distribution function of X. Letting $G(x) = 1-F(x)$, it follows that $G'(x) = -f(x)$ and the expression for $q(x)$ becomes

$$q(x) = \frac{-G'(x)}{G(x)}$$

Integrating both sides from 0 to some x, the following is obtained:

$$-\int_0^x q(u)du = \int_0^x \frac{G'(u)}{G(u)}du$$

Letting $Q(x) = \int_0^x q(u)du$, the above equation is simply

$$-Q(x) = \ln G(x) - \ln G(0)$$

But $G(0) = 1 - F(0) = 1$ so $\ln G(0) = 0$ so that

$$-Q(x) = \ln G(x) = \ln[1 - F(x)]$$

It follows that

$$F(x) = 1 - \exp[-Q(x)]$$

From the above expression, the probability density function, $f(x) = \frac{dF(x)}{dx}$, is

$$f(x) = q(x) \cdot \exp\left(- \int_0^x q(u)du \right) \qquad \textbf{Equation 57}$$

The above equation relates the probability density function of the location, X, to the hazard function, $q(x)$. For a specific example, Rabinovitch and Bahat (1999) assumed the following piecewise function for $q(x)$:

$$q(x) = \begin{cases} \dfrac{\lambda x^{\alpha}}{2\mu^{\alpha}} & , \quad 0 \le x \le \mu \\ \lambda\left[1 - \dfrac{(2\mu - x)^{\alpha}}{2\mu^{\alpha}}\right] & , \quad \mu \le x \le 2\mu \\ \lambda & , \quad x \ge 2\mu \end{cases} \qquad \textbf{Equation 58}$$

Figure 71 shows sample curves of $q(x)$ for $\lambda = 0.1\,\text{cm}^{-1}$, $\mu = 5\,\text{cm}$ and four different α values. As **Figure 71** shows, $q(x)$ increases up to a distance of $x = 2\mu$ then remains constant thereafter. It is clear that for fixed values of λ and μ, there is a greater "jointing hazard" (i.e., probability that a joint occurs in an interval $(x, x + dx)$ given no new joints up to x) for smaller values of α in locations where $x \le \mu$. However, the, reverse is true for the interval, $\mu \le x \le 2\mu$ since a greater jointing hazard is assigned to larger values of α. The relationship between the parameters of $q(x)$ and the material properties of the rocks involved is not clear.

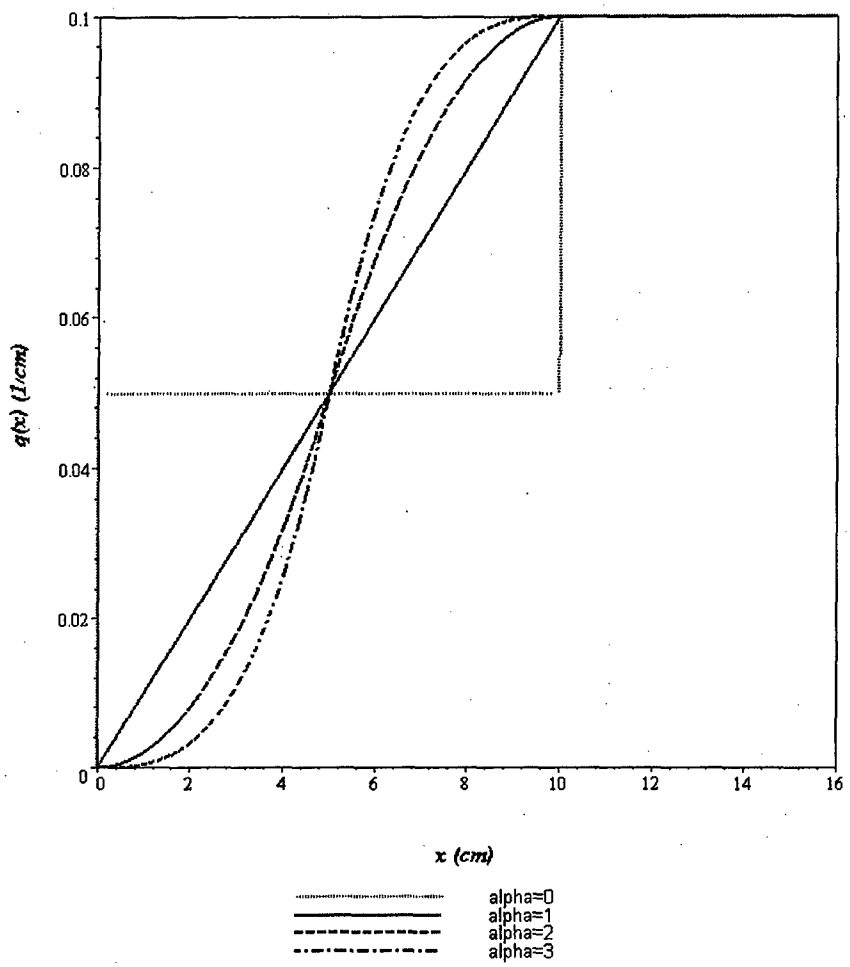


Figure 71 – Plots of $q(x)$ with parameters $\lambda = 0.1$ (cm^{-1}), $\mu = 5$ cm for $\alpha = 0$, 1, 2 and 3.

Using the piecewise form of $q(x)$ in **Equation 58**, the probability density function of X,

$$f(x) = q(x) \cdot \exp\left(- \int_0^x q(u)du \right)$$

expands to the following equation:

$$f(x) = \begin{cases} \dfrac{Bx^{\alpha}}{2\mu^{\alpha}} \cdot \exp\left(-\dfrac{\lambda x^{\alpha+1}}{2\mu^{\alpha}(\alpha+1)} \right) & , \quad 0 \le x \le \mu \\ B\left(1 - \dfrac{(2\mu - x)^{\alpha}}{2\mu^{\alpha}} \right) \cdot \exp\left(\lambda(\mu - x) - \dfrac{\lambda(2\mu - x)^{\alpha+1}}{2\mu^{\alpha}(\alpha+1)} \right) & , \quad \mu \le x \le 2\mu \\ B \cdot \exp[\lambda(\mu - x)] & , \quad x \ge 2\mu \end{cases}$$

Equation 59

The quantity, B, is a normalizing constant (Rabinovitch and Bahat, 1999). It can be seen that the tail of the distribution (i.e., the third part of the piecewise function, $f(x)$) is exponential. **Figure 72** shows how $f(x)$ is affected by the parameter α.

Given that the random variable X is the distance from a single existing joint to where a new joint is formed, how can one obtain a joint spacing distribution from $f(x)$? One way would be to use $f(x)$ to generate random values of X. These X values would represent joint locations from which a joint spacing histogram or distribution can be obtained. However, the formation of each new joint must have an effect on $f(x)$! Therefore, $f(x)$ should only be used to generate the location of one new joint not multiple new joints. This is one shortcoming of using a hazard function to represent the jointing process: it allows only for one new joint to form. In order to simulate further jointing, $f(x)$ should be revised to reflect the presence of each new joint. Note also that new joints can form on the other side of an existing joint (i.e., negative x- values). In order to consider negative x- values when generating one new joint, one can assign a 50-50 chance that the new joint is to the left or right of the single existing joint. In this sense, the use of a hazard function is also unusual. Hazard functions are typically used for uni-directional variables such as time (e.g., in time to failure problems).

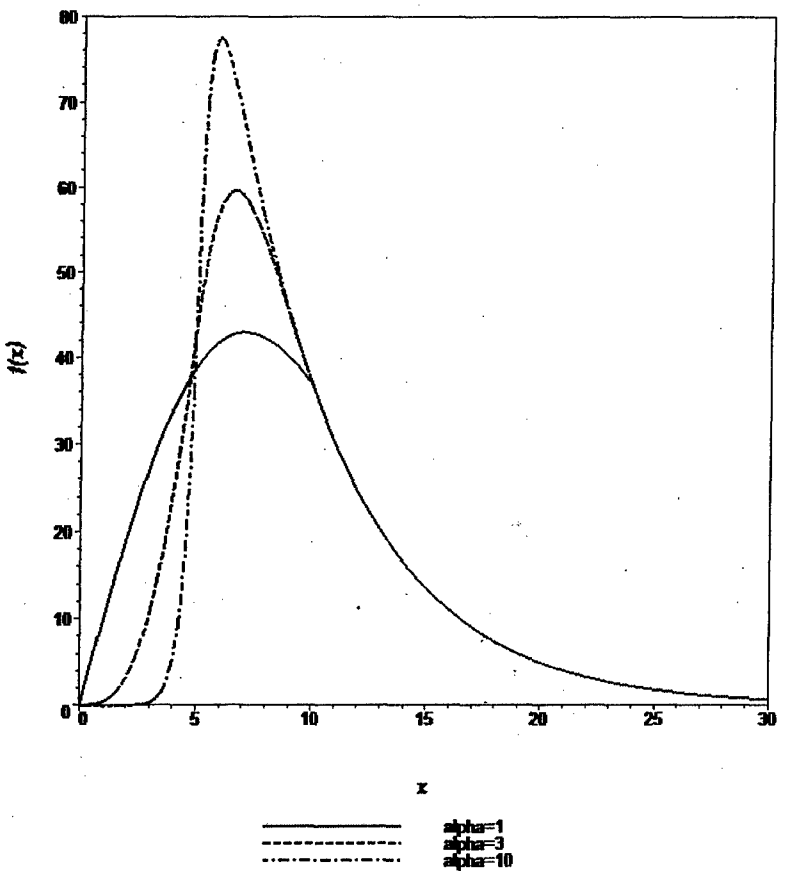


Figure 72 – Resulting probability density functions of x all with $B = 100$, $\lambda = 0.2$ (cm^{-1}), $\mu = 5$ cm for $\alpha = 1, 3$ and 10.

Purely geometric joint models such as Geofrac (Ivanova, 1998) also do not rely on the stress state to determine the locations of joints. These models use stochastic processes to simulate joint characteristics. Geofrac makes use of a primary process in order to model the stress field orientations and thus the joint orientations. In Geofrac, the planes are generated using a Poisson point process in the region:

$$\{(D,\theta,\phi): -\infty < D < \infty, 0 \le \theta \le \pi, 0 \le \phi \le \pi\}$$

Where D is the shortest distance from the generated plane to the origin, and the pair (θ,ϕ) describes the mean pole orientation of the joint set (i.e., the global azimuth and latitude, respectively). However, for the type of jointing under consideration, the mean orientation does not vary much from layer-perpendicular. For simplicity, the global azimuth and latitude could be assumed to be constant. Therefore, the generation of planes reduces to a Poisson point process in the region $\{D: -\infty < D < \infty\}$. This leads to an exponential distribution of joint spacing. As indicated earlier (in section **2.1**), the exponential distribution is not always the most suitable form that can be used to describe the joint spacing in layered sedimentary rock.

5.2 Numerical Approach

Joint patterns have also been simulated numerically using plausible mechanical/jointing processes. For example, Rives et al. (1992) used segment midpoint and random bisection procedures to generate spacing data. Segment midpoint bisection is mechanically plausible because the largest tensile stress occurs midway between two joints. Segment random bisection may also make mechanical sense if the strength along the layer is non-uniform and that, combined with the tensile stress distribution, may effectively lead to a random bisection process. A number of versions of this approach is presented in the following paragraphs and are then followed by an assessment of their effectiveness based on the actual observed nature of joint spacing statistics. Note that, unless otherwise indicated, all the plots in this section were produced independently and specificallt for this analysis.

It has been observed from laboratory experiments that the spacing distribution of layer perpendicular joints in tension changes as the joint intensity increases (Rives et al., 1992; Wu and Pollard, 1995). At low intensity, the observed spacing distribution is a shifted negative exponential; at intermediate intensity, log-normal; and at high intensity, quasi-normal. Negative exponential and log-normal distributions for field data have often been reported in the literature (e.g., Priest and Hudson, 1976; Narr and Suppe, 1991; Becker and Gross, 1996). The Gamma distribution has also been used to describe the joint spacing distribution (Huang and Angelier, 1989). Note that the negative exponential distribution is a special case of the Gamma distribution. A normal joint spacing distribution, however, is never observed. Rives et al. (1992) used simple numerical processes to model the occurrence of layer perpendicular joints in an effort to reproduce the evolution of joint spacing as intensity increases. These processes determine the locations of joints based on the stress distribution by Hobbs (1967).

Before proceeding, the assumptions should first be presented:

- The jointing layer is homogeneous. If the layer-parallel normal tensile stress (or σ_{xx}) at every point along the layer is equal to the tensile strength of the layer material (**Figure 73**), a joint can form at any point with equal probability.
- At a constant applied strain, no joint can form within the stress reduction shadows of existing joints. This is in contrast to the approach taken by Rabinovitch and Bahat (1999) where a joint can form inside the stress reduction shadow with a certain probability that is a function of distance from an existing joint. If additional strain is applied to the neighboring non-jointing layers (i.e., shear stress magnitudes at the interface increase), regions between existing joints in the jointing layer may have σ_{xx} approaching the tensile strength of the jointing layer and new joints may form
- A joint forms at a point in the layer if the stress, σ_{xx}, equals or exceeds the tensile strength of the layer (i.e., a strength of materials approach). The formation of a joint is instantaneous.
- The stress distribution derived by Hobbs (1967) applies.

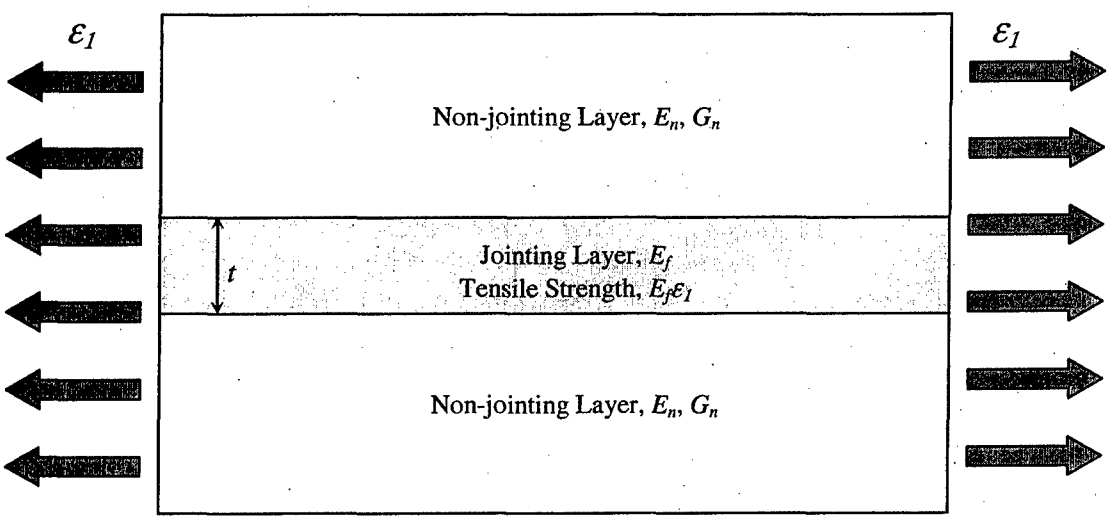


Figure 73 – Jointing layer sandwiched between two non-jointing layers. All layers are subjected to an equal amount of strain, ε_1.

For convenience, the equation describing the stress at some distance away from a joint derived by Hobbs (1967) is repeated here:

$$\frac{\sigma_{local}}{\sigma_{farfield}} = 1 + \sinh\sqrt{\frac{G_n}{E_f}}\frac{2x}{t} - \cosh\sqrt{\frac{G_n}{E_f}}\frac{2x}{t}$$

where x is the distance from the joint, $\sigma_{local} = \sigma_{xx}$, E_f is the modulus of elasticity of the jointing layer, G_n is the shear modulus of the neighboring non-jointing layers, t is the thickness of the jointing layer and $\sigma_{farfield}$ is the remote stress. Example plots of the normalized stress ($\sigma_{local}/\sigma_{farfield}$) as a function of distance from a joint for different E_f/G_n ratios are shown in **Figure 74**.

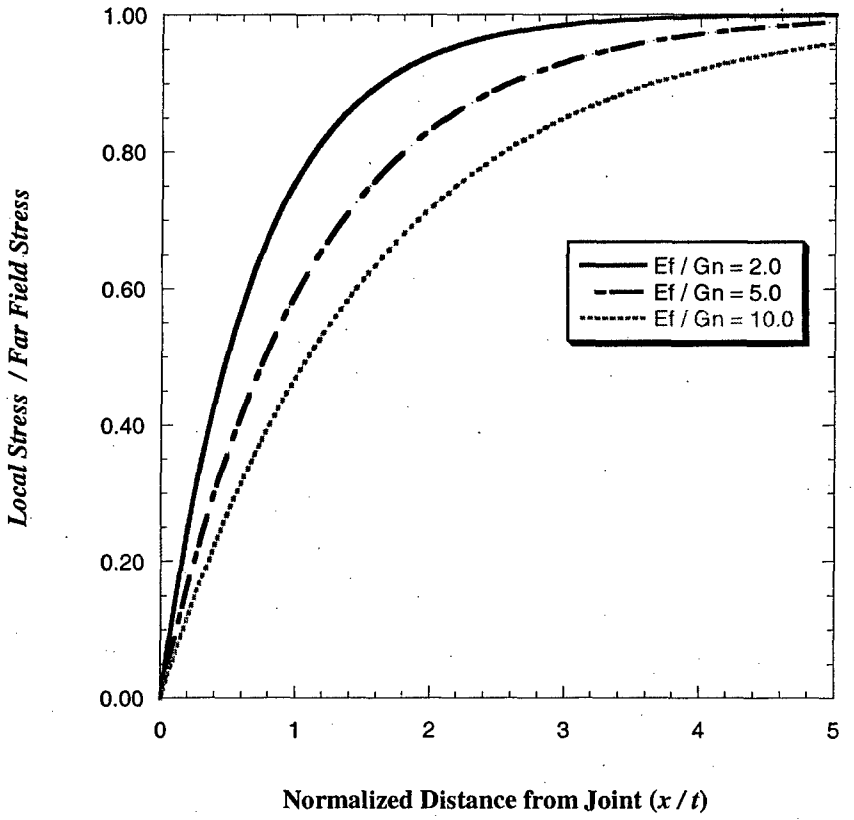


Figure 74 – Variation of normalized stress with distance away from a joint using different E_f/G_n ratios.

As one of the assumptions for the numerical jointing process, the region where a joint can form relative to pre-existing joints must be determined when $\sigma_{farfield}$ is equal to the tensile strength of the rock. **Figure 74** shows that the ratio $\sigma_{local}/\sigma_{farfield}$ approaches 1.0 asymptotically. This means that the distance where $\sigma_{local}/\sigma_{farfield} = 1.0$ cannot be defined. It must then be assumed that a joint can form at distances where at least a certain percentage of $\sigma_{farfield}$ exists. Solving for x/t in the equation for the normalized stress, the following is obtained:

$$\frac{x}{t} = \frac{1}{2} \frac{\ln\left(\frac{1}{1-\frac{\sigma_{local}}{\sigma_{farfield}}}\right)}{\sqrt{\frac{G_n}{E_f}}}$$

A value for $\sigma_{local}/\sigma_{farfield}$ can then be substituted into this equation to find the distance to the desired percentage of the far field stress. **Figure 75** shows how the distance to a certain percentage of the far field stress varies with the E_f/G_n ratio. It shows that the normalized distance to a certain percentage of the far field stress is sensitive to the chosen percentage as well as the E_f/G_n ratio. **Table 4** shows specific numbers for the normalized distance to 95% and 99% of the far field stress for different values of E_f/G_n. It shows that smaller E_f/G_n values require less distance from a joint in order to reach stresses near the remote or farfield stress. This is simply another way to look at the results in **Figure 74**.

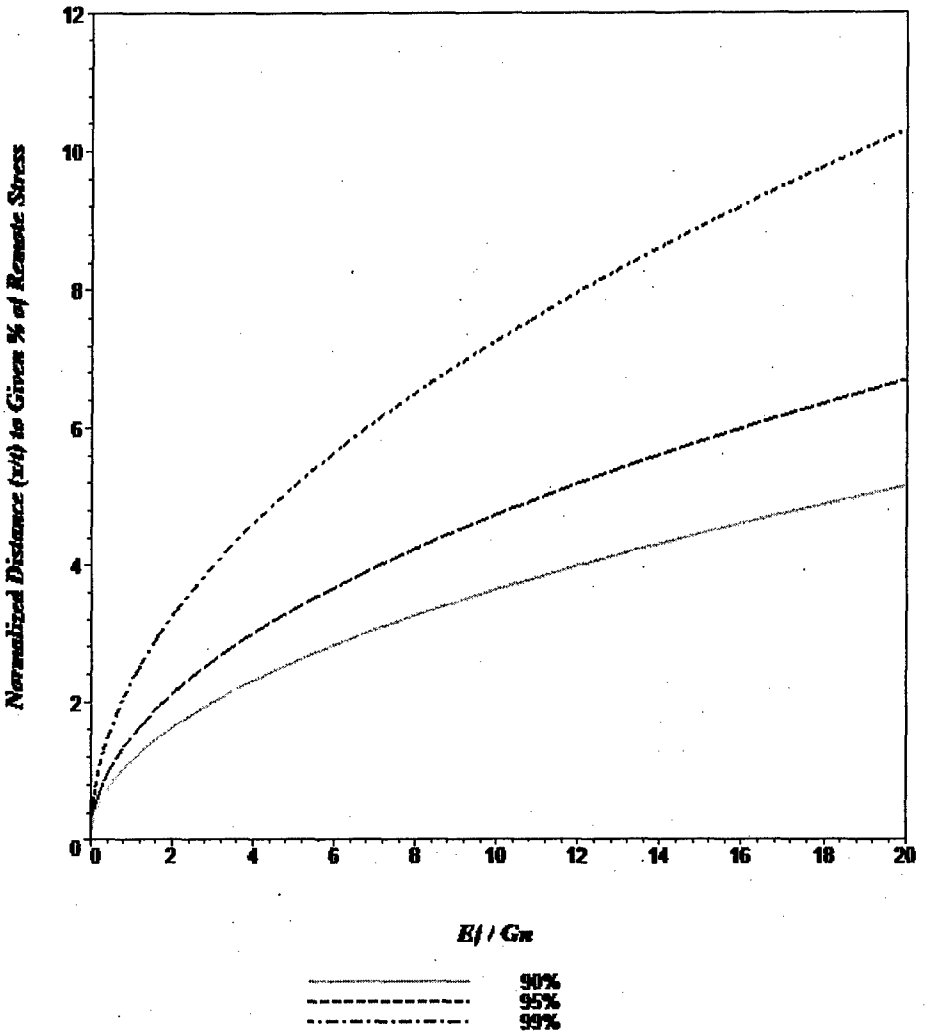


Figure 75 – Normalized distance from the joint to a particular percentage of the remote stress as a function of the E_f/G_n ratio.

Table 4 – The normalized distance from a joint to specific percentages of the remote stress as a function of the E_f/G_n ratio.

$\frac{E_f}{G_n}$	**2.0**	**5.0**	**10.0**
Normalized distance to 95% of remote stress	2.12	3.35	4.74
Normalized distance to 99% of remote stress	3.26	5.15	7.28

Before constructing the initial joint pattern, the meaning of this term must be clarified. The initial pattern occurs when every point along the jointing layer has reached a stress ($\sigma_{local} = \sigma_{xx}$) equal to the tensile strength of the rock. At this instant, a joint may form at any point along the layer with equal probability since the layer is assumed to be homogeneous. After the formation of this first joint, the stress distribution in the layer will have been altered by its presence (i.e., the stress reduction shadow, **Figure 76**). The extent of this stress reduction shadow determines where other joints may be formed. For example, **Figure 77** shows where other joints may still form with equal probability with respect to an existing joint. This process is repeated until all points along the layer are affected by the stress reduction shadows of the joints. The minimum joint spacing at the end of this process is illustrated in **Figure 78**. For this case, a joint is formed just at the tip of the stress reduction shadow of an existing joint. Meanwhile, the maximum spacing at the end of the initial process is shown in **Figure 79**. In this case, a joint forms at a distance just close enough for the resulting stress reduction shadows to touch each other. Also note that in the initial joint pattern, the maximum spacing will be twice the minimum spacing.

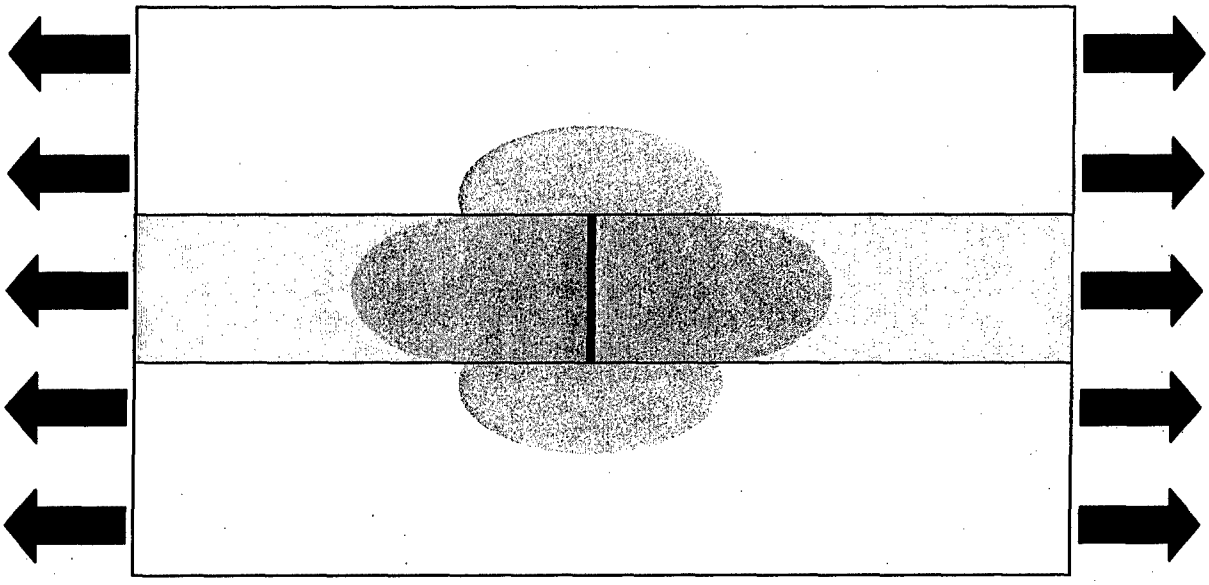


Figure 76 – Illustration of the stress reduction shadow.

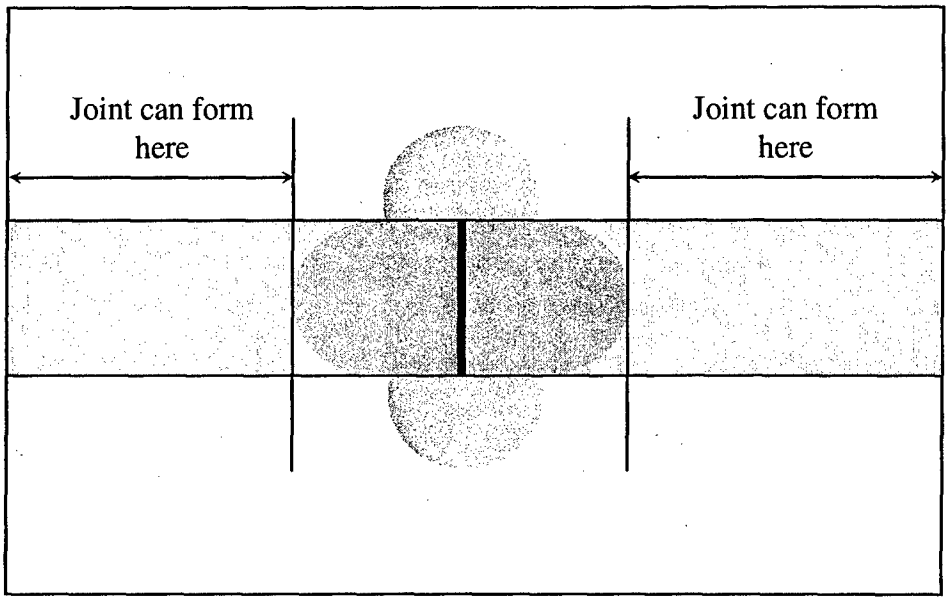


Figure 77 – Schematic of the stress reduction shadow.

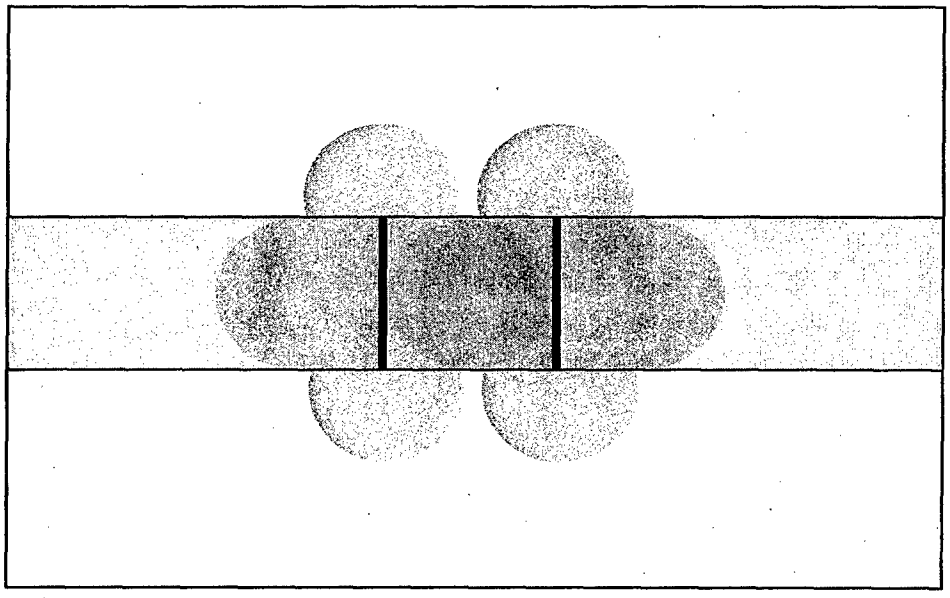


Figure 78 – Completely overlapping stress reduction shadows. The second joint forms just at the edge of the stress reduction shadow of the existing joint.

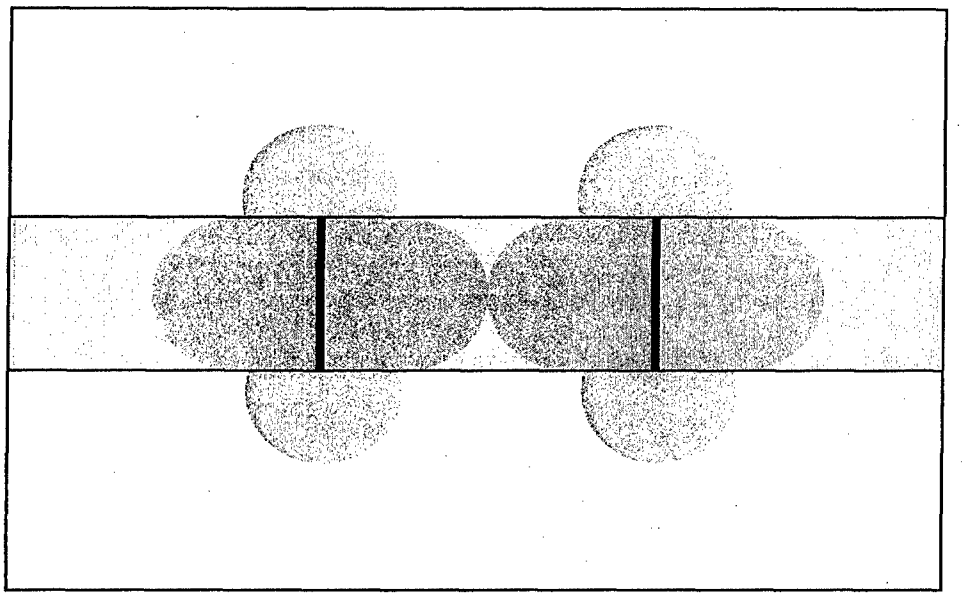


Figure 79 – Touching stress reduction shadows.

After the initial pattern is formed, it is then assumed that the applied strain is increased. Consequently, this increase in applied strain will cause an increase in the σ_{xx} within the individual segments formed by the joints in the initial pattern. Hobbs (1967) as well as Ji and Saruwatari (1998) have shown that the maximum value of σ_{xx} occurs at the midpoint of any segment. However, the maximum value of σ_{xx} also depends on the length of the segment. The models (Hobbs, 1967; Ji and Saruwatari, 1998) show that longer segments have greater midpoint σ_{xx} values than do the shorter ones. This line of reasoning leads one to believe that any additional jointing as a result of an increase in strain will likely occur first at the midpoint of the longest segment.

The four different algorithms used in the numerical process based on plausible jointing mechanisms are:

- Longest segment halving – New joints are placed at the midpoint of the longest segment. Rives et al. (1992) also used this process.
- Randomly selected segment halving – A random segment is chosen and the new joint is placed at the midpoint of this segment.
- Longest segment is divided randomly – The longest segment is found and the new joint is located randomly within that segment. Rives et al. (1992) also used this process.
- Randomly selected segment divided randomly – A random segment is chosen and the new joint is located randomly within that segment.

Now consider how this numerical process performs compared to observations made in laboratory experiments and in the field. Specifically, the change in shape of the joint spacing distribution (as defined by the skewness and the relative magnitudes of the minimum, mean and maximum joint spacing) as well as the changes in the variance (or

standard deviation) of spacing with increasing number of joints are considered. For clarity, a segment is defined as that piece formed between two joints. The length of a segment is therefore the spacing between the two joints that bound the segment. An increase in the number of segments is an increase in the number of joints and vice-versa.

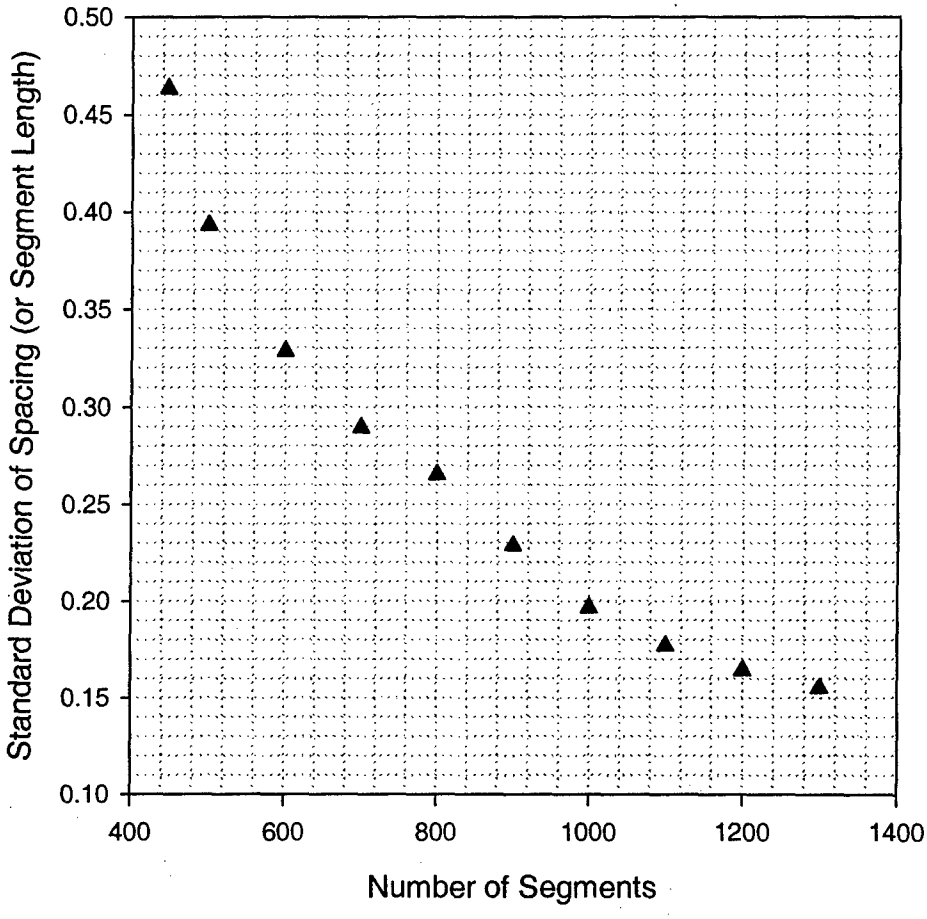


Figure 80 – Change in the standard deviation as the number of segments increases. In this algorithm, the longest segment is halved.

Figure 80 shows how the standard deviation of spacing changes as the number of joints or segments increases or as additional joints are added to the initial pattern. In the algorithm used here, after the initial pattern is complete, a joint is placed between the two joints that are the farthest apart (i.e., the longest existing segment is halved). One can see that the standard deviation decreases as the number of segments or joints increases. This means that all the spacing values begin to cluster together as additional joints are formed.

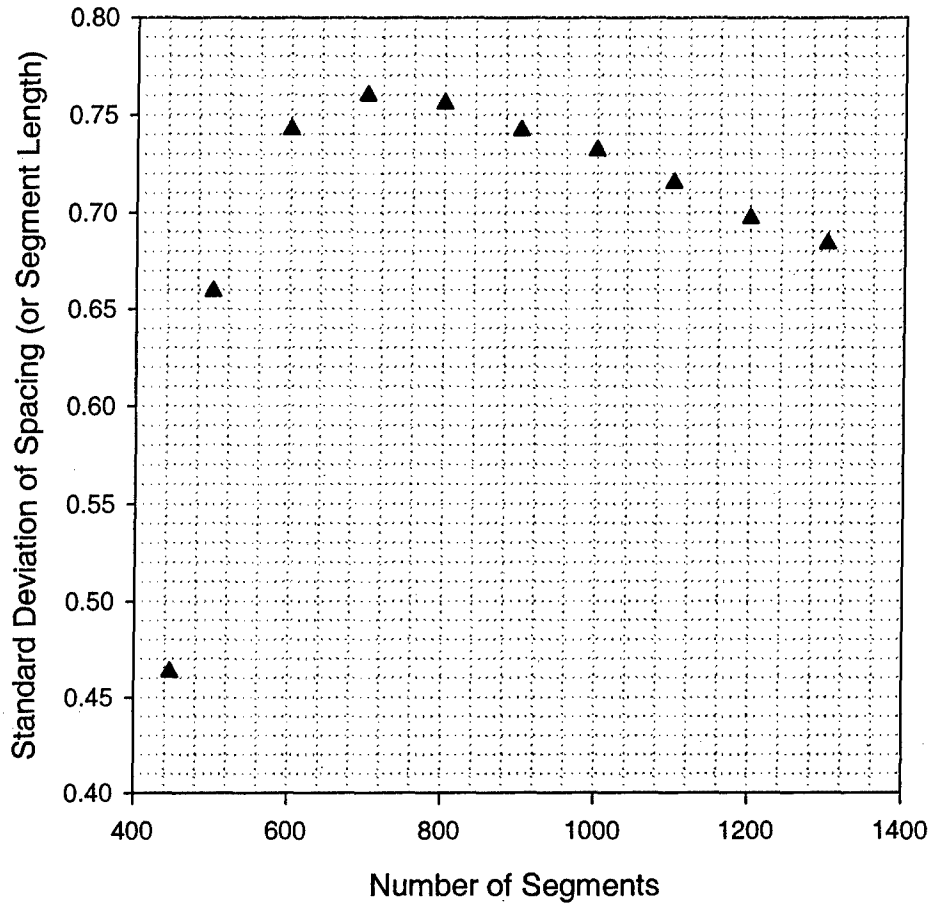


Figure 81 – Change in the standard deviation as the number of segments increases. In this algorithm, a randomly selected segment is halved.

Figure 81 shows how the standard deviation of spacing changes with the number of joints or segments when a randomly selected segment is halved. It shows an initially sharp increase in the standard deviation of spacing followed by a steady decrease as the number of segments or joints increases.

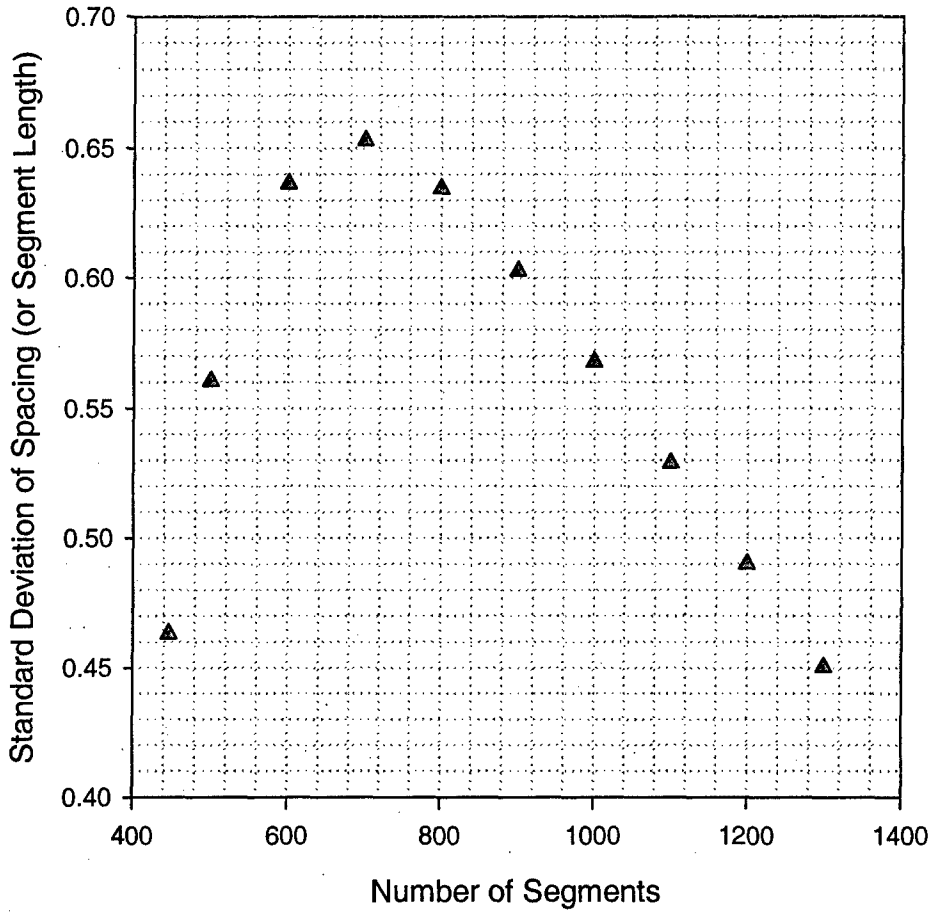


Figure 82 – Change in the standard deviation as the number of segments increases. In this algorithm, the longest segment is divided randomly.

Figure 82 shows how the standard deviation of the spacing or segment length changes with increasing number of joints or segments. **Figure 82** is for the algorithm where the longest segment is divided randomly. One can see from the plot that there is an initial increase in the standard deviation as the number of segments or joints increases. This is followed by an approximately linear decrease in the standard deviation with increasing number of segments or joints.

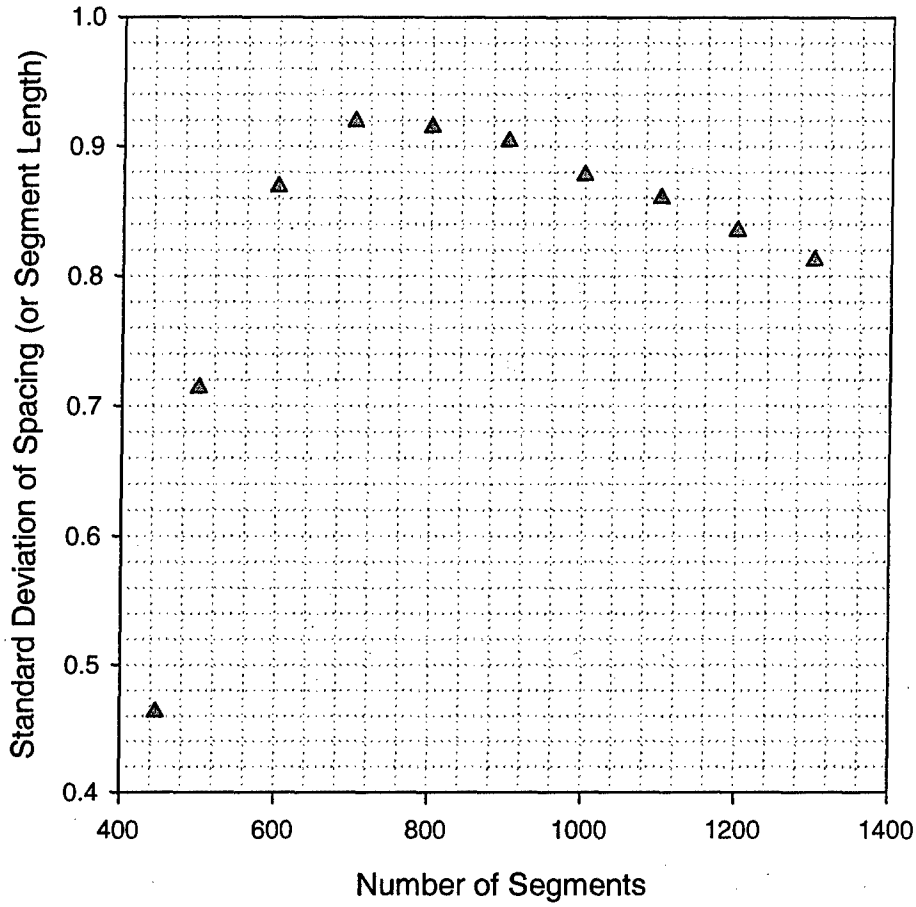


Figure 83 – Change in the standard deviation as the number of segments increases. In this algorithm, a randomly selected segment is divided randomly.

Figure 83 shows how the standard deviation varies with increasing number of segments or joints for the algorithm where first, a segment is chosen at random and then a new joint is placed at a random location within that chosen segment. Again, there is an initial increase in the standard deviation of spacing with each additional segment or joint formed up to a peak value. This is then followed by a steady decrease with increasing number of segments or joints.

The basic difference in the behavior of the standard deviation of spacing (or segment length) between halving the longest segment (**Figure 80**) and the other three processes (**Figure 81** to **Figure 83**) is the initial trend of the standard deviation as the joint intensity increases. The initial increase in the standard deviation of spacing is due to the random processes that are involved in **Figure 81** to **Figure 83** since a random process may produce segment lengths that differ much more from each other than if the longest segment is simply halved. A large difference in the lengths of the newly formed segments can increase the standard deviation at least initially.

Based solely on the behavior of the standard deviation of spacing as additional segments or joints are formed, it is difficult to say which one of the algorithms is a reasonable process for modeling the jointing mechanism under consideration. All of the algorithms show decreasing standard deviation of spacing as the number of segments increases although three out of the four show an initial increase instead of a decrease from the onset. This decrease in standard deviation is consistent with the observation that as the joint intensity increases the spacing values become more or less close to each other. This regularity may depict a tight clustering of the spacing values about the mean spacing (e.g., quasi-normal distribution).

Another characteristic of the observed joint spacing distributions presented in one of the previous sections is their usually positive skewness. Positive skewness means that the probability distribution is heavy towards smaller values and possesses a decaying tail towards larger values. This means that the skewness of the joint spacing distributions would ideally be positive and decreasing to zero as the joint spacing distribution goes from negative exponential to log-normal to quasi-normal (**Figure 84**). Note that a quasi-normal joint spacing distribution is never observed in field data so in reality, the skewness may not actually go to zero. On the other hand, it is obviously impossible to observe a progression of joint spacing distribution in the field. For the purposes of this comparison, one may expect the skewness to decrease, not necessarily all the way to zero, as joint intensity increases.

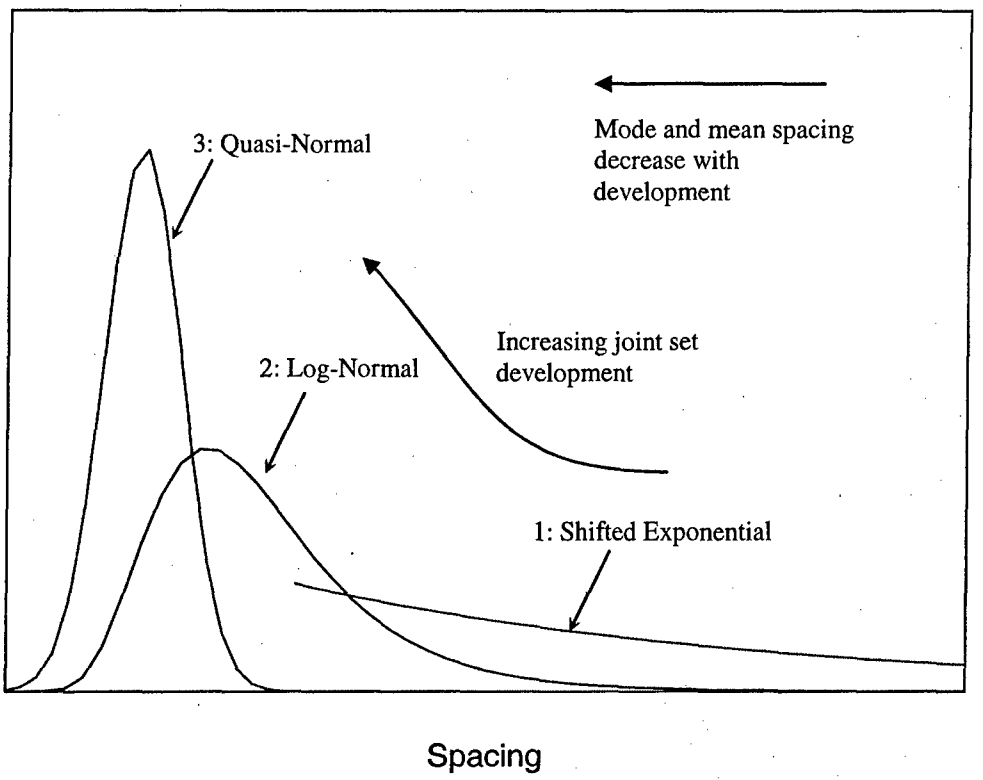


Figure 84 – The skewness values of the different joint spacing distributions approach zero for the quasi-normal distribution. This figure follows Fig. 7 in Rives et al. (1992).

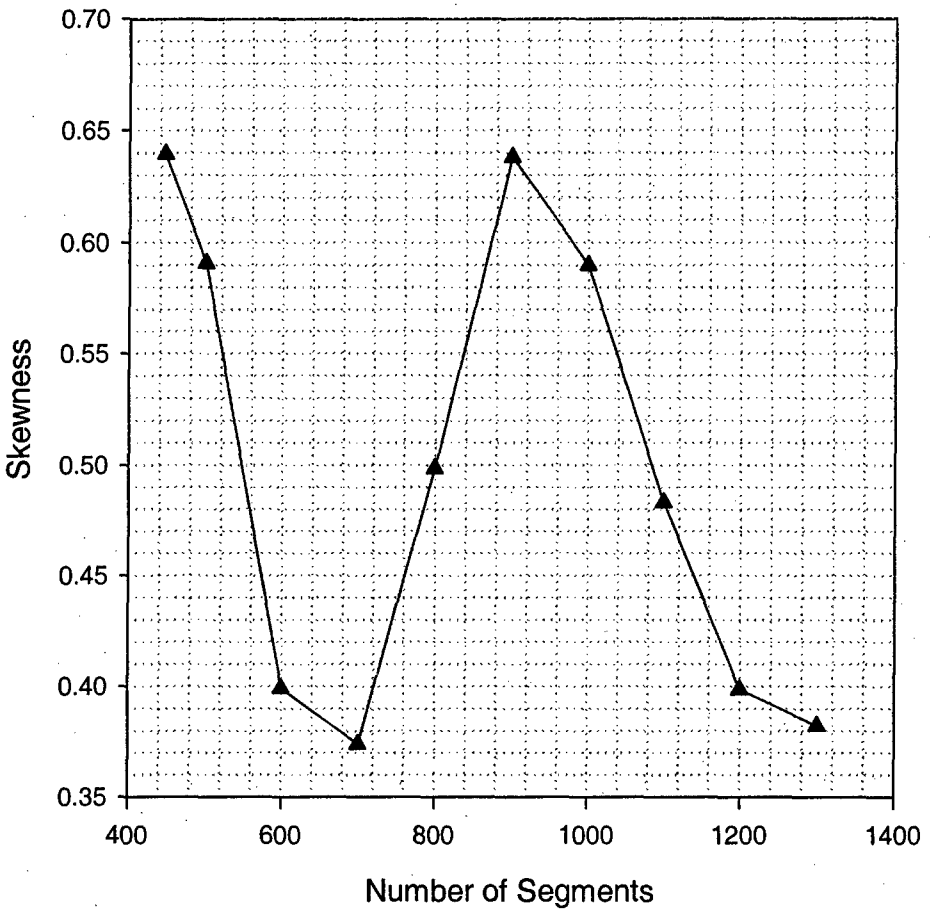


Figure 85 – Skewness with increasing number of segments. In this algorithm, the longest segment is halved.

Figure 85 shows the relationship between the skewness of the joint spacing distribution (or the segment length) and the number of segments or joints. The skewness is always positive but undergoes a series of decreases and increases as the number of segments increases. The skewness is also reflected in the relationship among the mean, minimum and maximum joint spacing values. **Figure 86** shows the relationship among these three parameters for the longest-segment-halving algorithm as the number of segments increases. **Figure 86** shows that after the initial pattern is generated, the mean is closer to the minimum spacing than it is to the maximum spacing. This indicates a positive skewness. As new joints are added, the mean still remains closer to the maximum but at varying degrees maintaining a positive skewness. Additional simulations were carried out to investigate how the skewness vs. number of segments relationship behaves as more joints are added.

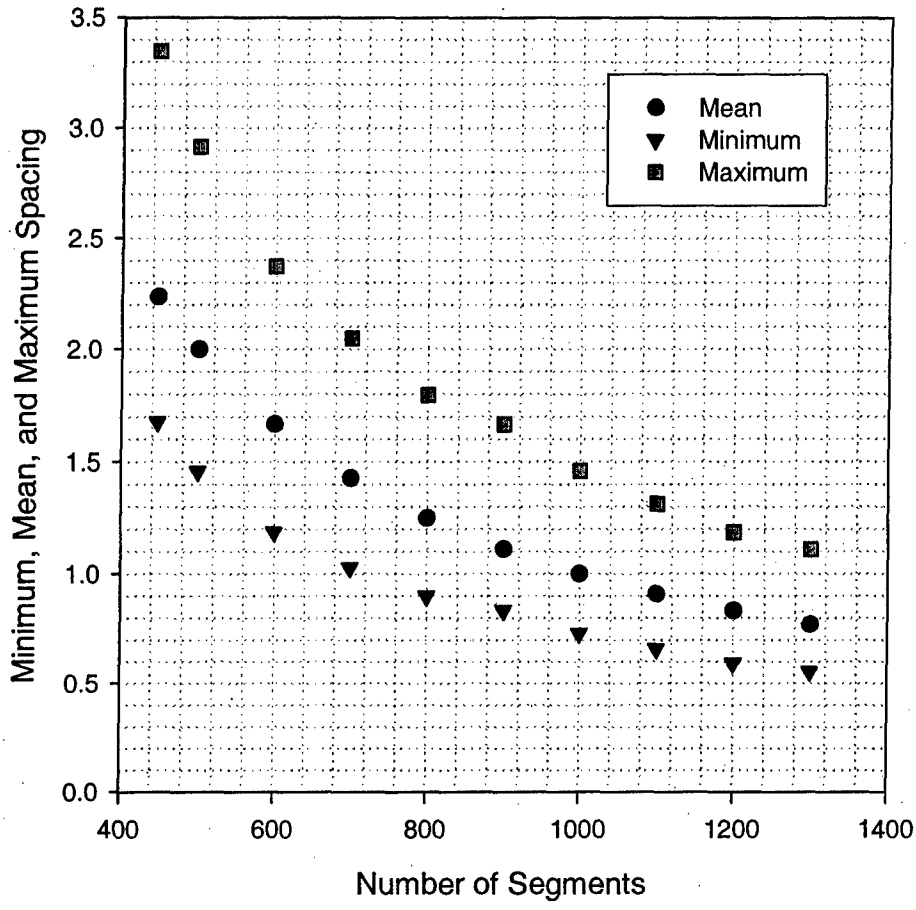


Figure 86 – Relationship among the mean, minimum and maximum joint spacing values for longest segment halving.

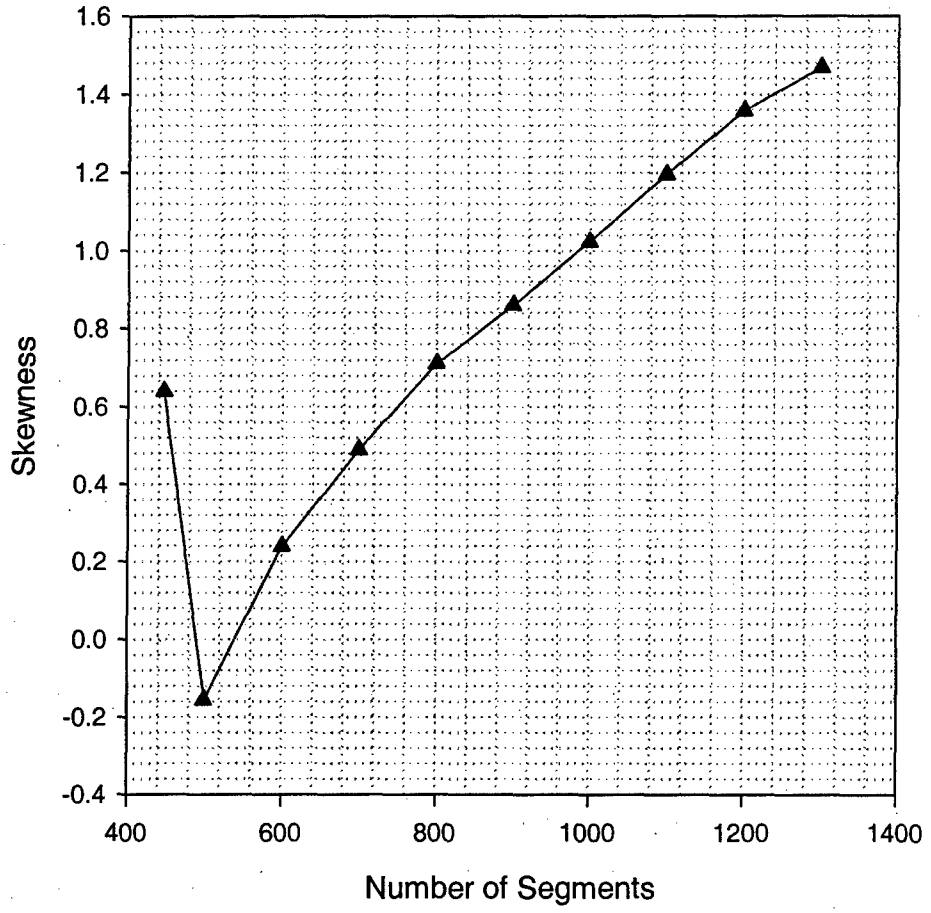


Figure 87 – Skewness with increasing number of segments. In this algorithm, a randomly selected segment is halved.

Figure 87 shows the skewness with increasing number of segments for the algorithm where a randomly selected segment is halved. This does not seem to be a suitable process because the skewness becomes negative at one point and then increases and becomes positive as the number of segments increases. This is also apparent in **Figure 88** when looking at the second set of minimum, mean and maximum spacing points. For this set of points, the mean is slightly closer to the maximum than it is to the minimum (negative skewness). However, as the number of segments increases, the mean spacing becomes closer to the minimum spacing than it is to the maximum spacing suggesting that a larger part of the distribution is concentrated in the smaller values. The maximum spacing remains the same while the minimum spacing quickly approaches zero and remains constant.

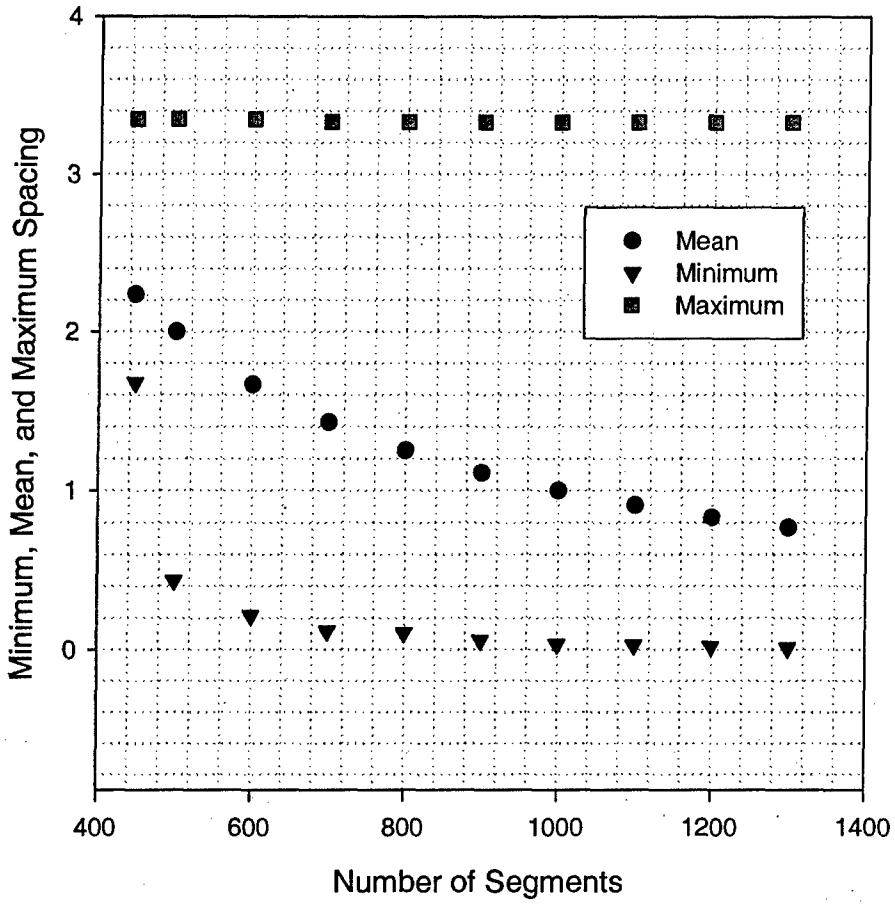


Figure 88 – Relationship among the mean, minimum and maximum joint spacing values for halving a randomly selected segment.

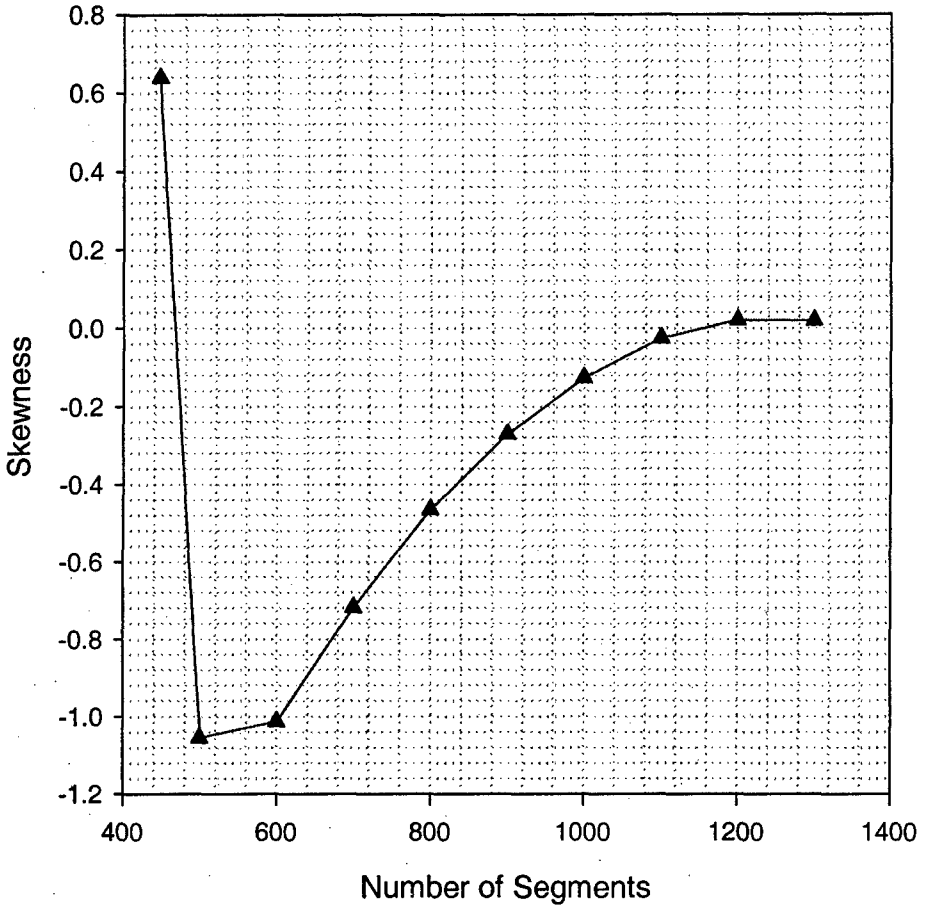


Figure 89 – Skewness with increasing number of segments. In this algorithm, the longest segment is divided randomly.

Figure 89 illustrates the relationship between skewness and the number of segments if additional joints are formed by randomly dividing the longest segment. This algorithm does not seem to describe the process of jointing well because the skewness values immediately drop to negative values upon the addition of new joints to the initial pattern. The skewness then increases but seems to tend to zero as the number of segments or joints grows larger. This result is expected since the final shape of the joint spacing distribution for this kind of algorithm would be a uniform distribution and this type of distribution should have zero skewness. A uniform joint spacing distribution will result because each time, the new joint is placed at a random location within the longest segment. This means that the resulting two segments will have lengths that are equally probable between the original length of the divided segment and zero. **Figure 90** shows that in the initial pattern, the mean spacing is closer to the minimum spacing than it is to the maximum spacing (positive skewness). The minimum spacing quickly reduces to zero as more segments are added. This is accompanied by a decrease in the maximum spacing. However, the mean spacing is still closer to the maximum spacing (negative

skewness). As the number of segments increases, the mean approaches midway between the minimum and maximum joint spacing (zero skewness).

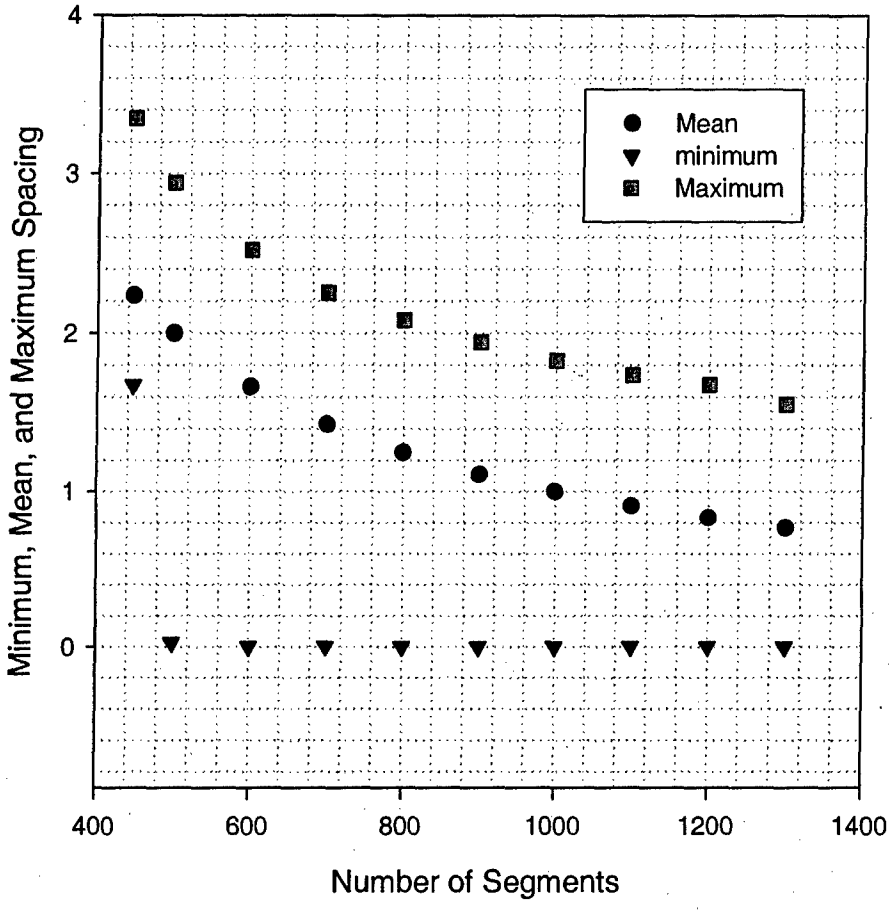


Figure 90 – Relationship among the mean, minimum and maximum joint spacing values for randomly dividing the longest segment.

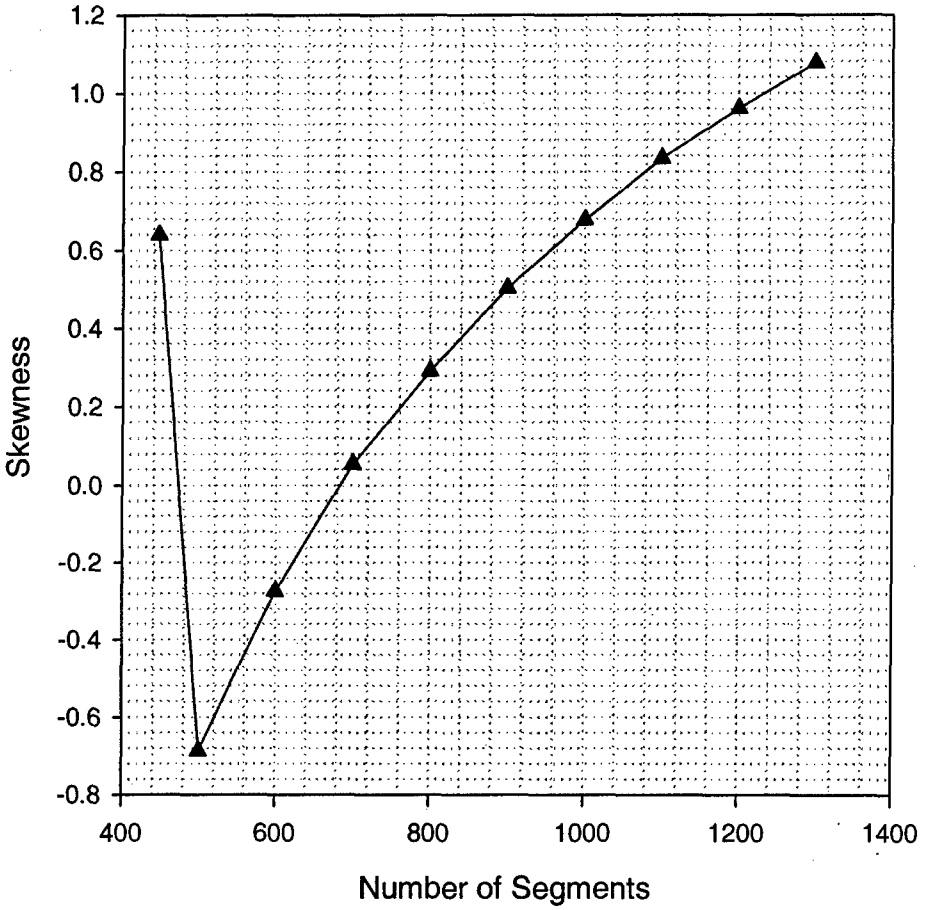


Figure 91 – Skewness with increasing number of segments. In this algorithm, a randomly selected segment is divided randomly.

Figure 91 shows that the skewness quickly becomes negative when new segments are added at random locations within randomly chosen segments. However, it gradually increases and becomes positive as more segments are added. This is also shown in **Figure 92**. The skewness for the initial pattern is positive. When additional segments are formed by the additional joints, the minimum spacing suddenly becomes zero but the mean spacing is still close to the maximum spacing (negative skewness). The maximum spacing remains constant and the minimum spacing remains at zero. The mean spacing decreases and becomes closer to the minimum spacing causing the skewness to become positive and increasing.

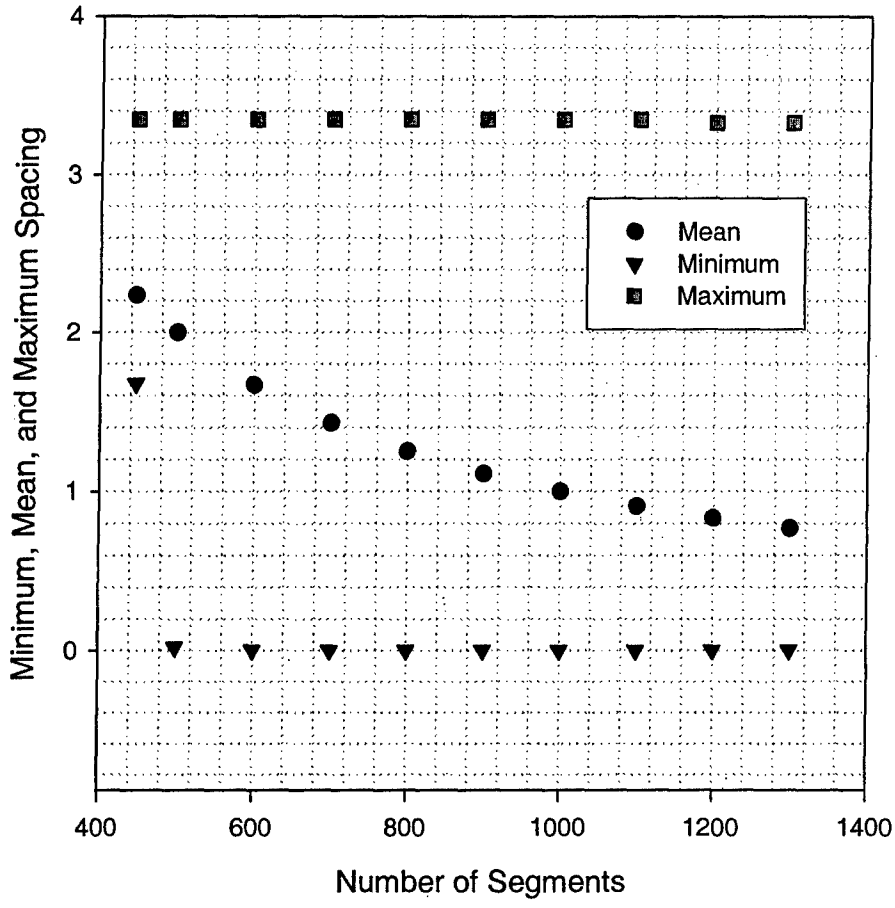


Figure 92 – Relationship among the mean, minimum and maximum joint spacing values for randomly dividing a randomly selected segment.

Based on the skewness of the resulting joint spacing distributions, it seems that the longest-segment-halving algorithm (**Figure 85**) shows the most promise. It is the only algorithm that produces joint spacing distributions that always have positive skewness and does not increase steadily with increasing joint intensity. However, the skewness versus number of segments plot does not seem to show a decrease towards zero which would reflect the supposedly final quasi-normal distribution. Additional simulations were performed by adding more joints forming more segments. The results are shown in **Figure 93**. It seems that the skewness of the joint spacing distribution cycles between a low of about 0.37 to a high of about 0.64 and never approaches zero.

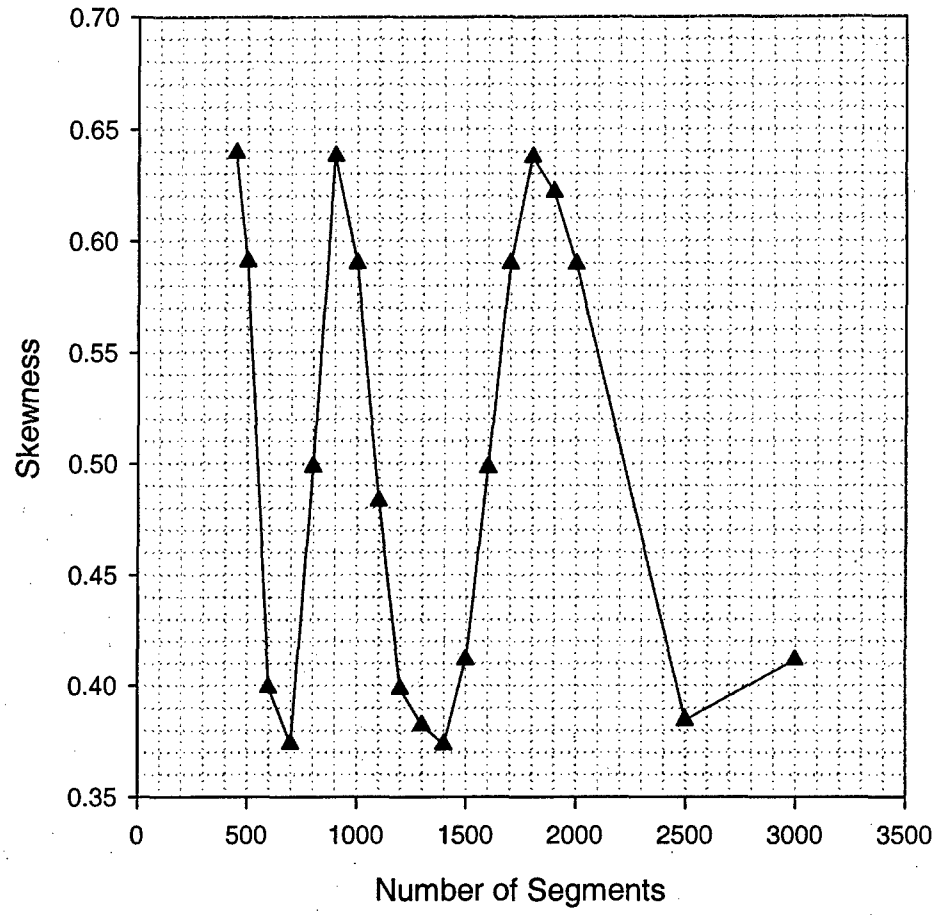


Figure 93 – Skewness versus number of segments for the longest segment halving algorithm (additional results).

The cyclical nature of the relationship between the skewness and the number of segments can be explained by looking at the segment length (or joint spacing) distribution and how it changes as the longest segment is halved. The segment length or joint spacing distribution for the initial pattern is shown in **Figure 94**. As the longest segments are halved, the frequency of the largest segment length values decrease. In the case of **Figure 94**, the frequency of the spacing or length values in the 0.20 m bin will decrease. This will be accompanied by an increase in the frequency of spacing or length values in the 0.10 m bin. If the process continues until all the spacing values just above 0.10 m have been halved, the process will have effectively "shifted" the initial pattern distribution to the interval 0.05 to 0.10. Of course, this new distribution will not have the same frequencies as that in the initial pattern because 1) there are more segments and 2) the segment length or spacing interval is more narrow (0.05 m compared to 0.1 m for the initial pattern). However, the shape will essentially be the same. At this point, the skewness will be the same as the initial pattern skewness. If additional jointing continues, the cycle is repeated as already shown by the results in **Figure 93**.

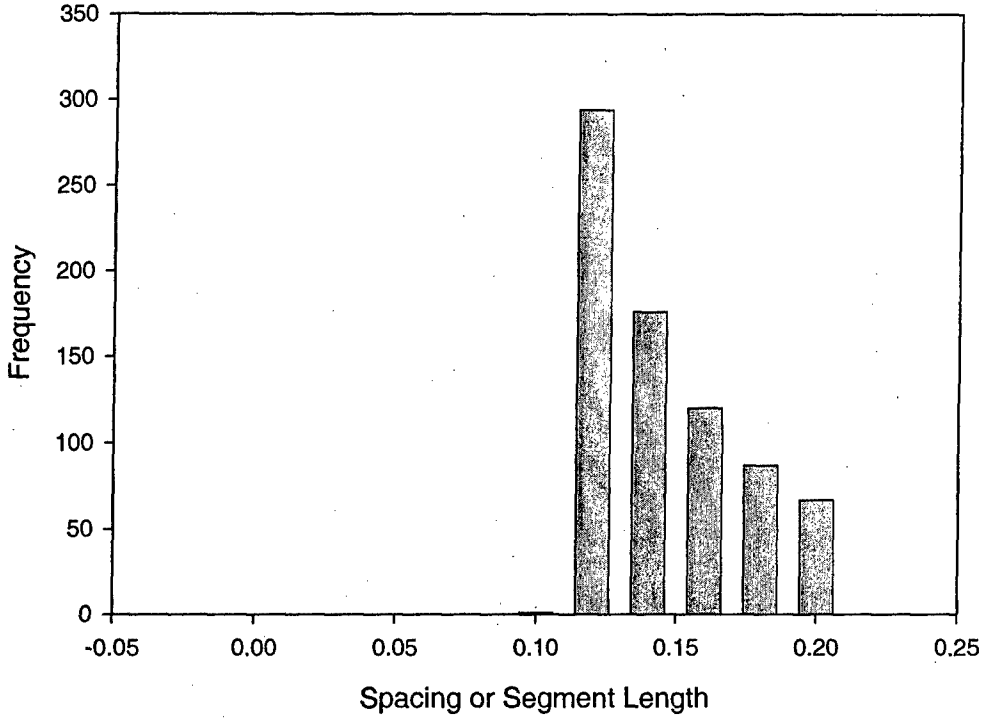


Figure 94 – Spacing distribution after the initial pattern is generated.

The results presented in this section indicate that, although somewhat mechanically plausible numerical jointing processes are used, the resulting behavior fails to mimic that observed in laboratory experiments and in the field. Considering the behavior of the standard deviation with additional jointing alone, the longest-segment-halving algorithm seemed to have the most promise. However, upon inspection of the skewness versus intensity (i.e., number of segments or joints), it is found that skewness behaves in some kind of cyclic manner (**Figure 93**). The three other algorithms, although showing decreasing standard deviation of spacing with increased jointing, have their skewness values either approaching zero from the negative range (**Figure 89**) or increasing monotonically from the negative range (**Figure 87** and **Figure 91**).

6 New Models

6.1 Introduction and Overview

It is clear that the joint spacing distributions suggested by the Hobbs (1967) and Ji and Saruwatari (1998) stress distribution models (**Figure 70** page 126) are inadequate to describe true joint spacing distributions. The probabilistic approach suggested by Rabinovitch and Bahat (1999) only considered the formation of one new joint given the existence of a single joint, not multiple joints (i.e., in-filling between joints). Also, the parameters of the hazard function, $q(x)$, were not clearly linked to rock material properties. Numerical processes based on some plausible jointing process (e.g., midpoint bisection, random division; Rives et al., 1992) were also not effective in describing the statistics of the joint spacing distribution. The geometric model by Ivanova (1998) produces an exponential joint spacing distribution for joints in layered sedimentary rock subjected to far-field extension. The resulting exponential distribution of spacing from Ivanova (1998) is inherent in the process used to generate the joints in the model (i.e., a Poisson process). Narr and Suppe (1991) used Hobbs' (1967) model in a jointing layer with random "flaws" to generate joint spacing distributions. They assumed that these "flaws" weakened the layer at random points by random amounts. As the strain is increased, a new joint is formed at a point where the normal stress exceeds the tensile strength. Narr and Suppe (1991) observed that this process could mimic the shape of the joint spacing distributions found for field data they collected (i.e., log-normal). However, the comparison was not detailed and none was performed with laboratory observations. The effects of joint saturation mechanisms were also not included in their study. The effect of the rock material properties on the resulting joint spacing probability distribution was not studied. From all this, it is evident that better models are needed and must be validated through comparison with field data. This will be done in **Chapter 7**.

In this chapter, two new jointing models (the flaw model and the rejection procedure) are presented and their capabilities demonstrated. Each model uses a combination of probabilistic and mechanical concepts in an attempt to duplicate the jointing sequence that takes place in a layered sedimentary rock subjected to remote extensional strain. The jointing sequence is instrumental to the kind of joint spacing distributions that have been observed in lab and field data. The flaw model is made up of two main components: a stress distribution model and a strength model. The stress distribution model, as the name suggests, describes how the stresses vary within the jointing layer. The strength model, on the other hand, describes the variation of the tensile strength along the length of the jointing layer. The flaw model relies on a comparison between the stress and the strength at some location in the jointing layer in order to determine if a joint forms or not. The rejection procedure, on the other hand, uses a single component, the stress distribution model to describe the probability density function of joint location, $f(x)$. This function is then used to determine where new joints form. A simple form of $f(x)$ that depends only on the stress distribution is used (i.e., no strength model). One can see that the two main differences between the flaw model and the rejection procedure are the manner in which each utilizes the stress distribution model and the presence or absence of a strength model.

In the following sections, the development of the two new jointing models is presented, first the flaw model, then the rejection procedure. The presentation structure for each jointing model is as follows:

1. A description of the stress distribution model and the strength model for the flaw model and the probability density function, $f(x)$, for the rejection procedure.

2. Jointing model algorithm without saturation mechanisms.

3. Jointing model algorithm with saturation mechanisms.

4. Parametric study for the mean joint spacing at saturation (e.g., for flaw model: effects of stress distribution and strength model parameters in the saturation mean spacing).

5. Study of the joint spacing distributions (i.e., effects of joint intensity, stress distribution and strength model parameters in the shape of the joint spacing distribution).

6.2 Flaw Model

The first jointing model, termed a **flaw model**, is based on a mechanical approach and is similar to the model formulated by Narr and Suppe (1991). For the flaw model, the strength model component is an important aspect because it strongly affects the resulting joint patterns and thus the joint spacing distribution. If the jointing layer is assumed to have the same tensile strength all along its length, one should expect new joints to form midway between two existing joints (i.e., where the tensile stress is a maximum). In the previous section, this process (midpoint bisection) has been shown to be incapable of producing realistic joint spacing distributions. A more realistic approach to modeling the tensile strength would be to assume that the strength is not constant along the length jointing layer. To achieve this, random flaws are added to the jointing layer (thus the term "flaw model"). Each flaw lowers the tensile strength of the jointing layer at its location. At locations where no flaws exist, the tensile strength is assumed equal to some maximum value (e.g., the intact rock tensile strength). In other words, at each flaw location a random tensile strength lower than that of the intact rock is assigned. The random tensile strength value at each flaw could be generated using some kind of probability distribution. For simplicity, a uniform distribution of tensile strength is used to assign these values. Other probability distributions can also be used.

The issue of joint saturation is also considered in the flaw model. Two saturation mechanisms are incorporated into the flaw model: saturation due to interface slippage and saturation due to the development of compressive stresses. These mechanisms were described in previous sections and will be repeated later in the development of the model algorithms for convenience.

As mentioned above, the flaw model makes explicit use of both a stress distribution model and a strength model. The model by Ji et al. (1998) will be used to define the tensile stresses in the jointing layer. According to Ji et al. (1998), the tensile stress distribution between two adjacent joints is given by:

$$\sigma_{local} = E_f \varepsilon \left[1 - \frac{\cosh \beta x}{\cosh\left(\frac{\beta L}{2}\right)} \right] \qquad \textbf{Equation 60}$$

where $\beta = \left[\frac{8G_n}{E_f t d}\right]^{\frac{1}{2}}$ (β is in units of $1/length$ so that βx and $\beta L/2$ are dimensionless), t = thickness of the jointing layer, d = thickness of the non-jointing bounding layers, E_f = Young's modulus of the jointing layer, G_n = shear modulus of the non-jointing bounding layers, ε = applied extensional strain, x = distance from the segment midpoint where σ_{local} occurs and L = length of the segment (**Figure 95**).

This stress distribution model includes the effects of the elastic contrast between the jointing and non-jointing bounding layers as well as the geometry of the non-jointing layer (d) on the tensile stresses. One could use other stress distribution models based on the shear-lag approach such as Hobbs (1967) or Ji and Saruwatari (1998) but Ji et al. (1998) also provide a framework for working with interface slippage. An analytical solution based on a full elastic approach for this specific problem does not yet exist. Numerical approaches such as finite-elements could also be used (e.g., FRANC2D) but the process becomes too computationally intensive when one needs to re-calculate the stresses each time a new joint is added. In two dimensions, the tensile stress is a maximum at the interface and minimum at the midpoint of the jointing layer (**Figure 96**). This profile changes and becomes shallower with distance away from an existing joint (**Figure 96** at distances *a*, *b* and *c*). The simplified stress distribution models provide a reasonable alternative since they can be thought of as representing the average tensile strength with distance away from an existing joint (**Figure 97**).

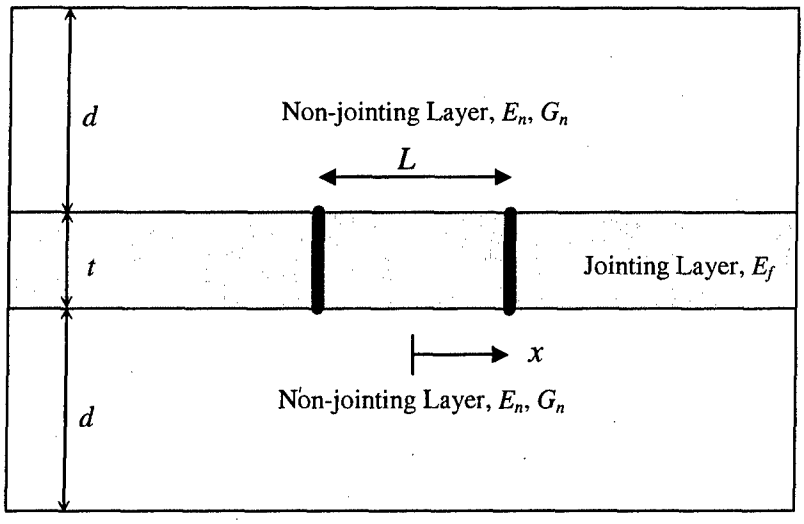


Figure 95 – Geometry of the problem.

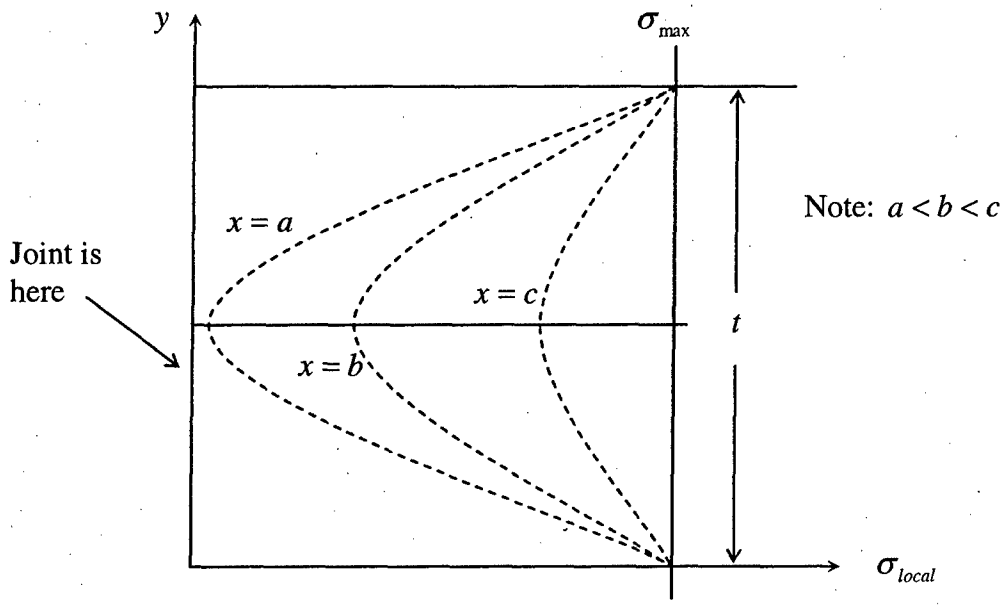


Figure 96 – Schematic of the local tensile stress profile along the *y*-direction at different distances from an existing joint.

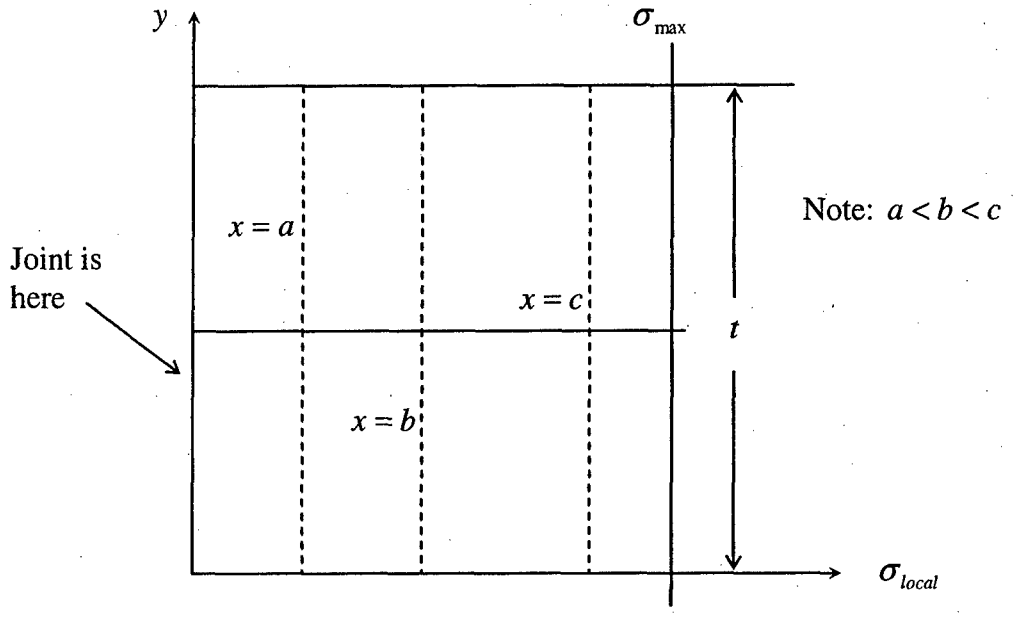


Figure 97 – Schematic of the average tensile stress at different distances from an existing joint.

As for the strength model, a uniform probability distribution is first used to assign the tensile strength value at each flaw (**Figure 98**).

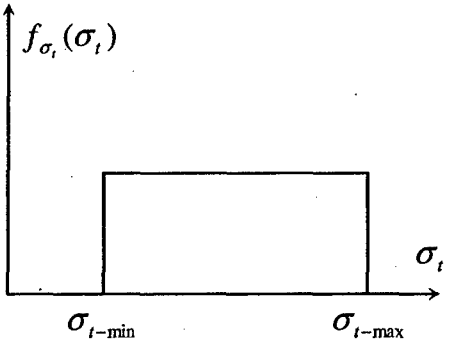


Figure 98 – Uniform probability distribution of tensile strength.

Before proceeding to the algorithm for the flaw model jointing process, one must first generate the flaws and assign the individual tensile strength values. This is done by generating a random number between zero and the length of the jointing layer (i.e., the unjointed length). For example, if the length of the jointing layer is 500 m, random numbers between 0 and 500 m should be generated (i.e., $U[0,500]$). After the desired number of flaws is generated, each is assigned a random tensile strength based on the chosen probability distribution (e.g., **Figure 98**). It is found that the appropriate number of flaws is generally greater than the number of joints. Otherwise, midpoint bisection occurs and the resulting joint spacing distributions become unrealistic.

Now that the two main components of the flaw model are in place (i.e., stress distribution model and strength model), the jointing algorithm can now be described. The algorithm

for the jointing process is presented next, first, without considering the saturation mechanism.

6.2.1 Flaw Model without Saturation Mechanisms

The following steps outline the algorithm used in the flaw model to determine where joints may form starting from the unjointed layer without considering saturation:

At each flaw location, the strain required to form a joint is calculated. The tensile stress due to the applied extensional strain is given by Ji et al. (1998) as

$$\sigma_{local} = E_f \varepsilon \left[1 - \frac{\cosh \beta x}{\cosh\left(\frac{\beta L}{2}\right)} \right] \qquad \textbf{Equation 60}$$

where the variables are as defined on **page 157**. Initially (i.e., when the layer is unjointed, **Figure 99**), L would be the length of the entire layer. Also, it would contain all the flaws (**Figure 99**). Letting $\sigma_{local} = \sigma_{t-flaw}$ = the tensile strength at the flaw, the extensional strain required for jointing for a specific flaw can be calculated.

$$\varepsilon_f = \frac{\sigma_{t-flaw}}{E_f} \cdot \frac{1}{\left[1 - \frac{\cosh \beta x}{\cosh\left(\frac{\beta L}{2}\right)} \right]} \qquad \textbf{Equation 61}$$

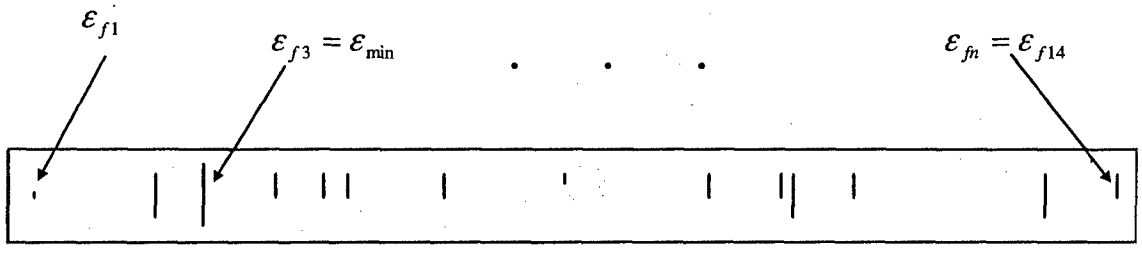


Figure 99 – Example of the initial unjointed layer containing flaws (there are 14 in this case). The unjointed layer is basically one big segment containing all the flaws. The strain required to form a joint at each flaw is calculated (shown). These strains will differ for each flaw based on the tensile strength at the flaw as well as the location of the flaw with respect to the midpoint of the layer. A new joint is located at the flaw that requires the lowest strain to form a joint.

Each flaw will have its own value of the required extensional strain to form a joint given the length of the segment it is located in and its position within that segment (e.g., **Figure 99**). Another possibility is that a joint forms at the segment midpoint where the tensile

stress is a maximum. The strain required for this to happen is obtained by substituting $\sigma_{local} = \sigma_t$ = intact strength of the layer and $x = 0$ in the above equation.

$$\varepsilon_m = \frac{\sigma_t}{E_f} \cdot \frac{1}{\left[1 - \frac{1}{\cosh\left(\frac{\beta L}{2}\right)}\right]}$$

After all the required jointing strains are calculated for a segment, the minimum strain ($\varepsilon_{\min}$) required is found (i.e., smallest of all the ε_f's and the ε_m for a segment, e.g., in **Figure 99**, the smallest strain required for jointing is $\varepsilon_{f3} = \varepsilon_{\min}$). This is done for all segments so that each segment has its own $\varepsilon_{\min}$ after this step (in **Figure 99** there is only one segment, the entire unjointed layer).

A new joint is added inside the segment requiring the least amount of strain to form a joint (i.e., the segment with the smallest $\varepsilon_{\min}$). For the case shown in **Figure 99**, there is only one segment and the new joint is added at the location of flaw number 3 (where the strain required for jointing is a minimum). The new joint is shown in **Figure 100** below.

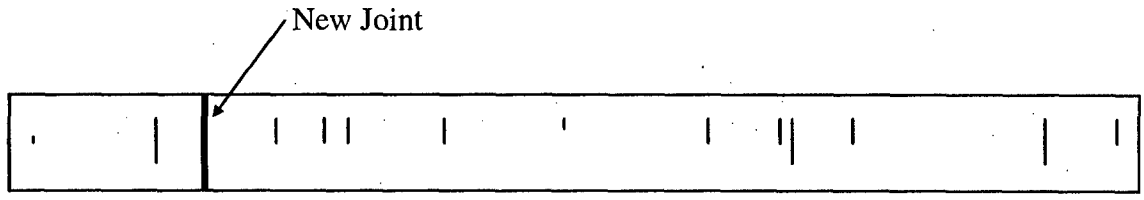


Figure 100 – Jointing layer after the formation of a single joint. There are now two segments and all the flaws are no longer contained within a single segment as in Figure 99.

The addition of a new joint leads to the formation of two new segments (as shown in **Figure 100**). The strains required to form joints inside these two new segments need to be updated because the segment lengths have changed as have the locations of the flaws with respect to the midpoint of the segment in which they belong (compare **Figure 99** and **Figure 100**). This brings the algorithm back to step 1. Note that this updating of strains needs to be performed only on the newly formed segments and the flaws that they contain. Midpoint jointing strains also need to be updated for these new segments. There is no need to perform the update for all the other segments and their respective flaws because no change in geometry occurs. This consideration is important when the model is past the unjointed stage and a large number of segments already exist. The algorithm then proceeds to step 2 and the process is repeated until the desired number of joints or the target level of strain is reached.

These steps are relatively easy to follow. Because of the absence of a saturation mechanism, the above process can be carried on without end. However, one can also

modify these steps to include saturation mechanisms, thereby providing a stopping point to the jointing process. Such modifications are presented next.

6.2.2 Flaw Model with Saturation Mechanisms

The algorithm just presented allows the jointing process to go on indefinitely. In reality, there may be a physical limit to how closely joints can be spaced. The flaw model jointing algorithm must be modified in order to consider these physical limits. Here, two saturation mechanisms are introduced and then incorporated into the algorithm. These are the saturation mechanisms due to (1) interface slippage and (2) development of compressive stresses. First, each of these saturation mechanisms is considered separately. Later, their combined effect is considered.

6.2.2.1 Interface Slippage Mechanism for Saturation

The most frequently mentioned mechanisms for saturation are the development of compressive stresses (Bai and Pollard, 2001) and slippage at the interface between the jointing and non-jointing layers (Narr and Suppe, 1991). Here, interface slippage as a saturation mechanism is incorporated into the model. Before proceeding, this mechanism is described using a stress distribution model. The phenomenon of interface slippage is going to be described using a simplified approach by Ji et al. (1998). Allowing for interfacial slip causes the shape of the shear stress distribution along the interface to take the form shown in **Figure 101**. A limit to the interface shear stress equal to τ_0 is enforced.

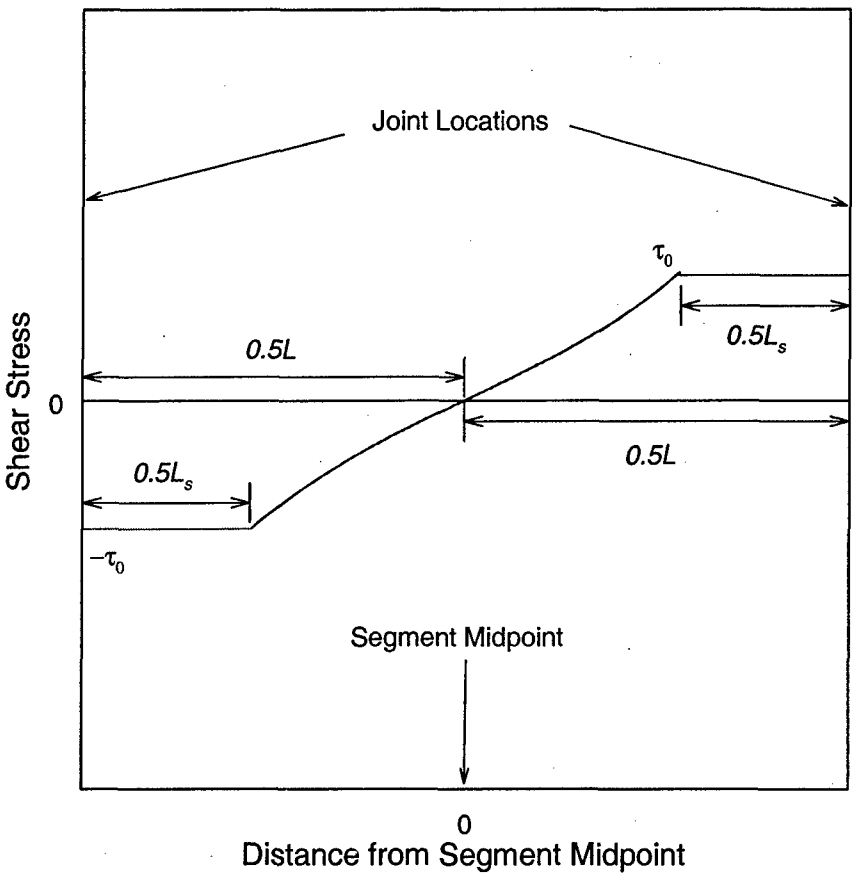


Figure 101 – Shear stress distribution allowing for interface slippage.

Ji et al. (1998) used the same approach as Hobbs (1967) and Ji and Saruwatari (1998) in deriving the stress distributions. The solution is of the form:

$$\sigma_{local} = E_f \varepsilon + \frac{A}{t}\sinh \beta x + \frac{B}{t}\cosh \beta x \qquad \textbf{Equation 62}$$

However, the boundary conditions are different. These are given by:

$$\sigma_{local} = \sigma_{fc} \text{ at } x = \pm\frac{(L - L_s)}{2}$$

where L is the length of the segment (or the spacing between two adjacent joints), L_s is that part of L that is experiencing interfacial slippage and σ_{fc} is the local normal stress at a distance $\frac{L - L_s}{2}$ from the segment midpoint (refer to **Figure 101**). Applying the boundary conditions, the solution becomes

$$\sigma_{local} = E_f \varepsilon + (\sigma_{fc} - E_f \varepsilon) \frac{\cosh \beta x}{\cosh\left(\beta \frac{(L - L_s)}{2}\right)}$$ **Equation 63**

where $\beta = \left[\frac{8G_n}{E_f t d}\right]^{\frac{1}{2}}$ as before.

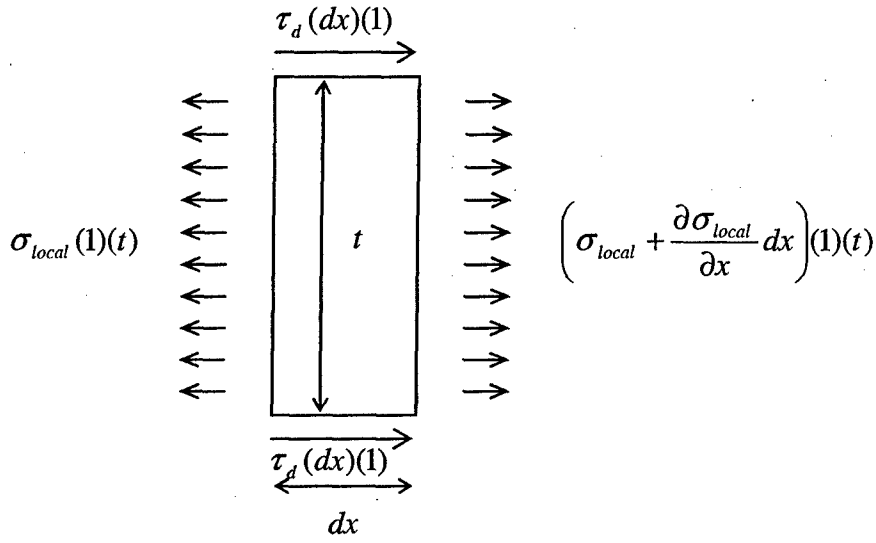


Figure 102 – Forces acting on a slice of jointing layer.

Recall that in the model, the magnitude of the local normal stress can be calculated directly from the shear stress distribution at the interface, τ_d (i.e., from equilibrium of forces in **Figure 102**, one obtains $\tau_d = -\frac{t}{2} \cdot \frac{\partial \sigma_{local}}{\partial x} = -\frac{t}{2} \cdot \frac{d\sigma_{local}}{dx}$ or conversely $\sigma_{local} = -\int \frac{2}{t} \tau_d \cdot dx$). The shear stress at the interface, τ_d ,can be calculated as:

$$\tau_d = -\frac{t}{2} \cdot \frac{d\sigma_{local}}{dx} = -\frac{t}{2} \cdot \beta(\sigma_{fc} - E_f \varepsilon) \frac{\sinh \beta x}{\cosh\left(\beta \frac{(L - L_s)}{2}\right)}$$

Substituting $x = \pm \frac{L - L_s}{2}$ and $\tau_d = \tau_0$ (the interface shear strength) and solving for σ_{fc}

$$\left|\sigma_{fc}\right| = \left| E_f \varepsilon - \frac{2\tau_0}{t\beta} \cdot \frac{1}{\tanh\left(\beta \frac{(L-L_s)}{2}\right)} \right| \qquad \textbf{Equation 64}$$

The local stress, σ_{fc}, can also be expressed as

$$\left|\sigma_{fc}\right| = \left| -\int \frac{2}{t}\tau_0 \cdot dx \right| = \left| -\frac{2}{t}\tau_0 \frac{L_s}{2} \right| = \left| \tau_0 \frac{L_s}{t} \right| \qquad \textbf{Equation 65}$$

directly from equilibrium of forces (**Figure 102**). Equating these two expressions (**Equation 64** and **Equation 65**) one derives the expression for L_s:

$$L_s = \frac{E_f \varepsilon t}{\tau_0} - \frac{2}{\beta} \cdot \frac{1}{\tanh\left(\beta \frac{(L-L_s)}{2}\right)} \qquad \textbf{Equation 66}$$

As can be seen, L_s cannot be isolated in the above equation. The value of L_s can be determined numerically. Substituting **Equation 65** into **Equation 63** yields:

$$\sigma_{local} = E_f \varepsilon - (E_f \varepsilon - \tau_0 \frac{L_s}{t}) \frac{\cosh \beta x}{\cosh\left(\beta \frac{(L-L_s)}{2}\right)}$$

The quantity $(E_f \varepsilon - \tau_0 \frac{L_s}{t})$ is always greater than zero because without the presence of jointing, this is the stress due to the applied strain. The minimum value of $\cosh(\beta x)$ occurs at $x = 0$ so that the maximum local normal stress also occurs at $x = 0$. The shape of the σ_{local} curve is linear with x in the intervals $\frac{L-L_s}{2} \le x \le \frac{L}{2}$ and $-\frac{L}{2} \le x \le -\frac{L-L_s}{2}$ because the interface shear stress in these intervals is constant (τ_0, also see **Figure 103**). In the interval $-\frac{L-L_s}{2} \le x \le \frac{L-L_s}{2}$, σ_{local} is non-linear in x as described by the equation above (**Figure 103**). The tensile stress distribution is described completely by the following equation:

$$\sigma_{local} = \begin{cases} \frac{2}{t}\tau_0\left(x+\frac{L}{2}\right) & , \quad -\frac{L}{2} \le x \le -\frac{L-L_s}{2} \\ E_f\varepsilon - \left(E_f\varepsilon - \tau_0\frac{L_s}{t}\right)\frac{\cosh\beta x}{\cosh\left(\beta\frac{(L-L_s)}{2}\right)} & , \quad -\frac{L-L_s}{2} \le x \le \frac{L-L_s}{2} \\ \frac{2}{t}\tau_0\left(-x+\frac{L}{2}\right) & , \quad \frac{L-L_s}{2} \le x \le \frac{L}{2} \end{cases} \qquad \textbf{Equation 67}$$

On the other hand, if slippage were disregarded (i.e., if the interface were assumed to have infinite shear strength so that $L_s = 0$ always), the tensile stress distribution would be given simply by:

$$\sigma_{local} = E_f\varepsilon\left[1 - \frac{\cosh\beta x}{\cosh\left(\frac{\beta L}{2}\right)}\right]$$

for $-\frac{L}{2} \le x \le \frac{L}{2}$.

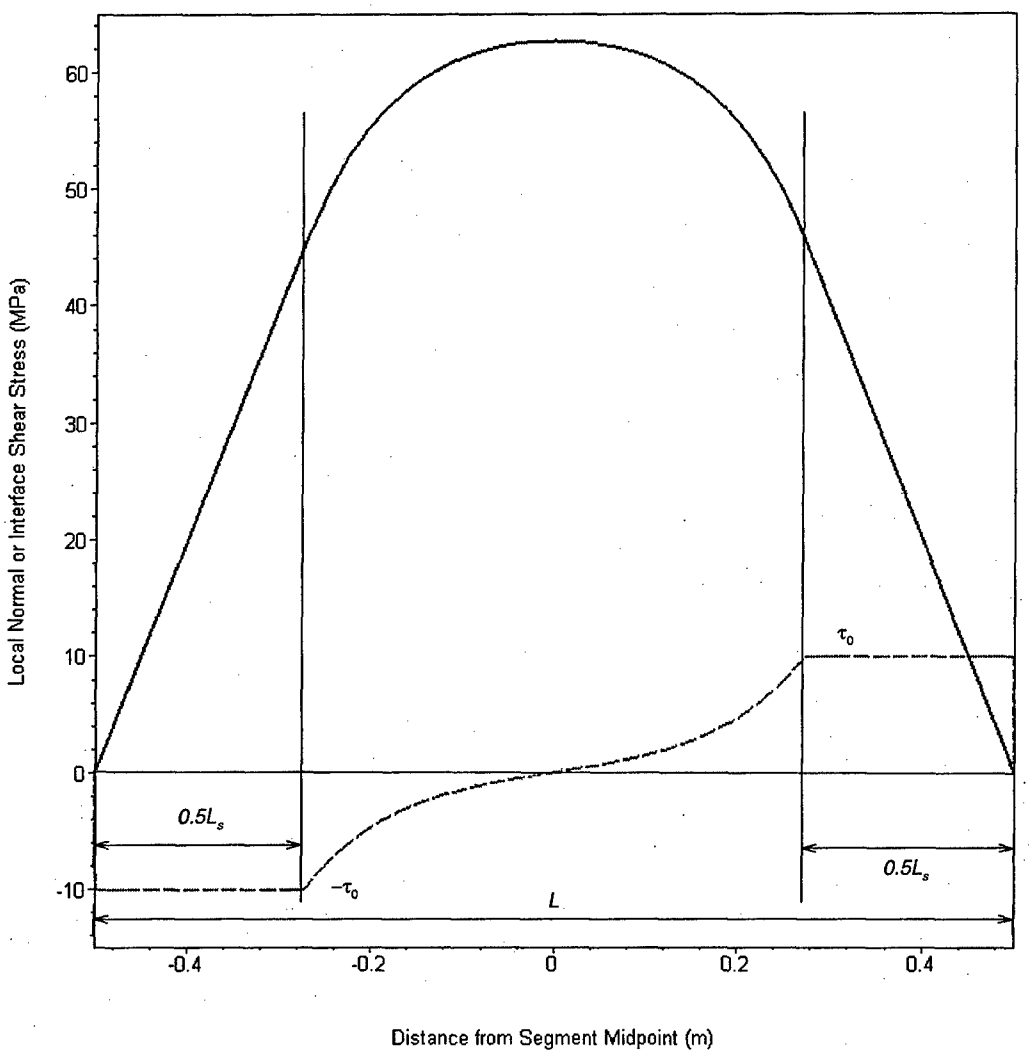


Figure 103 – Example of the plot of shear stress distribution considering slippage and the corresponding tensile stress distribution.

The question now is how does one use this model of interface slippage to bring about joint saturation in the model? To answer this, one must first look at the stress distribution at the instant when slippage occurs (i.e., just when $L_s = 0$) and when slippage has already occurred ($L_s > 0$). When $L_s = 0$, the stress distribution is given by

$$\sigma_{local} = E_f \varepsilon \left[1 - \frac{\cosh \beta x}{\cosh\left(\frac{\beta L}{2}\right)} \right]$$

for $-\frac{L}{2} \le x \le \frac{L}{2}$. This is the same stress distribution if interface slippage is not considered at all (i.e., **Equation 60**). The strain required to reach impending slippage is obtained by substituting $L_s = 0$ into the expression for L_s:

$$L_s = \frac{E_f \varepsilon t}{\tau_0} - \frac{2}{\beta} \cdot \frac{1}{\tanh\left(\beta \frac{(L - L_s)}{2}\right)}$$

and solving for ε.

$$\varepsilon = \varepsilon_0 = \frac{\tau_0}{E_f t} \cdot \frac{2}{\beta} \cdot \frac{1}{\tanh\left(\frac{\beta L}{2}\right)} \qquad \textbf{Equation 68}$$

The strain ε_0 in **Equation 68** can be considered as the slippage strain. For a numerical example, consider the stress distribution for both models (considering and disregarding interface slippage, **Equation 67** and **Equation 60**, respectively), using $t = 0.2$, $d = 0.1$, $E_f = 50000, G_n = 5000$, $\tau_0 = 300$, $L = 1.0$. The strain at impending slippage for this case is calculated as $\varepsilon_0 = 0.009520890312$ from **Equation 68**. The stress distributions are shown in **Figure 104** below and are exactly identical before and up to impending slippage because **Equation 67** reduces to **Equation 60** at strains less than or equal to ε_0.

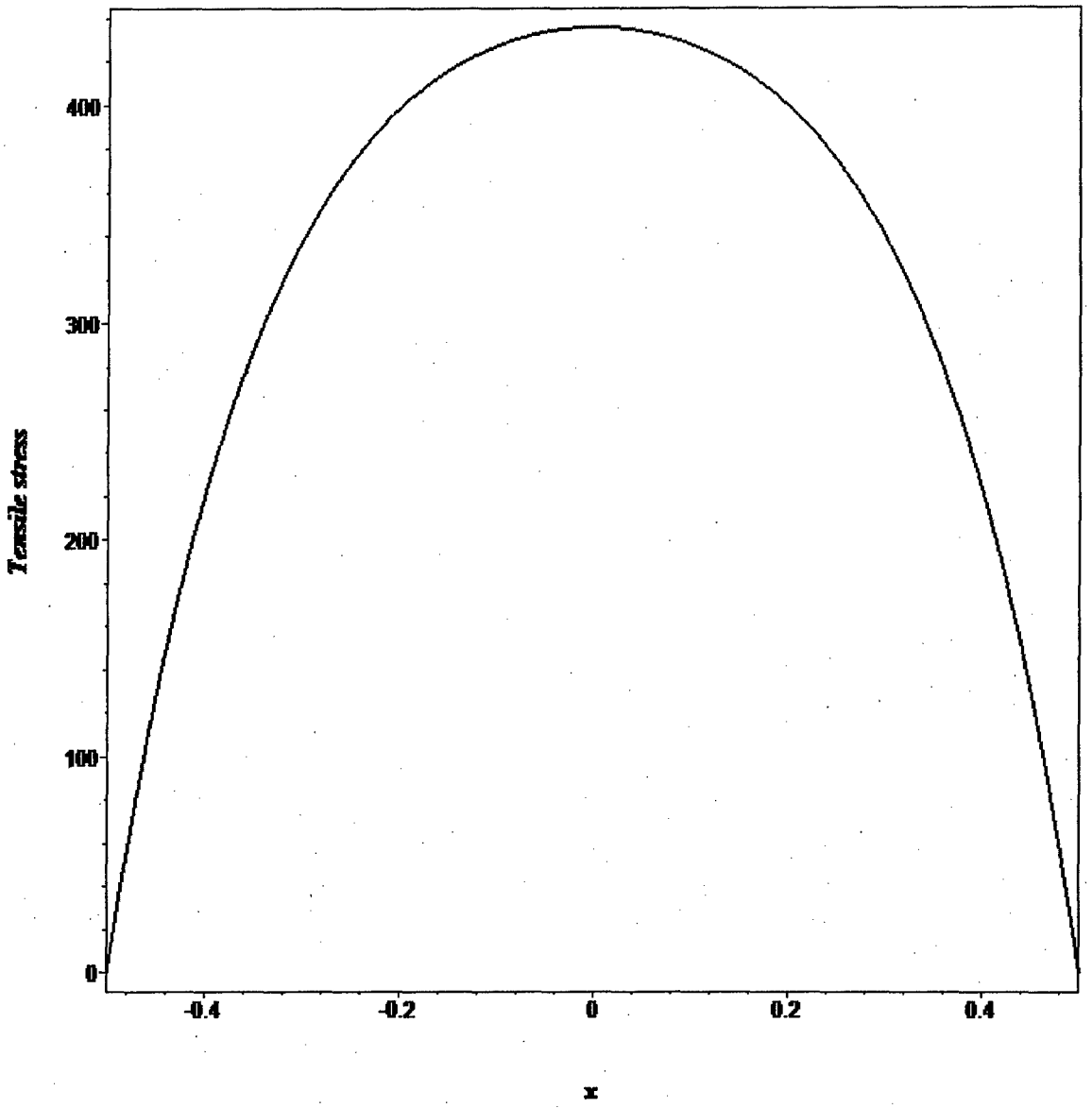


Figure 104 – Tensile stress distribution at impending slippage. The stress distributions for both models (considering and disregarding interface slippage) are identical.

Now consider the stress distributions when $L_s > 0$ or when interface slippage has already occurred. In the present case, the applied strain has to be greater than $\varepsilon_0 = 0.009520890312$, the slippage strain. For example, consider a strain $\varepsilon_{applied} = 0.02 > \varepsilon_0$. At this strain level, the slippage length is calculated as $L_s = 0.3405217847 > 0$ from **Equation 66**. The stress distributions for both **Equation 60** and **Equation 67** are shown in **Figure 105** below. It is clear that the stresses considering slippage are lower than those when slippage is not considered.

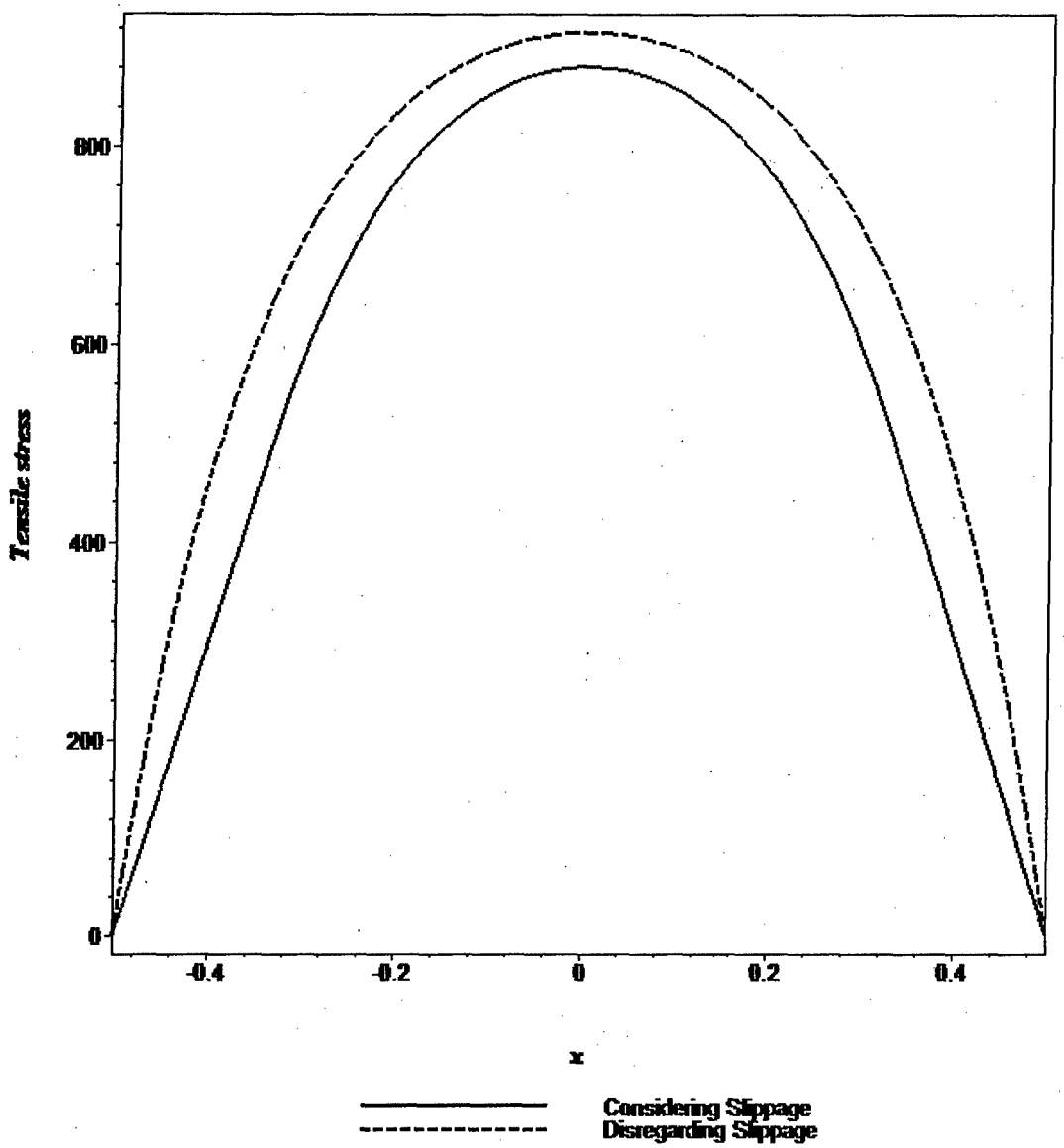


Figure 105 – Tensile stress distributions when the extensional strain is increased to 0.02. Model with slippage predicts lower stresses compared to model without slippage.

If the strain continues to increase (say, a strain $\varepsilon_{applied} = 0.039486832$), the stress distributions given by **Equation 60** and **Equation 67** would be those shown in **Figure 106**. It becomes apparent that the difference between the two distributions becomes larger as the slippage length increases (see progression from **Figure 104** to **Figure 106**). It is not hard to imagine that the limiting tensile stress distribution for the slippage model is triangular with a maximum value of $\frac{\tau_0 L}{t}$ at the segment midpoint. This can be seen by substituting $L_s = L$ in **Equation 67**. The middle portion vanishes and only the two linear parts remain, the maximum being equal to $\frac{\tau_0 L}{t}$ at $x = 0$.

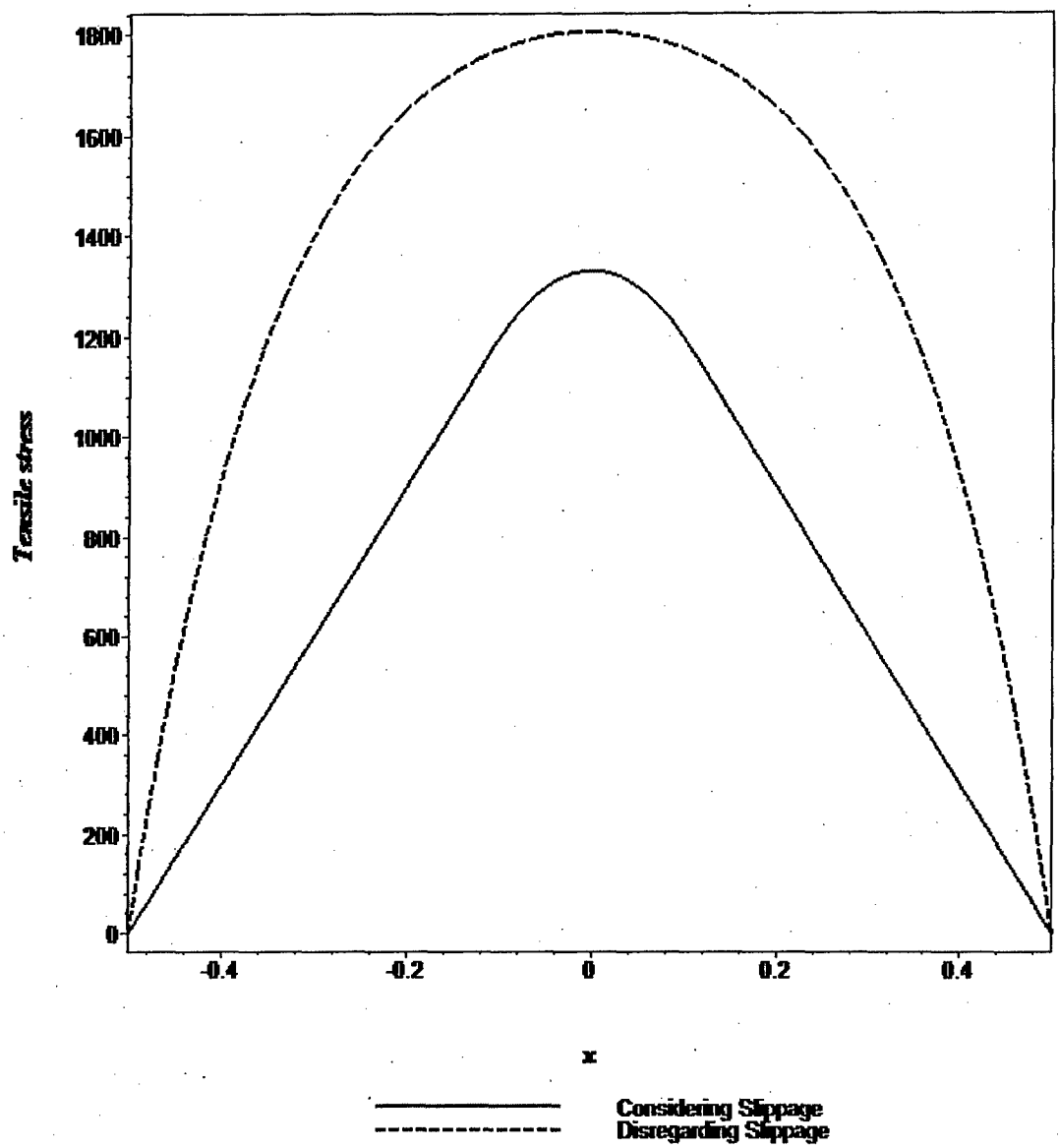


Figure 106 – Tensile stress distributions when the extensional strain reaches about 0.039. At this stage, the model considering slippage predicts stresses way below those from the model without slippage.

Figure 104, **Figure 105**, and **Figure 106** demonstrate that the tensile stress in the model considering slippage is less than that when slippage is not considered. As mentioned earlier, the tensile stress at the midpoint in the model considering slippage reaches a limiting value ($\frac{\tau_0 L}{t}$). Now consider the model that uses slippage alone and see how the tensile stress distribution changes from the point where impending slippage occurs to full slippage. **Figure 107** shows the progression of the tensile stress distribution considering interface slippage as the applied strain increases. It clearly shows the limiting tensile stress distribution (i.e., the triangular stress distribution). The strain at which this first occurs cannot be determined. In **Equation 66**, the value of ε cannot be determined if

$L_s = L$. This value of ε is the full-slippage strain. This poses a problem in the program. However, a simple assumption is used in order to handle this in the modified algorithm presented later in this section.

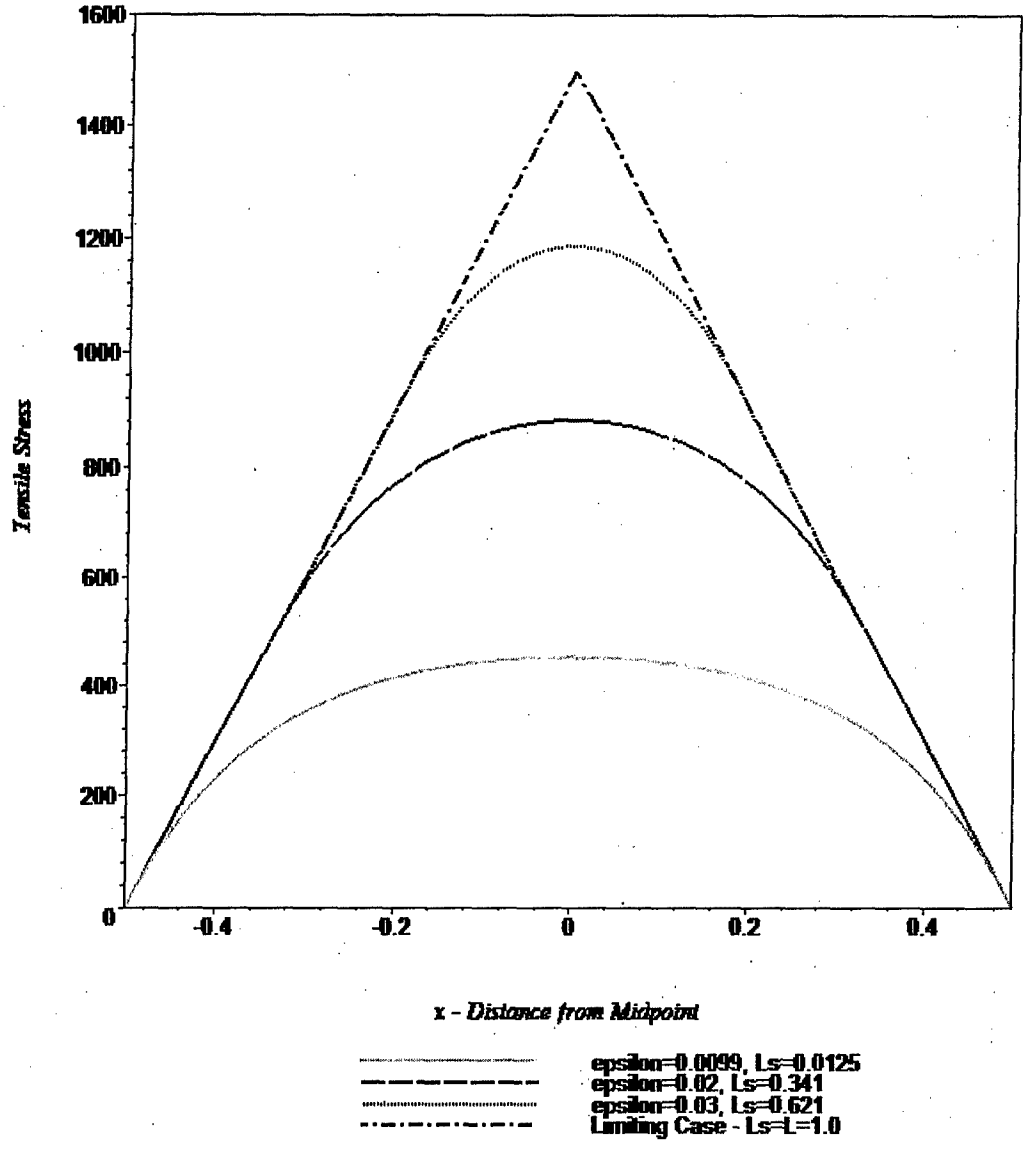


Figure 107 – Progression of the tensile stress distribution until the limiting condition (i.e., full slippage).

The observations that may help in constructing the new algorithm are now summarized. **Figure 104** to **Figure 107** show that, first, the tensile stress distribution not considering slippage (**Equation 60**) is always greater than or equal to the tensile stress distribution considering slippage (**Equation 67**). Second, the tensile stress distribution considering slippage reaches a limiting form when the slippage length equals the length of the segment (i.e., $L_s = L$ in **Equation 67**). This suggests that joints cannot increase in number indefinitely. If the strength at any point in the segment lies above the limiting

triangular tensile stress distribution, joints can no longer form in the segment. Third, the value of the maximum tensile stress at full slippage is proportional to the length of the segment (i.e., $\frac{\tau_0 L}{t}$ at the tip of the triangular stress distribution). This means that shorter segments develop smaller limiting tensile stresses decreasing the chance of additional joint formation. Fourth, the tensile stress distribution not considering slippage does not have a limiting form. It allows the stress to increase without bound and therefore allows for an infinite number of joints to form inside the segment. This can be concluded from **Equation 60**. For a given length of segment (L), an increase in strain leads directly to an increase in the tensile stress. Consequently, the mean joint spacing is allowed to reach zero if the applied strain is allowed to increase indefinitely.

In order to incorporate the limiting tensile stress distribution as a mechanism of joint saturation into the flaw model, a procedure was developed. At strains below the slippage strain (given in **Equation 68**), the three-step algorithm given in the beginning of this section is applicable. Recall that the strain required for jointing is calculated for each flaw in a segment and at the segment midpoint (where the tensile stress is a maximum). For a particular flaw, if the strain calculated from **Equation 61** exceeds the slippage strain (**Equation 68**) calculated for the segment that contains it, the first step in the previous algorithm is replaced by the following:

1. Given the location of the flaw within the segment being considered, plot where the strength at the flaw lies with respect to the limiting tensile stress distribution (e.g., **Figure 108**). If the location-strength point lies outside (or above) the triangle (Point C in **Figure 108**), jointing is no longer possible at that flaw location under this mechanism. There is also the special case referred to earlier where full slippage is required to reach the tensile strength at the midpoint (Point D in **Figure 108**). Recall that the strain cannot be calculated for this case. In order to handle this situation in the algorithm, it is assumed that no jointing can occur at the midpoint for this case. In effect, the location-strength point is considered to be outside the triangle even if it is exactly at the tip of the triangle. Remember that it is still possible for a new joint to form inside the segment because there are other flaws to consider (as well as midpoint jointing) but it is certain that the two new segments formed by the addition of this new joint will only be able to develop limiting stresses lower than that of the original segment. This is due to the observation that was made pertaining to the limiting tensile stress distribution being directly proportional to the length of the segment (i.e., shorter segments, lower limiting stresses). If the location-strength point (i.e., the (x, σ_{t-flaw}) pair) lies on (except at the tip) or below the triangle (Point A and B in **Figure 108**), then jointing is still possible at the flaw. These two cases are treated separately. For the case where the (x, σ_{t-flaw}) point lies exactly on the triangle (Point A), the minimum strain required to form a joint is that which develops slippage from the segment-end nearest the flaw up to the location of the flaw itself (see **Figure 108**, note point A with respect to the joint locations). In other words, the location (x) completely defines the slippage length in this case. **Equation 66** is used:

$$L_s = \frac{E_f \varepsilon t}{\tau_0} - \frac{2}{\beta} \cdot \frac{1}{\tanh\left(\beta \frac{(L - L_s)}{2}\right)}$$

Solving for the strain, ε, yields

$$\varepsilon = \frac{\tau_0}{E_f t}\left[L_s + \frac{2}{\beta} \cdot \frac{1}{\tanh\left(\beta \frac{(L - L_s)}{2}\right)} \right]$$

Recognizing that $L_s = 2\left|\frac{L}{2} - x\right|$ (note that L_s is the total slippage length so it is twice the slippage length from each end of the segment, see **Figure 103** or **Figure 108**), the minimum strain required for jointing at the flaw is therefore,

$$\varepsilon = \frac{\tau_0}{E_f t}\left[2\left|\frac{L}{2} - x\right| + \frac{2}{\beta} \cdot \frac{1}{\tanh\left(\beta \frac{\left(L - 2\left|\frac{L}{2} - x\right|\right)}{2}\right)} \right]$$

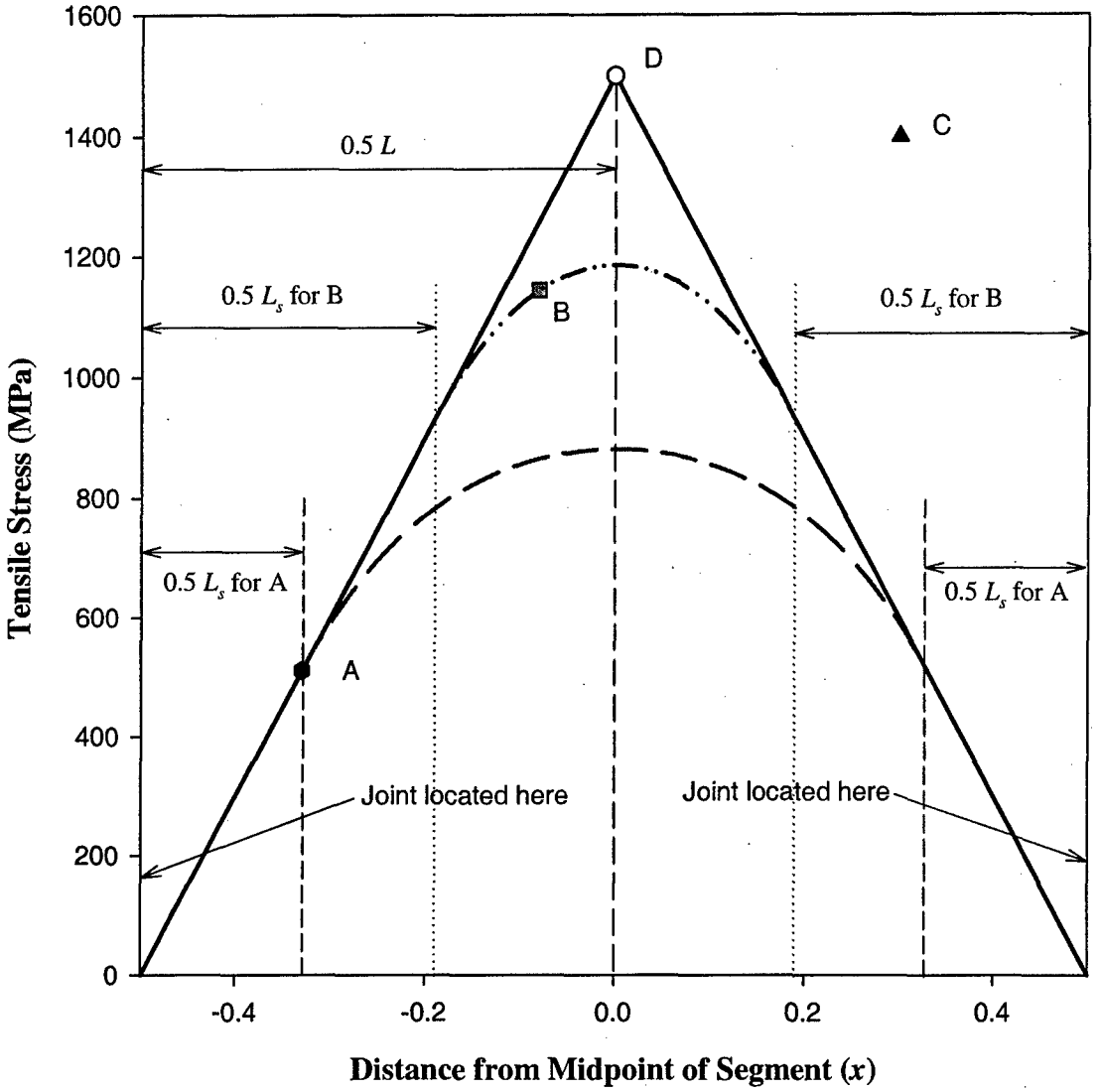


Figure 108 – Illustration of the possible scenarios for the (x, σ_{t-flaw}) pairs with respect to the limiting stress distribution in the initial step of the new algorithm. Point A is right on the limiting stress distribution triangle (jointing is possible). Slippage has to occur up to point A for jointing at A to occur. Point B is inside the triangle (jointing is possible). Point C is outside the triangle and point D is right at the tip (jointing not possible in both cases).

For the case where the (x, σ_{t-flaw}) point lies inside (or below) the triangle (Point B), the calculations are a little bit more complicated. This suggests that the stress required for jointing is attained in the middle portion of the stress distribution described by **Equation 67**. Unlike point A, the location of B does not define the slippage length completely. So, two things need to be calculated in this case: ε and L_s. The first equation needed to do

this is the middle portion of **Equation 67** and the second equation required is **Equation 66**. These are repeated here for convenience.

$$\sigma_{local} = E_f \varepsilon - (E_f \varepsilon - \tau_0 \frac{L_s}{t}) \frac{\cosh \beta x}{\cosh\left(\beta \frac{(L - L_s)}{2}\right)}$$

Middle portion of Equation 67

and

$$L_s = \frac{E_f \varepsilon t}{\tau_0} - \frac{2}{\beta} \cdot \frac{1}{\tanh\left(\beta \frac{(L - L_s)}{2}\right)}$$

Equation 66

Substituting $\sigma_{local} = \sigma_{t-flaw}$ (i.e., the strength at the flaw) and the location of the flaw within the segment into x, the strain, ε, is determined from the above equations to get the following:

$$\varepsilon = \left[\sigma_{t-flaw} - \tau_0 \frac{L_s}{t} \frac{\cosh \beta x}{\cosh\left(\beta \frac{(L - L_s)}{2}\right)}\right] \frac{1}{E_f \left[1 - \frac{\cosh \beta x}{\cosh\left(\beta \frac{(L - L_s)}{2}\right)}\right]}$$

Equation 69

and

$$\varepsilon = \frac{\tau_0}{E_f t}\left[L_s + \frac{2}{\beta} \cdot \frac{1}{\tanh\left(\beta \frac{(L - L_s)}{2}\right)}\right]$$

Equation 70

Equating these two, one obtains an equation where the only unknown is the slippage length, L_s.

$$\left[\sigma_{t-flaw} - \tau_0 \frac{L_s}{t} \frac{\cosh \beta x}{\cosh\left(\beta \frac{(L-L_s)}{2}\right)}\right] \cdot \frac{1}{E_f\left[1 - \frac{\cosh \beta x}{\cosh\left(\beta \frac{(L-L_s)}{2}\right)}\right]} \qquad \textbf{Equation 71}$$

$$-\frac{\tau_0}{E_f t}\left[L_s + \frac{2}{\beta} \cdot \frac{1}{\tanh\left(\beta \frac{(L-L_s)}{2}\right)}\right] = 0$$

Close inspection reveals that the value of L_s that satisfies **Equation 71** lies in the interval $0 < L_s < 2\left|\frac{L}{2} - x\right|$ (as opposed to using the wider interval, $0 < L_s < L$) where x is the location of the flaw with respect to the segment midpoint. The bisection method can be used to solve **Equation 71**. The calculated value of L_s is substituted into either **Equation 69** or **Equation 70** to get the strain, ε. This is the strain required to form a joint at the flaw and it should be greater than the ε_0 calculated from **Equation 68** for the segment containing the flaw because slippage will have occurred at this point.

Steps 2 and 3 of the original (without saturation) algorithm on **page 161** remain the same.

Next, the saturation mechanism due to the development of compressive stresses is considered.

6.2.2.2 Compressive Stress Development Mechanism for Saturation

So far, the flaw model has considered the saturation mechanism brought about by interface slippage. Another saturation mechanism is the development of compressive stresses in the horizontal (x-) direction within a segment that precludes the formation of additional joints. Bai and Pollard (2000) determined a critical spacing-to-thickness ratio, $(\frac{s}{t})_{cr}$, below which no new joints can form because of the development of compressive stresses. This critical ratio depends on the elastic properties of both the jointing layer and the bounding layers as well as the overburden stress. Recall that the $(\frac{s}{t})_{cr}$ ratio increases with:

- Increasing E_f/E_n ratio, where E_f and E_n are the Young's moduli of the jointing and non-jointing layers, respectively.
- Increasing overburden stress, S_v

and decreases with

- Increasing value of D (see equation below). Note that the value of D increases when ν_f decreases (for a fixed value of ν_n) or when ν_n increases (for a fixed value of ν_f), where ν_f and ν_n are the Poisson's ratios of the jointing and non-jointing layers, respectively. Also, D is positive if $\nu_f < \nu_n$ and negative if $\nu_f > \nu_n$.

$$D = \frac{(1-2\nu_f)(1+\nu_f)-(1-2\nu_n)(1+\nu_n)}{(1-\nu_f^2)+(1-\nu_n^2)} \qquad \textbf{Equation 44}$$

(repeated here from page 112)

The combined effect of these three factors can be expressed in the following equation:

$$\left(\frac{s}{t}\right)_{cr} = \beta\gamma\left[0.792+0.328\left(1-\exp\left[-0.824\left(\frac{E_f}{E_n}-0.0025\right)^{0.824}\right]\right)\right] \qquad \textbf{Equation 47}$$

(repeated here from page 116)

where

$$\beta = \frac{0.976-0.302D-0.129D^2+0.117D^3}{0.976}$$

and

$$\gamma = \frac{0.976+1.118\times10^{-4}S_v-7.562\times10^{-8}S_v^2+2.806\times10^{-9}S_v^2}{0.976}$$

In order to incorporate this saturation mechanism into the flaw model, the original algorithm (see page 160) must be modifeid as follows:

1. Calculate the value of $(\frac{s}{t})_{cr}$ using **Equation 47**. Note that this has to be done only once for the entire layer and that the value of this critical ratio does not change throughout the simulation. In **Equation 47**, $(\frac{s}{t})_{cr}$ depends only on the material properties (i.e., E_f, ν_f and E_n, ν_n) and the overburden. These do not change throughout the jointing process, although this assumption has to be made explicitly for the overburden (S_v). At each flaw location, the strain required to form a joint is calculated using the stress distribution model (i.e., Ji et al., 1998).

2. A new joint is added inside the segment requiring the least amount of strain to form a joint (i.e., the segment with the smallest $\varepsilon_{\min}$ of all the segments) and whose spacing-to-thickness ratio (i.e., segment length divided by layer thickness) is greater than $(\frac{s}{t})_{cr}$. Otherwise, a joint cannot form within that segment and the segment requiring

the next larger strain is selected and its spacing-to-thickness ratio checked. This is done until a segment satisfying both conditions (least strain required and spacing-to-thickness ratio > $(\frac{s}{t})_{cr}$) is found. If none are found to satisfy these conditions, saturation has been reached and the program terminates.

3. **Step 3** of the algorithm (i.e., updating the minimum strains for the newly formed segments) remains the same.

An immediate consequence of implementing these saturation mechanisms (interface slippage and compressive stress development) is the existence of a "saturation mean spacing" or SMS. This is the mean joint spacing at saturation. This is different from the critical spacing (or $t \cdot \left(\frac{s}{t}\right)_{cr}$) because it is quite possible for segments longer than the critical spacing to be jointed into segments that are shorter than the critical spacing. The effects of different model parameters on the SMS are investigated in the following section.

6.2.3 Saturation Mean Spacing Parametric Study

In this section, the effects of the various flaw model and saturation mechanism parameters on the SMS are investigated. The saturation mechanisms are first considered individually and are then combined. To start, the interface slippage mechanism is considered.

6.2.3.1 Interface Slippage

A number of simulations were performed using the flaw model in order to understand how the parameters in the model affect the jointing process. **Figure 109** to **Figure 114** illustrate such parameter effects specifically on the saturation mean spacing. The saturation mean spacing is the mean spacing at the point where a further increase in strain cannot cause additional jointing. Since the literature typically looks at the relationship between spacing and the jointing layer thickness at saturation, the same is done here for different parameter values.

First, the effect of the non-jointing layer thickness (i.e., the thickness of the bounding layers) is investigated. **Figure 109** shows that for all other parameters being equal, the use of different non-jointing layer thickness values does not appear to have a significant effect on the relationship between saturation mean spacing and jointing layer thickness. **Figure 110** shows the same effect more clearly and for a wider range of non-jointing layer thickness values. Note that in the contour plots, the relationship between the saturation mean spacing (SMS) and the jointing layer thickness can be obtained by drawing a horizontal line through a given value of non-jointing layer thickness (or any other parameter, for that matter) and picking off the values of the SMS (i.e., the intersection points between the contour lines and the horizontal line) at the corresponding jointing layer thickness. Note also that vertical contour lines indicate that the parameter in consideration does not affect the relationship between saturation mean spacing and

jointing layer thickness. Another characteristic found in these contour plots is that jumps in the data, common in the simulations, can be magnified. The insignificance of the effect of the non-jointing layer thickness is expected because when saturation is reached, the tensile stress in the jointing layer is governed only by the interface shear strength and the thickness of the jointing layer. This is not to say that the bounding layer thickness has no effect on the jointing process. In fact, in the earlier stages of joint set development, its effect is significant. This is demonstrated in **Figure 111** where various bounding layer thickness values were used with all other parameters being equal. It is clear that at the same strain (below saturation) a smaller bounding layer thickness leads to a lower mean spacing.

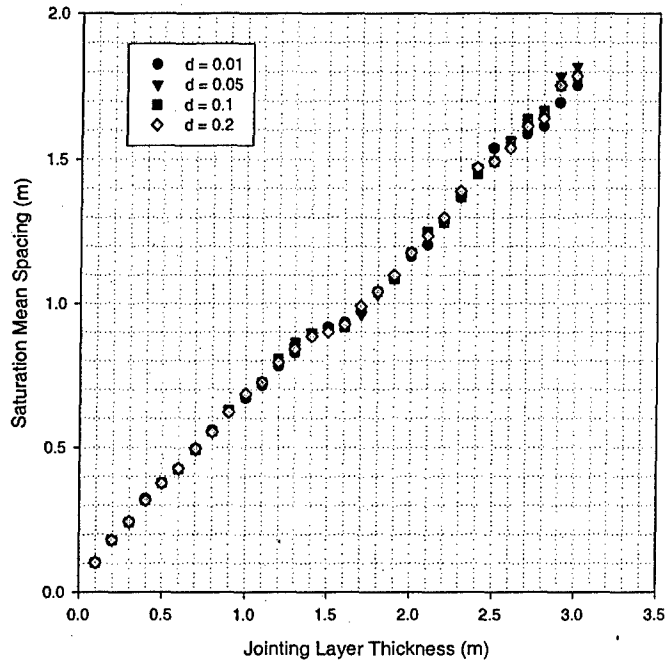


Figure 109 – Illustration of the effect of the non-jointing (bounding) layer thickness (d) on the relationship between saturation mean spacing and jointing layer thickness.

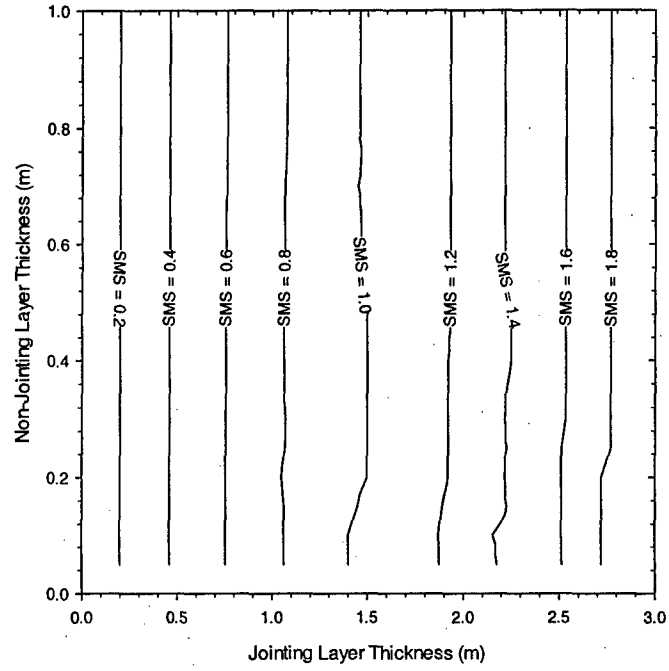


Figure 110 – Contours of saturation mean spacing (SMS) as a function of the jointing layer thickness and non-jointing layer thickness for the interface slippage model.

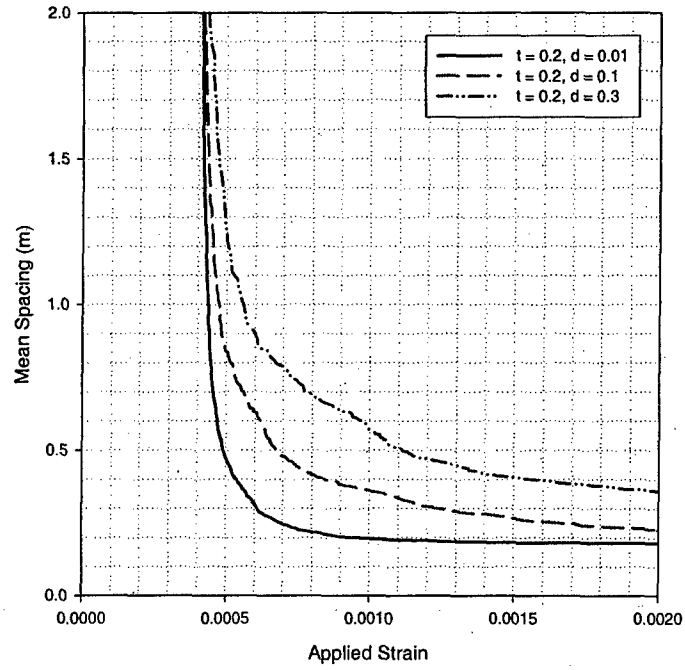


Figure 111 – Mean joint spacing as the applied strain increases for different bounding layer thickness (d) values. Note: t is the jointing layer thickness.

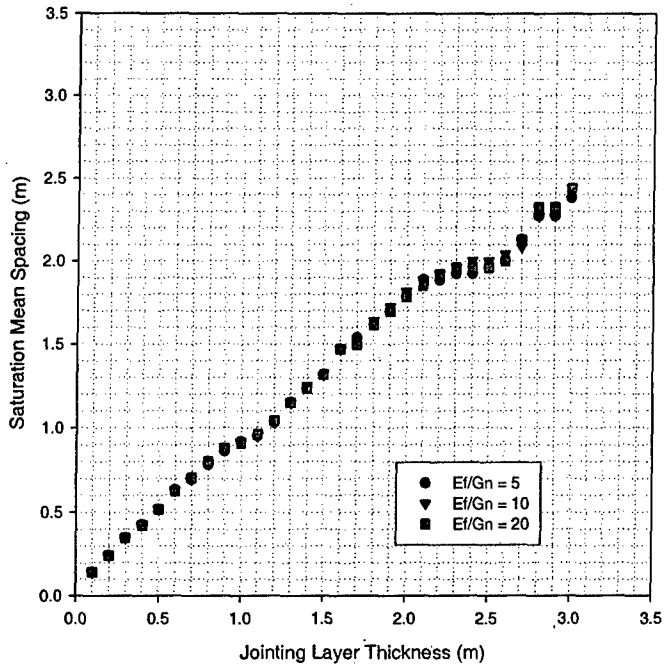


Figure 112 – Illustration of the effect of the ratio between the jointing layer modulus of elasticity and the bounding layer shear modulus.

Figure 112 shows that the $\frac{E_f}{G_n}$ ratio does not appear to have a significant effect on the relationship between the jointing layer thickness and the saturation mean spacing. Similar to the case of the bounding layer thickness, this observation was also expected because the only parameters that determine the tensile stress at saturation are the interface shear strength and the jointing layer thickness. The contours of saturation mean spacing in **Figure 113** also show this trend for a wider range of $\frac{E_f}{G_n}$ values. The contours in **Figure 113** are essentially vertical except for a few jumps (e.g., SMS=1.0 and SMS=1.4). These jumps are not sufficiently substantial to say that the $\frac{E_f}{G_n}$ ratio has a significant effect on the relationship between the saturation mean spacing and the jointing layer thickness. However, the $\frac{E_f}{G_n}$ ratio plays a significant role in the formation of joints below saturation level. This is demonstrated in **Figure 114** where the mean spacing is plotted against the applied strain. It is clear that at strains below saturation, a larger $\frac{E_f}{G_n}$ ratio leads to a larger mean spacing. The results in **Figure 112** suggest that these curves approach the same mean spacing as the strain increases.

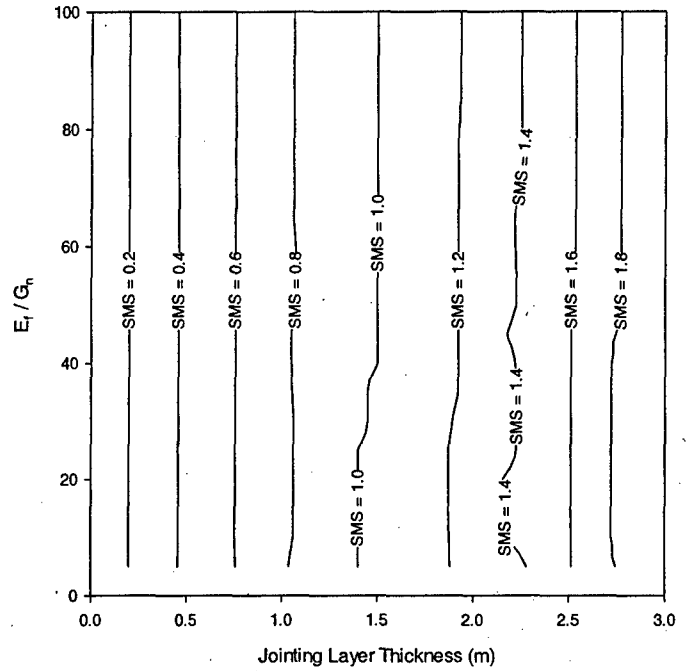


Figure 113 – Contours of saturation mean spacing (SMS) as a function of both the jointing layer thickness and the $\frac{E_f}{G_n}$ ratio for the interface slippage model.

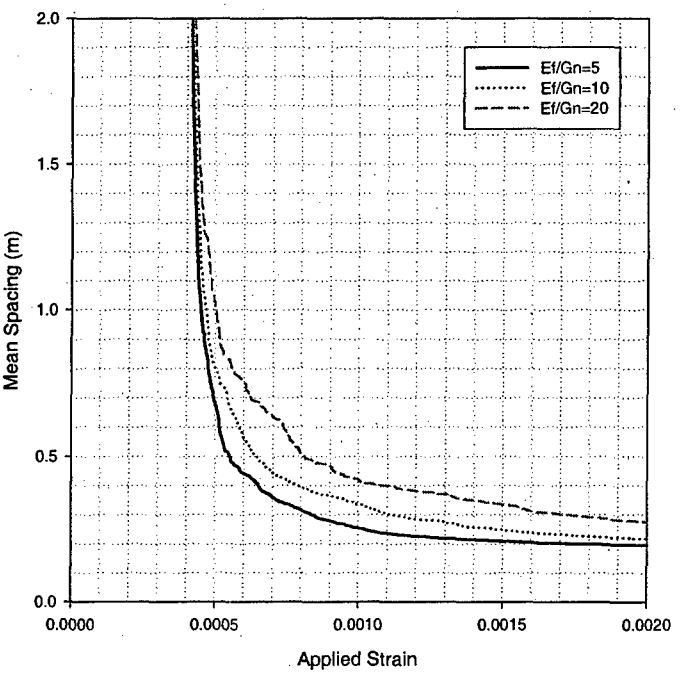


Figure 114 – Mean joint spacing as the applied strain increases for different values of the $\frac{E_f}{G_n}$ ratio.

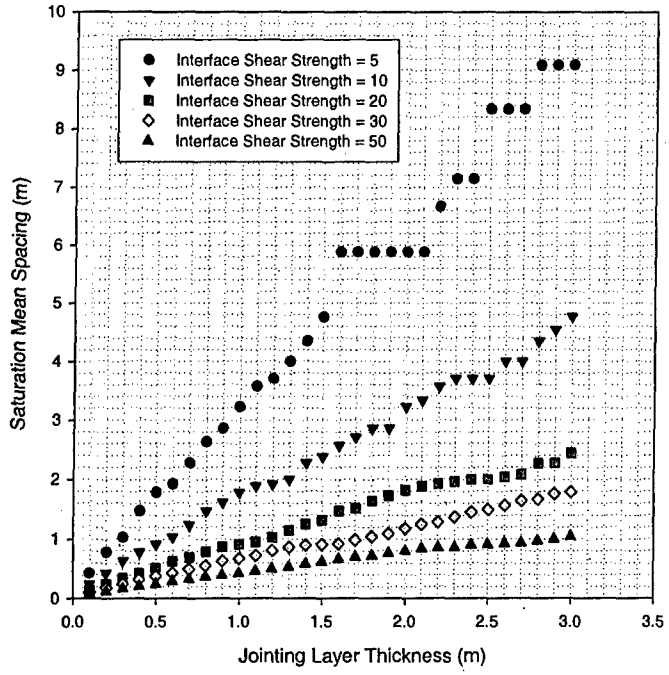


Figure 115 – Illustration of the effect of interface shear strength (in MPa) on the relationship between jointing layer thickness (t) and the saturation mean spacing.

Figure 115 shows the effect of the interface shear strength on the thickness-spacing relationship at saturation. Clearly, as the interface shear strength increases, the slope of the relationship decreases. For the same thickness, one expects a lower saturation mean spacing for higher interface shear strength values. Higher interface shear strength means that larger shear stresses are allowed to develop at the interface and in this model the tensile stresses in the jointing layer are directly proportional to the interface shear stress. Consequently, these larger tensile stresses translate to more jointing. The contour lines in **Figure 116** show the same trend for interface shear strength values up to 100 MPa. If one draws a horizontal line at a value of interface shear strength in **Figure 116** (in order to determine the SMS-jointing layer thickness relationship at that interface shear strength), the SMS values on the line become smaller as the horizontal line is moved up along the interface shear strength axis (i.e., the slope of the SMS-jointing layer thickness relationship becomes flatter).

Another notable characteristic of the plot in **Figure 115** is the periodic flattening of the relationship between the SMS and the jointing layer thickness followed by an almost sudden increase. This occurs especially as the interface shear strength becomes smaller. This observation makes sense because the use of the interface slippage saturation mechanism means that a maximum tensile stress ($\frac{\tau_0 L}{t}$, L is the length of the segment; see **Figure 107**) that is controlled in part by the interface shear strength occurs. This expression for the maximum tensile stress may be enough to cause jointing over a range of jointing layer thickness (t) values but once the jointing layer thickness is out of this

range, the maximum tensile stress may no longer be sufficient to cause jointing (t in $\frac{\tau_0 L}{t}$ decreases the maximum tensile stress significantly given the same τ_0) . This is why there is such a flattening of the relationship over a range of jointing layer thickness values then a sudden increase at some larger value of jointing layer thickness.

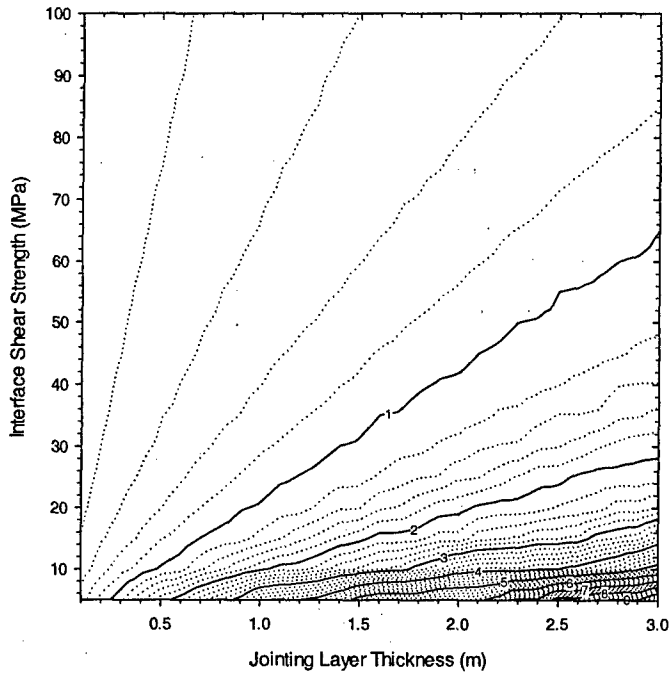


Figure 116 – Contours of saturation mean spacing (SMS) as a function of the jointing layer thickness and interface shear strength for the interface slippage model.

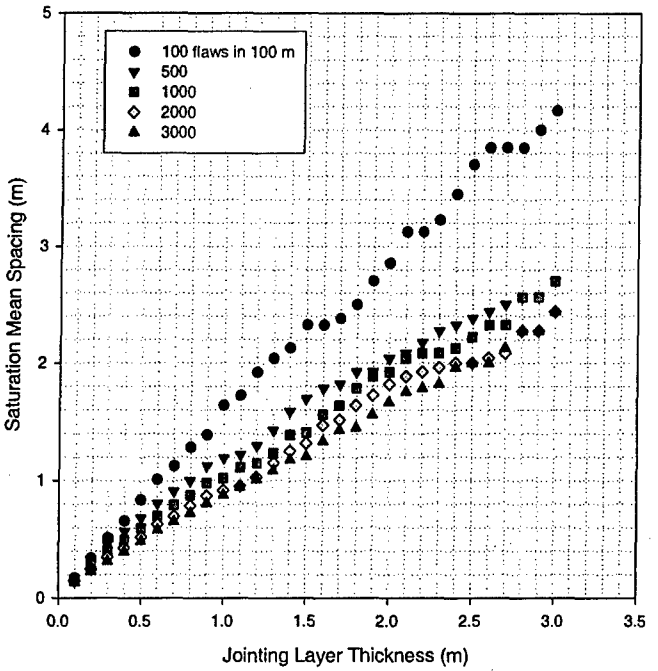


Figure 117 – Illustration of the effect of flaw density on the relationship between jointing layer thickness and the saturation mean spacing.

Another factor that affects the spacing-thickness relationship at saturation is the flaw density in the jointing layer. **Figure 117** shows that higher flaw densities lead to a smaller saturation mean spacing given the same jointing layer thickness. This makes sense because at higher flaw densities, the average strength of the jointing layer would be lower than it would be if a smaller number of flaws were present.

There is also a notable characteristic in the thickness-spacing relationships presented in the above figures. It appears that a flattening of the slope of the relationship occurs at certain jointing layer thickness values and then the slope increases again. This seems to occur periodically as the jointing layer is increased. This may serve to explain the bi-linear relationship that Ladeira and Price (1981) have observed in field data. However, further understanding of the model and their data is needed before this can be made certain.

Next, the saturation mechanism due to compressive stress development is considered and the parameter effects on the saturation mean spacing are investigated.

6.2.3.2 Compressive Stress Development

Simulations were performed using the flaw model algorithm with the compressive stress mechanism and the results are presented in **Figure 118** to **Figure 122**. As before, the results are presented in terms of the relationship between the saturation mean spacing and the jointing layer thickness.

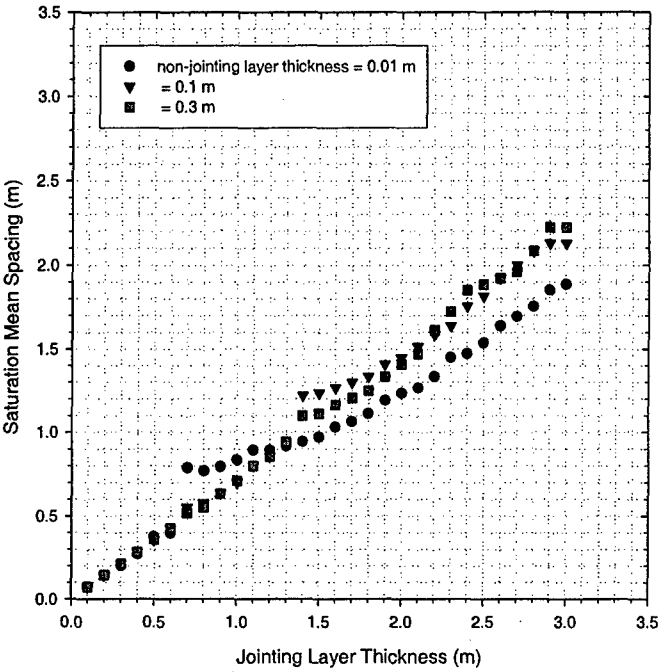


Figure 118 – Effect of the non-jointing layer thickness on the relationship between saturation mean spacing and jointing layer thickness.

Figure 118 shows the effect of the non-jointing layer thickness on the relationship between the saturation mean spacing and the jointing layer thickness. At jointing layer thickness values below 0.7 m (in this case), the non-jointing layer thickness does not appear to affect the relationship. However, there is a sudden jump in the case of the 0.01 m non-jointing layer thickness at a jointing layer thickness of about 0.7 m. There is no explanation for this behavior at this point. At higher jointing layer thickness values (here, > 1.2 m), smaller non-jointing layer thickness leads to lower saturation mean spacing. However, the effect appears to become smaller as the non-jointing layer thickness is increased (note the relatively small difference between the non-jointing layer thicknesses of 0.1 m and 0.3 m). **Figure 119** shows the effect of the same parameter but for a wider range of values. A jump in the data used in **Figure 118** is also apparent in **Figure 119**. Looking at the SMS-jointing layer thickness curve for a non-jointing thickness of 0.1 m in **Figure 118**, a jump in the SMS occurs between about 1.3 and 1.4 m on the jointing layer thickness axis. In **Figure 119**, a jump in the SMS contours for a non-jointing layer thickness of 0.1 m also occurs (i.e., the contours are spaced closely at that value of non-jointing layer thickness). At values below about 0.2 m in this case, the non-jointing layer thickness seems to have a significant effect on the relationship between the saturation mean spacing and the jointing layer thickness. However, above a non-jointing layer thickness of 0.2 m for this case, the relationship appears to be less dependent on this parameter. This dependence is not dictated by the equations that are used to determine $(\frac{s}{t})_{cr}$ because the non-jointing layer thickness is not one of the parameters considered (**Equation 47**). The dependence on the non-jointing layer thickness is brought about by

using **Equation 60** in determining the stresses in the jointing layer but this should only make a difference at strains below saturation (similar to what was demonstrated for the interface slippage model in **Figure 111**). Given the results in **Figure 118** and **Figure 119**, one can simply say that for low values of non-jointing layer thickness, there is some dependence, but this dependence disappears when the non-jointing layer thickness becomes large. Ladeira and Price (1981) have gathered field data showing lower joint spacing in layers bounded by thinner layers than in those bounded by thicker layers. However, they did not establish whether or not these jointing layers were already at saturation level with respect to this type of jointing.

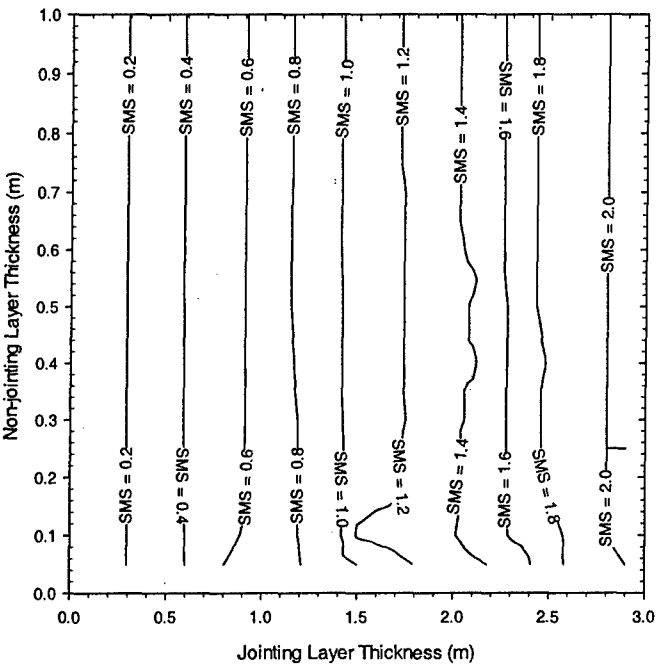


Figure 119 – Contours of saturation mean spacing (SMS) as a function of jointing layer thickness and non-jointing layer thickness for the compressive stress model.

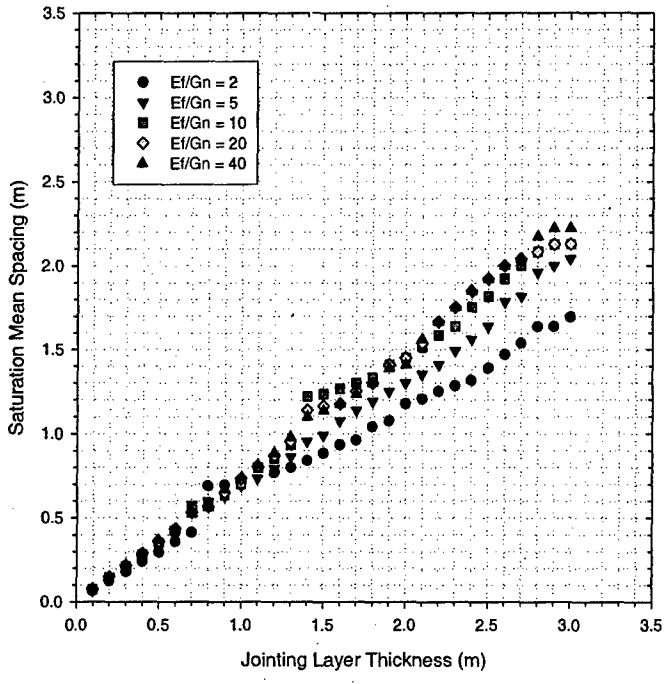


Figure 120 – Effect of the $\frac{E_f}{G_n}$ ratio on the relationship between saturation mean spacing and jointing layer thickness.

Figure 120 shows the effect of the ratio between the jointing layer Young's modulus and the non-jointing layer shear modulus on the relationship. One could also use $\frac{E_f}{E_n}$ as E_n and G_n are related but for reasons of consistency with previous plots (e.g., **Figure 112** and **Figure 114**) $\frac{E_f}{G_n}$ is used. At jointing layer thickness values below about 1.0 m, the effect of the $\frac{E_f}{G_n}$ ratio appears negligible. However, above 1.0 m, larger values of the $\frac{E_f}{G_n}$ ratio lead to a wider spacing. This behavior is notably different from that in the model with interface slippage as the saturation mechanism (**Figure 112**) but was expected because, unlike in the model with interface slippage, the stresses at saturation in this model are still controlled by the "elastic contrast", as Hobbs (1967) would call it (i.e., $\frac{E_f}{G_n}$ in **Equation 60**), between the jointing layer and the non-jointing layer. In the model considering interface slippage, on the other hand, the stresses in a segment at saturation are controlled by the interface shear strength and the length of the segment (or the spacing). **Figure 121** shows the effect of the elastic contrast for a wider range of values. At low jointing layer thickness (up to about 1.0 m), the $\frac{E_f}{G_n}$ ratio does not appear to have an effect on the relationship. This can be seen in both **Figure 120** and **Figure 121**. At high jointing layer thickness values, the $\frac{E_f}{G_n}$ ratio appears to have a significant effect on the SMS-jointing layer thickness relationship when $\frac{E_f}{G_n}$ is less than about 25 (**Figure 121**). However, the SMS-jointing layer thickness relationship appears less affected by

large values of the $\frac{E_f}{G_n}$ ratio. The contour lines become approximately vertical in **Figure 121** and the curves seem to cluster in **Figure 120** as $\frac{E_f}{G_n}$ is increased. Jumps in the data are apparent in both **Figure 120** and **Figure 121**. This can be explained by looking at **Figure 62** where the effect of $\frac{E_f}{E_n}$ (which is directly proportional to $\frac{E_f}{G_n}$ in elastic theory) is illustrated. The value of $(\frac{s}{t})_{cr}$ is no longer affected by $\frac{E_f}{E_n}$ when the latter becomes large (**Figure 62**).

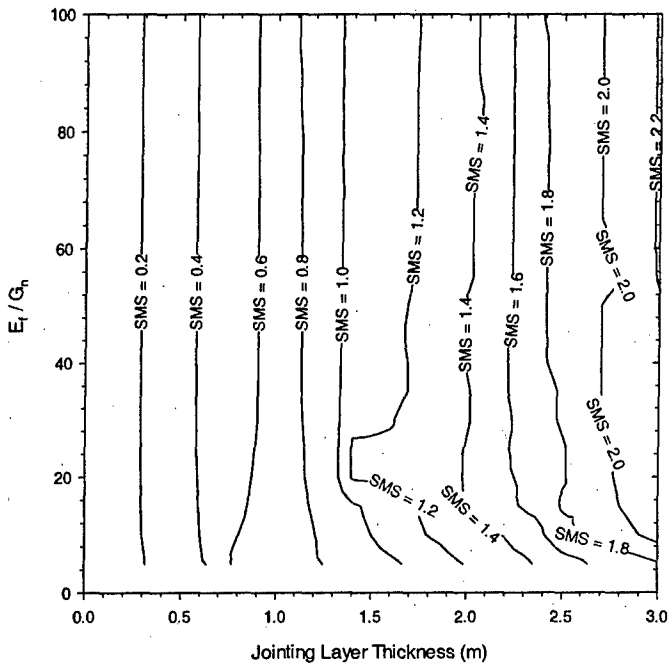


Figure 121 – Contours of saturation mean spacing (SMS) as a function of jointing layer thickness and the $\frac{E_f}{G_n}$ ratio for the compressive stress model.

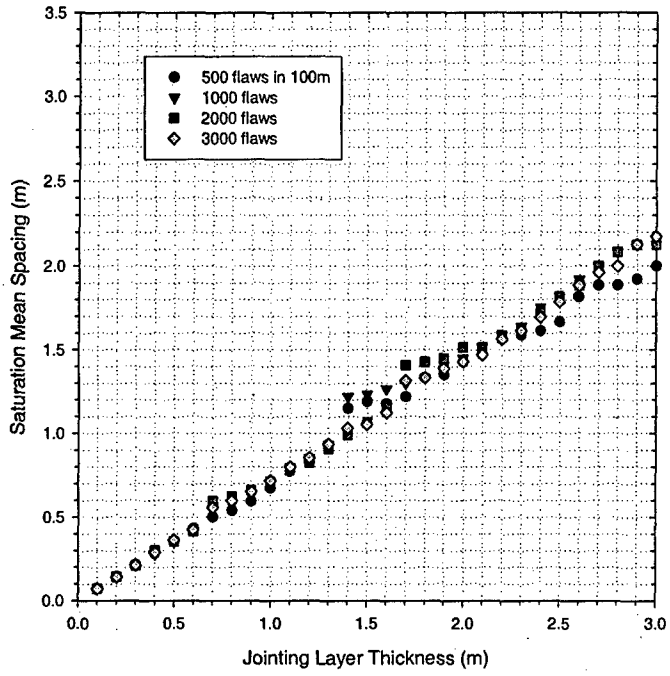


Figure 122 – Effect of the flaw density in the jointing layer on the relationship between saturation mean spacing and jointing layer thickness.

Figure 122 shows the effect of flaw density on the relationship between saturation mean spacing and jointing layer thickness. Apparently, the flaw density does not affect the relationship significantly. The relationship when there are 500 flaws is essentially the same as when there are 3000 flaws. This differs from the model having interface slippage as the saturation mechanism where the relationship between the saturation mean spacing and the jointing layer thickness is affected strongly by the flaw density (**Figure 117**). This behavior makes sense because in the flaw model with interface slippage, there is a limit to the tensile stress that can be developed (controlled by the interface shear strength, τ_0), whereas here there is none as long as the segment is above the critical spacing, $t \cdot \left(\frac{s}{t}\right)_{cr}$. This is shown better in **Figure 123** and **Figure 124**. In **Figure 123**, it matters if there are flaws or not because the tensile stress is limited. On the other hand, **Figure 124** shows that it does not matter if flaws exist because there is no limit to the tensile stress that can be developed as long as the spacing is above critical. New joints can always form, albeit at different locations as shown in **Figure 124**. Note that the resulting mean spacing in **Figure 124** is the same no matter where this new joint forms. This is the reason for the apparent independence of the SMS on the flaw density shown in **Figure 122**.

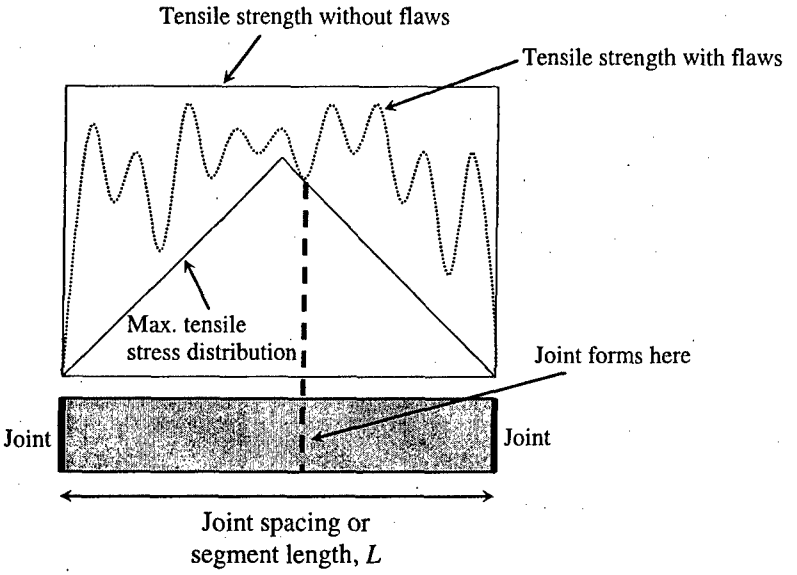


Figure 123 – Tensile stress vs. tensile strength for the interface slippage saturation mechanism for the case with and without flaws. New joint formation is only possible with the existence of flaws because there is a limit to the tensile stress that can be achieved.

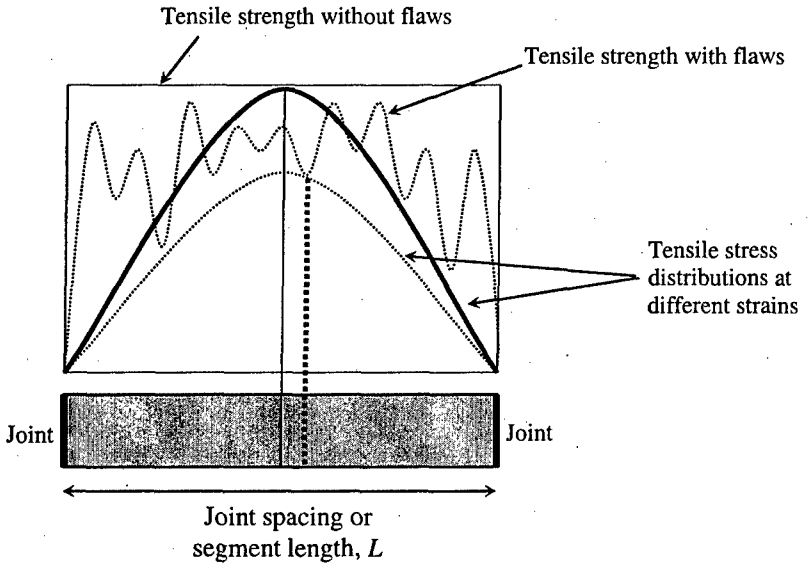


Figure 124 – Tensile stress vs. tensile strength for the compressive stress saturation mechanism for the case with and without flaws. The existing joints are spaced above the critical spacing, $t \cdot \left(\frac{\varepsilon}{t}\right)_{cr}$. A new joint can form with or without the flaws (the two dropdown lines) because there is no limit to the tensile stress as long as the spacing is above critical.

The combined effect of both saturation mechanisms on the saturation mean spacing is investigated in the next section.

6.2.3.3 Combined Interface Slippage and Compressive Stress Development Mechanisms

Before proceeding with the simulations to study the effects of the combined saturation mechanisms on the SMS, the jointing algorithm must again be modified. Since the necessary additions to the algorithm for each mechanism are already mapped out, combining them is relatively easy. Step 1 for this algorithm combines both the first steps from the flaw model considering interface slippage (i.e., the jointing strain calculations, **page 173**) and the flaw model considering the development of compressive stresses (i.e., the calculation of $(\frac{s}{t})_{cr}$). Step 2 is the same as in the model considering compressive stress development as the saturation mechanism. Step 3 remains unchanged from the original algorithm where no saturation mechanism was implemented (**page 161**). For convenience, a brief version of the steps is presented here.

1. Calculate the strains required for jointing at each flaw and at the midpoints of each segment (in the beginning, there is only one segment: the entire jointing layer). If the strain required to achieve the necessary stress for jointing exceeds the slippage strain, use the slippage equations. In other words, first assume no slippage when calculating the strain required for jointing and compare it with the slippage strain (which depends on the interface shear strength as well as the length of the segment). If it is greater than the slippage strain, re-calculate the strain using the slippage equations. Calculate the value of $(\frac{s}{t})_{cr}$. For each segment, find the smallest strain required for jointing and note the location where this is possible (e.g., at a flaw or at the midpoint).

2. A new joint is added to the segment requiring the least amount of strain for jointing and whose length to thickness ratio is greater than $(\frac{s}{t})_{cr}$. If there is no such segment, saturation has been reached and the program terminates.

3. Perform step 1 on the new segments formed by the new joint (if applicable). There is no need to re-calculate $(\frac{s}{t})_{cr}$.

Figure 125 shows the how the relationship between the saturation mean spacing and the jointing layer thickness is affected by the type of saturation mechanism used. In this case, the compressive stress mechanism data lie very close to the combined mechanisms data. This suggests the dominance of the compressive stress mechanism in the combined model. However, other parameters in the model may affect this relationship. One clear parameter is the interface shear strength. Simulations were performed using all three models at different interface shear strength values. The results are presented in **Figure 126** to **Figure 128**.

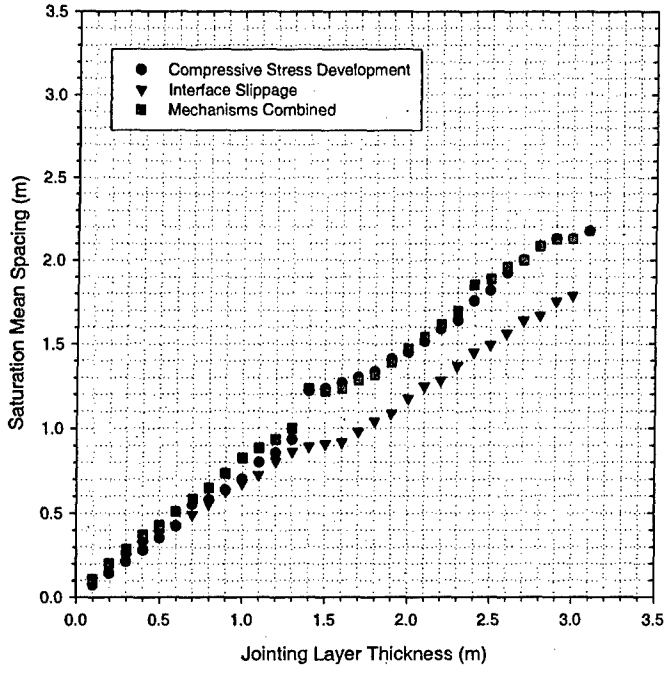


Figure 125 – Example of the relationship between saturation mean spacing and jointing layer thickness for the three different models.

Figure 126 to **Figure 128** show how the interface shear strength influences the difference among the three saturation mechanisms (compressive stress development only, interface slippage only, the two mechanisms combined). It is important to note that the compressive stress mechanism is not affected by the interface shear strength because it is assumed that the interface has infinite strength in that model. Consequently, the data for the compressive stress mechanism are the same in the three plots. The model considering interface slippage is strongly affected by the interface shear strength as was shown in **Figure 115**. The model using the combined mechanisms will be influenced by the interface shear strength but not to the same degree that the interface slippage model is. It is interesting to see that the location of each of the three curves with respect to each other is dependent on the interface shear strength (compare **Figure 126**, **Figure 127** and **Figure 128**). At low interface shear strength, the interface slippage mechanism governs in the combined model such that their curves coincide (**Figure 126**). In this case, the model using only the compressive stress mechanism allows higher tensile stresses to develop in the model, forming more joints (i.e., spacing is closer). For the combined mechanism model, the compressive stress mechanism has essentially no effect. At the intermediate level (**Figure 127**), none of the curves coincide as both mechanisms probably contribute to saturation, not just one. At high interface shear strength (**Figure 128**), the compressive stress development data coincide with the combined mechanism data. This indicates that the compressive stress mechanism dominates the interface slippage mechanism in the combined model. The compressive stress mechanism does not allow the development of interface shear stresses to reach the interface shear strength (i.e., the existing segments are not long enough). If it did, the spacing would be closer as exhibited by the interface slippage model data. The transition from one saturation

mechanism to the other (i.e., interface slippage to compressive stress) as the interface shear strength increases is more clearly shown in **Figure 131** with **Figure 129** and **Figure 130** serving as a guide. The first two figures (**Figure 129** and **Figure 130**) show the effect of the interface shear strength in the models that use each saturation mechanism as the sole saturation mechanism. **Figure 131** shows the effect of the interface shear strength in the model combining these two mechanisms (i.e., interface slippage and compressive stress mechanisms). It is clear in **Figure 131** that the combined model transitions from the behavior shown in **Figure 129** (interface slippage is the saturation mechanism) at low interface shear strength values to the behavior shown in **Figure 130** (compressive stress is the saturation mechanism) at high interface shear strength values. This behavior makes sense because at low interface shear strength, smaller tensile stresses are allowed to develop in the layer (recall that tensile stress in layer $\propto$ interface shear stress, see **Figure 102** and accompanying equations) and not enough jointing occurs in order to make $(\frac{s}{t})_{cr}$ (i.e., the criterion for saturation in the compressive stress mechanism) relevant. At high interface shear strength, larger interface shear stresses can occur and these lead to higher tensile stresses in the layer such that jointing can only be halted by the compressive stress mechanism (i.e., the $(\frac{s}{t})_{cr}$ criterion).

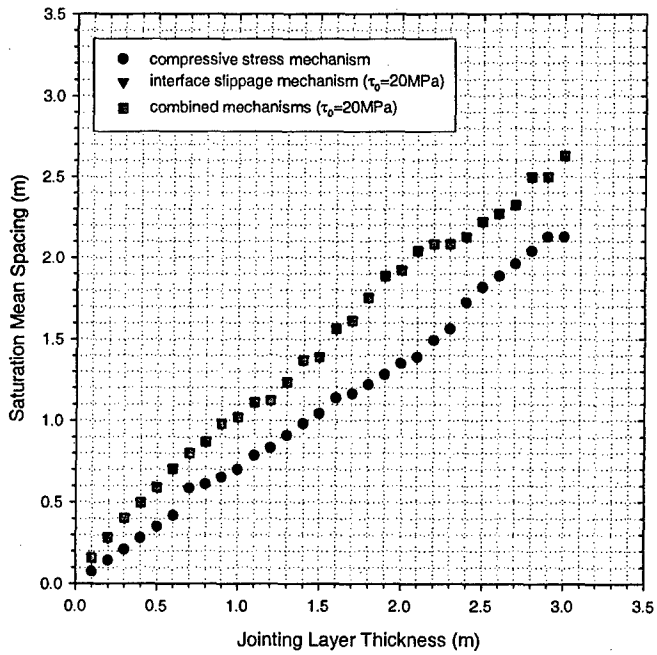


Figure 126 – The three saturation mechanisms at an interface shear strength of 20MPa. Note that the interface slip and combined mechanism data coincide almost perfectly.

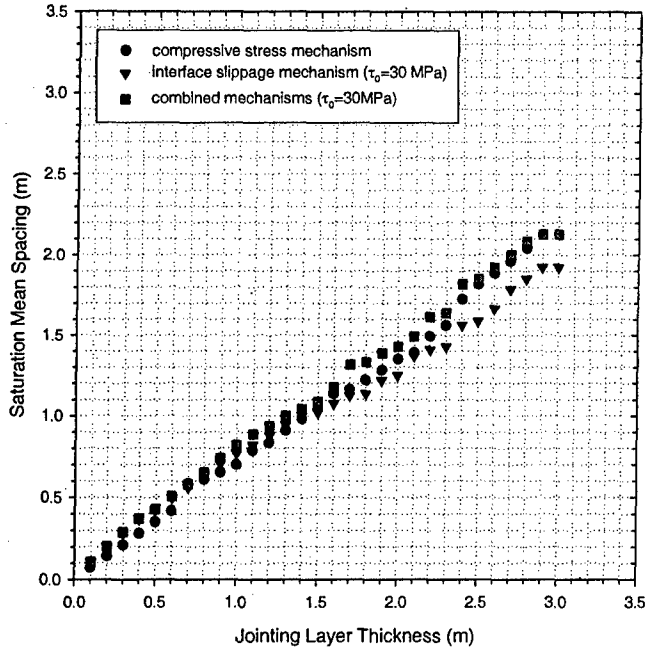


Figure 127 – The three saturation mechanisms at an interface shear strength of 30MPa.

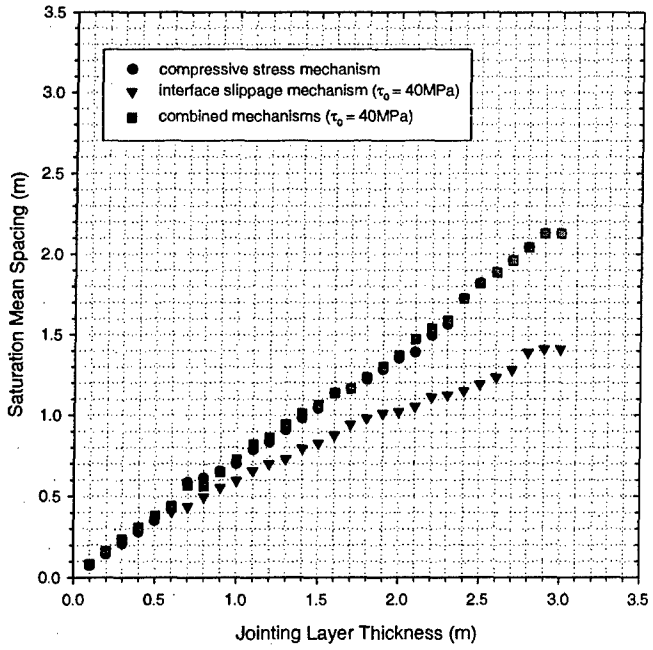


Figure 128 – The three saturation mechanisms at an interface shear strength of 40MPa.

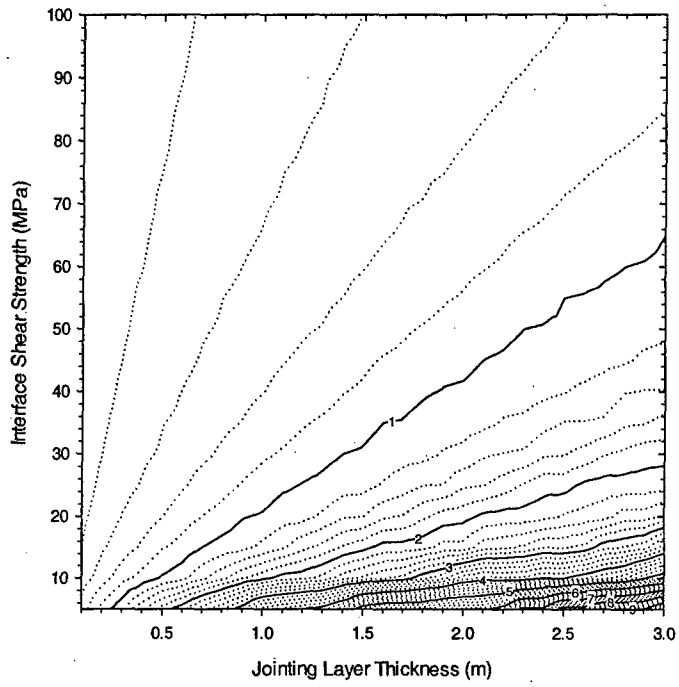


Figure 129 – Contours of the saturation mean spacing (SMS) as a function of the jointing layer thickness and the interface shear strength in the model considering only interface slippage as the saturation mechanism (same as Figure 116).

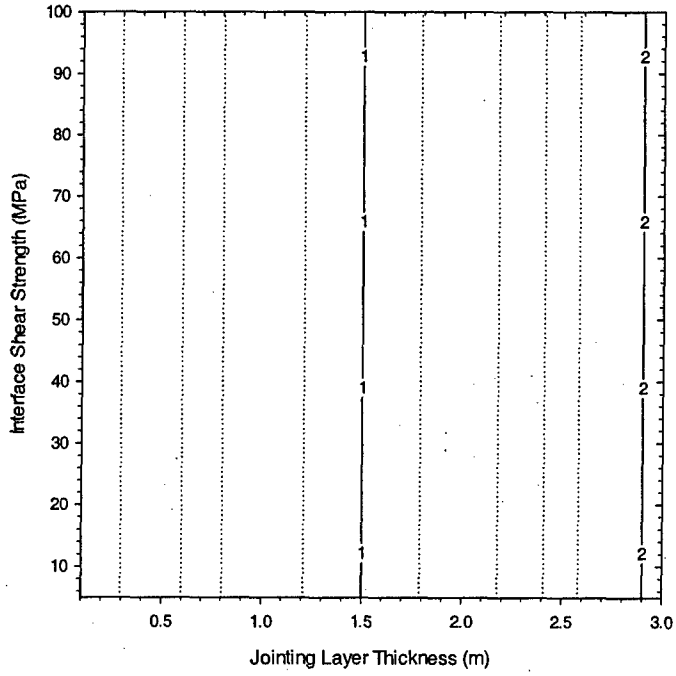


Figure 130 – Contours of saturation mean spacing (SMS) as a function of the jointing layer thickness and the interface shear strength in the model considering only the compressive stress as the saturation mechanism.

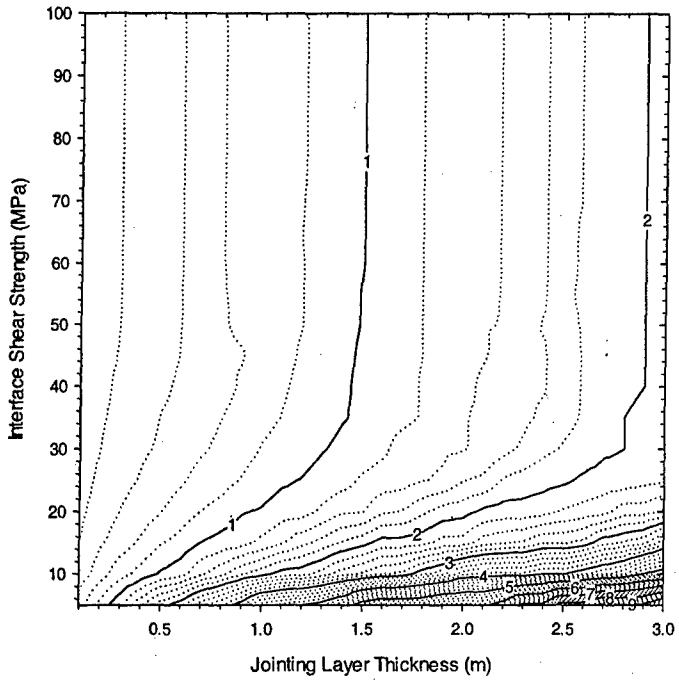


Figure 131 – Contours of saturation mean spacing (SMS) as a function of the jointing layer thickness and the interface shear strength in the model considering both interface slippage and compressive stress as saturation mechanisms.

The effects of the other model parameters may influence the results as well. For example, **Figure 132** to **Figure 134** show the effect of $\frac{E_f}{G_n}$. At low $\frac{E_f}{G_n}$ (**Figure 132**), the model using only the compressive stress mechanism and the model using only the interface slippage yield close results. Recall that the model using only the interface slippage mechanism is not affected by the $\frac{E_f}{G_n}$ ratio at saturation (see **Figure 112**). The model using the combined mechanism generally yields larger saturation mean spacing for a given value of jointing layer thickness. At intermediate $\frac{E_f}{G_n}$ (**Figure 133**), there is no significant difference among the three models at lower jointing layer thickness values but it appears that at higher jointing layer thickness values, the compressive stress mechanism model and the combined model yield close results. This suggests that the compressive stress mechanism dominates in the combined model at these values of jointing layer thickness. At high $\frac{E_f}{G_n}$ (**Figure 134**), it is clear that the results for the combined model and the model using only the compressive stress mechanism produce very close results. This suggests that the compressive stress mechanism governs saturation in the combined model for high values of the $\frac{E_f}{G_n}$ ratio. **Figure 135** to **Figure 137** show contours of the saturation mean spacing as a function of both the $\frac{E_f}{G_n}$ ratio and the jointing layer thickness for the interface slippage, compressive stress and combined mechanism models, respectively. In these figures, it is clear that the interface slippage

model and the combined mechanism model yield very close results for saturation mean spacing (SMS) values of up to 0.8 m. However, the contours for SMS values greater than or equal to 1.0 m in the combined mechanism model appear similar to those of the compressive stress model. This was expected because as mentioned earlier, the interface slippage model is not affected by the $\frac{E_f}{G_n}$ ratio at saturation so it is reasonable to believe that in this regard, the compressive stress model results will be similar to the combined mechanism results.

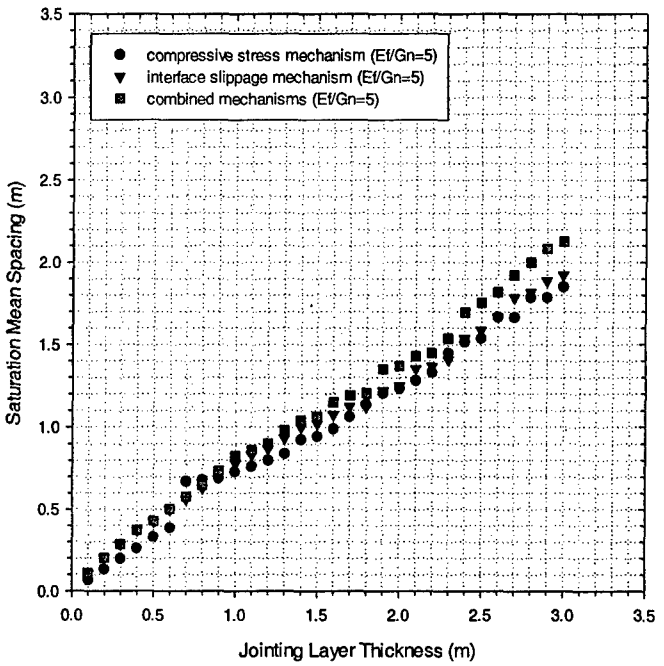


Figure 132 – Saturation mean spacing results from the three different models for a $\frac{E_f}{G_n}$ ratio of 5.0.

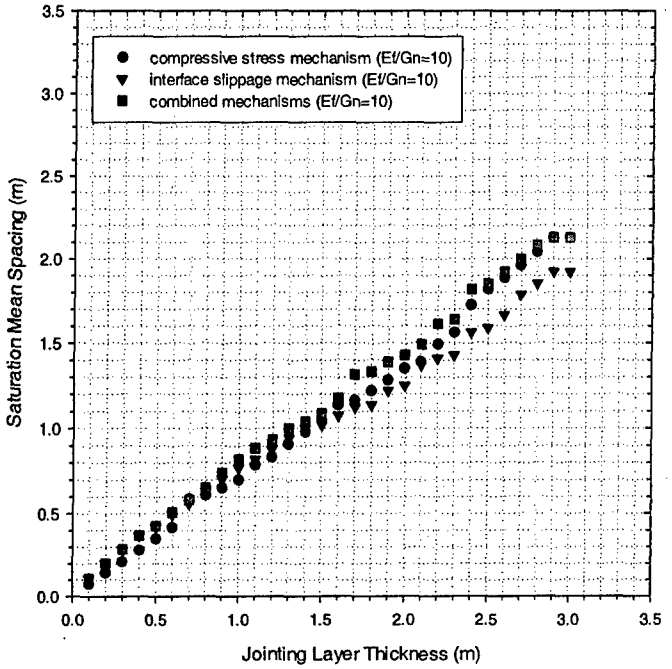


Figure 133 – Saturation mean spacing results from the three different models for a $\frac{E_f}{G_n}$ ratio of 10.

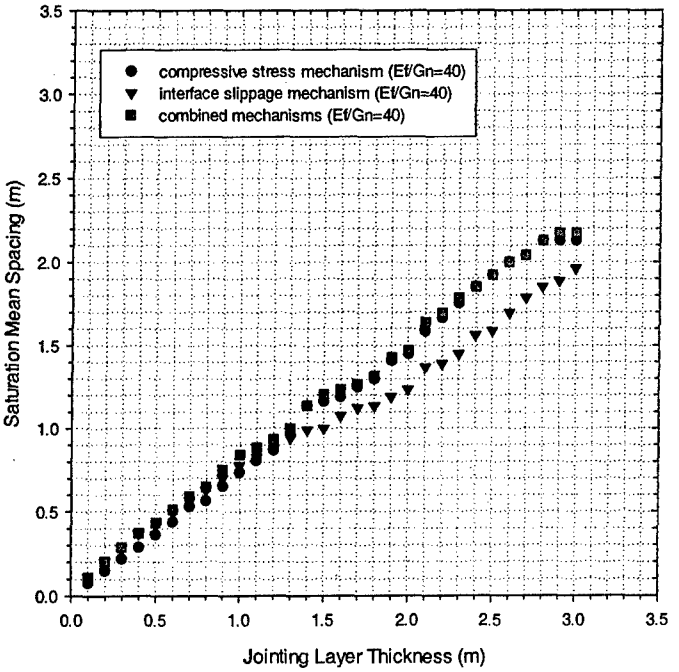


Figure 134 – Saturation mean spacing results from the three different models for a $\frac{E_f}{G_n}$ ratio of 40.

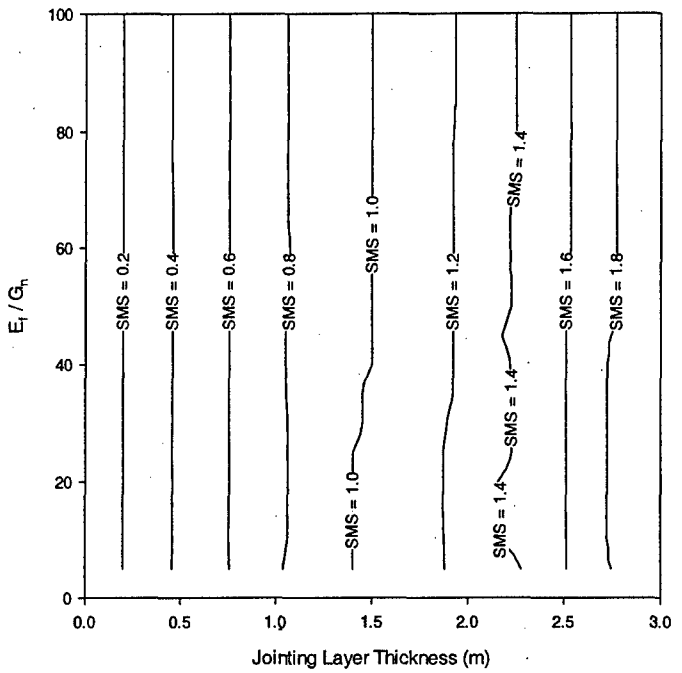


Figure 135 – Contours of saturation mean spacing (SMS) as a function of the jointing layer thickness and the $\frac{E_f}{G_n}$ ratio in the model considering only interface slippage as the saturation mechanism.

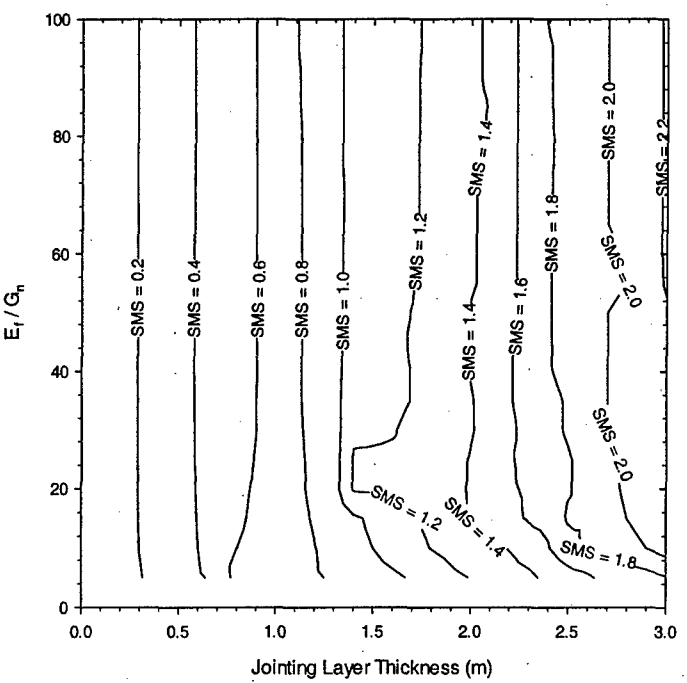


Figure 136 – Contours of saturation mean spacing (SMS) as a function of the jointing layer thickness and the $\frac{E_f}{G_n}$ ratio in the model considering only compressive stress as the saturation mechanism.

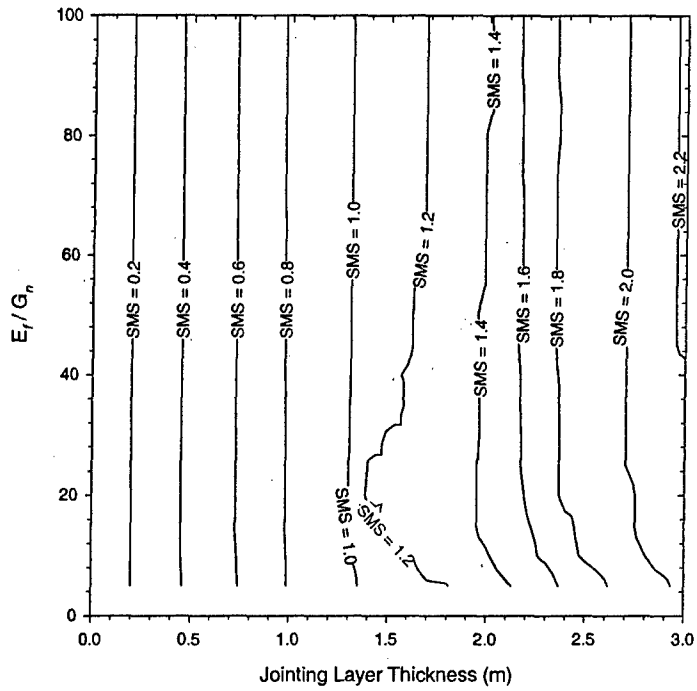


Figure 137 – Contours of saturation mean spacing (SMS) as a function of the jointing layer thickness and the $\frac{E_f}{G_n}$ ratio in the combined mechanism model.

Figure 138 to **Figure 140** show the effect of D (**Equation 44**) on the relationship between saturation mean spacing and jointing layer thickness for the three models. For a positive value of D (i.e., $\nu_f < \nu_n$), there does not appear to be a significant difference among the three models (**Figure 138**). However, it also appears that the compressive stress model and the interface slippage model yield results that are closer to each other than to the combined model results. This is also true where D equals zero (**Figure 139**). Both of these observations appear to be coincidental because the interface slippage model is not affected by D. For a negative value of D (i.e., $\nu_f > \nu_n$), it seems that the compressive stress mechanism is the dominant saturation mechanism in the combined model (**Figure 140**). This was be expected because the compressive stress model uses D in the calculation of $(\frac{s}{t})_{cr}$. This does not mean that the interface slippage mechanism does not play a role in the jointing process. It is clear in **Figure 141** and **Figure 142** that the contours of saturation mean spacing from the compressive stress model differ from those in the combined mechanism model. The contours in **Figure 142** seem to be shifted to the left with respect to the contours in **Figure 141**.

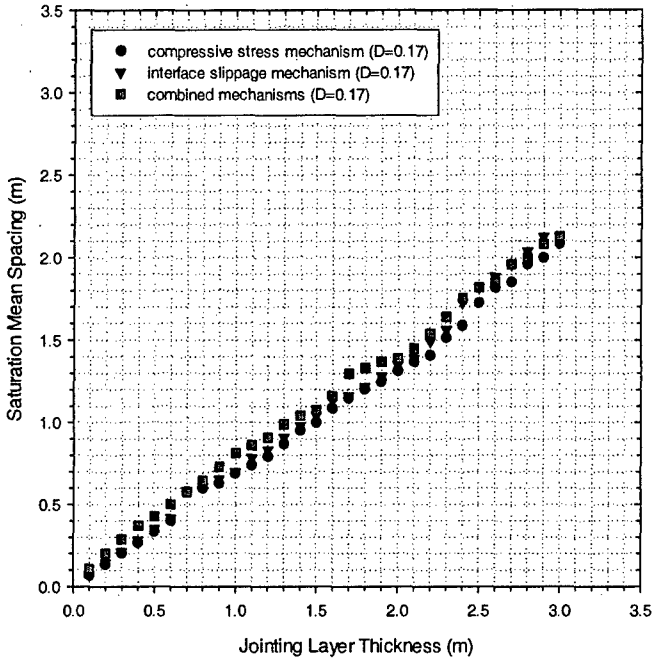


Figure 138 - Saturation mean spacing results from the three different models for $D = 0.17$.

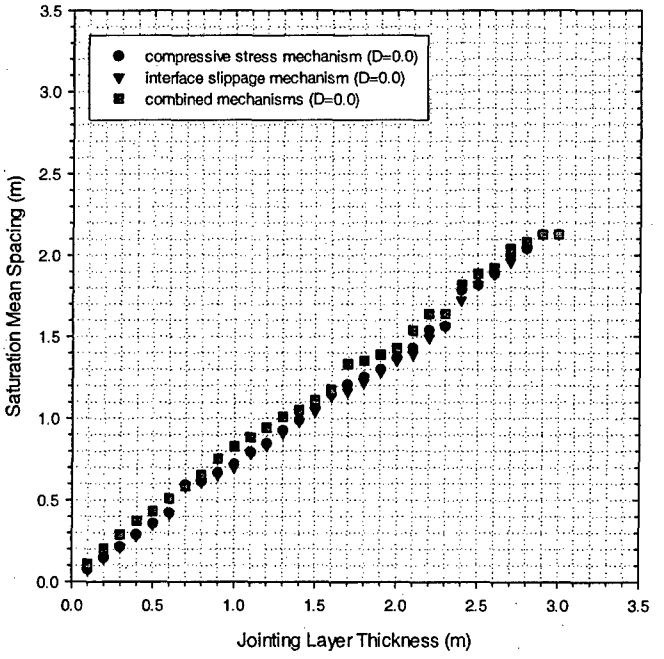


Figure 139 - Saturation mean spacing results from the three different models for $D = 0.0$.

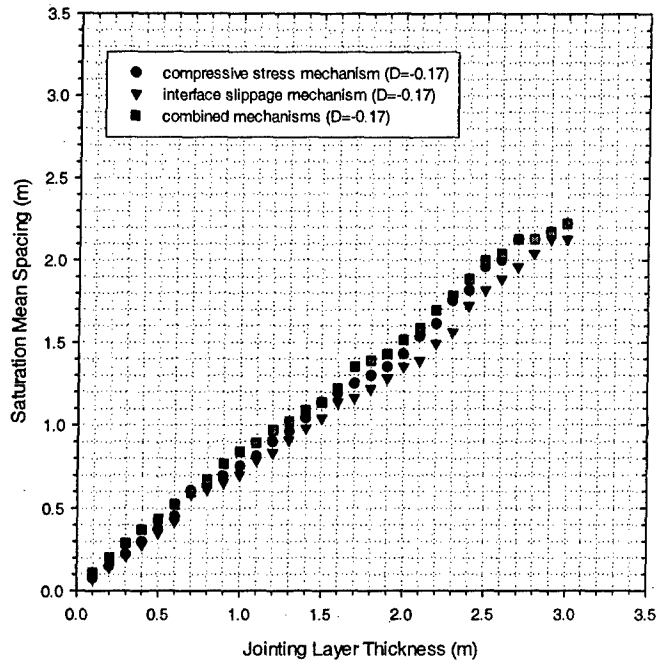


Figure 140 - Saturation mean spacing results from the three different models for D = -0.17.

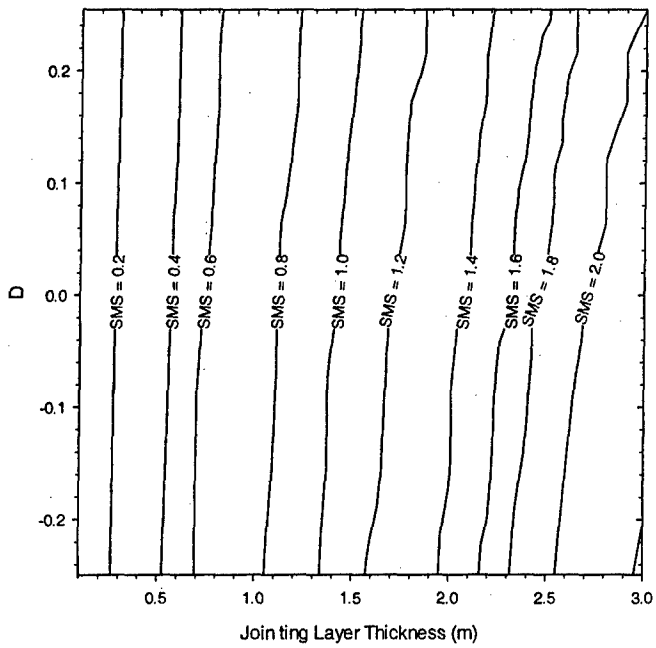


Figure 141 – Contours of saturation mean spacing (SMS) as a function of the jointing layer thickness and the parameter D in the model considering only compressive stress as the saturation mechanism.

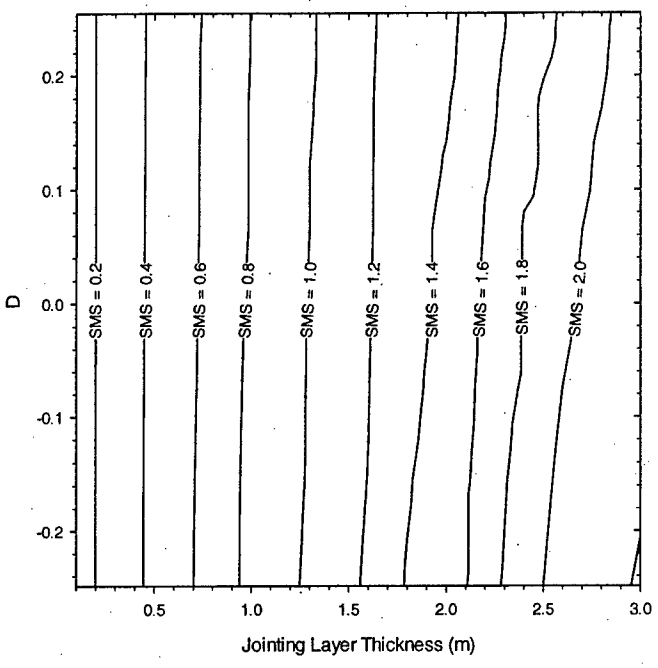


Figure 142 – Contours of saturation mean spacing (SMS) as a function of the jointing layer thickness and the parameter *D* in the combined mechanism model.

Another parameter that affects the relationship is the non-jointing layer (or bounding layer) thickness. Its effect is illustrated in **Figure 143** to **Figure 145**. For very thin bounding layers, no single saturation mechanism dominates in the combined model (**Figure 143**). The curve for the combined mechanism lies above the curves for both the compressive stress and the interface slippage models. However, as bounding layer thickness is increased, the compressive stress mechanism begins to dominate in the combined model (**Figure 144** and **Figure 145**). This is also apparent in the contour plots in **Figure 146**, **Figure 147** and **Figure 148**. The lower part of the plot in **Figure 148** appears to be a combination of the lower parts of the plots in **Figure 146** and **Figure 147**. However, the upper portion of the plot in **Figure 148** more strongly resembles the upper part of the plot in **Figure 147**. It is reasonable to expect the compressive stress mechanism to dominate in the combined model in this case because the model using only the compressive stress mechanism is affected more by the non-jointing layer thickness than the model using only the interface slippage mechanism. However, it must be noted that the effect of this parameter in both models (i.e., interface slippage only and compressive stress only) is not significant (i.e., contour lines appear mostly vertical except for some jumps in the data, **Figure 146** and **Figure 147**).

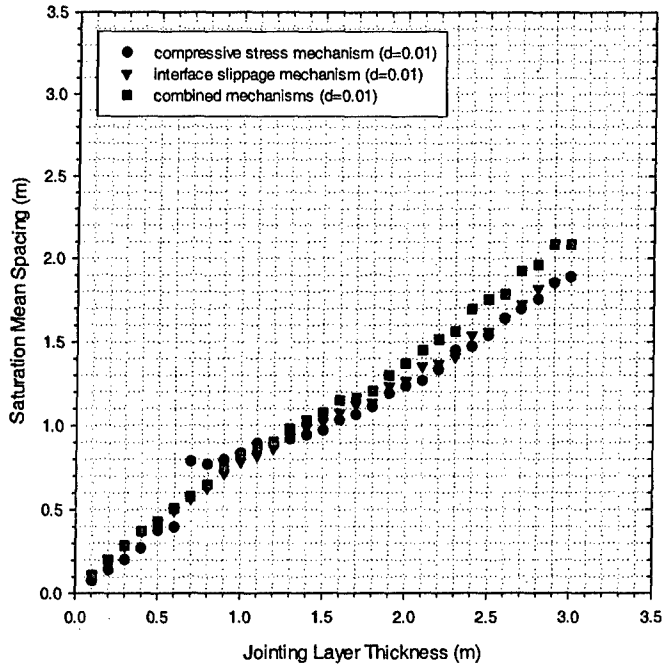


Figure 143 - Saturation mean spacing results from the three different models for a non-jointing layer thickness value of 0.01 m.

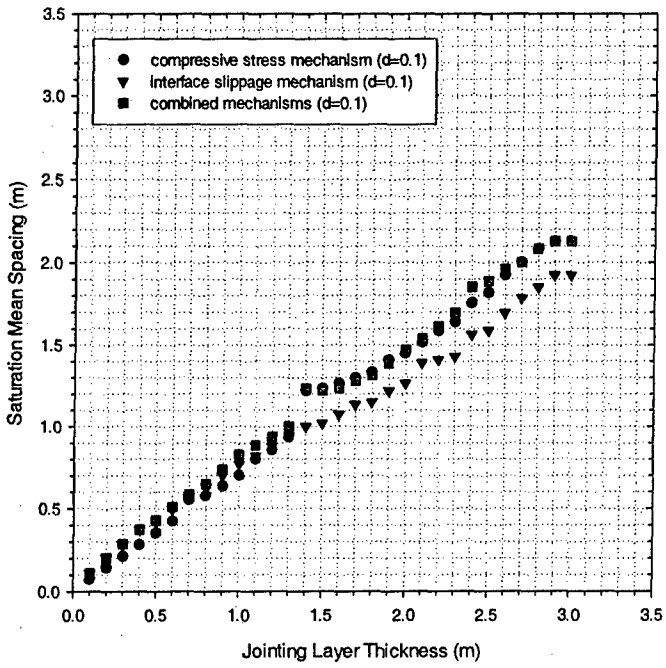


Figure 144 - Saturation mean spacing results from the three different models for a non-jointing layer thickness value of 0.1 m.

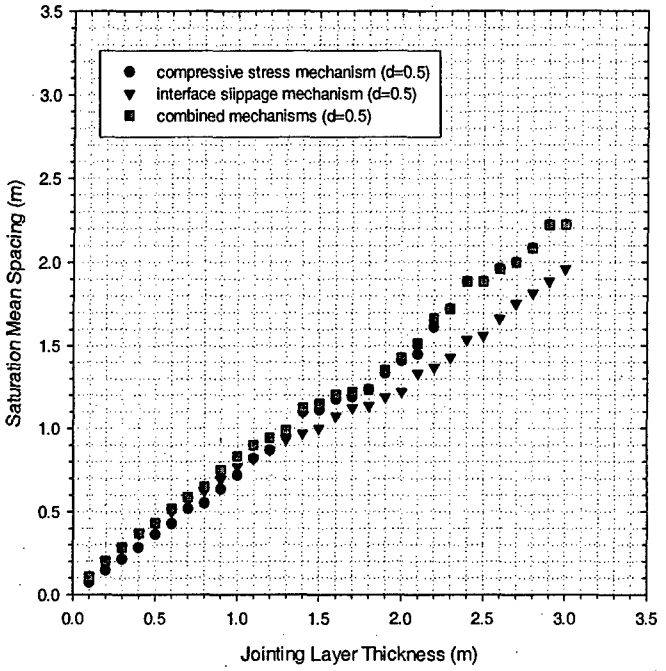


Figure 145 - Saturation mean spacing results from the three different models for a non-jointing layer thickness value of 0.5 m.

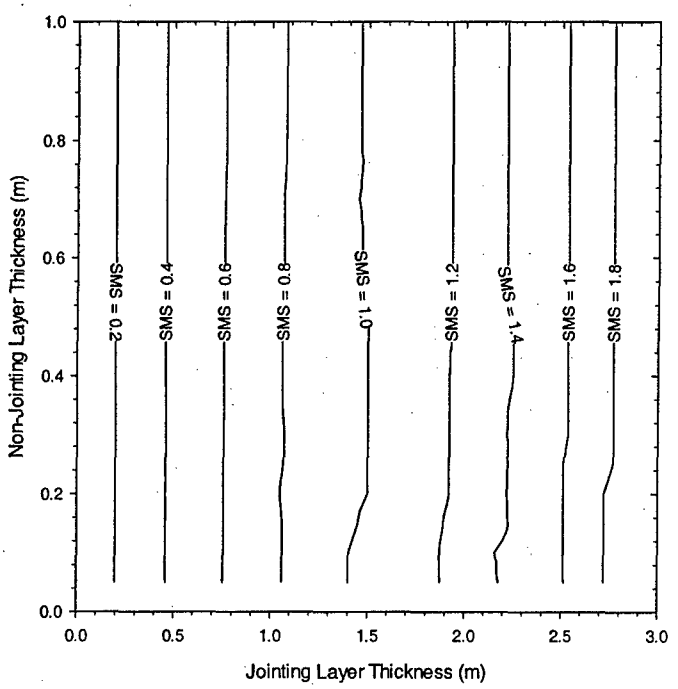


Figure 146 – Contours of saturation mean spacing (SMS) as a function of the jointing layer thickness and the non-jointing layer thickness in the model considering only interface slippage as the saturation mechanism.

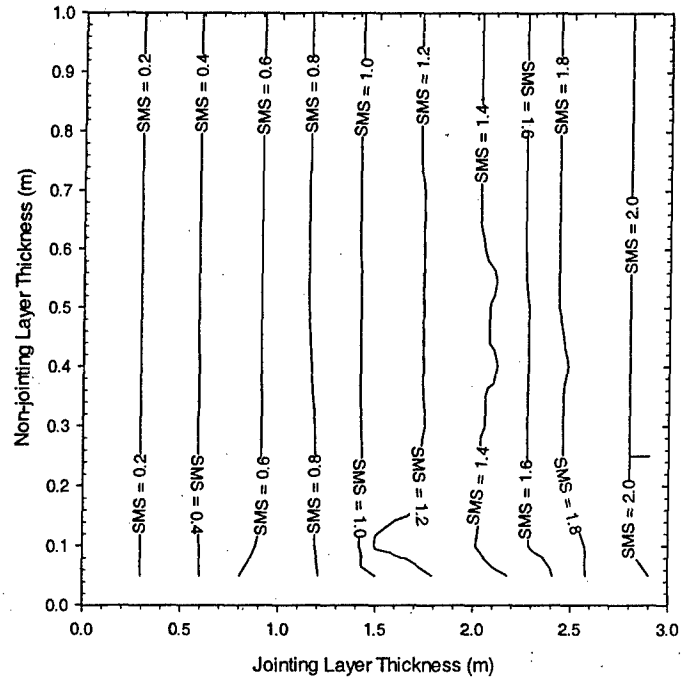


Figure 147 – Contours of saturation mean spacing (SMS) as a function of the jointing layer thickness and the non-jointing layer thickness in the model considering only the compressive stress as the saturation mechanism.

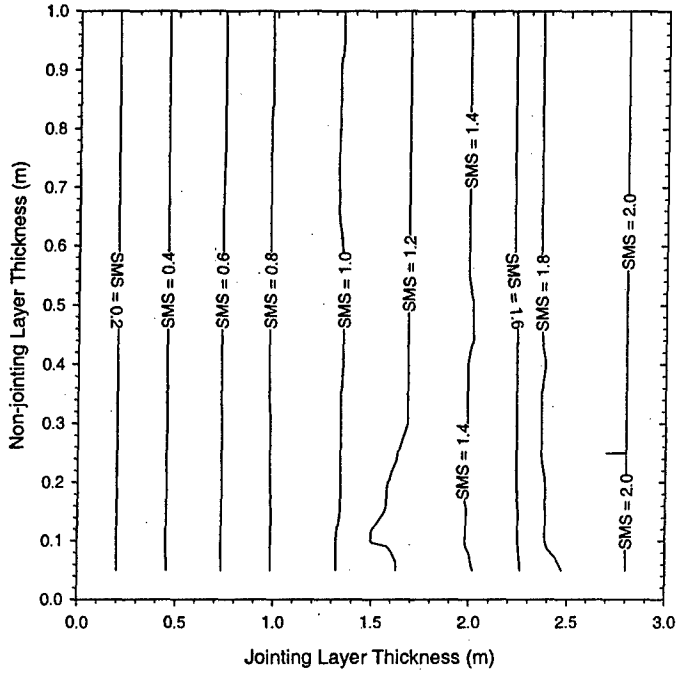


Figure 148 – Contours of saturation mean spacing (SMS) as a function of the jointing layer thickness and the non-jointing layer thickness in the combined mechanism model.

Figure 149 to **Figure 151** show the effect of flaw density on each of the three models. As with the previous simulations, the length of the jointing layer is 100 m. It can be observed that as the number of flaws increases, the dominant mechanism in the combined model also becomes clear. At low flaw density (e.g., 500 flaws in 100 m), the interface slippage mechanism governs in the combined model at lower jointing layer thickness values. However, at higher jointing layer thickness values, it is unclear which of these two mechanisms dominate in the combined model (**Figure 149**). At intermediate flaw density (e.g., 1000 flaws in 100 m), it seems that, in the combined model, the interface slippage mechanism dominates at low jointing layer thickness values whereas the compressive stress mechanism governs at higher jointing layer thickness values (**Figure 150**). At high flaw density (e.g., 2000 flaws in 100 m), the compressive stress mechanism is the dominant saturation mechanism in the combined model (**Figure 151**).

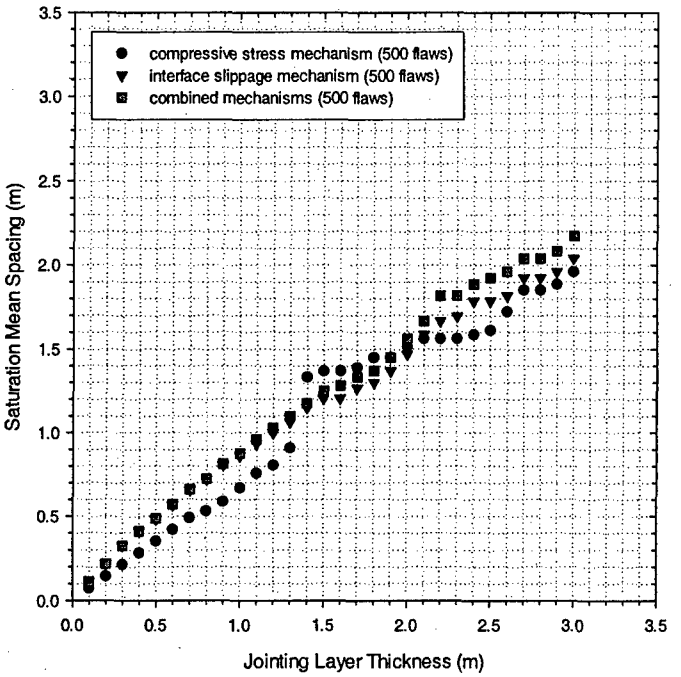


Figure 149 - Saturation mean spacing results from the three different models for a jointing layer with 500 flaws.

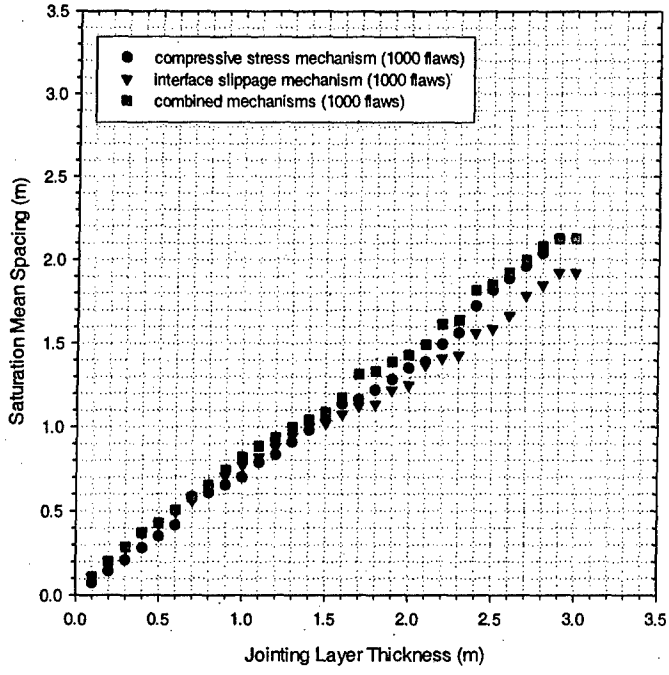


Figure 150 - Saturation mean spacing results from the three different models for a jointing layer with 1000 flaws.

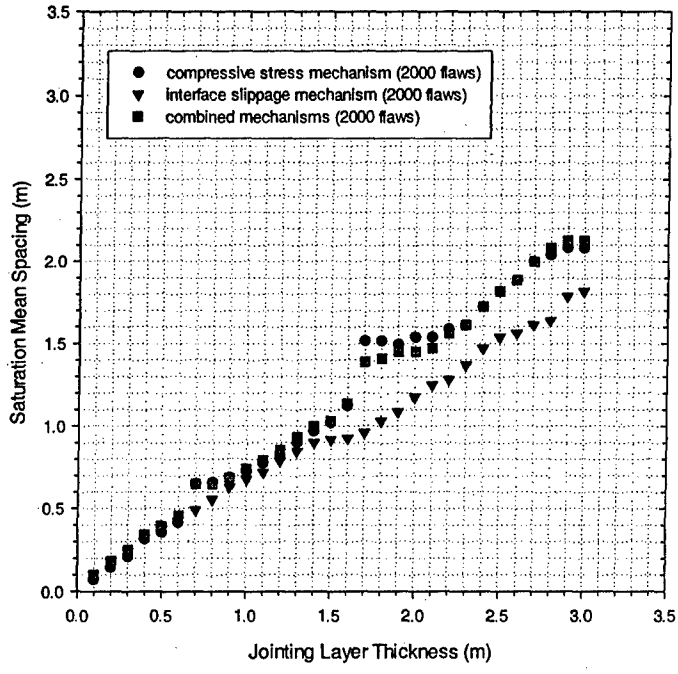


Figure 151 - Saturation mean spacing results from the three different models for a jointing layer with 2000 flaws.

The results presented in the last three sections showed the effects of the different flaw model parameters on the relationship between the mean spacing and the jointing layer thickness at saturation. It was found that the influence of some flaw model parameters on the SMS depends on the kind of saturation mechanism that is present. For example, the non-jointing layer thickness and the $\frac{E_f}{G_n}$ ratio do not appear to affect the SMS when the interface slippage mechanism is in place, but do affect the SMS when the compressive stress mechanism is present.

It must be noted, however, that saturation is only one stage of joint set development and that the mean spacing does not give a complete view of an entire joint pattern. Also, it is quite possible to find jointed sedimentary layers that are below (or even beyond) saturation and joint spacing is often observed to follow some form of probability distribution. For these reasons, one needs to look at the joint spacing distribution forms that are produced by the flaw model at different joint intensities using different parameter values and compare these to actual field observations (e.g., Rives et al., 1992).

6.2.4 Simulated Joint Spacing Distributions for Flaw Model

The results in the previous section demonstrated how each parameter affects saturation mean spacing (SMS) in the flaw model. However, saturation mean spacing is only one aspect of the joint patterns in layered sedimentary rock. It only represents the mean spacing at the final stage of joint set development (i.e., further jointing using the same mechanism is no longer possible). One would also want to look at the joint spacing distributions that are generated at different stages of joint set development before saturation. First, the shapes of joint spacing distributions for the flaw model with and without the saturation mechanism at different joint intensities are investigated. Here, only the compressive stress development saturation mechanism is considered because in the field data against which these models (flaw model and later, the rejection procedure) will be compared later, there is no evidence of interface slippage. Also, the effects of the parameters of the stress distribution model and the strength model (i.e., the two main components of the flaw model) on joint spacing distribution are studied. For this section on simulated joint spacing distributions, the structure is as follows:

1. Simulated joint spacing distribution vs. joint intensity for flaw model with and without saturation mechanism.

2. Effect of stress distribution model parameters on simulated joint spacing distributions at fixed joint intensity.

3. Effect of strength model parameters on simulated joint spacing distributions at fixed joint intensity.

6.2.4.1 Evolution with Increasing Joint Intensity and Effect of Saturation Mechanism

Recall that previous models (e.g., Narr and Suppe, 1991; Rabinovitch and Bahat, 1999) also generated joint spacing distributions but each had some shortcomings. For example, Rabinovitch and Bahat (1999) did not consider an in-filling process. In effect, their model could only represent joints whose stress reduction shadows do not interact (i.e., are far away from each other). Narr and Suppe (1991) used an approach similar to the flaw model. However, they did not consider the effects of non-jointing layer thickness and saturation mechanisms. Narr and Suppe (1991) also compared their model results to a combined set of spacings from several layers where interbed slippage was observed. The spacings from the different layers were combined into a single set because the joint intensities were similar. In effect, a comparison was made only for a single joint intensity.

First, consider how the flaw model with and then without the saturation mechanism represents the evolution of the joint spacing distribution as the joint intensity increases. In the simulations that follow, the term "saturation mechanism" only refers to the saturation mechanism due to the development of compressive stresses. The field data with which the new models are compared did not show evidence of interface slippage. For the purpose of looking at the evolution of joint spacing distribution, joint spacing cumulative probability distributions are used instead of joint spacing histograms because cumulative probability distributions are easier to compare visually than histograms. The phenomenon of evolution of the joint spacing distribution was only observed in laboratory experiments (e.g., Rives et al., 1992). It would not be possible to observe such an evolution in nature. Recall that Rives et al. (1992) observed the joint spacing distribution change from shifted exponential at low joint intensity to log-normal at intermediate joint intensity and quasi-normal at high joint intensity. **Figure 152** to **Figure 154** show how the simulated joint spacing cumulative distributions at different joint intensity compare to some known cumulative distribution functions or CDFs (e.g., exponential, log-normal and normal) for the flaw model with saturation mechanism. The parameters (e.g., mean and standard deviation of spacing) for each known distribution form are calculated using the maximum likelihood method (see **Table 5**). The cumulative probability is then plotted on a Gaussian-logarithmic plot. The cumulative distribution function for a normal or quasi-normal distribution will show as a straight line on a Gaussian-logarithmic plot. At low joint intensity (**Figure 152**), it is clear that the joint spacing distribution is not quasi-normal (i.e., cumulative probability is not a straight line). However, either an exponential or a log-normal distribution would describe the simulated distribution nicely. The better fit here appears to be the log-normal distribution. **Figure 153** shows how the simulated joint spacing cumulative distribution function at medium-high joint intensity compares to the exponential and log-normal CDFs. It is clear that the exponential CDF does not fit the simulated joint spacing cumulative distribution as well as a log-normal CDF does. At joint saturation (**Figure 154**), both the normal and log-normal CDFs provide a good fit to the simulated joint spacing CDF although the normal CDF is marginally better specifically at the tails.

Table 5 – Known probability distribution forms, their parameters and the corresponding maximum likelihood (ML) parameter estimates. Note: n is the number of joint spacing data.

Dist. Type	Equation	Param.	ML Estimates
Exp.	$f_s(s) = \lambda e^{-\lambda s}$	λ	$\hat{\lambda} = \frac{1}{\left(\frac{\sum_{i=1}^{n} s_i}{n}\right)} = \frac{1}{\bar{s}}$
Log-Normal (Note: ln s is normal)	$f_s(s) = \frac{1}{s\sigma_{\ln s}\sqrt{2\pi}} \exp\left(-\frac{1}{2}\left[\frac{\ln s - \mu_{\ln s}}{\sigma_{\ln s}}\right]^2\right)$	$\mu_{\ln s}, \sigma^2_{\ln s}$	$\hat{\mu}_{\ln s} = \frac{\sum_{i=1}^{n} \ln s_i}{n}$ $\hat{\sigma}^2_{\ln s} = \frac{1}{n}\sum_{i=1}^{n}\left(\ln s_i - \hat{\mu}_{\ln s}\right)^2$
Normal	$f_s(s) = \frac{1}{\sqrt{2\pi\sigma^2}} \exp\left(-\frac{(s-\mu)^2}{2\sigma^2}\right)$	μ, σ^2	$\hat{\mu} = \frac{\sum_{i=1}^{n} s_i}{n} = \bar{s}$ $\hat{\sigma}^2 = \frac{1}{n}\sum_{i=1}^{n}(s_i - \bar{s})^2$

It appears that the flaw model incorporated with a saturation mechanism (in this case, the development of compressive stresses at and below a critical spacing-to-thickness ratio) is capable of reflecting the evolution of the joint spacing distribution from exponential to log-normal to quasi-normal (**Figure 152** to **Figure 154**) that has been observed in laboratory experiments (Rives et al., 1992).

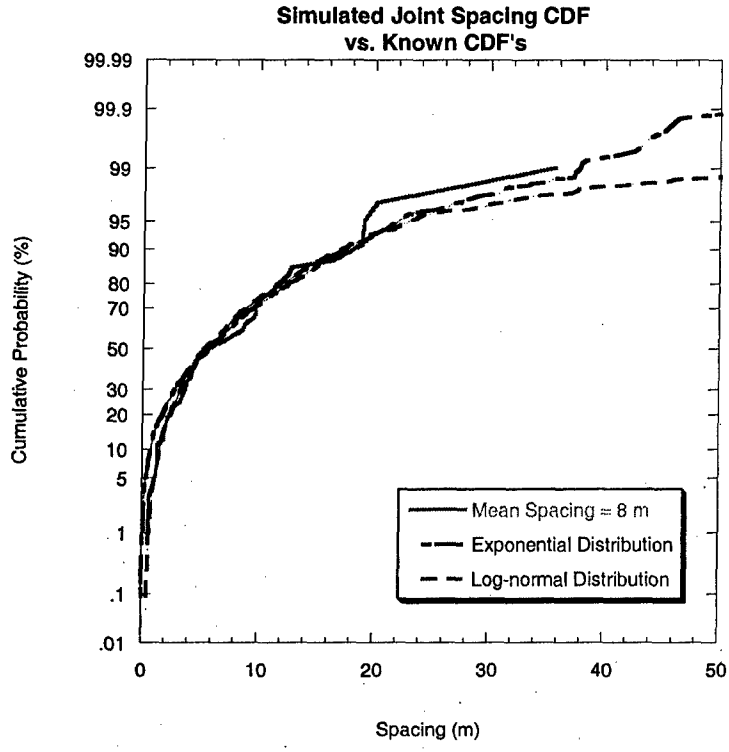


Figure 152 – Cumulative probability distribution comparison between a simulated joint pattern of low intensity (0.125 joints/m) and two known cumulative distribution forms (exponential and log-normal). The flaw model with saturation mechanism is used.

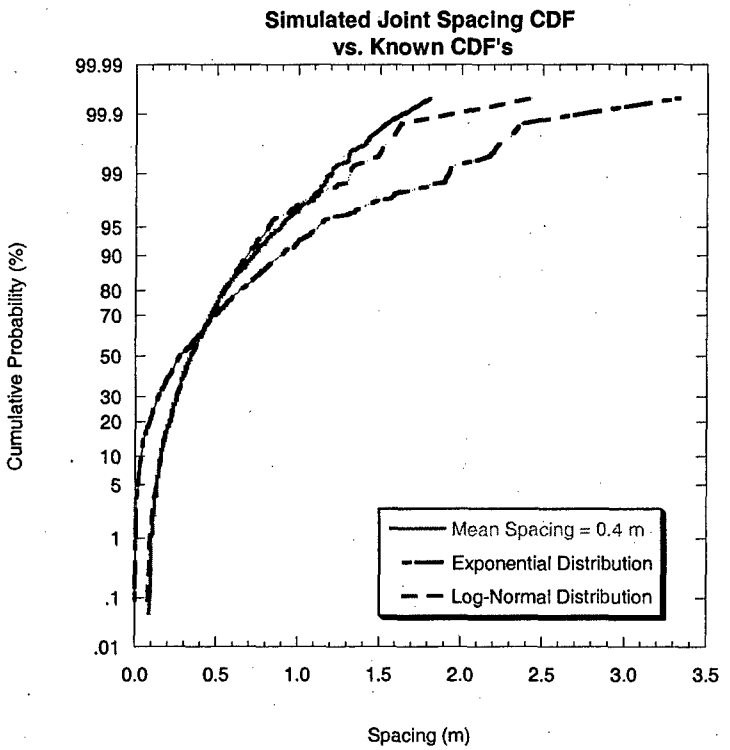


Figure 153 – Cumulative probability distribution comparison between a simulated joint pattern of medium-high intensity (2.5 joints/m) and two known cumulative distribution forms (exponential and log-normal). The flaw model with saturation mechanism is used.

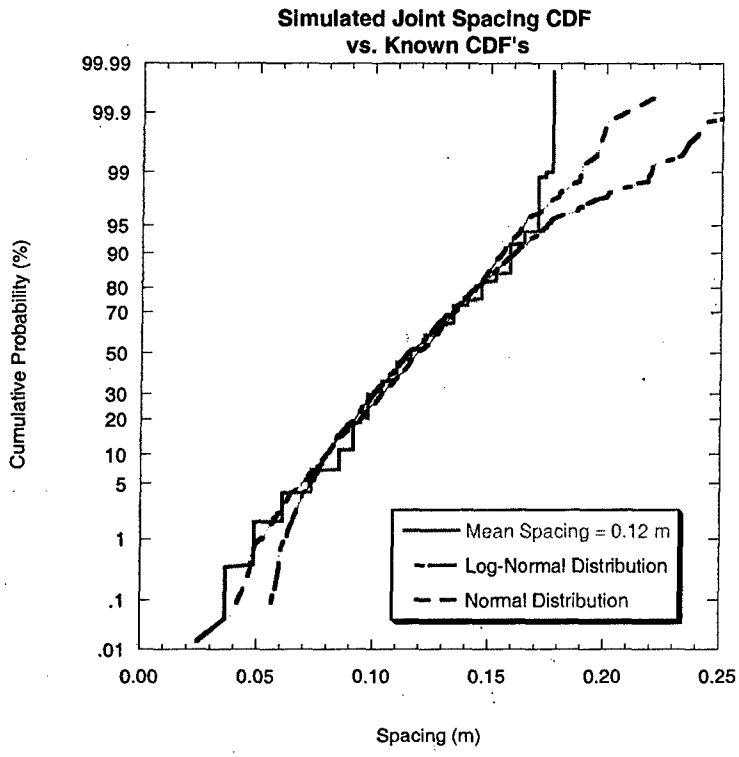


Figure 154 – Cumulative probability distribution comparison between a simulated joint pattern at saturation (~8.3 joints/m in this case) and known cumulative distribution forms (log-normal and normal). The flaw model with saturation mechanism is used.

Figure 155 to **Figure 157** show how the simulated joint spacing distribution (through the use of CDFs) evolves with joint intensity when the flaw model without a saturation mechanism is used. At low joint intensity, the joint spacing distribution appears to resemble a log-normal distribution more closely than it does an exponential distribution (**Figure 155**). At a higher joint intensity (or smaller mean joint spacing, **Figure 156**), the simulated joint spacing distribution clearly becomes log-normal. At high joint intensity (equal to the intensity at saturation in **Figure 154**), the simulated joint spacing distribution more closely resembles a normal distribution than it does a log-normal distribution (**Figure 157**). A log-normal distribution will still have some curvature when plotted in a Gaussian-logarithmic plot but the simulated joint spacing produces a somewhat straighter line than the log-normal.

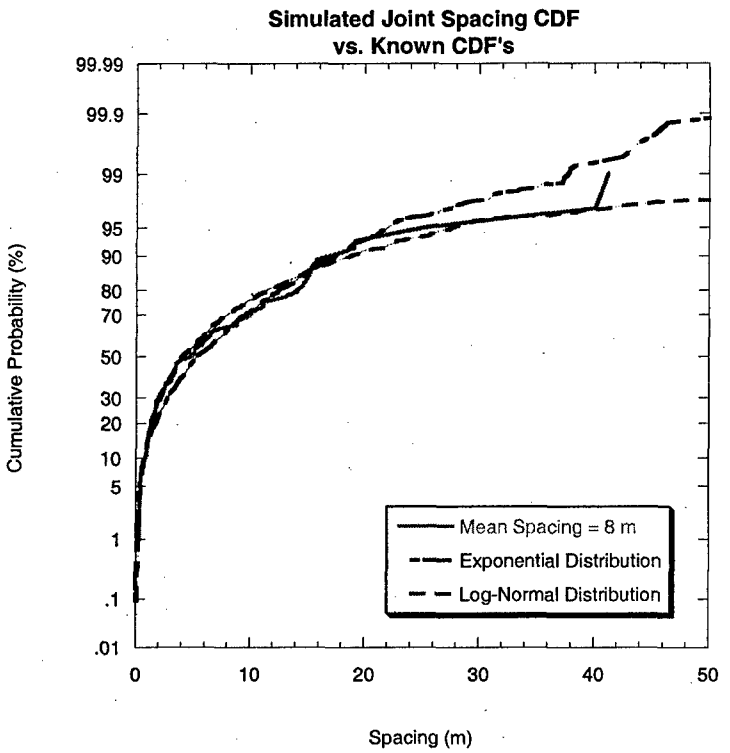


Figure 155 – Cumulative probability distribution comparison between a simulated joint pattern of low intensity (0.125 joints/m) and two known cumulative distribution forms (exponential and log-normal). The flaw model WITHOUT saturation mechanism is used.

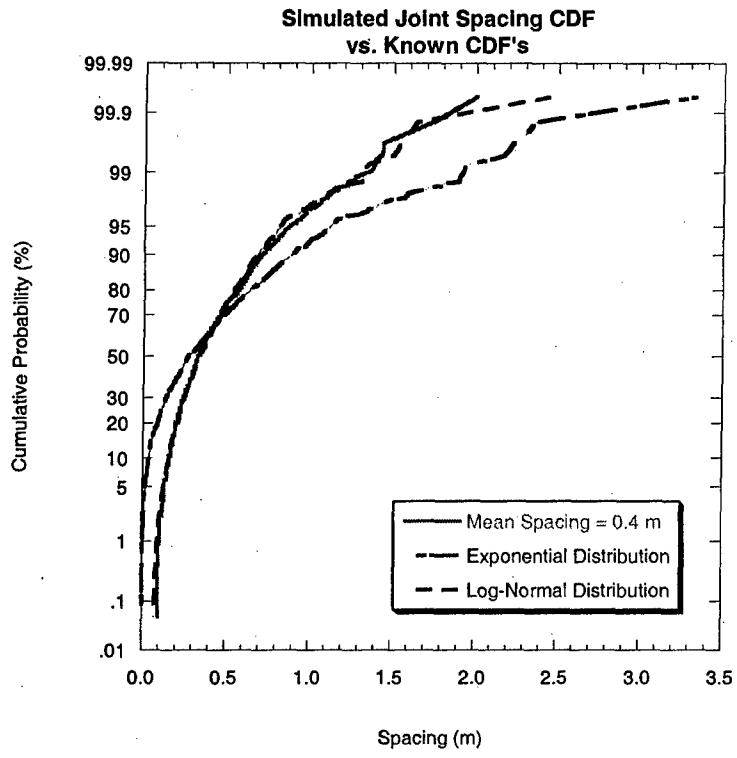


Figure 156 – Cumulative probability distribution comparison between a simulated joint pattern of medium-high intensity (2.5 joints/m) and two known cumulative distribution forms (exponential and log-normal). The flaw model WITHOUT saturation mechanism is used.

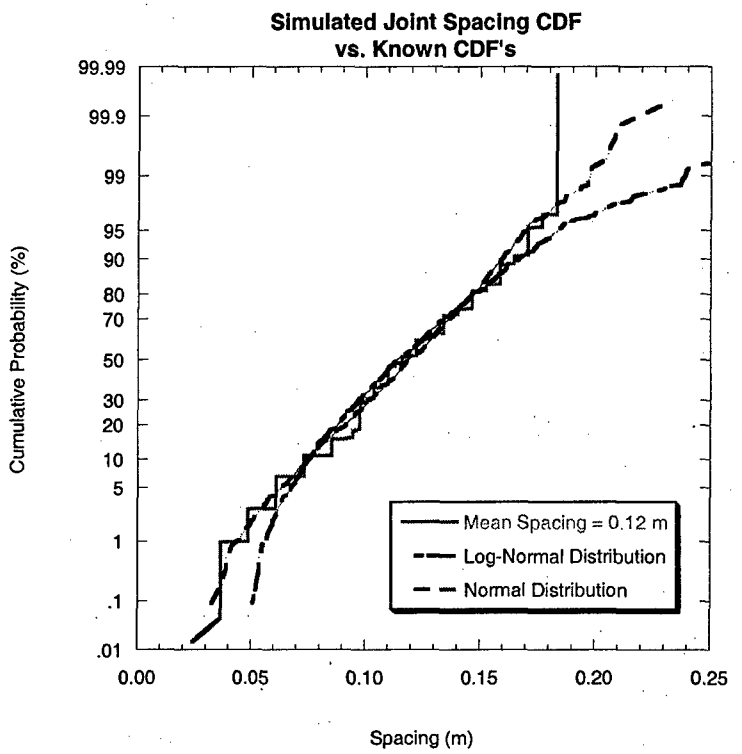


Figure 157 – Cumulative probability distribution comparison between a simulated joint pattern of high intensity (~8.3 joints/m) and known cumulative distribution forms (log-normal and normal). The flaw model WITHOUT saturation mechanism is used.

There is only a slight difference in the simulated joint spacing distributions at the different joint intensities (as reflected in the CDFs) between the flaw model that uses the saturation mechanism (in this case, the compressive stress development) and the flaw model that does not (**Figure 158** to **Figure 160**). The main difference is that without the saturation mechanism, the flaw model can produce higher joint intensities (past **Figure 160** in this case). The slight difference is the low cumulative probability at the smaller spacing values. This makes sense because the saturation mechanism limits the size of the segments that can still form a joint. Without the saturation mechanism, smaller segments can still form new joints. Naturally, jointing in a shorter segment as opposed to a longer one will likely lead to shorter new segments, thus the increased frequency of smaller spacing values for the flaw model without saturation. The important point that these figures (**Figure 158** to **Figure 160**) make is that the shape of the joint spacing probability distribution (depicted through the CDFs) from the flaw model does not appear to differ depending on whether or not the compressive stress saturation mechanism is used. However, the importance of the saturation mechanism is that it tells the model the physical limit to the jointing process (i.e., it provides a stopping point).

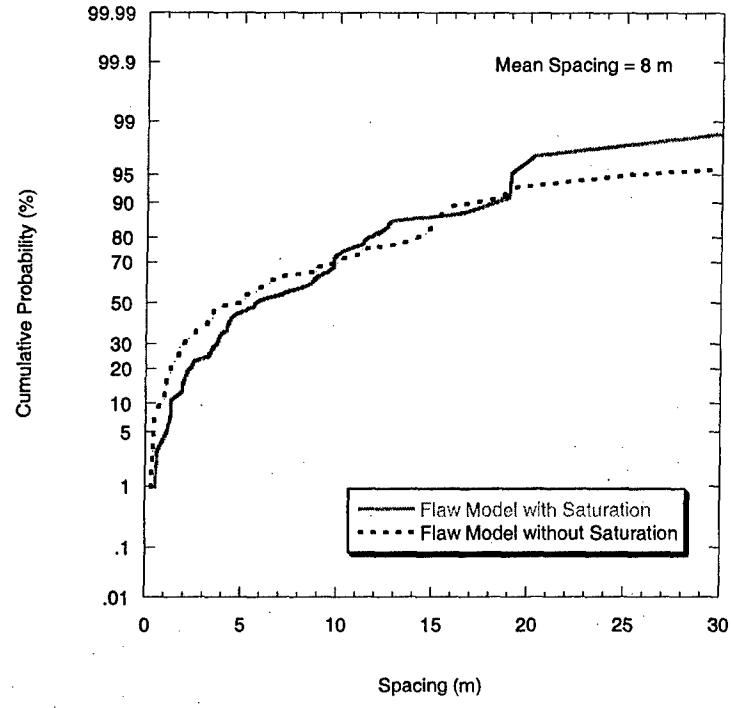


Figure 158 – Comparison between the simulated joint spacing CDFs at high joint intensity (0.125 joints/m) from the flaw model using the saturation mechanism and the flaw model that does not.

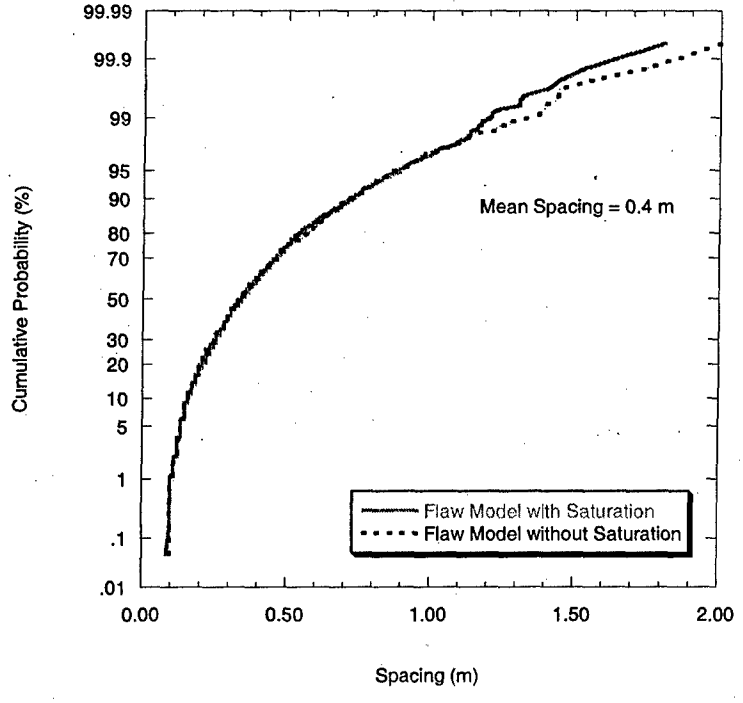


Figure 159 – Comparison between the simulated joint spacing CDFs at medium-high joint intensity (2.5 joints/m) from the flaw model using the saturation mechanism and the flaw model that does not.

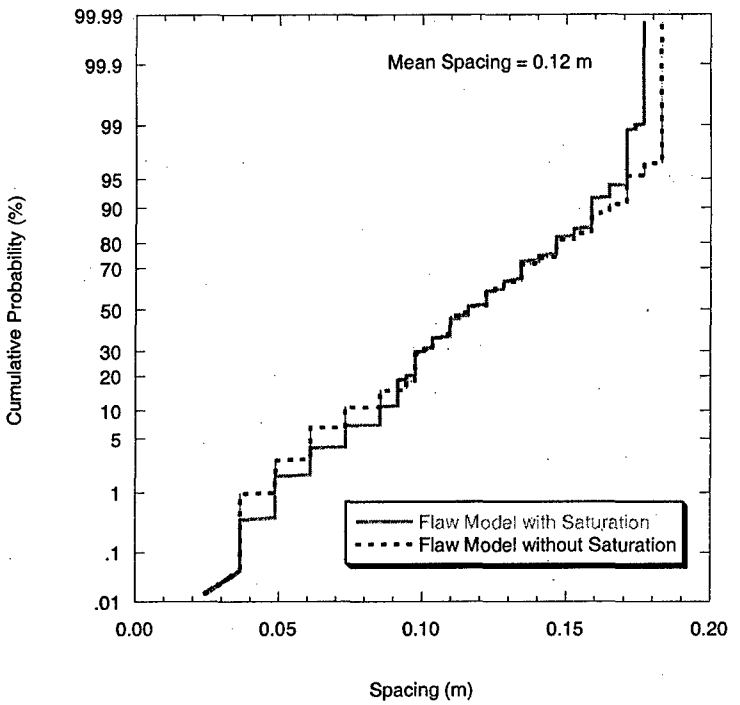


Figure 160 – Comparison between the simulated joint spacing CDFs at high joint intensity (~8.3 joints/m) from the flaw model using the saturation mechanism and the flaw model that does not.

These results show that the flaw model (with or without saturation) is able to reproduce laboratory joint spacing distributions at different joint intensities. The results also showed that there is only a slight difference in the joint spacing distribution between the flaw model with and without the saturation mechanism.

Now, attention is turned to the two main components of the flaw model: the stress distribution and strength models. First, the effects of the stress distribution model parameters on the resulting joint spacing distribution are studied. Then the effects of the strength model parameters are considered.

6.2.4.2 Effect of Stress Distribution Model Parameters

The parameters of the stress distribution model may have an effect on the simulated joint spacing distribution produced by the flaw model. In this section, these possible effects are investigated. To do this, the joint intensity is fixed at a constant value and the stress distribution parameters are varied. There are two main variables that affect the magnitude of the stress in stress distribution model (see **Equation 60, page 157**):

1. The $\frac{E_f}{G_n}$ ratio.

2. The non-jointing layer thickness, *d*.

Figure 161 shows that for a fixed joint intensity, the joint spacing distribution (shown using CDFs) changes with increasing $\frac{E_f}{G_n}$ ratio using the flaw model with saturation. The joint spacing distributions become tighter (i.e., smaller standard deviation, **Figure 162**) as the $\frac{E_f}{G_n}$ ratio increases. This makes sense because a larger $\frac{E_f}{G_n}$ ratio means that the tensile stress recovers to the maximum tensile stress more slowly with distance from the joint than it would for a smaller $\frac{E_f}{G_n}$ ratio (e.g., Hobbs' model, **Figure 163**). The model by Ji et al. (1998) behaves in the same way with regard to $\frac{E_f}{G_n}$. This slow recovery of the stress with distance exposes a small part of the segment between two joints to the largest stress. This limits the locations at which new joints may form. This, in turn, decreases the variance of spacing and the spread of the joint spacing distribution. On the other hand, if the tensile stress reaches its maximum a short distance from the joint (i.e., $\frac{E_f}{G_n}$ is small), a larger portion of the segment is susceptible to new jointing (i.e., a wider range of spacing values are possible). This increases the variance of the spacing and thus increases the spread of the joint spacing distribution. **Table 6** summarizes the effect of $\frac{E_f}{G_n}$ on the joint spacing distribution.

Table 6 – Summary of the effect of the $\frac{E_f}{G_n}$ on the variance of spacing.

Value of $\frac{E_f}{G_n}$	Stress Recovery with Distance from Joints Forming the Segment	Portion of Segment Exposed to Larger Tensile Stresses	Possible Locations of New Joints	Resulting Variance of Spacing
Small	Fast	Long	Many	High (wide joint spacing distribution)
Large	Slow	Short	Few	Low (narrow joint spacing distribution)

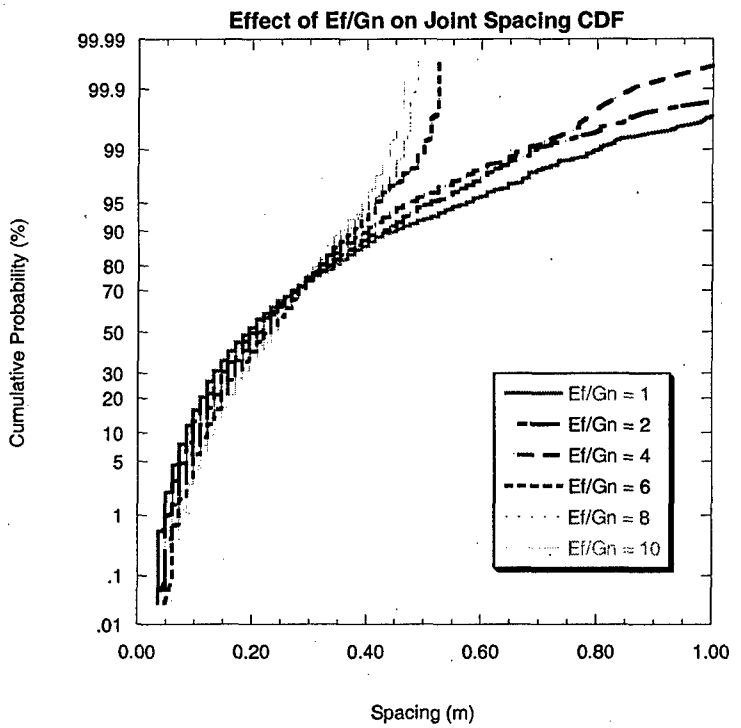


Figure 161 – Effect of $\frac{E_f}{G_n}$ ratio on the joint spacing CDF or the joint spacing distribution in the flaw model with saturation mechanism. Joint intensity is fixed at ~4.2 joints/m.

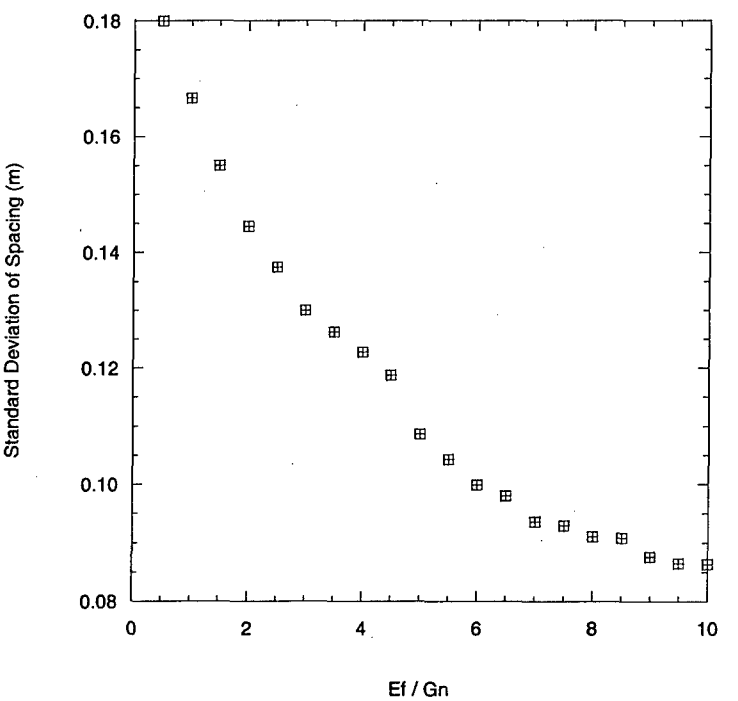


Figure 162 – Effect of $\frac{E_f}{G_n}$ ratio on the standard deviation of spacing for a fixed joint intensity (~4.2 joints/m).

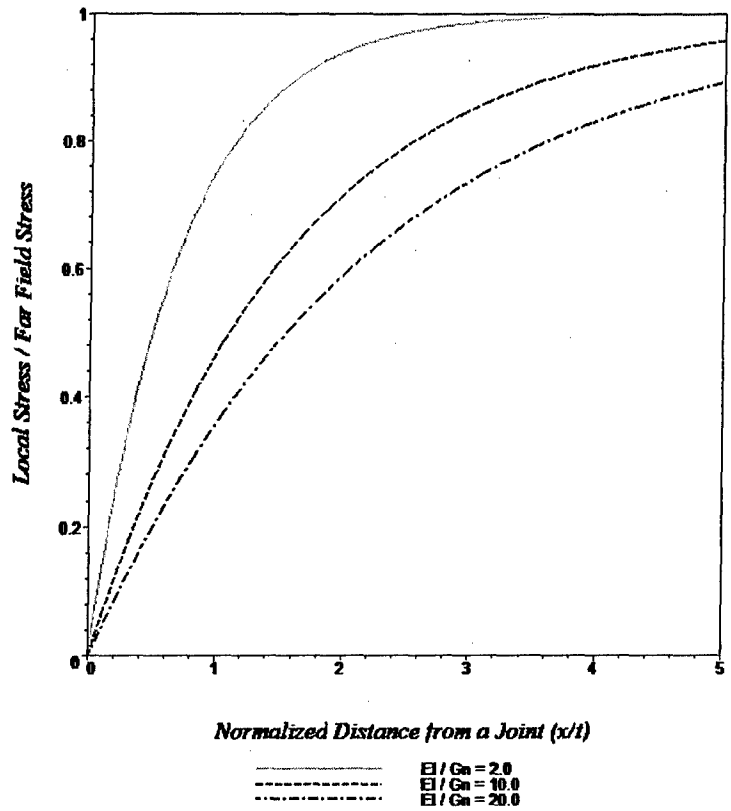


Figure 163 – Tensile stress distribution with distance from a joint (x/t) according to Hobbs' (1967) model.

To see this effect of $\frac{E_f}{G_n}$ on the joint spacing distribution form more clearly, the CDF of simulated joint spacing for some specific $\frac{E_f}{G_n}$ values taken from **Figure 161** are compared to some known CDFs (**Figure 164** to **Figure 168**). As before, the parameters for these CDFs are obtained using maximum likelihood estimation. **Figure 164** to **Figure 168** suggest that the value of $\frac{E_f}{G_n}$ does indeed affect the form of the joint spacing distribution even at a fixed joint intensity. An $\frac{E_f}{G_n}$ value of 2.0 in this particular case leads to an approximately log-normal joint spacing distribution (**Figure 164**). As the $\frac{E_f}{G_n}$ ratio is increased the joint spacing distribution transitions from log-normal (**Figure 165** and **Figure 166** at $\frac{E_f}{G_n}$ of about 8.0) to approximately normal (**Figure 167** and **Figure 168** at $\frac{E_f}{G_n}$ of about 15.0).

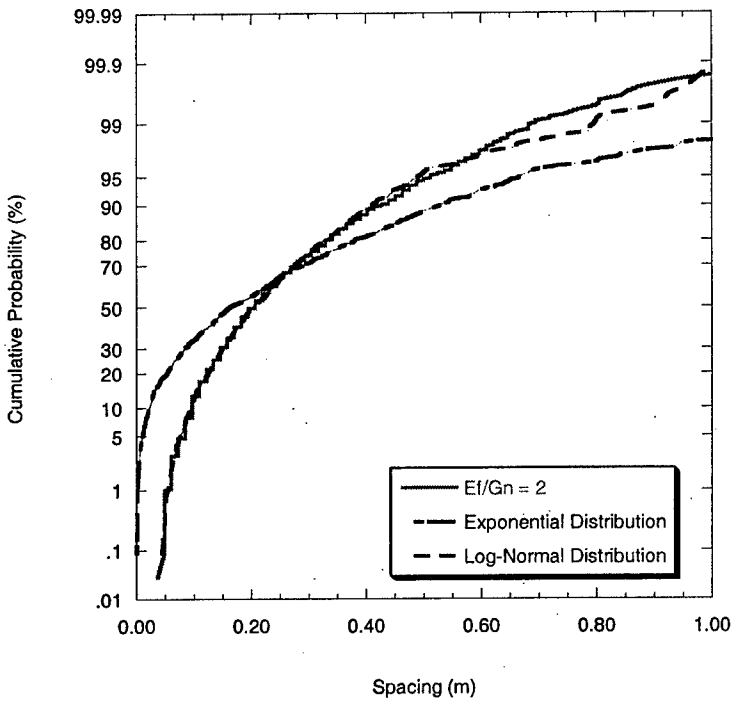


Figure 164 – Simulated cumulative distribution for $\frac{E_f}{G_n} = 2.0$ and the corresponding exponential and and log-normal CDFs. Flaw model with saturation is used.

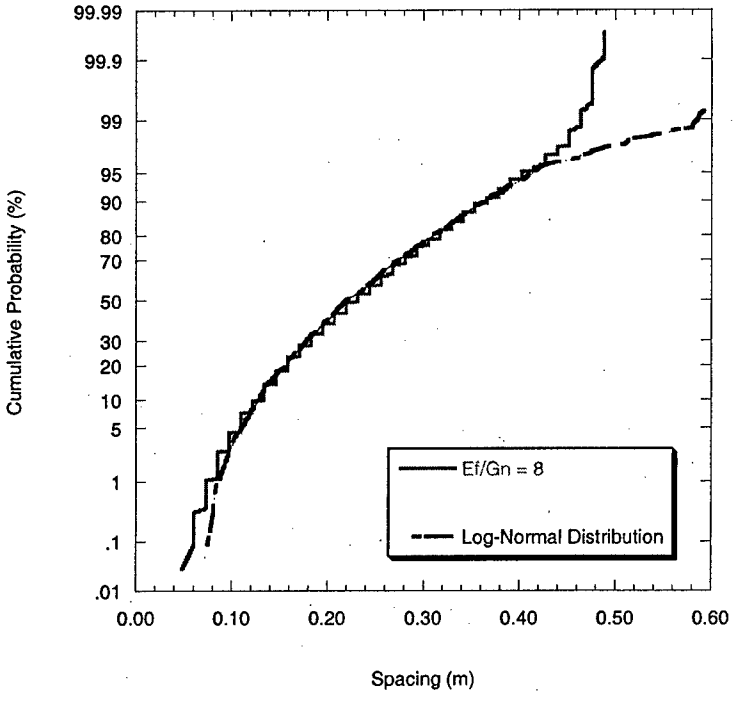


Figure 165 – Simulated cumulative distribution for $\frac{E_f}{G_n} = 8.0$ and the corresponding log-normal CDF. Flaw model with saturation is used.

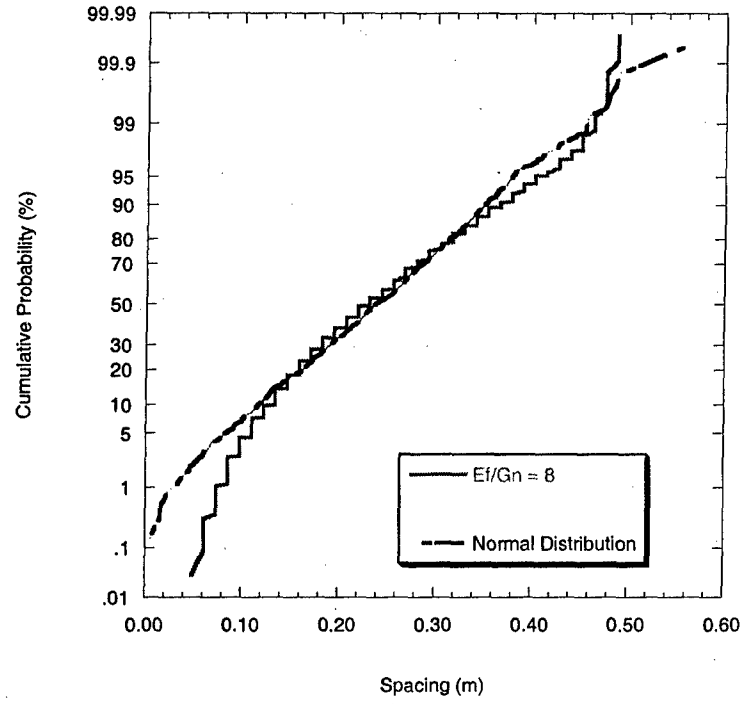


Figure 166 – Simulated cumulative distribution for $\frac{E_f}{G_n} = 8.0$ (same data as Figure 165) and the corresponding normal CDF. Flaw model with saturation is used.

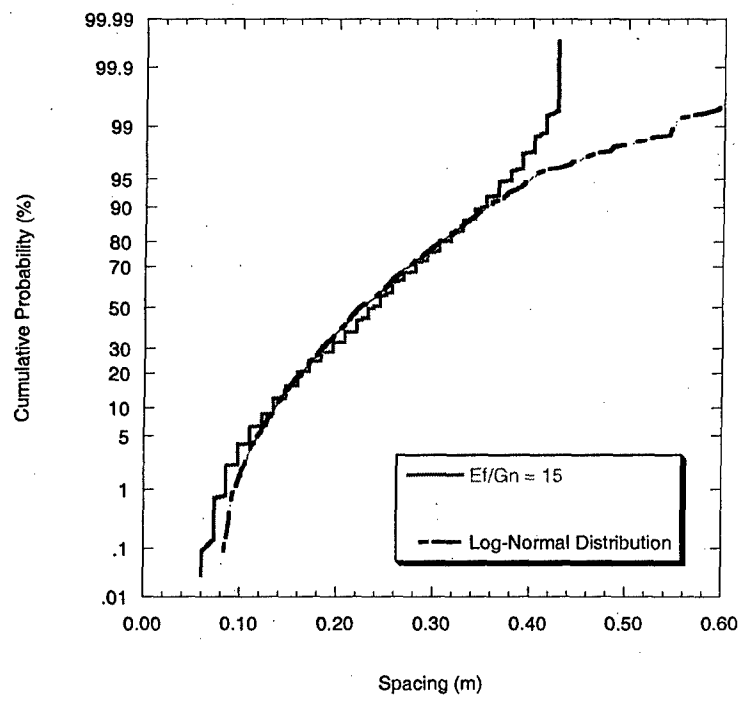


Figure 167 – Simulated cumulative distribution for $\frac{E_f}{G_n} = 15.0$ and the corresponding log-normal CDF. Flaw model with saturation is used.

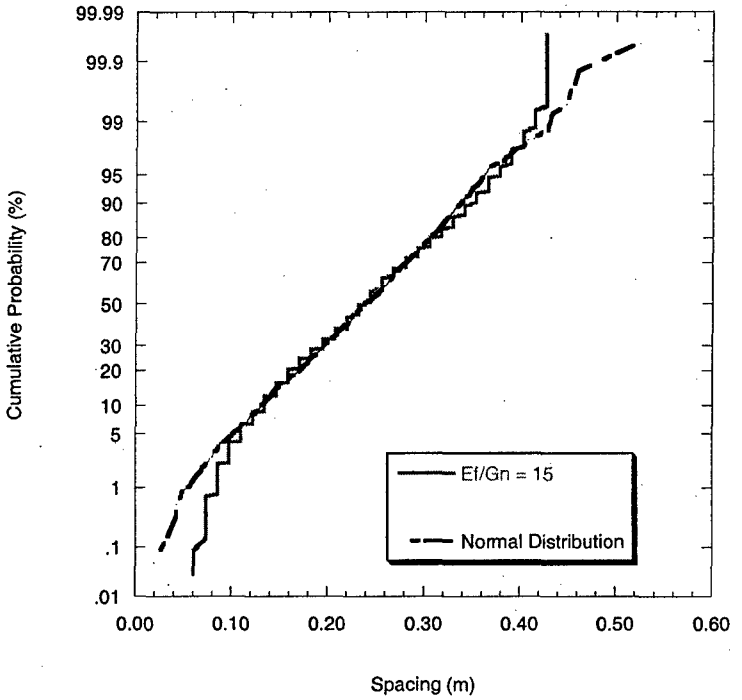


Figure 168 – Simulated cumulative distribution for $\frac{E_f}{G_n}$ = 15.0 (same data as Figure 167) and the corresponding normal CDF. Flaw model with saturation is used.

Figure 169 shows the effect of the non-jointing layer thickness (*d*) on the standard deviation of the simulated joint spacing distribution. Holding all other parameters constant, **Figure 169** shows that the standard deviation of spacing decreases as the non-jointing layer thickness increases for a given joint intensity. The explanation for this is similar to that used to explain the effect of $\frac{E_f}{G_n}$ ratio. A smaller non-jointing layer thickness allows a faster recovery of stresses with increasing distance from a joint. This allows a larger part of a segment to support new joints and thus a wider range of spacing values. The standard deviation alone cannot reveal the shape of the probability distribution of joint spacing so one must also look at the resulting joint spacing CDFs. **Figure 170** shows the cumulative distribution for simulated joint spacing. **Figure 170** shows that a thicker non-jointing layer produces a joint spacing distribution that may have a different form than that of a thinner non-jointing layer thickness. For example, **Figure 171** shows the simulated joint spacing CDF for a non-jointing layer thickness of 0.01 m. Using the same simulated joint spacing data, the corresponding exponential and log-normal CDFs are also constructed using maximum likelihood (**Figure 171**). It appears that a log-normal distribution fits the simulated joint spacing data quite well. The same is true when the non-jointing layer thickness is increased to 0.05 m (**Figure 172**). However, if the non-jointing layer thickness of 0.2 m is used, the joint spacing CDF tends to be normal instead of log-normal (**Figure 173** and **Figure 174**). In other words, the fit between the simulated joint spacing and the distribution from the maximum likelihood appears to be better in **Figure 174**, normal, than it is in **Figure 173**, log-

normal). This observation suggests that in the flaw model, the joint spacing distribution of two layers with exactly the same material properties, layer thickness and the same joint intensity may have different joint spacing distributions if the non-jointing layer thicknesses differ.

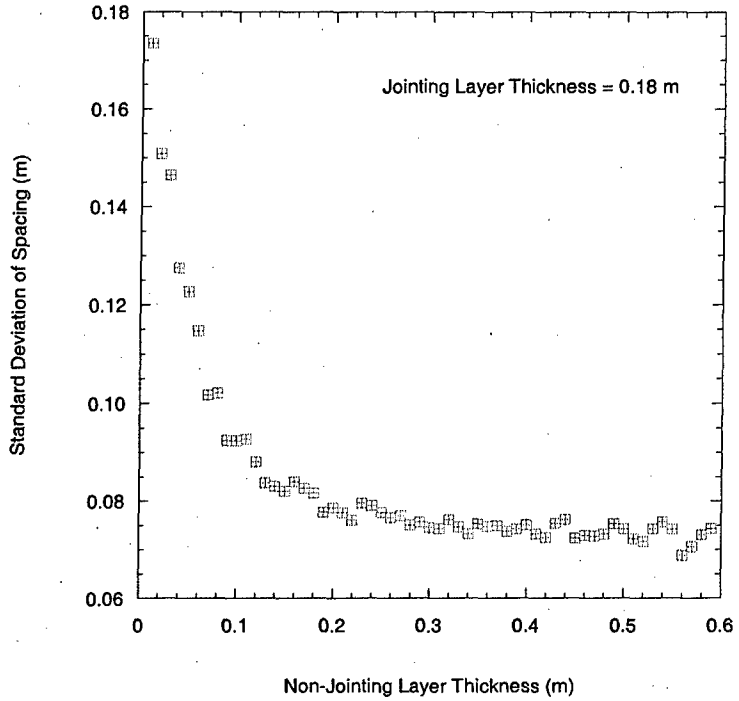


Figure 169 – Effect of the non-jointing layer thickness (d) on the standard deviation of joint spacing holding all other parameters fixed.

Table 7 shows a summary of the effect of the non-jointing layer thickness on the resulting joint spacing distribution. Its effect is similar to that of the $\frac{E_f}{G_n}$ ratio.

Table 7 – Summary of the effect of the non-jointing layer thicknes, d, on the variance of spacing.

Value of Non-Jointing Layer Thickness (d)	Stress Recovery with Distance from Joints Forming the Segment	Portion of Segment Exposed to Larger Tensile Stresses	Possible Locations of New Joints	Resulting Variance of Spacing
Small	Fast	Long	Many	High (wide joint spacing distribution)
Large	Slow	Short	Few	Low (narrow joint spacing distribution)

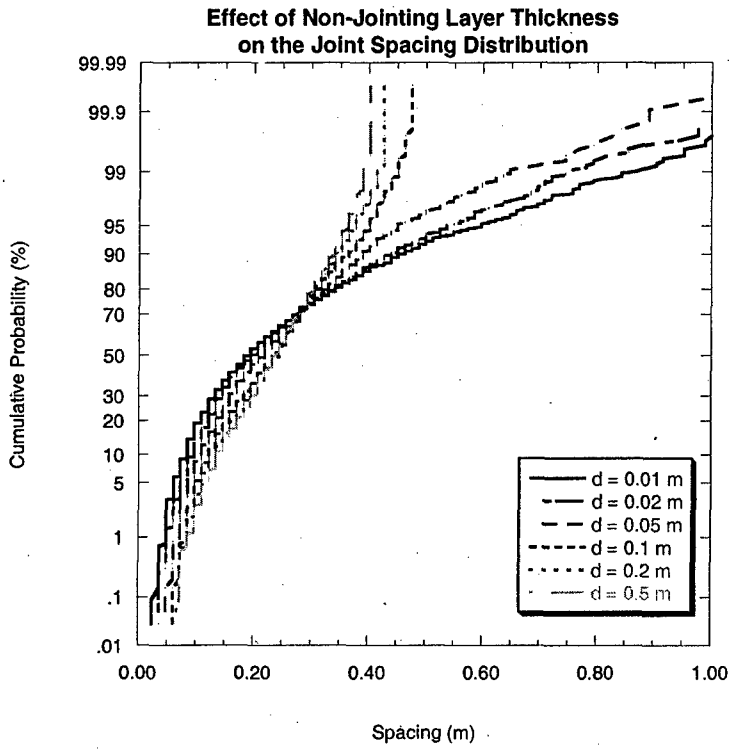


Figure 170 – Effect of the non-jointing layer thickness (*d*) on the joint spacing CDF or the joint spacing distribution in the flaw model using a saturation mechanism.

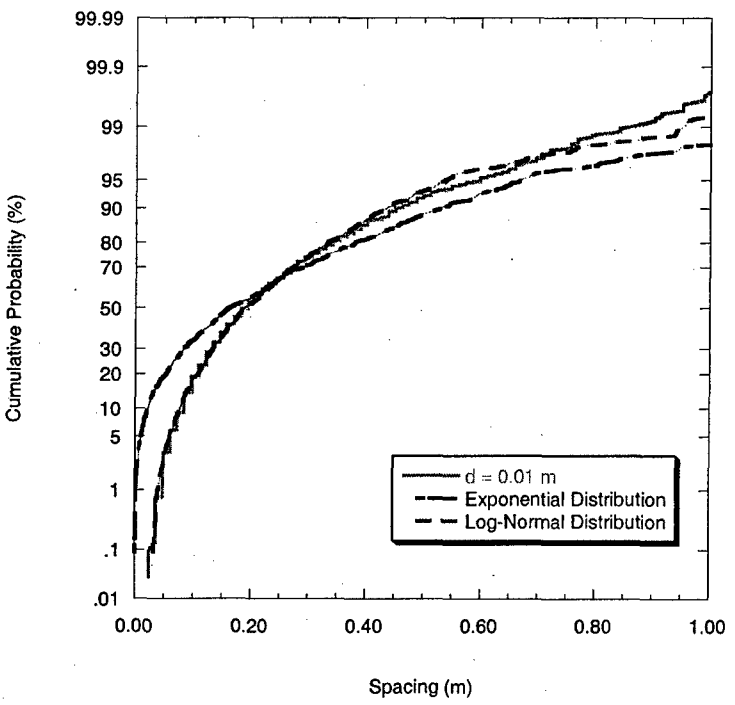


Figure 171 – Joint spacing CDF for a non-jointing layer thickness of 0.01 m (jointing layer thickness = 0.18 m) and the corresponding exponential and log-normal distributions. Flaw model using saturation mechanism is used.

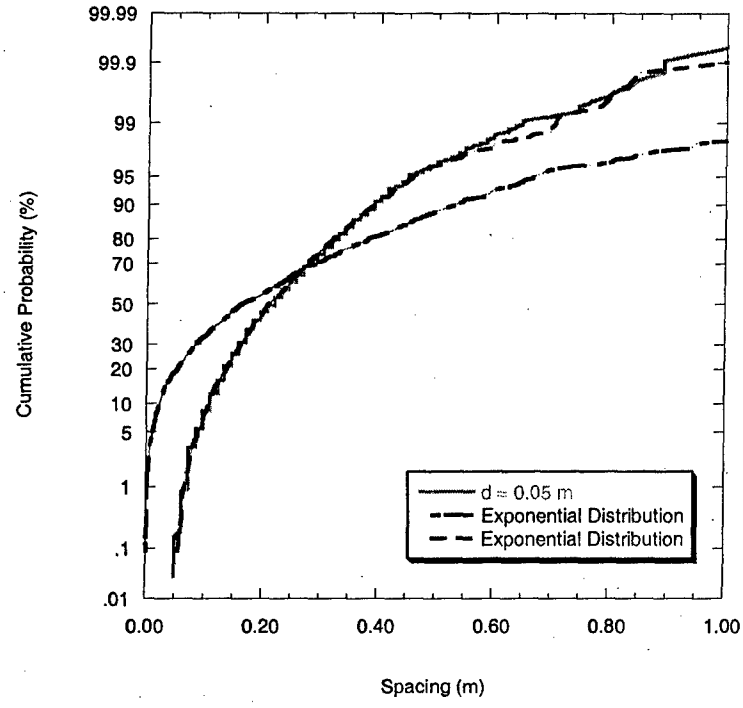


Figure 172 – Joint spacing CDF for a non-jointing layer thickness of 0.05 m (jointing layer thickness = 0.18 m) and the corresponding exponential and log-normal distributions. Flaw model using saturation mechanism is used.

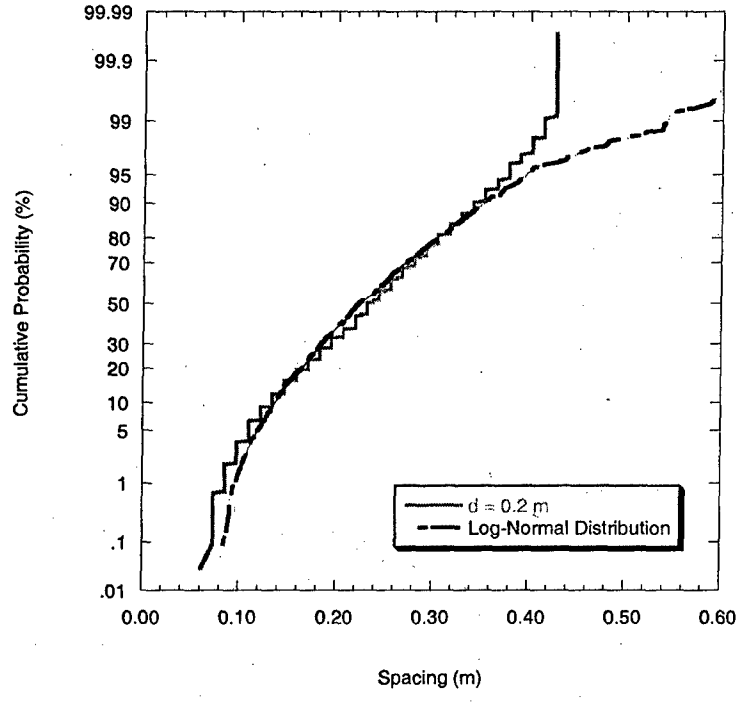


Figure 173 – Joint spacing CDF for a non-jointing layer thickness of 0.2 m (jointing layer thickness = 0.18 m) and the corresponding log-normal distribution. Flaw model using saturation mechanism is used.

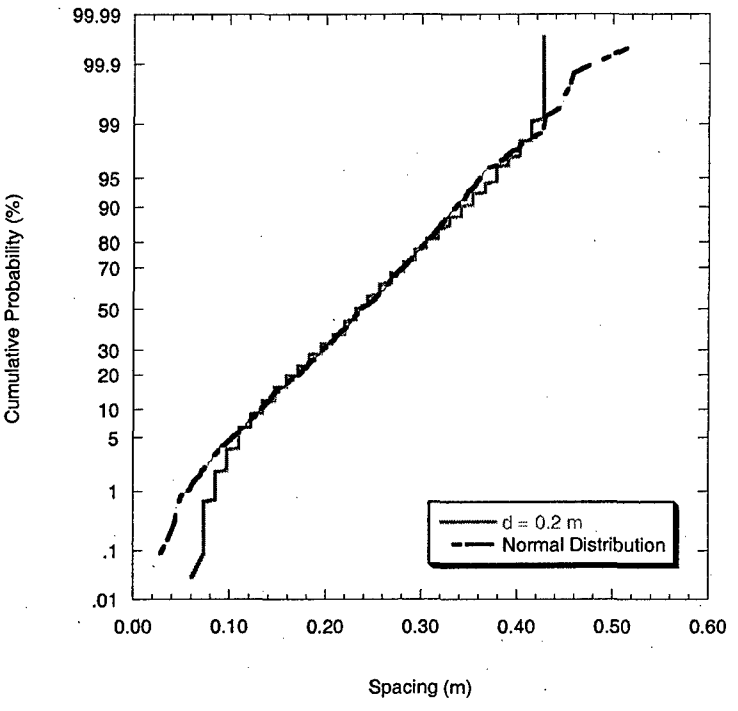


Figure 174 – Joint spacing CDF for a non-jointing layer thickness of 0.2 m (jointing layer thickness = 0.18 m) and the corresponding normal distribution. The simulated spacing data here is the same as in Figure 173. Flaw model using saturation mechanism is used.

In the above discussion, it was shown that the flaw model closely mimiced the change in form of the joint spacing distribution observed in laboratory experiments (e.g., Rives et al., 1992) as the joint intensity increases. The flaw model does this with or without a saturation mechanism in place. However, there are still slight differences in the joint spacing distribution between the two flaw model versions as demonstrated in **Figure 158** to **Figure 160**.

The effects of several parameters describing the stress distribution on the joint spacing distribution were also presented and it was shown that both the $\frac{E_f}{G_n}$ ratio and the non-jointing layer thickness (d) influence the type of joint spacing distribution that results even for the same joint intensity. Specifically, larger $\frac{E_f}{G_n}$ ratios or larger d values cause the joint spacing distribution to tend towards a normal or quasi-normal distribution. This effect on the joint spacing distribution was explained in terms of the effect each of these two parameters have on the stress distribution. Basically, larger $\frac{E_f}{G_n}$ ratios or larger d values lead to a slow stress recovery with increasing distance away from a joint. This means that a smaller portion of the segment is subjected to the high stresses. This decreases the possible number of locations for new joints and thus decreases the variance of the lengths of the newly formed segments (i.e., the spacing). These effects are summarized in **Table 6** and **Table 7**. So far, only the effect of the stress distribution on

the jointing process and the resulting spacing distribution has been considered. Now, attention is turned to the other aspect of these models: the strength model.

6.2.4.3 Effect of Strength Model

Recall that the joint patterns resulting from the flaw model depend on two parts: the stress distribution model and the strength model. The stress distribution model (e.g., Hobbs, 1967; Ji et al., 1998) determines the variation of the tensile stress along the jointing layer whereas the strength model represents the variation of the tensile strength along the same layer. The parameters that factor into the stress distribution model are the material properties (e.g., $\frac{E_f}{G_n}$) and the geometry of both jointing and non-jointing layers (e.g., t and d, as well as the lengths of individual segments). Strength models, as applied here, can be classified into two main types: uncorrelated or correlated.

For an uncorrelated model, the strength at one location along the jointing layer is independent of the strength at adjacent locations. This results in a jointing layer that has non-uniform tensile strength along its length. Here, the important factors are the flaw density and the probability distribution of tensile strength at each flaw. The flaw density controls the uniformity/non-uniformity of tensile strength along the length of the layer. Where no flaws exist, it is assumed that the intact tensile strength of the rock prevails. Where flaws exist, the tensile strength is assigned using the assumed probability distribution of tensile strength. The smaller the number of flaws, the more uniform the strength along the layer. Using a uniform probability distribution for tensile strength does not mean that the layer has uniform tensile strength. A probability distribution is used only to assign a specific value of tensile strength at a flaw. Different flaws will be assigned different values of strength using the same probability distribution leading to a layer with non-uniform tensile strength along its length.

In a correlated strength model, the strength at a point is dependent on the strength at an adjacent point and the form of the relationship between the strengths at adjacent points may be prescribed. This also results in a jointing layer that has non-uniform tensile strength along its length.

Although the uncorrelated and correlated strength models both result in non-uniform tensile strength along the length of the jointing layer, the jointing behavior should differ. In an uncorrelated strength model, the tensile strength may change abruptly going from one point to another close by. There are no clear sections of weakness or strength so that joints do not tend to form or not form in specific sections. In a correlated strength model, the change in tensile strength from one point to an adjacent point is controlled by the correlation. It can be abrupt (low correlation) or gradual (high correlation). As a result, clear sections of weakness or strength will result and joints will tend to form in these sections. Consequently, the joint spacing distributions using the two strength models will differ.

In what follows, the effect of strength on the joint pattern is investigated. Specifically, the influence of the strength model parameters on the standard deviation and the shape of the probability distribution of joint spacing are studied.

Uncorrelated Strength Model

The first uncorrelated tensile strength model used here assumes that the tensile strength at a flaw has a uniform probability distribution between some minimum and maximum value, say the tensile strength of intact rock. In reality, it might be difficult to ascertain the appropriate minimum and maximum tensile strength of the rock, let alone the probability distribution of the tensile strength. For this reason, it is helpful to look at the effect of the choice of minimum and maximum tensile strength values on the simulated joint spacing distribution.

Simulations using the flaw model (with or without the compressive stress development saturation mechanism) show that as long as the ratio between the maximum and minimum stresses remains constant, the standard deviation of joint spacing is largely unaffected given that all other parameters stay the same (i.e., material properties and joint intensity). This is demonstrated in **Figure 175** to **Figure 177** where different minimum and maximum tensile strength values are utilized to achieve the same max-to-min strength ratio. The standard deviation of simulated joint spacing is plotted against different $\frac{E_f}{G_n}$ values. The points for each max-to-min strength ratio coincide reasonably regardless of the actual values of the maximum and minimum tensile strength values.

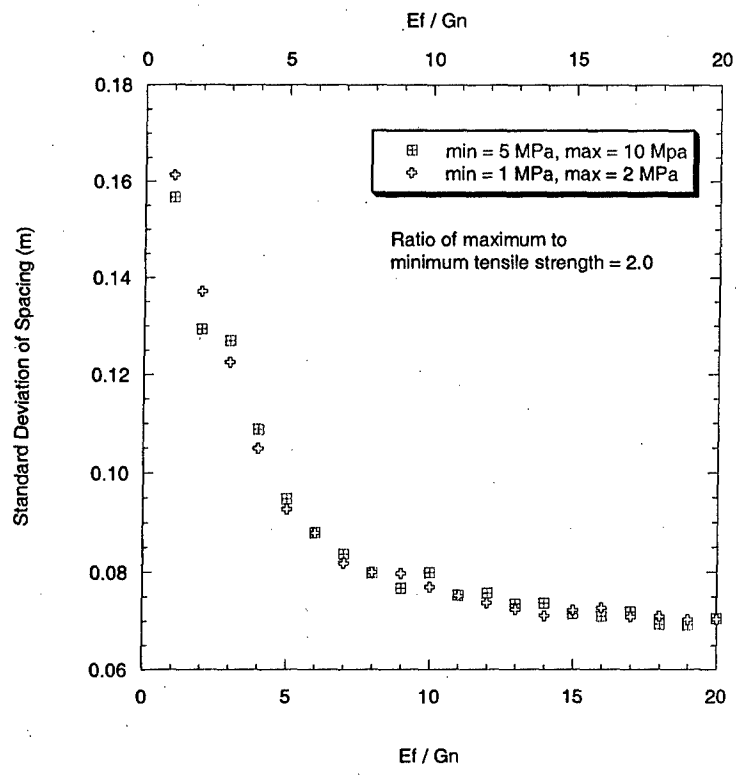


Figure 175 – Standard deviation of spacing as a function of the $\frac{E_f}{G_n}$ ratio for two different sets of minimum and maximum tensile strengths with the same max-to-min ratio (= 2.0). Flaw model with saturation.

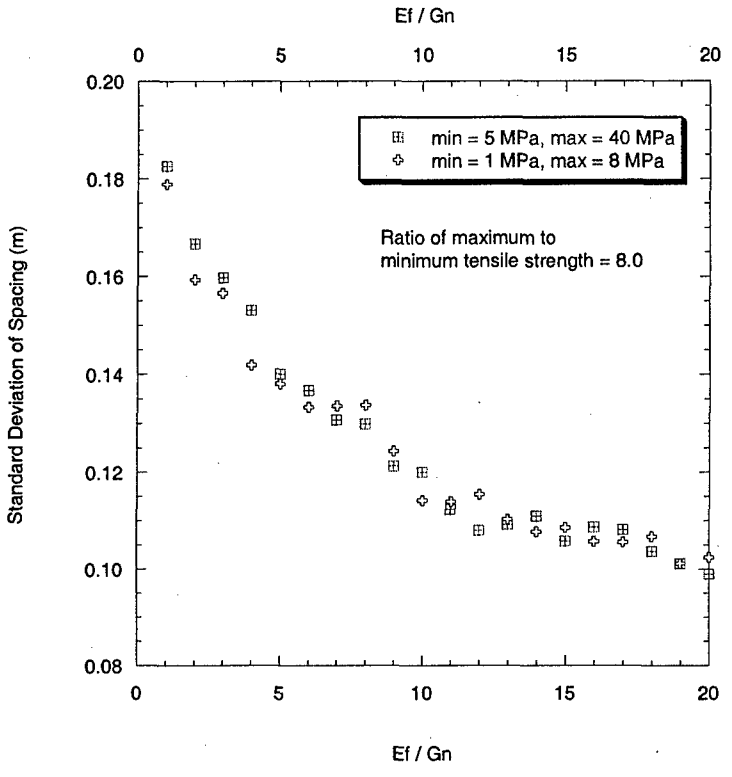


Figure 176 – Standard deviation of spacing as a function of the $\frac{E_f}{G_n}$ ratio for two different sets of minimum and maximum tensile strengths with the same max-to-min ratio (= 8.0). Flaw model with saturation.

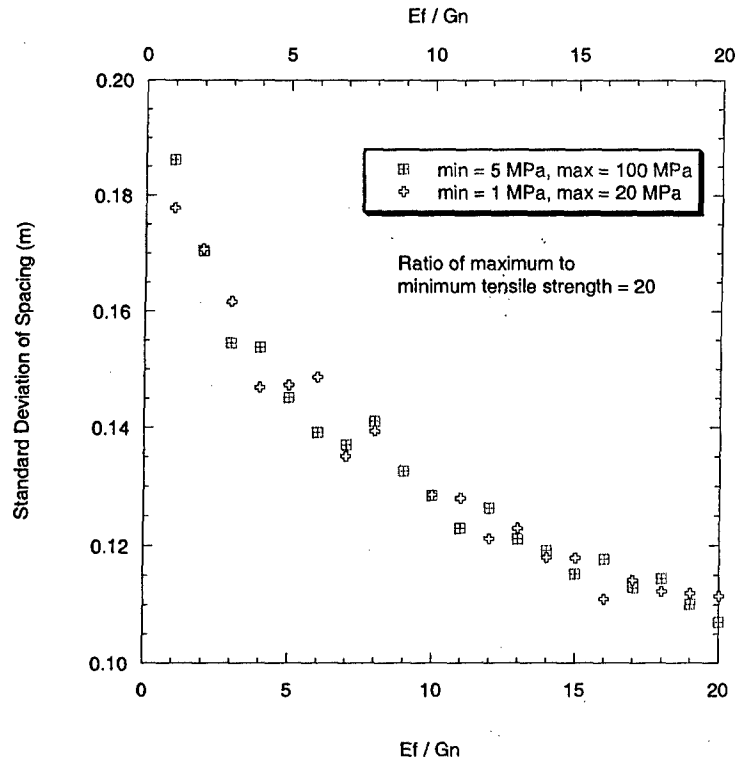


Figure 177 – Standard deviation of spacing as a function of the $\frac{E_f}{G_n}$ ratio for two different sets of minimum and maximum tensile strengths with the same max-to-min ratio (= 20.0). Flaw model with saturation.

Whereas **Figure 175** to **Figure 177** show that the standard deviation of spacing remains essentially the same for a particular max-to-min tensile strength ratio, **Figure 178** shows that the joint spacing CDF remains the same for the same max-to-min tensile strength ratio also. This is true for a range of intensities up to saturation (**Figure 178**).

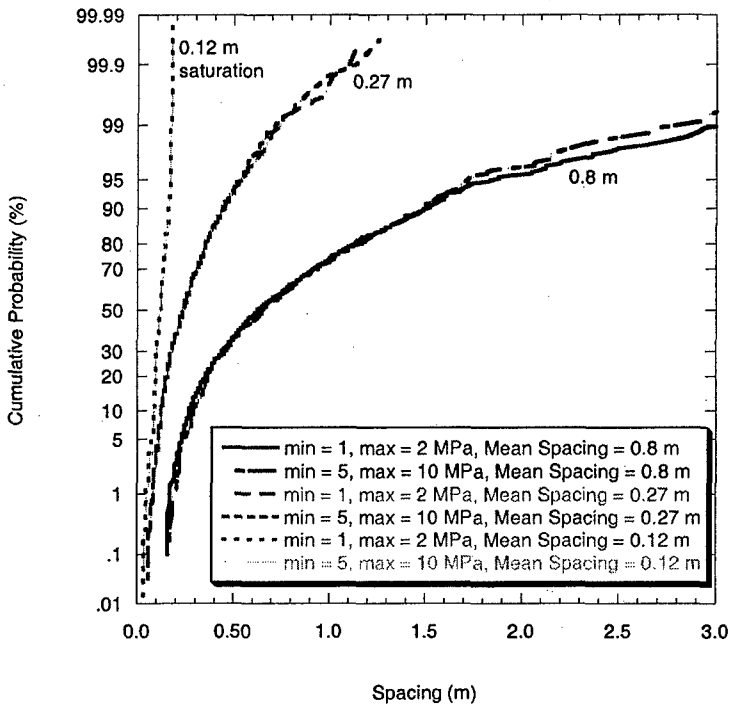


Figure 178 – Simulated joint spacing CDFs at different joint intensities for different choices of the minimum and maximum tensile strength values but with constant max-to-min ratio = 2.0. Flaw model with saturation is used.

An example of the sensitivity of the standard deviation of simulated joint spacing on the ratio between the maximum and minimum tensile strength is shown in **Figure 179**. The standard deviation of simulated joint spacing is shown as a function of the $\frac{E_f}{G_n}$ ratio. The joint intensity is also fixed to a single value (~4.2 joints/m) in all the simulations. **Figure 179** shows that at a given $\frac{E_f}{G_n}$, the standard deviation of spacing increases with the max-to-min ratio of tensile strength.

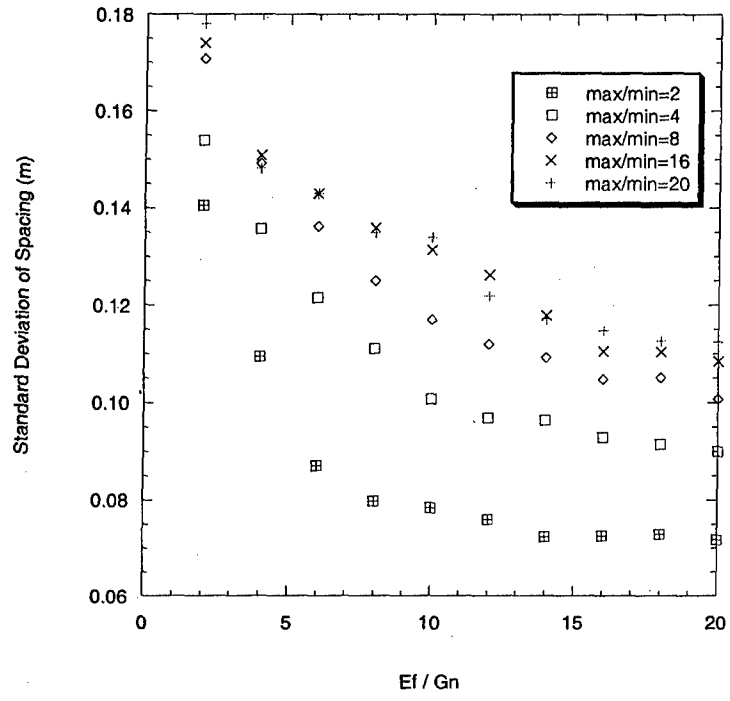


Figure 179 – Effect of the ratio between the maximum and minimum tensile strength on the standard deviation of simulated joint spacing for different values of $\frac{E_f}{G_n}$ at a fixed joint intensity (~4.2 joints/m). Flaw model with saturation mechanism is used. Minimum tensile strength = 1.0 MPa.

As for the joint spacing CDF, different max-to-min tensile strength ratios lead to different joint spacing distributions (**Figure 180**). However, increasing the max-to-min tensile strength ratio given a fixed joint intensity does not change the form of the joint spacing CDF (**Figure 181** to **Figure 183**).

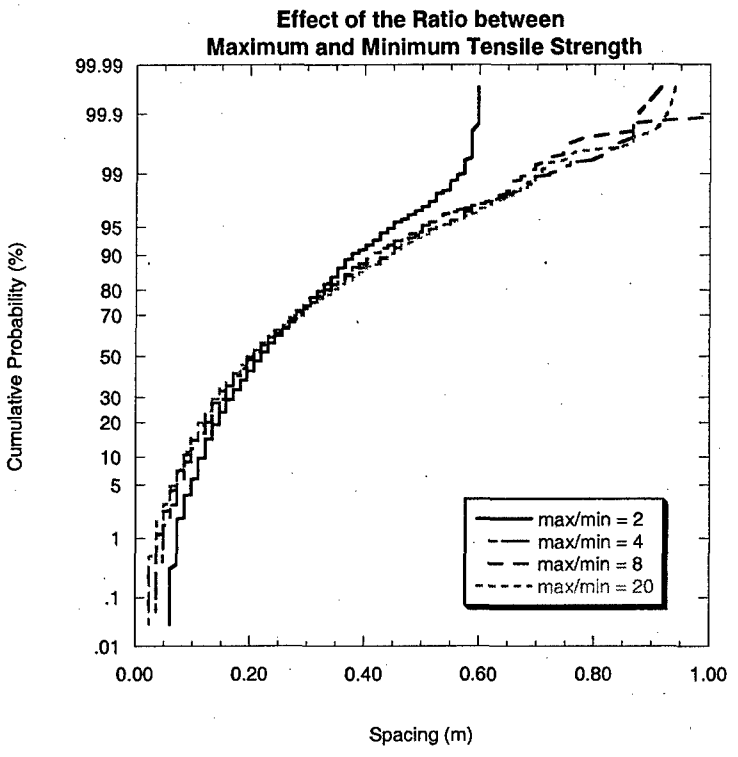


Figure 180 – Effect of the ratio between the maximum and minimum tensile strength on the simulated joint spacing CDF. Flaw model with saturation mechanism is used.

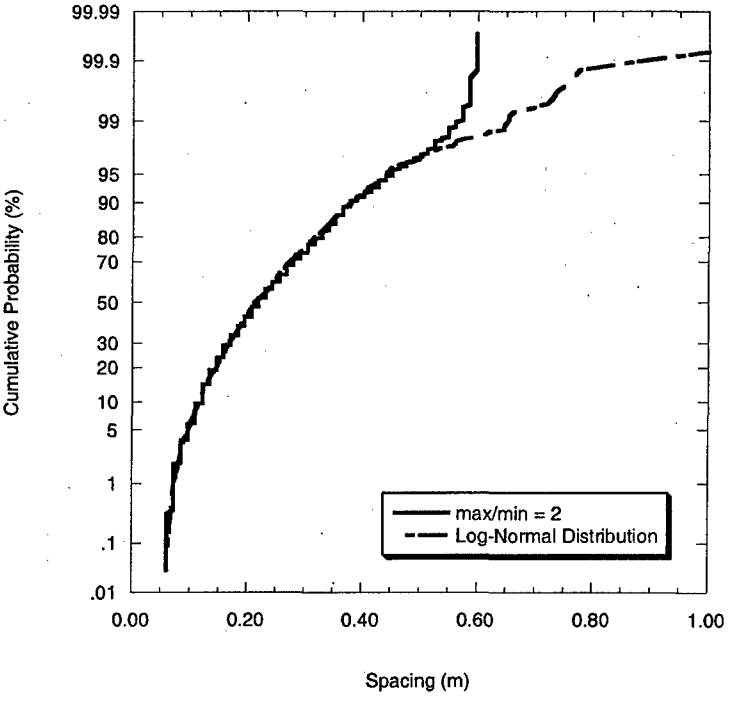


Figure 181 – Joint spacing CDF for a maximum to minimum tensile strength ratio of 2.0 and the corresponding log-normal CDF. Flaw model with saturation is used.

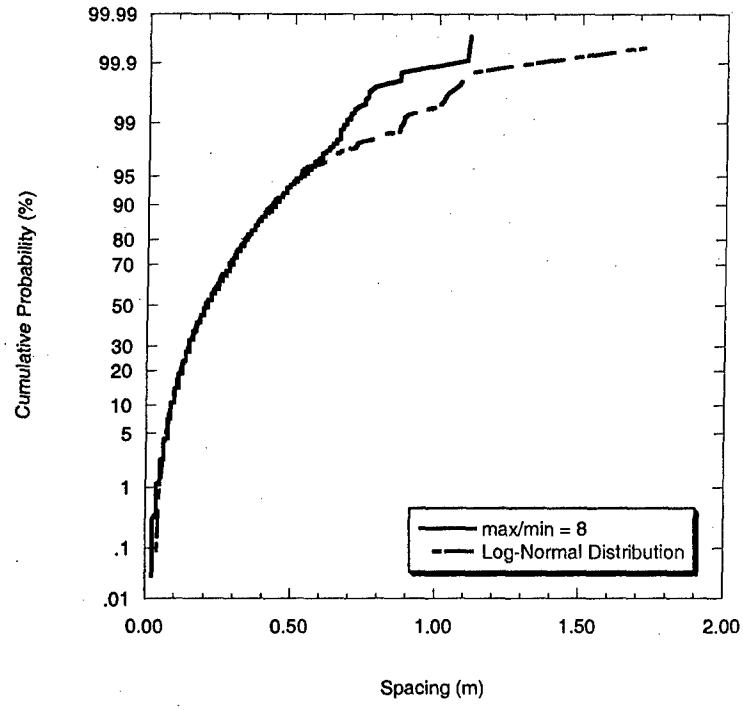


Figure 182 – Joint spacing CDF for a maximum to minimum tensile strength ratio of 8.0 and the corresponding log-normal CDF. Flaw model with saturation is used.

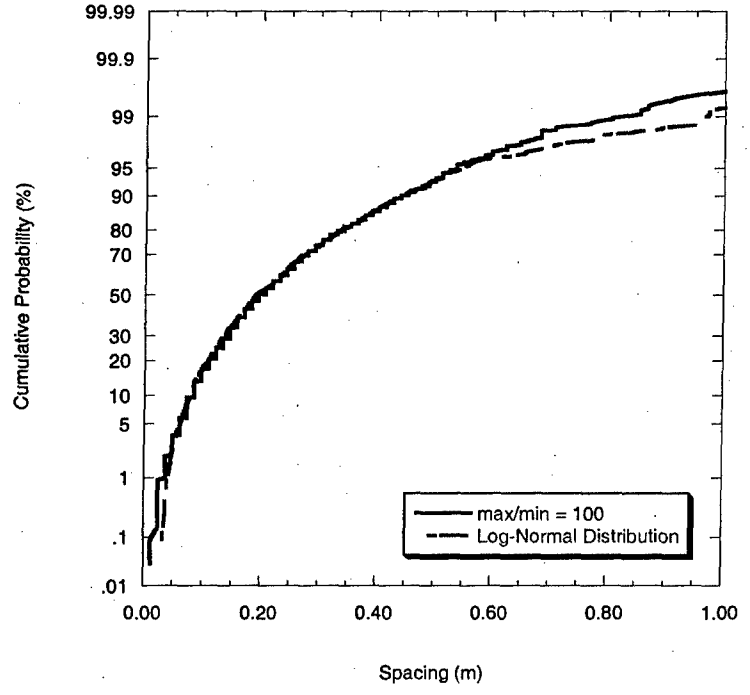


Figure 183 – Joint spacing CDF for a maximum to minimum tensile strength ratio of 100.0 and the corresponding log-normal CDF. Flaw model with saturation is used.

It was mentioned that part of the strength model is the probability distribution of tensile strength. So far, the results shown above used a uniform probability distribution for the tensile strength or the strength at a point is a uniformly distributed random variable. It was also shown that with such a strength model, the standard deviation of spacing and the shape of the joint spacing distribution depend only on the ratio between the maximum and minimum tensile strength that has been assumed. Other probability distributions can also be used to describe the tensile strength at a point. In what follows, the use of a normal probability distribution for tensile strength in an uncorrelated strength model is investigated.

The flaw model using a strength model that assumes a normally distributed tensile strength at any point behaves quite differently from that with a uniform distribution of tensile strength. **Figure 184** shows that the standard deviation of spacing is affected by the standard deviation of the tensile strength. This effect is similar to that of the strength model that uses a uniform probability distribution where a larger max-to-min tensile strength ratio leads to a larger standard deviation for joint spacing. The larger strength standard deviation in the case of the normally distributed strength model could be thought of as having a larger max-to-min tensile strength ratio (even though there is no way to determine the maximum and minimum values in a normal distribution). The similarity ends there, however, since the standard deviation for joint spacing here is also affected by the choice of the mean tensile strength. For example, using a mean strength of 7.0 MPa with a standard deviation of 3.0 MPa will yield a different joint spacing standard deviation than a mean strength of 17 MPa with the same 3.0 MPa standard deviation.

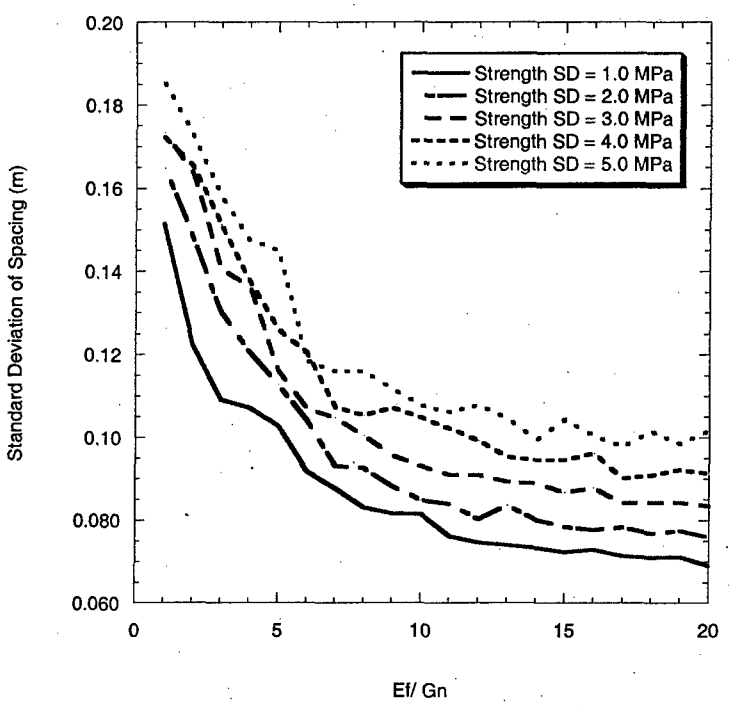


Figure 184 – Effect of the standard deviation of tensile strength using the flaw model WITH the compressive stress saturation mechanism at joint intensity below saturation (~4.2 joints/m). Tensile strength is NORMALLY distributed. Mean tensile strength is 7.0 MPa.

So far, only uncorrelated strength models have been considered and it has been shown that the flaw model behavior (in terms of the joint spacing distribution) depends on the probability distribution of tensile strength that was assumed (e.g., uniform probability distribution vs. normal probability distribution). For a uniform probability distribution of tensile strength, the joint spacing distribution depends only on the ratio between the maximum and minimum tensile strength. For a normal probability distribution, however, the joint spacing distribution depends not only on the standard deviation of the tensile strength but also on the mean tensile strength.

Next, a correlated strength model is presented and its effects on the resulting joint spacing distribution are investigated.

Correlated Strength Model

The second type of strength model is the correlated strength model. The previously described strength models assume that the tensile strength at one location is independent of the tensile strength at another location (i.e., uncorrelated strength models). **Figure 185** shows the variation of the tensile strength along a 200 m long layer for an uncorrelated tensile strength model assuming a uniform probability distribution for the tensile strength at a point. In this example, the minimum tensile strength is 4.0 MPa and the maximum is 10.0 MPa. Having a uniform probability distribution must not be confused with being uniform (i.e., constant). It shows that the tensile strength changes rapidly from one location to the next. This is the result of the assumed independence of the tensile strength at one location to the tensile strength at an adjacent location. Such a tensile strength variation may not be realistic. For this reason a correlated tensile strength model may need to be explored. A simple correlated tensile strength model relates the tensile strength at some location *i* to the tensile strength at a previous, adjacent location (*i*-1) or

$$\ln\left(\frac{\sigma_{t_i}}{\mu_{\sigma_t}}\right) = \phi \ln\left(\frac{\sigma_{t_{i-1}}}{\mu_{\sigma_t}}\right) + \varepsilon_i \qquad \textbf{Equation 72}$$

where σ_{t_i} is the tensile strength at location *i*, $\sigma_{t_{i-1}}$ is the tensile strength at the previous adjacent location (*i*-1), μ_{σ_t} is the mean tensile strength, ϕ is the correlation factor ($0 < \phi < 1$) and ε_i is a normal random variable with mean equal to zero and a standard deviation of σ_ε. In order to appreciate how each parameter affects the tensile strength variation along the jointing layer, some examples are shown. **Figure 186** and **Figure 187** show the tensile strength variation for a correlation coefficient of $\phi = 0.1$, a mean tensile strength $\mu_{\sigma_t} = 7.0$ MPa and two different σ_ε values (0.05 and 0.1). The tensile strength is defined at 1000 points along the layer. It can be observed that for the same value of the correlation factor, the range in tensile strength values along the layer increases as the value of σ_ε increases. It can also be seen that the low correlation factor leads to a rapid change in strength from one location to another. In other words, the tensile strength variations in **Figure 186** and **Figure 187** resemble that in **Figure 185** save for the fact

that **Figure 185** exhibits a wider range of tensile strength values. **Figure 188** and **Figure 189** show the tensile strength variation along the layer for a correlation factor of 0.9, a mean tensile strength of 7.0 MPa and two different σ_ε values (0.05 and 0.1). As a result of the increased correlation factor, the crests and troughs of the variation of the tensile strength along the layer are clearer than those in **Figure 186** and **Figure 187** where the correlation factor is 0.1. Note that as in **Figure 186** and **Figure 187**, the tensile strength is also defined at 1000 points along the layer in **Figure 188** and **Figure 189**. The effect of each parameter is summarized in the following items:

1. An increase in σ_ε leads to a wider range of tensile strength values for a given value of ϕ and μ_{σ_t} (e.g., **Figure 186** vs. **Figure 187** and **Figure 188** vs. **Figure 189**).

2. An increase in the correlation factor, ϕ, leads to a wider range of tensile strength values for a given value of σ_ε and μ_{σ_t} (e.g., **Figure 186** vs. **Figure 188** and **Figure 187** vs. **Figure 189**). Also, regions of low and high tensile become more clearly defined with larger ϕ values.

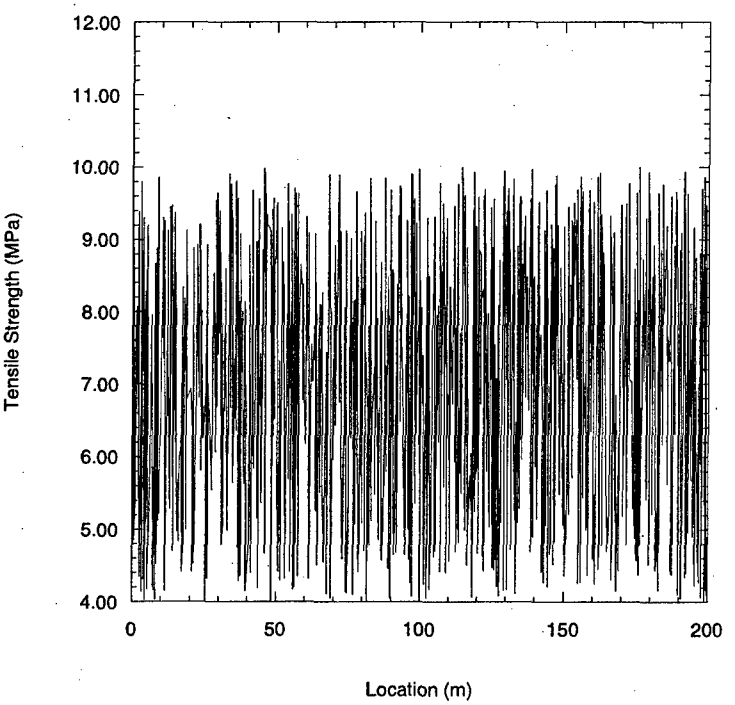


Figure 185 – Variation of tensile strength along the jointing layer for the uncorrelated strength model. The tensile strength has a uniform probability distribution between 4.0 and 10.0 MPa. The strength is defined at 1000 points along the layer.

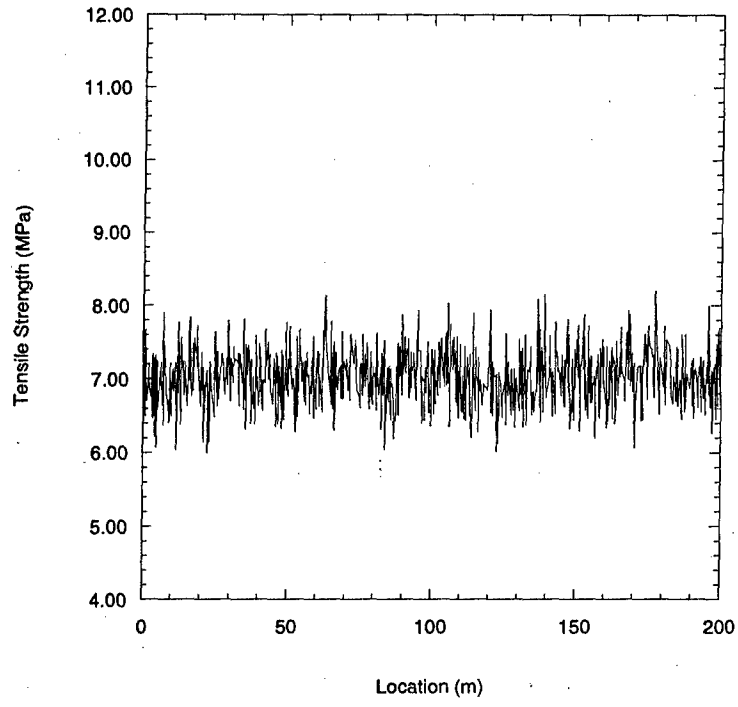


Figure 186 – Variation of tensile strength along the jointing layer for a correlated strength model. Parameter values: $\phi = 0.1$, $\sigma_\varepsilon = 0.05$ and $\mu_{\sigma_t} = 7.0$ MPa.

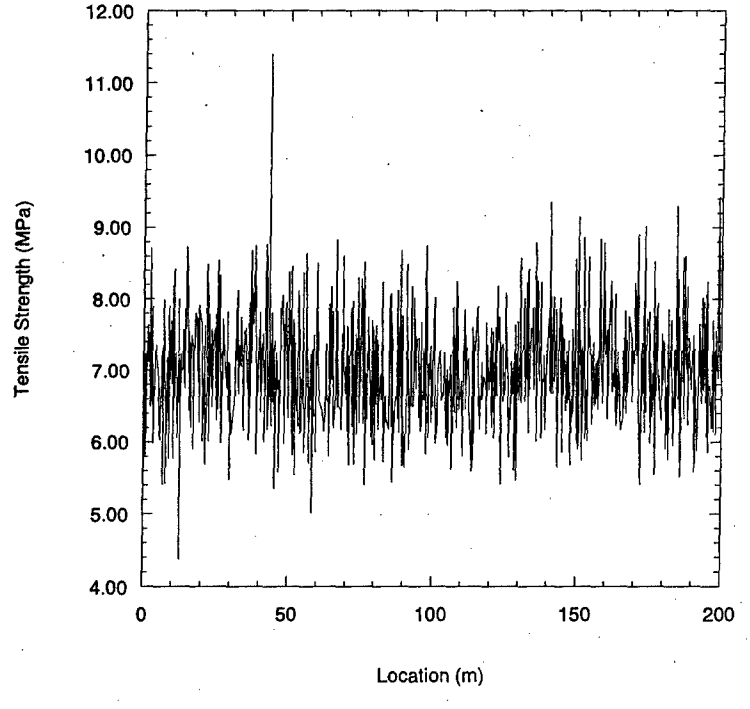


Figure 187 – Variation of tensile strength along the jointing layer for a correlated strength model. Parameter values: $\phi = 0.1$, $\sigma_\varepsilon = 0.1$ and $\mu_{\sigma_t} = 7.0$ MPa.

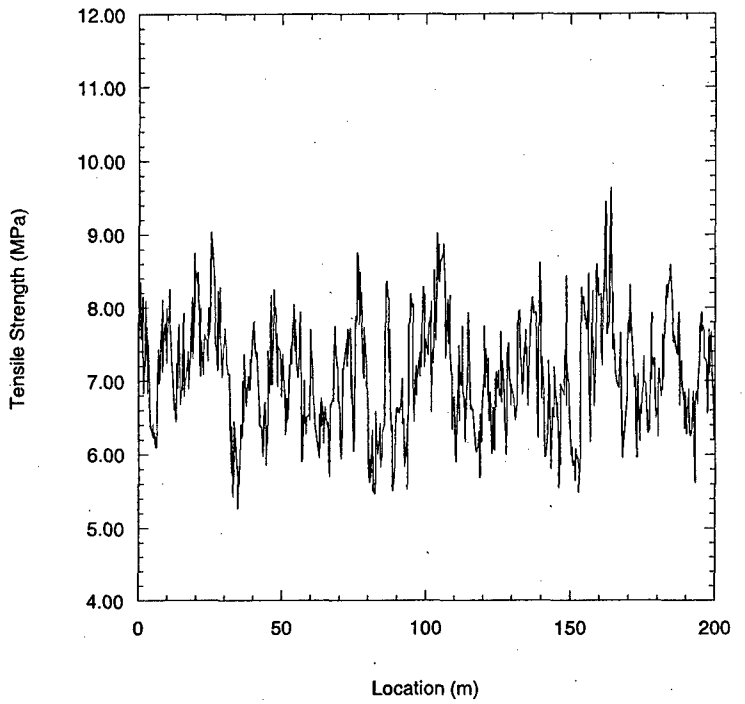


Figure 188 – Variation of tensile strength along the jointing layer for a correlated strength model. Parameter values: $\phi = 0.9$, $\sigma_\varepsilon = 0.05$ and $\mu_{\sigma_t} = 7.0$ MPa.

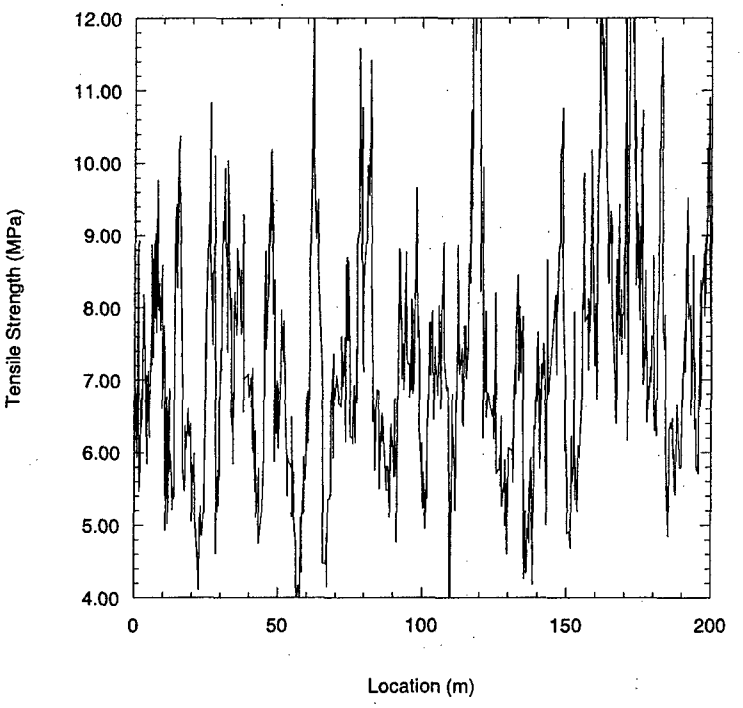


Figure 189 – Variation of tensile strength along the jointing layer for a correlated strength model. Parameter values: $\phi = 0.9$, $\sigma_\varepsilon = 0.1$ and $\mu_{\sigma_t} = 7.0$ MPa.

Perhaps a clearer way to differentiate the correlated strength model from an uncorrelated strength model would be to show how the ratio between the tensile strength values at adjacent locations (i.e., $\frac{\sigma_{t_i}}{\sigma_{t_{i-1}}}$) varies along the layer. For the correlated strength model, one expects this ratio to hover around 1.0 and deviate from it with magnitudes depending on the correlation factor, ϕ, as well as the parameter σ_ε. For the uncorrelated model using a uniform probability distribution of tensile strength at a point, this ratio fluctuates between the ratio between the maximum and minimum tensile strength and its inverse. For example, **Figure 190** shows the variation of the ratio between tensile strength values at adjacent locations for the uncorrelated model using a uniform probability distribution of tensile strength with a maximum of 10.0 MPa and a minimum of 4.0 MPa. The ratios fluctuate between about 0.4 and 2.5 (i.e., between 4/10 and 10/4). **Figure 191** and **Figure 192** show the variation of the strength ratios along the layer for the correlated strength model for two different values of the correlation factor (0.1 and 0.9) but the same σ_ε (= 0.1). The larger correlation factor leads to smaller fluctuations about 1.0. **Figure 193** and **Figure 194** show the variation of the ratios for the two correlation factor values (0.1 and 0.9) but with a smaller σ_ε (= 0.01). It can be seen that the fluctuations about 1.0 for both cases are smaller regardless of the correlation factor. One can also change the value of μ_{σ_t} to increase or decrease the overall tensile strength of the layer (**Figure 195**, $\mu_{\sigma_t} = 7.0$ and $\mu_{\sigma_t} = 15.5$ MPa). It can be observed that increasing the μ_{σ_t} also increases the range of tensile strength values for fixed ϕ and σ_ε (**Figure 195**).

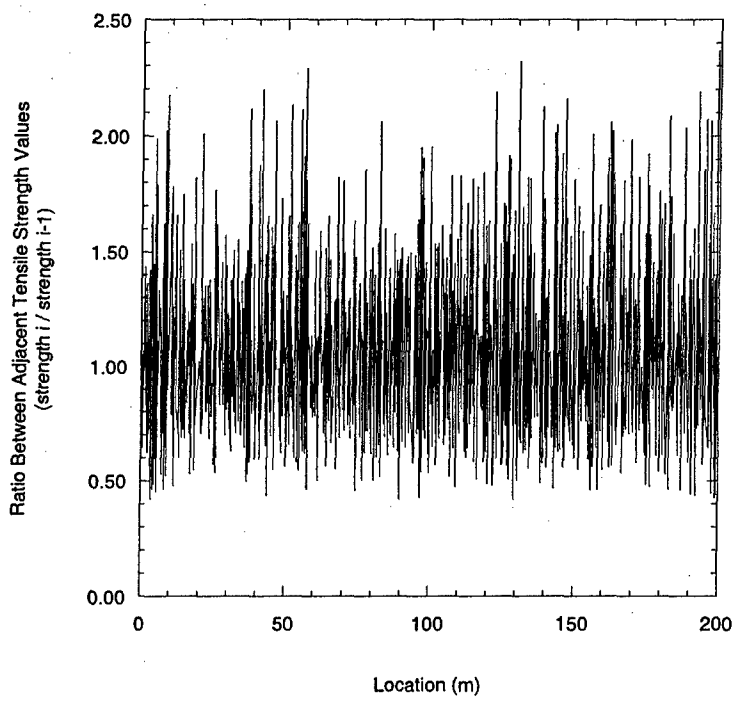


Figure 190 – Ratio between adjacent strength values for a minimum of 4.0 MPa and a maximum of 10.0 MPa using a uniform probability distribution of tensile strength in an uncorrelated strength model.

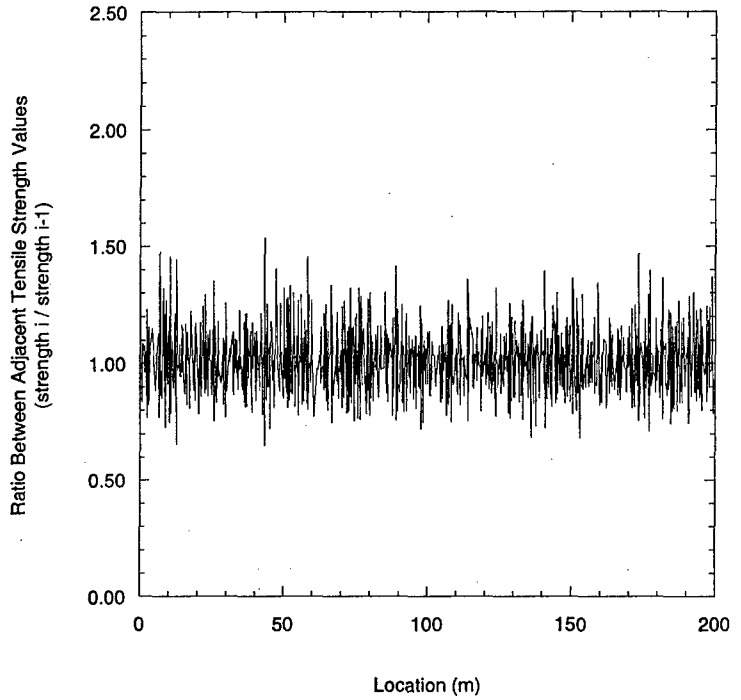


Figure 191 – Ratio between adjacent strength values for the correlated strength model with parameters $\phi = 0.1$, $\sigma_\varepsilon = 0.1$ and $\mu_{\sigma_t} = 7.0$ MPa.

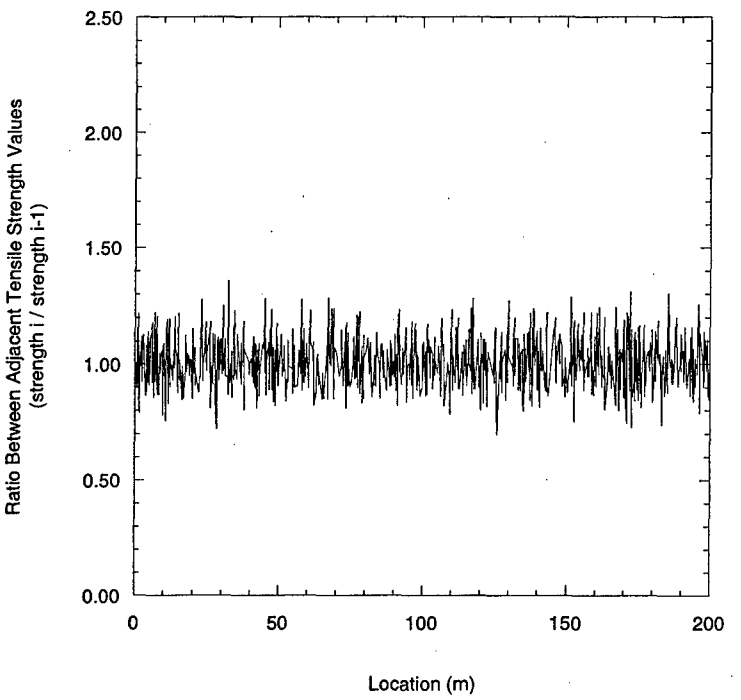


Figure 192 – Ratio between adjacent strength values for the correlated strength model with parameters $\phi = 0.9$, $\sigma_\varepsilon = 0.1$ and $\mu_{\sigma_t} = 7.0$ MPa.

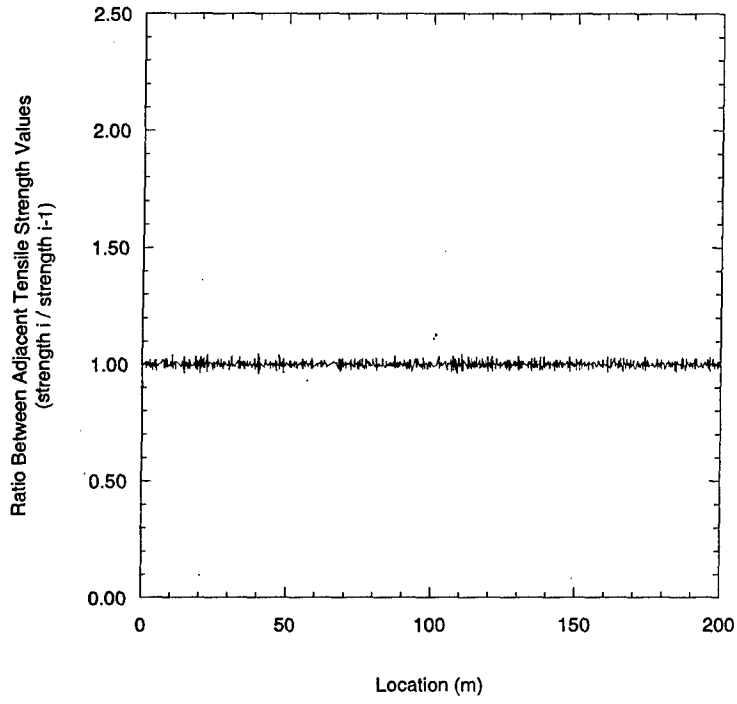


Figure 193 – Ratio between adjacent strength values for the correlated strength model with parameters $\phi = 0.1$, $\sigma_\varepsilon = 0.01$ and $\mu_{\sigma_t} = 7.0$ MPa.

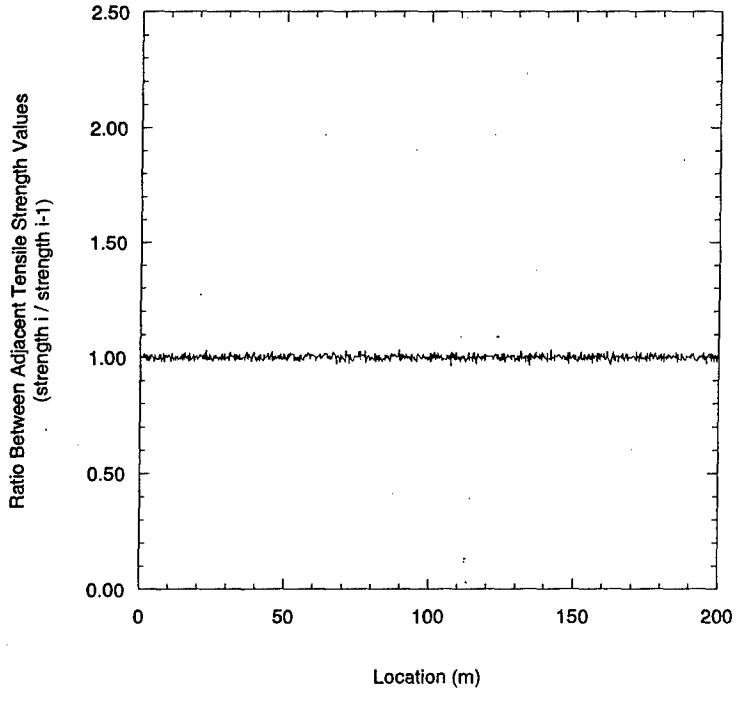


Figure 194 – Ratio between adjacent strength values for the correlated strength model with parameters $\phi = 0.9$, $\sigma_\varepsilon = 0.01$ and $\mu_{\sigma_t} = 7.0$ MPa.

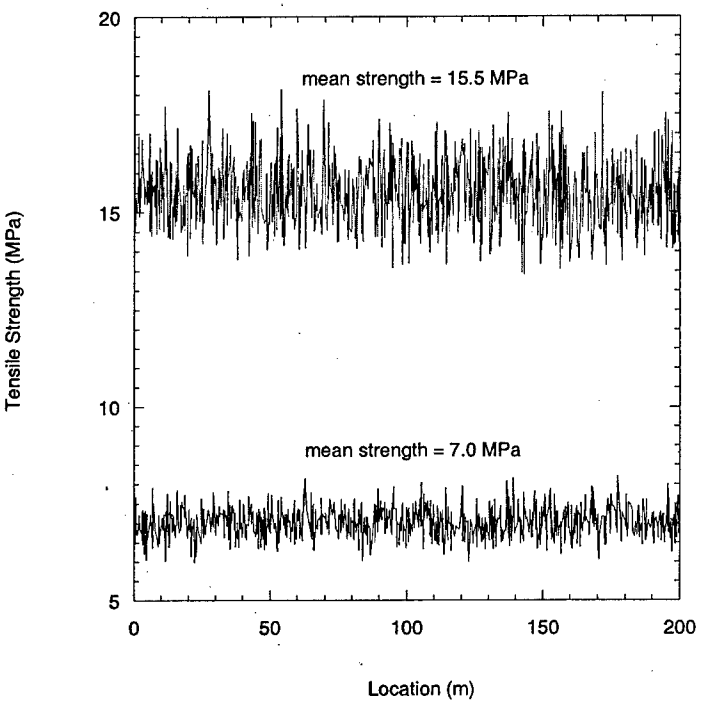


Figure 195 – Variation of tensile strength along the jointing layer for two different mean strength values. For both cases, $\phi = 0.1$, and $\sigma_\varepsilon = 0.05$.

The joint spacing distributions from a correlated strength model are now considered. **Figure 196** shows that the standard deviation of joint spacing increases as the correlation factor increases with all other parameters fixed. This makes sense because larger ϕ values lead to clear regions of high tensile strength and low tensile strength (e.g., **Figure 188** vs. **Figure 186**). New joints are more likely to form in the regions of low tensile strength whereas the regions of high tensile strength may remain largely unjointed. This leads to a greater variance in spacing, the trend shown in **Figure 196**. **Figure 197** shows the effect of σ_ε on the standard deviation of spacing. A larger σ_ε value leads to a larger standard deviation for spacing. This effect is similar to that of the correlation factor, ϕ. A larger σ_ε for a given ϕ and μ_{σ_t} merely enhances the absolute difference in the low and high tensile strength values (e.g., **Figure 188** vs. **Figure 189**). It also enhances the chance that new joint formation will be confined to the low tensile strength areas, thus increasing the standard deviation of joint spacing.

Figure 198 and **Figure 199** show how the joint spacing CDFs are affected by the correlation factor, ϕ, and σ_ε. **Figure 198** shows that as the correlation factor increases, there is an increase in the relative frequency of the smaller joint spacing values accompanied by a decrease in the relative frequency of the larger joint spacing values. This is related to the observation that was made regarding the standard deviation vs. ϕ in **Figure 196** in that new joint formation is possibly limited to the low tensile strength areas which are better defined for larger ϕ values. Meanwhile, **Figure 199** shows that

larger σ_ε values also lead to an increase in the relative frequency of the smaller joint spacing values. Again, this is related to the fact that an increase in σ_ε leads to a larger absolute difference between tensile strength in the weaker regions and the stronger regions thus confining new joint formation to the weaker regions.

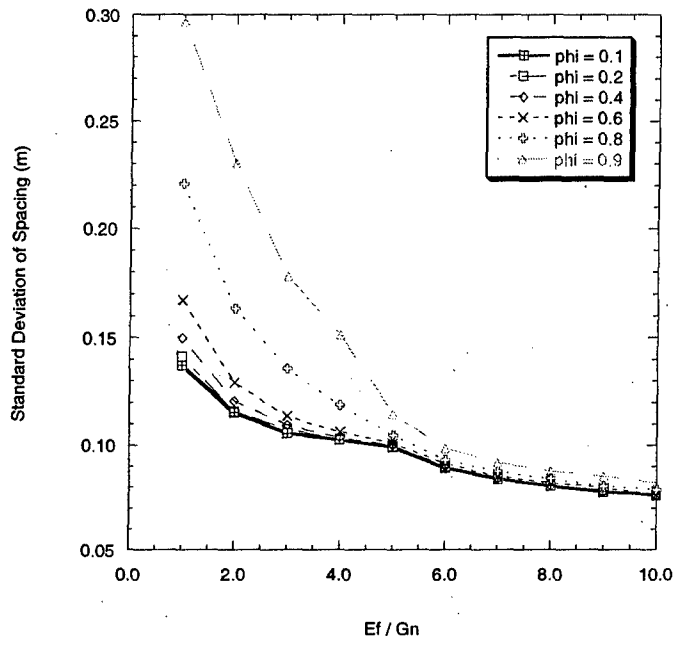


Figure 196 – Effect of the correlation factor, ϕ, on the standard deviation of joint spacing for different $\frac{E_f}{G_n}$ values. The joint intensity is fixed (~4.2 /m), jointing layer thickness is 0.18 m, non-jointing layer thickness is 0.05 m, $\mu_s = 7.0$ MPa and $\sigma_\varepsilon = 0.1$.

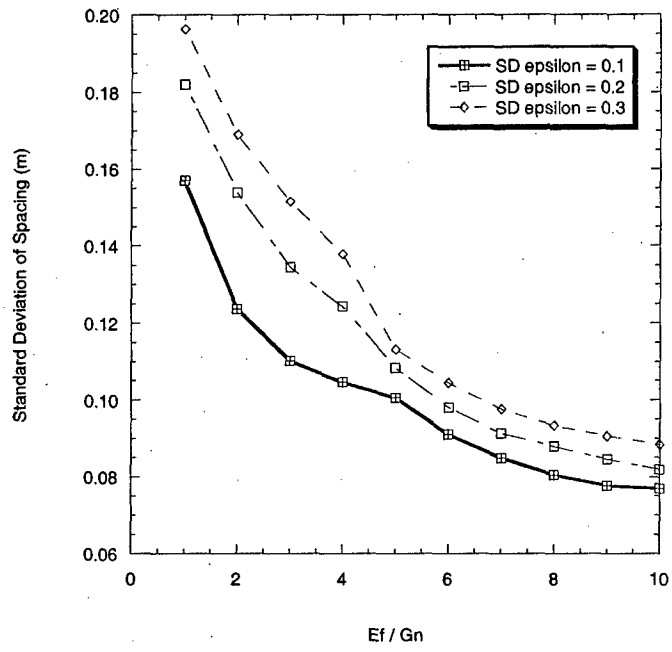


Figure 197 – Effect of the parameter σ_ε (shown as SD epsilon) on the standard deviation of spacing for different $\frac{E_f}{G_n}$ values. The joint intensity is fixed (~4.2 /m), jointing layer thickness is 0.18 m, non-jointing layer thickness is 0.05 m, $\mu_{\sigma_t} = 7.0$ MPa and $\phi = 0.5$.

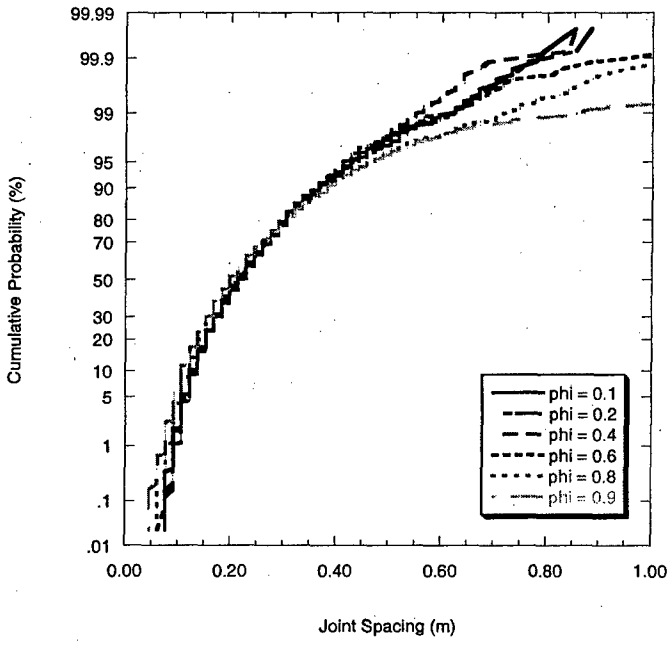


Figure 198 – Effect of the correlation factor on the resulting joint spacing CDF. The joint intensity is fixed (~4.2 /m), jointing layer thickness is 0.18 m, non-jointing layer thickness is 0.05 m, $\sigma_\varepsilon = 0.1$ and $\mu_{\sigma_t} = 7.0$ MPa.

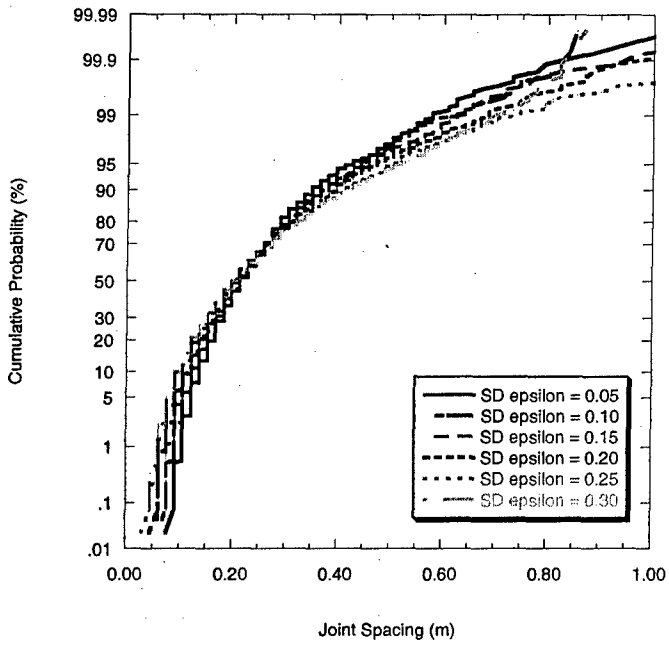


Figure 199 – Effect of the parameter σ_ε (noted as SD epsilon) on the resulting joint spacing CDF. The joint intensity is fixed (~4.2 /m), jointing layer thickness is 0.18 m, non-jointing layer thickness is 0.05 m, $\phi = 0.5$ and $\mu_{\sigma_t} = 7.0$ MPa.

Now consider the joint spacing distributions that result when a correlated strength model is used in the flaw model. As before, the simulated joint spacing CDF is compared with known distribution forms whose parameters are estimated using maximum likelihood. **Figure 200** to **Figure 202** show the simulated joint spacing CDFs at three different joint intensities for a correlation factor of $\phi = 0.1$ and $\sigma_\varepsilon = 0.1$. The behavior is similar to that produced by the uncorrelated strength model in that the joint CDF resembles either an exponential or log-normal CDF at low joint intensity (**Figure 200**), a log-normal CDF at intermediate joint intensity (**Figure 201**) and a normal CDF at very high joint intensity (**Figure 202**). This is expected because a low correlation factor means that the strength is modeled close to an uncorrelated model.

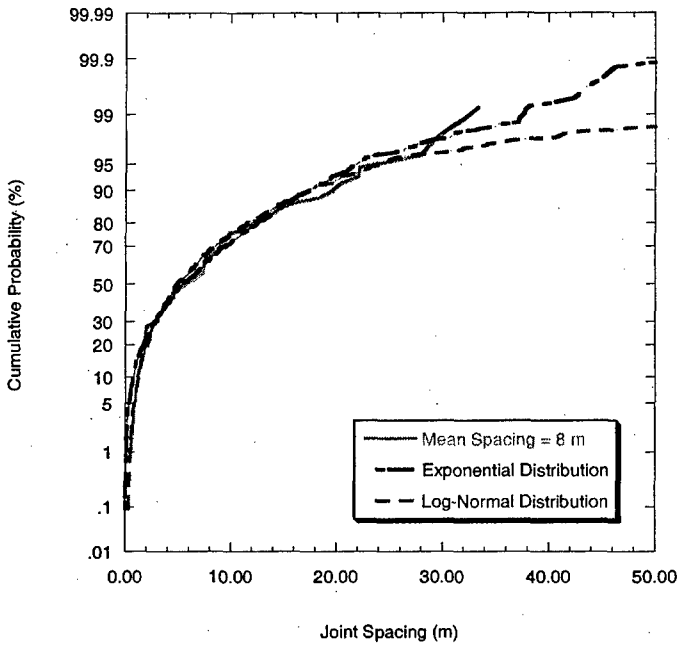


Figure 200 – Comparison between the simulated joint spacing CDF and those of known probability distribution forms at a joint intensity of ~0.125 joints/m. The parameter values are $\phi = 0.1$, $\mu_{\sigma_t} = 7.0$ MPa and $\sigma_\varepsilon = 0.1$.

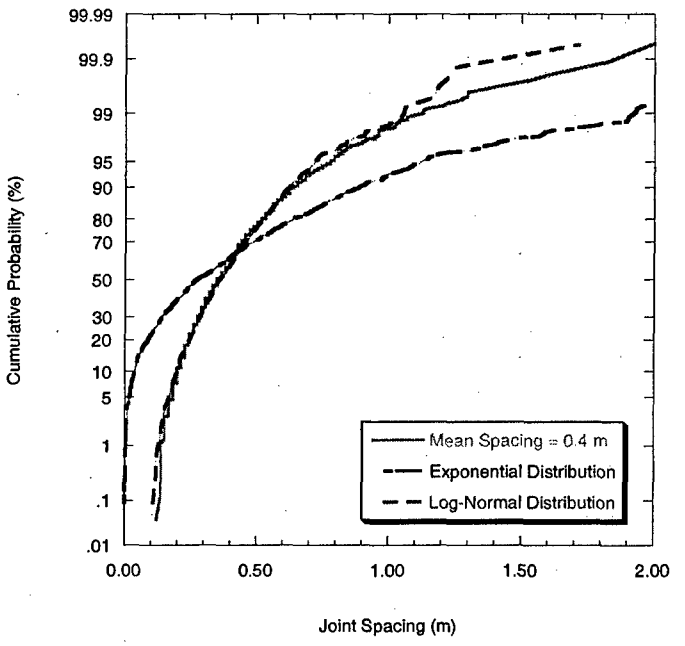


Figure 201 – Comparison between the simulated joint spacing CDF and those of known probability distribution forms at a joint intensity of ~2.5 joints/m. The parameter values are $\phi = 0.1$, $\mu_{\sigma_t} = 7.0$ MPa and $\sigma_\varepsilon = 0.1$.

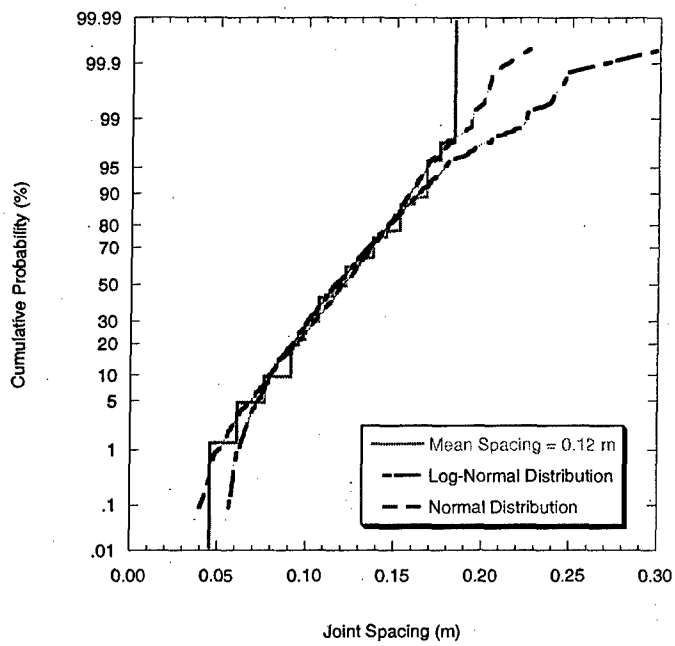


Figure 202 – Comparison between the simulated joint spacing CDF and those of known probability distribution forms at a joint intensity of ~8.3 joints/m. The parameter values are $\phi = 0.1$, $\mu_{\sigma_t} = 7.0$ MPa and $\sigma_\varepsilon = 0.1$.

Figure 203 to **Figure 205** show the joint spacing CDFs for $\phi = 0.5$ and $\sigma_\varepsilon = 0.1$ compared to some typical probability distribution forms at different joint intensities. **Figure 203** shows that the joint CDF resembles neither an exponential nor a log-normal CDF (but close) at low joint intensity. **Figure 204** shows that the joint spacing CDF closely resembles a log-normal CDF at intermediate joint intensity. At very high joint intensity, the joint CDF may be described by a normal CDF (**Figure 205**).

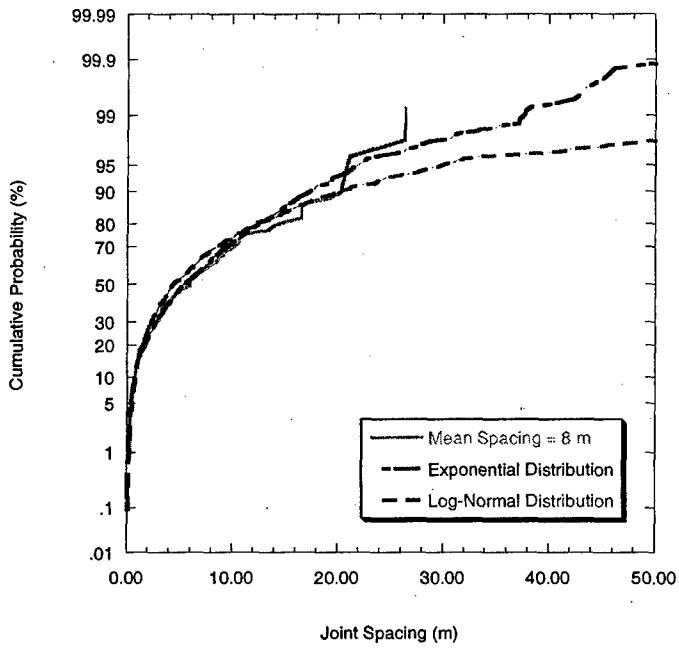


Figure 203 – Comparison between the simulated joint spacing CDF and those of known probability distribution forms at a joint intensity of ~0.125 joints/m. The parameter values are $\phi = 0.5$, $\mu_{\sigma_t} = 7.0$ MPa and $\sigma_\varepsilon = 0.1$.

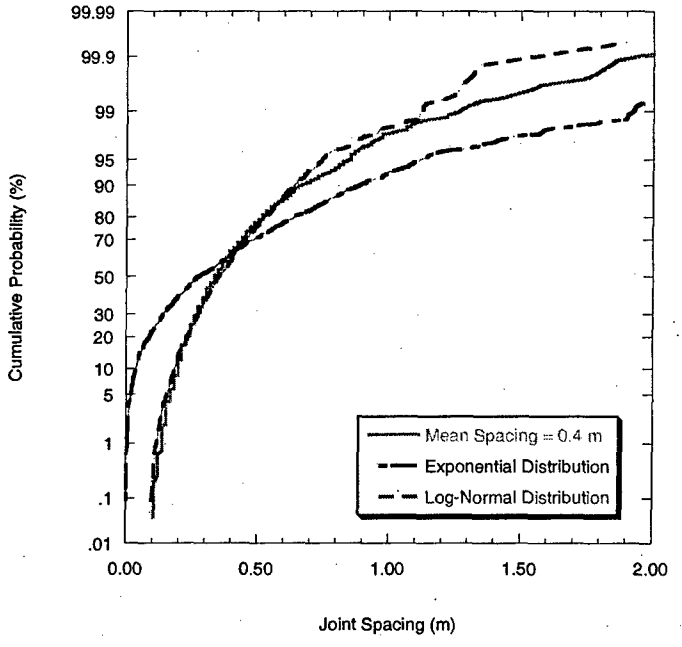


Figure 204 – Comparison between the simulated joint spacing CDF and those of known probability distribution forms at a joint intensity of ~2.5 joints/m. The parameter values are $\phi = 0.5$, $\mu_{\sigma_t} = 7.0$ MPa and $\sigma_\varepsilon = 0.1$.

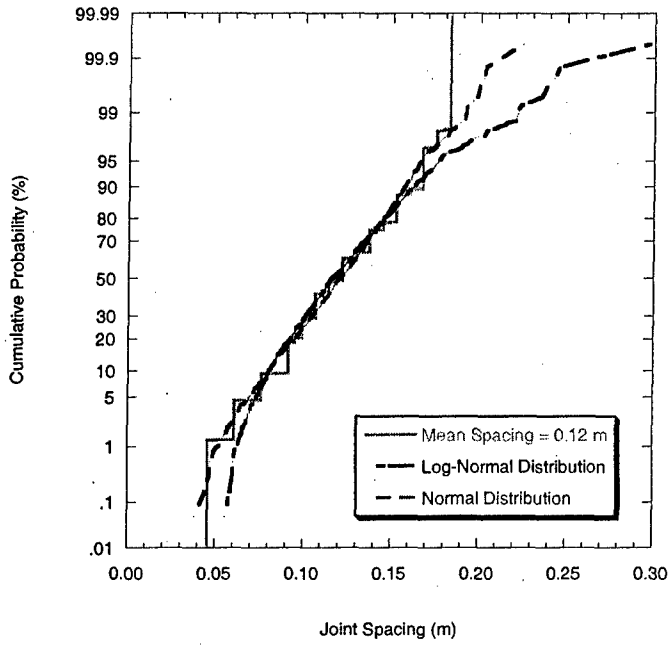


Figure 205 – Comparison between the simulated joint spacing CDF and those of known probability distribution forms at a joint intensity of ~8.3 joints/m. The parameter values are $\phi = 0.5$, $\mu_{\sigma_t} = 7.0$ MPa and $\sigma_\varepsilon = 0.1$.

Figure 206 to **Figure 208** shows the joint spacing CDFs for a higher correlation factor ($\phi = 0.9$) and a $\sigma_\varepsilon = 0.1$. The same joint intensities as those in **Figure 203** to **Figure 205** are used. **Figure 206** shows that at low joint intensity, the simulated joint spacing CDF does not resemble an exponential or a log-normal CDF. At intermediate joint intensity (**Figure 207**), the resemblance of the joint spacing CDF to a log-normal CDF is not as strong as that when $\phi = 0.5$. However, at very high joint intensity (**Figure 208**), it appears that the joint spacing CDF can be represented by a normal CDF.

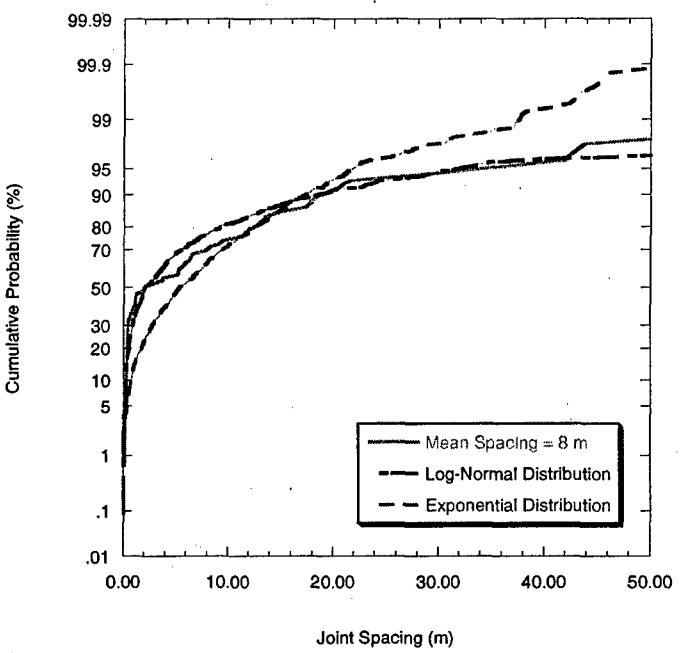


Figure 206 – Comparison between the simulated joint spacing CDF and those of known probability distribution forms at a joint intensity of ~0.125 joints/m. The parameter values are $\phi = 0.9$, $\mu_{\sigma_t} = 7.0$ MPa and $\sigma_\varepsilon = 0.1$.

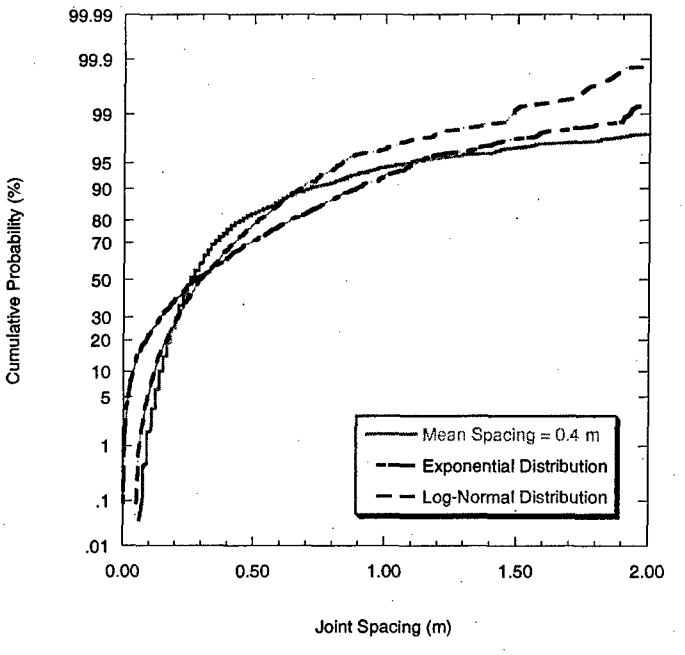


Figure 207 – Comparison between the simulated joint spacing CDF and those of known probability distribution forms at a joint intensity of ~2.5 joints/m. The parameter values are $\phi = 0.9$, $\mu_{\sigma_t} = 7.0$ MPa and $\sigma_\varepsilon = 0.1$.

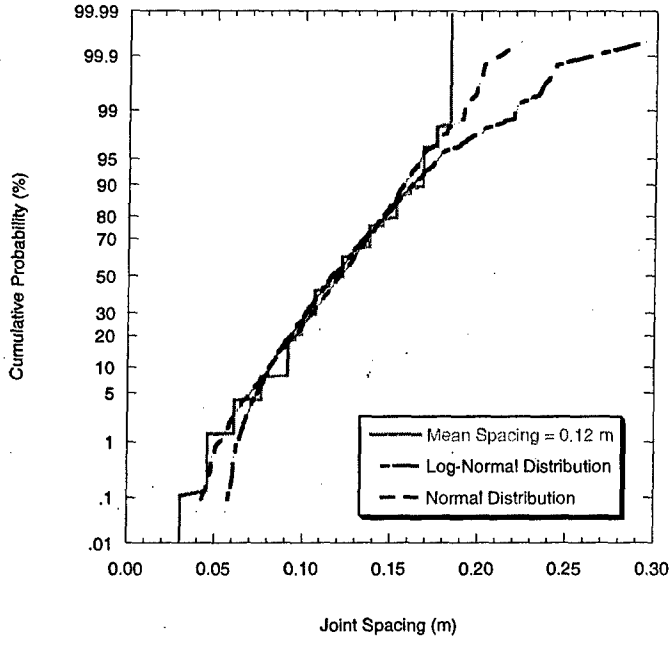


Figure 208 – Comparison between the simulated joint spacing CDF and those of known probability distribution forms at a joint intensity of ~8.3 joints/m. The parameter values are $\phi = 0.9$, $\mu_{\sigma_t} = 7.0$ MPa and $\sigma_\varepsilon = 0.1$.

Figure 209 to **Figure 211** show the joint spacing CDFs if σ_ε is equal to 0.5 instead of 0.1. It can be seen that this change in the value of σ_ε does not cause the simulated joint spacing CDF to resemble the known distribution forms more closely for the low and intermediate joint intensities (**Figure 209** and **Figure 210**). The resemblance at very high joint intensity appears to be about the same. There is also a marked increase in the relative frequency of smaller spacing values at each value of joint intensity compared to those in **Figure 206** to **Figure 208**.

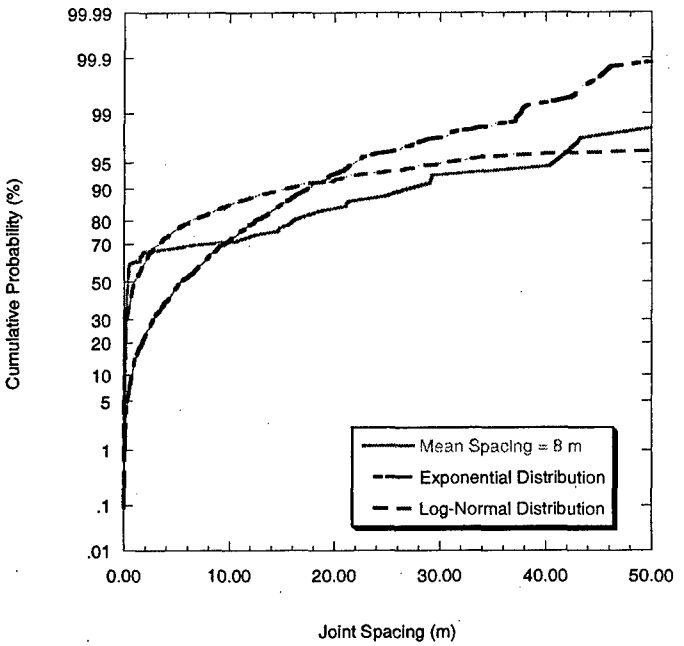


Figure 209 – Comparison between the simulated joint spacing CDF and those of known probability distribution forms at a joint intensity of ~0.125 joints/m. The parameter values are $\phi = 0.9$, $\mu_{\sigma_t} = 7.0$ MPa and $\sigma_\varepsilon = 0.5$.

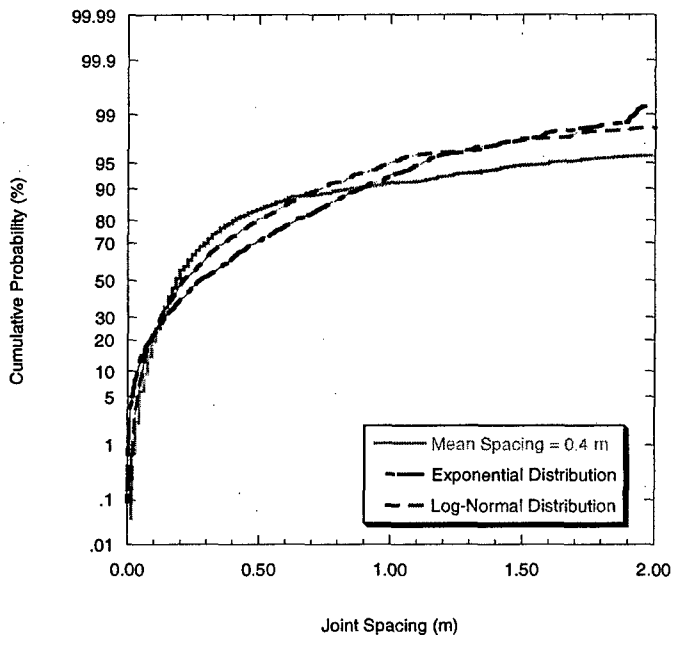


Figure 210 – Comparison between the simulated joint spacing CDF and those of known probability distribution forms at a joint intensity of ~2.5 joints/m. The parameter values are $\phi = 0.9$, $\mu_{\sigma_t} = 7.0$ MPa and $\sigma_\varepsilon = 0.5$.

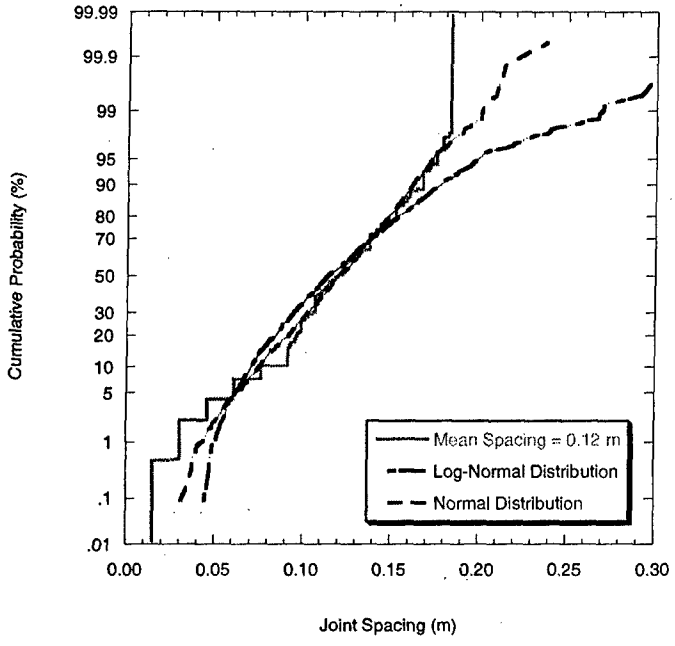


Figure 211 – Comparison between the simulated joint spacing CDF and those of known probability distribution forms at a joint intensity of ~8.3 joints/m. The parameter values are $\phi = 0.9$, $\mu_{\sigma_t} = 7.0$ MPa and $\sigma_\varepsilon = 0.5$.

From this investigation, it is found that the use of a correlated strength model in the flaw model does indeed produce joint spacing distributions with different characteristics than those produced using an uncorrelated strength model. It is also shown that joint spacing distributions with characteristics similar to those from an uncorrelated strength model can also be obtained using the correlated strength model if the correlation factor (ϕ) is lowered. With regard to strength models in general, whether correlated or uncorrelated, the influential element is the variance of the strength values. The results have consistently shown that a larger variance of strength leads to a larger standard deviation of spacing as well as a different joint spacing CDF given the same joint intensity.

This completes a detailed look into the development and behavior of the flaw model. Attention will now be turned to the second jointing model: the rejection procedure. The same structure used to describe the flaw model will be followed in the presentation of the rejection procedure.

6.3 Rejection Procedure

The second model, termed **rejection procedure** after the process that is involved in choosing the location of a newly formed joint, mainly uses a probabilistic approach. Whereas Rabinovitch and Bahat's (1999) model considered the case where only a single pre-existing joint was present (**Figure 212**), the rejection procedure considers the case where multiple joints exist (**Figure 213**). In **Figure 212**, stress reduction shadows do not overlap (Region A), whereas in **Figure 213**, they do (Region B). The formation of new joints between pre-existing joints in **Figure 213** constitutes a joint interaction and an in-filling process that were not included in Rabinovitch and Bahat's (1999) model.

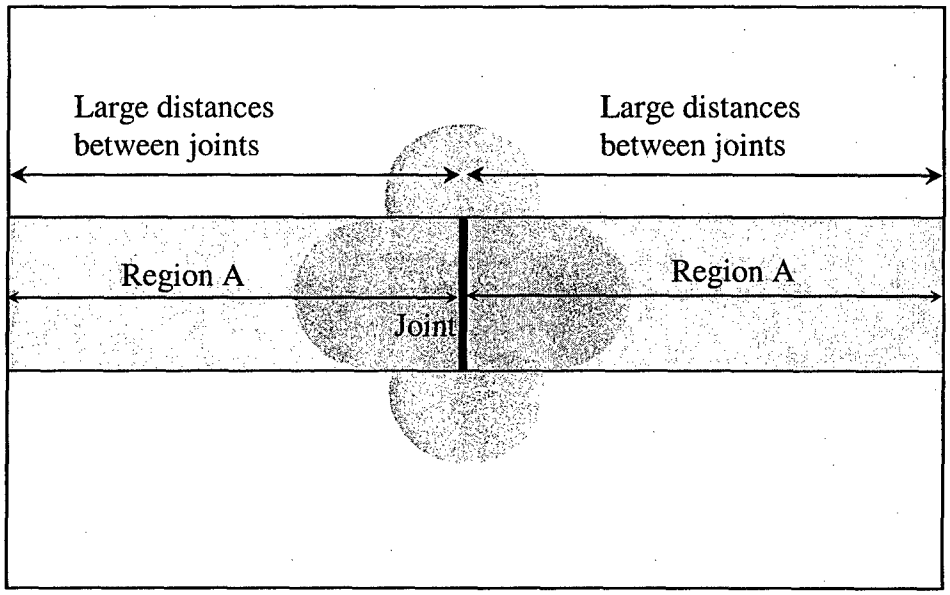


Figure 212 – Single joint and schematic of its stress reduction shadow.

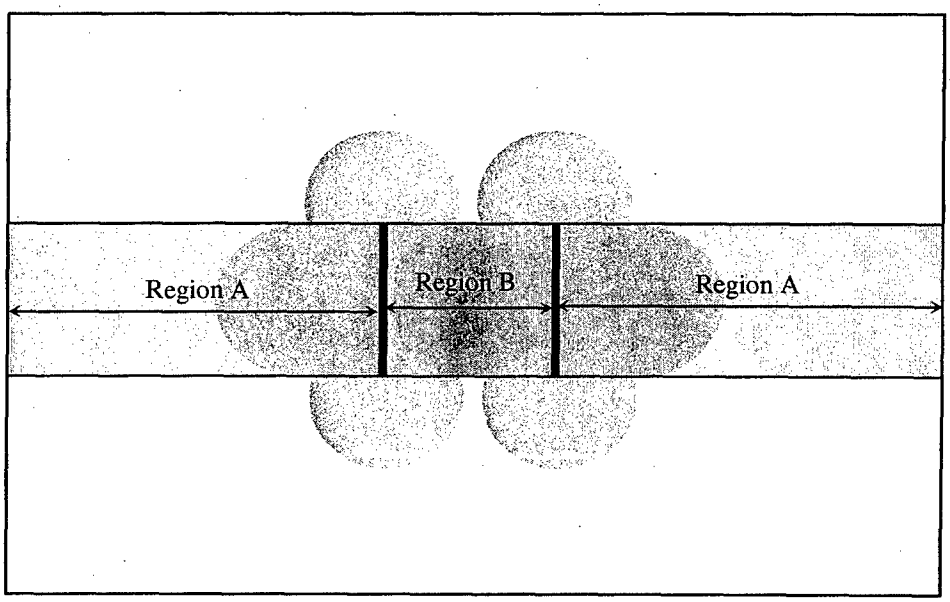


Figure 213 – Two joints with overlapping stress-reduction shadows.

The approach by Rabinovitch and Bahat (1999) used a hazard function, $q(x)$, that increases to a maximum value and then remains constant with distance from an existing joint. From this hazard function, they derived a probability density function, $f(x)$, for the location of a new joint. However, the resulting $f(x)$ is quite limited for use in representing multiple jointing. First of all, it is one-sided because it does not consider joint formation on both sides of the existing joint (i.e., negative x- values are not considered), a characteristic of hazard functions which are usually applied to problems involving time (i.e., uni-directional). This can be remedied by assigning a 50-50 chance that the new joint location is to the left or to the right of the existing joint. Even with this adjustment, it is still applicable only to the formation of one new joint. Lastly, the probability density function, $f(x)$, considers only the presence of a single existing joint. In reality, multiple joints may exist in the layer at any time and $f(x)$, must be updated to reflect the presence of each newly-formed joint.

One can address these issues by working directly with $f(x)$ instead of $q(x)$. Factors that affect the location of a new joint may be incorporated directly into $f(x)$. Note that $f(x)$ must be updated after each newly-formed joint. From each updated $f(x)$, a single value of x can be generated. The generated x-values define locations of joints from which a spacing distribution can be obtained. To generate a value of x from $f(x)$, a "rejection procedure" can be used. The rejection procedure is simply a method of generating values of a random variable that follow some probability distribution. Intuitively, the probability density function of the location of a new joint should be a function of both the tensile stress (σ_{local}) and the tensile strength of the layer (σ_t) or $f(x) = g(\sigma_{local}, \sigma_t)$. The tensile stress, σ_{local}, depends on location and increases with strain, ε, and changes with the addition of new joints (i.e., $\sigma_{local} = \sigma(x, \varepsilon)$). The tensile strength can be a function of location along the layer (i.e., $\sigma_t = \sigma_t(x)$). If the jointing layer has constant tensile strength, the probability $f(x)dx$ depends only on the tensile stress in the layer. However, the tensile stress is a maximum at the midpoint of the two widest-spaced joints (i.e., the longest segment) so that a new joint forms there with probability 1.0. On the other hand, $f(x)$ will be different if the tensile strength at each point ($\sigma_t = \sigma_t(x)$) is a random variable with probability density function $f_{\sigma_t}(\sigma_t)$. A simple model for $f(x)$ would be to assume that $f(x) \propto \frac{\sigma_{local}}{\sigma_{farfield}} = \frac{\sigma(x)}{\sigma_{farfield}} = \frac{\sigma(x)}{E_f \varepsilon}$. The maximum possible value that $\frac{\sigma(x)}{\sigma_{farfield}}$ can attain is 1.0. Also, the function $\frac{\sigma(x)}{\sigma_{farfield}}$ reaches larger values in longer segments than in shorter ones (e.g., Hobbs, 1967; Ji et al., 1998). Given this, the assumption simply means that a new joint is more likely to form inside longer segments than inside shorter ones. Using the simplified stress distribution models (e.g., Hobbs, 1967; Ji et al., 1998), the function $\frac{\sigma(x)}{\sigma_{farfield}}$ does not change with increasing strain. Only a change in the geometry of the segments can alter it (e.g., when a new joint

is added and one segment is divided into two shorter segments). **Figure 214** shows a schematic of how $\frac{\sigma(x)}{\sigma_{farfield}}$ might vary along the jointing layer.

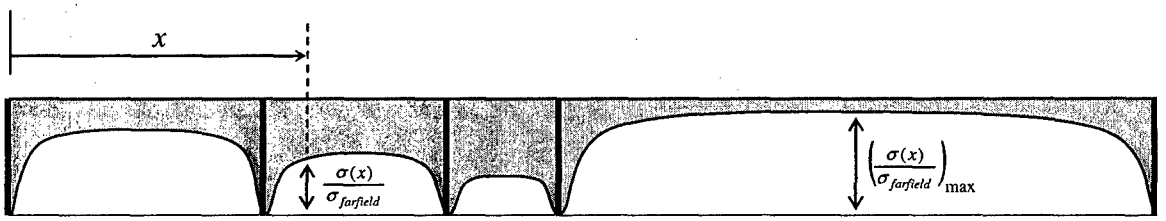


Figure 214 – Illustration of the variation of normalized tensile stress along a jointed layer. The maximum tensile stress occurs within the longest segment.

Joint locations can then be generated from $f(x)$ and from these joint locations, the joint spacing histogram or distribution can be obtained. The calculation of the proportionality constant in $f(x) \propto \frac{\sigma(x)}{\sigma_{farfield}}$ is not necessary. A rejection procedure can be employed to generate new joint locations given only $f(x) \propto \frac{\sigma(x)}{\sigma_{farfield}}$. This procedure is described in the following section.

6.3.1 Rejection Procedure without Saturation Mechanisms

Values of X are generated from $f(x) \propto \frac{\sigma(x)}{\sigma_{farfield}}$ using a rejection procedure. In the following steps, one sees that the proportionality constant in $f(x) \propto \frac{\sigma(x)}{\sigma_{farfield}}$ need not be determined because it cancels out in calculations. Starting with an unjointed layer, the following steps are performed:

1. The location of a new joint is chosen at random. It is assumed that the new joint can form at any location along the entire layer with equal probability. A random number between zero and 1.0 is generated, then is multiplied by the length of the entire layer to obtain the preliminary location of the new joint.

2. The value of $\frac{\sigma(x)}{\sigma_{farfield}}$ at this location is calculated (e.g., using Ji et al., 1998). It is then divided by $\left(\frac{\sigma(x)}{\sigma_{farfield}}\right)_{max}$ (i.e., the maximum value of $\frac{\sigma(x)}{\sigma_{farfield}}$ in the entire layer, which is located at the midpoint of the longest existing segment).

3. A random number between zero and 1.0 is generated using a uniform probability distribution.

4. If the ratio calculated in item 2 exceeds the random number generated in item 3, the location of the new joint is retained. If not, the location is rejected and the process is repeated until a new joint is retained. The process is repeated from step 1 until a

desired number of new joints are formed. Note that in an unjointed layer, $\frac{\sigma(x)}{\sigma_{farfield}} = \left(\frac{\sigma(x)}{\sigma_{farfield}}\right)_{\max}$ everywhere so a new joint can form anywhere (rejections are unlikely). However, as more and more joints are formed, more rejections will occur before a valid location is produced. This reflects the increasing influence of the existing joints on the tensile stress as the joint intensity increases. The existing joints limit the mechanically possible locations for new joints.

The rejection procedure produces joint spacing distributions that have characteristics similar to those observed in the field. The simulated spacing distributions are unimodal, skewed towards smaller spacing values have tails towards large spacing values. Because of the assumption that $f(x) \propto \frac{\sigma(x)}{\sigma_{farfield}}$, this model is devoid of an explicit strength model. In other words, no direct comparison between stress and strength is made to determine the locations of new joints.

In the next section, the compressive stress saturation mechanism is included in the rejection procedure.

6.3.2 Rejection Procedure with Saturation Mechanisms

Unlike in the flaw model, the saturation mechanism due to interface slippage cannot be applied directly to the rejection procedure because no strains are calculated. However, the compressive stress saturation mechanism can be implemented in the rejection procedure because only the geometry of the segments is important in determining whether or not compressive stresses are developed. The critical spacing-to-thickness ratio, $\left(\frac{s}{t}\right)_{cr}$, is the only important parameter. Bai and Pollard (2000) showed that $\left(\frac{s}{t}\right)_{cr}$ increases with:

- Increasing E_f/E_n ratio
- Increasing overburden stress, S_v

and decreases with

- Increasing value of D (see equation below). Note that the value of D increases when ν_f decreases (for a fixed value of ν_n) or when ν_n increases (for a fixed value of ν_f). Also, D is positive if $\nu_f < \nu_n$ and negative if $\nu_f > \nu_n$.

$$D = \frac{(1-2\nu_f)(1+\nu_f)-(1-2\nu_n)(1+\nu_n)}{(1-\nu_f^2)+(1-\nu_n^2)} \qquad \textbf{Equation 44}$$

(repeated here)

The combined effect of these three factors can be expressed as:

$$\left(\frac{s}{t}\right)_{cr} = \beta\gamma\left[0.792+0.328\left(1-\exp\left[-0.824\left(\frac{E_f}{E_n}-0.0025\right)^{0.824}\right]\right)\right] \qquad \textbf{Equation 47}$$

(repeated here)

where

$$\beta = \frac{0.976-0.302D-0.129D^2+0.117D^3}{0.976}$$

and

$$\gamma = \frac{0.976+1.118\times10^{-4}S_v-7.562\times10^{-8}S_v^2+2.806\times10^{-9}S_v^2}{0.976}$$

Using the expression for $\left(\frac{s}{t}\right)_{cr}$, the algorithm for the rejection procedure can be modified to reflect the compressive stress saturation mechanism in $f(x) \propto \frac{\sigma(x)}{\sigma_{farfield}}$. This can be done by letting $f(x) \propto \frac{\sigma(x)}{\sigma_{farfield}} = 0$ whenever x defines a point inside a segment that has a length equal to or below the critical spacing. **Figure 215** shows $\frac{\sigma(x)}{\sigma_{farfield}}$ when one of the segments (i.e., the third one from the left) is below critical spacing.

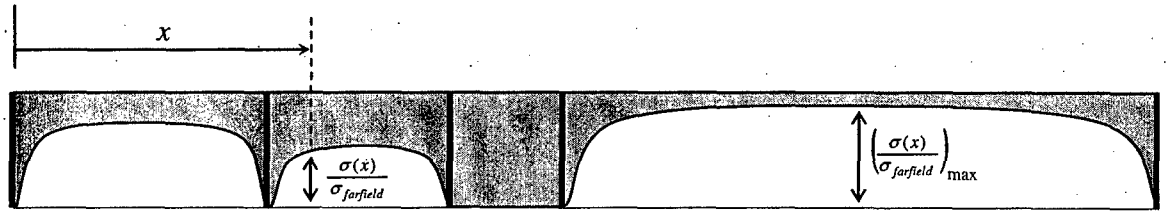


Figure 215 – Illustration of the variation of normalized tensile stress along a jointed layer when saturation mechanism is included. The third segment from the left has a spacing below critical.

The following steps outline the rejection procedure considering the saturation mechanism due to compressive stress development. Starting from the unjointed layer:

1. Calculate the value of $\left(\frac{s}{t}\right)_{cr}$. Note that this is calculated only once and does not change throughout the jointing process. The location of a new joint is chosen at random. For this step, it is assumed that the new joint can form at any location along the entire layer with equal probability. To do this, a random number between zero and 1.0 is generated. This number is then multiplied by the length of the entire layer to obtain the preliminary location of the new joint. Check the length of the segment that contains the preliminary location. If it is greater than the critical spacing (i.e., $t \cdot \left(\frac{s}{t}\right)_{cr}$), then proceed to step 2. Otherwise, generate a new location until a valid

segment is found (i.e., segment length is longer than $t \cdot (\frac{s}{t})_{cr}$). A segment whose length ratio is less than $t \cdot (\frac{s}{t})_{cr}$ will have developed compressive stresses and therefore, the probability that a new joint occurs there is zero (i.e., $f(x) = 0$ inside that segment).

2. The value of $\frac{\sigma(x)}{\sigma_{farfield}}$ at this new location is calculated (e.g., using Ji et al., 1998). It is then divided by $\left(\frac{\sigma(x)}{\sigma_{farfield}}\right)_{\max}$ (i.e., the maximum value of $\frac{\sigma(x)}{\sigma_{farfield}}$ in the entire layer, which is located at the midpoint of the longest existing segment).

3. A random number between zero and 1.0 is generated using a uniform probability distribution.

4. If the ratio calculated in item 2 exceeds the random number generated in item 3, the location of the new joint is retained. If not, the location is rejected and the process is repeated until a new joint is retained. The process is repeated from step 1 until a desired number of new joints are formed. Note that in an unjointed layer, $\frac{\sigma(x)}{\sigma_{farfield}} = \left(\frac{\sigma(x)}{\sigma_{farfield}}\right)_{\max}$ everywhere so a new joint can form anywhere (rejections are unlikely). However, as more and more joints are formed, more rejections will occur before a valid location is produced. This reflects the increasing influence of the existing joints as the joint intensity increases. The existing joints limit the mechanically possible locations for new joints.

As shown above, the incorporation of the saturation mechanism into the rejection procedure is relatively straightforward. The only step that was added to the procedure on 263 is the comparison of segment length to the critical spacing.

Next, the effects of parameters that describe the function $\frac{\sigma(x)}{\sigma_{farfield}}$ on the saturation mean spacing are investigated. The following section shows the results of simulations using the rejection procedure using different parameter values in $\frac{\sigma(x)}{\sigma_{farfield}}$.

6.3.3 Saturation Mean Spacing Parametric Study

For the rejection procedure, there are only two important parameters in $f(x) \propto \frac{\sigma(x)}{\sigma_{farfield}}$ that factor into the jointing process: the $\frac{E_f}{G_n}$ ratio and the non-jointing layer thickness, d. Since the probability density function $f(x)$ is proportional to the tensile stress, one can expect the rejection procedure to behave similar to the flaw model.

Figure 216 shows that the $\frac{E_f}{G_n}$ ratio affects the slope of the relationship between the saturation mean spacing and the jointing layer thickness. This is consistent with the effect of $\frac{E_f}{G_n}$ on the relationship in the flaw model (**Figure 120**). Larger $\frac{E_f}{G_n}$ values lead to larger saturation mean spacing values given the same jointing layer thickness. However, the difference between the slopes is more pronounced in the flaw model (**Figure 120**). Smaller $\frac{E_f}{G_n}$ leads to a larger portion of the segment being exposed to the highest value of $f(x)$ so there is a greater chance that the segment could be divided into one short segment (below the critical spacing) and one long segment rather than into two segments of approximately the same length if only a small portion of the segment were exposed to the highest value of $f(x)$ (i.e., if the $\frac{E_f}{G_n}$ is large). Dividing the segment into one short and one long segment (as in the case of small $\frac{E_f}{G_n}$) is a slow way to make all resulting segments reach critical or below critical spacing. Dividing the segment into two that are approximately the same length is a faster way to make all resulting segments reach critical or below critical (as in the case of large $\frac{E_f}{G_n}$). If the resulting segments do not fall below the critical spacing fast enough, more joints can form. This leads to a smaller saturation mean spacing. Intuitively, the kind of segment division just described for small and large $\frac{E_f}{G_n}$ values leads one to think that a smaller value of $\frac{E_f}{G_n}$ leads to a larger variance (or standard deviation) of spacing and vice-versa. However, **Figure 217** shows that this may not always be the case. In fact, **Figure 217** shows that the saturation standard deviation of spacing is smaller for small values of $\frac{E_f}{G_n}$. One must note, however, that for smaller values of $\frac{E_f}{G_n}$, one is dealing with smaller joint spacing values because a smaller $\frac{E_f}{G_n}$ allows more jointing than a larger $\frac{E_f}{G_n}$. Thus, the standard deviation can possibly be smaller for small $\frac{E_f}{G_n}$ ratios! If one were to normalize the saturation standard deviation (SSD) of spacing using the SMS, then as seen in **Figure 218**, despite the scatter, that smaller $\frac{E_f}{G_n}$ ratios do lead to relatively larger standard deviation of spacing values.

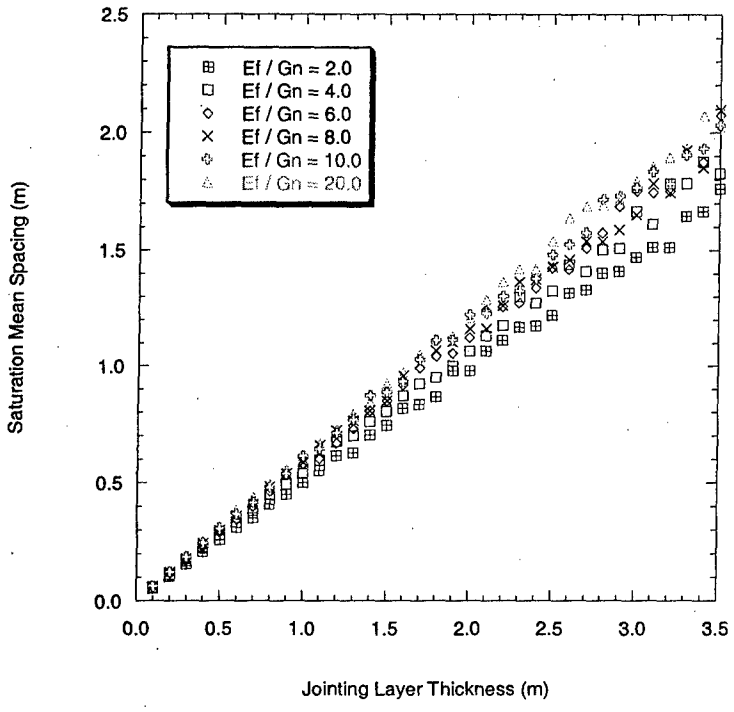


Figure 216 – Effect of the $\frac{E_f}{G_n}$ ratio on the saturation mean spacing in the rejection procedure with saturation mechanism. The non-jointing layer thickness is 0.04 m, ν_f is 0.25, and ν_n is 0.30.

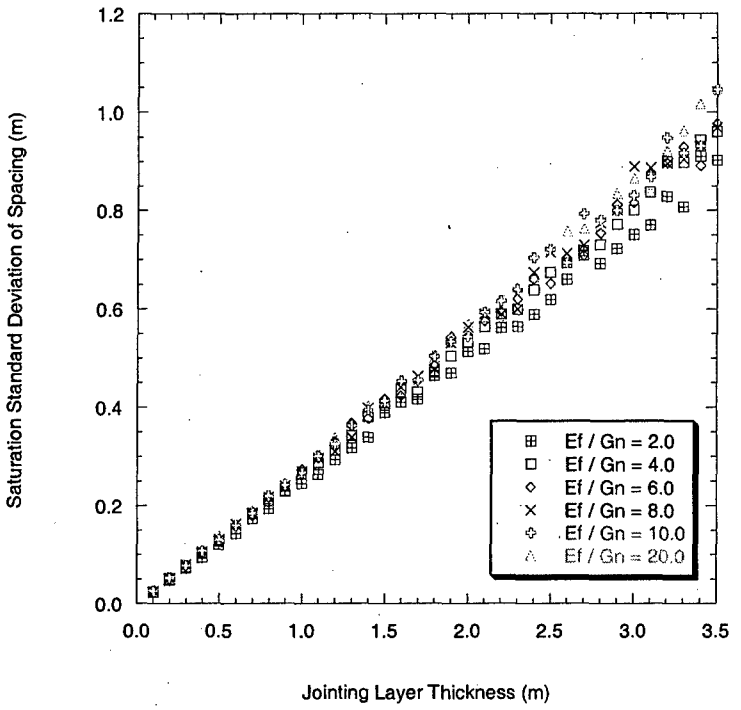


Figure 217 – Effect of the $\frac{E_f}{G_n}$ ratio on the saturation standard deviation of spacing. Rejection procedure with saturation mechanism. The non-jointing layer thickness is 0.04 m, ν_f is 0.25, and ν_n is 0.30.

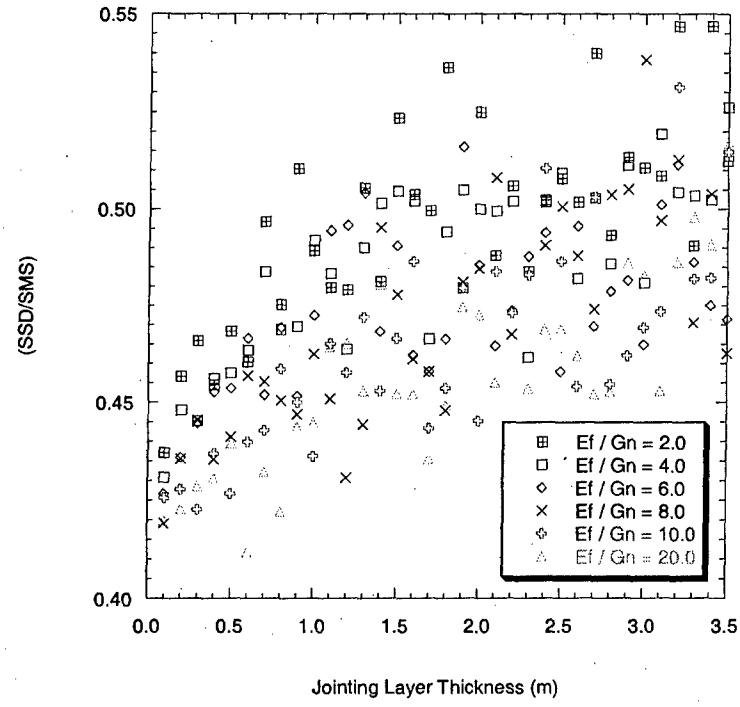


Figure 218 – Effect of the $\frac{E_f}{G_n}$ ratio on the ratio between the standard deviation and mean spacing at saturation (SSD/SMS). Rejection procedure with saturation mechanism. The non-jointing layer thickness is 0.04 m, ν_f is 0.25, and ν_n is 0.30.

Figure 219 shows the effect of the non-jointing layer thickness on the relationship between the SMS and the jointing layer thickness. The influence of the non-jointing layer thickness is very slight but greater non-jointing layer thickness leads to greater saturation mean spacing. Conversely, a smaller non-jointing layer thickness leads to smaller SMS. The same explanation used for the effect of $\frac{E_f}{G_n}$ can be used here because d influences $f(x)$ in the same way. A small value for non-jointing layer thickness means that $f(x)$ is at its highest value only in a short portion of a segment. This means that there is a greater chance that segments are divided into smaller segments of approximately equal length. This, as explained before, is a faster way to make all resulting segments below critical in terms of the compressive stress saturation mechanism. For example, a segment that has length 1.5 times the critical spacing, when divided into two segments that have approximately equal length (0.75 times the critical spacing), will no longer allow further jointing. On the other hand, if it were divided into two segments that are 1.1 and 0.4 times the critical spacing, at least one more joint can form (in the longer segment which is still above critical). Again, intuition leads one to think that a smaller non-jointing layer thickness will lead to a larger variance in spacing. **Figure 220** shows that such is the case regarding the effect of the non-jointing layer thickness. Normalizing the SSD with the SMS (**Figure 221**) yields the following trend: smaller non-jointing layer thickness values lead to relatively larger variance in spacing at saturation.

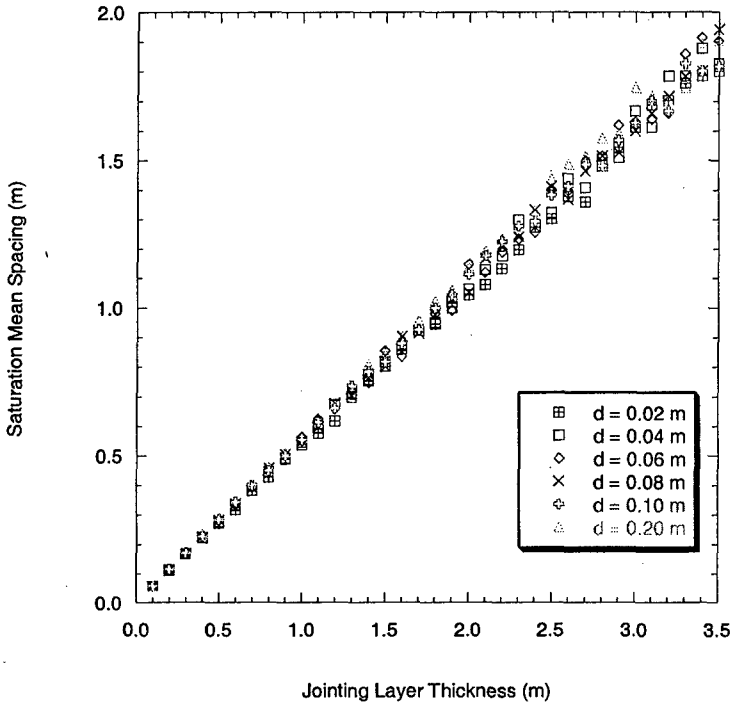


Figure 219 – Effect of the non-jointing layer thickness (d) on the saturation mean spacing in the rejection procedure. $\frac{E_f}{G_n}$ is 4.0, ν_f is 0.25, and ν_n is 0.30.

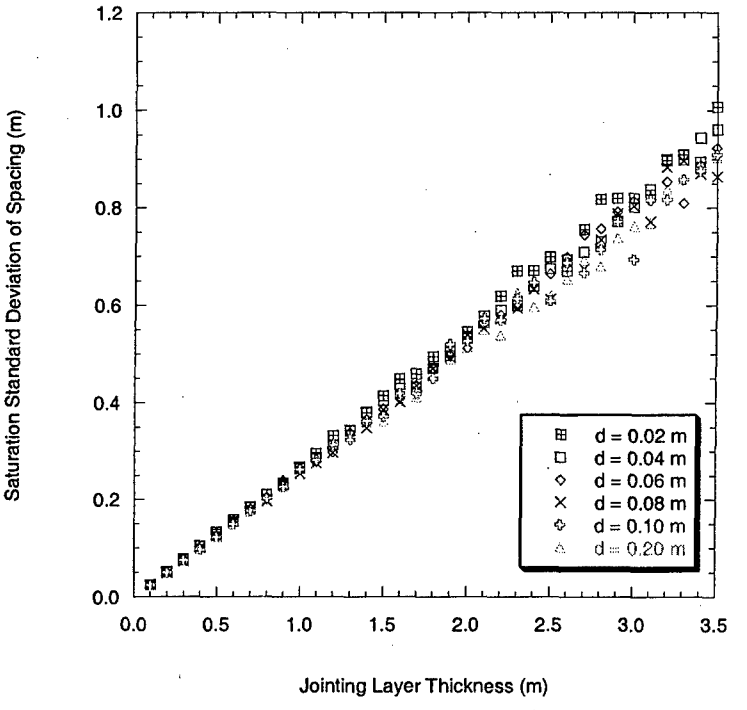


Figure 220 – Effect of the non-jointing layer thickness (d) on the saturation standard deviation of spacing in the rejection procedure. $\frac{E_f}{G_n}$ is 4.0, ν_f is 0.25, and ν_n is 0.30.

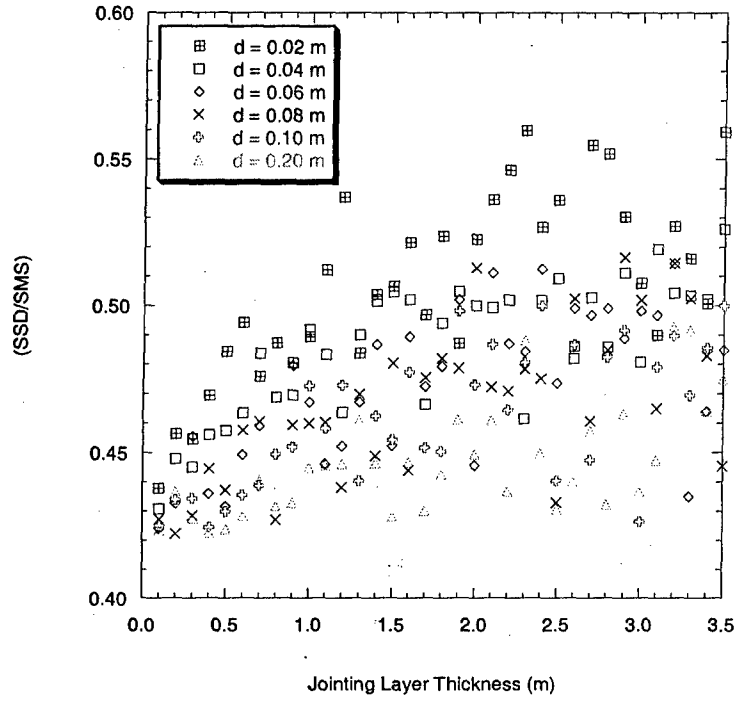


Figure 221 – Effect of the non-jointing layer thickness on the ratio between the standard deviation and mean spacing at saturation (SSD/SMS). Rejection procedure with saturation mechanism. The $\frac{E_f}{G_n}$ is 4.0, ν_f is 0.25, and ν_n is 0.30.

Another aspect of the jointing process is the observed relationship between the joint spacing distribution and the joint intensity. In the next section, this relationship for the rejection procedure is investigated and compared with laboratory observations found in the literature.

6.3.4 Simulated Joint Spacing Distributions

6.3.4.1 Evolution with Increasing Joint Intensity and Effect of Saturation Mechanism

As in the flaw model, the evolution of the joint spacing distribution with increasing joint intensity can also be observed in the rejection procedure. **Figure 222** to **Figure 224** show the simulated joint spacing CDFs for a jointing layer at three different joint intensities. At low joint intensity (**Figure 222**), the simulated joint spacing distribution more closely resembles a log-normal distribution but is also similar to an exponential distribution. The same is true at medium-high joint intensity (**Figure 223**), although the difference is less discernible. At joint saturation (**Figure 224**), the joint spacing distribution resembles neither an exponential nor a log-normal distribution. However, the middle portion of the curve which contains the majority of the joint spacing data (about 90%), appears to form a straight line indicating a possible normal distribution. Deviation at the tail ends is understandable especially at the right end of the distribution (i.e., wider

spacing). In both the rejection procedure and the flaw model, the length of the jointing layer is set at a constant value. As more and more joints are formed within the layer, the tail end of the distribution representing larger spacing values is inevitably being cut because the longer segments are divided into smaller and smaller parts. This cutting of the joint spacing distribution tail is seen in the CDFs as a sudden rise towards a cumulative probability of 1.0. On the other hand, if one generates random spacing data based on some probability distribution (as is done with the known distributions here), it is possible to produce values that are part of the tail end of the probability distribution. This prevents the CDF from rising abruptly in the plots.

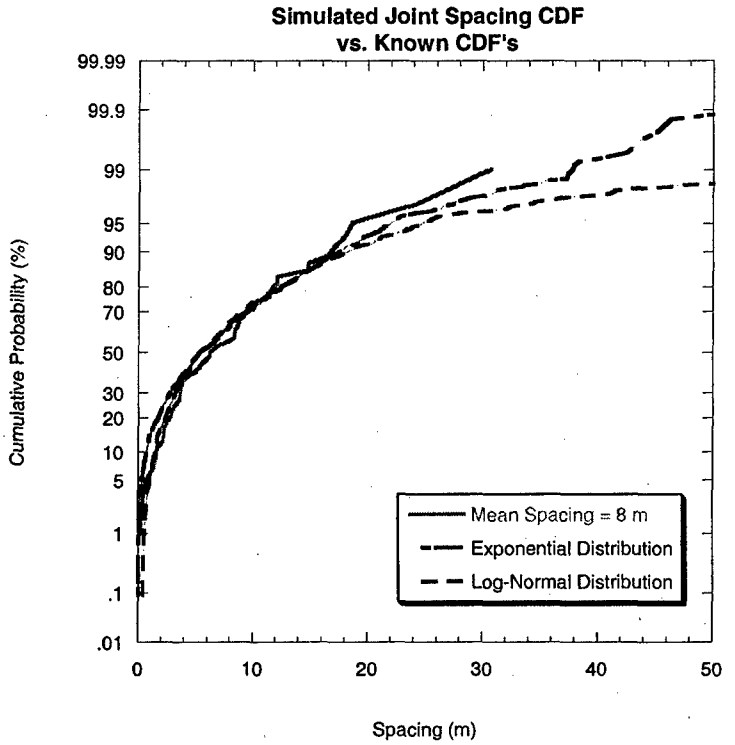


Figure 222 – Cumulative probability distribution comparison between a simulated joint pattern at low joint intensity (0.125 joints/m) and two known cumulative distribution forms (exponential and log-normal). Rejection procedure with saturation mechanism is used.

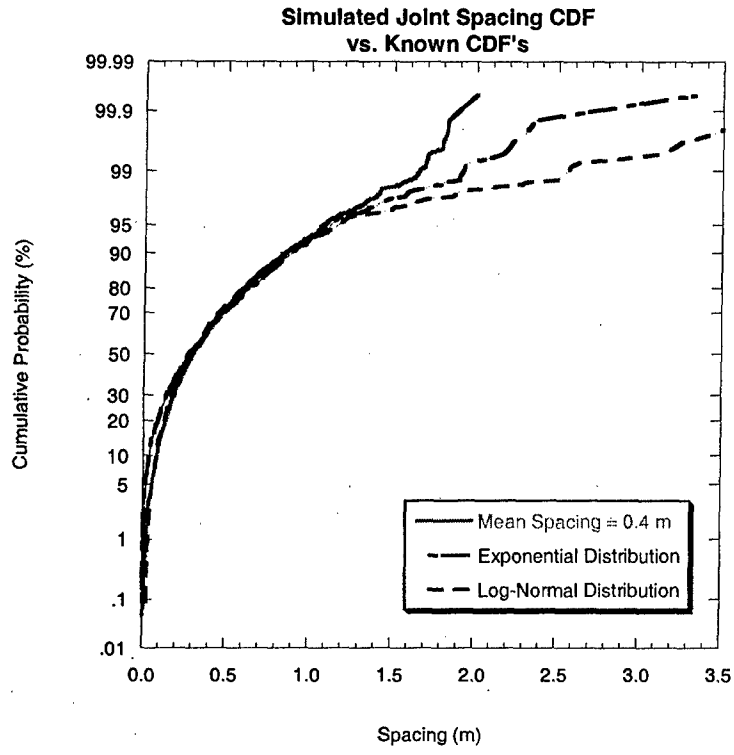


Figure 223 – Cumulative probability distribution comparison between a simulated joint pattern at medium-high joint intensity (2.5 joints/m) and two known cumulative distribution forms (exponential and log-normal). Rejection procedure with saturation mechanism is used.

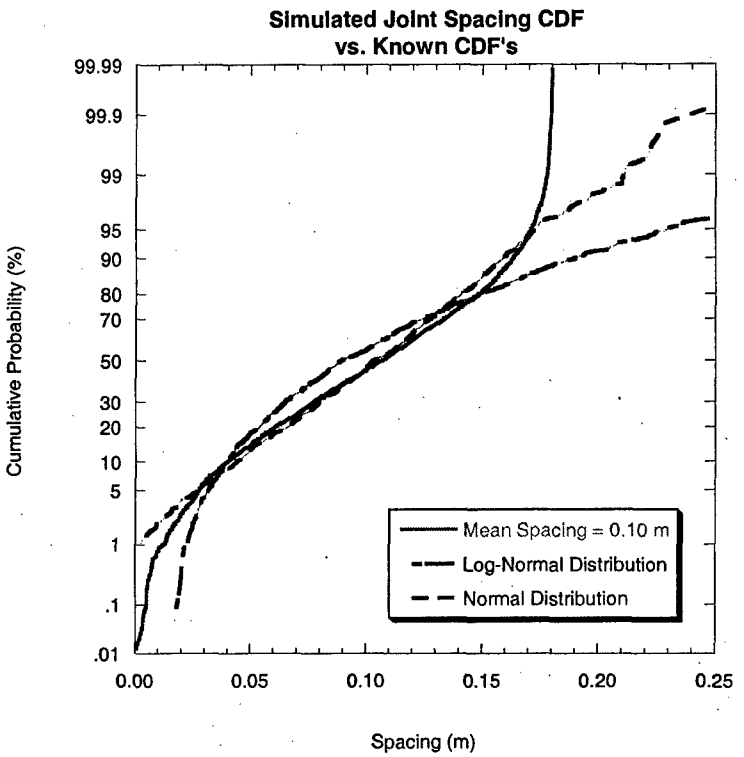


Figure 224 – Cumulative probability distribution comparison between a simulated joint pattern at saturation (10 joints/m) and known cumulative distribution forms (log-normal and normal). Rejection procedure with saturation mechanism is used.

Figure 225 to **Figure 227** show the evolution with increasing joint intensity of the joint spacing CDF when using the rejection procedure but without the saturation mechanism. These exhibit essentially the same behavior as the rejection procedure with the saturation mechanism except at intensities that would be near or at saturation (e.g., the joint intensity in **Figure 224**). Without the saturation mechanism, the joint spacing CDF does not resemble a normal or quasi-normal CDF (**Figure 227**). This makes sense because if a saturation mechanism were in place, the procedure would reject locations within critical segments but accept locations within non-critical segments. Accepting only the locations within non-critical segments allows the formation of segments with lengths near those of the critical segments as more joints are added, thereby causing the joint spacing distribution to resemble a normal or a quasi-normal distribution. Even with the saturation mechanism in place, the form of the joint spacing CDF does not change much with increasing joint intensity below saturation (**Figure 222** to **Figure 223**). **Figure 225** to **Figure 227** show that this behavior extends to even higher joint intensity if a saturation mechanism is not utilized. Another point regarding the rejection procedure is that there is not much difference between implementing or disregarding the saturation mechanism if one considers joint intensities below saturation as suggested by the joint spacing CDFs (i.e., **Figure 222**, **Figure 223** and **Figure 225**, **Figure 226**).

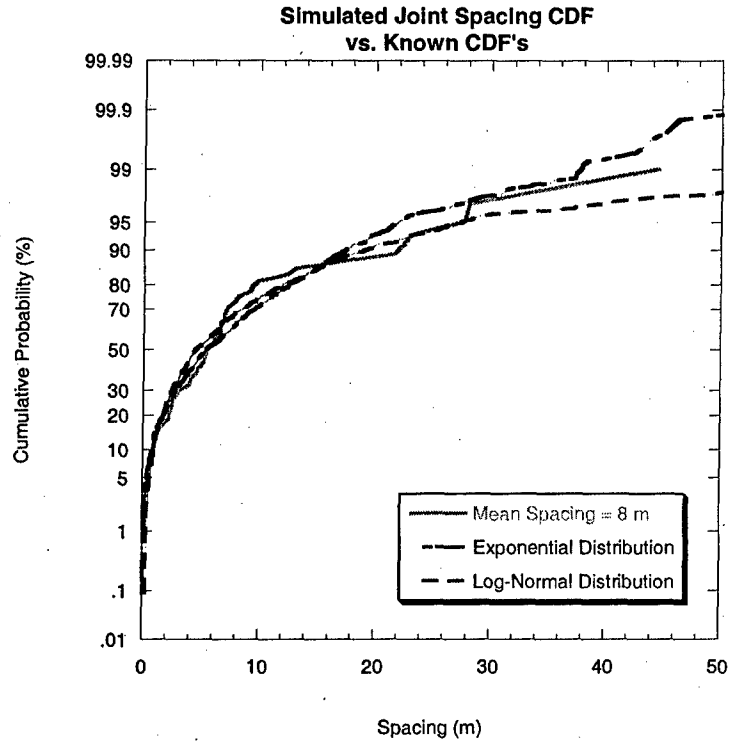


Figure 225 – Cumulative probability distribution comparison between a simulated joint pattern at low intensity (0.125 joints/m) and two known cumulative distribution forms (exponential and log-normal). Rejection procedure WITHOUT saturation mechanism is used.

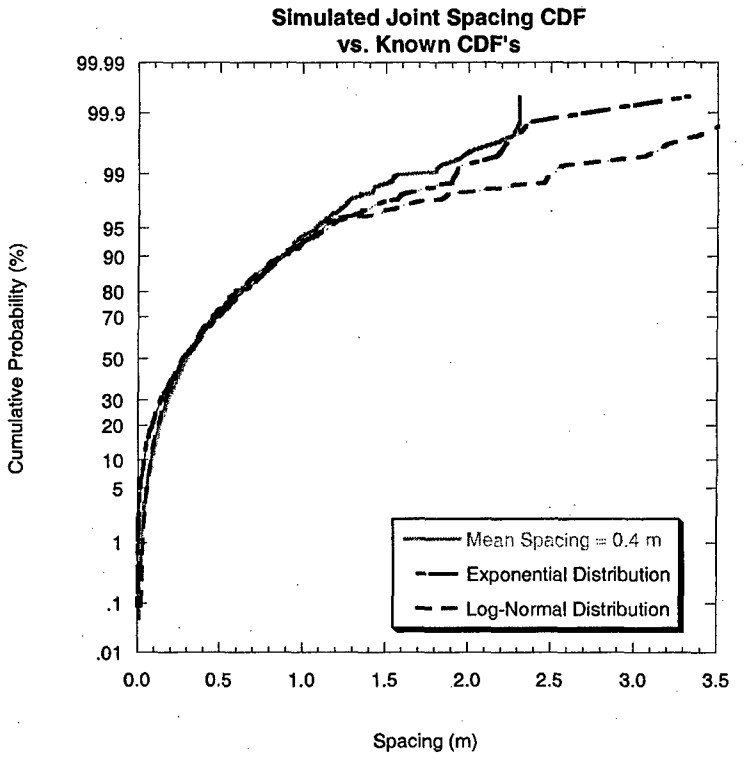


Figure 226 – Cumulative probability distribution comparison between a simulated joint pattern at medium-high joint intensity (2.5 joints/m) and two known cumulative distribution forms (exponential and log-normal). Rejection procedure WITHOUT saturation mechanism is used.

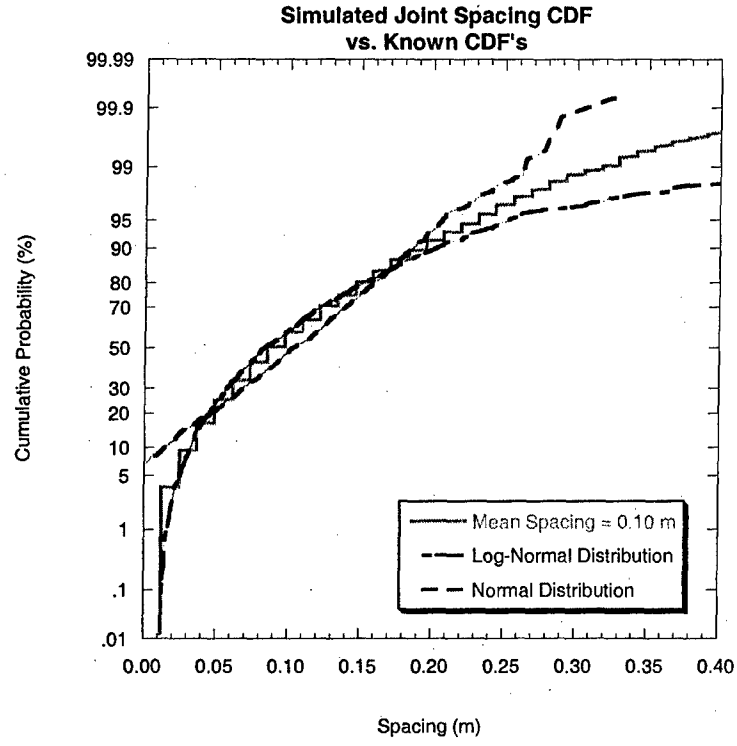


Figure 227 – Cumulative probability distribution comparison between a simulated joint pattern at high intensity (10 joints/m) and known cumulative distribution forms (log-normal and normal). Rejection procedure WITHOUT saturation mechanism is used.

In this section, it has been shown that the rejection procedure must rely on the saturation mechanism to cause a change in the form of the joint spacing distribution when intensity increases from medium-high close or equal to saturation. This is in contrast to the flaw model in which there was no considerable difference between the simulations with and without the saturation mechanism.

Next, the effects of the parameters of the probability density function, $f(x)$, on the resulting joint spacing distributions are studied given a fixed joint intensity.

6.3.4.2 Effect of Parameters in $f(x)$

Unlike the flaw model, the rejection procedure does not rely on direct comparison of tensile stress and tensile strength to determine the locations of new joints. Nonetheless, the rejection procedure is a probabilistic approach that is grounded in mechanics, nonetheless. The link to mechanical concepts is made through the probability density function of joint location, $f(x)$. The shape of this function relies on material properties ($\frac{E_f}{G_n}$) as well as layer geometry (d). Based on the assumption that a higher tensile stress leads to a higher probability density, the locations of new joints can be determined.

Here, the effects of the parameters in $f(x)$ on the joint spacing distribution for a fixed joint intensity are investigated. In all the simulations, the rejection procedure with saturation mechanism is used. **Figure 228** shows that the standard deviation of joint spacing decreases as the $\frac{E_f}{G_n}$ increases. This effect can be explained in much the same way as in the flaw model. The reason is because the function $f(x)$ is proportional to the tensile stress in the flaw model. This explanation is summarized in **Table 8**. In the joint spacing CDFs in (**Figure 229**), an increase in $\frac{E_f}{G_n}$ causes a slight decrease in the relative frequency of the smaller joint spacing values and an accompanying increase in the larger joint spacing values.

Table 8 – Summary of the effect of $\frac{E_f}{G_n}$ on the resulting joint spacing.

Value of $\frac{E_f}{G_n}$ in $q(x)$	Increase in Probability Density with Distance from Joints Forming the Segment	Portion of Segment Exposed to Larger Probability Density	Possible Locations of New Joints	Resulting Variance of Spacing
Small	Fast	Long	Many	High (wide joint spacing distribution)
Large	Slow	Short	Few	Low (narrow joint spacing distribution)

Figure 230 to **Figure 233** show that the shape of the joint spacing distribution changes, but not dramatically, with increasing $\frac{E_f}{G_n}$. The joint spacing CDF in **Figure 230** for an $\frac{E_f}{G_n}$ of 2.0 is closer to a log-normal distribution than the CDF in **Figure 233** for an $\frac{E_f}{G_n}$ of 40 even though joint intensity is the same. The exponential and normal probability distribution forms were left out in this case because the resemblance is not as close as that to the log-normal. Other probability distributions could be explored but it would not have the same benefit as a comparison with actual data.

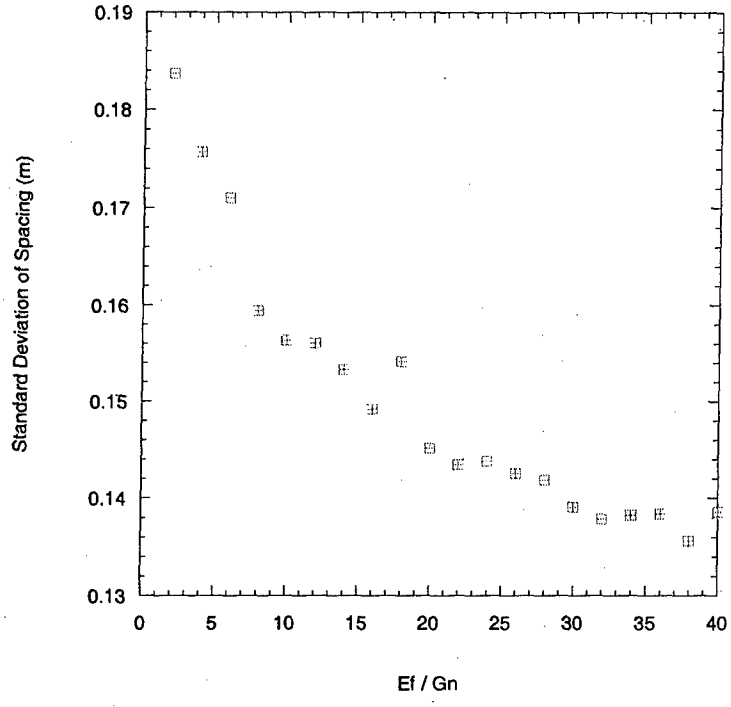


Figure 228 – Effect of the $\frac{E_f}{G_n}$ ratio on the standard deviation of spacing. All other parameters held constant and joint intensity is ~4.2 joints/m.

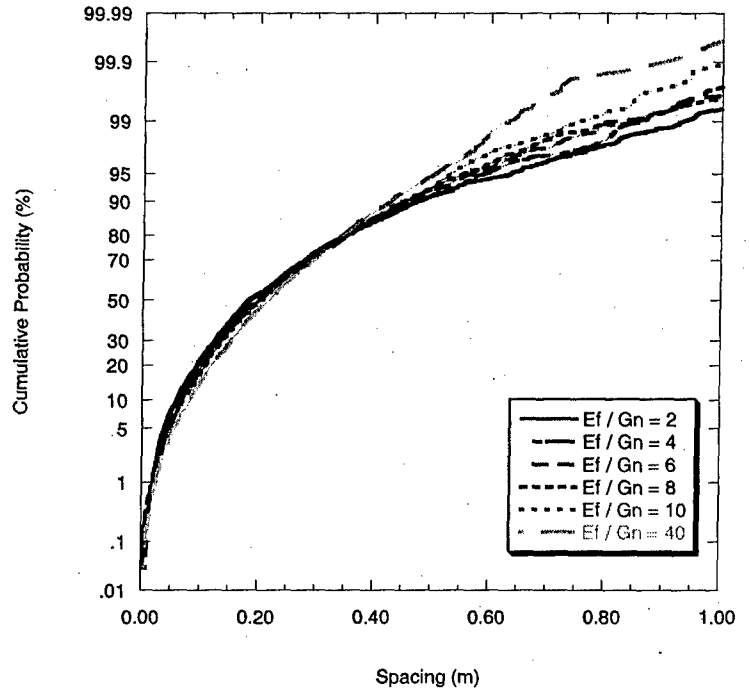


Figure 229 – Effect of $\frac{E_f}{G_n}$ ratio on the joint spacing CDF for the rejection procedure with saturation mechanism. All other parameters are fixed. Joint intensity is fixed at ~4.2 joints/m.

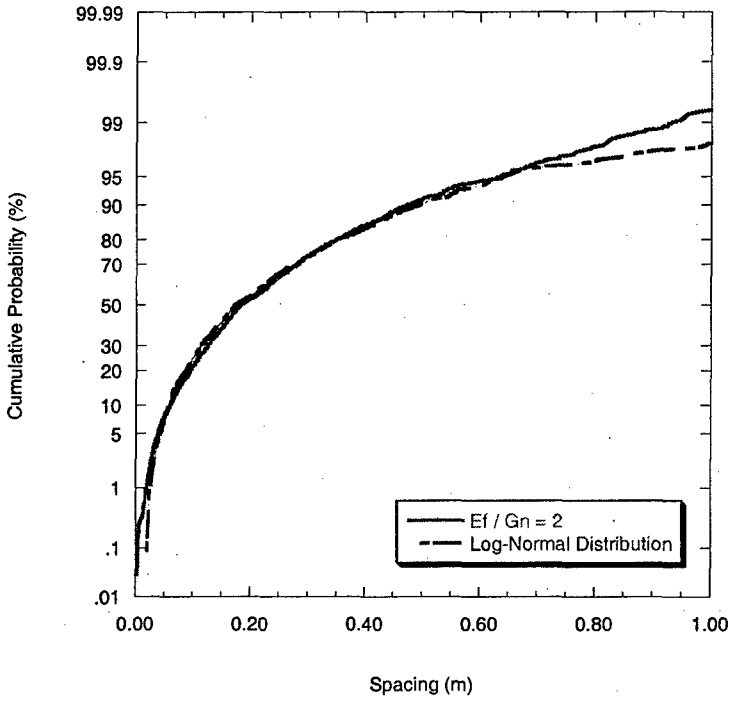


Figure 230 – Comparison between the joint CDF at $\frac{E_f}{G_n}$ = 2.0 in Figure 229 and the corresponding log-normal distribution obtained via maximum likelihood.

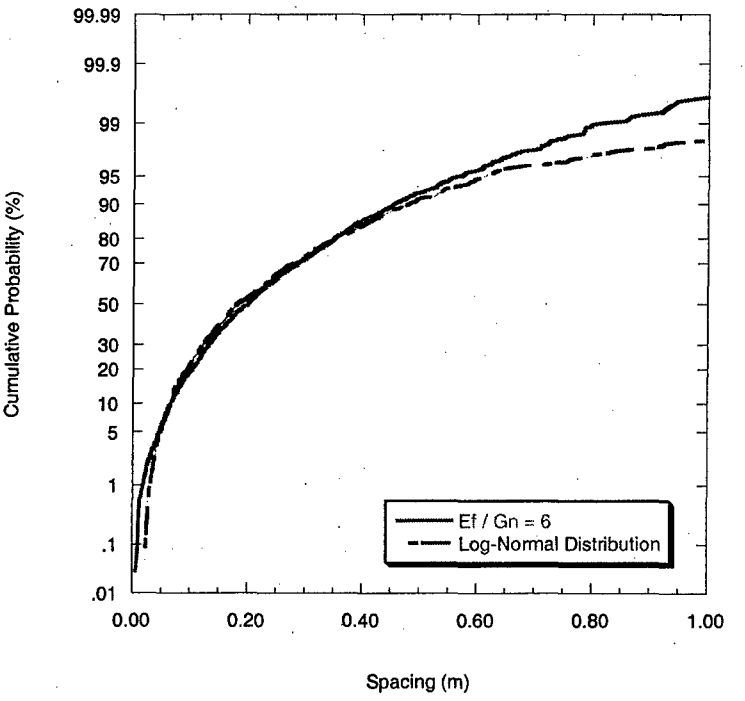


Figure 231 – Comparison between the joint CDF at $\frac{E_f}{G_n}$ = 6.0 in Figure 229 and the corresponding log-normal distribution obtained via maximum likelihood.

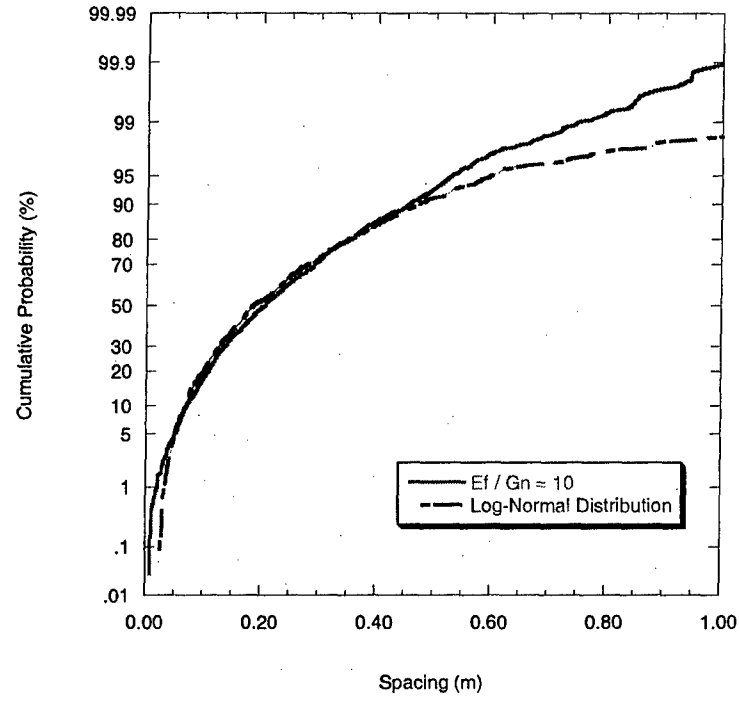


Figure 232 – Comparison between the joint CDF at $\frac{E_f}{G_n}$ = 10.0 in Figure 229 and the corresponding log-normal distribution obtained via maximum likelihood.

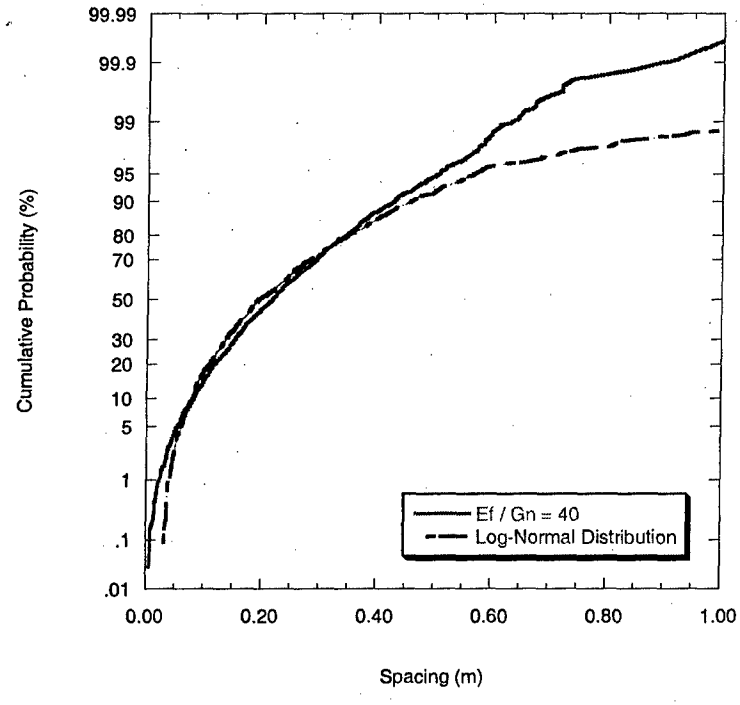


Figure 233 – Comparison between the joint CDF at $\frac{E_f}{G_n}$ = 40.0 in Figure 229 and the corresponding log-normal distribution obtained via maximum likelihood.

Figure 234 shows the effect of the non-jointing layer thickness on the standard deviation of spacing. It appears that a thicker non-jointing layer leads to a smaller standard deviation of spacing. Making use of the fact that $f(x)$ is proportional to the tensile stress in the flaw model, the explanation for this trend is given in **Table 9**. In **Figure 235**, the joint spacing CDFs show that an increase in the non-jointing layer thickness is accompanied by a decrease in the relative frequency of the smaller spacing values and an accompanying increase in the relative frequency of larger spacing values. This is the same effect as the $\frac{E_f}{G_n}$ ratio because they both influence the probability density function, $f(x)$, in very much the same way.

Table 9 – Summary of the effect of the non-jointing layer thickness on the resulting joint spacing.

Value of Non-Jointing Layer Thickness (d)	Increase in Probability density with Distance from Joints Forming the Segment	Portion of Segment Exposed to Larger Probability density	Possible Locations of New Joints	Resulting Variance of Spacing
Small	Fast	Long	Many	High (wide joint spacing distribution)
Large	Slow	Short	Few	Low (narrow joint spacing distribution)

Figure 236 to **Figure 239** show that the non-jointing layer thickness also affects the form of the joint spacing distribution even at the same joint intensity. The shape tends to become less and less log-normal especially at the larger spacing values as the non-jointing layer becomes thicker. The exponential and normal distributions were left out because the resemblance is better for the log-normal distribution.

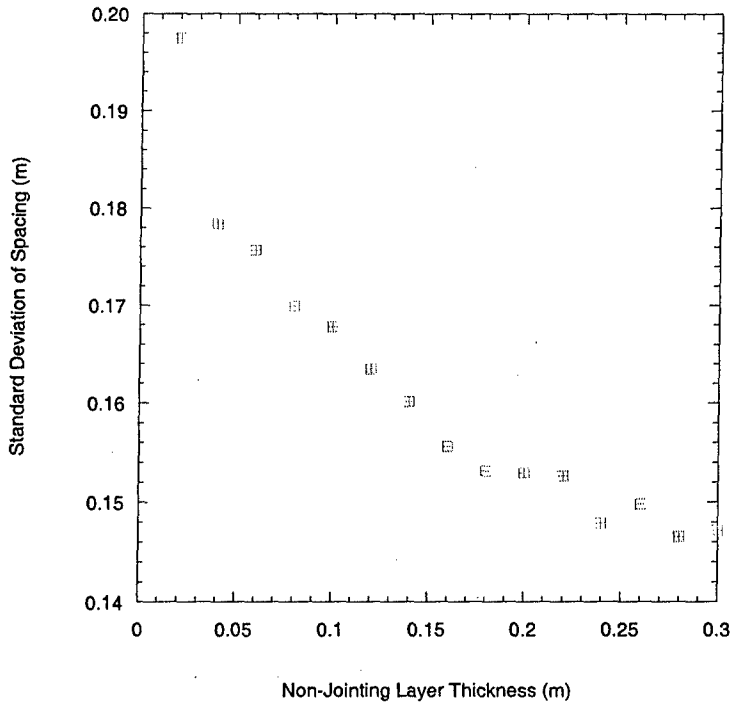


Figure 234 – Effect of the non-jointing layer thickness on the standard deviation of spacing. All other parameters held constant and joint intensity is ~4.2 joints/m.

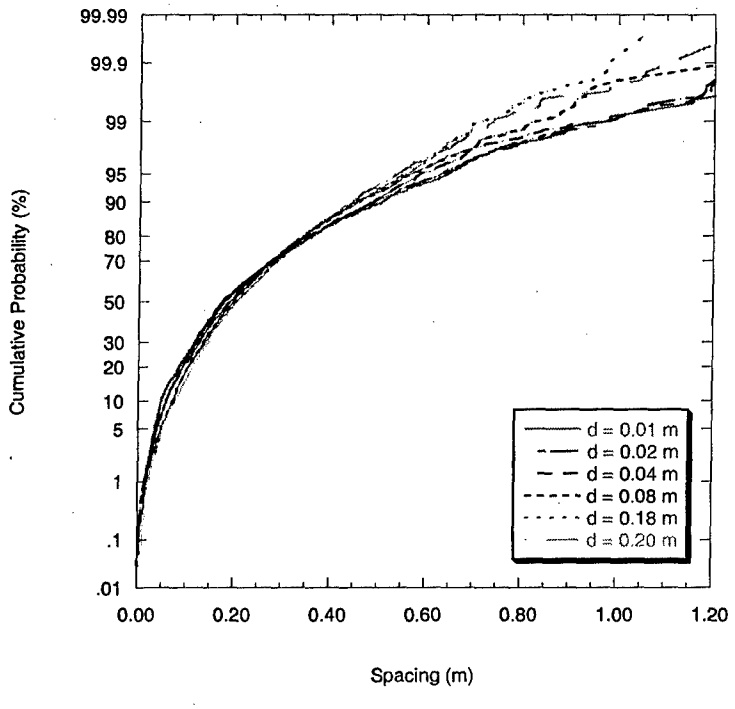


Figure 235 – Effect of the non-jointing layer thickness (*d*) on the joint spacing CDF for the rejection procedure with saturation mechanism. All other parameters fixed. Joint intensity is fixed at ~4.2 joints/m.

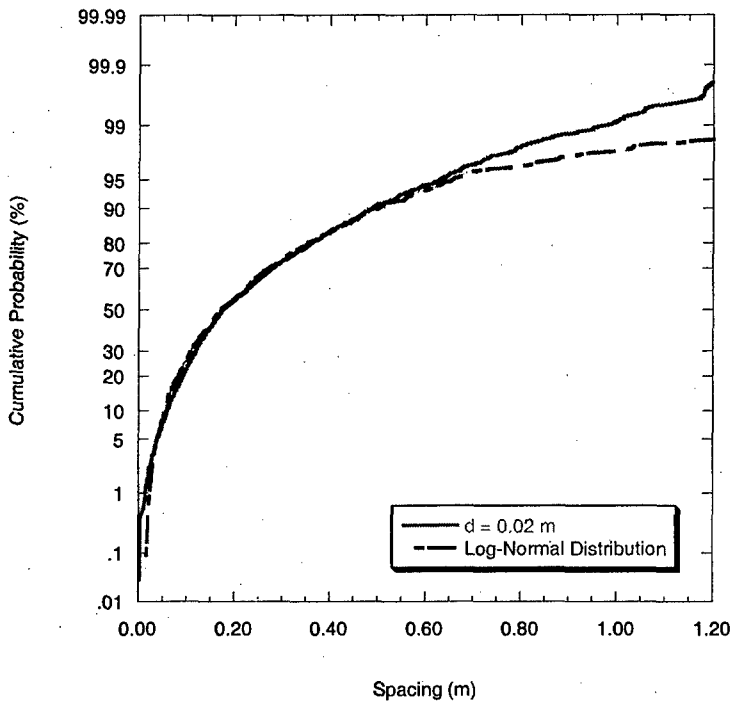


Figure 236 – Comparison between the joint CDF at d = 0.02 m in Figure 235 and the corresponding log-normal distribution obtained via maximum likelihood.

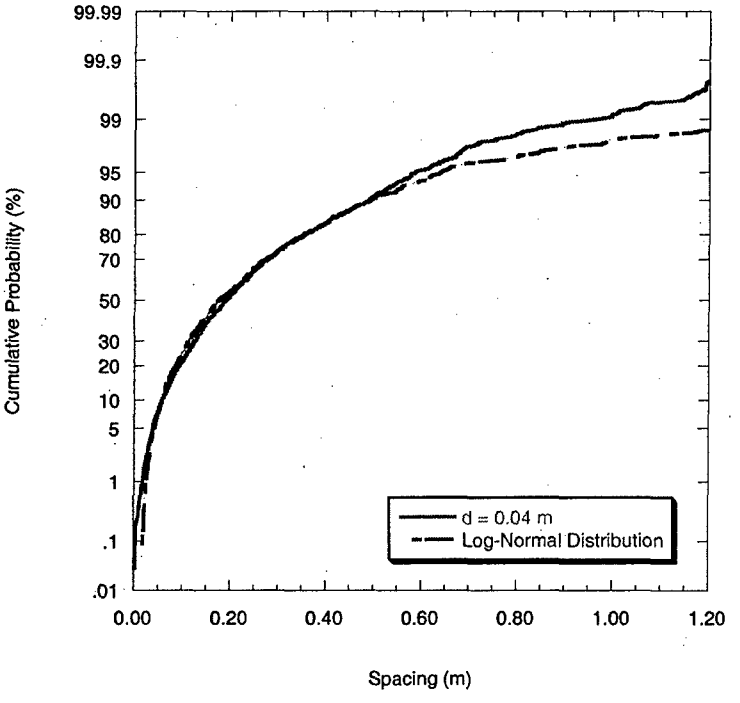


Figure 237 – Comparison between the joint CDF at d = 0.04 m in Figure 235 and the corresponding log-normal distribution obtained via maximum likelihood.

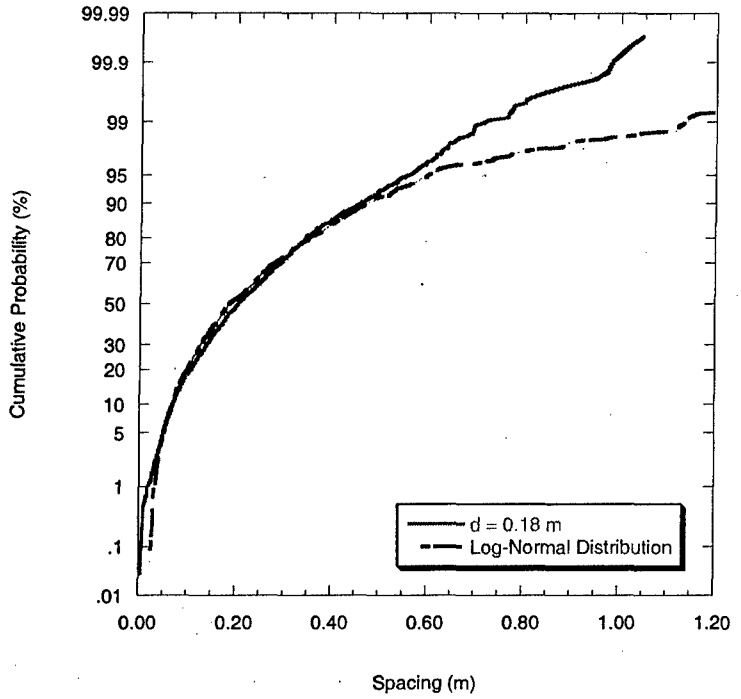


Figure 238 – Comparison between the joint CDF at d = 0.18 m in Figure 235 and the corresponding log-normal distribution obtained via maximum likelihood.

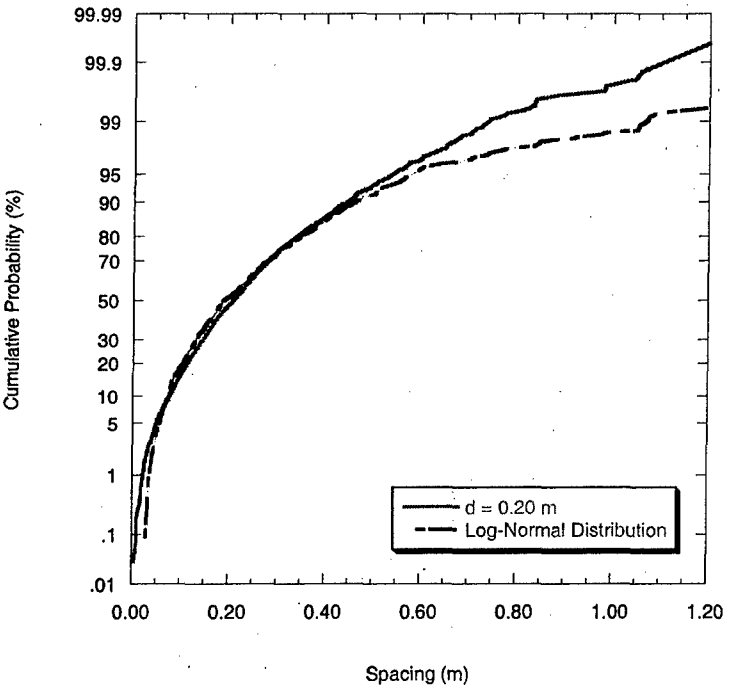


Figure 239 – Comparison between the joint CDF at d = 0.20 m in Figure 235 and the corresponding log-normal distribution obtained via maximum likelihood.

7 Comparison: New Models vs. Field Data

7.1 Introduction

In the previous section, the new flaw and rejection procedure jointing models were presented in an attempt to duplicate the pattern of layer-perpendicular joints in sedimentary rock. Saturation mechanisms which determine the stopping point of the jointing process were also incorporated into both models. The behavior of each model in terms of the joint spacing distribution with increasing joint intensity was demonstrated. In the flaw model, the effects of the stress distribution and strength models on the saturation mean spacing and the joint spacing distribution were also demonstrated. For the rejection procedure, the effect of the probability density function, $f(x)$, was also shown. Recall that the rejection procedure does not make use of an explicit strength model. Its use of a stress distribution model is mainly to define the probability density function, $f(x)$. New joint locations are then chosen based on this function. The flaw model and rejection procedure, when equipped with saturation mechanisms, appear to mimic the laboratory-observed evolution of joint spacing distribution in a brittle layer on a ductile substrate (Rives et al., 1992) with different degrees of success. The flaw model appears to produce joint spacing distributions that are more consistent with observations than the rejection procedure.

So far, the flaw model and rejection procedure results have only been compared to laboratory observations regarding the shape of the joint spacing distributions. The next step in the analysis of these models is direct comparison of the simulated joint spacing distributions with actual field data. This will help clarify the applicability of such simplified mechanisms of jointing to actual cases as well as determine their limitations. Four different cases will be used here and each will follow the structure of presentation below:

1. General Observations
2. Joint Spacing Data
3. Model Parameter Values
4. Simulation Results and Discussion

In essence, a summary of the data is first presented and then the model parameters are estimated. The results from model simulations are then compared with the field data. Comparative measures consist mainly of standard deviation and joint spacing cumulative probability (i.e., CDF). Model parameter estimation is problematic because there is a discrepancy between what is required in the models and what is reported in joint surveys. Field data normally consist of the following:

1. Jointing layer thickness – usually refers to bed thickness or MLT controlled by changes in lithology.

2. Non-jointing layer thickness – thickness of non-jointing bed, also controlled by changes in lithology; this is not typically reported.

3. Joint spacing or frequency – from this data the joint spacing distribution and the accompanying statistics can be calculated.

4. Scanline direction.

5. Joint orientation – strike and dip; also for this kind of jointing pattern, the joints of concern are perpendicular to bedding.

One must also note that different field workers collect different data. For example, some measure trace length but others do not. Also, people measure the same thing differently. For example, spacing may be areal or scanline. Additionally, some field workers are very explicit about how they collect data but others less so.

The models require the following:

1. Material properties – Young's moduli and Poisson's ratios of the jointing and non-jointing layers.

2. Layer geometry – thickness, uniformity of thickness (both jointing and non-jointing layers).

3. Extensional strain – provides the stopping point in the jointing process.

4. Type of saturation mechanism involved – either interface slippage or compressive stress development. Interface slippage is observable, compressive stress development is not.

5. Flaw density – this parameter controls the non-uniformity of the tensile strength of the jointing layer. Recall that the jointing layer without flaws is assumed to have uniform strength along its length and the presence of flaws reduces tensile strength at random points along the layer. This produces a jointing layer with what is effectively a non-uniform tensile strength along its length. Non-uniformity of tensile strength affects the resulting joint spacing distribution because it partly controls where new joints form. Without flaws, the locations of new joints are controlled entirely by the stress distribution which means that midpoint jointing will occur (i.e., maximum stress is at the midpoint of a segment). It has been shown that midpoint jointing does not lead to a realistic joint spacing distribution. As a result, a high concentration of flaws is required in order to avoid midpoint jointing.

It is clear from the above lists that there are significant differences between typical field data and those that are required in the model. Material properties usually require laboratory methods to determine. Strain estimates are impractical. As a consequence, a

number of assumptions need to be made on a case by case basis in order to estimate the values of the parameters required in the two new models. In the four comparisons that follow, general observations are presented first. These observations are mainly those of the fieldworkers themselves and additional information is taken from the literature. In each of the four cases, sections following the general observations (i.e., sections on Joint Spacing Data, Model Parameter Values, Simulation Results and Discussion) are mainly the result of new work unless noted otherwise. Sections named "Joint Spacing Data" contain analyses of the joint spacing data sets in each case. Sections named "Model Parameter Values" outline how the parameters of the flaw model and rejection procedure are estimated. Sections named "Simulation Results and Discussion" present the simulated spacing data and comparisons with the actual joint spacing data.

7.2 Case 1: Becker & Gross (1996)

7.2.1 General Observations

Becker and Gross (1996) gathered joint spacing data from a single flat-lying limestone/dolostone layer in the Gerofit Formation in Israel. The limestone/dolostone jointing layer is approximately of uniform thickness (18 ± 1.2 cm) and bounded by marlstone. Measurements were made along a scanline approximately 190 m long. Although at least four vertical joint sets can be found in the Gerofit Formation, Becker and Gross (1996) focused on the ~293°-striking joint set. The other prominent joint set strikes ~345° or ~165° (Eyal et al., 2001). Both of these sets dip vertically. Eyal et al. (2001) find that the ~293° and ~345° sets strike parallel to the trend of the maximum compressive stress directions associated with the Syrian Arc stress field (SAS) and the Dead Sea Transform stress field (DSS), respectively (**Figure 240**). **Figure 240** is not intended to demonstrate the abutting relationships between the ~293° and the ~345° or ~165° joint sets but merely to illustrate the difference in their orientations. The relationships among the maximum horizontal stress (S_H), the joint set orientation and the minimum and maximum extensional strains (ε_3 and ε_1, respectively) for the SAS are shown in **Figure 241**. The Syrian Arc stress field is older (Cretaceous to present) than the Dead Sea Transform stress field (Miocene to present). However, this does not necessarily mean that the joints associated with each stress field follow the same age relationship. In fact, according to Eyal et al. (2001), in the dolostone/limestone layer studied by Becker and Gross (1996), the ~293° is the first-formed joint set (note: Eyal et al., 2001 included the spacing data collected by Becker and Gross, 1996 in their study). In other layers in the same formation, the ~345° joint set is the first-formed joint set (e.g., Saltzman, 2001, later in this chapter). The difference between the two joint sets is not limited to orientation. Eyal et al. (2001) also observed that, generally, the joints belonging to the ~345° set are more closely-spaced than those belonging to the ~293° set.

No material properties were measured for the jointing and non-jointing layers. Many of the joints are filled with sparry calcite (Becker and Gross, 1996). However, they also noted that these were filled after the formation of the joint set. This is important because filling of joints during formation may change their mechanical behavior. Recall that Gross (personal communication, 2004) noted that closely spaced joints may result from mineralization because the mechanical behavior of existing joints is altered (i.e., the layer behaves much like intact rock). Another observation is that in locations where the top of the layer is exposed, joint trace length is much greater than joint height (typically the thickness of the layer; **Figure 242**). In this case, joint height is the same as the jointing layer thickness. The authors noted that no slippage has occurred between the jointing layer and the non-jointing layers. This indicates that either the interface slippage mechanism does not apply in this case or that the applied strain has not been enough to reach saturation and, therefore, not large enough to activate slippage between the layers. Becker and Gross (1996) also noted the existence of fracture zones along the length of the layer. These fracture zones were classified as either a fault zone or a joint zone. The locations of these fracture zones along the limestone/dolostone layer are shown in **Figure 243**. A fracture zone is typically composed of a single large discontinuity that spans

more than one layer (i.e., it is not confined to the jointing layer). If the discontinuity exhibits displacement along its surface (in this case, as evidenced by tectonic breccia) then it is classified as a fault zone (solid vertical lines in **Figure 243**, relative vertical displacement is also sketched). If it is purely an opening mode fracture, it is classified as a joint zone (dashed vertical lines in **Figure 243**). Along the layer being studied, there are four of each kind of fracture zone. These zones occur mainly in the middle portion of the measured layer. The joints in most of these zones could not be measured properly by the authors because of intense weathering. However, the authors were able to measure the joint spacing near one of the fault zones (the last fault zone going from left to right). Becker and Gross (1996) constructed a plot of the moving average of joint spacing with respect to location along the scanline and found that the mean spacing near the middle portion of the layer (i.e., adjacent to where the fracture zones are situated) is smaller than the mean spacing near the ends. This prompted them to believe that the strain in the middle portion of the layer is greater than that near the ends. They also believe that the through-going fracture zones functioned as some sort of saturation mechanism. Instead of adding more joints inside the jointing layer as strain was increased, some of the existing joints continued through to the adjacent layers. The stress reduction caused by these through-going joints precluded additional joint formation in the jointing layer. This may be a case of "apparent" saturation (Becker and Gross, 1996). The saturation is deemed apparent because the jointing layer could have taken on more joints if no through-going joints had developed.

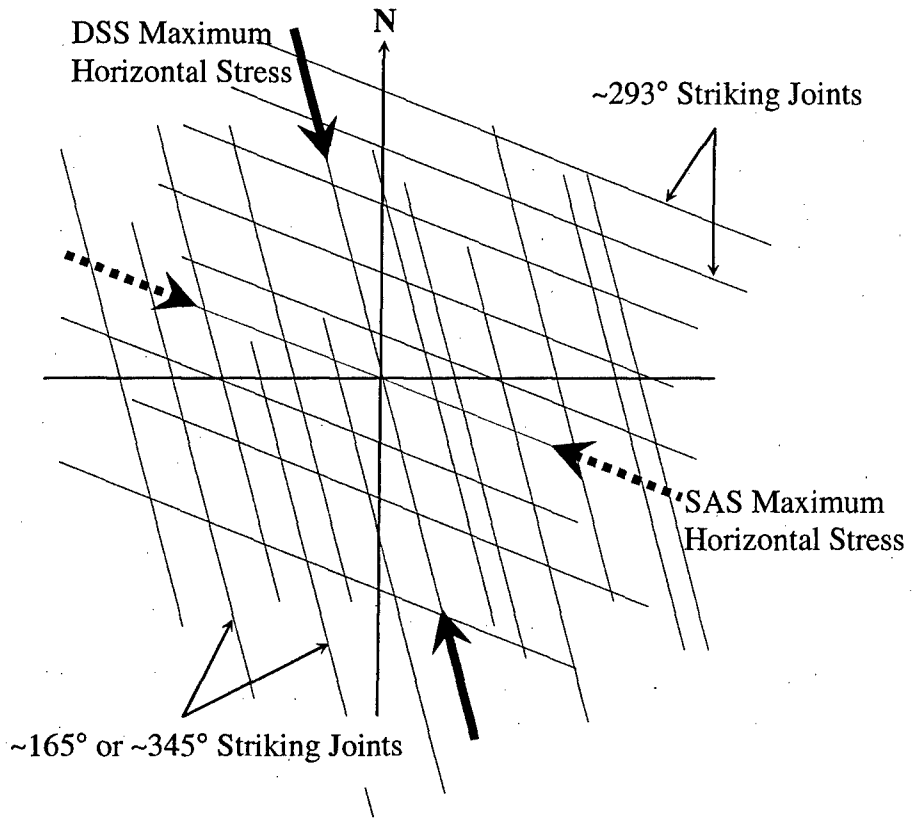


Figure 240 – Schematic of the two joint sets (~293° and ~345° or ~165°) superimposed. This figure is does not depict the actual abutting relationship between the two joint sets in layers where both are present. Sketched from information in Fig. 12 in Eyal et al. (2001).

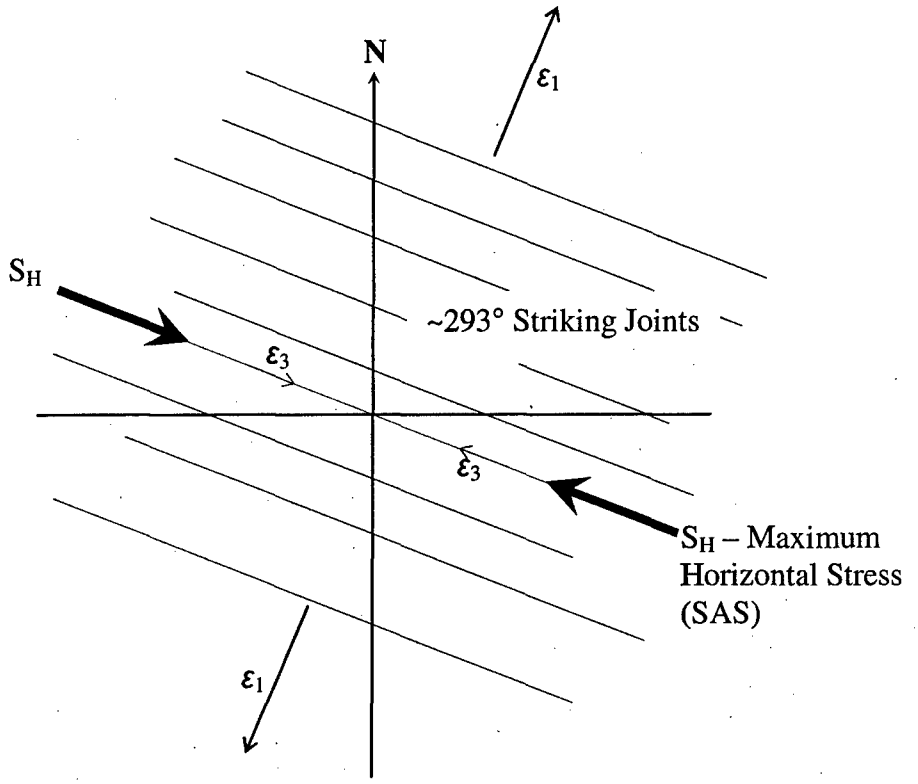


Figure 241 – Schematic of the relationship among the maximum horizontal (compressive) stress direction, the maximum extensional strain direction and the ~293° joint set orientation. Sketched from information in Fig. 12 in Eyal et al. (2001).

Next, the joint spacing data are presented for the four different sections. Note that measurements were not made along the entire length of the 190 m scanline. In fact, the sum of all spacing measurements is 117.2 m. The divisions in the spacing data are not solely based on the variation of the moving average of spacing. The divisions are also physical due to accessibility and weathering issues along the scanline. This clarification is important in order to avoid any impression that the four sections identified by Becker and Gross (1996) were made only by eye. It just so happens that the more highly jointed sections of the scanline are those which contain all the fracture zones that were observed (Becker and Gross, 1996).

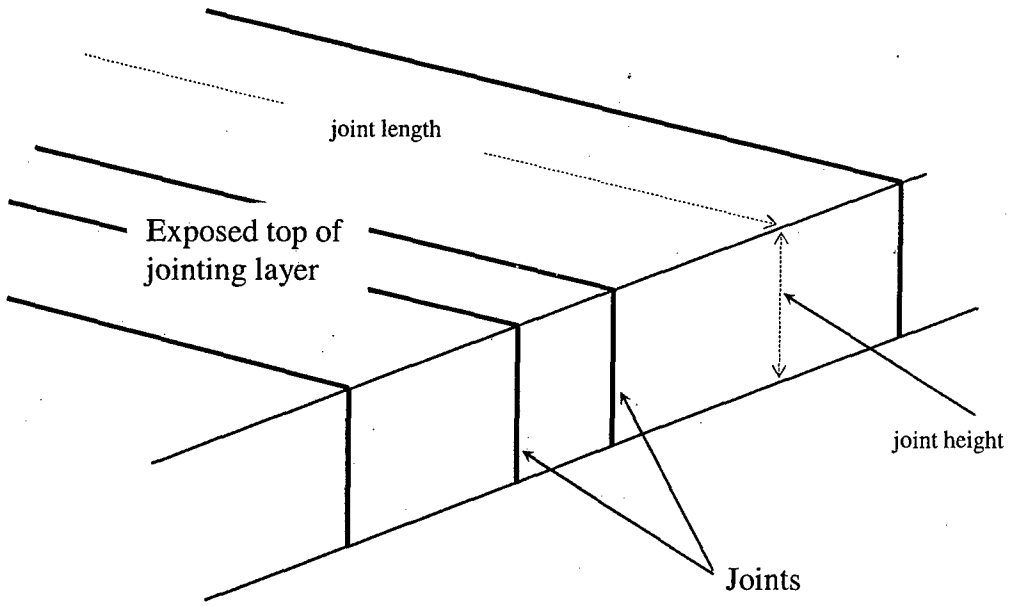


Figure 242 – Jointing layer with an illustration of joint height vs. joint length.

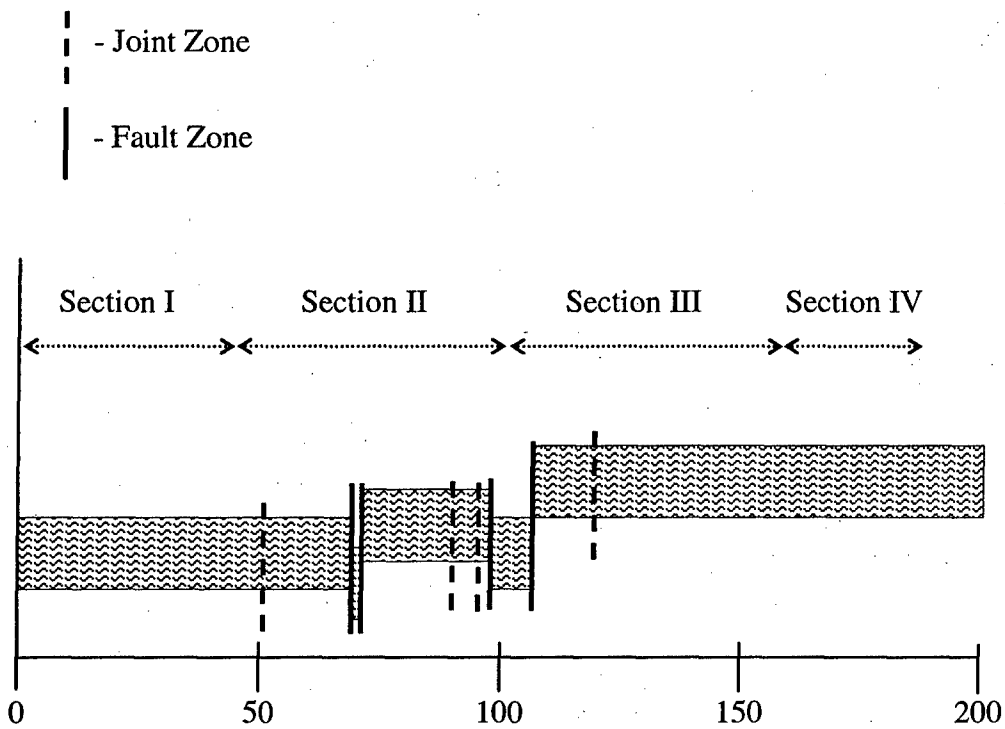


Figure 243 – Schematic of the joint and faults zones as well as the four different sections along the 190-m long scanline laid on the limestone/dolostone jointing layer in Becker and Gross (1996). Horizontal axis is shown to scale, vertical axis is not. For fault zones, relative displacement is also shown (magnitudes of these displacements are not to scale). Sketched from Fig. 7 in Becker and Gross (1996) but without the vertical scale.

7.2.2 Joint Spacing Data

Due to physical and measurement issues, the layer or scanline is divided by Becker and Gross (1996) into four parts as noted above (sections I, II, III and IV shown to scale in **Figure 243**). Note that spacing measurements were not made along the entire length of each section, only where it was possible (Becker and Gross, 1996). Note also that the fracture zones that were observed are located in sections II and III (**Figure 243**). Statistically, this also appears to be the appropriate procedure because the average joint spacing and standard deviation also vary according to these sections. **Table 10** shows a brief summary of the spacing data in each section. It is clear that sections II and III both have smaller mean joint spacing and standard deviation than sections I and IV. **Figure 244** shows the joint spacing histogram for the entire data set. It appears that the joint spacing distribution is best described by a log-normal distribution. **Figure 245** to **Figure 248** show the joint spacing histograms for each section (I to IV). Note that the spacing histograms from sections I and IV (the less strained portions) appear to be different from those in sections II and III (the more strained portions). Sections II and III appear to have log-normal joint spacing distributions (**Figure 246** and **Figure 247**) but Becker and Gross (1996) found, using statistical analysis, that this is not the case. On the other hand, they found that the histograms from sections I and IV (**Figure 245** and **Figure 248**) may be described by log-normal distributions. Hypothesis testing by the authors also revealed that the joint spacing in sections I and IV may come from the same distribution. Independent Chi-squared goodness-of-fit tests confirm these observations. Regarding the joint spacing histograms, one should note that a larger number of data generally leads to a more well-defined or complete distribution (compare **Figure 244** to histograms for each section). So a larger data set is generally more desirable than a smaller one.

Table 10 – Summary of joint spacing data and statistics for each section (Becker and Gross, 1996). Measurements are in m.

ACTUAL DATA	Section I	Section II	Section III	Section IV
Number of Spacing Data	110	237	271	94
Sum of Spacing Data	26.026	32.762	39.014	19.432
Mean	0.2366	0.1382	0.1440	0.2067
Standard Deviation	0.1496	0.0776	0.0931	0.1285
Skewness	1.068	0.993	1.218	1.084
Minimum	0.020	0.020	0.003	0.023
Maximum	0.750	0.397	0.670	0.640
Mean Spacing / Layer Thickness	1.31	0.77	0.80	1.15

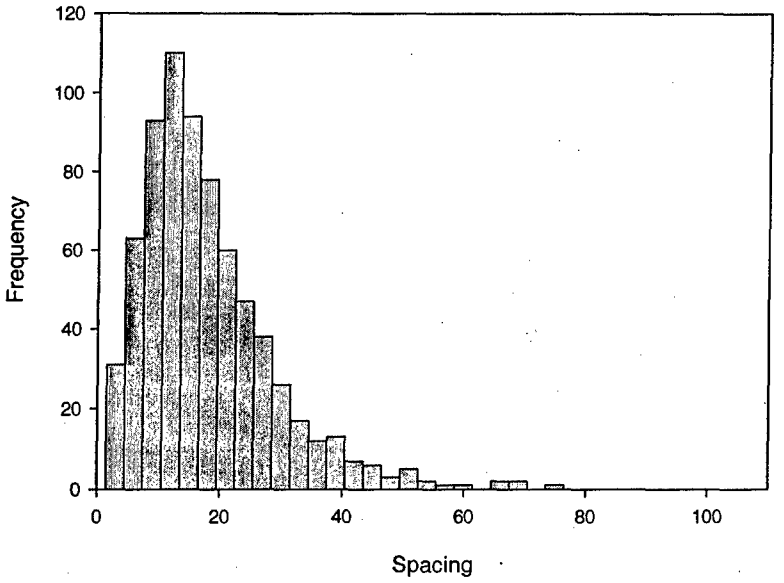


Figure 244 – Histogram of joint spacing data for the entire 190 m scanline (constructed from joint spacing data in Becker and Gross, 1996). Spacing is in cm.

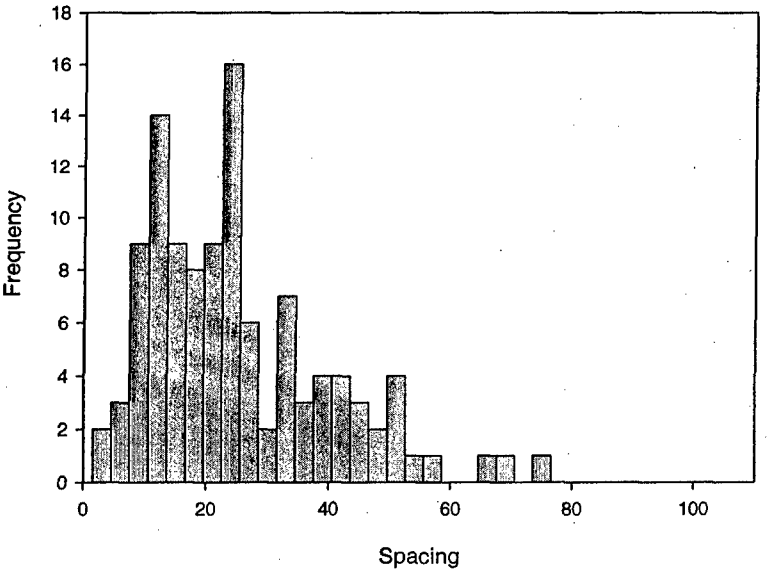


Figure 245 – Joint spacing histogram for section I (constructed from joint spacing data in Becker and Gross, 1996). Spacing is in cm.

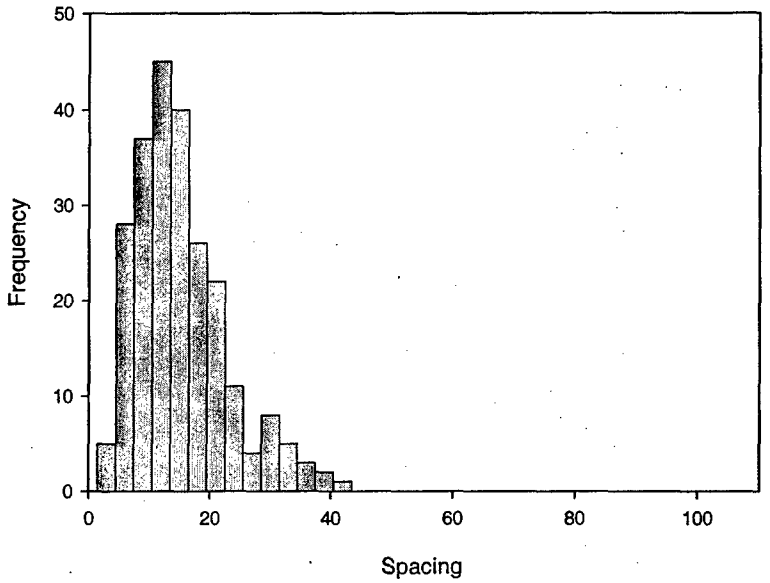


Figure 246 – Joint spacing histogram for section II (constructed from joint spacing data in Becker and Gross, 1996). Spacing is in cm.

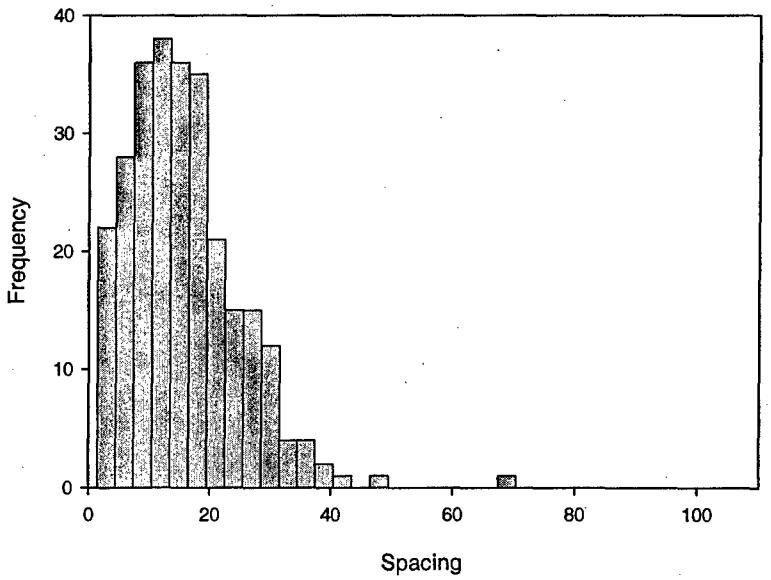


Figure 247 – Joint spacing histogram for section III (constructed from joint spacing data in Becker and Gross, 1996). Spacing is in cm.

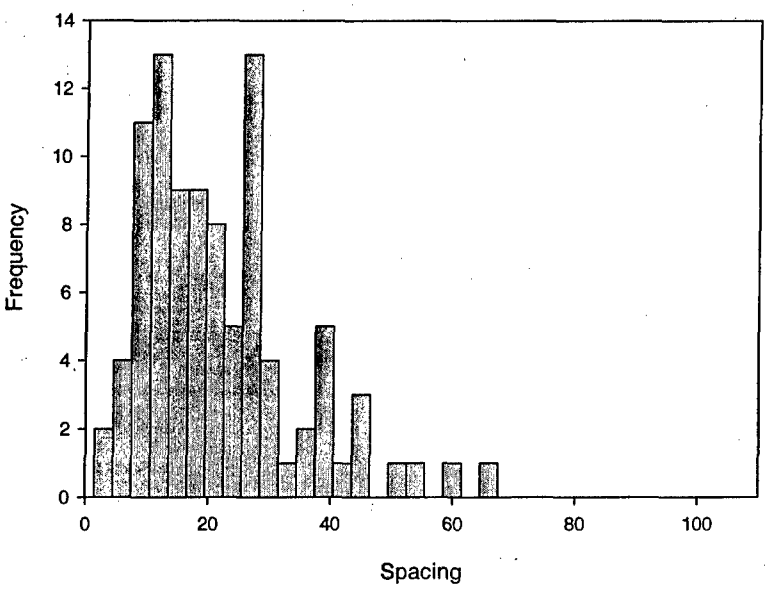


Figure 248 – Joint spacing histogram for section IV (constructed from joint spacing data in Becker and Gross, 1996). Spacing is in cm.

7.2.3 Model Parameter Values

Given the data and the physical observations, the model parameters will now be estimated. First, the observations must be translated into a form that can be used in the models. **Table 11** shows each field observation and its corresponding implications in the model. Also, as mentioned earlier, a high flaw density is used in order to avoid midpoint jointing which, from experience in an older model, leads to unrealistic joint spacing distributions.

Table 11 – Field observations by Becker and Gross (1996) and their corresponding implications in the model.

Field Observations	Model Implications
The jointing layer is limestone/dolostone bounded by marlstone. The limestone layer is approximately constant in thickness (18±1.2 cm) but the thickness of the marlstone was not measured. Photographs, however, suggest that the marlstone layer is approximately 5 cm thick.	Simulations can be performed using only a single value of layer thickness (18 cm). This helps reduce the number of simulations that need to be performed.
Length of joints is much greater than the height of joints (i.e., the jointing layer thickness). See **Figure 242** for illustration of joint length.	The use of a one-dimensional model may be reasonable. The flaw model and rejection procedure are both one-dimensional.
Eyal et al. (2001) indicate that the ~293° joint set is the first-formed joint set in the specific layer Becker and Gross (1996) investigated.	The effects of other joints on the formation of the ~293° joint set can be ignored.
No slip between jointing and non-jointing layers is evident.	The interface slippage saturation mechanism is not applicable.
There is variation in mean spacing along the layer. The middle portion appears to be more densely jointed than the ends. These divisions are both physical and statistical.	Each section can be modeled separately.
No strain measurements were taken.	A stopping point for the jointing process needs to be defined. The actual mean joint spacing may be used for this purpose. The actual standard deviation may also be used but utilizing the mean joint spacing is easier because it can only decrease with additional jointing. The behavior of standard deviation is less clear especially at the start of the jointing process.
Existence of through-going fractures in the form of fracture zones.	Through-going fractures are not handled in the model. However, an indirect implication is that their existence may suggest that the jointing layer is below saturation level.
Many joints are filled with sparry calcite.	Since the joints were filled after joint set formation, it does not affect the mechanical behavior of joints during the jointing process.
No material properties for the limestone/dolostone and marlstone layers were measured.	These material properties need to be estimated or obtained from other sources.

The above observations may aid in defining the modeling approach but still lack material property data. Fortunately, Saltzman (2001) studied joints in limestone/dolostone layers from the same formation but in a different area and measured some material properties. Four different layers of varying thickness were sampled and tested. Note that the samples consist of intact rock and did not include joints.

Static tests by Saltzman (2001) indicate that the Young's modulus of the limestone/dolostone layer ranges from 40 to 50 GPa. Dynamic testing was also performed in order to capture more of the variation in the Young's modulus due to porosity and grain size (Saltzman, 2001). The results of the dynamic tests are summarized in the histogram in **Figure 249**. The Young's modulus ranges from about 30 GPa to 80 GPa. Since most of the samples had Young's moduli around 50 GPa; this value will be used in the model simulations.

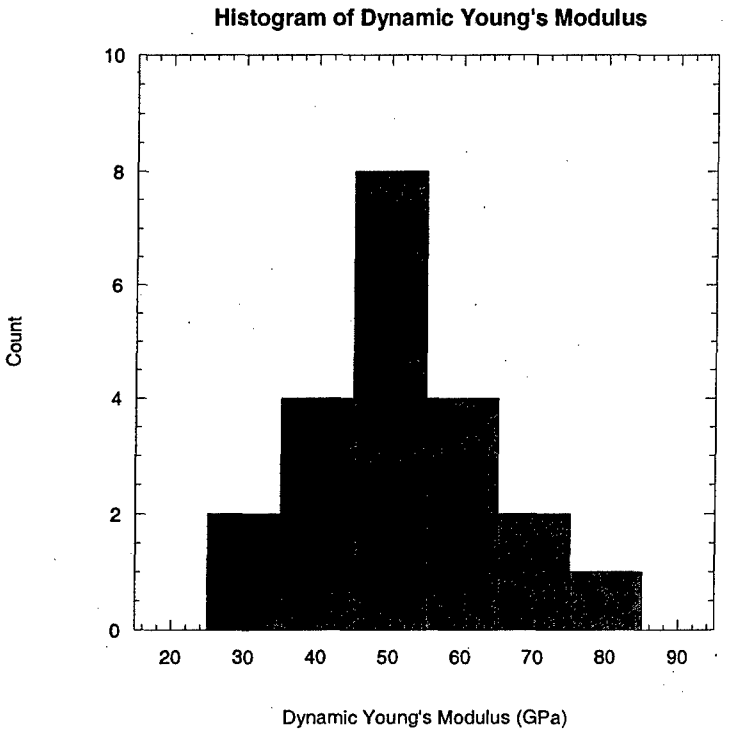


Figure 249 – Histogram of dynamic Young's Modulus (constructed from data in Saltzman, 2001).

As for the $\frac{E_f}{G_n}$ ratio, the material properties of the marlstone are needed. No measurements were made for this particular marlstone. Available data from the literature indicate that marlstone may have a Young's modulus between about 21.0 and 25.0 GPa. For Poisson's ratios between about 0.15 and 0.25, this leads to shear modulus values between 8.0 and 11.0 GPa. Assuming that the Young's modulus of the limstone/dolostone layer is 50 GPa, this leads to $\frac{E_f}{G_n}$ values that range from about 4.5 to about 6.25. A range of 3.0 to 6.0 for $\frac{E_f}{G_n}$ is used in the simulations as it appears to be reasonable for this case.

Saltzman (2001) also performed tensile strength tests on the limestone/dolostone samples from the four layers. **Figure 250** shows the histogram of tensile strength data. The tensile strength values of intact samples range from about 4.0 MPa to 10.0 MPa (Saltzman, 2001). The limited sample appears to have an approximately uniform probability distribution between these two values. This set of data provides a good starting point with regard to strength ranges as well as the shape of the strength probability distribution.

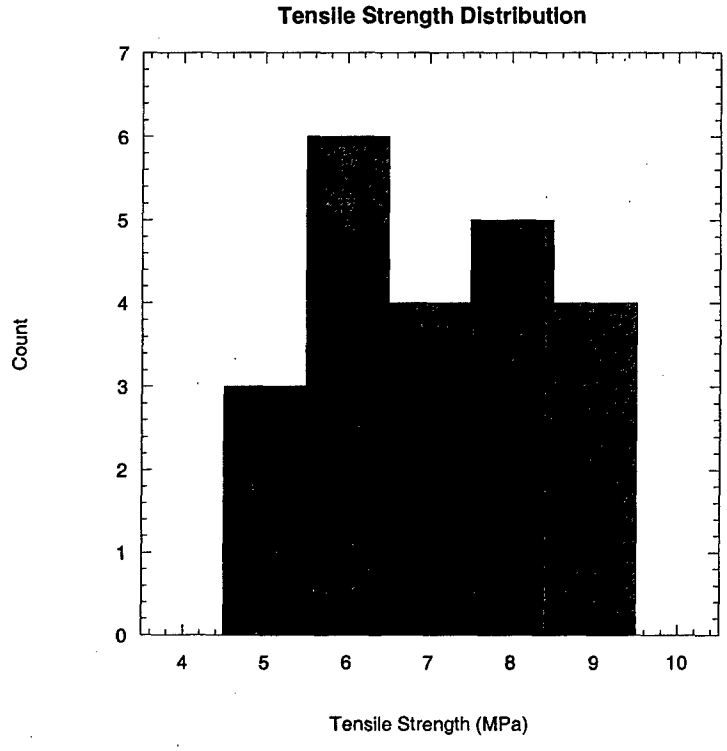


Figure 250 – Histogram of tensile strength (constructed from data in Saltzman, 2001).

Using the observations in **Table 11** and the material property data from Saltzman (2001), the simulations and comparisons can now be performed.

7.2.4 Simulation Results and Discussion

Given the parameter estimates in the previous section, a comparison between the field spacing data and simulated joint spacing data can now be performed. First, this comparison will be done using the flaw model and then using the rejection procedure. Two aspects of the simulated spacing data are then compared to the actual data: the joint spacing standard deviation and the joint spacing cumulative probability (or joint CDF).

7.2.4.1 Flaw Model Results

Uncorrelated Strength Model

The first issue to resolve before making this comparison is whether or not the jointing layer is at saturation with respect to jointing. This will help in the assessment of the flaw model performance. If the actual mean joint spacing is below the predicted value of the saturation mean spacing (SMS) then the model may not perform very well. Such a result may suggest that the actual jointing pattern is not the result of remote extension alone. Other jointing mechanisms may have already caused additional jointing in addition to the remote extension. One must also note that a range of SMS values must be considered because of the uncertainty in the material property and strength data that are available. This means that a number of simulations need to be run using different combinations of parameter values in order to get a reasonable range of SMS values. The parametric studies on the SMS in the previous chapter may provide useful in reducing the number of these simulations. Specifically, the following behavior was observed:

1. The SMS increases with increasing $\frac{E_f}{G_n}$. Recall also that the $\frac{E_f}{G_n}$ factors into both the stress distribution model (e.g., Ji et al., 1998) and the critical spacing-to-thickness ratio (specifically, as the ratio $\frac{E_f}{E_n}$ in Bai and Pollard, 2000). A larger $\frac{E_f}{G_n}$ or $\frac{E_f}{E_n}$ ratio leads to a larger $\left(\frac{s}{t}\right)_{cr}$ which, in turn, leads to a larger SMS. At the same time, a larger $\frac{E_f}{G_n}$ means that the tensile stress recovers slowly with distance from a joint (**Figure 251**). This means that a shorter portion of a segment is exposed to high stresses thereby limiting the possible location of new joints toward the middle of the segment. This leads to less jointing because segments are divided more quickly into smaller ones that are likely below the critical spacing.

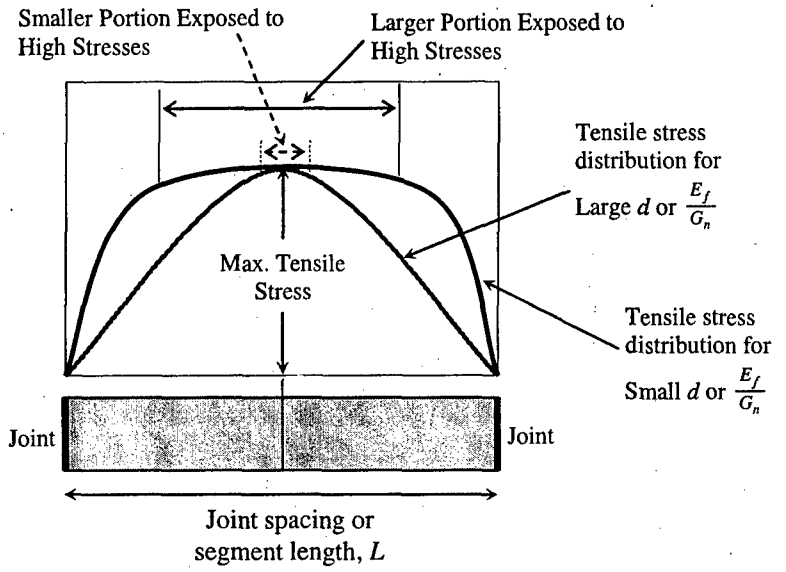


Figure 251 – Shape of the tensile stress distribution for small and large $\frac{E_f}{G_n}$ or d values.

2. The SMS increases with increasing non-jointing layer thickness, d. The non-jointing layer thickness does not influence the critical spacing-to-thickness ratio. However, its effect on the stress distribution is the same as that of the $\frac{E_f}{G_n}$ ratio and its consequent effect on the SMS can be explained in much the same way (**Figure 251**).

3. The SMS increases with decreasing D which represents relationship between the Poisson's ratios of the jointing and non-jointing layers in the following manner:

$$D = \frac{(1-2\nu_f)(1+\nu_f)-(1-2\nu_n)(1+\nu_n)}{(1-\nu_f^2)+(1-\nu_n^2)}$$

where ν_f and ν_n are the Poisson's ratios of the jointing and non-jointing layers, respectively. D is positive if $\nu_f < \nu_n$ and negative if $\nu_f > \nu_n$. Numerical simulations by Bai and Pollard (2000) showed that the critical spacing-to-thickness ratio is affected by the $\frac{E_f}{E_n}$ (or $\frac{E_f}{G_n}$) ratio and D in the following manner:

$$\left(\frac{S}{t}\right)_{cr} = \alpha\left[0.792+0.328\left(1-\exp\left[-0.824\left(\frac{E_f}{E_n}-0.0025\right)^{0.824}\right]\right)\right]$$

where

$$\alpha = \frac{0.976 - 0.302D - 0.129D^2 + 0.117D^3}{0.976}$$

Note that this factor, α, increases with decreasing D.

4. The SMS increases with decreasing flaw density. This makes sense because low flaw density will promote midpoint jointing. In other words, the jointing layer will effectively have uniform tensile strength so jointing occurs at the location of maximum tensile stress which is the midpoint between two joints. It has been explained that midpoint jointing is a quicker way to produce segments having lengths below the critical spacing, $t \cdot \left(\frac{s}{t}\right)_{cr}$ (e.g., **Figure 251**) than non-midpoint jointing. However, at high flaw densities, any increment of flaw density should not have a significant impact on the SMS. This insignificant effect of an increment of flaw density at high flaw densities was shown in the chapter 6.

5. The SMS is <u>not affected</u> by the ratio between the maximum and minimum tensile strength values. This makes sense because for the compressive stress development saturation mechanism, there is no limit to the tensile stress that can be developed within a segment as long as its length is above the critical spacing. Therefore, it does not really matter what the tensile strength values at the flaws are because segments longer than the critical spacing will always be able to attain stresses equal to them. The same is not true of the interface slippage saturation mechanism where the tensile stresses are limited by the interface shear strength.

In the SMS simulations, the non-jointing layer thickness (d), $\frac{E_f}{G_n}$ ratio, and D are varied. Recall that both d and $\frac{E_f}{G_n}$ affect the tensile stress distribution whereas D and also $\frac{E_f}{G_n}$ affect $\left(\frac{s}{t}\right)_{cr}$. The SMS simulations are done at different flaw densities.

In order to determine if joint saturation has occurred, it is not sufficient to compare the mean or median actual joint spacings to the critical joint spacing, $t \cdot \left(\frac{s}{t}\right)_{cr}$, as Bai and Pollard (2000) suggest. Remember that the critical spacing is the spacing at or below which no further jointing under this mechanism can occur. However, it is quite possible that segments shorter than $t \cdot \left(\frac{s}{t}\right)_{cr}$ exist as a product of the division of segments longer than $t \cdot \left(\frac{s}{t}\right)_{cr}$! Therefore, one can reason that jointing layers at or near saturation should have a mean or median spacing smaller than $t \cdot \left(\frac{s}{t}\right)_{cr}$ because anything longer than this will have already been jointed. For the same reason, the maximum spacing at saturation should be less than or equal to $t \cdot \left(\frac{s}{t}\right)_{cr}$. The question now becomes how much smaller than $t \cdot \left(\frac{s}{t}\right)_{cr}$ should one expect the mean spacing to be? First, the range of values that $\left(\frac{s}{t}\right)_{cr}$ can take is determined. Using the equation for $\left(\frac{s}{t}\right)_{cr}$ and figuring that $1 < \frac{E_f}{E_n} < \infty$ and $-0.5 < D < 0.5$, it is found that $0.8 < \left(\frac{s}{t}\right)_{cr} < 1.2$. The flaw model is then used to run

simulations while varying the non-jointing layer thickness, the $\frac{E_f}{G_n}$ ratio and D. Note that changing $\frac{E_f}{G_n}$ and D also changes $\left(\frac{s}{t}\right)_{cr}$. These simulations show that, for the various parameter value combinations, the saturation mean spacing (SMS) ranges from about 65% to 70% of the calculated critical joint spacing or:

$$SMS = (0.65 - 0.70)t \cdot \left(\frac{s}{t}\right)_{cr} \qquad \textbf{Equation 73}$$

Substituting $t = 0.18\,\text{m}$ and the minimum and maximum values of $\left(\frac{s}{t}\right)_{cr}$, one finds that the saturation mean spacing ranges from **0.094 m** to **0.151 m** for this particular case. Looking at the actual mean spacing values from Becker and Gross (1996) (**Table 12**), one finds that there is a possibility that sections II and III may be at or near saturation. On the other hand, sections I and IV have mean joint spacing that are greater than the calculated saturation mean spacing values. This information may be of use later in the assessment of the performance of the flaw model when the simulated spacing data are compared with the actual.

Table 12 – Actual mean spacing values from Becker and Gross (1996) data. Measurements are in m.

ACTUAL DATA	**Section I**	**Section II**	**Section III**	**Section IV**
Mean	0.2366	0.1382	0.1440	0.2067

So far, the SMS simulations have indicated the possibility that sections II and III may be at saturation or close to it. If the sections are below saturation, then the parameters that did not affect the joint spacing at saturation may actually have an effect. For example, the ratio between the maximum and minimum tensile strength will have an effect on the spacing below saturation. In **Figure 250**, it was shown that tensile strength could have a uniform probability distribution with a minimum of 4.0 MPa and a maximum of 10.0 MPa. This serves as a starting point for the range of tensile strength in the simulations. The following parameter values will also be used in the simulations:

1. Jointing layer thickness = 0.18 m (actual measurement).

2. Non-jointing layer thickness ~ 0.05 m (scaled from a photograph).

3. Young's modulus of jointing layer ≈ 50000 MPa (from Saltzman, 2001).

4. $\frac{E_f}{G_n}$ ranges from 3.0 to 6.0. This represents a reasonable range of values for a limestone/dolostone jointing layer with marlstone bounding layers.

5. Poisson's ratio for limestone/dolostone jointing layer is assumed to be 0.25 and 0.30 for the marlstone non-jointing layer. The Poisson's ratios affect the $\left(\frac{s}{t}\right)_{cr}$ used in the simulations.

Another consequence of the sections being below saturation is that a stopping point for the jointing process must be indicated. In this case, the actual mean spacing can be used. In the following simulations, the jointing process stops when the simulated mean spacing reaches the actual mean spacing. Two elements are then studied: the standard deviation of joint spacing and the joint spacing cumulative probability. An attempt to include skewness was made but it was realized that the skewness varies so much from one simulation to another that it would be impossible to obtain a value that would be representative for a given set of input parameters. It would also be unreasonable to expect that the actual joint spacing skewness is representative of the skewness for some level of jointing. Also, when comparing simulated to actual joint spacing distributions, CDF plots are used instead of histograms because they are easier to compare visually. Note, however, that a histogram can show details about the distribution that may not be clear in a CDF. Be reminded also that the simulation results that follow are from the flaw model with saturation mechanism.

Section I

Figure 252 shows the standard deviation vs. $\frac{E_f}{G_n}$ relationship for section I for two different ranges of tensile strength. In these flaw model comparisons, the strength at the flaws is assumed to have a uniform probability distribution between a minimum and maximum value (as suggested by the Saltzman, 2001 data). The first range is that which is suggested by the Saltzman (2001) data. This is then increases by 2.0 MPa in both directions. **Figure 252** shows that the standard deviation of joint spacing is sensitive to this change in strength range. The wider tensile strength range produces higher standard deviation values that are closer to the actual value (~ 0.15 m) for reasonable $\frac{E_f}{G_n}$ ratios (3.0 to 6.0).

Using these two tensile strength ranges, the joint spacing CDFs for section I were also generated using the reasonable range of $\frac{E_f}{G_n}$ ratios. **Figure 253** shows the actual vs. simulated joint spacing CDFs for a tensile strength range between 4.0 MPa and 10.0 MPa. This range of tensile strength is obtained from Saltzman (2001). **Figure 253** shows that for the range of $\frac{E_f}{G_n}$ ratios used, the simulations underestimate the number of small spacing data and overestimate the number of large spacing data. The simulated joint spacing CDFs lie below the actual at small spacing values and above the actual at large spacing values. Basically, the flaw model does not represent the actual joint spacing distribution well for this tensile strength range. Kolmogorov-Smirnov (K-S) testing accepts the hypothesis that the actual data and the simulated spacing data come from the same distribution (i.e., **hypothesis** H_0) at the 0.05 level only for $\frac{E_f}{G_n} = 3.0$ in **Figure 253**.

Figure 254 compares the actual joint spacing CDF with the simulated CDFs using a range of $\frac{E_f}{G_n}$ ratios but now with a slightly wider range of tensile strength (2.0 to 12.0 MPa). It shows a better agreement between the actual joint spacing CDF and the

simulated data than that demonstrated in **Figure 253** although there is still a very small underestimation for smaller spacings (**Figure 254**). This also coincides with the improvement in the simulated standard deviation of spacing that was shown in **Figure 252**. There is also not much difference in the simulated curves for the different $\frac{E_f}{G_n}$ ratios. K-S testing accepts H_0 at the 0.05 level for all $\frac{E_f}{G_n}$ ratios used in **Figure 254**.

An even better fit is achieved if the tensile strength range is increased such that the minimum is much smaller than the maximum (**Figure 255**). K-S testing accepts the hypothesis that the actual and simulated spacing data in **Figure 255** are from the same probability distribution. Remember that the tensile strength range given by Saltzman (2001) is a possible tensile strength range. One should realize that the actual range may be narrower or wider than that. Considering that the tensile strength data come from intact samples, one can expect the actual tensile strength range to be wider. However, it should be noted that for the simulations where the minimum tensile strength is << than the maximum (e.g., **Figure 255** and the corresponding plots for the other sections), the tensile strength range used is highly unlikely (min = 1.0 MPa, max = 1×10^7 MPa) and serves only to demonstrate the limit of the joint CDF as the range of tensile strength is increased.

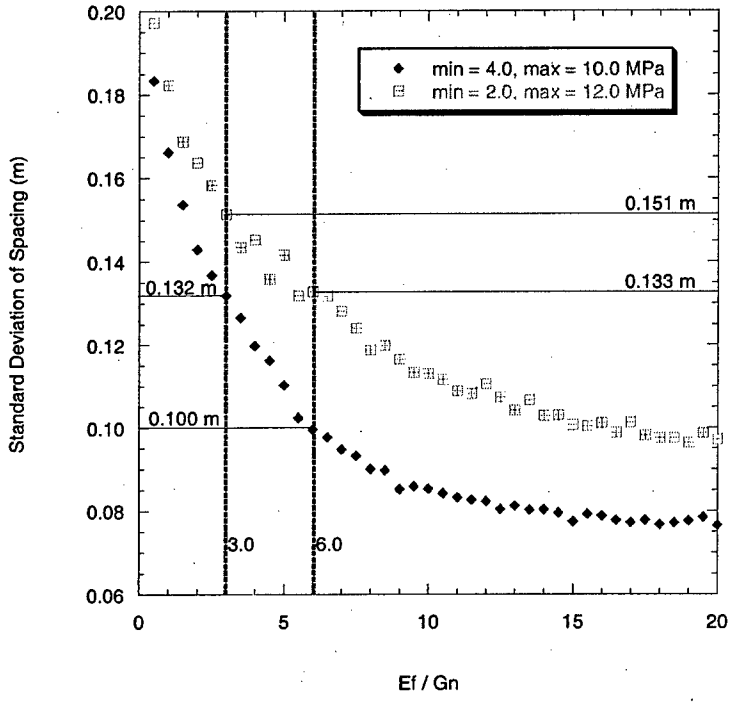


Figure 252 – Standard deviation vs. $\frac{E_f}{G_n}$ ratio for section I (two tensile strength ranges). Actual standard deviation of joint spacing ~ 0.15 m.

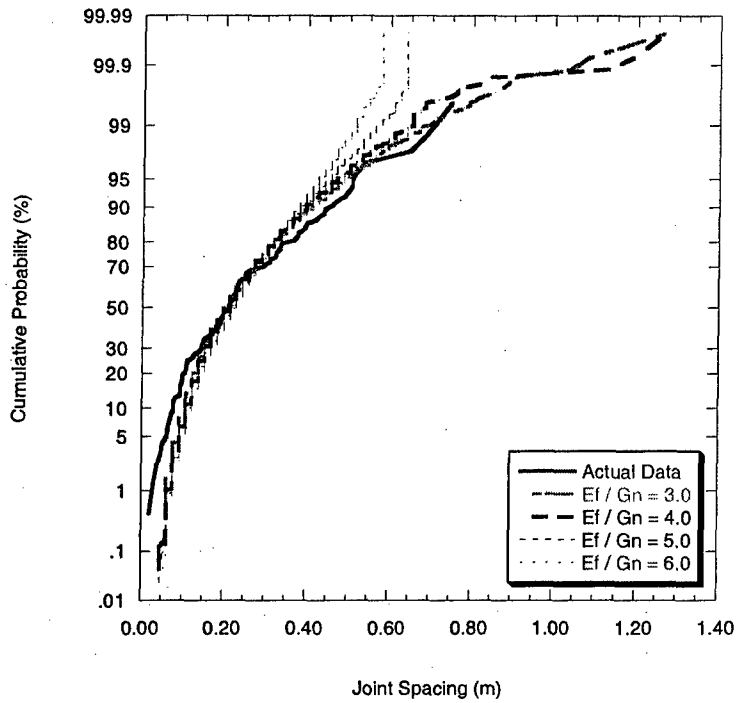


Figure 253 – Comparison between actual and simulated joint spacing CDFs for section I using four different $\frac{E_f}{G_n}$ ratios for a minimum tensile strength of 4.0 MPa and a maximum of 10.0 MPa.

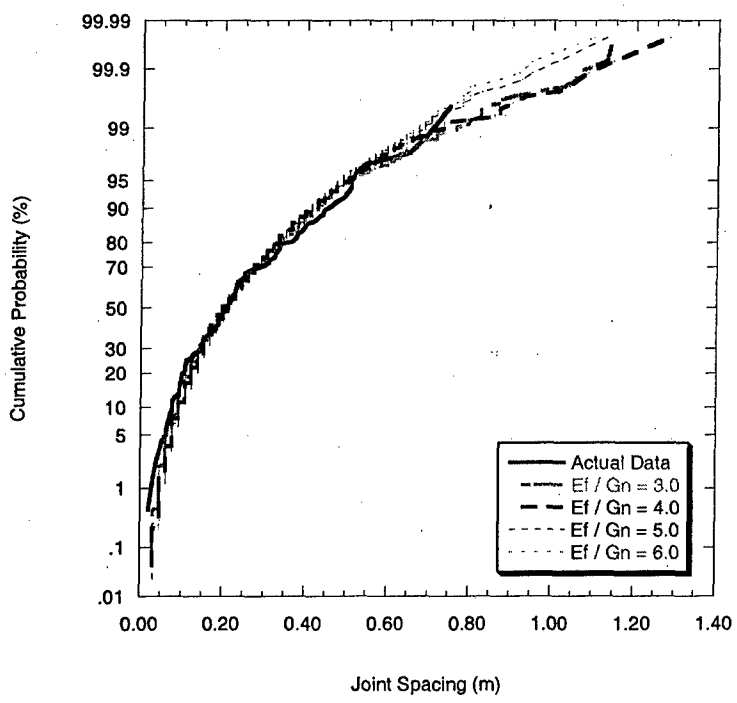


Figure 254 – Comparison between actual and simulated joint spacing CDFs for section I using four different $\frac{E_f}{G_n}$ ratios for a minimum tensile strength of 2.0 MPa and a maximum of 12.0 MPa.

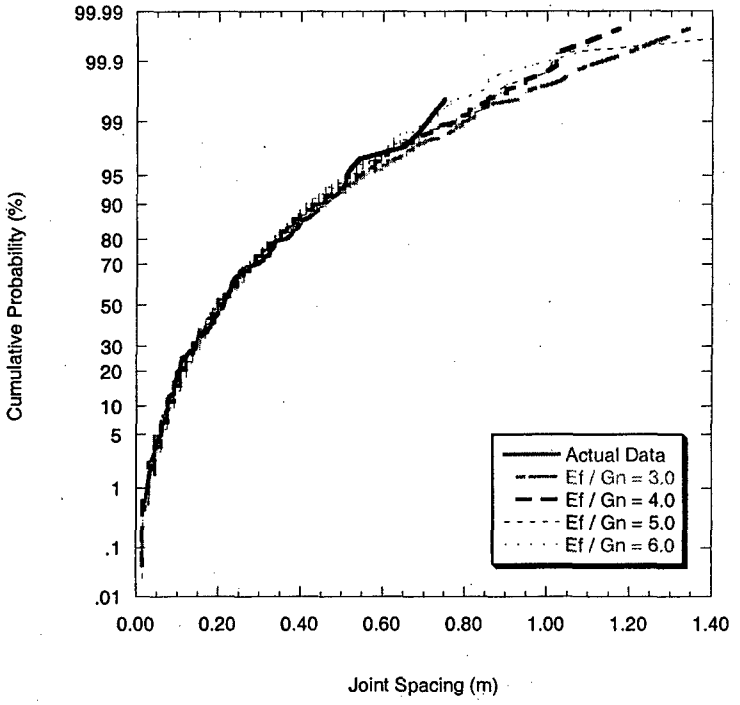


Figure 255 – Comparison between actual and simulated joint spacing CDFs for section I using four different $\frac{E_f}{G_n}$ ratios for a minimum tensile strength << the maximum.

Section II

Figure 256 shows the relationship between the simulated standard deviation of joint spacing and the $\frac{E_f}{G_n}$ ratio for section II using the two different tensile strength ranges. Recall that section II and section III are more densely jointed than sections I and IV. As a result, the mean joint spacing and standard deviation take on smaller values than those in sections I and IV. In **Figure 256**, it is apparent that the flaw model underestimates the joint spacing standard deviation (actual ~ 0.08 m) for reasonable values of $\frac{E_f}{G_n}$ (3.0 to 6.0).

Figure 257 to **Figure 259** show the simulated joint spacing CDFs for the range of reasonable $\frac{E_f}{G_n}$ values using different tensile strength ranges. Unlike in section I, the improvement in the joint spacing distribution fit is less pronounced as the tensile strength range is widened. For the section II results, in general, the flaw model underestimates the number of smaller spacings and overestimates the number of larger spacings. In other words, the simulated joint CDFs lie below the actual joint CDF in the small spacing data range but lie above the actual joint CDF in the large spacing data range (**Figure 257** to **Figure 259**). The flaw model is unable to produce the more closely spaced joints that are found in the actual data. Even for the extremely wide tensile strength range (**Figure 259**), the fit is not as good as that for section I (**Figure 255**). Kolmogorov-Smirnov testing reveals that H_0 is rejected at the 0.05 level for all cases in **Figure 257** and **Figure 258** and for $\frac{E_f}{G_n} = 6.0$ in **Figure 259**. For $\frac{E_f}{G_n} = 3.0, 4.0$ and 5.0 in **Figure 259**, hypothesis H_0 is accepted at the 0.05 level.

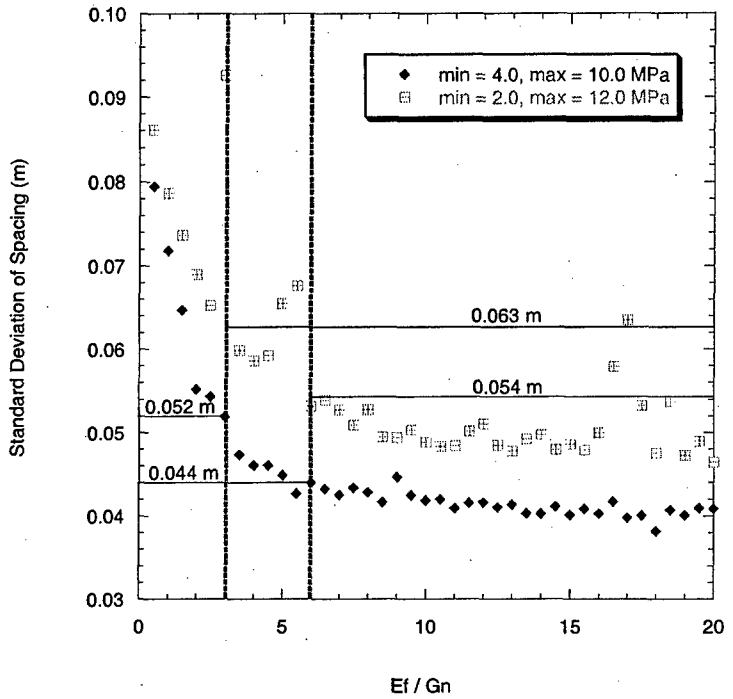


Figure 256 – Standard deviation vs. $\frac{E_f}{G_n}$ ratio for section II (two tensile strength ranges). Actual standard deviation of joint spacing ~ 0.08 m.

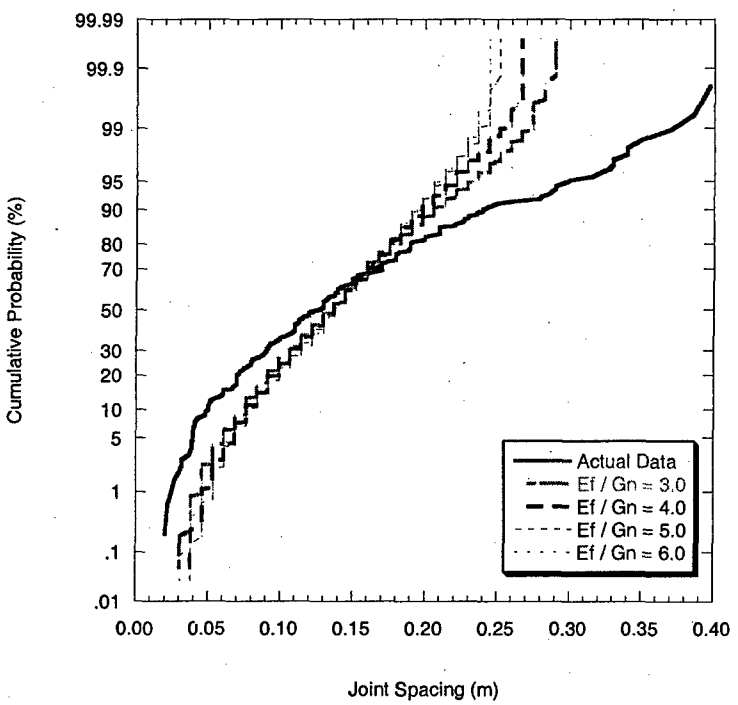


Figure 257 – Comparison between actual and simulated joint spacing CDFs for section II using four different $\frac{E_f}{G_n}$ ratios for a minimum tensile strength of 4.0 MPa and a maximum of 10.0 MPa.

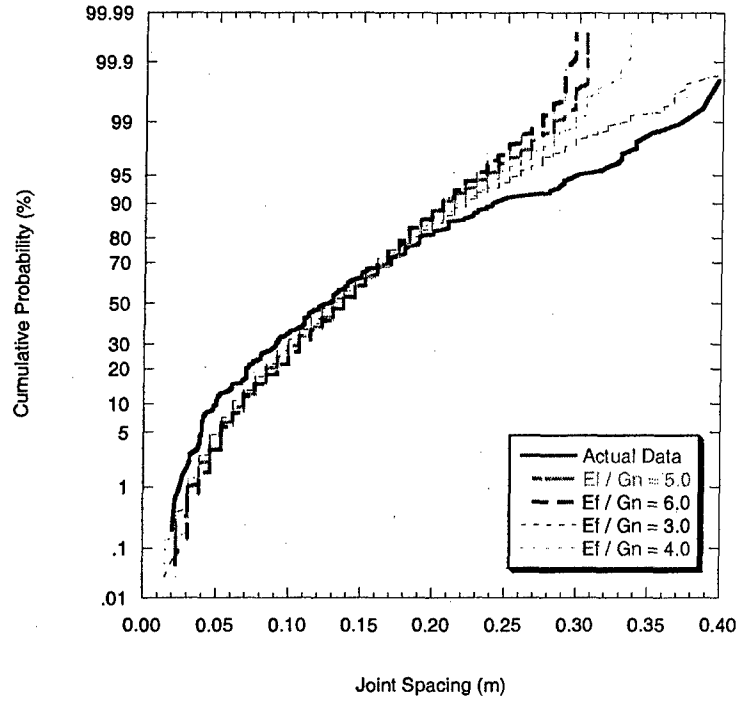


Figure 258 – Comparison between actual and simulated joint spacing CDFs for section II using four different $\frac{E_f}{G_n}$ ratios for a minimum tensile strength of 2.0 MPa and a maximum of 12.0 MPa.

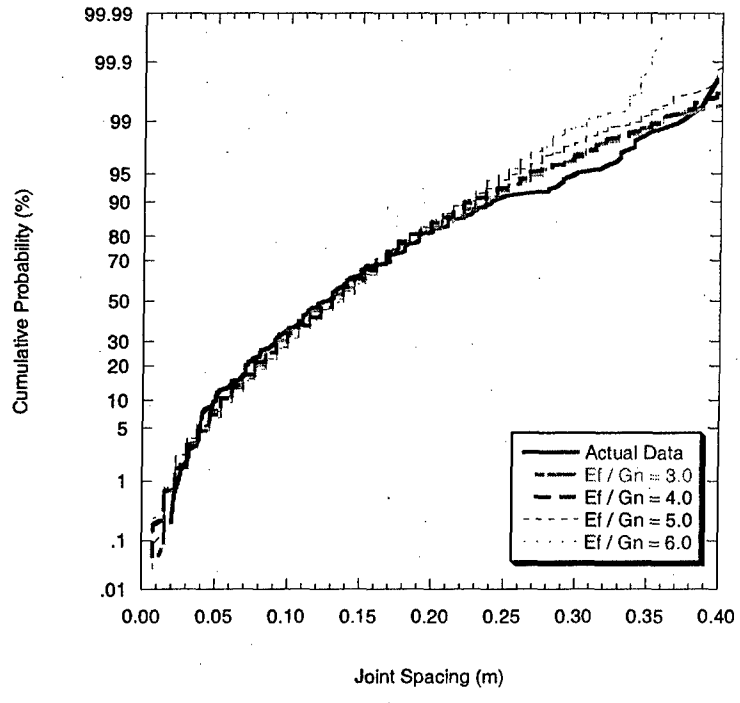


Figure 259 – Comparison between actual and simulated joint spacing CDFs for section II using four different $\frac{E_f}{G_n}$ ratios for a minimum tensile strength << the maximum.

Section III

As in section II, the flaw model grossly underestimates the standard deviation of spacing for a reasonable range of $\frac{E_f}{G_n}$ values (**Figure 260** for section III). Like section II, section III is more densely jointed than sections I and IV. It appears that the flaw model behaves the same way for both of these sections.

Figure 261 to **Figure 263** show the simulated joint spacing CDFs together with the actual joint spacing CDFs. As before, three different tensile strength ranges are used. In this case, the improvement in the simulated joint spacing CDF expected with the widening of the tensile strength range does not occur. The flaw model again underestimates the number of smaller spacings and overestimates the number of larger spacings. This behavior is similar to that observed in the simulations for section II; sections II and III have almost the same joint intensity. However, it appears that the deviation between the joint spacing CDFs is worse here. No matter how wide the tensile strength range is, there is still a discrepancy in the cumulative probability distribution (**Figure 263**). Kolmogorov-Smirnov testing confirms this observation as H_0 is rejected at the 0.05 level in all cases in **Figure 261** to **Figure 263**.

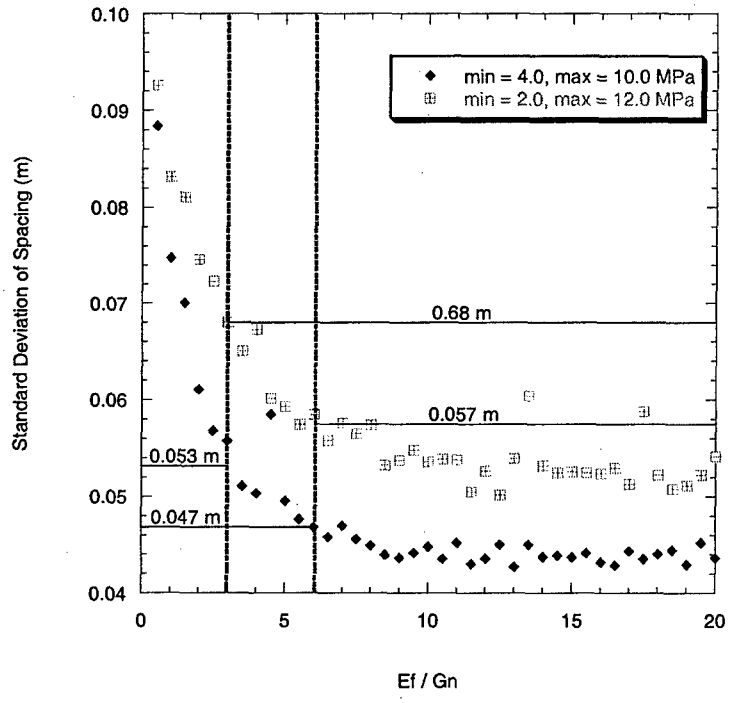


Figure 260 – Standard deviation vs. $\frac{E_f}{G_n}$ ratio for section III (two tensile strength ranges). Actual standard deviation of joint spacing ~ 0.09 m.

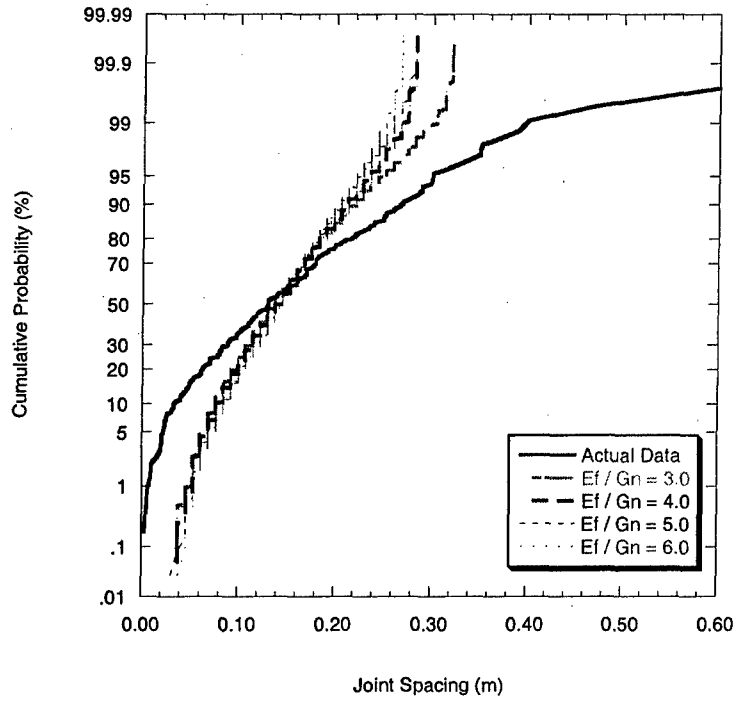


Figure 261 – Comparison between actual and simulated joint spacing CDFs for section III using four different $\frac{E_f}{G_n}$ ratios for a minimum tensile strength of 4.0 MPa and a maximum of 10.0 MPa.

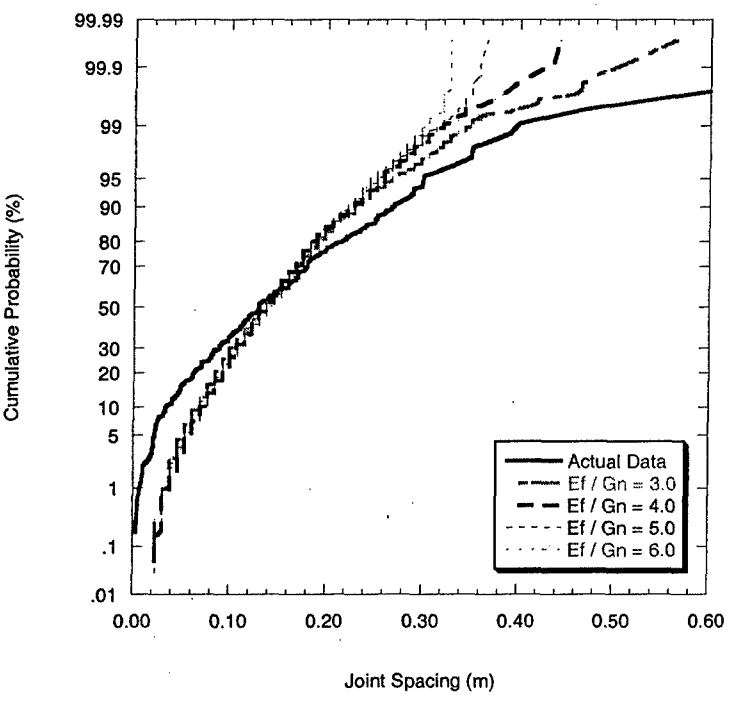


Figure 262 – Comparison between actual and simulated joint spacing CDFs for section III using four different $\frac{E_f}{G_n}$ ratios for a minimum tensile strength of 2.0 MPa and a maximum of 12.0 MPa.

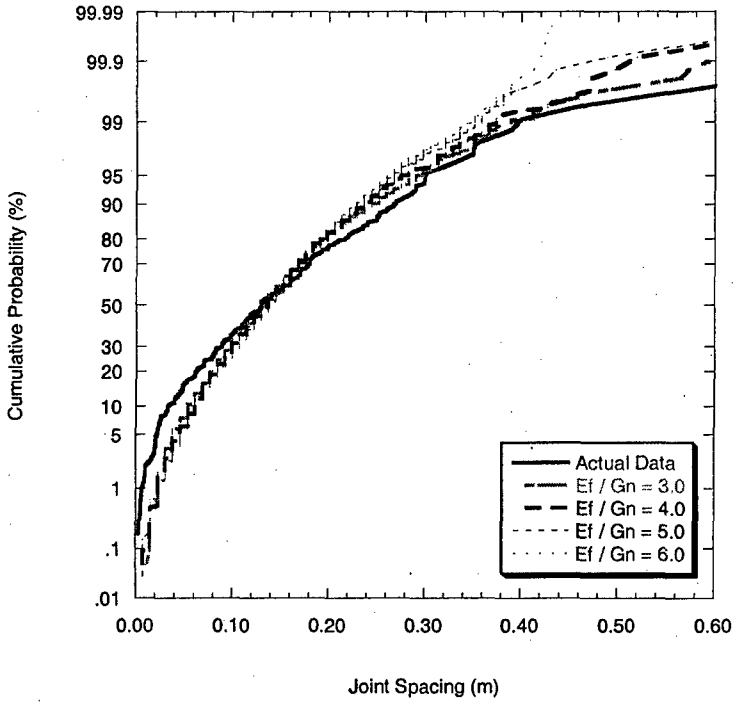


Figure 263 – Comparison between actual and simulated joint spacing CDFs for section III using four different $\frac{E_f}{G_n}$ ratios for a minimum tensile strength << the maximum.

Section IV

Figure 264 shows the simulated joint spacing standard deviation vs. $\frac{E_f}{G_n}$ relationship for section IV. For reasonable $\frac{E_f}{G_n}$ values (i.e., 3.0 to 6.0), the flaw model underestimates the standard deviation (actual value is 0.1285 m). Recall that section IV has a mean spacing that is a bit smaller than section I (0.2067 m vs. 0.2366 m). **Figure 265** to **Figure 267** show the simulated joint CDFs compared with the actual CDFs for the three different strength ranges and for the reasonable range of $\frac{E_f}{G_n}$ values. They show that the flaw model again underestimates the number of small spacings. This is especially true when the tensile strength range is the narrowest (**Figure 265**). Kolmogorov-Smirnov testing rejects H_0 at the 0.05 level for all cases in **Figure 265**. Improvement can be observed as the tensile strength range is widened (**Figure 266** and **Figure 267**). However, the fit between the simulated and actual CDFs is not as good as for section I (**Figure 266** and **Figure 267** vs. **Figure 254** and **Figure 255**). On the other hand, the fit in **Figure 266** and **Figure 267** is clearly better than that in sections II and III (**Figure 258** and **Figure 259** for section II and **Figure 262** and **Figure 263** for section III). K-S testing accepts H_0 at the 0.05 level in all cases in **Figure 266** and **Figure 267**.

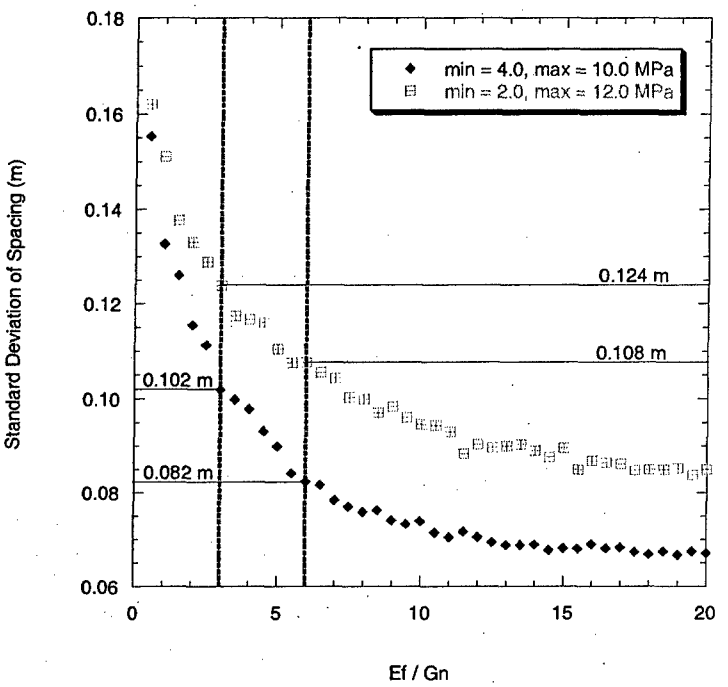


Figure 264 – Standard deviation vs. $\frac{E_f}{G_n}$ ratio for section IV (two tensile strength ranges). Actual standard deviation of joint spacing ~ 0.13 m.

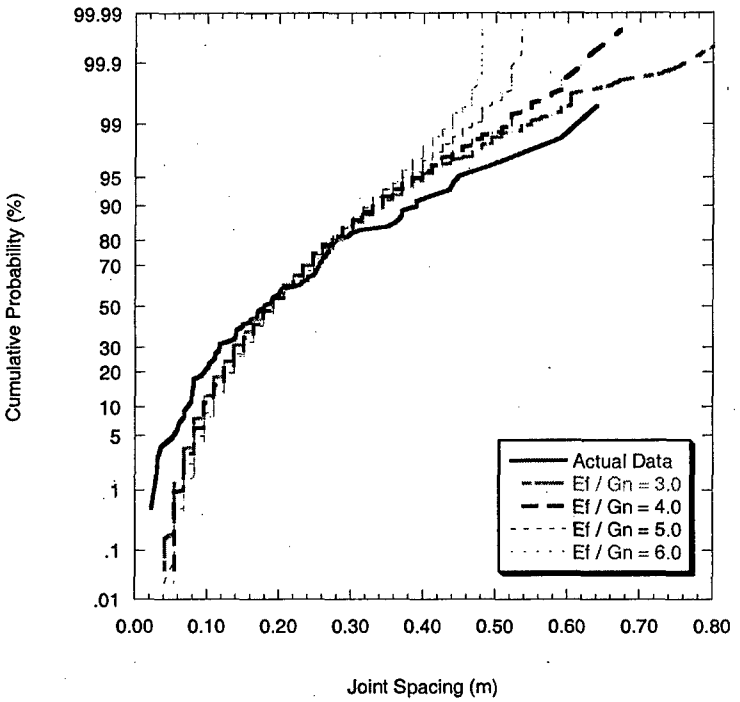


Figure 265 – Comparison between actual and simulated joint spacing CDFs for section IV using four different $\frac{E_f}{G_n}$ ratios for a minimum tensile strength of 4.0 MPa and a maximum of 10.0 MPa.

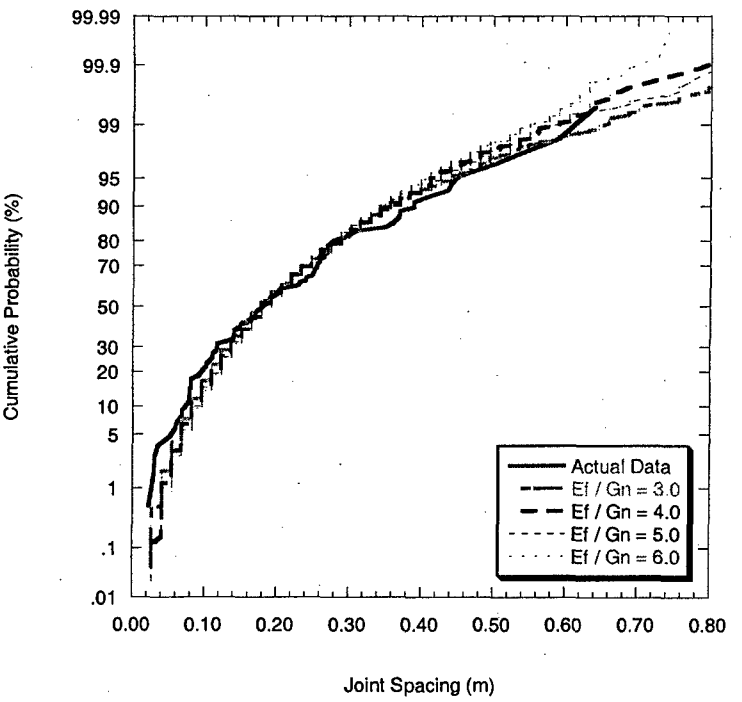


Figure 266 – Comparison between actual and simulated joint spacing CDFs for section IV using four different $\frac{E_f}{G_n}$ ratios for a minimum tensile strength of 2.0 MPa and a maximum of 12.0 MPa.

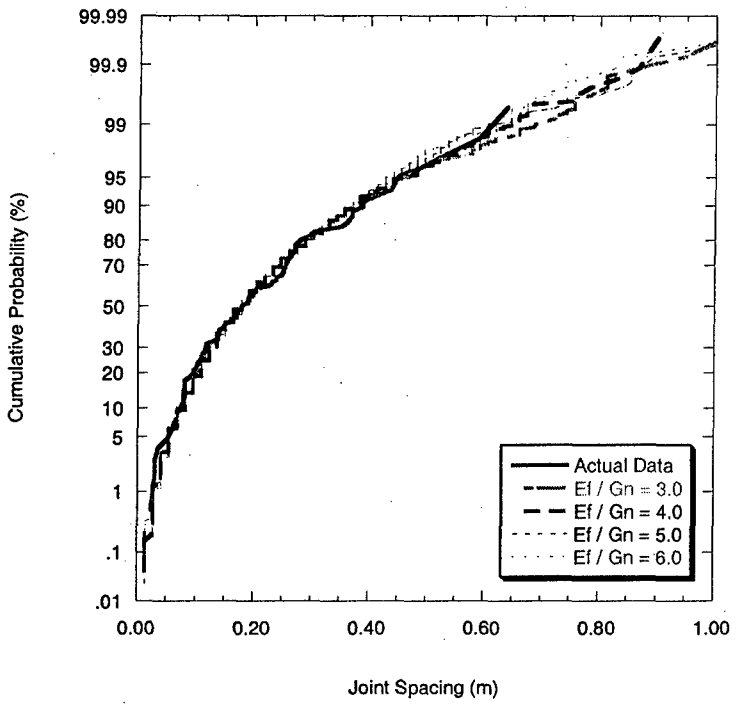


Figure 267 – Comparison between actual and simulated joint spacing CDFs for section IV using four different $\frac{E_f}{G_n}$ ratios for a minimum tensile strength << the maximum.

Discussion

Overall, the flaw model appears to consistently underestimate the standard deviation of spacing but is able to simulate the joint spacing CDFs for sections I and IV more effectively than for sections II and III. Sections II and III were shown to be more densely jointed than sections I and IV. In fact, the mean spacing values for sections II and III (~0.14 m and ~0.144, respectively) lie inside the calculated saturation mean spacing range of 0.094 m to 0.151 m for this case. This indicates a possibility that sections II and III are jointed beyond the saturation because their mean spacing values are below the upper bound of the SMS. Additional jointing may have occurred beyond saturation and such a process is beyond the scope of the flaw model. Another possibility lies in the fact that sections II and III contain all the fracture zones (i.e., the joint and fault zones, see **Figure 243**) that were observed along the 190 m scanline. These may have influenced the joint formation in the limestone/dolostone layer not just in sections II and III but in sections I and IV as well (possibly to a lesser degree). The jointing process that may result from the formation of these fracture zones may differ from that being modeled by the flaw model.

The above comparison demonstrates one of the limitations of the flaw model and indicates that it may no longer be applicable when the joint pattern is beyond saturation. Jointing beyond saturation may be brought about by a process that is different from the remote extension of the layer on which the flaw model is based. As for the strength model it appears that an assumed uniform probability distribution of tensile strength at a

point appears to suffice. However, the use of a correlated strength model is also investigated in the following section.

Correlated Strength Model

So far, the tensile strength at a point along the jointing layer was assumed to be independent of the tensile strength at an adjacent point. This may not be a realistic way of representing the non-uniform tensile strength of a layer. For this reason, the use of a correlated strength model was explored. In such a strength model, the tensile strength at a point is related to that at an adjacent point. A correlated strength model produces tensile strength variations that are different from an uncorrelated strength model in that there are clear peaks and valleys in the strength profile along the length of the layer. New joint formation is likely to be concentrated in the valleys. The correlated strength model is now used to simulate joint spacing for comparison with actual joint spacing.

First, the values of the correlated strength model parameters (see **Equation 74** below) need to be estimated. Recall from section **0 - Correlated Strength Model** (page 242) that the correlated strength model is given by

$$\ln\left(\frac{\sigma_{t_i}}{\mu_{\sigma_t}}\right) = \phi \ln\left(\frac{\sigma_{t_{i-1}}}{\mu_{\sigma_t}}\right) + \varepsilon_i \qquad \textbf{Equation 74}$$

where σ_{t_i} is the tensile strength at location i, $\sigma_{t_{i-1}}$ is the tensile strength at the previous adjacent location (i-1), μ_{σ_t} is the mean tensile strength, ϕ is the correlation factor ($0<\phi<1$) and ε_i is a normal random variable with mean equal to zero and a standard deviation of σ_ε. Detailed knowledge of the locations along the layer where Saltzman (2001) obtained test samples is needed in order to estimate the parameter ϕ. Because this information is not available, simulations will be performed using different correlation factor values. In order to estimate the parameter σ_ε, the above expression is expanded to yield the following:

$$\ln\sigma_{t_i} - \ln\mu_{\sigma_t} = \phi \ln\sigma_{t_{i-1}} - \phi \ln\mu_{\sigma_t} + \varepsilon_i$$

It can be seen that the parameter ε_i is related to the natural logarithm of the tensile strength. As a first estimate, σ_ε is assumed equal to the standard deviation of the natural logarithms of the tensile strength from the data (i.e., from Saltzman, 2001) or $\sigma_\varepsilon = \sqrt{\sigma^2_{\ln\sigma_t}}$. This yields a value of $\sigma_\varepsilon \approx 0.2$ using Saltzman's (2001) tensile strength data. Also, from the tensile strength data, the minimum and maximum tensile strength values are ~4.0 and ~10.0 MPa, respectively. These give a mean tensile strength of $\mu_{\sigma_t} = 7.0$ MPa. These parameter values are used in the simulations.

Section I

Figure 268 shows the standard deviation of joint spacing as it varies with the $\frac{E_f}{G_n}$ ratio for different values of the correlation factor. The reasonable values for the $\frac{E_f}{G_n}$ ratio (i.e., 3.0 to 6.0) and the actual standard deviation of spacing are also shown. From **Figure 268**, it appears that the actual standard deviation can be achieved given $\sigma_\varepsilon \approx 0.2$, $\frac{E_f}{G_n}$ is between 3.0 and 6.0, and $\mu_{\sigma_t} = 7.0$ MPa when the correlation factor, ϕ, is greater than about 0.7 but less than 0.9. In other words, a highly correlated strength variation along the layer may lead to a realistic joint pattern in terms of the joint spacing distribution. However, **Figure 269** shows that this is not necessarily the case. **Figure 269** shows the actual and simulated joint spacing CDFs for different correlation factor values that are greater than 0.7 with $\sigma_\varepsilon \approx 0.2$, $\mu_{\sigma_t} = 7.0$ MPa and $\frac{E_f}{G_n} = 3.0$. The simulated joint spacing CDFs underestimate the relative frequency of the small joint spacing values, overestimate that of the intermediate spacing values and underestimate that of the large spacing values. Given this information, there is no need to look at the resulting joint spacing CDFs for $\frac{E_f}{G_n} > 3.0$ because the effect of increasing the $\frac{E_f}{G_n}$ ratio is to reduce the relative frequency of the smaller spacing values. Kolmogorov-Smirnov testing indicates that the hypothesis that the actual and simulated spacing data come from the same probability distribution (i.e., hypothesis H_0) is accepted at the 0.05 level for ϕ = 0.70, 0.75 and 0.80 in **Figure 269**. H_0 is rejected at the 0.05 level for $\phi > 0.80$ in **Figure 269**. Increasing the value of σ_ε does not appear to help even though it leads to an increase in the relative frequency of smaller spacings (**Figure 270**). In fact, hypothesis H_0 is rejected for all cases in **Figure 270**.

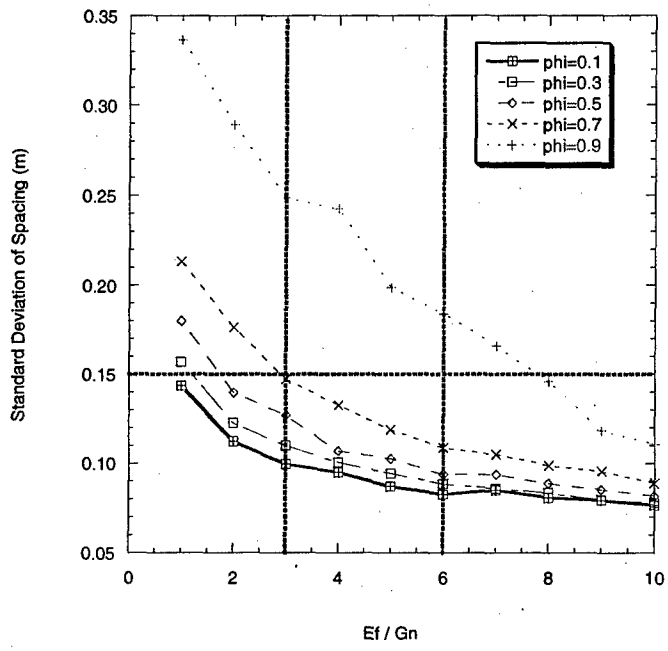


Figure 268 – Standard deviation of joint spacing vs. $\frac{E_f}{G_n}$ for section I using different values of the correlation factor, ϕ. Other parameter values are $\mu_{\sigma_t} = 7.0$ and $\sigma_\varepsilon = 0.2$.

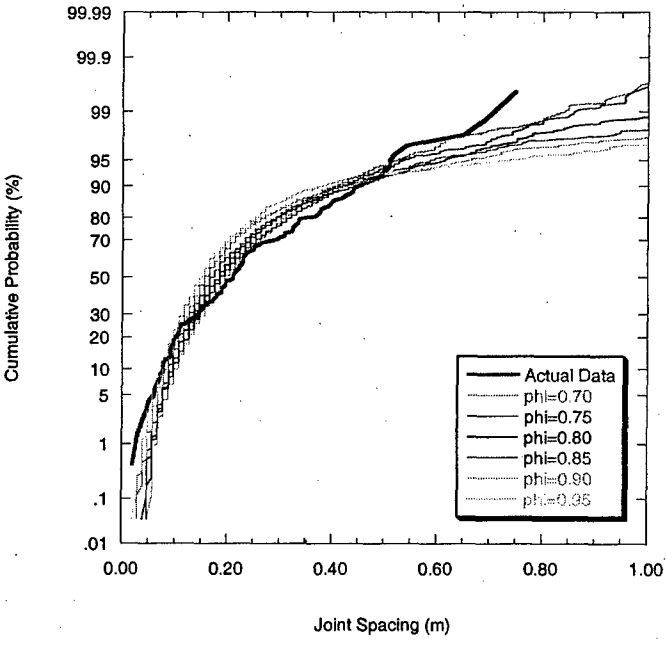


Figure 269 – Simulated joint spacing CDFs for different values of the correlation factor (≥ 0.7) together with the actual joint spacing CDF for section I. The simulation parameter values are: $\frac{E_f}{G_n} = 3.0$, $\sigma_\varepsilon = 0.2$ and $\mu_{\sigma_t} = 7.0$.

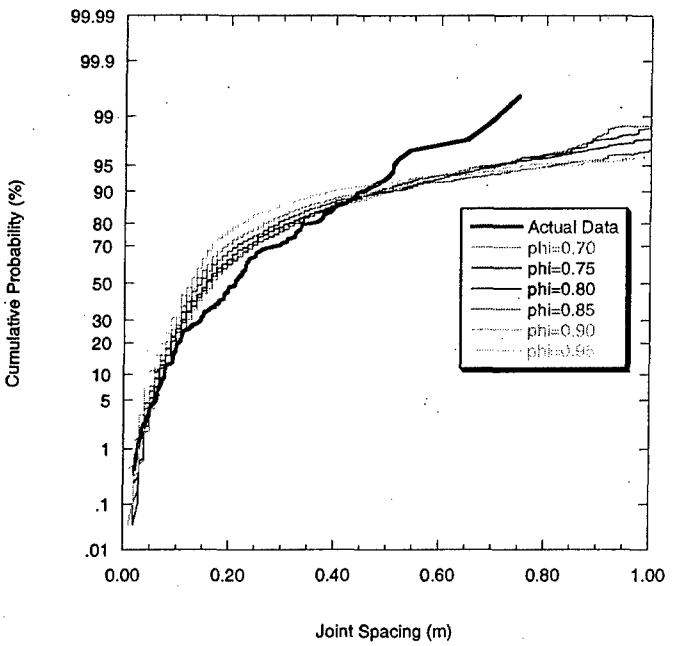


Figure 270 – Simulated joint spacing CDFs for different values of the correlation factor (≥ 0.7) together with the actual joint spacing CDF for section I. The simulation parameter values are: $\frac{E_f}{G_n} = 3.0$, $\sigma_\varepsilon = 0.5$ and $\mu_{\sigma_t} = 7.0$.

Section II

Figure 271 shows the standard deviation of joint spacing as it varies with the $\frac{E_f}{G_n}$ ratio for section II. The actual joint spacing standard deviation is about 0.08 m (shown). **Figure 271** also shows that for a reasonable range of $\frac{E_f}{G_n}$ values, the actual standard deviation of spacing may be achieved in simulations using a high correlation factor (greater than about 0.9). For the joint spacing CDF simulations, a range from 0.7 to 0.95 was used. Using the initial estimate of σ_ε, $\mu_{\sigma_t} = 7.0$ and $\frac{E_f}{G_n} = 3.0$, the joint spacing CDFs for section II are shown in **Figure 272**. It can be seen that the simulated joint spacing CDFs do not resemble the actual joint spacing CDF (**Figure 272**). As mentioned in the results for section I, an increase in the $\frac{E_f}{G_n}$ ratio only causes the simulated relative frequency of the small spacings to decrease and will not lead to an improvement in the comparison. An increase in the value of σ_ε (from which one can expect the increase in the relative frequency of smaller spacing values) does not appear to improve the fit between the actual and simulated joint spacing CDFs either (**Figure 273**). In K-S testing, the hypothesis H_0 is rejected at the 0.05 level for all cases in **Figure 272** and **Figure 273**. It must be noted in **Figure 273** that the joint CDF for $\phi = 0.85$ results from a simulation where the simulated joint intensity fell substantially below the target joint intensity due to the saturation mechanism. Simulations such as this result from time to time especially when the target joint intensity is within the range of simulated saturation joint intensity (i.e., **Equation 73**). In the case of Becker and Gross (1996), the simulated saturation

joint intensity ranges from 6.6 to 10.6 joints per meter (i.e., mean spacing of 0.094 m to 0.151 m). For section II, the actual observed joint intensity is 7.2 joints per meter (i.e., mean spacing of 0.1382 m). In any case, the curve for $\phi = 0.85$ **Figure 273** should lie closer to those of the other ϕ values if the target joint intensity were to be attained.

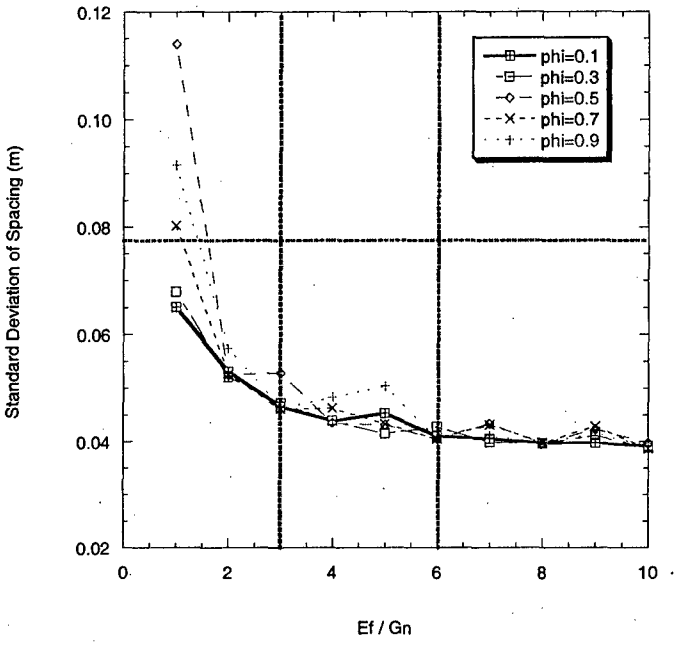


Figure 271 – Standard deviation of joint spacing vs. $\frac{E_f}{G_n}$ for section II using different values of the correlation factor, ϕ. Other parameter values are $\mu_{\sigma_t} = 7.0$ and $\sigma_\varepsilon = 0.2$.

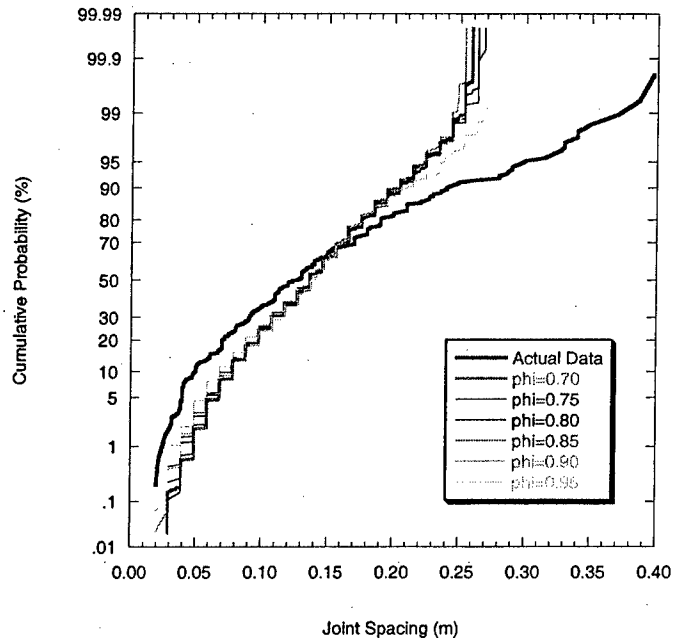


Figure 272 – Simulated joint spacing CDFs for different values of the correlation factor (≥ 0.7) together with the actual joint spacing CDF for section II. The simulation parameter values are: $\frac{E_f}{G_n} = 3.0$, $\sigma_\varepsilon = 0.2$ and $\mu_{\sigma_t} = 7.0$.

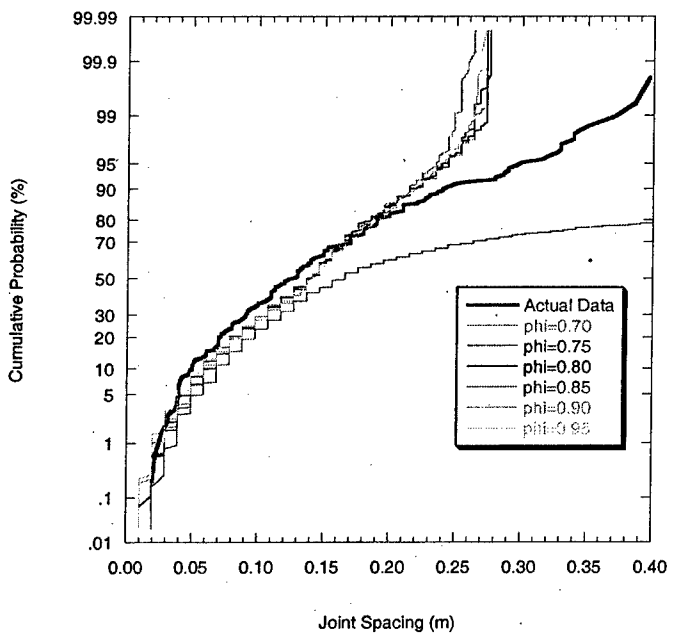


Figure 273 – Simulated joint spacing CDFs for different values of the correlation factor (≥ 0.7) together with the actual joint spacing CDF for section II. The simulation parameter values are: $\frac{E_f}{G_n} = 3.0$, $\sigma_\varepsilon = 0.5$ and $\mu_{\sigma_t} = 7.0$.

Section III

Figure 274 shows the relationship between the standard deviation of joint spacing and the $\frac{E_f}{G_n}$ ratio for different values of the correlation factor, ϕ, for section III. The actual standard deviation of spacing is about 0.09 m and **Figure 274** shows that this value could not be achieved in the simulations using different ϕ values. It also appears that the standard deviation does not vary much with ϕ for the range of reasonable $\frac{E_f}{G_n}$ ratios (**Figure 274**). In the simulations, the correlation factor is varied from 0.70 to 0.95. As for section II, the simulated joint spacing CDFs for an $\frac{E_f}{G_n}$ of 3.0 using $\phi > 0.7$ do not resemble the actual joint spacing CDF (**Figure 275**). If the value of σ_ε is increased to 0.5, the relative frequency of the smaller spacings is increased but the shapes of the simulated joint spacing CDFs are different from those of the actual joint spacing CDFs (**Figure 276**). In K-S testing, the hypothesis H_0 is rejected at the 0.05 level for all cases in **Figure 275** and **Figure 276**.

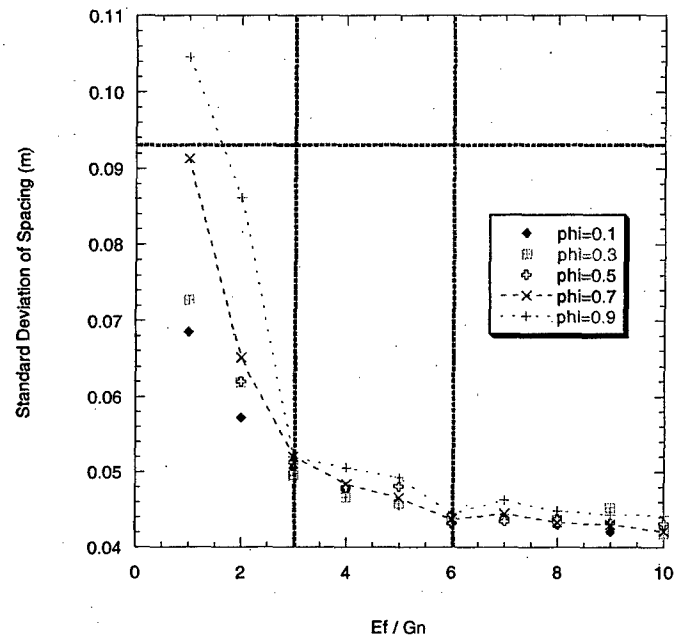


Figure 274 – Standard deviation of joint spacing vs. $\frac{E_f}{G_n}$ for section III using different values of the correlation factor, ϕ. Other parameter values are $\mu_{\sigma_t} = 7.0$ and $\sigma_\varepsilon = 0.2$.

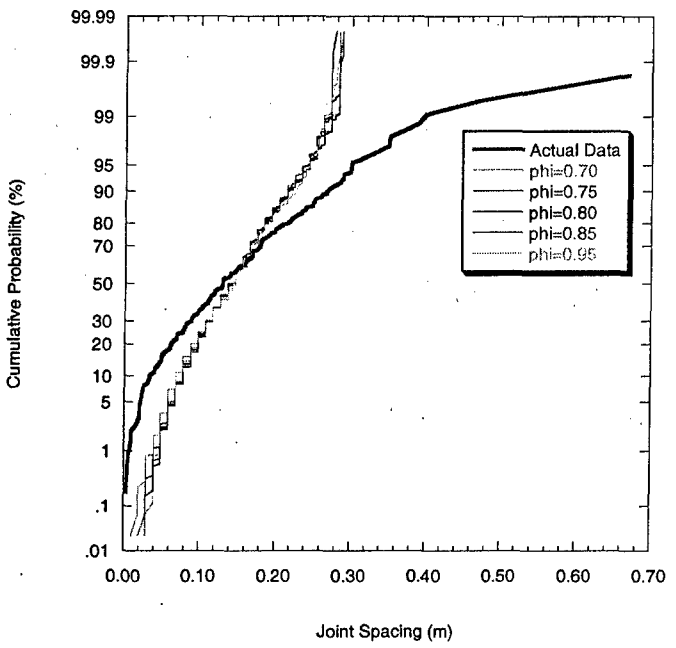


Figure 275 – Simulated joint spacing CDFs for different values of the correlation factor (≥ 0.7) together with the actual joint spacing CDF for section III. The simulation parameter values are: $\frac{E_f}{G_n} = 3.0$, $\sigma_\varepsilon = 0.2$ and $\mu_{\sigma_t} = 7.0$.

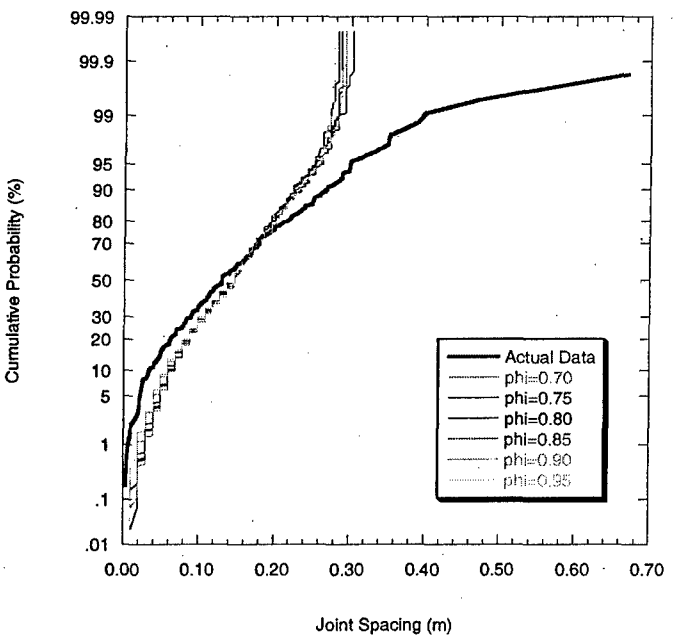


Figure 276 – Simulated joint spacing CDFs for different values of the correlation factor (≥ 0.7) together with the actual joint spacing CDF for section III. The simulation parameter values are: $\frac{E_f}{G_n} = 3.0$, $\sigma_\varepsilon = 0.5$ and $\mu_{\sigma_t} = 7.0$.

Section IV

Figure 277 shows the simulated standard deviation of joint spacing for various $\frac{E_f}{G_n}$ values using different correlation factor values for section IV. **Figure 277** shows that the actual standard deviation (0.13 m) can be achieved if the correlation factor is greater than about 0.7 for $\frac{E_f}{G_n}$ from 3.0 to 6.0. **Figure 278** shows the simulated joint spacing CDFs for an $\frac{E_f}{G_n}$ of 3.0 and correlation factors from 0.70 to 0.95. Like in section I, which has a similar joint intensity, the simulated joint spacing CDFs for section IV do not fit the actual data. The model underestimates the relative frequency of smaller spacings, overestimates the relative frequency of intermediate and underestimates those of larger spacings (**Figure 278**). K-S testing reveals that the hypothesis H_0 is accepted at the 0.05 level for ϕ = 0.70, 0.75 and 0.80 in **Figure 278**. H_0 is rejected at the 0.05 level for the other ϕ values in **Figure 278**. In order to increase the simulated relative frequency of smaller spacings, one can increase the value of σ_ε. However, **Figure 279** shows that although the relative frequency of the small spacings is indeed increased when this is done, the fit between the actual and simulated joint spacing CDFs is still not very good. Specifically, the discrepancy between the actual and simulated joint CDFs at intermediate and large spacings becomes bigger than that in **Figure 278**. In fact, hypothesis H_0 is rejected at the 0.05 level for all ϕ values in **Figure 279**.

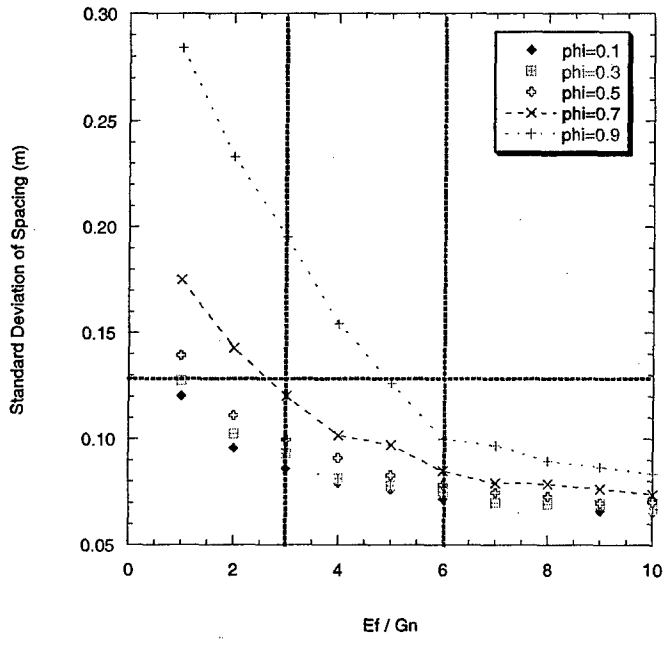


Figure 277 – Standard deviation of joint spacing vs. $\frac{E_f}{G_n}$ for section IV using different values of the correlation factor, ϕ. Other parameter values are $\mu_{\sigma_t} = 7.0$ and $\sigma_\varepsilon = 0.2$.

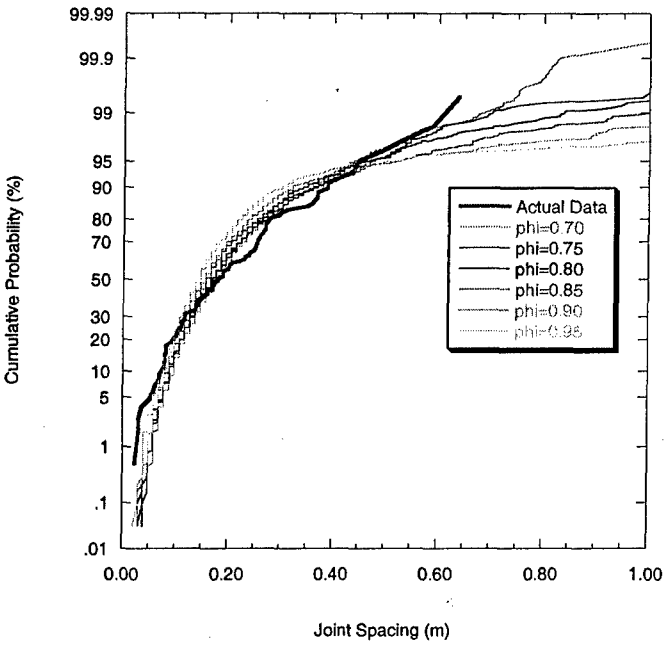


Figure 278 – Simulated joint spacing CDFs for different values of the correlation factor (≥ 0.7) together with the actual joint spacing CDF for section IV. The simulation parameter values are: $\frac{E_f}{G_n} = 3.0$, $\sigma_\varepsilon = 0.2$ and $\mu_{\sigma_t} = 7.0$.

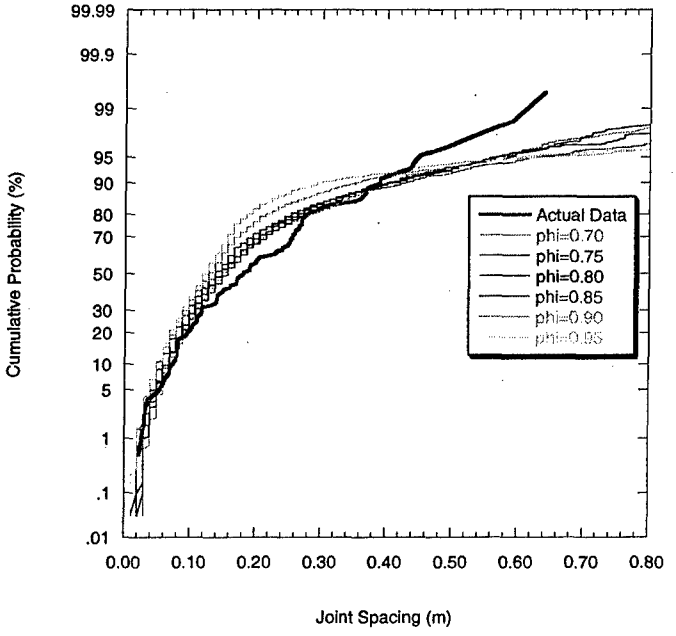


Figure 279 – Simulated joint spacing CDFs for different values of the correlation factor (≥ 0.7) together with the actual joint spacing CDF for section IV. The simulation parameter values are: $\frac{E_f}{G_n} = 3.0$, $\sigma_\varepsilon = 0.5$ and $\mu_{\sigma_t} = 7.0$.

Discussion

The correlated strength model does not appear to be an effective strength model for simulating the joint patterns in this case. For sections I and IV, chi-square goodness-of-fit tests indicate that the simulated spacing data (in **Figure 269** and **Figure 278**) cannot be described by log-normal probability distributions. On the other hand, the actual data for these two sections were effectively described by log-normal probability distributions in Becker and Gross (1996). Despite this, K-S testing accepts hypothesis H_0 (i.e., that the simulated and actual spacing data come from the same probability distribution) in some cases for sections I and IV (**Figure 269** and **Figure 278**). From the parametric studies described in the previous chapter (**6 - New Models**, page 155), the correlated strength model could produce log-normally-shaped joint spacing probability distributions at intermediate joint intensity when the correlation factor is low (<0.5). For high correlation factors, which were required in this case to produce realistic standard deviation values, those same studies showed that the resulting joint spacing probability distributions were largely different from log-normal. As for sections II and III, it was hoped that the correlated strength model would help to produce smaller spacings that could not be produced with the uncorrelated strength model. Recall that the discrepancies between the actual and simulated joint spacing CDFs using the uncorrelated strength model were essentially underestimation of the relative frequency of smaller spacings coupled with overestimation of that of larger spacings. Unfortunately, the results from the correlated strength model still cannot eliminate this discrepancy. This may be another indication that a different jointing process may have acted on the two middle sections to produce the final joint pattern. Recall also that the joint and fault zones are confined mainly within these two sections (**Figure 243**).

7.2.4.2 Rejection Procedure Results

The simulation results for each section using the rejection procedure with the saturation mechanism are now presented. The saturation mechanism basically assigns a zero probability density ($f(x)=0$) to a segment whose length is below the critical joint spacing. First, a standard deviation comparison is made followed by a comparison between the simulated and actual joint spacing CDFs.

Section I

Figure 280 shows the standard deviation vs. $\frac{E_f}{G_n}$ relationship for section I using the rejection procedure. As expected, the standard deviation is higher than that produced in the flaw model. In fact, for reasonable values of $\frac{E_f}{G_n}$ (3.0 to 6.0), the rejection procedure overestimates the actual standard deviation of spacing (~0.15 m). This is a reflection of the effectively wide range of strength values that implicitly results from the use of the rejection procedure.

Figure 281 shows the simulated joint CDF for section I for a range of $\frac{E_f}{G_n}$ values compared with the actual joint spacing CDF. It can be seen that the simulated joint spacing CDFs overestimate the number of small joint spacings. This is in contrast to the results from the flaw model for section I where the number of small spacings was

underestimated to various degrees depending on the range of tensile strength that was used (i.e., **Figure 253** to **Figure 255**). Overall, though, there appears to be good agreement between the simulated and the actual spacing data as suggested by **Figure 281**. Kolmogorov-Smirnov tests show that hypothesis H_0 (i.e., actual and simulated data come from the same probability distribution) is accepted at the 0.05 level for all cases in **Figure 281**.

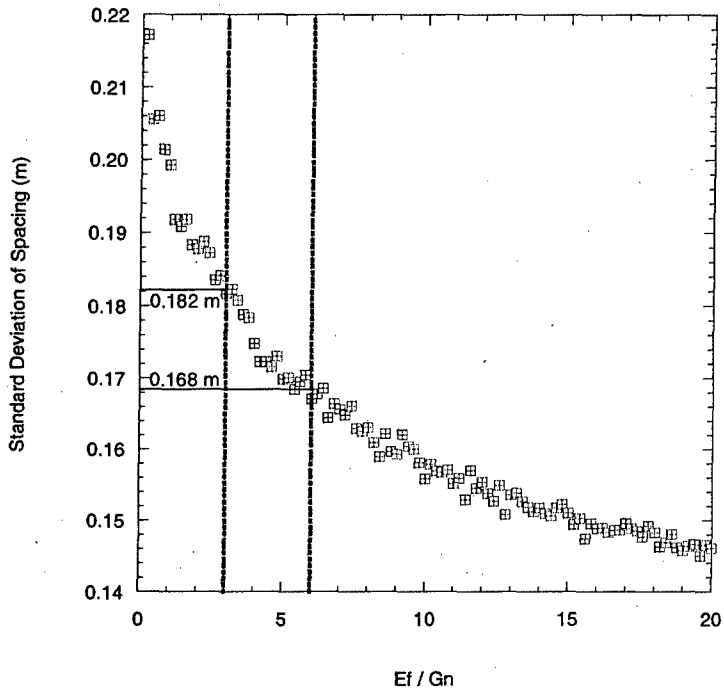


Figure 280 – Standard deviation vs. $\frac{E_f}{G_n}$ ratio for section I. Actual standard deviation of joint spacing ~ 0.15 m.

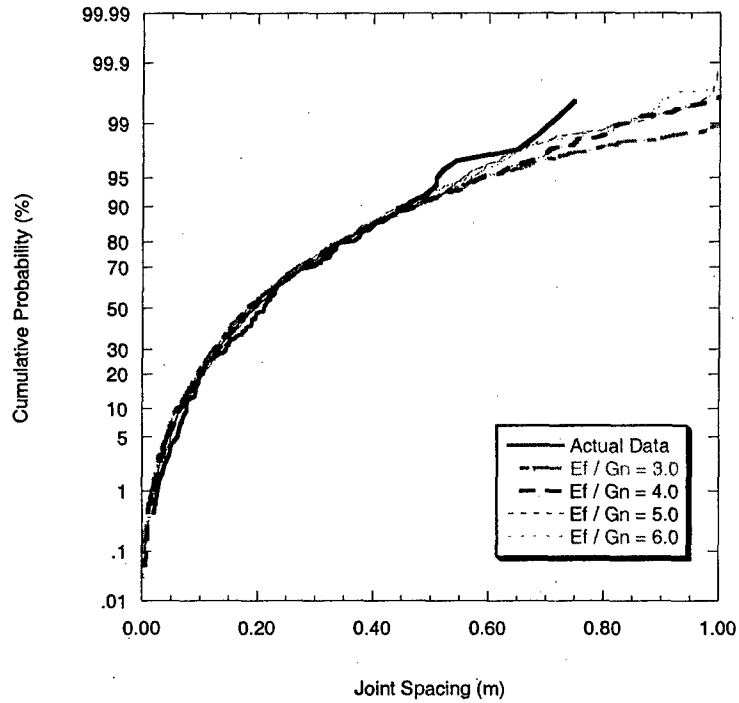


Figure 281 – Comparison between actual and simulated joint spacing CDFs for section I using four different $\frac{E_f}{G_n}$ ratios.

Section II

Figure 282 shows the standard deviation vs. $\frac{E_f}{G_n}$ relationship for section II using the rejection procedure with saturation mechanism. The rejection procedure appears to underestimate the actual standard deviation of spacing for reasonable values of $\frac{E_f}{G_n}$ (3.0 to 6.0) but there appears to be a good agreement between the simulated and actual joint spacing CDFs (**Figure 283**). In fact, the fit is better than that for the flaw model for the same section (**Figure 257**, **Figure 258** and **Figure 259**). In K-S testing, the hypothesis H_0 is accepted at the 0.05 level for all cases in **Figure 283**.

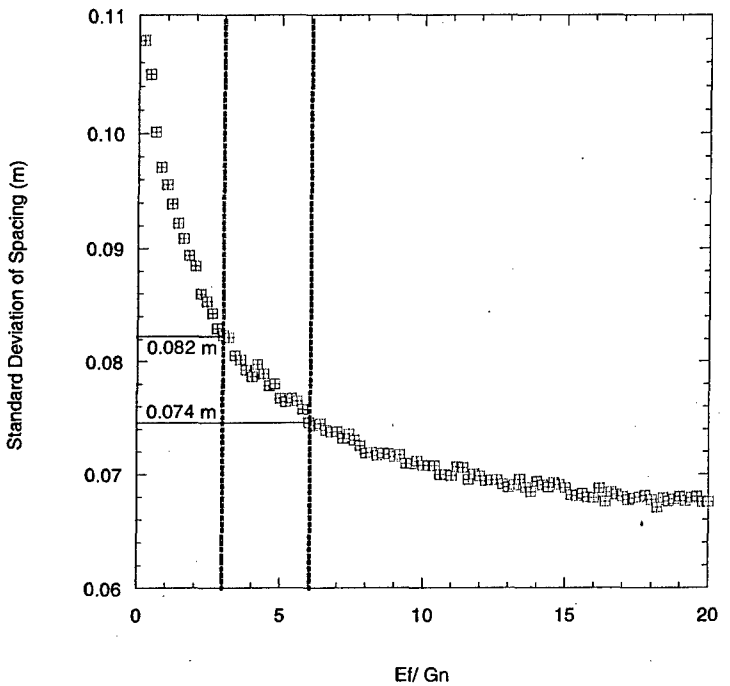


Figure 282 – Standard deviation vs. $\frac{E_f}{G_n}$ ratio for section II. Actual standard deviation of joint spacing ~ 0.08 m.

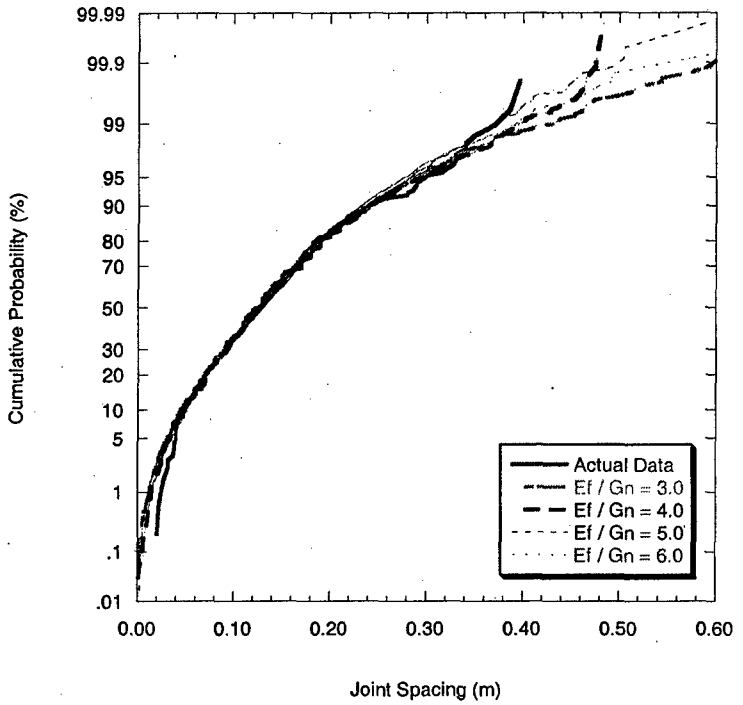


Figure 283 – Comparison between actual and simulated joint spacing CDFs for section II using four different $\frac{E_f}{G_n}$ ratios.

Section III

Figure 284 shows the standard deviation vs. $\frac{E_f}{G_n}$ relationship for section III using the rejection procedure with saturation mechanism. As in section II, the rejection procedure underestimates the standard deviation of joint spacing inside the reasonable range of $\frac{E_f}{G_n}$ values (3.0 to 6.0). The simulated joint CDFs also underestimate the number of smaller spacings (**Figure 285**). However, K-S testing accepts hypothesis H_0 at the 0.05 level in all cases in **Figure 285**.

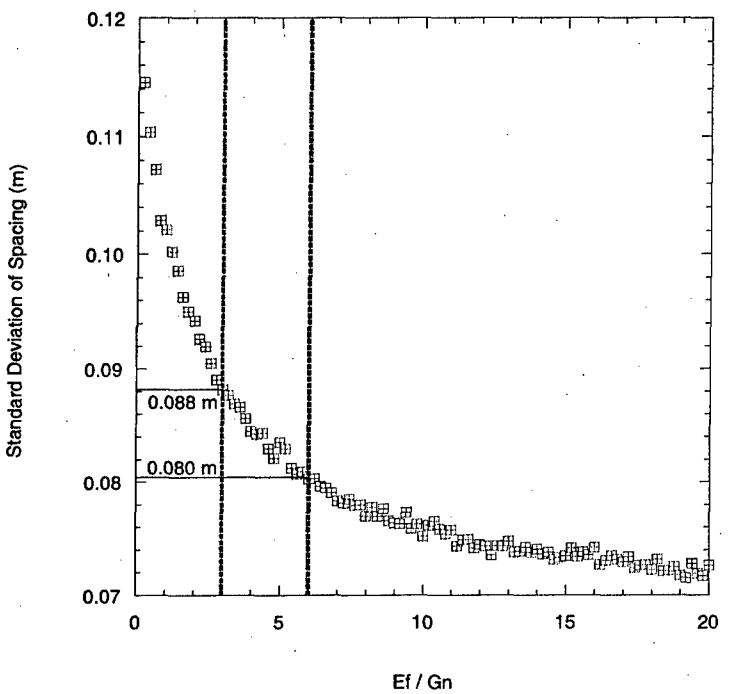


Figure 284 – Standard deviation vs. $\frac{E_f}{G_n}$ ratio for section III. Actual standard deviation of joint spacing ~ 0.09 m.

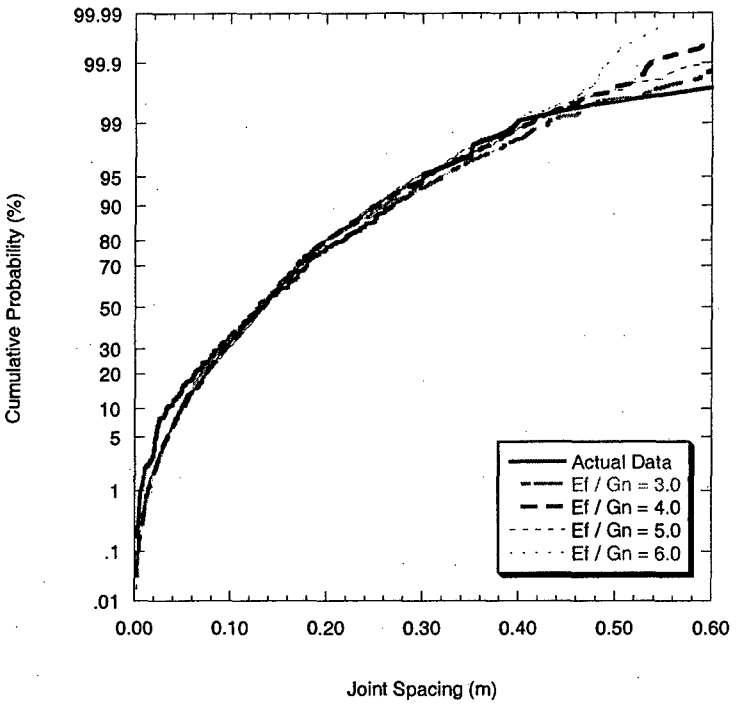


Figure 285 – Comparison between actual and simulated joint spacing CDFs for section III using four different $\frac{E_f}{G_n}$ ratios.

Section IV

Figure 286 shows that the rejection procedure overestimates the standard deviation of spacing for $\frac{E_f}{G_n}$ between 3.0 and 6.0 in section IV but there appears to be a good agreement between the simulated joint spacing CDFs and the actual joint spacing CDFs (**Figure 287**) although the number of smaller spacings is slightly overestimated by the rejection procedure. K-S testing reveals that the hypothesis H_0 is accepted at the 0.05 level for all cases in **Figure 287**.

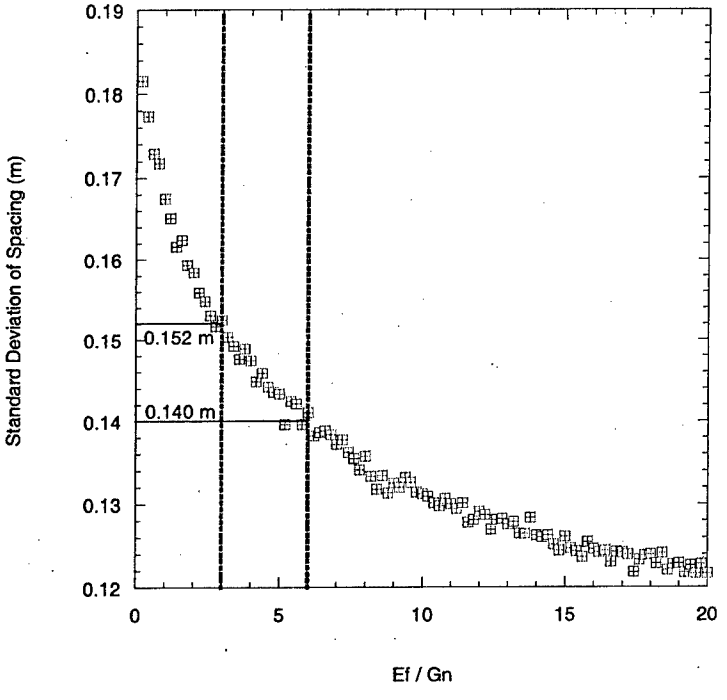


Figure 286 – Standard deviation vs. $\frac{E_f}{G_n}$ ratio for section IV. Actual standard deviation of joint spacing ~ 0.13 m.

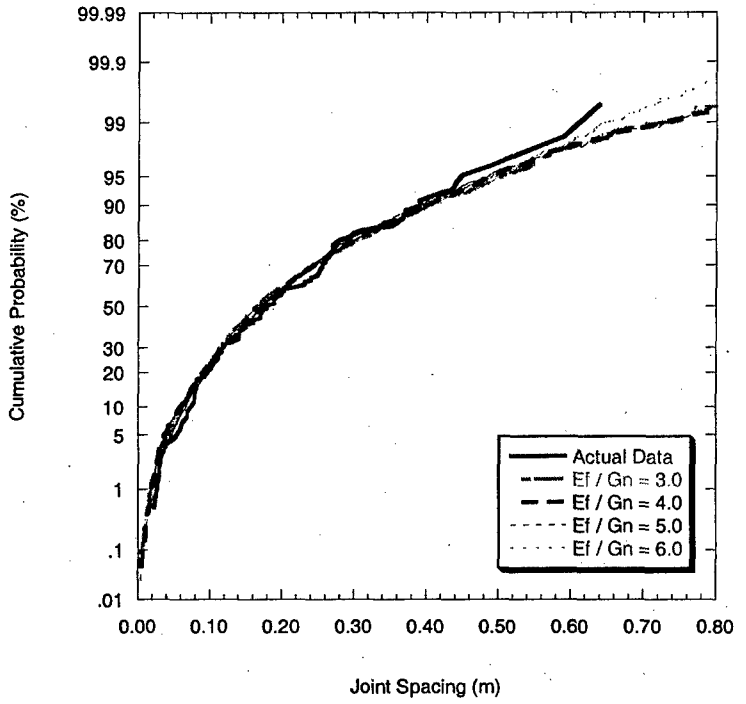


Figure 287 – Comparison between actual and simulated joint spacing CDFs for section IV using four different $\frac{E_f}{G_n}$ ratios.

Although the rejection procedure appears to work better than the flaw model in terms of the joint spacing CDF for all four sections, one must keep in mind that the rejection procedure is not a mechanical model. The rejection procedure effectively models the tensile strength as having a wider range of values than the ranges used in the flaw model, thus one should expect improvement in the joint spacing CDF fit over those in the flaw model especially for sections II and III. However, even this effectively increased range in tensile strength does not allow an increase in the simulated standard deviation of spacing sufficient to reach the actual value. The flaw model results should serve as a guide in assessing the performance of the rejection procedure. Based on the results for this case, it seems that the rejection procedure is reliable in the same joint intensity range as the flaw model even though it demonstrates the ability to reproduce the joint spacing CDFs at high joint intensity as it did in sections II and III. At lower intensities, the rejection procedure is a faster computational alternative to the flaw model because no flaws and stress to strength comparisons are ever handled.

7.3 Case 2: Saltzman (2001)

7.3.1 General Observations

Saltzman (2001) investigated the possibility of a correlation between joint spacing and material properties in layered sedimentary rock at Nahal Nekarot in southern Israel. Specifically, layer-confined vertical joints striking ~165° (or ~345°) were investigated in limestone/dolostone layers belonging to the Gerofit formation. These jointed layers are bounded by unjointed marlstone layers. Recall that Becker and Gross (1996) investigated layer-confined joints striking ~293° in different layers within the same formation in a nearby area. In Saltzman's (2001) study, joint spacing measurements from a single joint set found in four limestone/dolostone layers with thickness ranging from 12.0 cm (0.12 m) to 52.0 cm (0.52 m) were made (**Figure 288**). For unkown reasons, Saltzman (2001) did not make any joint measurements from the limestone/dolostone layer between layers 1 and 2 (**Figure 288**). The layers also appear to be numbered according to decreasing mean joint spacing (layer 1, 13.96 cm; layer 2, 10.38 cm; layer 3, 8.64 cm; layer 4, 5.91 cm). The ~165° striking joint set is the primary joint set in these four layers (Saltzman, 2001). In other words, it is the first-formed joint set in these layers.

Eyal et al. (2001) determined that the ~165° or ~345° joint set was formed under the Dead Sea Transform stress field (DSS). This pertains to a regional compressive stress oriented NNW-SSE. **Figure 289** shows the orientation of the DSS together with the maximum and minimum extensional strains (ε_1 and ε_3, respectively) as well as the ~165° joint set. The joints propagated normal to the maximum extensional strain (ε_1). Recall the in Becker and Gross (1996), the first-formed joints (striking ~293°) in the studied layer were associated with the Syrian Arc stress field (SAS) which strikes ~293°.

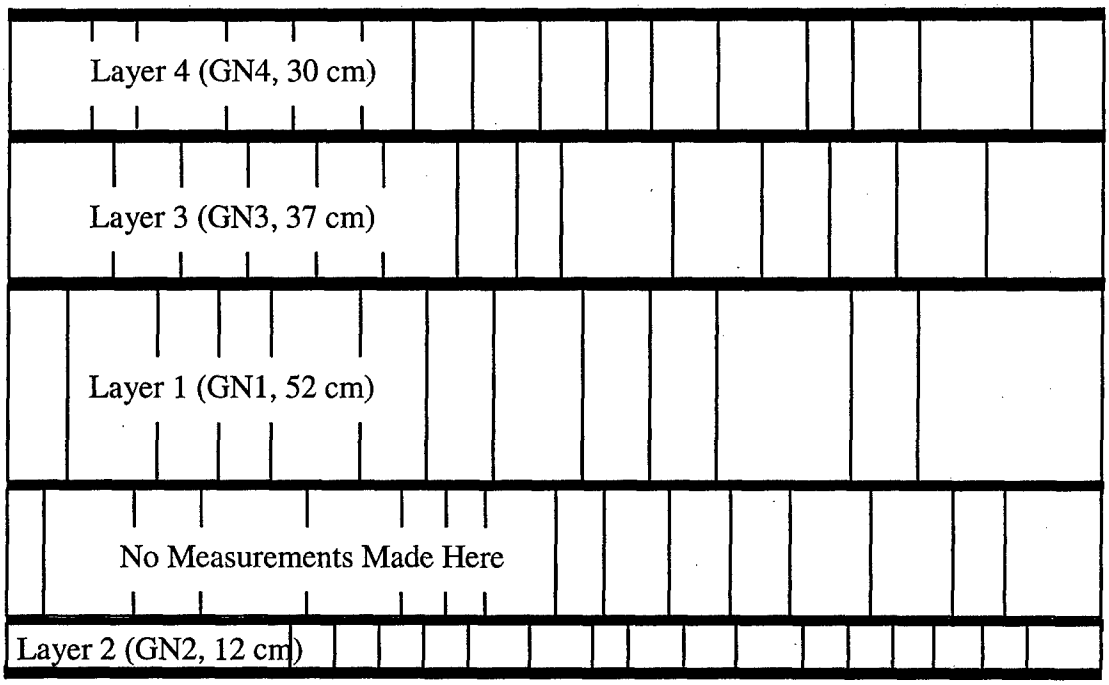


Figure 288 – Schematic of the limestone/dolostone layers studied by Saltzman (2001) (sketched from a photgraph in Saltzman, 2001). The layers are bounded by marlstone (represented by dark solid lines).

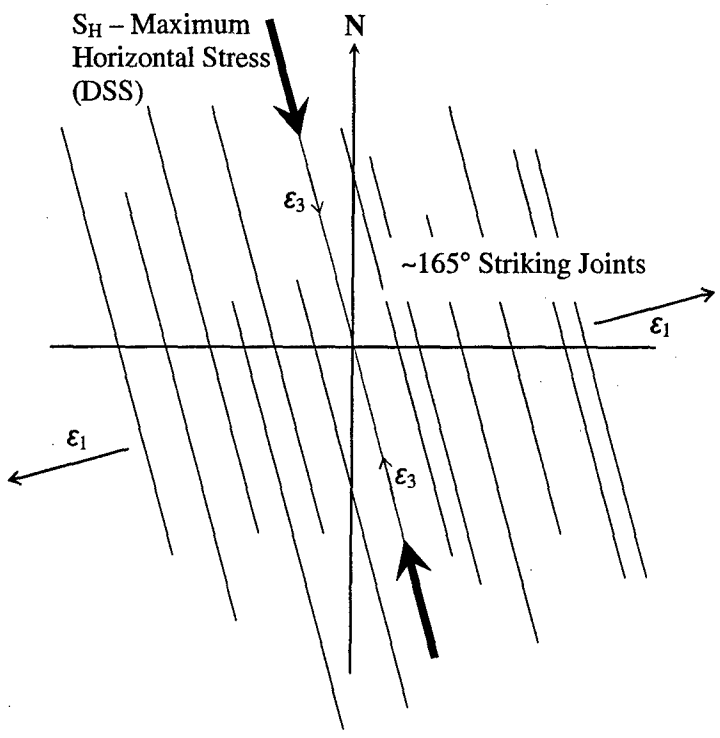


Figure 289 – Schematic of the relationship among the maximum horizontal stress, the maximum and minimum extensional strains and the ~165° joint set orientation. Sketched from information in Fig. 12 in Eyal et al. (2001).

7.3.2 Joint Spacing Data

Table 13 shows the spacing statistics for the ~165° joint set from each of the four layers (see also **Figure 288**). Compared to the data on the ~293° joint set gathered by Becker and Gross (1996) in another layer, the joint intensities here are generally much higher (i.e., mean spacing-to-thickness ratios are much smaller). Becker and Gross (1996) recorded mean spacing-to-thickness ratios from 0.77 to 1.31. Saltzman (2001), on the other hand, records mean spacing-to-thickness ratios in the 0.20 to 0.27 range for three of the four layers (**Table 13**). Eyal et al. (2001) also made the observation that joint intensities associated with the Dead Sea Transform stress field (DSS) tend to be higher than those associated with the Syrian Arc stress field (SAS).

Table 13 – Summary of joint spacing statistics for each layer. Measurements are in cm.

	Layer 1 (GN1)	Layer 2 (GN2)	Layer 3 (GN3)	Layer 4 (GN4)
Number of Spacings	30	59	49	62
Mean Spacing (cm)	13.96	10.38	8.64	5.91
Standard Deviation of Spacing (cm)	6.67	4.48	3.44	2.91
Layer Thickness (cm)	52	12	37	30
Mean Spacing / Layer Thickness	0.27	0.87	0.23	0.20

Figure 290 to **Figure 293** show the joint spacing histograms for each of the four layers. These follow the general shape of joint spacing distributions described in chapter **2**: unimodal and skewed towards small spacings. **Figure 294** to **Figure 297** show the joint spacing CDF for each layer along with the corresponding log-normal CDF estimated using maximum likelihood. There appears to be very good agreement between the spacing data and the corresponding estimated log-normal distributions. Chi-Squared goodness-of-fit tests accept the hypothesis that each of the four joint spacing datasets can be described by log-normal probability distributions. Also, despite the very high joint intensities observed here, none of the joint spacing data exhibit a quasi-normal distribution as Rives et al. (1992) observed in their laboratory experiments at high joint intensities.

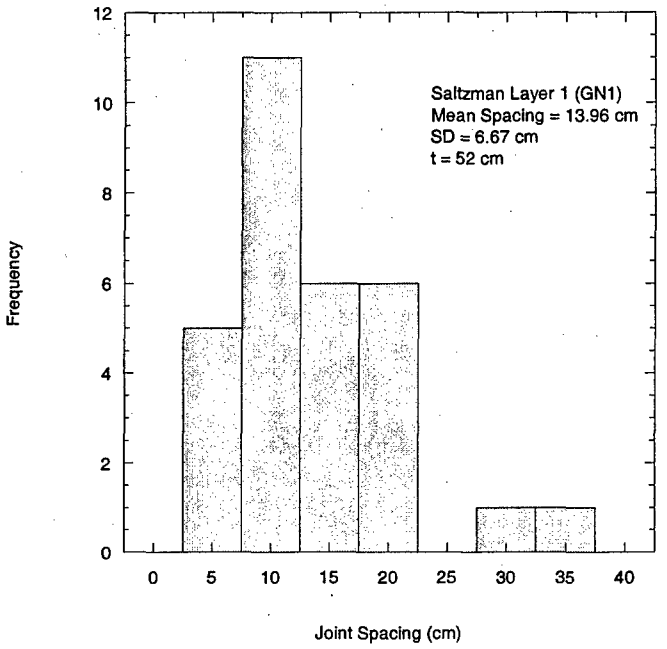


Figure 290 – Spacing histogram for layer 1 (GN1). Constructed from data in Saltzman (2001).

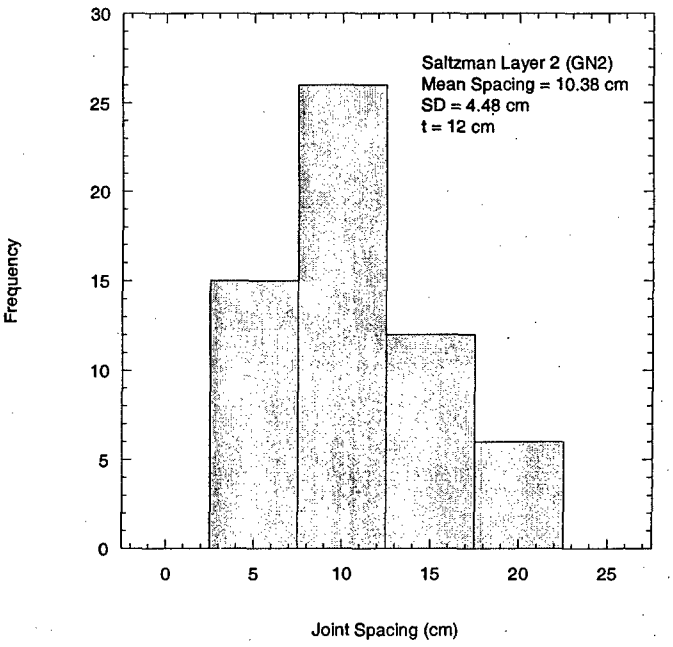


Figure 291 – Spacing histogram for layer 2 (GN2). Constructed from data in Saltzman (2001).

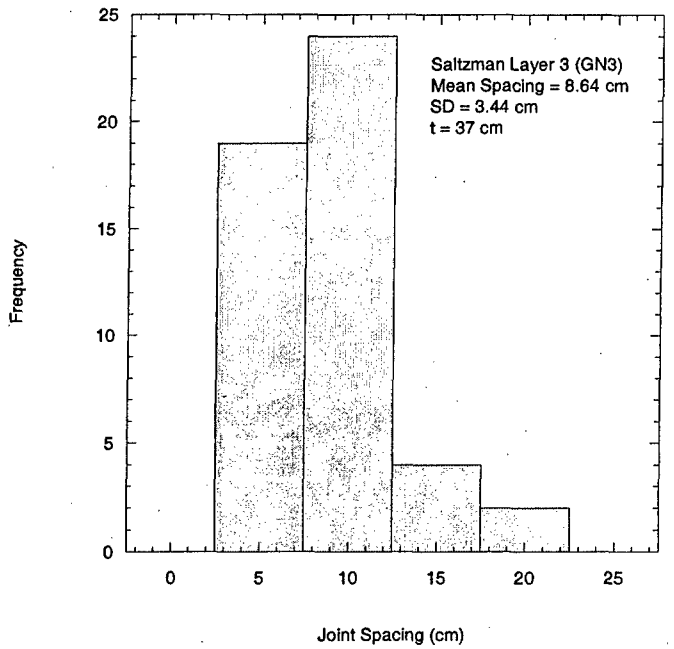


Figure 292 - Spacing histogram for layer 3 (GN3). Constructed from data in Saltzman (2001).

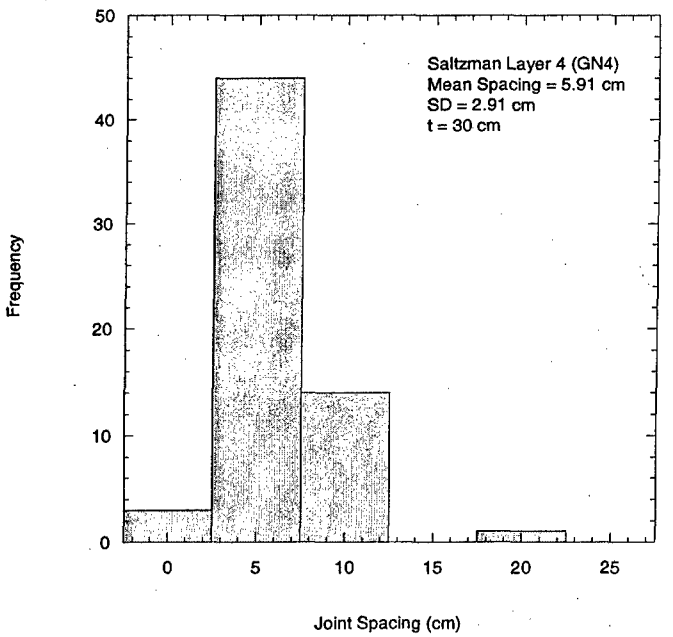


Figure 293 - Spacing histogram for layer 4 (GN4). Constructed from data in Saltzman (2001).

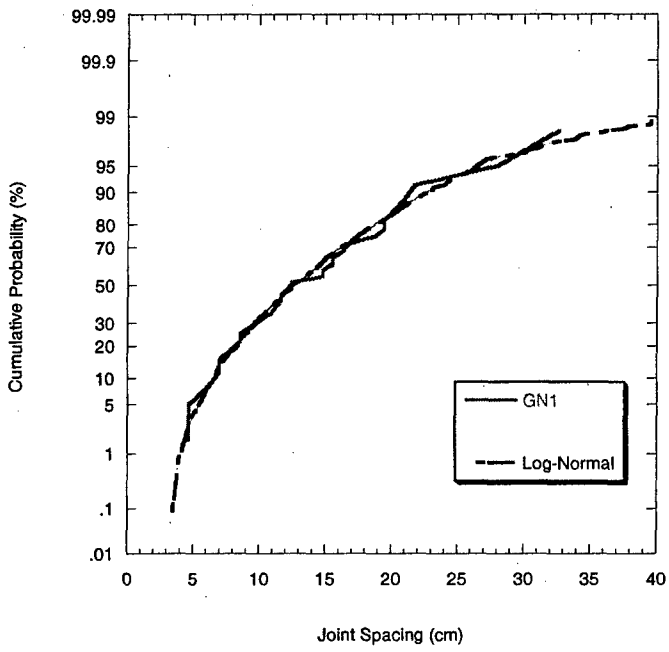


Figure 294 – Joint spacing CDF for layer 1 and a log-normal distribution. Chi-squared goodness-of-fit accepted at the 0.05 and 0.01 levels.

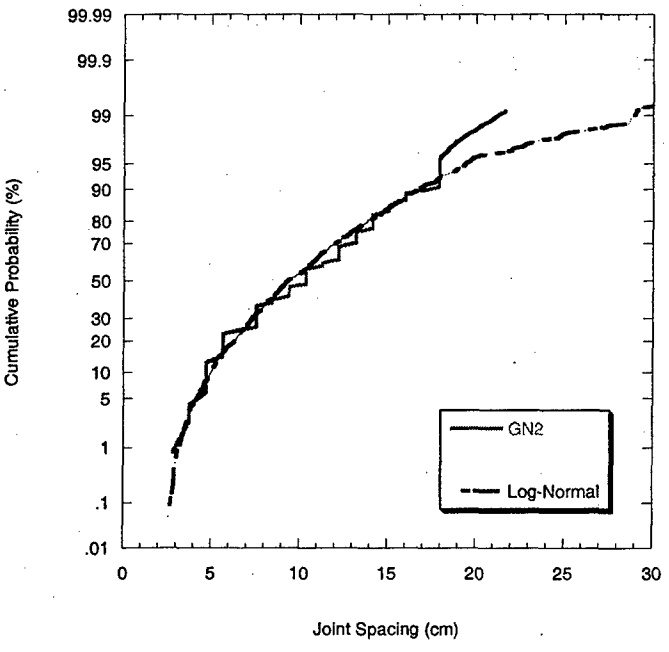


Figure 295 – Joint spacing CDF for layer 2 and a log-normal distribution. Chi-squared goodness-of-fit accepted at the 0.05 and 0.01 levels.

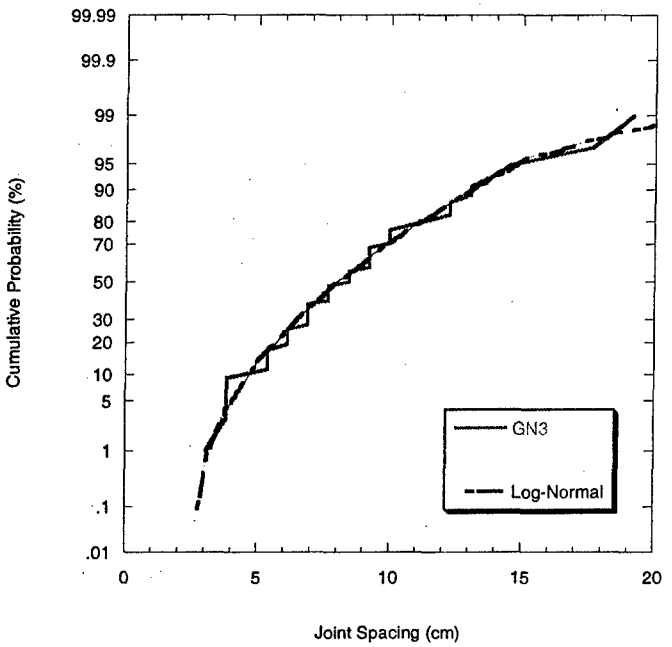


Figure 296 – Joint spacing CDF for layer 3 and a log-normal distribution. Chi-squared goodness-of-fit accepted at the 0.05 and 0.01 levels.

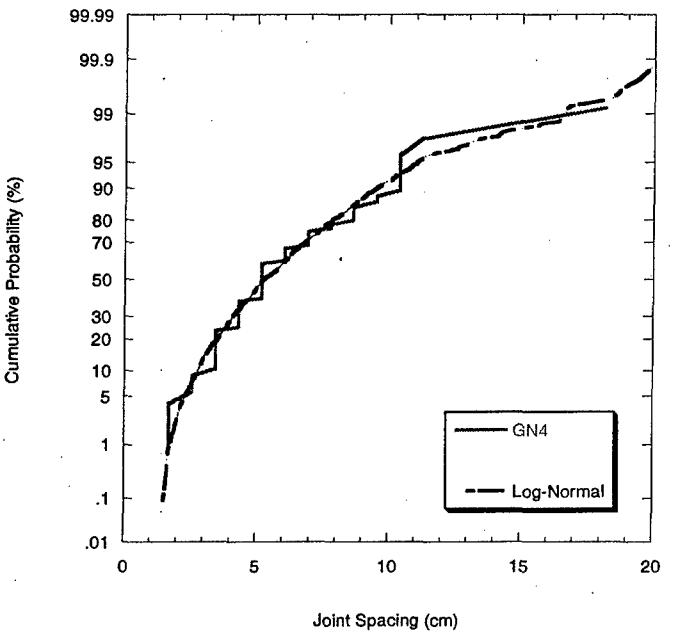


Figure 297 – Joint spacing CDF for layer 4 and a log-normal distribution. Chi-squared goodness-of-fit accepted at the 0.05 and 0.01 levels.

7.3.3 Model Parameter Values

Table 14 shows Saltzman's (2001) field observations together with their corresponding model implications. This information may provide some guidance in running the simulations.

Table 14 – Field observations with their corresponding model implications for the spacing data from Saltzman (2001).

Field Observations	Model Implications
Joint spacing measurements were made on limestone/dolostone layers bounded by unjointed marlstone layers.	Limestone/dolostone is generally stiffer than marlstone so the $\frac{E_f}{G_n}$ ratio used in the simulations should be > 1.0.
The joint spacing measurements were made on the primary joint set (strike ~165°, vertically dipping). Abutting relationships suggest that this joint set is the first-formed joint set in the layers. Eyal et al. (2001) confirm that this is the orientation of the predominant first-formed joint set in sedimentary layers in the area.	Effect of the other joint sets observed in the area on the formation of the ~165° joint set can be neglected since it is the first-formed joint set in the layers considered.
No slip between dolostone/limestone and marlstone layers is evident. Joint intensity is quite high.	The interface slippage saturation mechanism is not applicable but the compressive stress development mechanism may have an effect on the simulated joint pattern. In the model, the interface shear strength is set to a very high value so that it cannot be overcome (i.e., no slippage). Because the joint intensity is very high, investigate if saturation mechanism prevents models from reaching target joint intensity.
No strain measurements were taken.	A stopping point for the jointing process needs to be defined. The actual mean joint spacing may be used for this purpose.

Saltzman (2001) deals with essentially the same rocks as Becker and Gross (1996), but includes material property determinations. To avoid repetition, the same material property information derived from Saltzman (2001) used for the case of Becker and Gross (1996) will be used in the present case. This is summarized in **Table 15**.

Table 15 – Summary of simulation parameters for the case of Saltzman (2001).

Material Property	Values to be Used
Modulus of Elasticity of limestone/dolostone, E_f	Most test samples fall at around 50 GPa (from Saltzman, 2001 test data)
$\frac{E_f}{G_n}$ ratio	3.0 to 6.0 (see case for Becker and Gross, 1996; section 7.2.3, page 299)
Tensile strength of limestone/dolostone	4.0 to 10.0 MPa as a starting point (from Saltzman, 2001 test data)
Thickness of marlstone layers	~0.05 m (same as case for Becker and Gross, 1996; see section 7.2.3, page 299)

7.3.4 Simulation Results and Discussion

7.3.4.1 Flaw Model Results

Uncorrelated Strength Model

Before proceeding to the simulation results, it is worthwhile to note that the joint intensities in three of the four layers are very high. Specifically, in layers 1, 3, and 4 the mean spacing-to-thickness ratio ranges from 0.20 to 0.27. In layer 2, this ratio is 0.87. Flaw model simulations covering the possible range of $\frac{E_f}{G_n}$ (or $\frac{E_f}{E_n}$) ratios, and the Poisson's ratios of the jointing and non-jointing (or bounding) layers (ν_f and ν_n, respectively) both of which control the critical spacing-to-thickness ratio ($\left(\frac{s}{t}\right)_{cr}$ from Bai and Pollard, 2000), indicate that the saturation mean spacing-to-thickness ratio ranges from **0.52** to **0.84**. This demonstrates how high the joint intensities in the layers studied by Saltzman (2001) are compared to what the flaw model and Bai and Pollard (2000) consider saturated. In other words, the flaw model with saturation mechanism may only be expected to work for layer 2 where the mean spacing-to-thickness ratio is 0.87 which is greater than the upper bound of the saturation mean spacing-to-thickness ratio (**0.84**). In the other three layers (layers 1, 3, and 4), it is unlikely that the flaw model with saturation mechanism will be able to reproduce the actual joint intensities because they are below the lower bound of the saturation mean spacing-to-thickness ratio (**0.52**). In those cases, it would be interesting to see how the flaw model without the saturation mechanism would perform.

Layer 1

Figure 298 shows that with the saturation mechanism, the flaw model cannot reach the actual joint intensity for layer 1. The simulated joint spacing CDFs lie to the right of the actual CDF. K-S hypothesis testing rejects the hypothesis that the actual spacing data and the simulated spacing data come from the same distribution for each of the $\frac{E_f}{G_n}$ values used.

Figure 299 to **Figure 301** show the actual vs. simulated joint spacing CDFs when no saturation mechanism is used. Three different ranges of tensile strength are used (i.e., 4.0

to 10.0 MPa from tensile strength testing, and two wider ranges). It is possible that the actual range of tensile strength is wider than the test results indicate. In the flaw model, recall that the ratio between the maximum and minimum tensile strength affects the resulting joint spacing distribution. The standard deviation of spacing increases with increasing ratio between the maximum and minimum tensile strength (regardless of their individual values). Here, the flaw model is able to simulate the actual joint intensity. K-S hypothesis testing accepts the hypothesis that the actual and simulated data come from the same probability distribution at the 0.05 level for all cases in **Figure 299** to **Figure 301**. However, it can be seen that the fit becomes better as the tensile strength range becomes wider. Also, the K-S statistic (i.e., the largest absolute difference in the cumulative probability between the actual and simulated joint spacing CDFs) becomes smaller as one goes from **Figure 299** to **Figure 301**. This is a good example of why hypothesis testing should be accompanied by a visual fit (e.g., joint spacing CDF plots) because sometimes the visual fit can give an overall perspective of the comparison that a single statistic cannot provide (e.g., the K-S statistic). For example, K-S hypothesis testing indicates a good fit in **Figure 299** but a visual comparison does not. In fact, an improvement could still be made by using a wider range of tensile strength values (e.g., **Figure 300**).

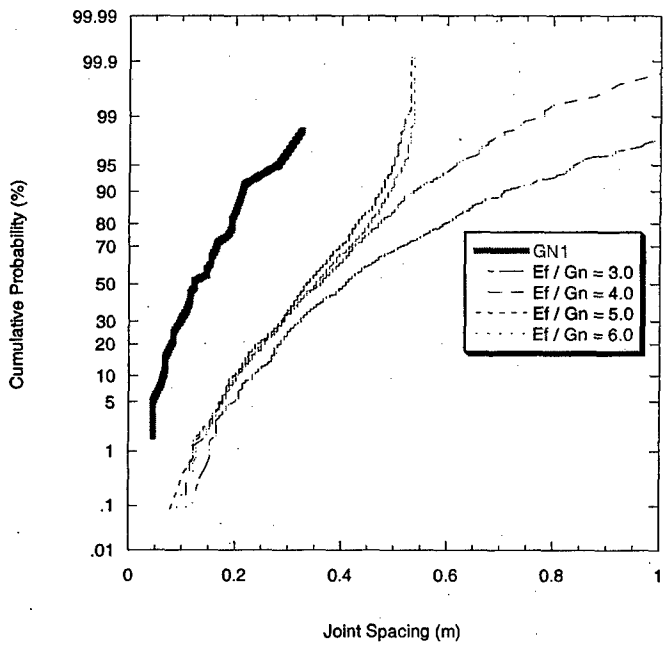


Figure 298 – Actual vs. simulated joint spacing CDFs using the flaw model with saturation for different values of $\frac{E_f}{G_n}$ for layer 1 (GN1). The minimum tensile strength is 4.0 MPa and the maximum 10.0 MPa.

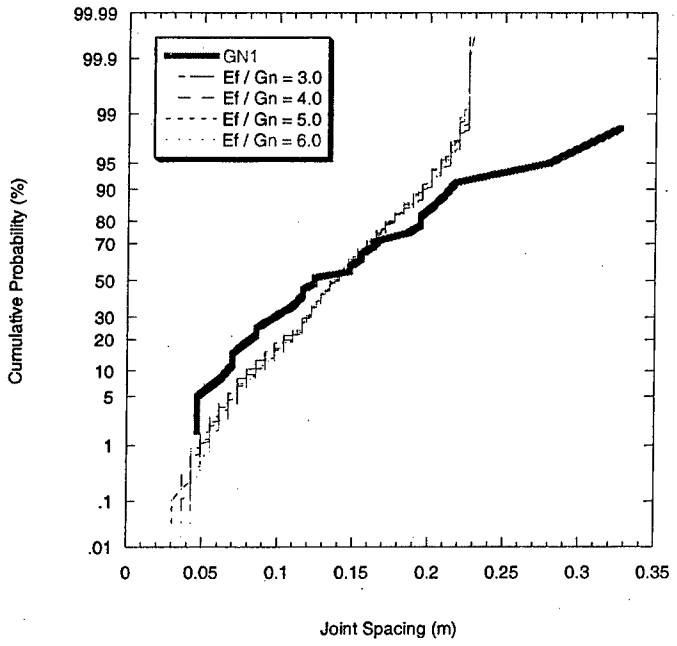


Figure 299 – Actual vs. simulated joint spacing CDFs using the flaw model without saturation for different values of $\frac{E_f}{G_n}$ for layer 1 (GN1). The minimum tensile strength is 4.0 MPa and the maximum 10.0 MPa.

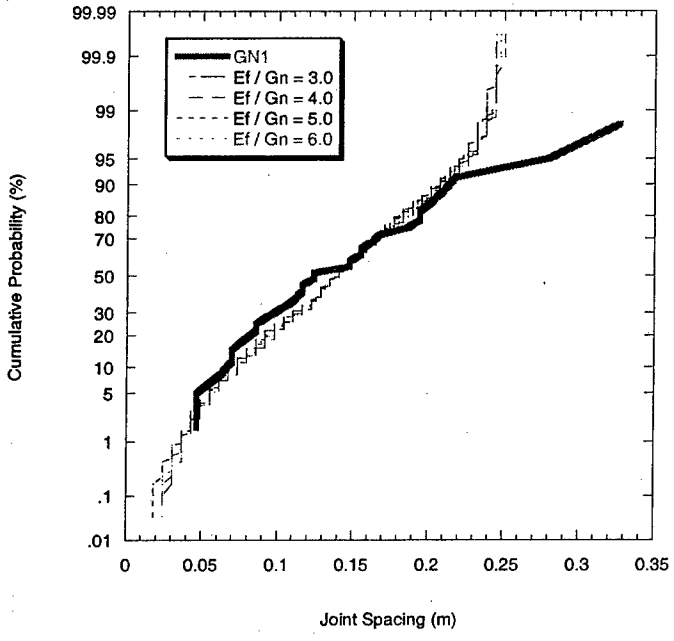


Figure 300 – Actual vs. simulated joint spacing CDFs using the flaw model without saturation for different values of $\frac{E_f}{G_n}$ for layer 1 (GN1). The minimum tensile strength is 2.0 MPa and the maximum 12.0 MPa.

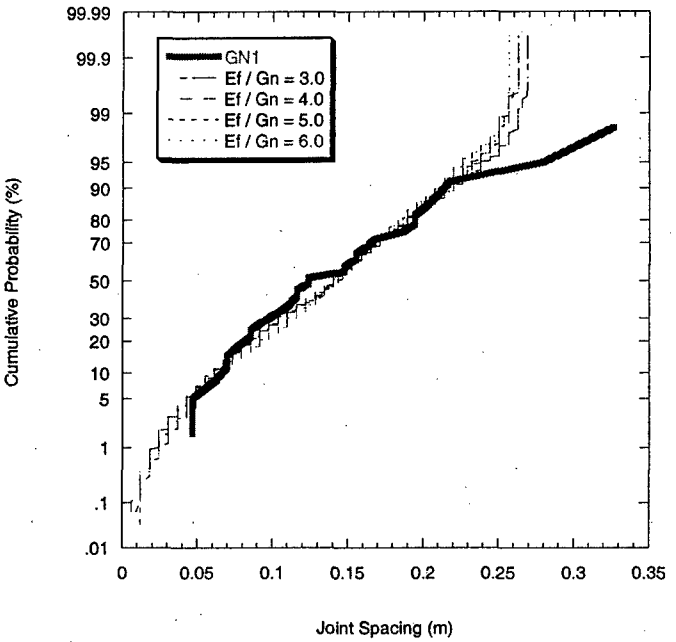


Figure 301 – Actual vs. simulated joint spacing CDFs using the flaw model without saturation for different values of $\frac{E_f}{G_n}$ for layer 1 (GN1). The minimum tensile strength is 1.0 MPa and the maximum 1.0e7 MPa.

Layer 2

Figure 302 to **Figure 304** show the actual vs. simulated joint spacing CDFs for layer 2 (GN2). Here, the joint intensity is not as high as the other three layers. As a consequence, the flaw model with saturation is able to simulate the actual joint intensity for layer 2. The flaw model with saturation mechanism gives a good fit between the actual and simulated joint spacing CDFs in **Figure 302** to **Figure 304**. K-S hypothesis testing confirms this for all plots in **Figure 302** to **Figure 304**.

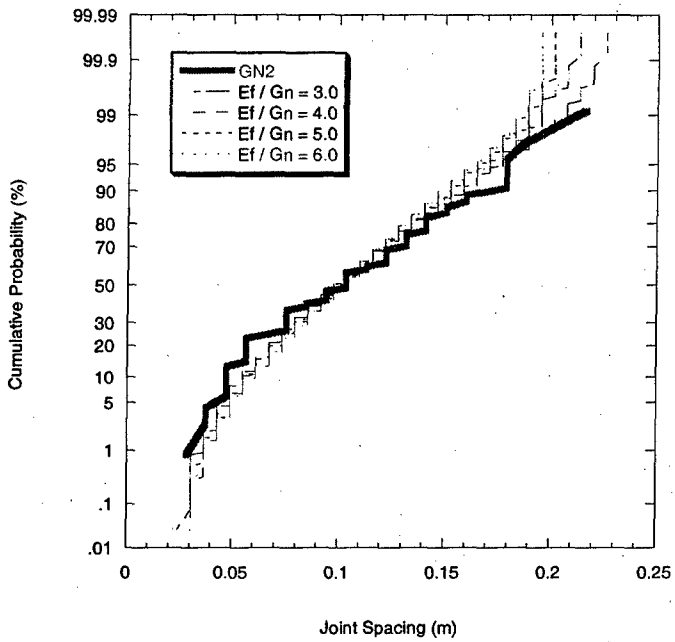


Figure 302 – Actual vs. simulated joint spacing CDFs using the flaw model with saturation for different values of $\frac{E_f}{G_n}$ for layer 2 (GN2). The minimum tensile strength is 4.0 MPa and the maximum 10.0 MPa.

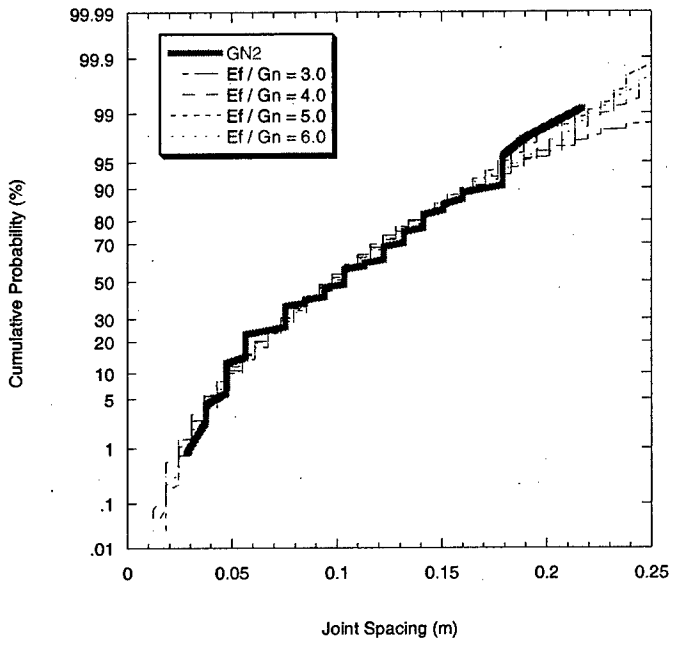


Figure 303 – Actual vs. simulated joint spacing CDFs using the flaw model with saturation for different values of $\frac{E_f}{G_n}$ for layer 2 (GN2). The minimum tensile strength is 2.0 MPa and the maximum 12.0 MPa.

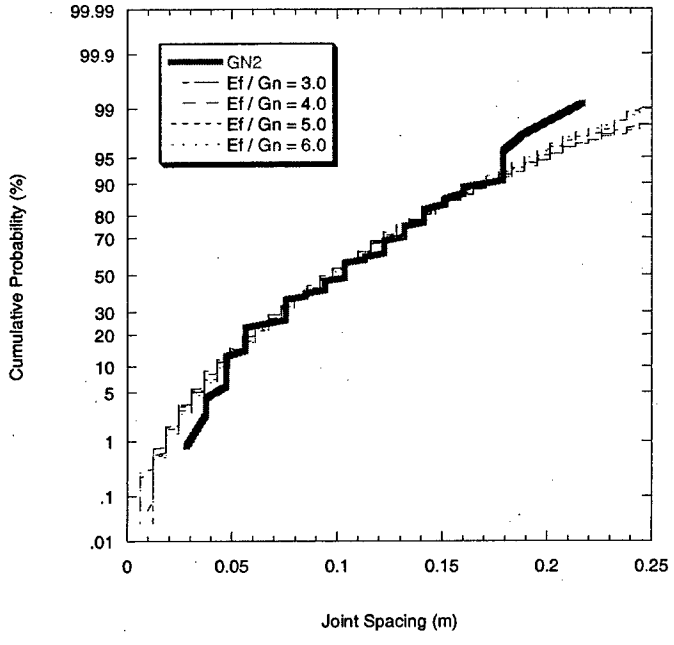


Figure 304 - Actual vs. simulated joint spacing CDFs using the flaw model with saturation for different values of $\frac{E_f}{G_n}$ for layer 2 (GN2). The minimum tensile strength is 1.0 MPa and the maximum 1.0e7 MPa.

Layer 3

Figure 305 shows the actual vs. simulated joint spacing CDFs for layer 3 (GN3). It is clear that with the saturation mechanism in place, the flaw model is unable to reach the actual joint intensity. Consequently, a good fit between the simulated and actual spacing data is never attained.

Figure 306 to **Figure 308** show that when the saturation mechanism is not applied, the flaw model is able to produce joint spacing CDFs that come close to the actual joint spacing CDF. K-S hypothesis testing indicates a good fit between the actual and simulated joint spacing CDFs for all cases in **Figure 306** to **Figure 308**. Visually, though, **Figure 307** appears to provide the best fit between the actual and simulated joint spacing CDFs.

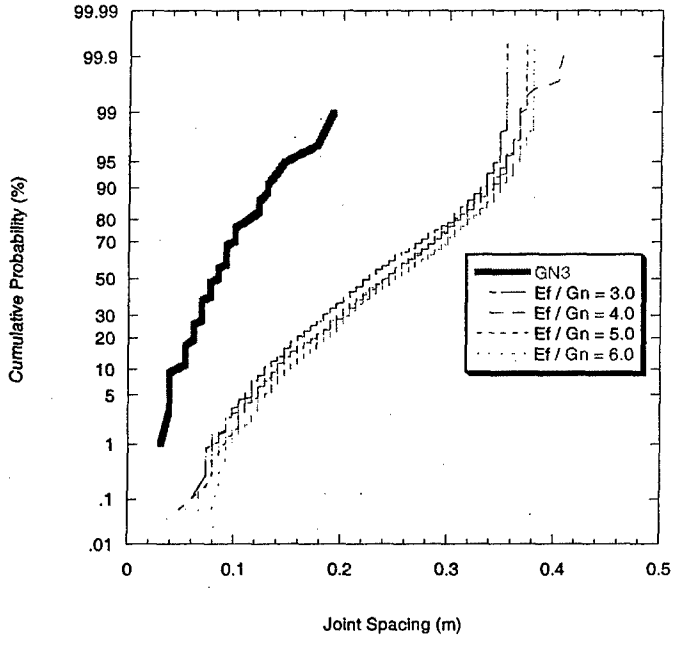


Figure 305 – Actual vs. simulated joint spacing CDFs using the flaw model with saturation for different values of $\frac{E_f}{G_n}$ for layer 3 (GN3). The minimum tensile strength is 4.0 MPa and the maximum 10.0 MPa.

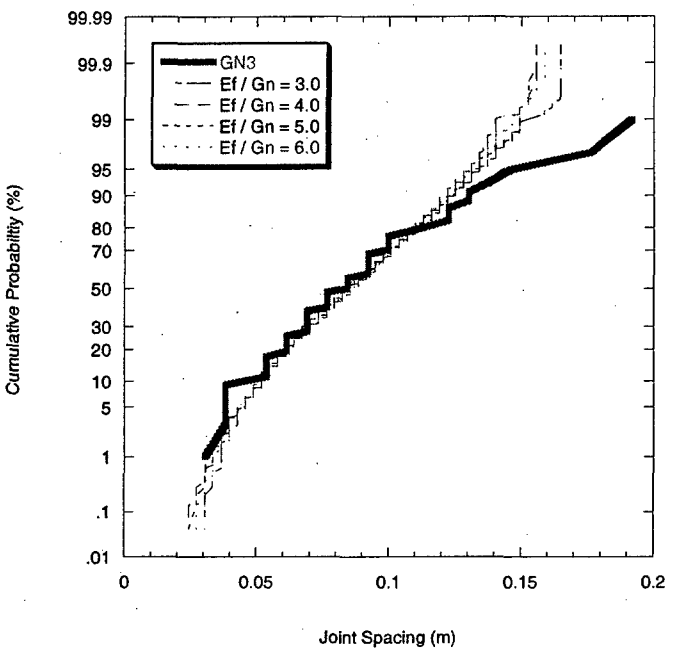


Figure 306 – Actual vs. simulated joint spacing CDFs using the flaw model without saturation for different values of $\frac{E_f}{G_n}$ for layer 3 (GN3). The minimum tensile strength is 4.0 MPa and the maximum 10.0 MPa.

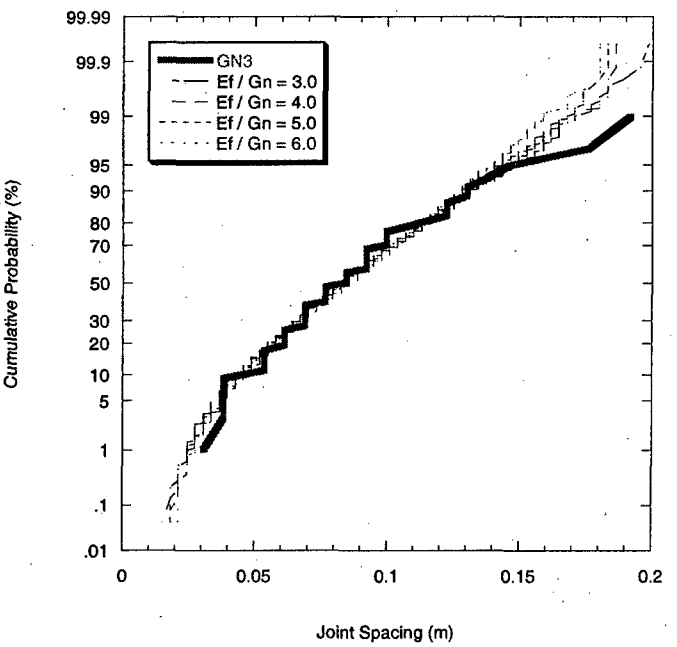


Figure 307 – Actual vs. simulated joint spacing CDFs using the flaw model without saturation for different values of $\frac{E_f}{G_n}$ for layer 3 (GN3). The minimum tensile strength is 2.0 MPa and the maximum 12.0 MPa.

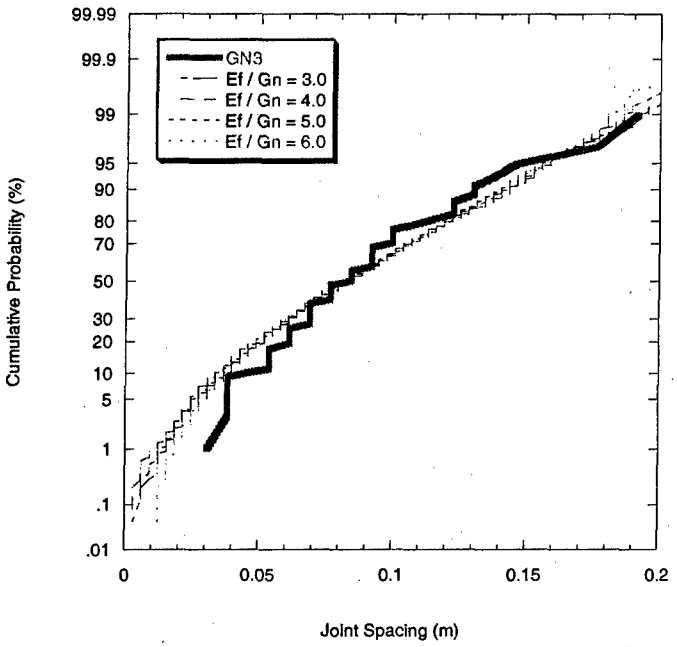


Figure 308 – Actual vs. simulated joint spacing CDFs using the flaw model without saturation for different values of $\frac{E_f}{G_n}$ for layer 3 (GN3). The minimum tensile strength is 1.0 MPa and the maximum 1.0e7 MPa.

Layer 4

Figure 309 shows the actual vs. simulated joint spacing CDFs for layer 4 (GN4). Like layers 1 and 3, the flaw model could not reach the actual joint intensity because of the saturation mechanism. Consequently, a good fit again could not be attained between the actual and simulated joint spacing CDFs.

Without the saturation mechanism, the flaw model is able to reach the actual joint intensity for layer 4. This results in a better fit than in that in **Figure 309**. **Figure 310** to **Figure 312** show the resulting joint spacing CDFs in the absence of the saturation mechanism. However, K-S hypothesis testing rejects the hypothesis that the actual and simulated joint spacing come from the same distribution at the 0.05 level for all cases in **Figure 310**. In **Figure 311**, the hypothesis is accepted at the 0.05 level in all but the $\frac{E_f}{G_n} = 6.0$ case. In **Figure 312**, the hypothesis is accepted at the 0.05 level in all cases. Visually, an improvement in the fit between actual and simulated joint spacing CDFs can be observed from **Figure 310** to **Figure 312**.

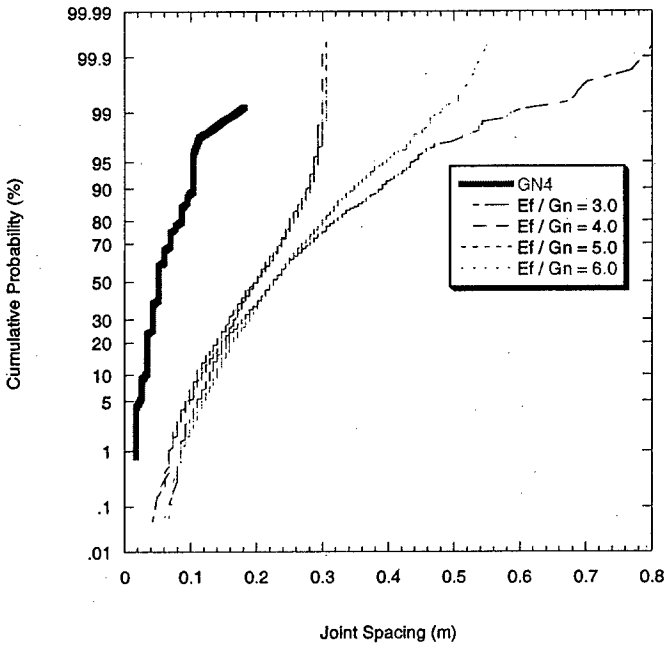


Figure 309 – Actual vs. simulated joint spacing CDFs using the flaw model with saturation for different values of $\frac{E_f}{G_n}$ for layer 4 (GN4). The minimum tensile strength is 4.0 MPa and the maximum 10.0 MPa.

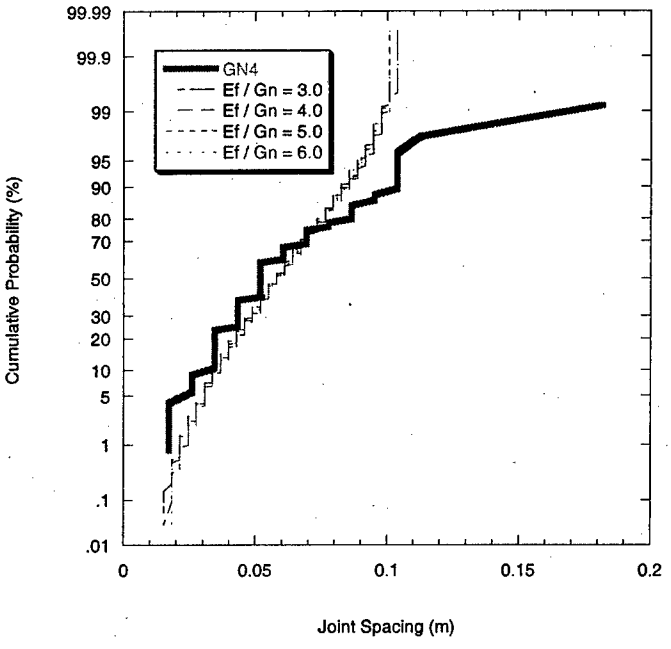


Figure 310 – Actual vs. simulated joint spacing CDFs using the flaw model without saturation for different values of $\frac{E_f}{G_n}$ for layer 4 (GN4). The minimum tensile strength is 4.0 MPa and the maximum 10.0 MPa.

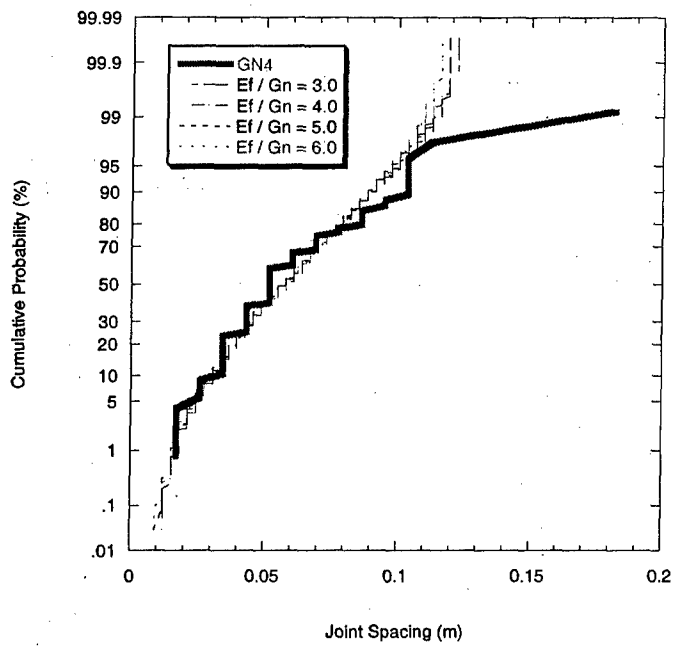


Figure 311 - Actual vs. simulated joint spacing CDFs using the flaw model without saturation for different values of $\frac{E_f}{G_n}$ for layer 4 (GN4). The minimum tensile strength is 2.0 MPa and the maximum 12.0 MPa.

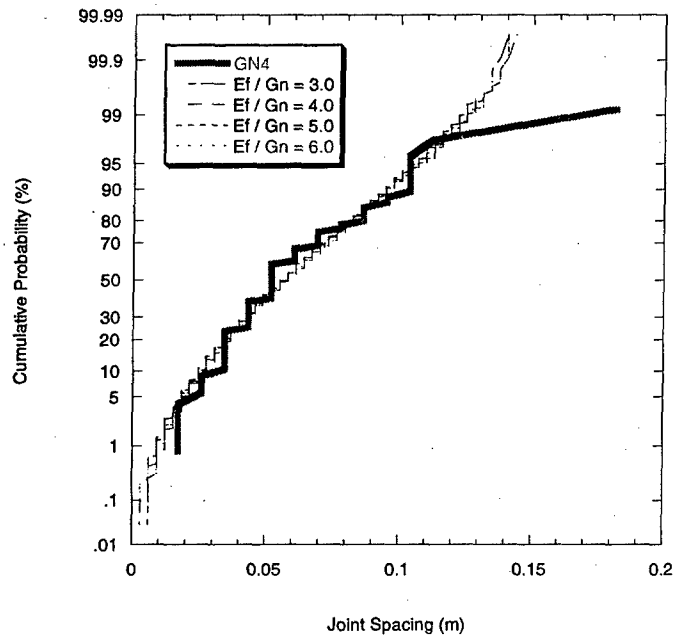


Figure 312 - Actual vs. simulated joint spacing CDFs using the flaw model without saturation for different values of $\frac{E_f}{G_n}$ for layer 4 (GN4). The minimum tensile strength is 1.0 MPa and the maximum 1.0e7 MPa.

Discussion

The flaw model with saturation does not appear capable of simulating joint spacing CDFs for very high joint intensities. For the only case where the joint intensity was not too high (i.e., layer 2, GN2), it provided good agreement between the actual and simulated joint spacing CDFs (**Figure 302** to **Figure 304**). In the other cases where the joint intensities are very high, the absence of a saturation mechanism appears to enable the flaw model to produce joint spacing CDFs that come close to the actual joint spacing CDFs. This means that the saturation mechanism proposed by Bai and Pollard (2000) may not be applicable to the Saltzman (2001) spacing data. It is also observed that a wider range of tensile strength leads to a better fit between the actual and simulated joint spacing CDFs. The wider tensile strength ranges here correspond to higher ratios between the maximum and minimum tensile strength (e.g., 4.0-10.0 for a ratio of 2.5; 2.0-12.0 for a ratio of 6.0). As explained before, a larger ratio between the maximum and minimum tensile strength values leads to a larger standard deviation of spacing. Another effect of increasing the tensile strength ratio is the increase in the relative frequency of smaller spacings as well as a corresponding relative decrease in larger spacings. In the simulations using a tensile strength range of 4.0-10.0 MPa, the relative frequency of smaller spacings is generally underestimated and the relative frequency of larger spacings is overestimated. Widening the range to 2.0-12.0 MPa improved the fit between the actual and simulated joint spacing CDFs. Two wider ranges were used: a realistic 2.0-12.0 MPa and a somewhat unrealistic 1.0-1.0e7 MPa range. Nevertheless, a good fit was observed when using the realistic 2.0-12.0 MPa tensile strength range.

Correlated Strength Model

Even though the uncorrelated strength model produces joint spacing CDFs that appear to agree with the actual joint spacing CDFs, a correlated strength model is also explored. In a correlated strength model, the strength at some location is dependent on the strength at an adjacent location. This prevents abrupt changes in tensile strength from one point to another and produces clear peaks and valleys of high and low tensile strength (for example, compare **Figure 313** and **Figure 314**).

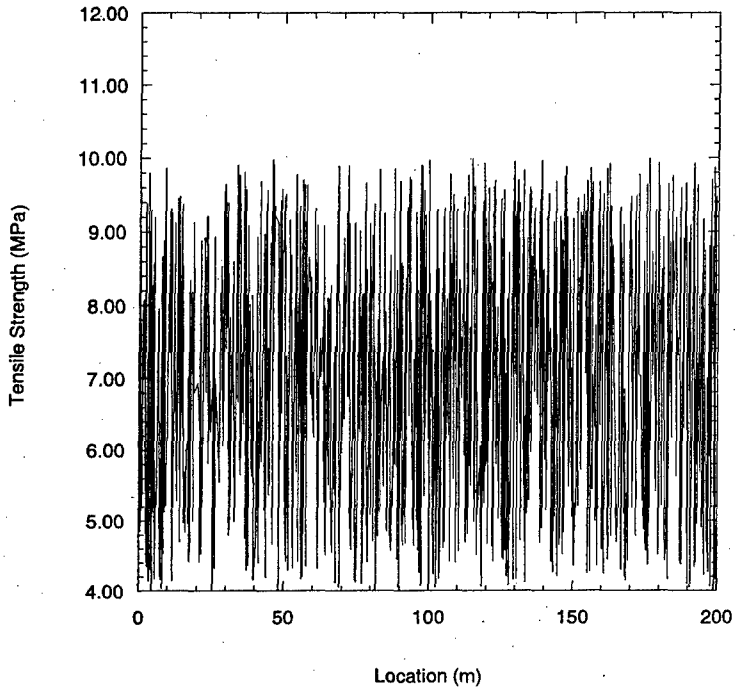


Figure 313 - Variation of tensile strength along the jointing layer for the uncorrelated strength model. The tensile strength has a uniform probability distribution between 4.0 and 10.0 MPa. The strength is defined at 1000 points along the layer.

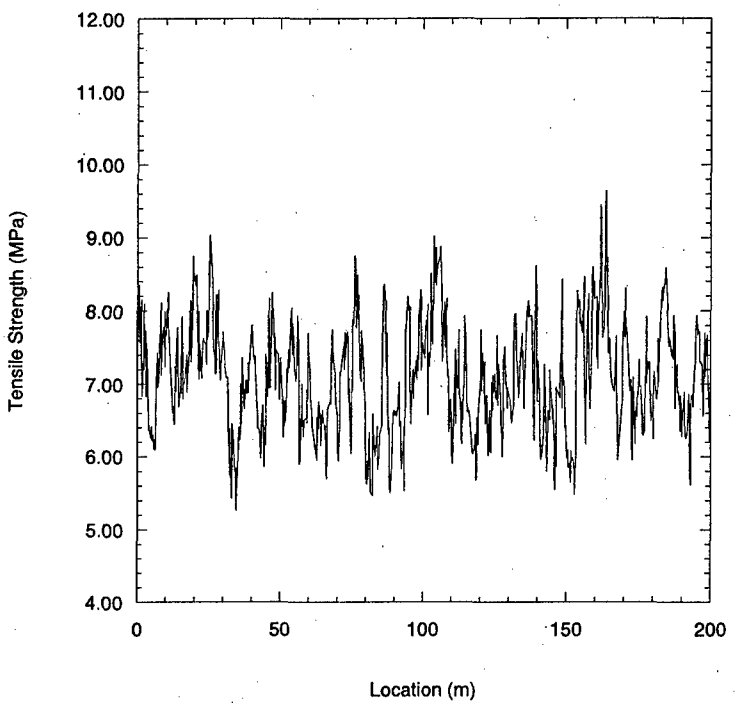


Figure 314 - Variation of tensile strength along the jointing layer for a correlated strength model. Parameter values: $\phi = 0.9$, $\sigma_\varepsilon = 0.05$ and $\mu_{\sigma_t} = 7.0$ MPa. The strength is defined at 1000 points along the layer.

Recall that the correlated strength model is given by:

$$\ln\left(\frac{\sigma_{t_i}}{\mu_{\sigma_t}}\right) = \phi \ln\left(\frac{\sigma_{t_{i-1}}}{\mu_{\sigma_t}}\right) + \varepsilon_i \qquad \textbf{Equation 72}$$

(repeated here from page 242)

where σ_{t_i} is the tensile strength at location i, $\sigma_{t_{i-1}}$ is the tensile strength at the previous adjacent location (i-1), μ_{σ_t} is the mean tensile strength, ϕ is the correlation factor ($0 < \phi < 1$) and ε_i is a normal random variable with mean equal to zero and a standard deviation of σ_ε. Saltzman (2001) measured tensile strength from rock samples and found that it ranges from ~4.0 to ~10.0 MPa. The histogram of tensile strength data from Saltzman (2001) is shown in **Figure 250**, page 301. The mean tensile strength is therefore $\mu_{\sigma_t} = 7.0$ MPa. In order to estimate σ_ε, the above expression is expanded to yield the following:

$$\ln \sigma_{t_i} - \ln \mu_{\sigma_t} = \phi \ln \sigma_{t_{i-1}} - \phi \ln \mu_{\sigma_t} + \varepsilon_i$$

It can be seen that ε_i is related to the natural logarithm of the tensile strength. As an estimate, let σ_ε equal the standard deviation of the natural logarithms of the tensile

strength from the data or $\sigma_\varepsilon = \sqrt{\sigma^2_{\ln \sigma_t}}$. This yields a value of $\sigma_\varepsilon \approx 0.2$ using Saltzman's (2001) tensile strength data. This value of σ_ε, when used in **Equation 72**, generates tensile strength values with a range that is generally wider than that observed by Saltzman (2001) in laboratory testing. It must be noted, however, that the range of tensile strength values produced by **Equation 72** also depends on the correlation factor, ϕ, and not on σ_ε alone. Consequently, even with the value of σ_ε held constant at 0.2, the range of generated tensile strength values from **Equation 72** widens as the correlation factor ϕ is increased.

As in the flaw model with an uncorrelated strength model, the presence of the saturation mechanism in this case does not allow the flaw model to reach the actual joint intensity except for layer 2 (GN2). Without the saturation mechanism, however, the flaw model is able to attain the target joint intensities in layers 1, 3, and 4.

Layer 1

Figure 315 and **Figure 316** show the actual vs. simulated joint spacing CDFs for layer 1 using the flaw model without saturation but with the correlated strength model. Two ranges of tensile strength are used: 4.0-10.0 MPa and 2.0-12.0 MPa. The $\frac{E_f}{G_n}$ ratio is fixed at 3.0. Also, $\sigma_\varepsilon \approx 0.2$ in all cases. Visually, the agreement between the actual and simulated joint spacing CDFs does not appear to be good. However, K-S hypothesis testing accepts the hypothesis that the simulated and actual spacing data come from the same distribution at the 0.05 level in all cases in **Figure 315** and **Figure 316**. In this case, a visual assessment indicates that the flaw model with correlated strength may not be applicable. There is a considerable discrepancy between the shapes of the actual and simulated joint spacing CDFs as well as the relative frequencies of small and large spacings.

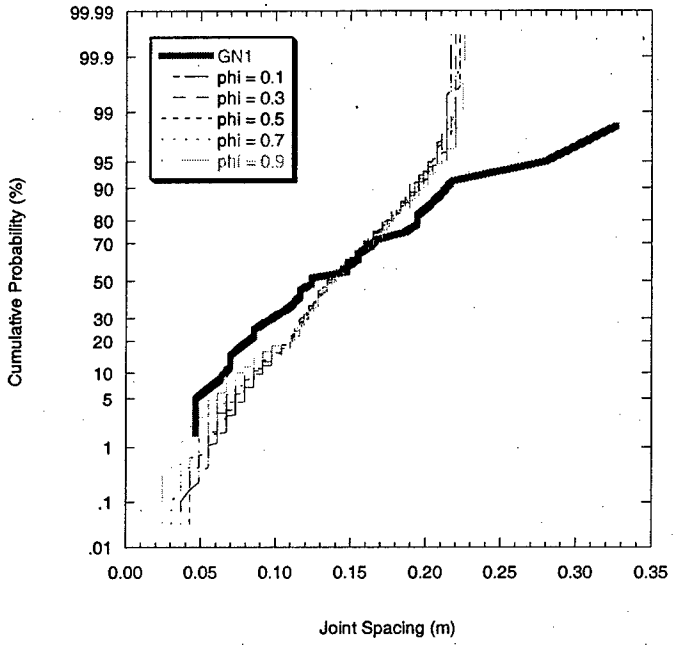


Figure 315 – Actual vs. simulated joint spacing CDFs using the flaw model with correlation without saturation for different values of ϕ for layer 1 (GN1). The minimum tensile strength is 4.0 MPa and the maximum 10.0 MPa. The $\frac{E_f}{G_n}$ ratio is fixed at 3.0.

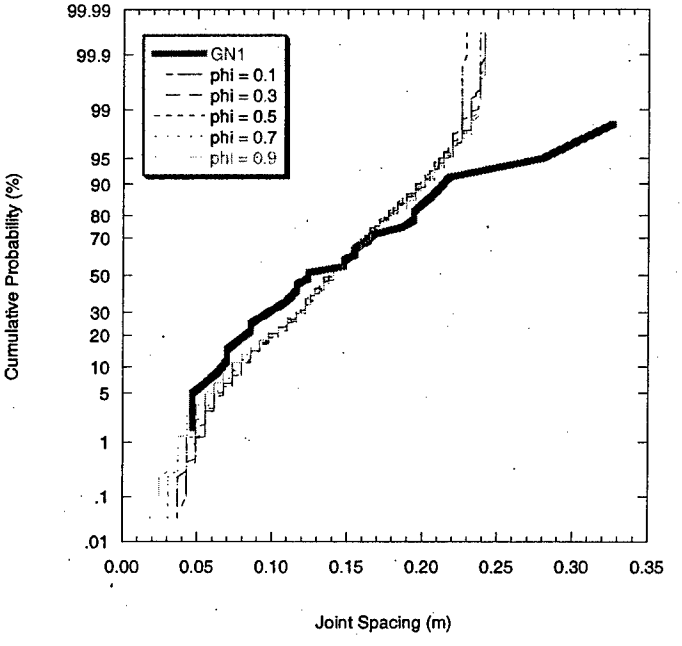


Figure 316 – Actual vs. simulated joint spacing CDFs using the flaw model with correlation without saturation for different values of ϕ for layer 1 (GN1). The minimum tensile strength is 2.0 MPa and the maximum 12.0 MPa. The $\frac{E_f}{G_n}$ ratio is fixed at 3.0.

Layer 2

The flaw model with saturation mechanism is able to reproduce the joint intensity in layer 2 (GN2) because it is not as high as those in the other layers. As shown in **Figure 317** and **Figure 318**, the flaw model with both the saturation mechanism and correlated strength model provides a good fit between the actual and simulated joint spacing CDFs especially at higher correlation factors. K-S hypothesis testing accepts the hypothesis that the actual and simulated joint spacing data come from the same distribution for all cases in **Figure 317** and **Figure 318**. It appears that in the case of layer 2 (GN2), the flaw model with saturation mechanism and correlated strength model performs well.

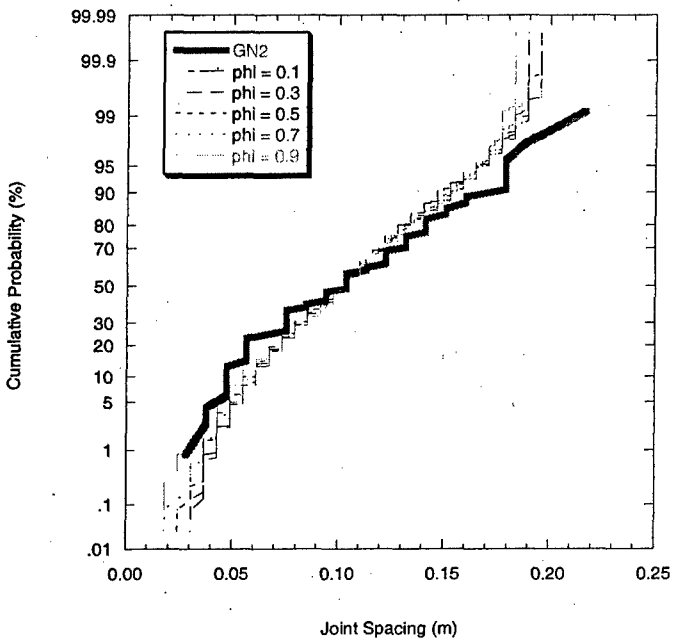


Figure 317 – Actual vs. simulated joint spacing CDFs using the flaw model with correlation and saturation for different values of ϕ for layer 2 (GN2). The minimum tensile strength is 4.0 MPa and the maximum 10.0 MPa. The $\frac{E_f}{G_n}$ ratio is fixed at 3.0.

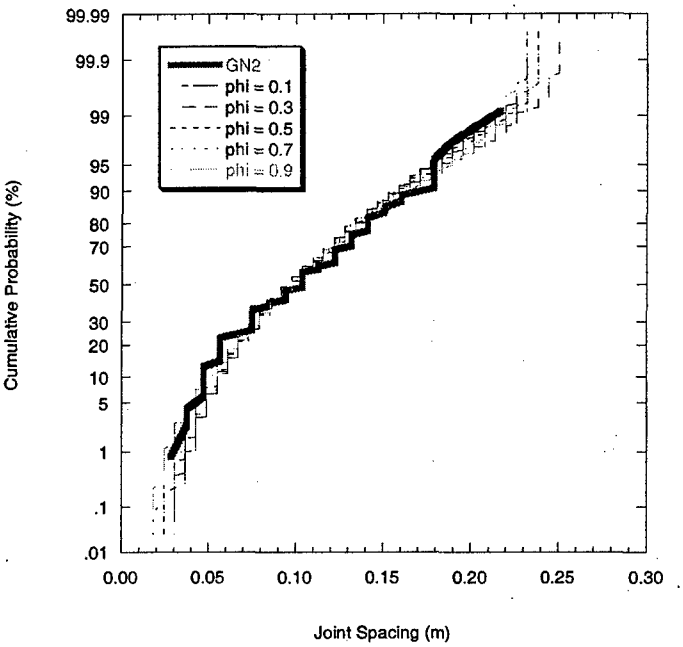


Figure 318 – Actual vs. simulated joint spacing CDFs using the flaw model with correlation and saturation for different values of ϕ for layer 2 (GN2). The minimum tensile strength is 2.0 MPa and the maximum 12.0 MPa. The $\frac{E_f}{G_n}$ ratio is fixed at 3.0.

Layer 3

Figure 319 and **Figure 320** show the actual vs. simulated joint spacing CDFs for layer 3 (GN3) using two different tensile strength ranges (4.0-10.0 MPa and 2.0-12.0 MPa). No saturation mechanism is used here because it prevents the flaw model from attaining the actual joint intensity. Visually, the agreement between the actual and the simulated joint spacing CDFs does not appear to be good. K-S hypothesis testing indicates otherwise. The hypothesis that the actual and simulated joint spacing data come from the same distribution is accepted at the 0.05 level for all cases in **Figure 319** and **Figure 320**. However, it is clear that the fit is not as good visually as that for layer 2 (**Figure 317** and **Figure 318**). Also, Chi-Squared goodness-of-fit tests indicate that the spacings in all four layers can be described by log-normal probability distributions (**Figure 294** to **Figure 297**) . The simulated spacing data in **Figure 319** and **Figure 320** appear to have middle portions that form a straight line indicating a quasi-normal distribution instead.

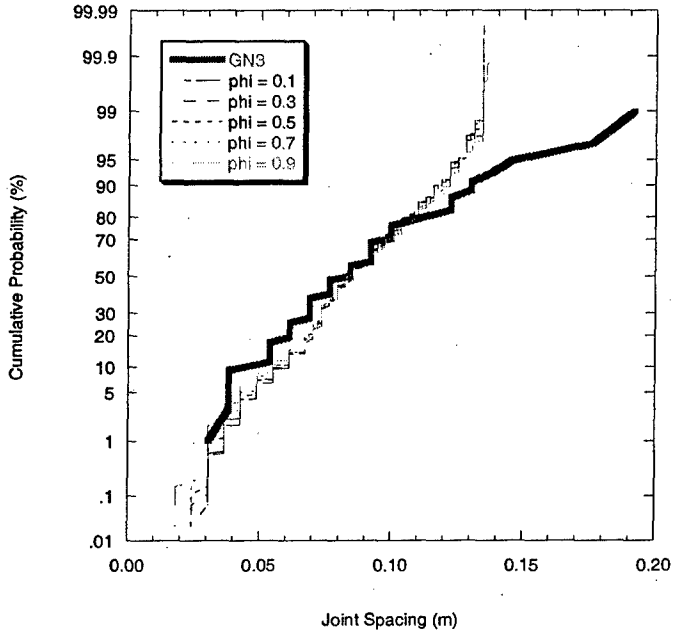


Figure 319 - Actual vs. simulated joint spacing CDFs using the flaw model with correlation without saturation for different values of ϕ for layer 3 (GN3). The minimum tensile strength is 4.0 MPa and the maximum 10.0 MPa. The $\frac{E_f}{G_n}$ ratio is fixed at 3.0.

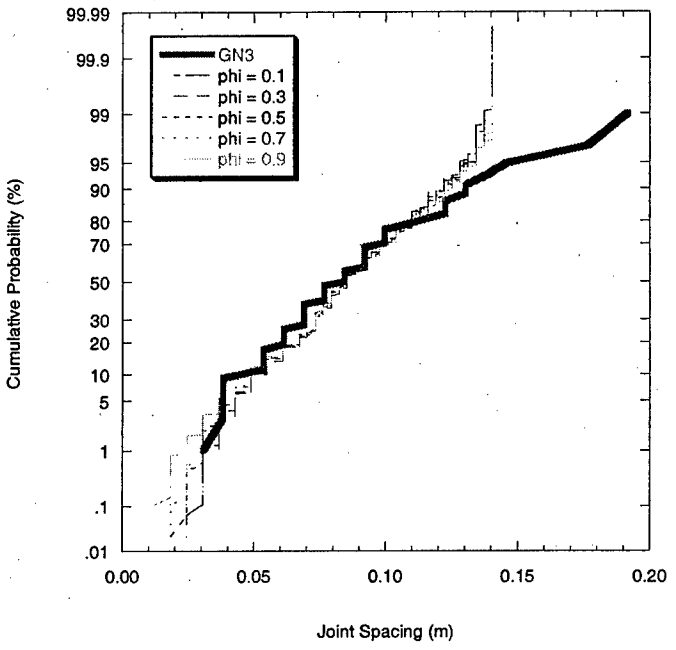


Figure 320 – Actual vs. simulated joint spacing CDFs using the flaw model with correlation without saturation for different values of ϕ for layer 3 (GN3). The minimum tensile strength is 2.0 MPa and the maximum 12.0 MPa. The $\frac{E_f}{G_n}$ ratio is fixed at 3.0.

Layer 4

Figure 321 to **Figure 322** show the actual vs. simulated joint spacing CDFs for layer 4 (GN4). Because the joint intensity here is very high, no saturation mechanism is applied so that the actual joint intensity can be reproduced. **Figure 321** shows that there is a poor agreement between the actual and simulated joint spacing CDFs. K-S hypothesis testing results agree with this visual assessment for all cases in **Figure 321**. The same is true when a wider tensile strength range is used (2.0-12.0 MPa in **Figure 322**). Visually, the fit between the actual and simulated joint spacing data does not appear to be good. K-S hypothesis testing confirms this for all cases in **Figure 322**.

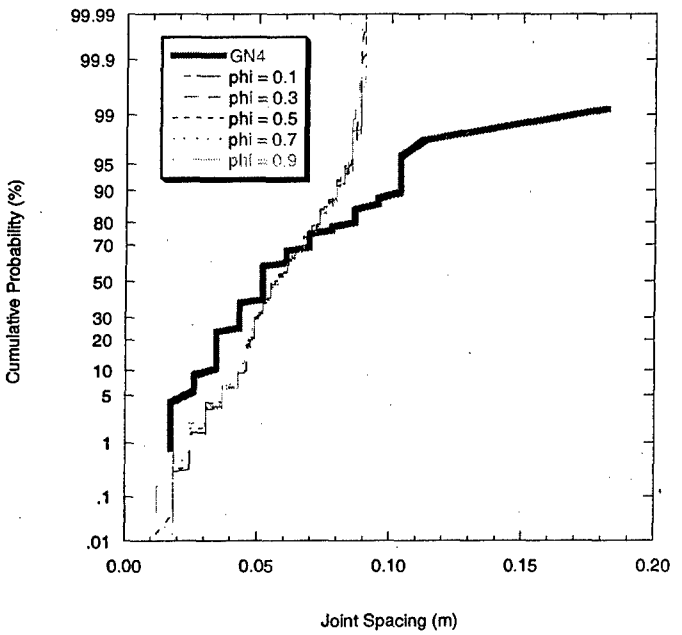


Figure 321 – Actual vs. simulated joint spacing CDFs using the flaw model with correlation without saturation for different values of ϕ for layer 4 (GN4). The minimum tensile strength is 4.0 MPa and the maximum 10.0 MPa. The $\frac{E_f}{G_n}$ ratio is fixed at 3.0.

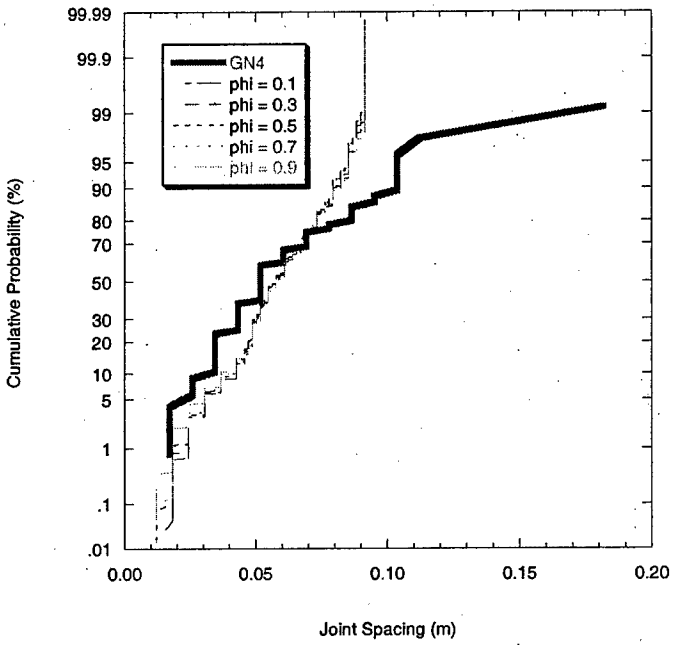


Figure 322 – Actual vs. simulated joint spacing CDFs using the flaw model with correlation without saturation for different values of ϕ for layer 4 (GN4). The minimum tensile strength is 2.0 MPa and the maximum 12.0 MPa. The $\frac{E_f}{G_n}$ ratio is fixed at 3.0.

For the flaw model with correlated strength, a good fit both visually and by hypothesis testing is achieved only for layer 2 where the joint intensity is lowest. For layers 1, 3, and 4, the visual and hypothesis testing results do not agree. Focusing on the visual assessment, the flaw model with correlated strength does not perform well when the joint intensity is very high (i.e., for layers 1, 3, and 4) even without the saturation mechanism. Note also that an $\frac{E_f}{G_n}$ of 3.0 represents the value that can produce the best fit (in the range of assumed $\frac{E_f}{G_n}$ values, 3.0 to 6.0) because increasing this ratio will only decrease the relative frequency of smaller spacings and increase the relative frequency of larger spacings. As observed in the comparisons above, such a change will only worsen the fit between the actual and simulated spacing data.

7.3.4.2 Rejection Procedure Results

Joint spacing data were also simulated for each layer using the rejection procedure and compared to the actual spacing data. As in the flaw model, the saturation mechanism prevented the rejection procedure from reaching the target joint intensity specifically in layers 1, 3, and 4.

Layer 1

Figure 323 shows the actual vs. simulated joint spacing CDFs for layer 1 (GN1) when the saturation mechanism is used. It is clear that the rejection procedure with saturation cannot simulate joint spacings that come close to the actual spacings. **Figure 324** shows the actual vs. simulated joint spacing CDFs for layer 1 (GN1) when the rejection procedure is used without a saturation mechanism. Visually, there appears to be some discrepancy between the actual and simulated. The simulations overestimate the relative frequency of smaller spacings while underestimating the relative frequency of larger spacings. However, K-S hypothesis testing deems these deviations acceptable. In other words, the hypothesis that the actual and simulated spacing data come from the same distribution is accepted at the 0.05 level for all cases in **Figure 324**.

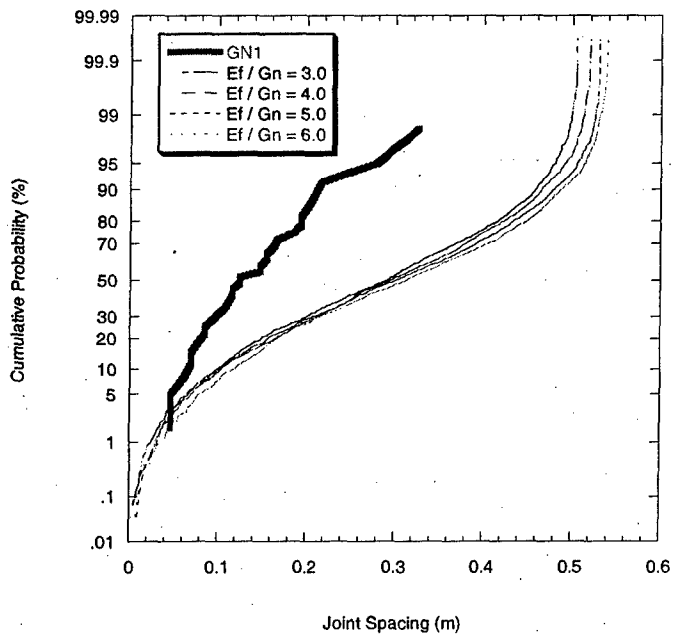


Figure 323 – Actual vs. simulated joint spacing CDFs using the rejection procedure with saturation for different values of $\frac{E_f}{G_n}$ for layer 1 (GN1).

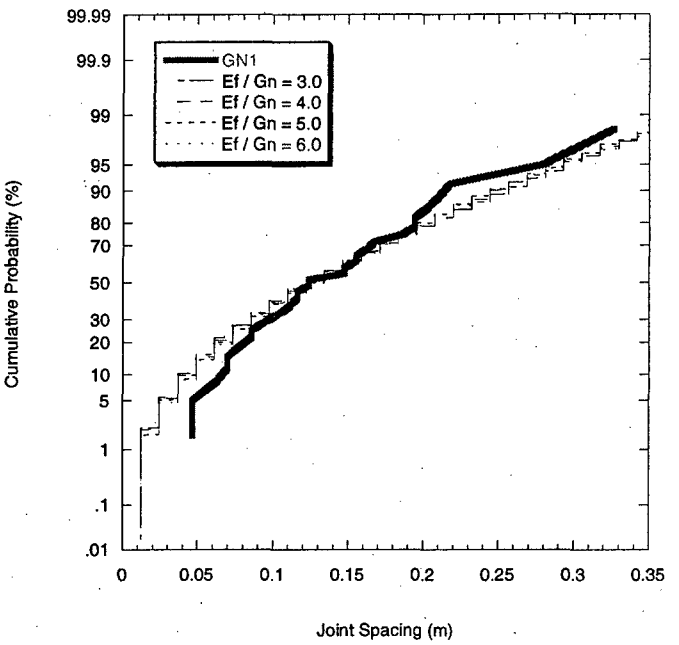


Figure 324 – Actual vs. simulated joint spacing CDFs using the rejection procedure without saturation for different values of $\frac{E_f}{G_n}$ for layer 1 (GN1).

Layer 2

For layer 2 (GN2), the saturation mechanism does not impede the rejection procedure from attaining the actual joint intensity. **Figure 325** shows the actual vs. simulated joint spacing CDFs. Visually, the rejection procedure with saturation mechanism underestimates the relative frequency of the smaller spacings while overestimating the relative frequency of the larger spacings. However, K-S hypothesis testing accepts the hypothesis that the actual and simulated spacing data come from the same distribution at the 0.05 level for all cases in **Figure 325**.

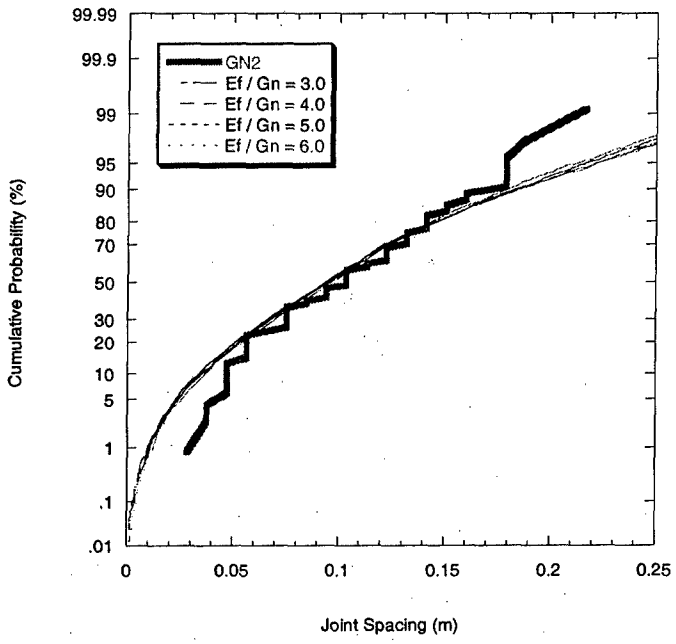


Figure 325 – Actual vs. simulated joint spacing CDFs using the rejection procedure with saturation for different values of $\frac{E_f}{G_n}$ for layer 2 (GN2).

Layer 3

Figure 326 shows the actual vs. simulated joint spacing CDFs for layer 3 (GN3) using the rejection procedure. Here, no saturation mechanism is used so that the target joint intensity can be reached. Visually, it appears that the rejection procedure does not perform well in this case. However, K-S hypothesis testing accepts the hypothesis that the actual and simulated joint spacing data come from the same distribution at the 0.05 level in all cases except $\frac{E_f}{G_n} = 6.0$ in **Figure 326**. In this case, it would be better to say that the rejection procedure without saturation does not work well based on a visual comparison (**Figure 326**).

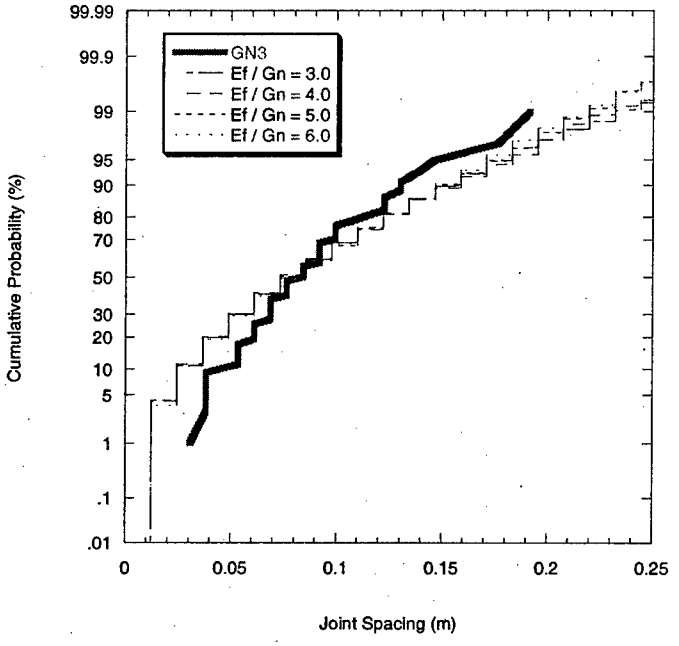


Figure 326 – Actual vs. simulated joint spacing CDFs using the rejection procedure without saturation for different values of $\frac{E_f}{G_n}$ for layer 3 (GN3).

Layer 4

Figure 327 shows the actual vs. simulated joint spacing CDFs for layer 4 (GN4) using the rejection procedure without saturation. It appears that, visually, the rejection procedure produces joint spacing CDFs in agreement with the actual data. K-S hypothesis testing indicates a good fit in all except the $\frac{E_J}{G_n} = 6.0$ case in **Figure 327**.

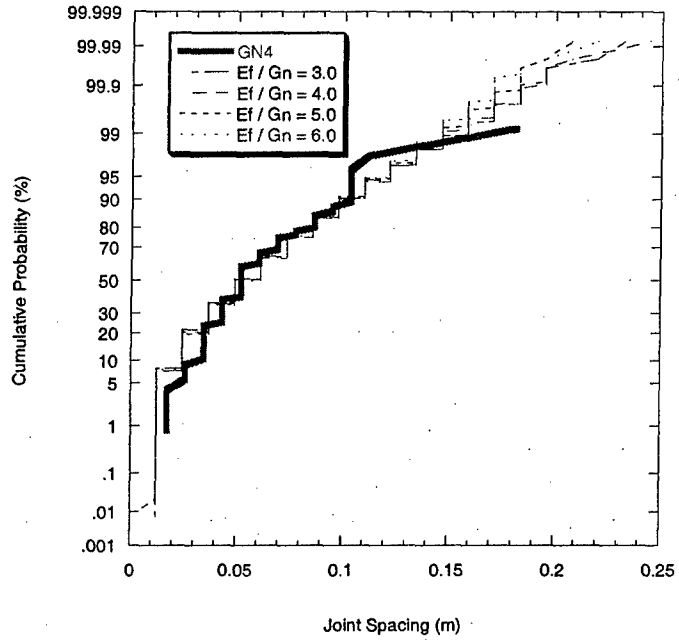


Figure 327 – Actual vs. simulated joint spacing CDFs using the rejection procedure without saturation for different values of $\frac{E_J}{G_n}$ for layer 4 (GN4).

Discussion

Overall, the rejection procedure is able to reproduce joint spacing CDFs that agree with the actual data based on hypothesis testing (i.e., K-S statistic). However, in some cases, visual observations do not agree with K-S hypothesis test results. Also, the saturation mechanism prevents the rejection procedure from reaching the actual joint intensity in all cases except layer 2 (GN2). In the layers with higher joint intensity (layers 1, 3, and 4), the saturation mechanism was deactivated in order to reach the desired intensity. This may indicate that the saturation mechanism suggested by Bai and Pollard (2000) may not be applicable to the Saltzman (2001) data.

7.3.4.3 Summary

Using the flaw model, the same phenomenon is observed: the saturation mechanism prevents the model from reaching the actual joint intensity except in layer 2. Without the saturation mechanism, the flaw model produced joint spacing CDFs that compare well (visually and statistically) with the actual joint spacing CDFs. This becomes especially true for a wider tensile strength range (e.g., 2.0-12.0 MPa) compared to that suggested by

Saltzman's (2001) laboratory tests. Also, the use of correlated strength in the flaw model does not improve upon the results when using uncorrelated strength. In fact, the fits between actual and simulated joint spacing CDFs were worse when using correlated strength. Larger visual discrepancies between CDF shape and relative frequency of spacing were observed when correlated strength is used. Overall, the flaw model with uncorrelated strength but without the saturation mechanism provided realistic joint spacing CDFs.

7.4 Case 3: Gross et al. (1997)

7.4.1 General Observations

Gross et al. (1997) studied joints in six chalk layers interbedded with chert near Beer Sheva, Israel (**Figure 328**). The layers belong to the lower Eocene Mor Formation and are exposed in a road cut (Gross et al., 1997). The layers have been slightly folded but are still essentially flat-lying (Bahat, 1988). Two sets of joints were observed in the area: cross-fold joints and strike joints. Cross-fold joints, as the name suggests, generally strike the perpendicular to the fold axis in the area. Strike joints, on the other hand, are oriented parallel to the fold axis. The cross-fold joints strike at about 326° and the strike joints strike about 055° and both sets are found throughout the Beer Sheva region. These joint sets have vertical dips and are confined mechanically within the chalk layers whose thicknesses in the studied area range from about 17 cm to 63 cm. The thicknesses of the interbedded chert layers were not measured. A normal fault zone is also evident in the exposure. The fault zone strikes 292°, dips 45°N and is made up of three segments (F1, F2, and F3 in **Figure 328** see also **Figure 329**). Slip along the fault is accommodated mostly across F1 (Gross et al., 1997). The aggregate slip across the fault zone should be uniform (i.e., each point along the fault zone displaces the same amount along the fault). However, Gross et al. (1997) noted that the slip is less along the segment of the fault zone crossing chalk layer 4 than anywhere else. The part of layer 4 north of the fault zone is more heavily jointed than the part that is south of the fault zone. Gross et al. (1997) believe that the energy that could not be accommodated by slipping along the fault crossing layer 4 was translated into additional jointing when the 055° joint set formed later. Gross et al. (1997) found evidence from cross-cutting relationships that the fault zone formed before the 055° joint set but after the 326° joint set. This is important because the fault zone appears to have affected the joint density of the 055° set in the northern part of chalk layer 4. However, the authors noted that the fault does not appear to affect the orientations of the 055° joint set, even near the fault. The strike joints are of more interest than the cross-fold joints because the mechanism involved in their formation is consistent with that modeled by the flaw model and rejection procedure. Folding provides a mechanism by which the layer could be subjected to extensional strain. Bahat (1988) also observed circular fracture markings on joints in both sets implying their extensional nature.

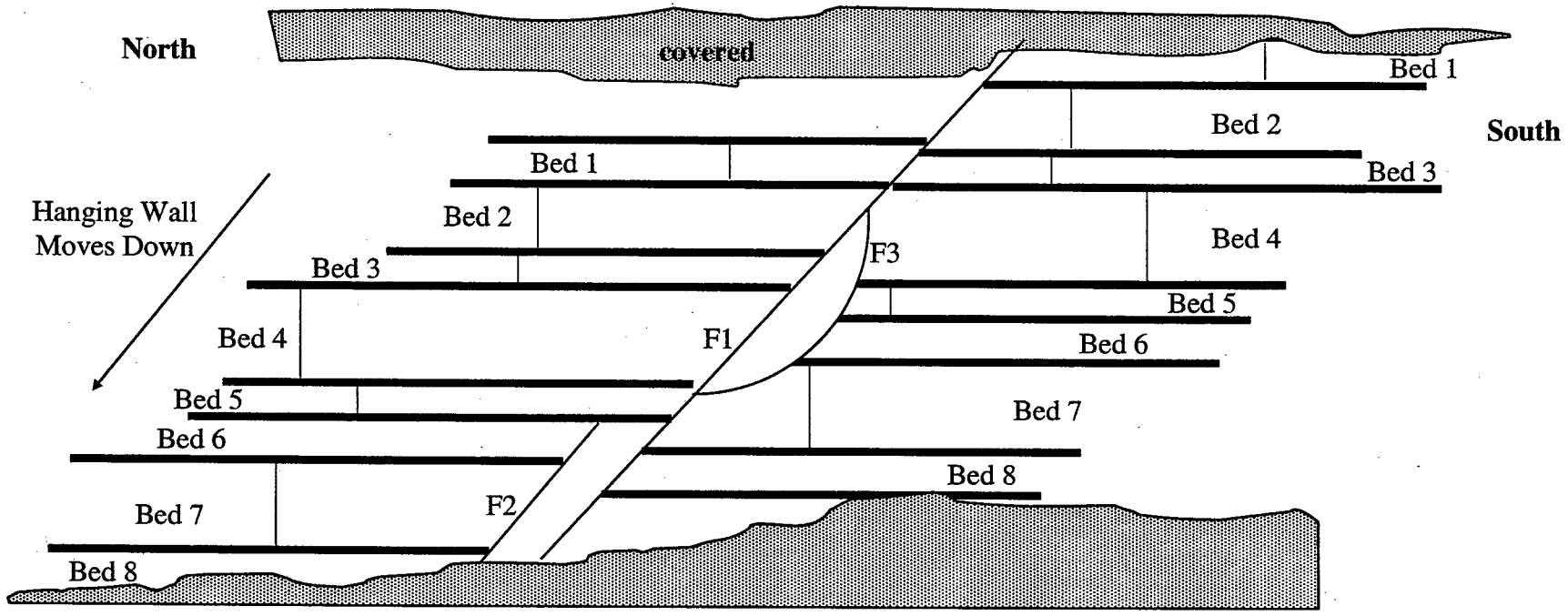


Figure 328 – Schematic of the outcrop from Gross et al. (1997). Chert layers are represented as thick solid lines. The normal fault is made up of three segments (F1, F2, and F3). The strike of the outcrop face is approximately 350°. Sketched from Fig. 2 in Gross et al. (1997).

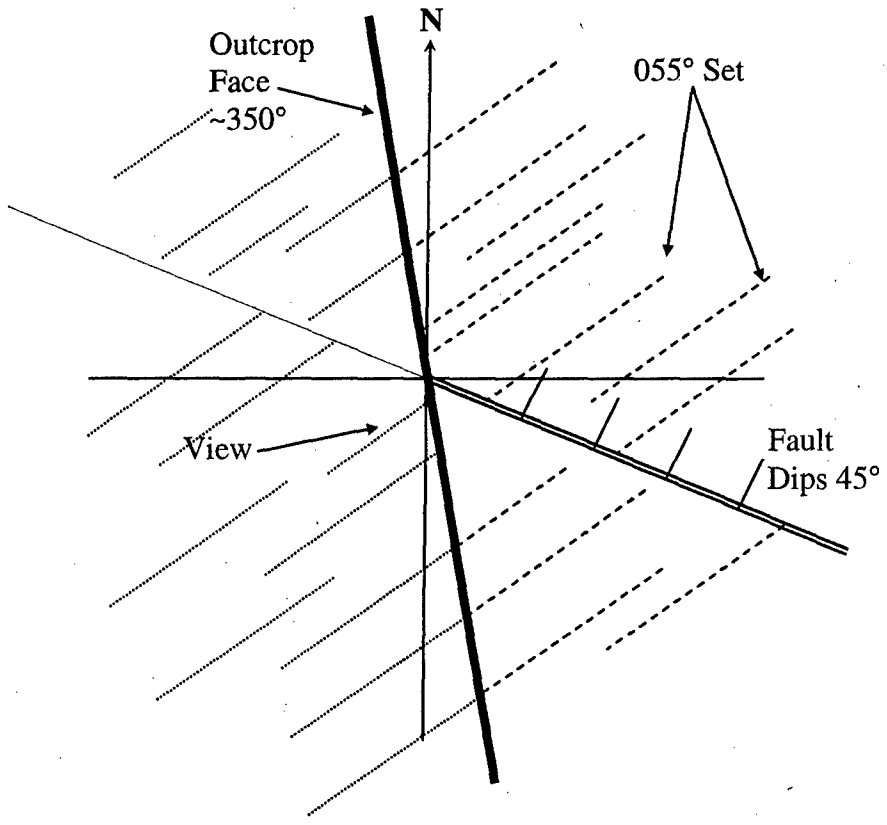


Figure 329 – Schematic of the orientations of the fault, outcrop and the 055° set. Sketched from descriptions in Gross et al. (1997).

7.4.2 Joint Spacing Data

The spacings between joints of the 055° set were measured by Gross et al. (1997) in each of the six layers. However, the number of spacings measured in each layer is small (**Table 16**) so it may become necessary to combine data from different layers to obtain larger datasets. As noted earlier, larger datasets lead to a more complete characterization of the spacing distribution. One has to be careful in doing this because the jointed chalk layers have different thicknesses so one cannot just combine all the data into a single set. This problem is addressed by normalizing each spacing with the thickness of the layer in which it is located. Another issue is that each layer may be at different stages of jointing so it may be appropriate to look at the normalized mean (or normalized median) spacing before combining the normalized spacing data. Gross et al. (1997) did not combine joint spacing data from different layers. In this analysis, data from layers with normalized mean values that are close to each other are combined to form one normalized dataset. **Table 16** shows a summary of these normalized statistics for each of the six layers. According to the information in **Table 16**, normalized data from layers 1, 3 and 5 can be combined to form a larger dataset because their normalized mean spacing values are similar. Using the same reasoning, data from layers 2 and 7 can also be combined. Layer 4 (combined North and South data) appears to be more intensely jointed than the other

layers so the data there cannot be combined with the others. Gross et al. (1997) divided the data in each layer according to location with respect to the fault. Specifically, the spacing data were divided into a set north of the fault and another set south of the fault (the fault strikes about 292°). When this is done for the data from layer 4, it is found that the mean spacing from the north side is significantly lower than that in the south side of the fault (about 0.45 compared to about 0.70 normalized). The other layers do not exhibit such a large discrepancy between North and South joint spacing. The normalized mean spacing of 0.70 is quite close to those from layers 2 and 7 so it may be reasonable to combine the South dataset of layer 4 with these sets. The combined set of data for layers 1, 3 and 5 is set A and the combined set of data for layers 2, 7 and the South dataset of layer 4 is set B (see **Table 16**). Statistical tests (K-S) indicate that combining spacings into datasets A and B is reasonable. K-S testing accepts the hypothesis that normalized spacings from layers 1, 3 and 5 come from the same distribution. The same is true for normalized spacings from layers 2, 7 and the south dataset of layer 4.

Table 16 – Mean and median normalized spacing for each of the six chalk layers. Layer 4 is divided into North and South parts due to large difference in joint intensity. Note that joints in layer 6 were not included in the dataset.

Layer (combined dataset) (thickness, cm)	Number of spacings	Normalized mean spacing	Normalized median spacing
1 (A)(26,29)	27	1.11	1.10
2 (B)(43,46)	47	0.76	0.76
3 (A)(22,17)	43	1.17	1.18
4 North of Fault (none)(62.5)	33	0.45	0.45
4 South of Fault (B)(62.5)	23	0.70	0.67
4 Combined (62.5,62.5)	56	0.56	0.52
5 (A)(19.5,17.4)	68	1.13	1.06
7 (B)(60,60)	71	0.75	0.75

Table 17 – Statistics of normalized spacing for the combined datasets.

Combined dataset	Number of Spacings	Normalized mean spacing	Normalized median Spacing	Skewness of normalized data	Standard deviation of normalized data
A	138	1.12	1.09	2.27	0.51
B	141	0.74	0.74	0.84	0.29

Table 17 shows the statistics for the combined datasets. The mean and median values are not far from the individual values from each of the layers being combined. **Figure 330** and **Figure 331** show the histograms for datasets A and B. These histograms illustrate that the normalized spacing data in set A are more spread out than those in B. Comparing

the cumulative distribution function for each dataset to typical probability distributions reveals that dataset A may follow a log-normal probability distribution (**Figure 332** for log-normal vs. **Figure 333** for normal). This is supported by chi-square goodness-of-fit tests. Dataset B, on the other hand, appears closer to a normal than it is to a log-normal probability distribution (**Figure 334** for log-normal vs. **Figure 335** for normal). The middle portion (i.e., 10% to 90% cumulative probability) of the joint spacing CDF of dataset B appears to be a straight line, as a normal CDF would in this plot. However, chi-square goodness-of-fit tests reject the hypotheses that dataset B can be described by either a log-normal or a normal probability distribution. The parameters of the log-normal and normal probability distributions were obtained using maximum likelihood estimation. A summary of the comparisons of the two datasets with typical probability distributions is shown in **Table 18**. The '×' symbol denotes a bad fit while the '√' denotes a possible fit.

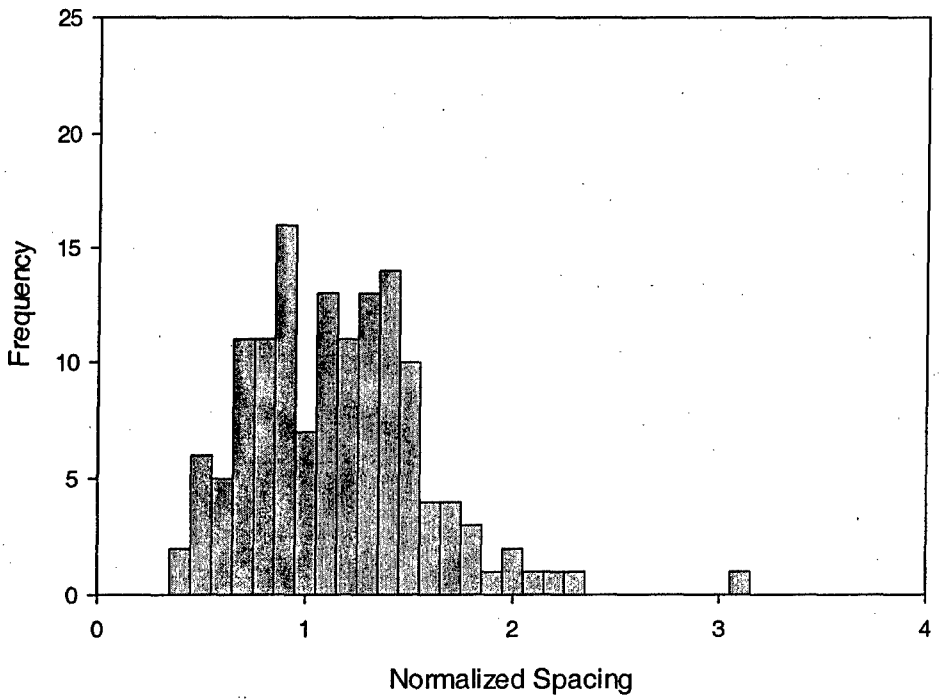


Figure 330 – Normalized spacing histogram for set A.

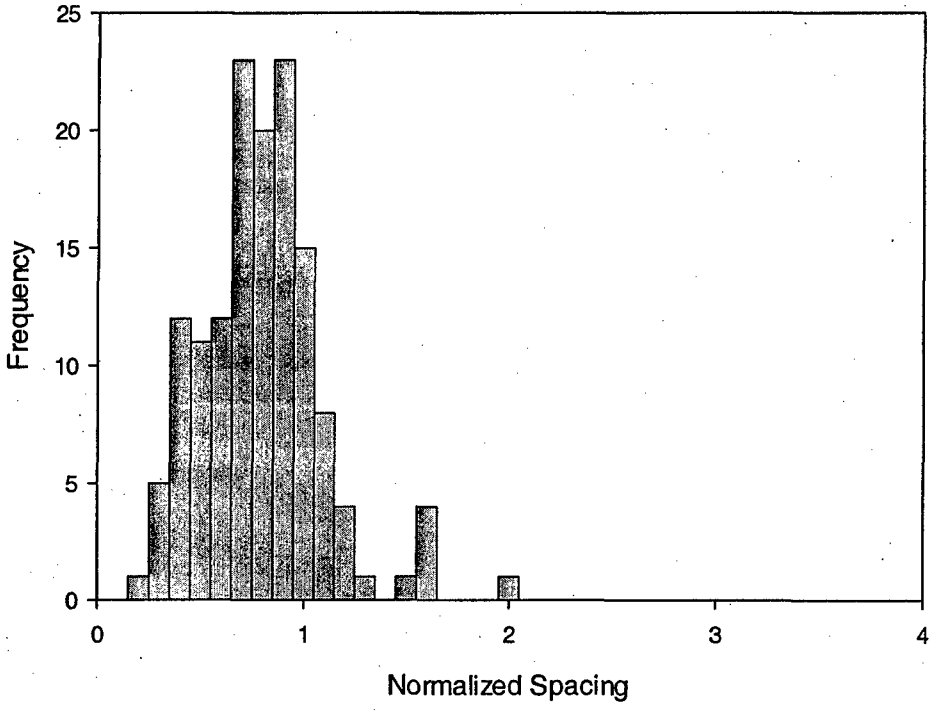


Figure 331 – Normalized spacing histogram for set B.

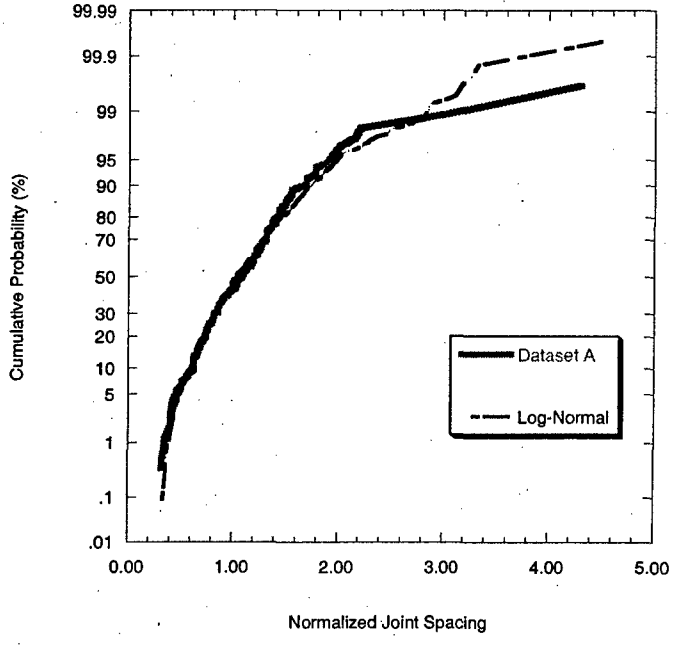


Figure 332 – Comparison between dataset A and a log-normal probability distribution. Mean normalized spacing is 1.12.

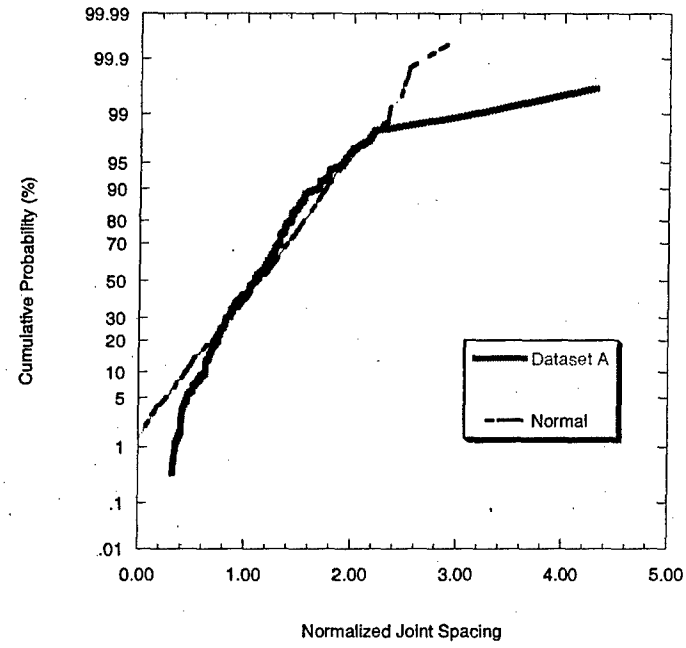


Figure 333 – Comparison between dataset A and a normal probability distribution. Mean normalized spacing is 1.12.

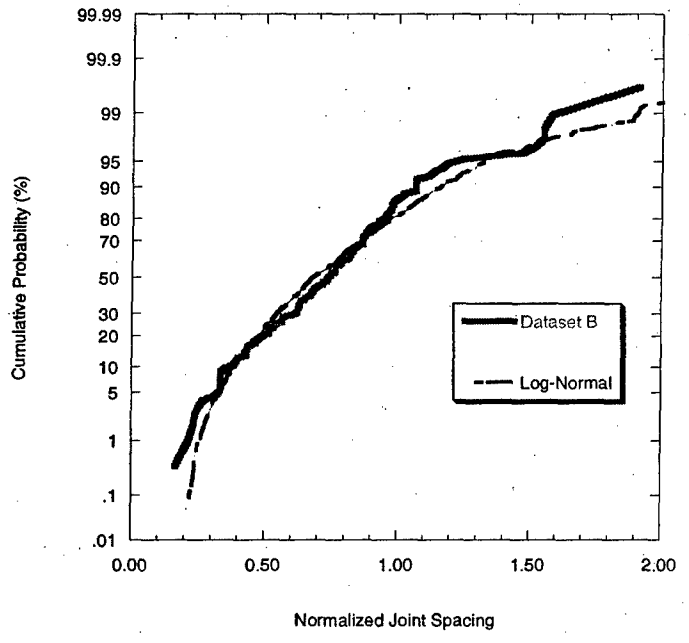


Figure 334 – Comparison between dataset B and a log-normal probability distribution. Mean normalized spacing is 0.74.

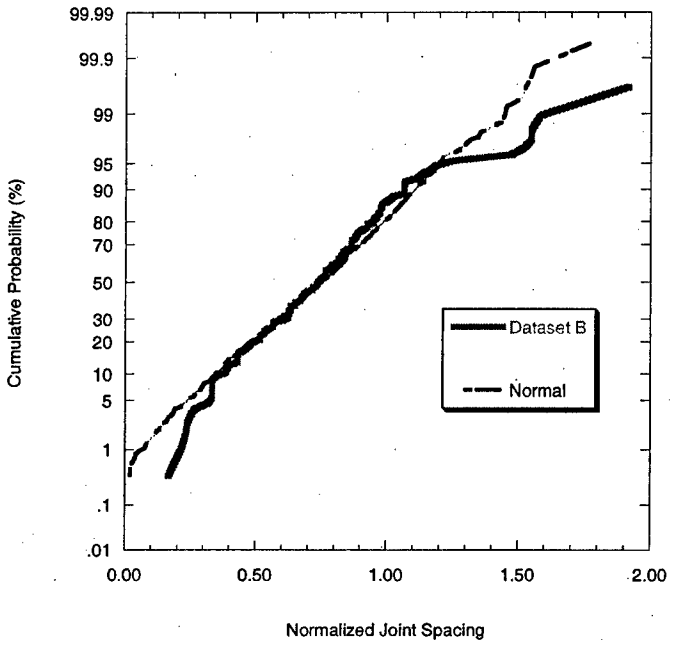


Figure 335 – Comparison between dataset B and a normal probability distribution. Mean normalized spacing is 0.74.

Table 18 – Summary of possible probability distribution functions for spacing datasets A and B based on a visual comparison with known probability distributions.

Dataset	Exponential	Log-Normal	Normal	Mean Spacing/Layer Thickness
A	×	√ (Chi-squared accepted)	×	1.12
B	×	×	√ (Chi-squared rejected)	0.74

Using the same graphical comparison, the spacing data from the individual layers are compared with typical probability distributions. **Table 19** shows the probability distribution functions that best describe the spacings from each layer based on the graphical comparison. The more densely jointed layers (i.e., smaller mean spacing-to-thickness ratio) appear to tend towards normal probability distributions. Among the layers with wider-spaced joints, only the data from layer 5 appears to be a typical probability distribution (i.e., log-normal). Overall, even with the small sets of data, it appears that the more densely jointed layers have spacings that may be described by a normal probability distribution whereas those that are less jointed do not appear to be described by either an exponential or a log-normal distribution except for layer 5.

Table 19 – Summary of possible probability distribution functions for spacing data from each layer based on a visual comparison with known probability distributions.

Layer	Number of Data	Exponential	Log-Normal	Normal	Mean Spacing/Layer Thickness
1	27	×	×	×	1.11
2	47	×	×	√	0.76
3	43	×	×	×	1.17
4 North of Fault	33	×	×	√	0.45
4 South of Fault	23	×	×	√	0.70
4 Combined	56	×	×	√	0.56
5	68	×	√	×	1.13
7	71	×	×	×	0.75

It would also help to look at the results in **Table 18** and **Table 19** in terms of the estimated saturation mean spacing. It was shown in the preceding comparison (Case 1: Becker and Gross, 1996) that the saturation mean spacing from flaw model simulations is given by:

$$SMS = (0.65 - 0.70)t \cdot \left(\frac{s}{t}\right)_{cr}$$

where t is the thickness of the jointing layer and $\left(\frac{s}{t}\right)_{cr}$ is the critical spacing-to-thickness ratio which ranges from 0.8 to about 1.2 (Bai and Pollard, 2000). This translates to $\left(\frac{SMS}{t}\right)$ ratios from 0.52 to 0.84. The entries in **Table 18** and **Table 19** that may be described by a normal probability distribution have mean spacing-to-thickness ratios that are below 0.84. On the other hand, those whose mean spacing-to-thickness ratios are above 0.84 cannot be described by normal probability distributions. Based on this observation, it is possible that some of the chalk layers are already at saturation with respect to layer-perpendicular jointing due to extension. In any case, the spacing data appear to possess behavior consistent with the mean spacing-to-thickness ratio vs. joint spacing distribution behavior in the flaw model.

7.4.3 Model Parameter Values

Before proceeding to estimate the model parameters, the field observations and their corresponding model implications are summarized (**Table 20**).

Table 20 – Summary of field observations and their corresponding model implications.

Field Observations	Model Implications
Joint spacing measurements were made in chalk layers that are bounded by chert.	Intact chert is stiffer than chalk so the $\frac{E_f}{G_n}$ ratio may be <1.0. However, the chert has been observed to be brecciated (i.e., heavily fractured) so that $\frac{E_f}{G_n}$ may not necessarily be <1.0. Investigate both $\frac{E_f}{G_n}$<1.0 and $\frac{E_f}{G_n}$>1.0.
Fault pre-dates the strike joint set (i.e., the 055° set). Fault slip profile is approximately uniform except where the fault zone crosses layer 4. No change in joint orientation with proximity to the fault.	Assume that presence of the fault does not influence formation of the 055° set except in the north part of layer 4 where the slip was not accommodated by the fault.
No slip between chalk and chert layers is evident.	The interface slippage saturation mechanism is not applicable but the compressive stress development mechanism may come into play. In the model, the interface shear strength is set to a very high value so that it cannot be overcome (i.e., no slippage).
Number of joint spacings from each chalk layer is small.	May be able to combine data from multiple layers to form larger dataset. Normalization of spacing data with joint layer thickness should be done before combining data from different layers.
No strain measurements were taken.	A stopping point for the jointing process needs to be defined. The actual mean joint spacing may be used for this purpose.
Cross-fold joint set (i.e., 326° set) pre-dates the 055° set).	Since the 326° set is approximately perpendicular to 055° set, its effect may be neglected. Bahat (1999) indicated that these two sets do not appear to interact.
No material properties for the chalk and chert layers are measured in the joint survey.	These material properties need to be estimated or obtained from other sources.

The thicknesses of the chert layers were not measured by Gross et al. (1997). However, Bahat (1988), in a separate study of lower Eocene formations, noted that chert beds in this area are about 0.07 m thick. This thickness value is used as a reference and the actual values used in the simulations will vary around this reference value.

As is typical of joint surveys, no material properties were measured. The $\frac{E_f}{G_n}$ ratio is an important parameter in both the flaw model and rejection procedure. Typical values of chert shear modulus found in literature range from 31.0 to 33.0 GPa (e.g., Gross et al.,

1995). The Young's modulus of chalk reported in the literature ranges from about 2.0 GPa to 20.0 GPa. This translates to $\frac{E_f}{G_n}$ ratios from 0.06 to 0.65. As expected, $\frac{E_f}{G_n}$ values are less than unity because intact chert is generally much stiffer than chalk. In the simulations, $\frac{E_f}{G_n}$ ratios of up to 1.05 will be used for the assumption that the chert layers are intact. For the case where the chert layers are brecciated (i.e., heavily fractured) the $\frac{E_f}{G_n}$ is allowed to vary from 2.0 to 10.0. Available tensile strength data on Lower Eocene Mor chalks in the area (Palchik and Hatzor, 2004) indicate a range between about 3.0 MPa to 9.0 MPa.

Now that the model parameter values have been estimated, simulations can be run. First, the flaw model will be used with an uncorrelated strength model and a correlated strength model, then the rejection procedure is used.

7.4.4 Simulation Results and Discussion

7.4.4.1 Flaw Model Results

Uncorrelated Strength Model

Simulations were performed for each individual layer using the uncorrelated strength model. The $\frac{E_f}{G_n}$ is first varied between 0.05 to about 1.0 based on the assumption that the bounding chert layers are intact and are therefore stiffer than the chalk layer. The chert layer thicknesses used are 0.05 and 0.10 m. This bounds the 0.07 m chert layer thickness reported by Bahat (1988).

Simulated joint spacing from the flaw model with an uncorrelated strength model does not compare well with the spacing data from the individual layers. For the range of $\frac{E_f}{G_n}$ and chert thickness values that are used (0.05 to 1.05 and 0.05 m to 0.1 m, respectively), the flaw model overestimates the relative frequency of smaller spacings and underestimates that of the larger spacings. This is true for all layers regardless of the individual mean spacing-to-thickness ratio. For example, **Figure 336** and **Figure 337** show the comparisons with data from layer 2 which has a mean spacing-to-thickness ratio of 0.76 whereas **Figure 338** and **Figure 339** show the same comparison for layer 5 where the mean spacing-to-thickness ratio is 1.13. One can see, however, that the shape of the simulated joint CDFs are drastically more different from the actual joint CDFs in **Figure 336** and **Figure 337** than they are in **Figure 338** and **Figure 339**. K-S testing rejects the hypothesis (H_0) that the actual and simulated spacing data come from the same probability distribution for all cases in **Figure 336** and **Figure 337**. In **Figure 338** and **Figure 339**, K-S testing rejects the hypothesis H_0 for the smaller $\frac{E_f}{G_n}$ values (0.05 and 0.45 in **Figure 338**, 0.05 in **Figure 339**) and accepts it for the rest of the cases. These results show that the assumption of intact chert bounding layers does not yield a good fit between the actual and simulated joint spacing.

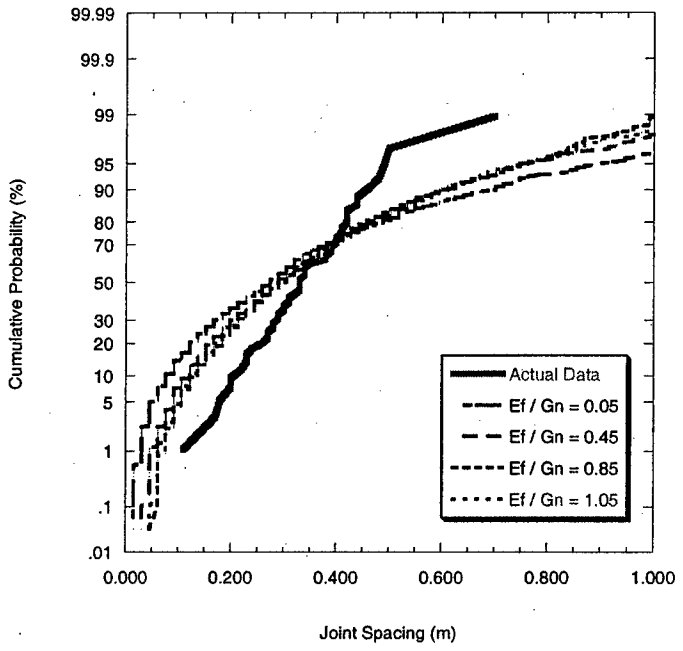


Figure 336 – Joint spacing CDF comparison for layer 2. Mean spacing-to-thickness ratio is 0.76. Chert layer thickness is 0.05 m. Spacings are not normalized.

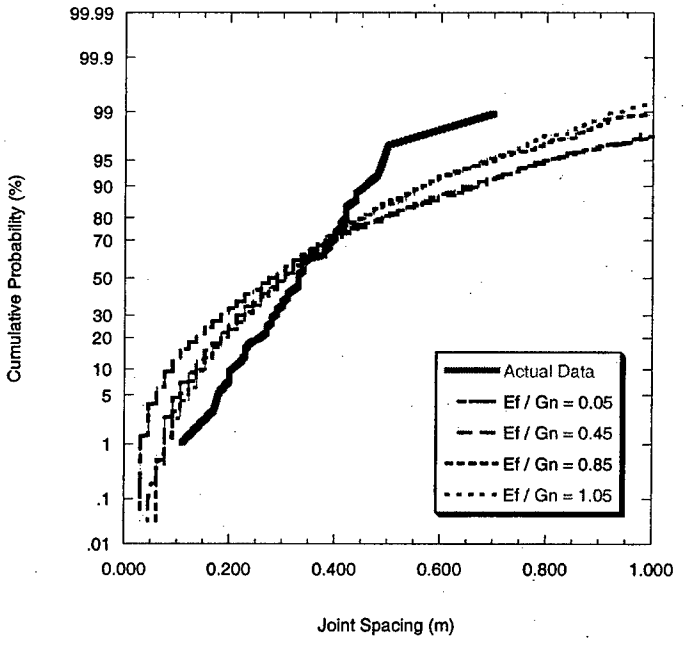


Figure 337 – Joint spacing CDF comparison for layer 2. Mean spacing-to-thickness ratio is 0.76. Chert layer thickness is 0.1 m. Spacings are not normalized.

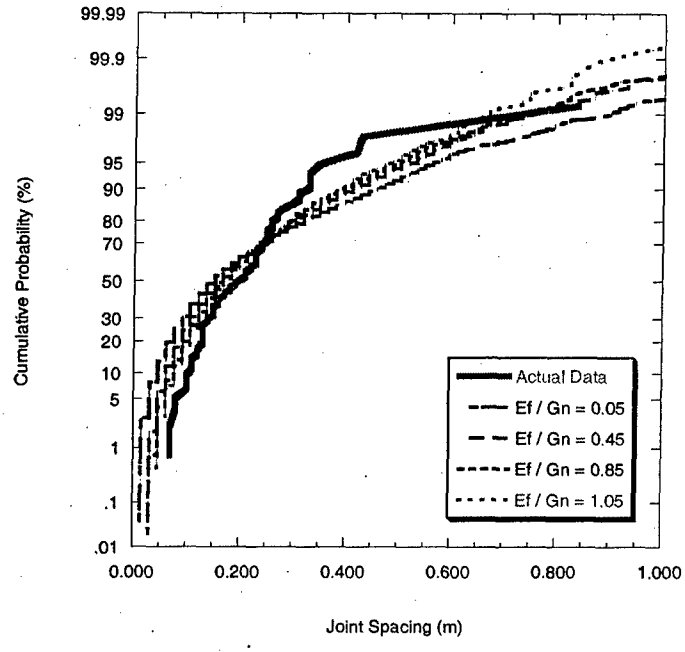


Figure 338 – Joint spacing CDF comparison for layer 5. Mean spacing-to-thickness ratio is 1.13. Chert layer thickness is 0.05 m. Spacings are not normalized.

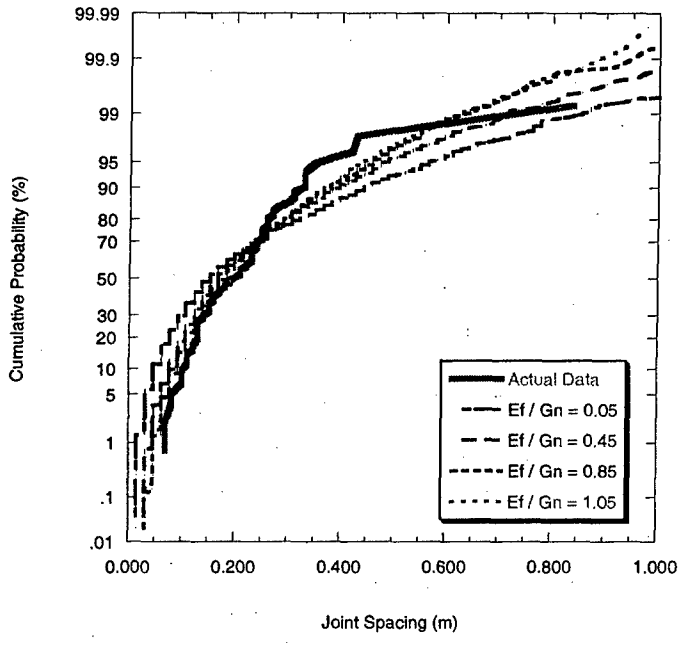


Figure 339 – Joint spacing CDF comparison for layer 5. Mean spacing-to-thickness ratio is 1.13. Chert layer thickness is 0.1 m. Spacings are not normalized.

In **Figure 340** and **Figure 341**, the joint spacing for layer 2 is simulated using the assumption that the bounding chert layers are less stiff compared to the chalk layers due to fracturing in the chert layers. As a consequence the $\frac{E_f}{G_n}$ ratio is allowed to assume values that exceed 1.0. Visually, one can see immediately the improvement in the fit

between the simulated and actual joint spacing CDFs in **Figure 340** and **Figure 341** compared to **Figure 336** and **Figure 337**. **Figure 342** and **Figure 343** show that the same is true for layer 5 where the improvement over **Figure 338** and **Figure 339** is quite noticeable. In fact, K-S testing accepts hypothesis H_0 for all cases in **Figure 340** to **Figure 343** except $\frac{E_f}{G_n}$ = 2.0 in **Figure 340**. Assuming that the chert stiffness is effectively lowered by brecciation or fracturing generally yields a better fit between the actual and simulated spacing data.

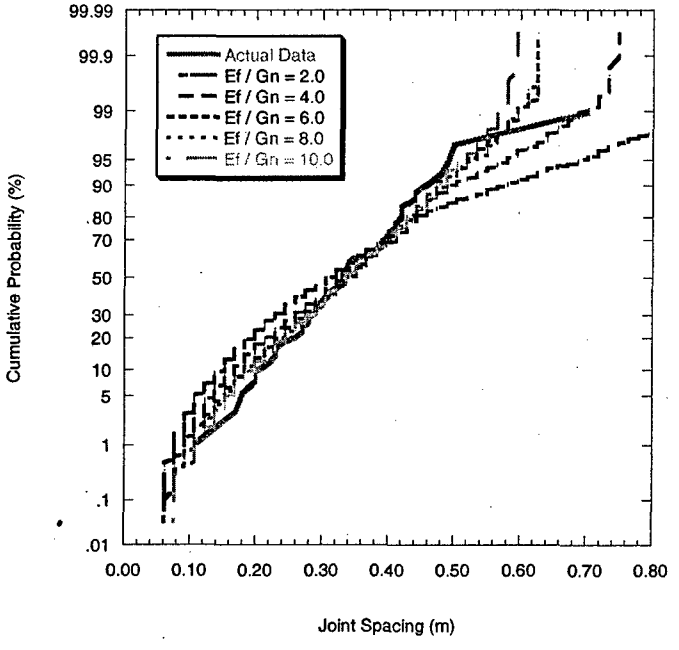


Figure 340 – Joint spacing CDF comparison for layer 2. Mean spacing-to-thickness ratio is 0.76. Chert layer thickness is 0.05 m. The $\frac{E_f}{G_n}$ values are allowed to exceed unity. Spacings are not normalized.

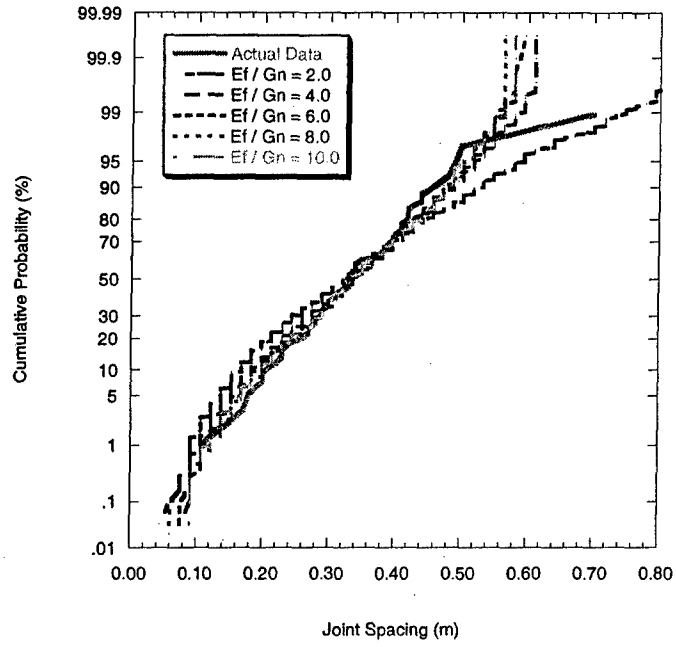


Figure 341 – Joint spacing CDF comparison for layer 2. Mean spacing-to-thickness ratio is 0.76. Chert layer thickness is 0.1 m. The $\frac{E_f}{G_n}$ values are allowed to exceed unity. Spacings are not normalized.

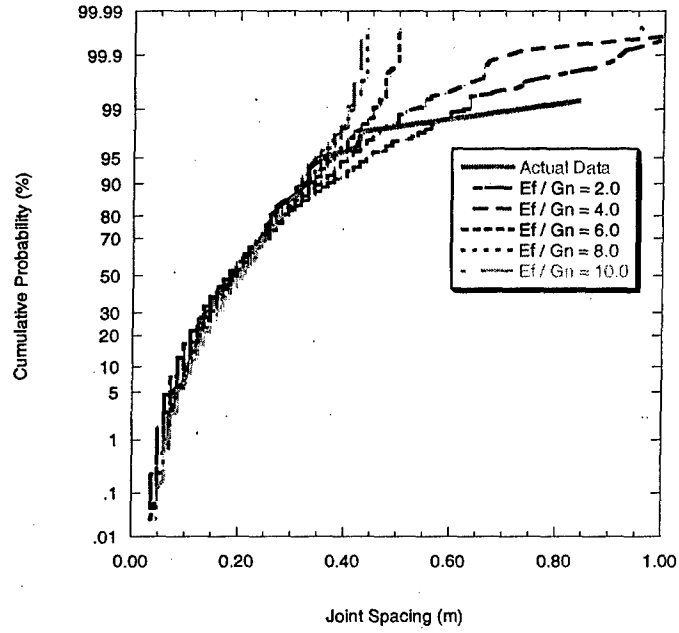


Figure 342 – Joint spacing CDF comparison for layer 5. Mean spacing-to-thickness ratio is 1.13. Chert layer thickness is 0.05 m. The $\frac{E_f}{G_n}$ values are allowed to exceed unity. Spacings are not normalized.

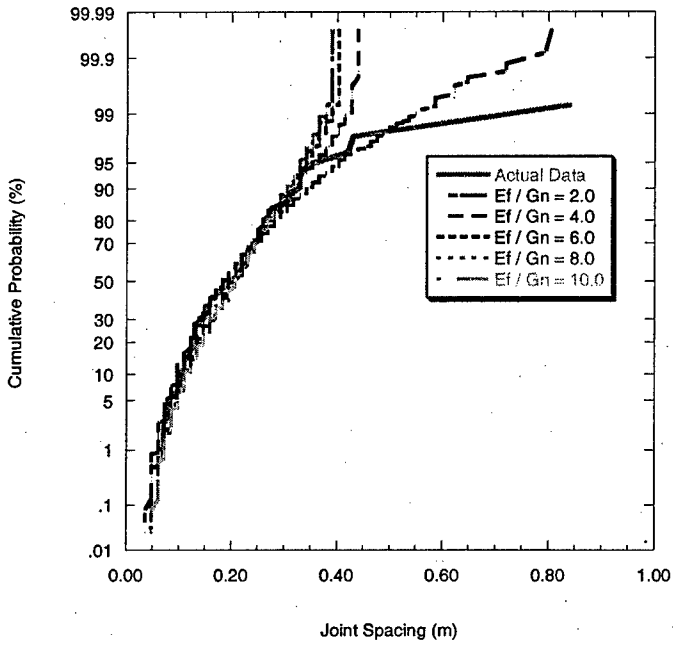


Figure 343 – Joint spacing CDF comparison for layer 5. Mean spacing-to-thickness ratio is 1.13. Chert layer thickness is 0.1 m. The $\frac{E_f}{G_n}$ values are allowed to exceed unity. Spacings are not normalized.

In the following comparisons, joint spacing data from the individual layers are addressed as datasets A and B. When the joint spacing data from the individual layers are combined into datasets A and B based on their mean spacing-to-thickness ratios, it was shown graphically that dataset A may be described by a log-normal distribution and dataset B by a normal distribution (**Figure 332** to **Figure 335**). In the first set of comparisons, it is first assumed that the chert layers are intact so that $\frac{E_f}{G_n}$<1.0. However, in initial simulations, it is observed that a good fit between the actual and simulated joint spacing could not be achieved with chert layer thickness values within the realistic range of 0.05-0.10 m. For this reason, the chert layer thickness (d) is varied while the $\frac{E_f}{G_n}$ ratio is maintained constant in order to see the range of d values for which a good fit is achieved.

Figure 344 to **Figure 349** show the comparison between the simulated and the actual joint spacing CDFs for dataset A for $\frac{E_f}{G_n}$ of 0.05, 0.5, 0.75 and 1.0. The same is done for dataset B in **Figure 350** to **Figure 355**. For both datasets, the flaw model comparison improves as the chert layer thickness (d) and the $\frac{E_f}{G_n}$ ratio approach unity (e.g., **Figure 347** and **Figure 349** for dataset A and **Figure 353** and **Figure 355** for dataset B). In all other cases, the flaw model overestimates the relative frequency of smaller spacings and underestimates that of larger spacings. Kolmogorov-Smirnov test results for each plot are included in the captions (note that H_0: the actual and simulated joint spacing data come from the same probability distribution). Recall that the same was true when the

spacing data sets from individual layers were considered with $\frac{E_f}{G_n}$<1.0 (**Figure 336** to **Figure 339**). Although the comparison between simulated and actual joint spacing CDFs was not good for the individual layers, an improvement in the fit would be seen if the chert layer thickness were increased to say 1.0 m (e.g., layer 5, **Figure 356**). However, a 1.0 m thick chert layer is not realistic based on what Bahat (1988) reported.

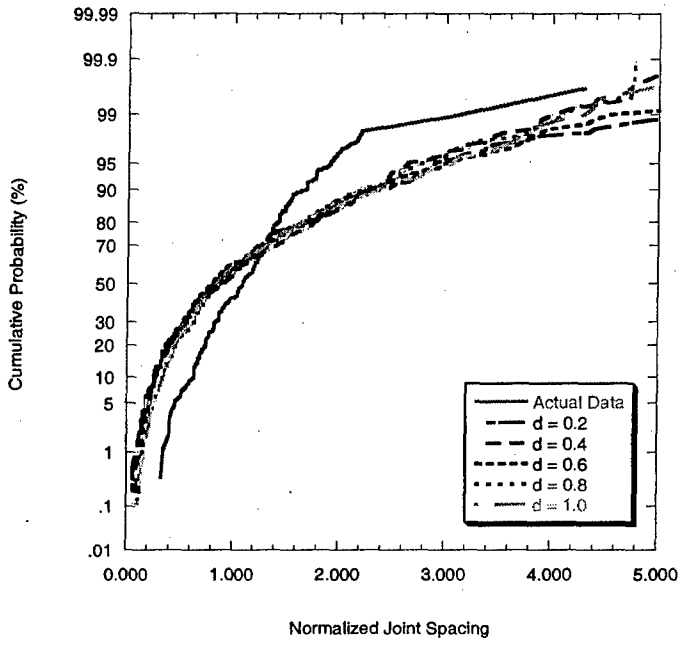


Figure 344 – Comparison between simulated and actual joint spacing CDFs for dataset A using various chert layer thickness values. The $\frac{E_f}{G_n}$ ratio is 0.05. H_0 is rejected for all values of *d*.

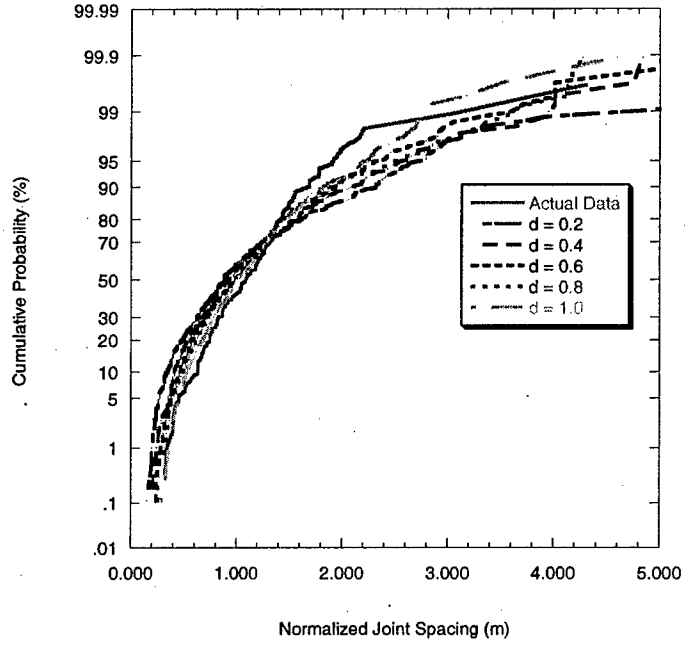


Figure 345 – Comparison between simulated and actual joint spacing CDFs for dataset A using various chert layer thickness values. The $\frac{E_f}{G_n}$ ratio is 0.5. H_0 is accepted only for d = 0.8 and 1.0 m.

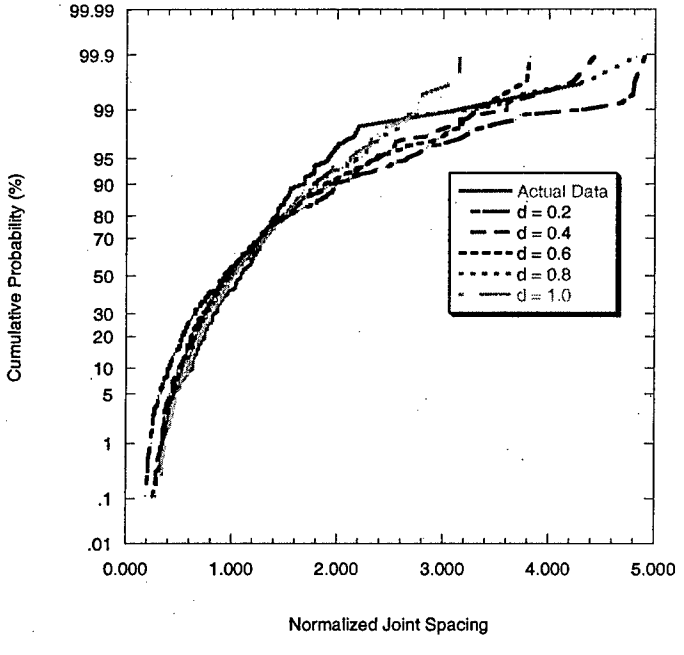


Figure 346 – Comparison between simulated and actual joint spacing CDFs for dataset A using various chert layer thickness values. The $\frac{E_f}{G_n}$ ratio is 0.75. H_0 is rejected only for d = 0.2 m.

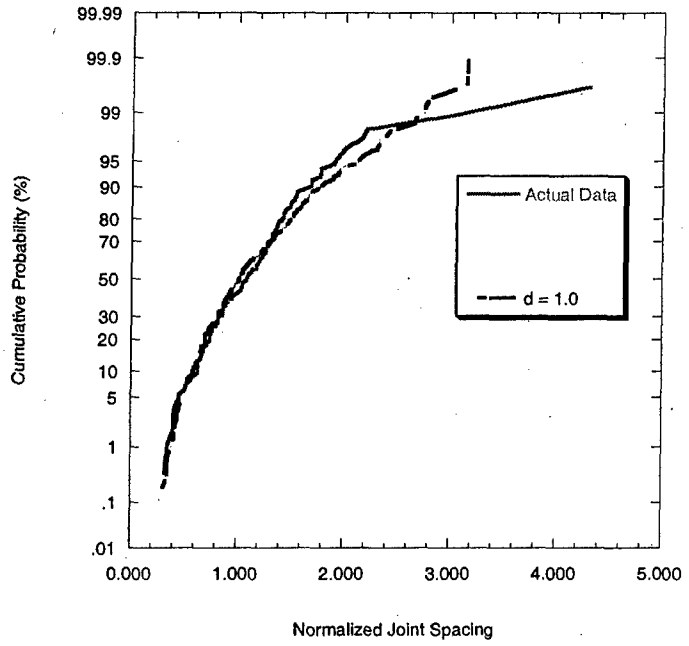


Figure 347 – Detail of d = 1.0 from Figure 346.

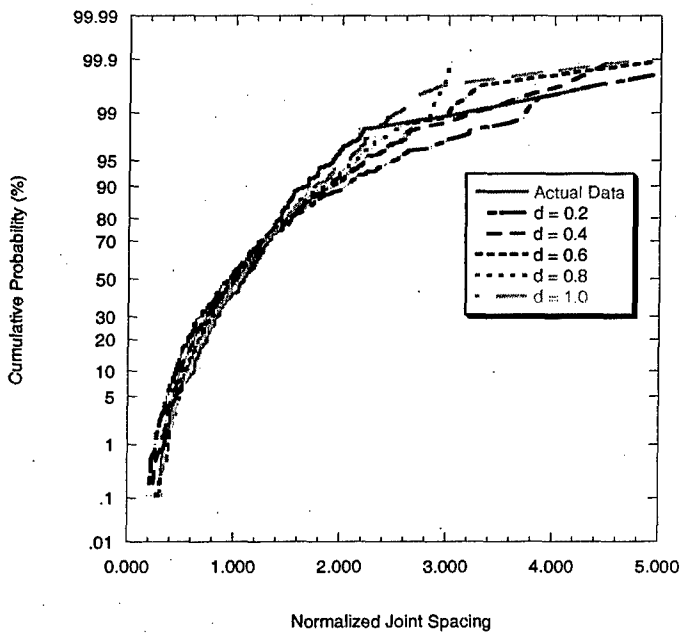


Figure 348 – Comparison between simulated and actual joint spacing CDFs for dataset A using various chert layer thickness values. The $\frac{E_f}{G_n}$ ratio is 1.0. H_0 is rejected only for d = 0.2 m.

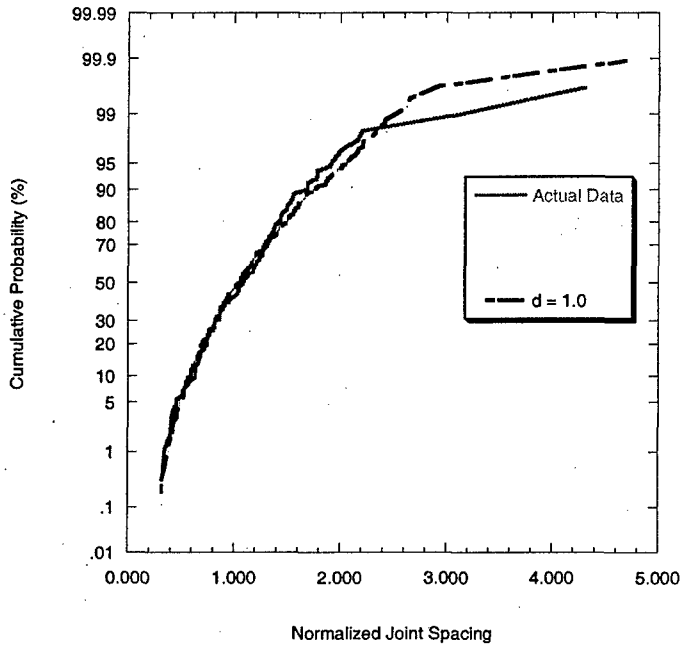


Figure 349 – Detail of d = 1.0 from Figure 348.

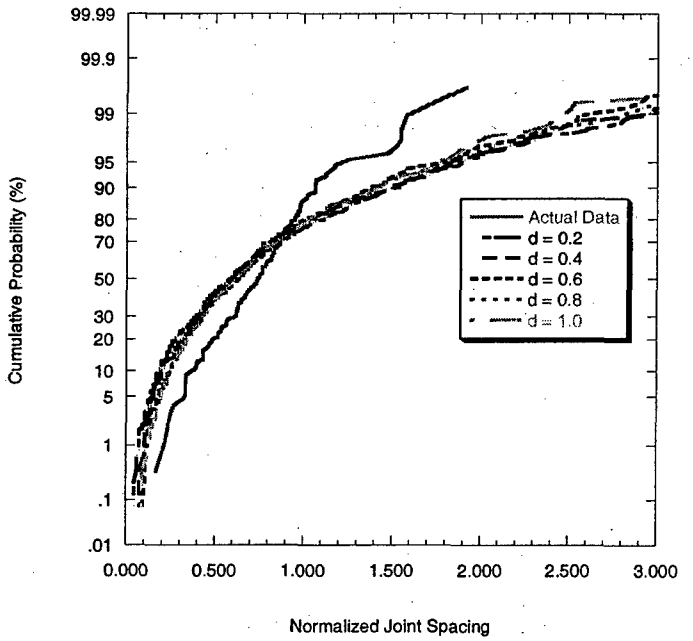


Figure 350 – Comparison between simulated and actual joint spacing CDFs for dataset B using various chert layer thickness values. The $\frac{E_f}{G_n}$ ratio is 0.05. H_0 is rejected for all values of d.

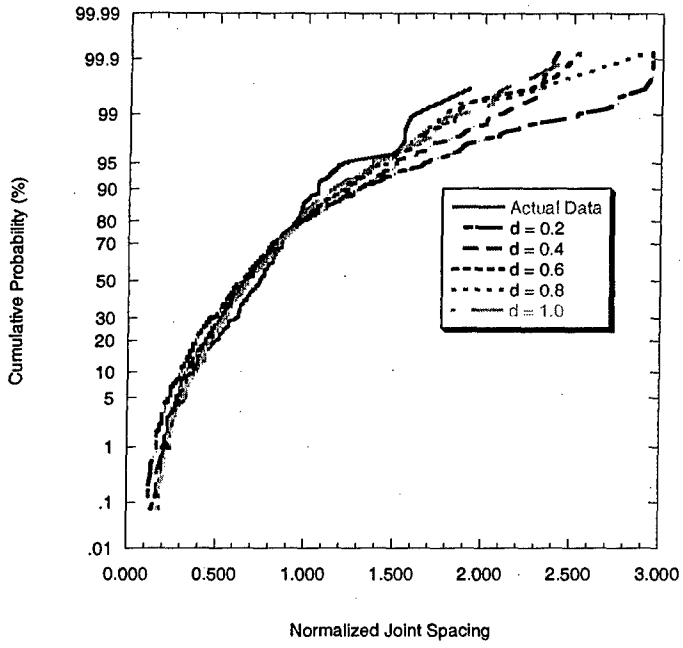


Figure 351 – Comparison between simulated and actual joint spacing CDFs for dataset B using various chert layer thickness values. The $\frac{E_f}{G_n}$ ratio is 0.5. H_0 is accepted only for $d = 1.0$ m.

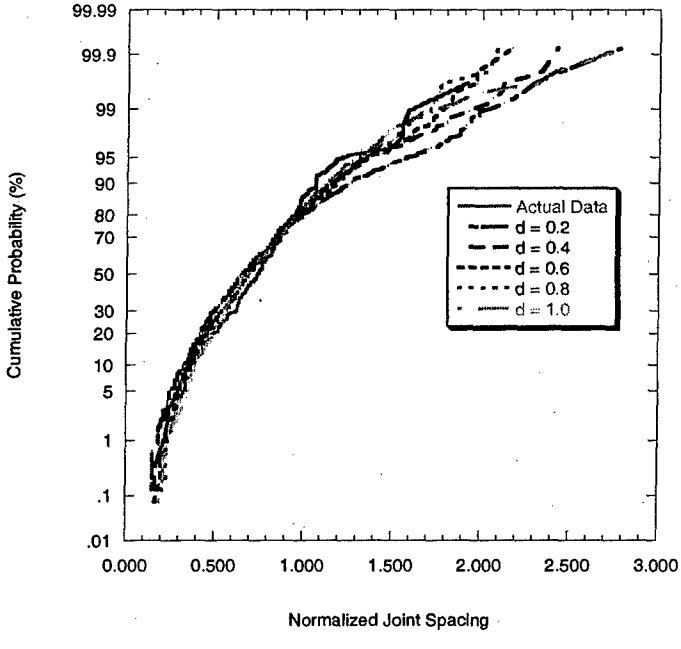


Figure 352 – Comparison between simulated and actual joint spacing CDFs for dataset B using various chert layer thickness values. The $\frac{E_f}{G_n}$ ratio is 0.75. H_0 is rejected only for $d = 0.2$ m.

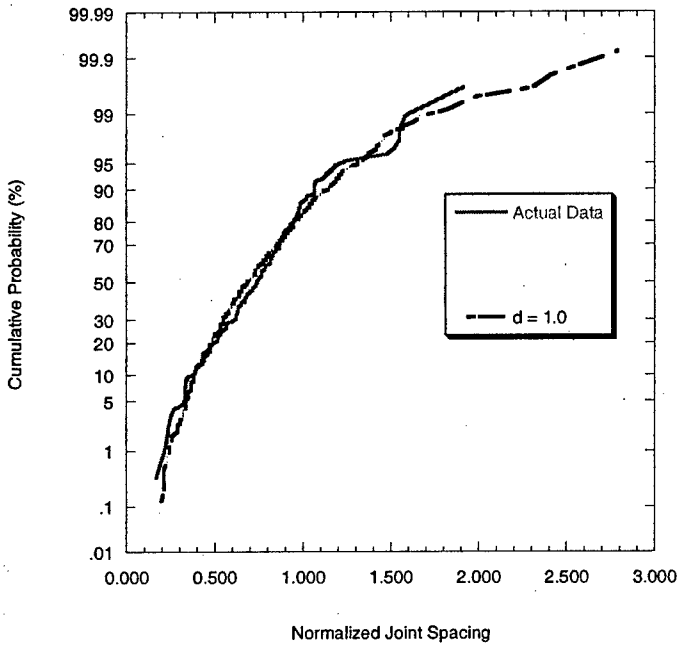


Figure 353 – Detail of d = 1.0 from Figure 352.

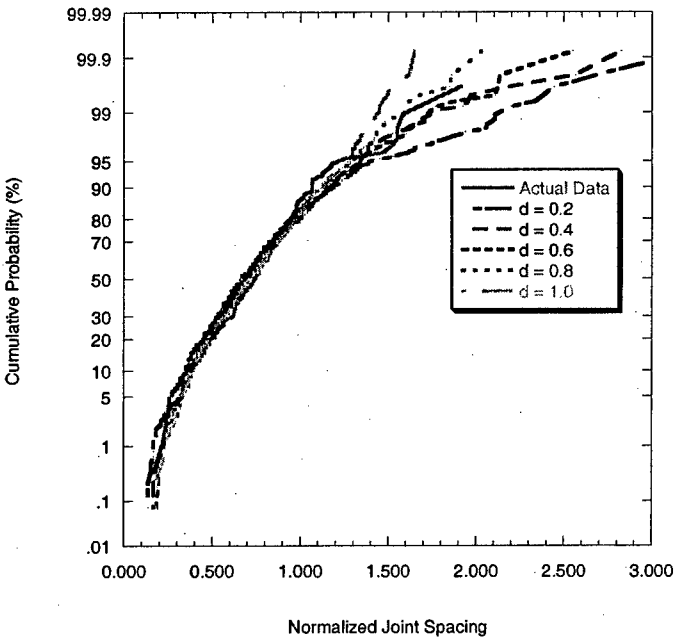


Figure 354 – Comparison between simulated and actual joint spacing CDFs for dataset B using various chert layer thickness values. The $\frac{E_f}{G_n}$ ratio is 1.0. H_0 is rejected only for d = 0.2 m.

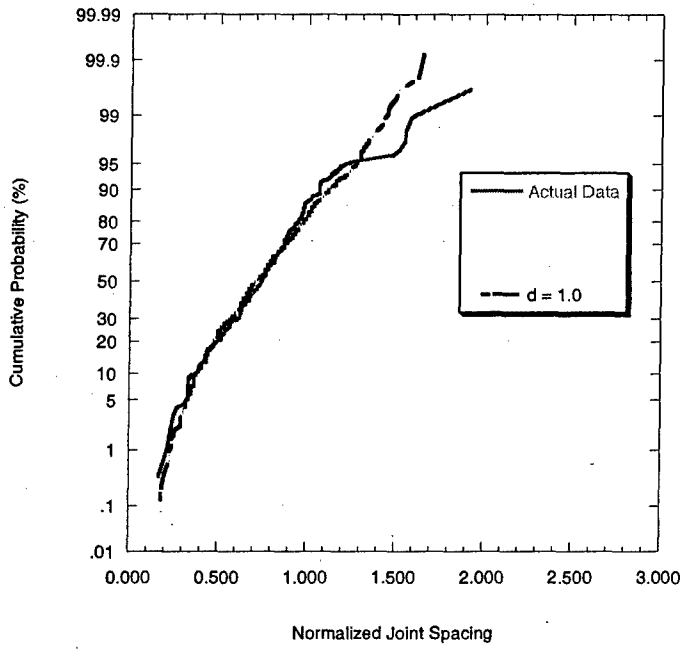


Figure 355 – Detail of d = 1.0 from Figure 354.

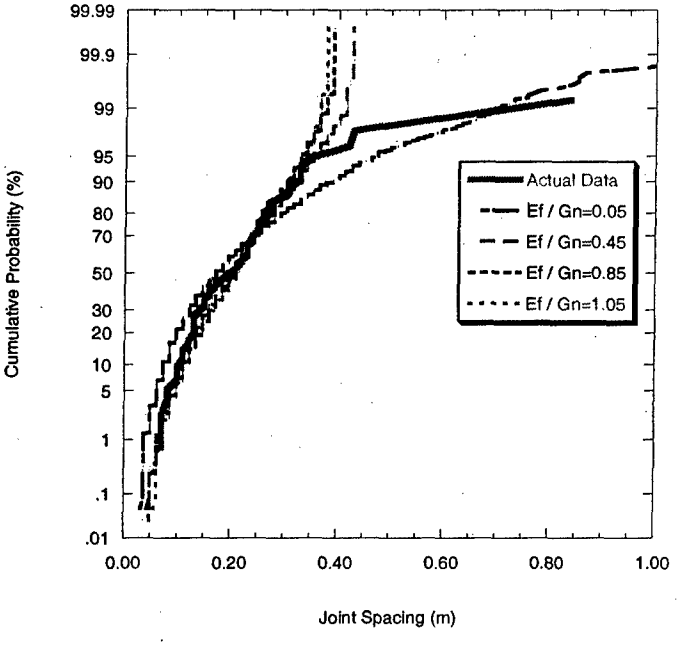


Figure 356 – Comparison between simulated and actual joint spacing CDFs for layer 5. Joint spacing is not normalized A thick chert layer is used here (d=1.0 m). Compare this comparison with Figure 338 and Figure 339. H_0 is accepted for all values of $\frac{E_f}{G_n}$. Note the change in vertical scale as the value of cumulative probability increases: near the tail differences in cumulative probability are less than 0.01 (or 1 percentage point).

There are several possible reasons why the comparisons between the simulated and actual joint spacing CDFs that have been shown above are not successful. One, the existence of the fault may have affected the formation of the 055° set in layers other than the North side of layer 4. However, field evidence does not support this except on the North side of layer 4. Gross et al. (1997) did not observe a change in orientation in the 055° set with proximity to the fault. They also did not note any changes in joint spacing with proximity to the fault. Another possible reason for the discrepancy is that the chert layers may be less stiff than assumed. Gross et al. (1997) observed breccia in the chert layers. This means that the chert may be heavily fractured. The material properties that were assumed for the chert in the preceding simulations were based on an intact chert. A brecciated chert will have an overall stiffness that is lower than the intact chert making $\frac{E_f}{G_n}$ ratios above 1.0 possible. Now consider what effect $\frac{E_f}{G_n}$ ratios larger than unity will have on some of the comparisons. **Figure 357** and **Figure 358** show the comparison for dataset A when larger $\frac{E_f}{G_n}$ ratios are used and the chert layer thickness is 0.05 and 0.10 m, respectively. **Figure 359** and **Figure 360** show the same for dataset B. The fit for dataset A is not as good as that for dataset B but the chert layer thickness values used are realistic. K-S testing rejects H_0 for $\frac{E_f}{G_n}$ = 2.0 and 4.0 in both **Figure 357** and **Figure 358** (H_0 is accepted for the other cases in **Figure 357** and **Figure 358**). In **Figure 359** and **Figure 360**, H_0 is accepted for all $\frac{E_f}{G_n}$ values.

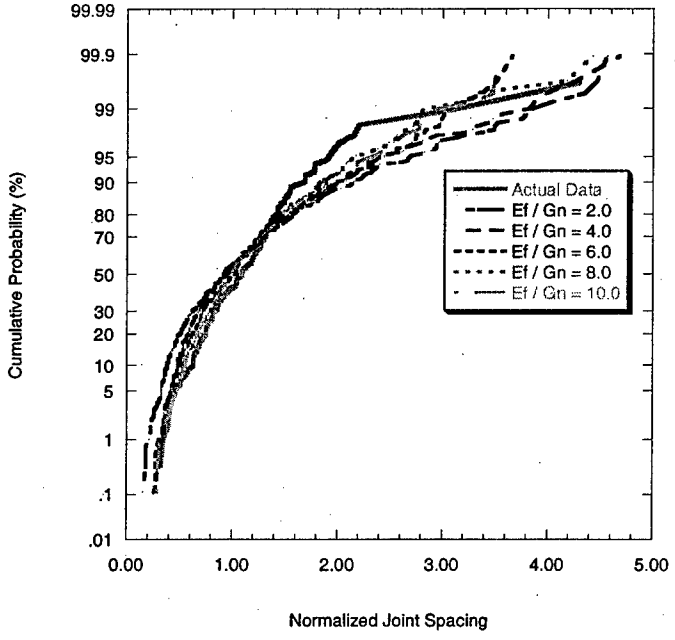


Figure 357 – Comparison of joint spacing CDFs for dataset A for a chert layer thickness of 0.05 m and $\frac{E_f}{G_n}$ values exceeding unity.

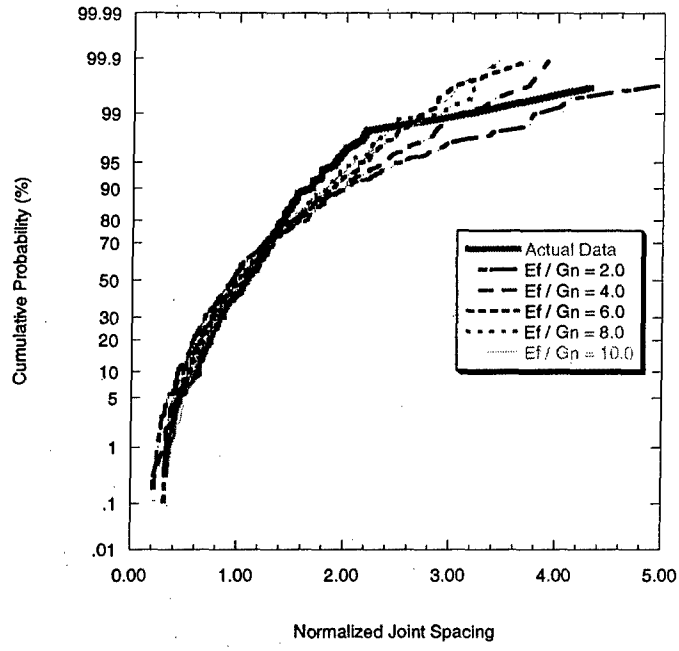


Figure 358 – Comparison of joint spacing CDFs for dataset A for a chert layer thickness of 0.1 m and $\frac{E_f}{G_n}$ values exceeding unity.

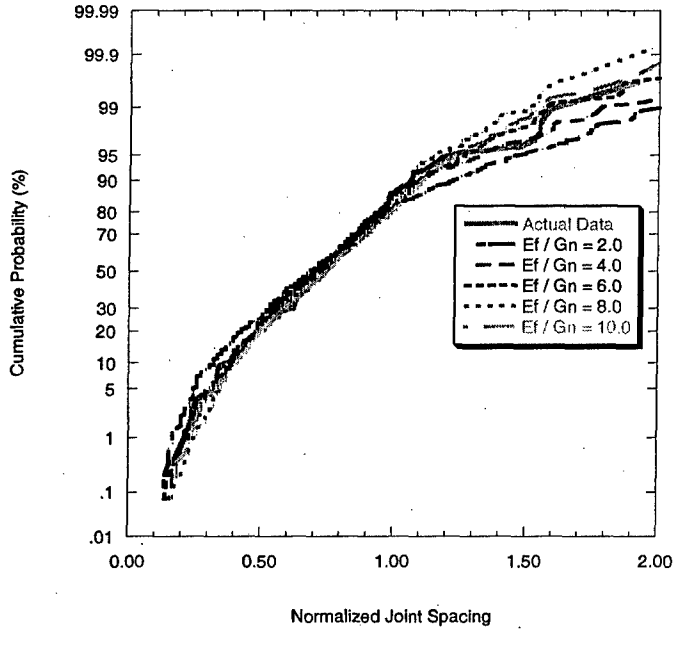


Figure 359 - Comparison of joint spacing CDFs for dataset B for a chert layer thickness of 0.05 m and $\frac{E_f}{G_n}$ values exceeding unity.

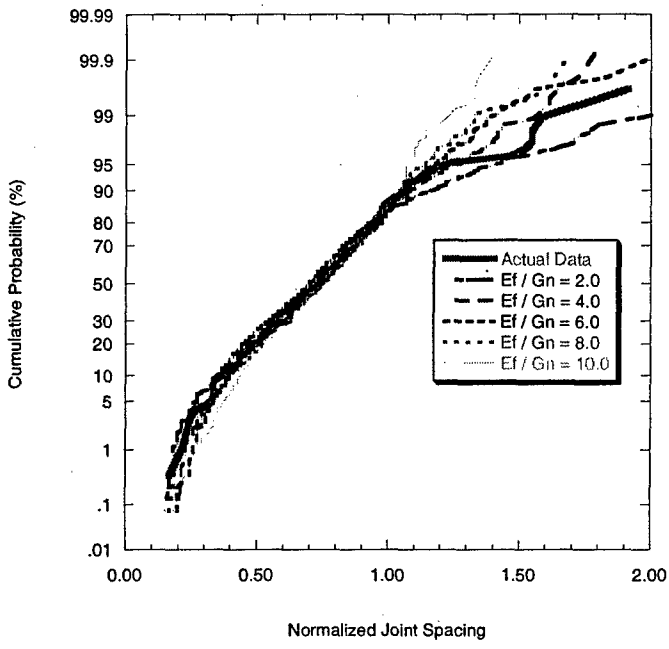


Figure 360 – Comparison of joint spacing CDFs for dataset B for a chert layer thickness of 0.1 m and $\frac{E_f}{G_n}$ values exceeding unity.

Correlated Strength Model

Now, joint spacing distributions produced by the flaw model with correlated strength are compared to actual spacing data. Recall that the correlated strength model is given by:

$$\ln\left(\frac{\sigma_{t_i}}{\mu_{\sigma_t}}\right) = \phi \ln\left(\frac{\sigma_{t_{i-1}}}{\mu_{\sigma_t}}\right) + \varepsilon_i$$

where σ_{t_i} is the tensile strength at location i, $\sigma_{t_{i-1}}$ is the tensile strength at the previous adjacent location (i-1), μ_{σ_t} is the mean tensile strength, ϕ is the correlation factor ($0 < \phi < 1$) and ε_i is a normal random variable with mean equal to zero and a standard deviation of σ_ε. As before, an estimate of the value of σ_ε is obtained from the natural logarithms of the tensile strength data. Specifically, it is assumed that $\sigma_\varepsilon = \sqrt{\sigma^2_{\ln \sigma_t}}$ (i.e., the standard deviation of the natural logarithms of the tensile strength). From the chalk tensile strength data from Palchik and Hatzor (2004) on Lower Eocene Mor chalks, σ_ε is about 0.37. In the comparisons that follow, the value of the correlation factor is varied while the chert layer thickness, $\frac{E_f}{G_n}$, and σ_ε remain constant. The $\frac{E_f}{G_n}$ ratio is increased from 0.05 to 10.0 (i.e., from intact chert to fractured chert). **Figure 361** to **Figure 365** show the comparison between the simulated and actual joint spacing CDFs for dataset A. The comparisons for dataset B are shown in **Figure 366** and **Figure 370**. The Kolmogorov-Smirnov hypothesis testing results are given in figure captions. Based on

these figures, it appears that the flaw model with a correlated strength model does not simulate the actual joint spacing CDFs very well. However, as in the flaw model with an uncorrelated strength model, the results are improved if $\frac{E_f}{G_n}$ is allowed to exceed unity (i.e., the chert is less stiff than expected due to fracturing). This is evidenced by the K-S test results for each dataset as $\frac{E_f}{G_n}$ increases.

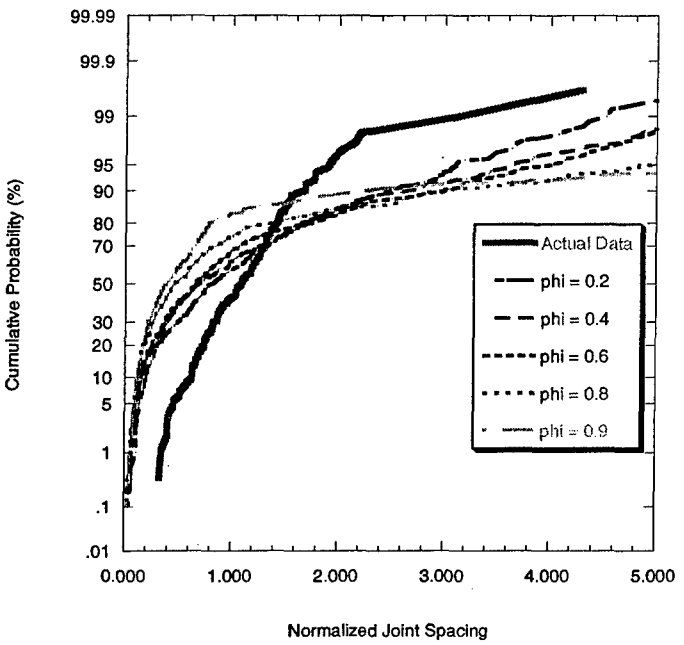


Figure 361 – Comparison between simulated and actual joint spacing CDFs using the flaw model with correlated strength model for dataset A. The chert layer thickness is d = 0 .1 and $\frac{E_f}{G_n}$ is 0.05. H_0 is rejected for all values of ϕ.

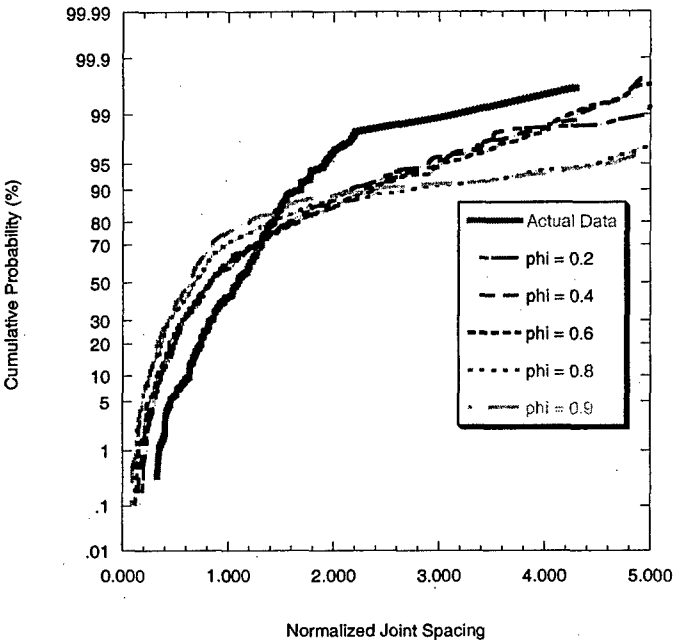


Figure 362 - Comparison between simulated and actual joint spacing CDFs using the flaw model with correlated strength model for dataset A. The chert layer thickness is d = 0 .1 and $\frac{E_f}{G_n}$ is 0.75. H_0 is rejected for all values of ϕ.

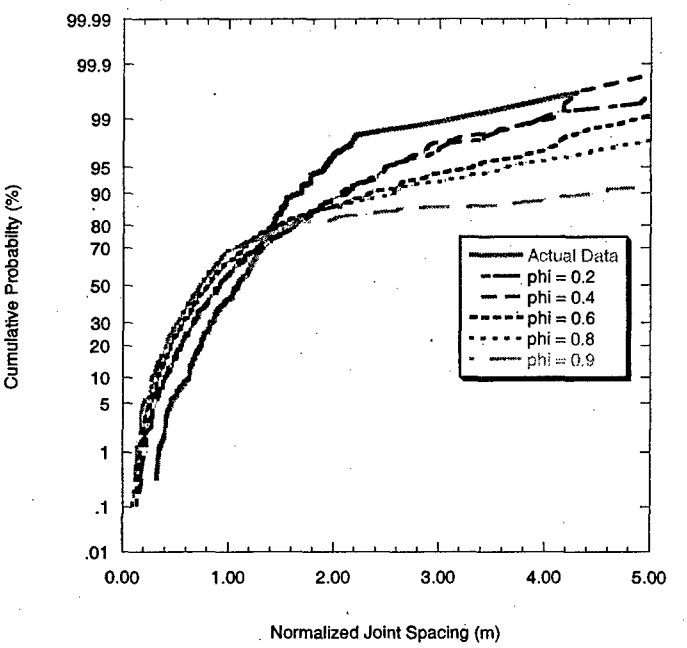


Figure 363 – Comparison between simulated and actual joint spacing CDFs using the flaw model with correlated strength model for dataset A. The chert layer thickness is d = 0 .1 and $\frac{E_f}{G_n}$ is 2.0. H_0 is rejected for all values of ϕ.

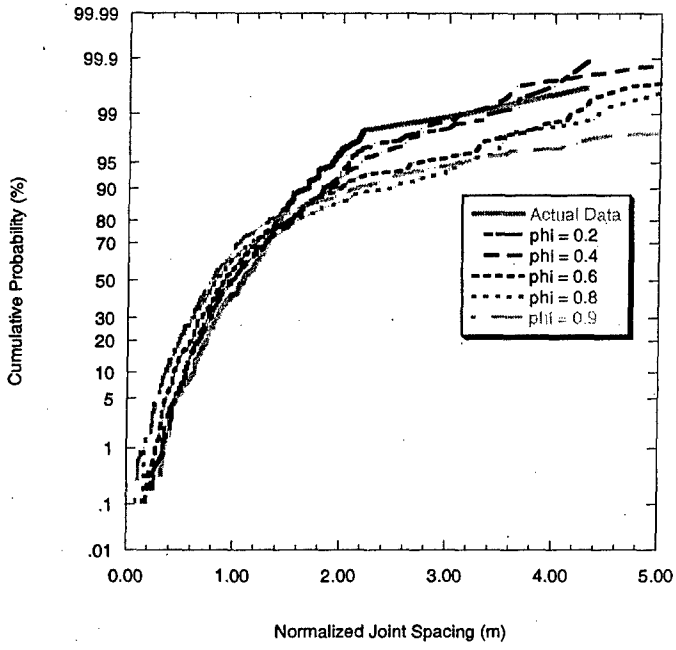


Figure 364 – Comparison between simulated and actual joint spacing CDFs using the flaw model with correlated strength model for dataset A. The chert layer thickness is d = 0 .1 and $\frac{E_f}{G_n}$ is 6.0. H_0 is rejected for ϕ =0.6 – 0.9.

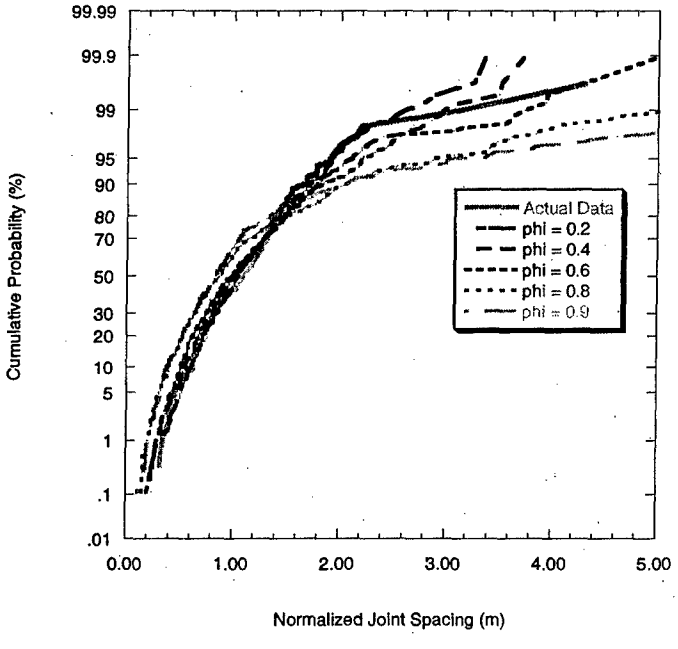


Figure 365 - Comparison between simulated and actual joint spacing CDFs using the flaw model with correlated strength model for dataset A. The chert layer thickness is d = 0 .1 and $\frac{E_f}{G_n}$ is 10.0. H_0 is rejected for ϕ =0.8 – 0.9.

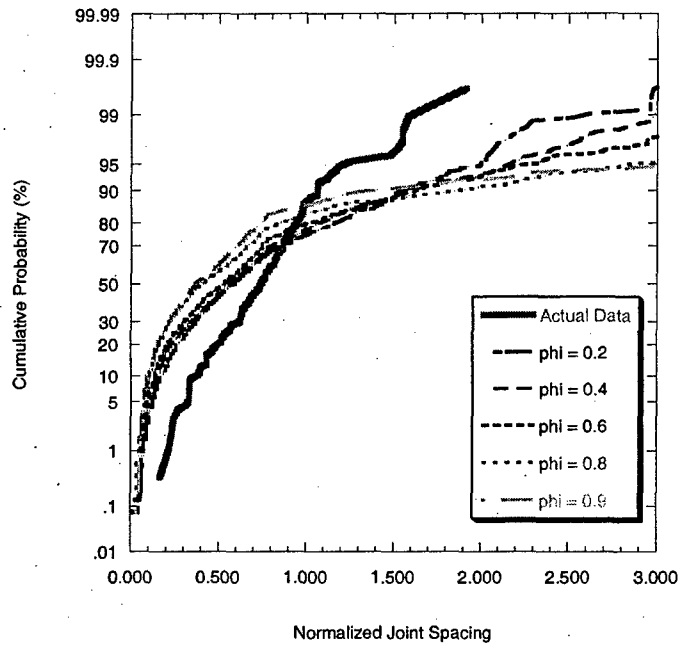


Figure 366 - Comparison between simulated and actual joint spacing CDFs using the flaw model with correlated strength model for dataset B. The chert layer thickness is d = 0 .1 and $\frac{E_f}{G_n}$ is 0.05. H_0 is rejected for all values of ϕ.

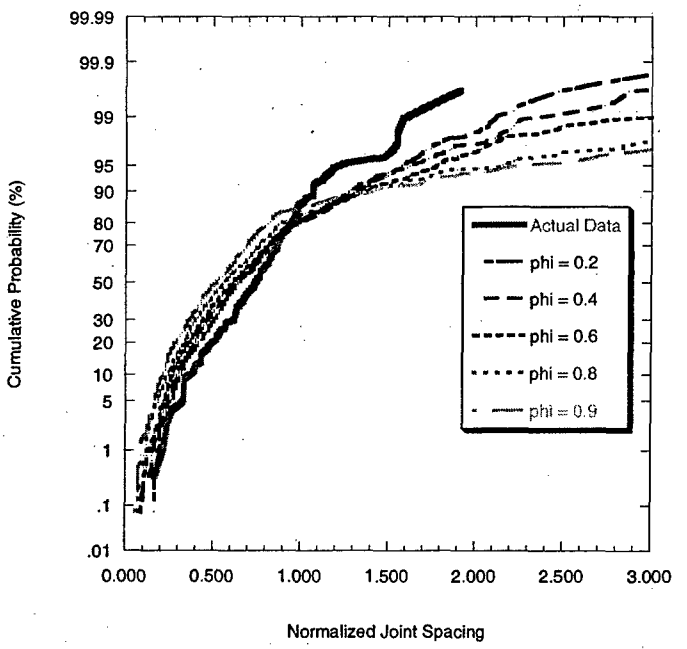


Figure 367 - Comparison between simulated and actual joint spacing CDFs using the flaw model with correlated strength model for dataset B. The chert layer thickness is d = 0 .1 and $\frac{E_f}{G_n}$ is 0.75. H_0 is rejected for all values of ϕ.

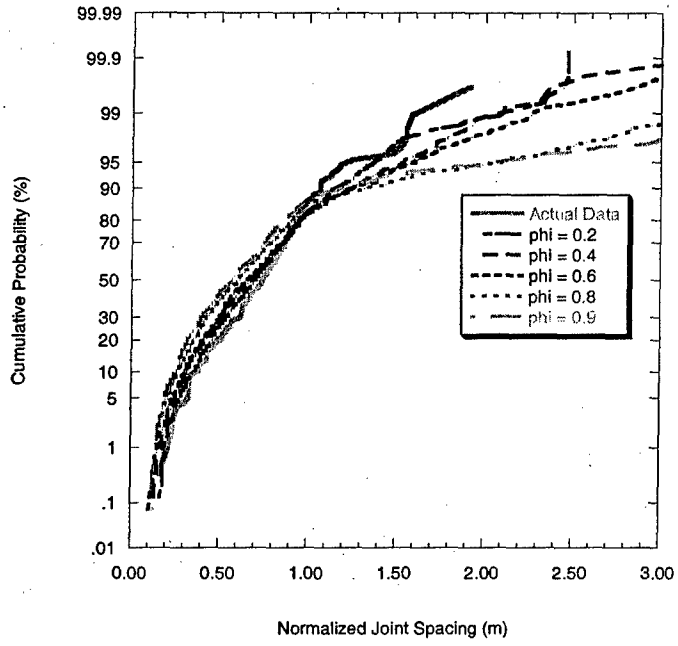


Figure 368 – Comparison between simulated and actual joint spacing CDFs using the flaw model with correlated strength model for dataset B. The chert layer thickness is d = 0 .1 and $\frac{E_f}{G_n}$ is 2.0. H_0 is rejected for ϕ =0.4 – 0.9.

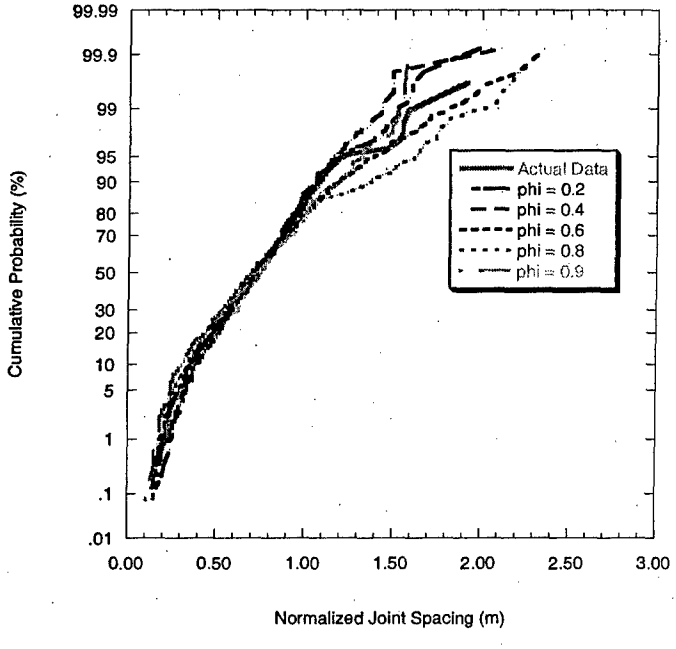


Figure 369 – Comparison between simulated and actual joint spacing CDFs using the flaw model with correlated strength model for dataset B. The chert layer thickness is d = 0 .1 and $\frac{E_f}{G_n}$ is 6.0. H_0 is accepted for all values of ϕ.

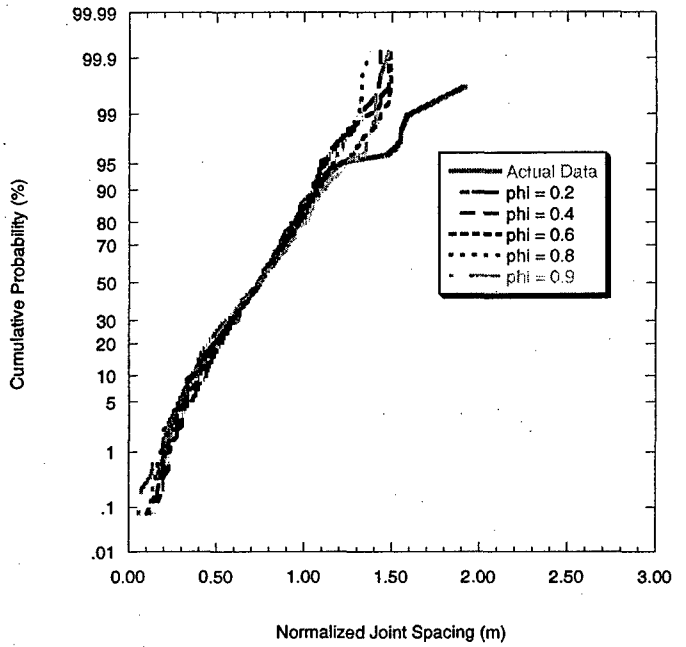


Figure 370 - Comparison between simulated and actual joint spacing CDFs using the flaw model with correlated strength model for dataset B. The chert layer thickness is d = 0 .1 and $\frac{E_f}{G_n}$ is 10.0. H_0 is accepted for all values of ϕ.

7.4.4.2 Rejection Procedure Results

Figure 371 and **Figure 372** show the comparisons between the simulated and actual joint spacing CDFs for dataset A using the rejection procedure when it is assumed that the bounding chert layers are intact and therefore stiffer than the chalk layers ($\frac{E_f}{G_n}$<1.0). **Figure 373** and **Figure 374** show the same for dataset B. In these plots, $\frac{E_f}{G_n}$ is held constant while the chert layer thickness is varied. In all four comparisons, it can be seen that the rejection procedure does not perform well. The rejection procedure does not capture the shape of the actual joint spacing probability distributions, and K-S testing rejects H_0 for all cases in **Figure 371** to **Figure 374**. This is true even if the $\frac{E_f}{G_n}$ ratio exceeds unity and the chert layer thickness takes on values closer to those observed in the field (i.e., 0.05 to 0.1 m). **Figure 375** and **Figure 376** demonstrate this for dataset A and **Figure 377** and **Figure 378** show this for dataset B. K-S testing rejects H_0 for all cases in **Figure 375** and **Figure 376** (dataset A). For dataset B, H_0 is rejected in all cases except for $\frac{E_f}{G_n}$ = 10.0 in **Figure 377** and $\frac{E_f}{G_n}$ = 8.0 and 10.0 in **Figure 378**.

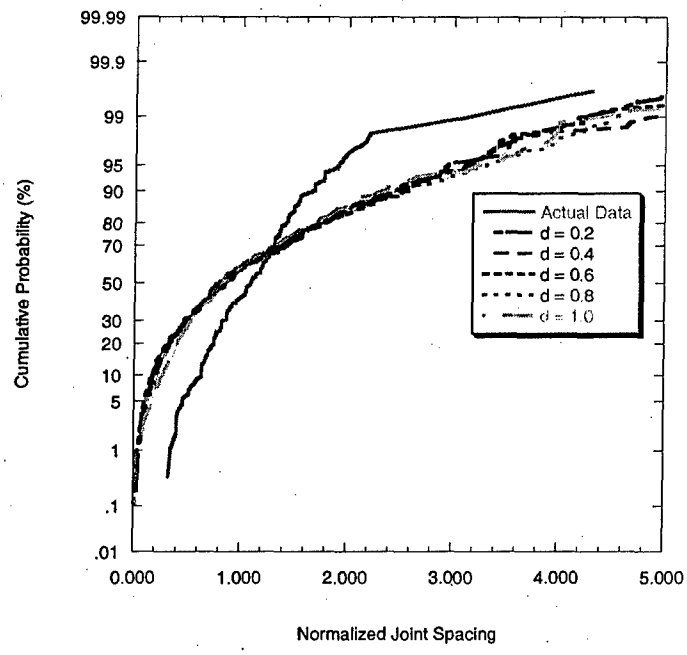


Figure 371 – Comparison between simulated and actual joint spacing CDFs for dataset A using the rejection procedure. The $\frac{E_f}{G_n}$ ratio is 0.05.

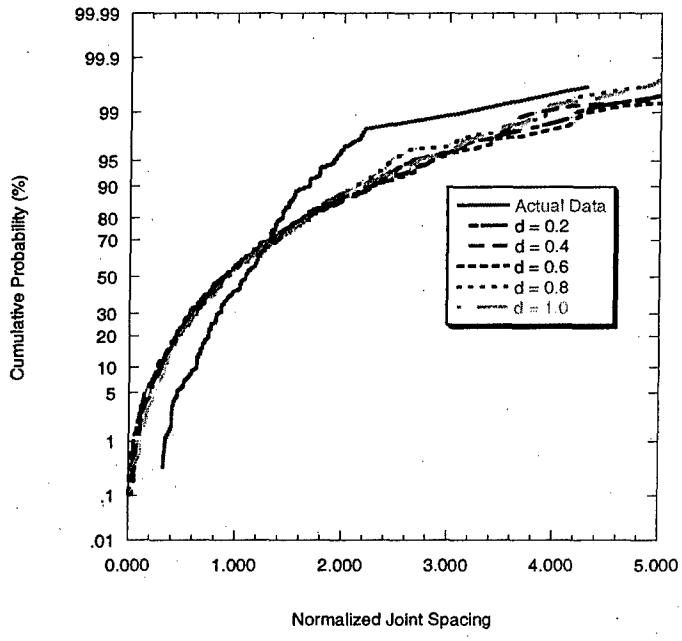


Figure 372 - Comparison between simulated and actual joint spacing CDFs for dataset A using the rejection procedure. The $\frac{E_f}{G_n}$ ratio is 1.0.

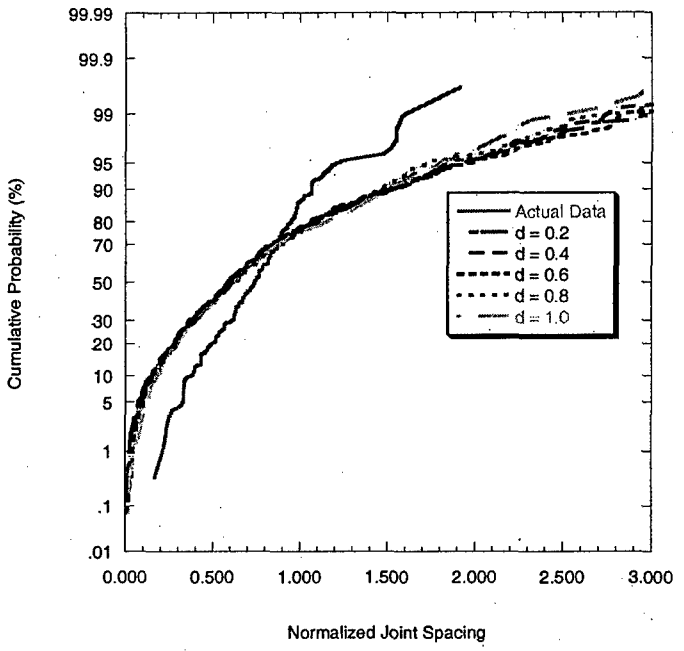


Figure 373 - Comparison between simulated and actual joint spacing CDFs for dataset B using the rejection procedure. The $\frac{E_f}{G_n}$ ratio is 0.05.

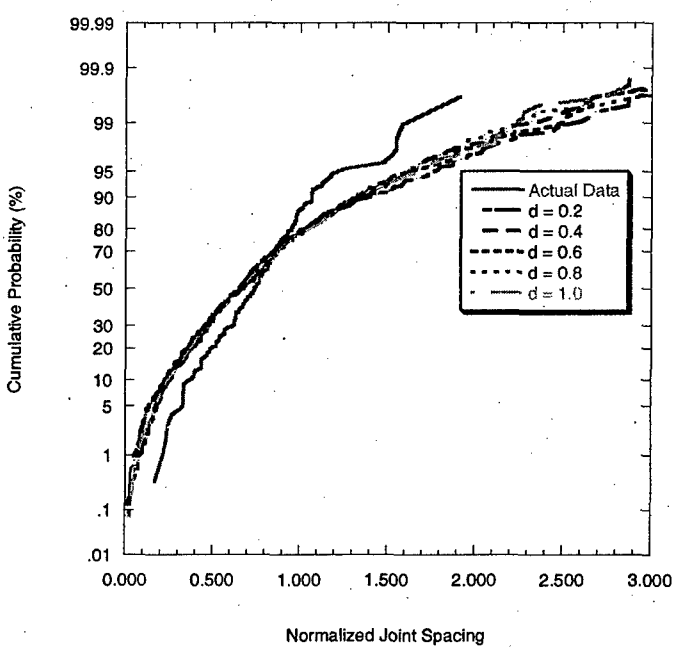


Figure 374 - Comparison between simulated and actual joint spacing CDFs for dataset B using the rejection procedure. The $\frac{E_f}{G_n}$ ratio is 1.0.

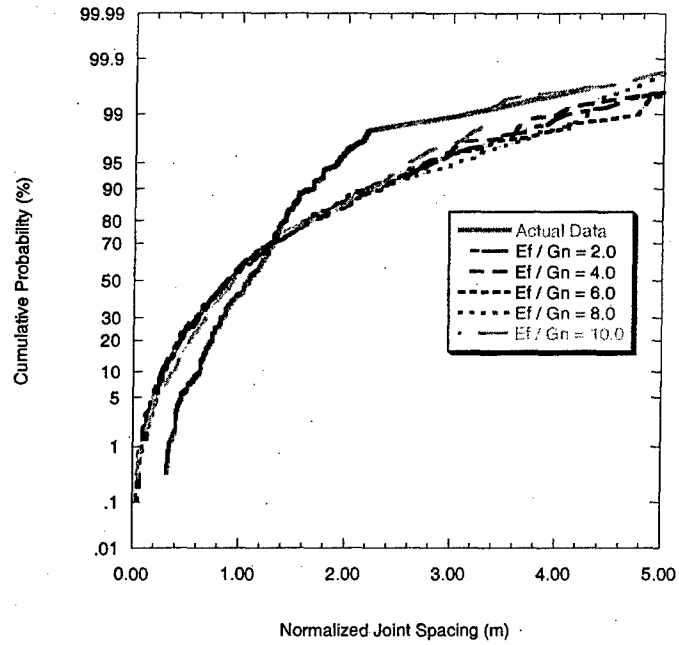


Figure 375 – Comparison between simulated and actual joint spacing CDFs for dataset A using the rejection procedure for a chert layer thickness of 0.05 m. The $\frac{E_f}{G_n}$ is allowed to exceed unity.

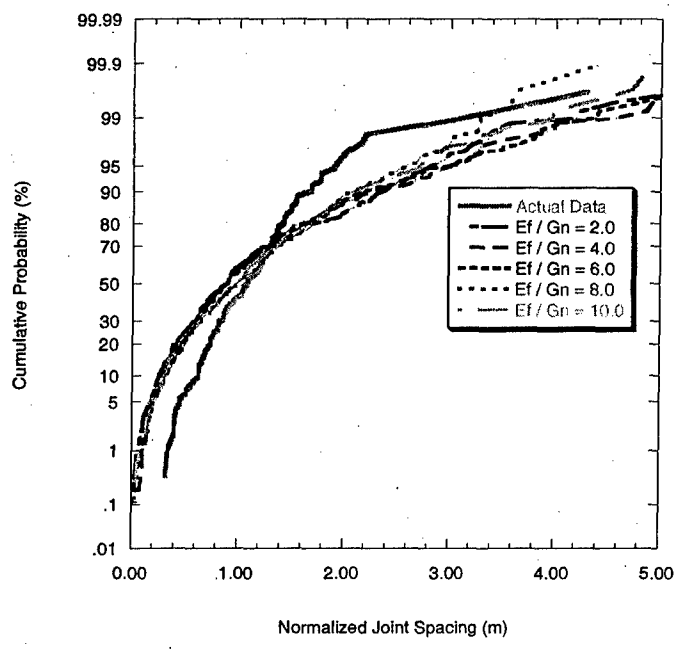


Figure 376 – Comparison between simulated and actual joint spacing CDFs for dataset A using the rejection procedure for a chert layer thickness of 0.1 m. The $\frac{E_f}{G_n}$ is allowed to exceed unity.

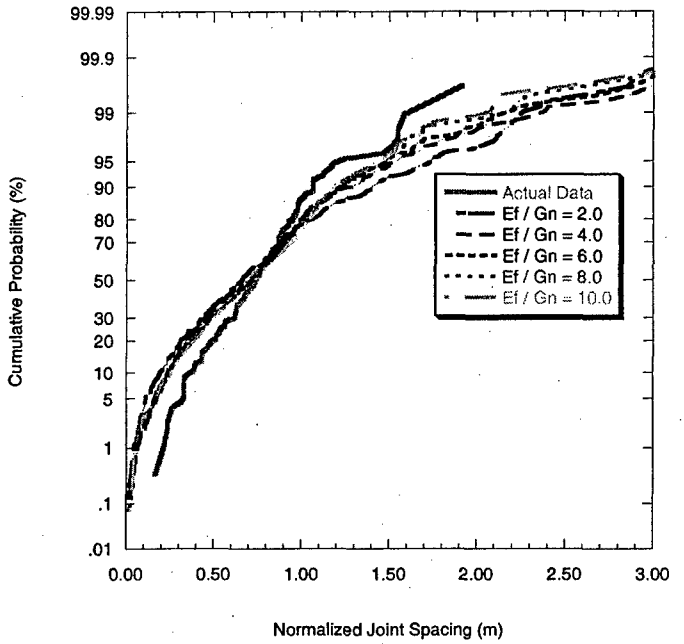


Figure 377 - Comparison between simulated and actual joint spacing CDFs for dataset B using the rejection procedure for a chert layer thickness of 0.05 m. The $\frac{E_f}{G_n}$ is allowed to exceed unity.

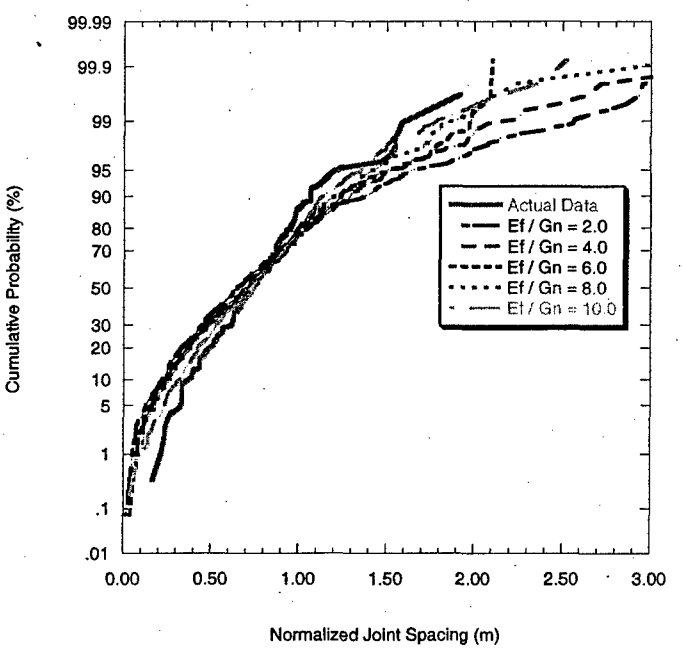


Figure 378 – Comparison between simulated and actual joint spacing CDFs for dataset B using the rejection procedure for a chert layer thickness of 0.1 m. The $\frac{E_f}{G_n}$ is allowed to exceed unity.

7.4.4.3 Discussion

The rejection procedure does not appear to be effective in producing joint spacing CDFs similar to those of the field data. Statistical tests confirm this and the hypothesis that the actual and simulated joint spacing data come from the same probability distribution is rejected in most cases. Visual comparisons are consistent with the statistical results.

The flaw model, on the other hand, models the actual joint spacing CDFs at different levels of success depending on whether or not the bounding chert layers are intact. If the bounding chert layers are assumed to be intact, the $\frac{E_f}{G_n}$ ratios should be less than 1.0 because chert is generally stiffer than chalk. If the bounding chert layers are fractured (as noted by Gross et al., 1997), their overall stiffness would decrease and $\frac{E_f}{G_n}$ ratios greater than 1.0 may be possible. When the bounding chert layers are considered intact (i.e., $\frac{E_f}{G_n}$<1.0), the flaw model with uncorrelated strength does not perform well. In that case, a good fit between the actual and simulated joint spacing data is achieved only at chert layer thicknesses (i.e., 0.2-1.0 m) greater than observed (~0.07 m). On the other hand, when the chert bounding layers are fractured (i.e., $\frac{E_f}{G_n}$>1.0), the flaw model with uncorrelated strength yields joint spacing CDFs that are close to the actual joint spacing CDFs while using chert layer thicknesses (i.e., 0.05 and 0.10 m) that are close to those observed in the area (~0.07 m).

When correlated strength is used in the flaw model, a good fit between the simulated and actual joint spacing CDFs is achieved when using $\frac{E_f}{G_n}$ values greater than unity for a fractured chert layer thickness of 0.1 m (~0.07 m thickness is typical in the area).

7.5 Case 4: Baudo (2001)

7.5.1 General Observations

Baudo (2001) gathered joint spacing data from sedimentary rocks in southwestern New York State. Specifically, the data were taken from layers of the Upper Canadaway Formation in the Appalachian Plateau in the South Branch gorge of Cattaraugus Creek (Baudo, 2001). Joint spacing measurements were made along numerous scanlines (totaling a length of 4 km) that trace the path of Cattaraugus Creek (**Figure 379**). Sandstones and shales of the Catskill Delta Complex are exposed along the creek (Baudo, 2001). Siltstones are also present (Engelder and Geiser, 1980). Whereas the sandstone beds can be massive (~2 m thick), most layers are less than 0.5 m thick (Engelder and Geiser, 1980). Although the area is on the plateau, folds with limbs dipping less than 2° are found in the area (Baudo, 2001).

Major joint sets in the Appalachian Plateau have been classified roughly into two groups (e.g., Engelder and Geiser, 1980) depending on their orientation with respect to the general trend of the folds in the area: cross-fold joints (set I) and strike joints (set II). Fold axes in the area generally strike northwest. Cross-fold joints are those that intersect the fold axes at high angles whereas strike joints are oriented sub-parallel to the fold axes (Engelder and Geiser, 1980). A third joint set (set III) that is geometrically unrelated to the fold orientations in the area is also present (Engelder and Geiser, 1980; Engelder, 1985). The set I joints generally strike northwest whereas the set II joints are generally oriented northeast (Baudo, 2001). Both sets dip approximately vertically (Baudo, 2001). In Baudo's (2001) study area both sets are generally widely spaced although joints in set I are typically more widely spaced than joints in set II. According to Engelder and Geiser (1980) set III joints cannot be clearly distinguished from set II joints in this area.

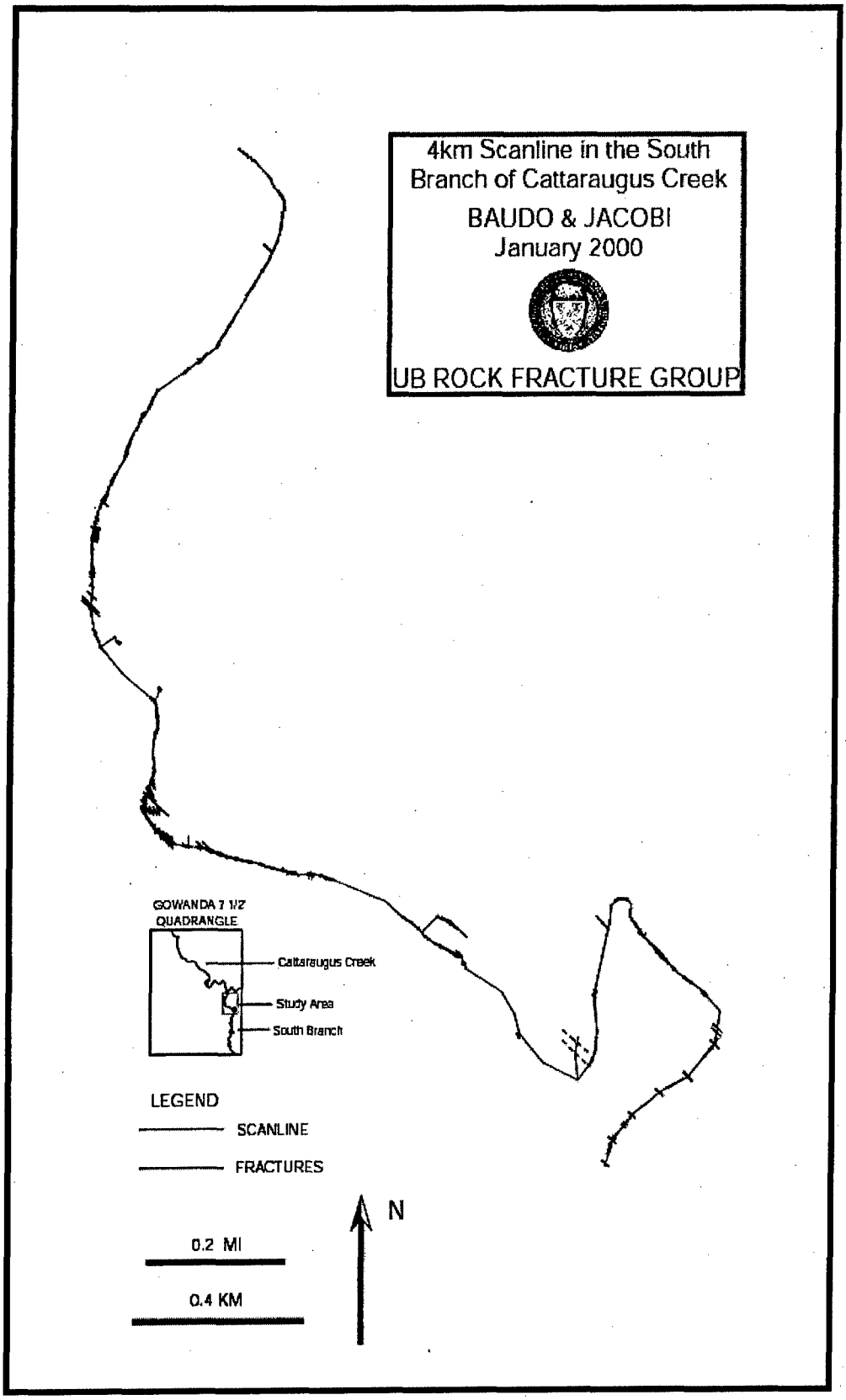


Figure 379 – The 4-km-long scanline tracing the path of the Cattaraugus Creek (from Baudo, 2001)

7.5.2 Joint Spacing Data

Due to the fact that the set I (northwest-striking) joints are very widely spaced, only a small number of them can be found in each segment of the 4-km-long scanline. Set II (northeast-striking) joints, although also widely spaced, are more abundant in than set I joints. However, the joint intensity varies from one scanline to another and there is much variation in the types of rock intersected. As a result, only three scanline segments are considered here. Also, along these three scanline segments, only set II joints are considered in the comparisons. Set I joints also intersect these three scanlines but are much too widely spaced to comprise data sets containing enough joints. Since the three scanline segments inersect different layers the datasets are referred to as layer 1, layer 2 and layer 3 datasets. The position of each layer relative to the other two within the rock formation is unclear in Baudo (2001).

Table 21 shows the different lithologies intersected by the three scanlines. One can see that more than one layer is often intersected by a single scanline. However, one layer is intersected more often than any the other. For example, scanline 1 mostly intersects one sandstone and one siltstone layer (Baudo, 2001 combined this into a single "sandstone + siltsone" layer). Scanline 2 mostly intersects a fine sandstone layer, as does scanline 3. As a result, layer 1 is defined as a sandstone/siltstone layer that is 0.09 m thick. Layers 2 and 3 are defined as fine sandstone layers that are 0.10 m thick.

The bounding layers noted by Baudo (2001) also change along each scanline. However, "representative" top and bottom bounding layers can be chosen based on which layers are most persistent along the length of the jointing layer. For example, for scanline 1, sandstone layers bound the jointing layer for most of its length. For scanlines 2 and 3, the representative bounding layers are fine sandstone.

Scanline spacings were reported in Baudo (2001). Here, scanline spacings are corrected using scanline orientation to obtain the perpendicular spacing between joints of the same set. For the rest of this section (**7.5**), "spacing" refers to corrected spacing.

Joint spacings are wide compared to layer thickness. For example, set II joints in layer 1 have a mean spacing of 0.72 m. This results in a mean spacing-to-thickness ratio of 8.0. Similarly, layers 2 and 3 have mean spacing-to-thickness ratios of 8.3 and 9.9, respectively. These ratios are much larger than those considered in the three previous cases in this chapter. Given such large ratios, it should be safe to say that these layers are below joint saturation.

Table 21 – Summary of lithologies of the layers intersected by the three scanlines considered (from data by Baudo, 2001).

Scanline (orientation)	Jointing Layer Lithologies	Jointing Layer Thickness	Top Bounding Layer	Top Bounding Layer Thickness	Bottom Bounding Layer	Bottom Bounding Layer Thickness
Scanline 1 (277°)	sandstone, siltstone, shaly siltstone, interbedded siltstone and shale, interbedded sandstone and siltstone	sandstone and siltstone have a combined thickness of 0.09 m, thickness for other lithologies not indicated	sandstone, shale, shaly siltstone, silty shale	sandstone layer is from 0.03 to 0.10 m thick, others are between 0.01 and 0.05 m thick	sandstone, shale, interbedded siltstone and shale, shaly siltstone, siltstone	sandstone layer is from 0.03 to 0.10 m thick, others are between 0.02 and 0.06 m thick
Scanline 2 (290°)	fine sandstone, silty shale, shaly siltstone, siltstone	fine sandstone is 0.10 m thick, silty shale is < 0.01 m thick, thickness for others not indicated	fine sandstone, silty shale	fine sandstone layer is from 0.03 to 0.10 m thick, silty shale is 0.005 m thick at some point	fine sandstone, silty shale	fine sandstone layer is 0.03 m thick, thickness for others not indicated
Scanline 3 (111°)	silty shale, fine sandstone, siltstone, interbedded siltstone and shale, interbedded sandstone and siltstone	fine sandstone is 0.10 m thick, others are between 0.01 to 0.05 m thick	silty shale, siltstone, fine sandstone	fine sandstone is 0.03 m, thickness for others not indicated	fine sandstone	fine sandstone layer is 0.05 m in some parts

Table 22 shows the statistics of spacings for case 4 followed by spacing histograms for each layer (**Figure 380** to **Figure 382**). The mean and standard deviation are not close to each other in all layers (**Table 22**). This suggests that the exponential distribution is not a suitable probability distribution to describe the spacing data. The shapes of the spacing histograms support this observation.

Table 22 – Spacing statistics for case 4. Calculated from data in Baudo (2001).

	Layer 1	Layer 2	Layer 3
Number of Spacings	70	39	38
Mean Spacing (m)	0.725	0.835	0.988
Standard Deviation (m)	0.546	1.785	0.815

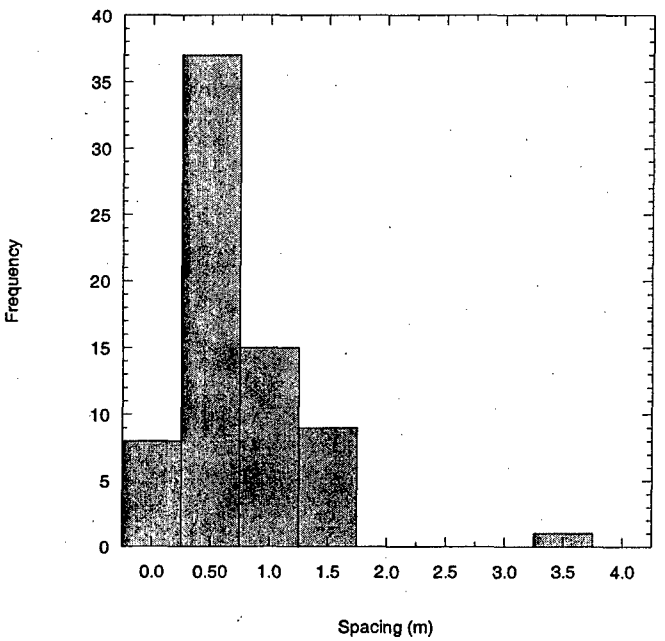


Figure 380 – Spacing histogram form layer 1. Constructed from data in Baudo (2001).

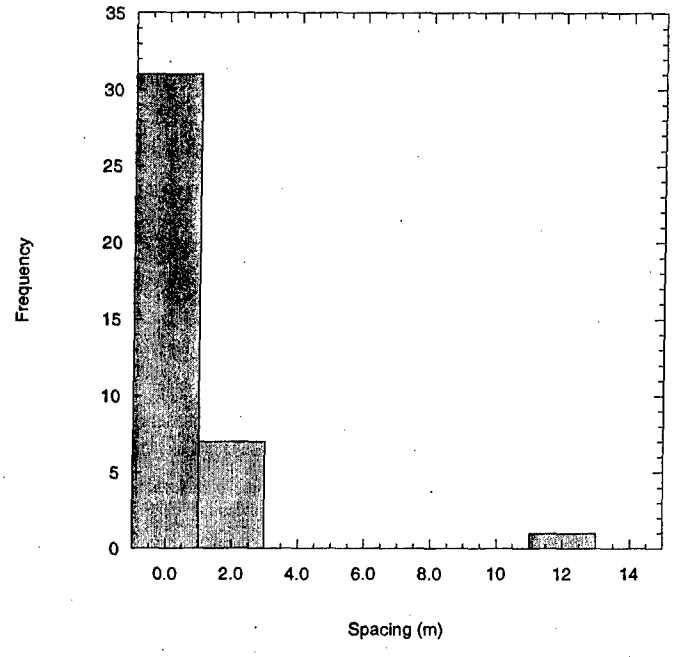


Figure 381 – Spacing histogram form layer 2. Constructed from data in Baudo (2001).

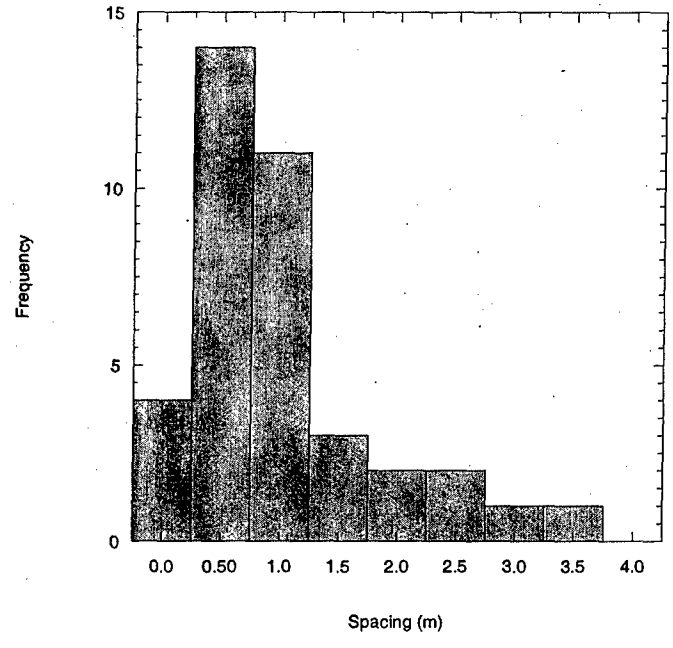


Figure 382 – Spacing histogram form layer 2. Constructed from data in Baudo (2001).

Figure 383 shows the CDF for joint spacing data for layer 1 together with the CDFs for corresponding exponential and log-normal distributions obtained via maximum likelihood. It appears that spacings from layer 1 can be described by a log-normal probability distribution. A chi-square goodness-of-fit test accepts the hypothesis at the 0.05 level. **Figure 384** shows the joint spacing CDF for layer 2 and the corresponding maximum likelihood exponential and log-normal CDFs. Neither probability distribution

appears to describe the joint spacing data well. In fact, chi-squared goodness-of-fit tests reject the hypotheses that either probability distribution can be used to describe these data. **Figure 385** shows that the joint spacing data in layer 3 may be best described by a log-normal probability distribution. A Chi-squared goodness-of-fit test is consistent with this observation (i.e., hypothesis that a log-normal distribution can be used to describe the joint spacing data from layer 3 is accepted at the 0.05 level).

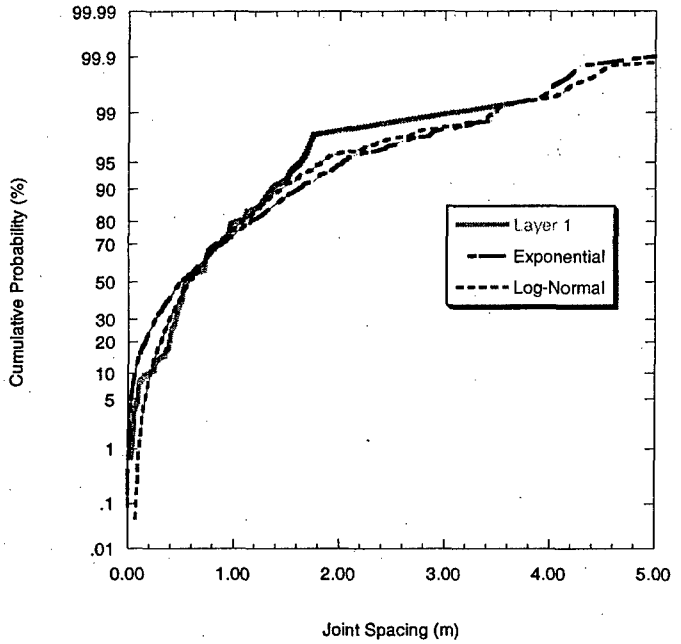


Figure 383 – Comparison of layer 1 joint spacing (set II, northeast-striking) CDF with exponential and log-normal CDFs. Chi-square accepted at 0.05 level for log-normal probability distribution.

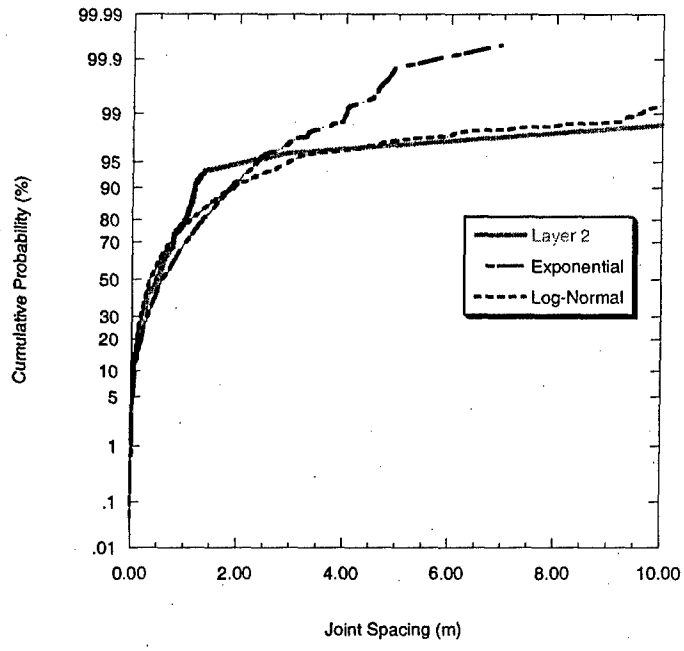


Figure 384 – Comparison of layer 2 joint spacing (set II, northeast-striking) CDF with exponential and log-normal CDFs. Chi-square rejected at 0.05 level for log-normal probability distribution.

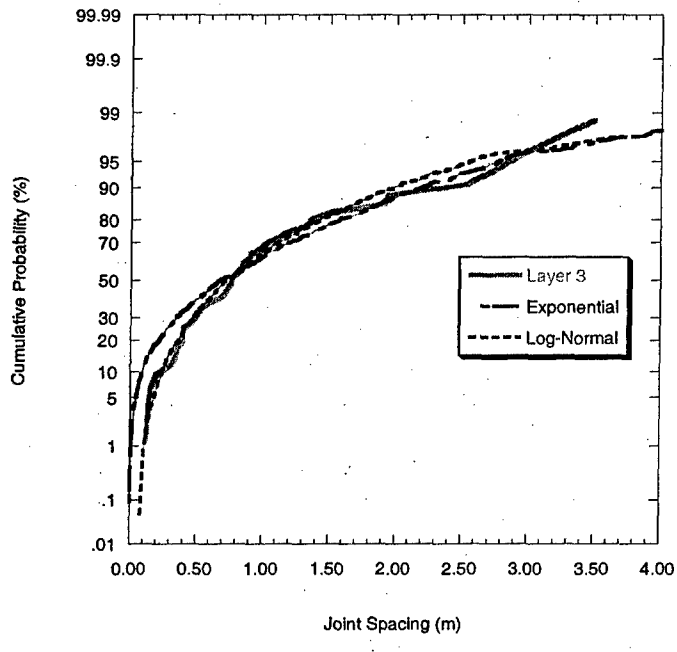


Figure 385 – Comparison of layer 3 joint spacing (set II, northeast-striking) CDF with exponential and log-normal CDFs. Chi-square accepted at 0.05 level for log-normal probability distribution.

7.5.3 Model Parameter Values

Table 23 below shows a summary of field observations along with the corresponding model implications.

Table 23 – Field observations and their corresponding model implications for case 4.

Field Observations	Model Implications
Joints are typically not confined to a single layer (i.e., joint height is greater than bed thickness).	This violates the assumption that the joints are layer-confined in the derivation of the stress distribution within the jointing layer. However, it is assumed that the joints are initially layer-confined when they are formed. As the strain increased, it is accommodated by propagation into the adjacent layers rather than the addition of new joints.
No slip between the layers is observed.	The interface slippage saturation mechanism is not applicable but the compressive stress development mechanism may come into play. In the model, the interface shear strength is set to a very high value so that it cannot be overcome (i.e., no slippage).
No strain measurements were taken.	A stopping point for the jointing process needs to be defined. The actual mean joint spacing may be used for this purpose.
Cross-fold joints (set I) and strike joints (set II) are both found in the area. Observations indicate that set I joints are older than set II joints (Engelder, 1985; Baudo, 2001). Set I joints are much more widely-spaced than set II joints. Data used in comparisons are from set II.	Set II joints are not first-formed joints and may be influenced by existing set I joints. Set I and set II joints are not necessarily perpendicular to each other in the study area (Engelder and Geiser, 1980; Baudo, 2001). However, set I joints are so widely spaced that many set II joints could be found in the area between two adjacent set I joints. It is assumed that in that area, the set II joints are only influenced by the existence of other set II joints (i.e., set I joints are essentially remote).
No material properties for the layers are measured in the joint survey.	These material properties need to be estimated or obtained from other sources. However, the low joint intensities in all three layers may allow some of these properties to be disregarded as their effects on the joint spacing probability distribution may be insignificant. Some parametric studies are needed.

Unlike in the previous three cases, no material properties could be found in the literature for the layers studied by Baudo (2001). However, because of the relatively low joint intensities, the effects of certain parameters on simulated joint spacing may not be significant in either the flaw model and rejection procedure. As an example, consider how the tensile strength may affect the simulated joint spacing distribution for layer 1 using the flaw model with uncorrelated tensile strength. It was shown in parametric studies that simulated joint spacing distributions are affected only by the ratio between the maximum and minimum tensile strength rather than by their exact values. **Figure 386** shows the effect of the tensile strength ratio for layer 1 and it appears that its effect

on the joint spacing CDF is not significant. There are some discrepancies at the tail ends but the vertical scale in the CDF is much smaller at high cumulative probabilities (i.e., the difference between the cumulative probabilities cannot be greater than one percentage point). This is helpful because tensile strength is one of the pieces of information that is not available for the layers being considered.

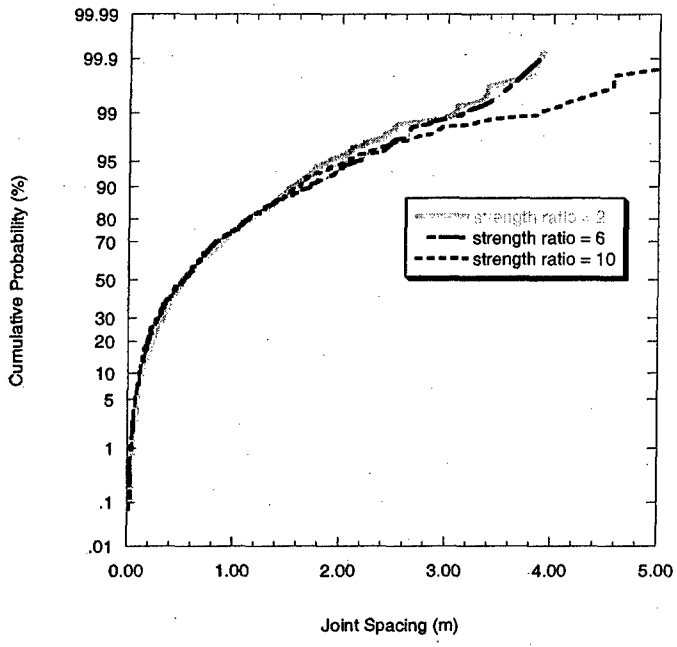


Figure 386 – Demonstration of the effect of the tensile strength ratio. Tensile strength ratio is the maximum tensile strength divided by the minimum tensile strength.

The jointing and bounding layer Poisson's ratios are needed to calculate the critical spacing-to-thickness ratio (Bai and Pollard, 2000) in the consideration of the compressive stress development saturation mechanism. However, at low joint intensities such as those encountered here, the saturation mechanism may not be important. **Figure 387** and **Figure 388** show the effects of the individual Poisson's ratios. From both plots, it appears that the effect of both Poisson's ratios on the joint spacing CDFs is not significant.

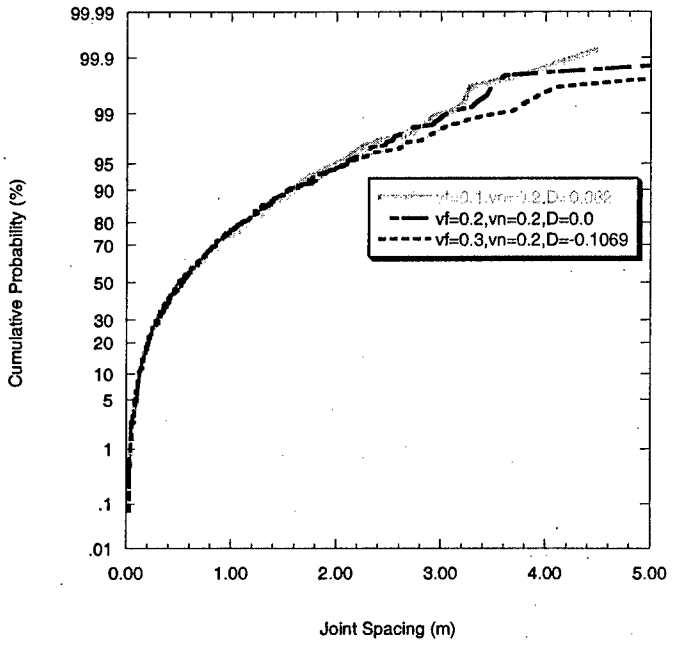


Figure 387 – Effect of the jointing layer Poisson's ratio (ν_f) on the simulated joint spacing CDF for layer 1. Note that *D* is a function of ν_f and ν_n (the bounding layer Poisson's ratio).

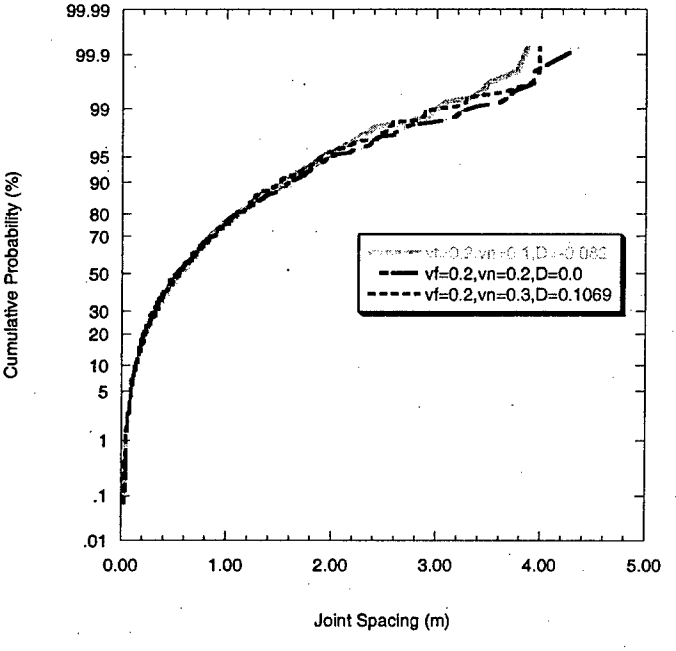


Figure 388 – Effect of the bounding layer Poisson's ratio (ν_n) on the simulated joint spacing CDF for layer 1. Note that *D* is a function of ν_f (the jointing layer Poisson's ratio) and ν_n.

Although bounding layer thicknesses are available for each of the three layers, they tend not to be uniform along the entire length of the individual scanline segments. Typically, bounding layer thicknesses range between about 0.03 m and 0.10 m along the three scanline segments. For this reason, it might be worthwhile to look at how the bounding layer thickness may affect the joint spacing distribution. **Figure 389** shows that the effect of the non-jointing layer thickness on the joint spacing distribution in this case is insignificant because of the low joint intensity. This means that a single value of bounding layer thickness between 0.03 and 0.10 m can be used in the simulations without expecting much difference in the resulting joint spacing CDF.

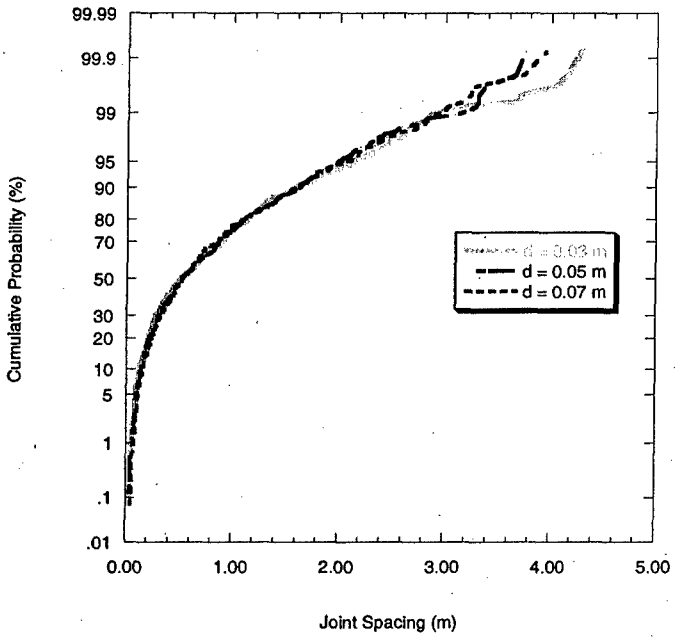


Figure 389 – Demonstration of the effect of the bounding layer thickness on the joint spacing CDF for layer 1.

Even though the above results pertain to layer 1, the same behavior applies to layers 2 and 3 because both of these layers have joint intensities similar to layer 1.

7.5.4 Simulation Results and Discussion

7.5.4.1 Flaw Model Results

Uncorrelated Strength Model

Two sets of simulations are performed for each layer. In one set, the minimum bounding layer thickness is used. The maximum bounding layer thickness is used in the other. This is done even though it was demonstrated in **Figure 389** that the bounding layer thickness does not influence the simulated joint spacing distribution significantly for the range of bounding layer thickness values observed in the field. The $\frac{E_f}{G_n}$ ratio is varied in

each set from 1.0 to 6.0. Note that there are no data available for the $\frac{E_f}{G_n}$ ratios in this particular case. The range being used represents a reasonable range of values that might be expected given the lithologies that are present.

Figure 390 and **Figure 391** show the actual and simulated joint spacing CDFs for layer 1. The minimum bounding layer thickness is 0.03 m and the maximum is 0.10 m. Some significant discrepancies between the actual and simulated joint spacing CDFs can be seen specifically at values of joint spacing below 1.0 m. There is also some deviation in the tails but these are actually only magnified because of the vertical scale. Kolmogorov-Smirnov tests reject the hypothesis (H_0) that the actual and simulated joint spacings come from the same probability distribution at the 0.05 level in all cases except for $\frac{E_f}{G_n}$ = 5.0 and 6.0 in **Figure 391**. The rejections are mainly due to the large vertical differences between the actual and simulated CDFs at joint spacings less than 1.0 m.

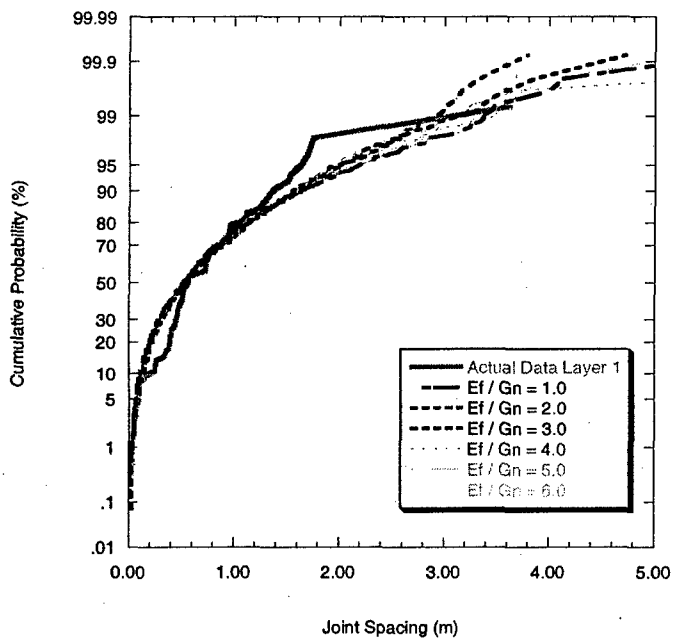


Figure 390 – Comparison between actual and simulated joint spacing CDFs for layer 1. The bounding layer thickness is 0.03 m.

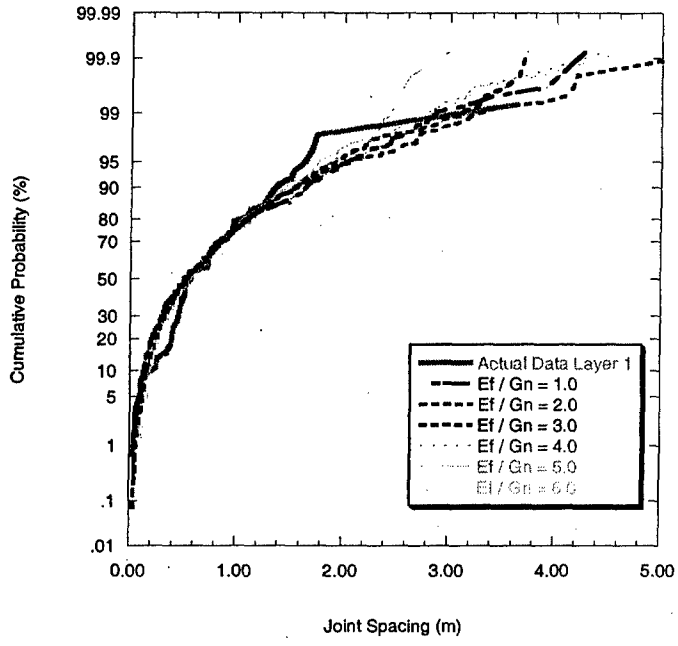


Figure 391 – Comparison between actual and simulated joint spacing CDFs for layer 1. The bounding layer thickness is 0.10 m.

Figure 392 and **Figure 393** show the actual and simulated joint spacing CDFs for layer 2. Visually, it does not appear that the simulated joint spacing CDFs can reproduce the shape of the actual curve and that the simulations underestimate the frequency of joint spacings smaller than about 2.5 m. However, K-S testing accepts H_0 in all cases in **Figure 392** and **Figure 393** except for $\frac{E_f}{G_n} = 6.0$ in **Figure 393**.

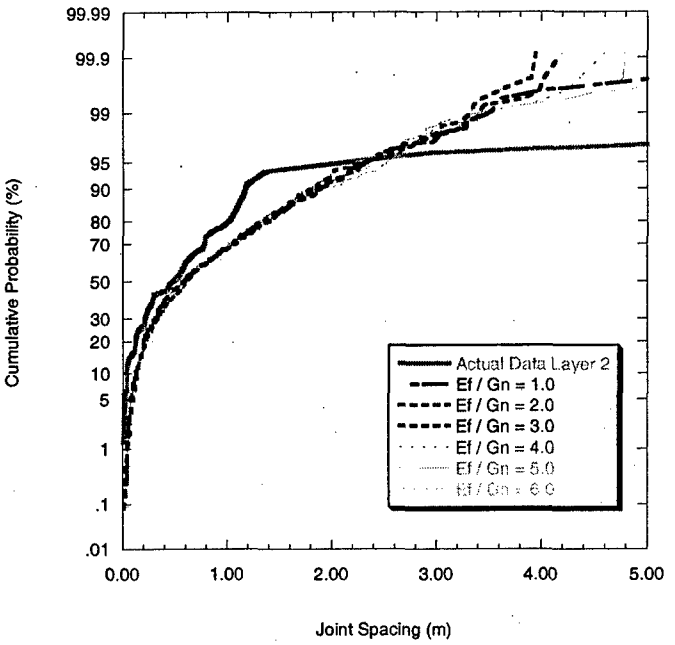


Figure 392 - Comparison between actual and simulated joint spacing CDFs for layer 2. The bounding layer thickness is 0.03 m.

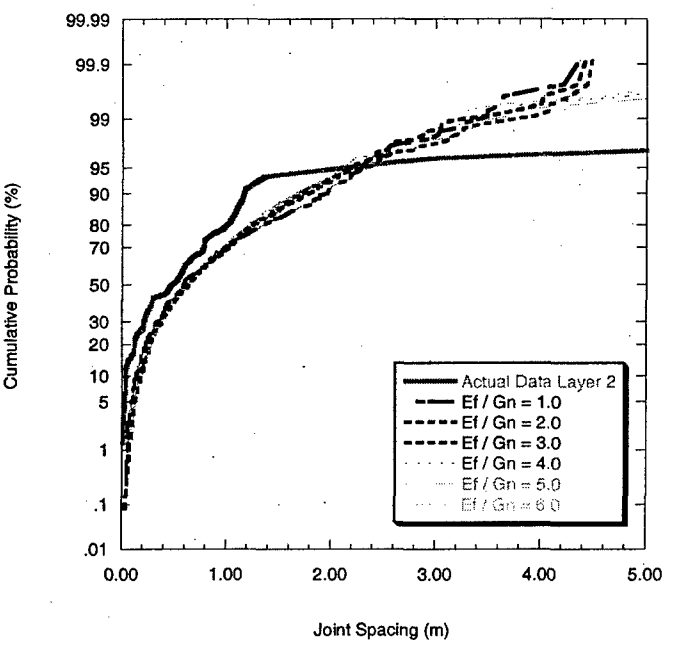


Figure 393 - Comparison between actual and simulated joint spacing CDFs for layer 2. The bounding layer thickness is 0.10 m.

Figure 394 and **Figure 395** show the comparison between the actual and simulated joint spacing CDFs for layer 3. The maximum bounding layer thickness observed for layer 3 is 0.05 m (**Figure 395**). Visually, the simulated joint spacing CDFs model the actual

joint spacing CDFs very well. K-S testing confirms this as the hypothesis H_0 is accepted for all cases.

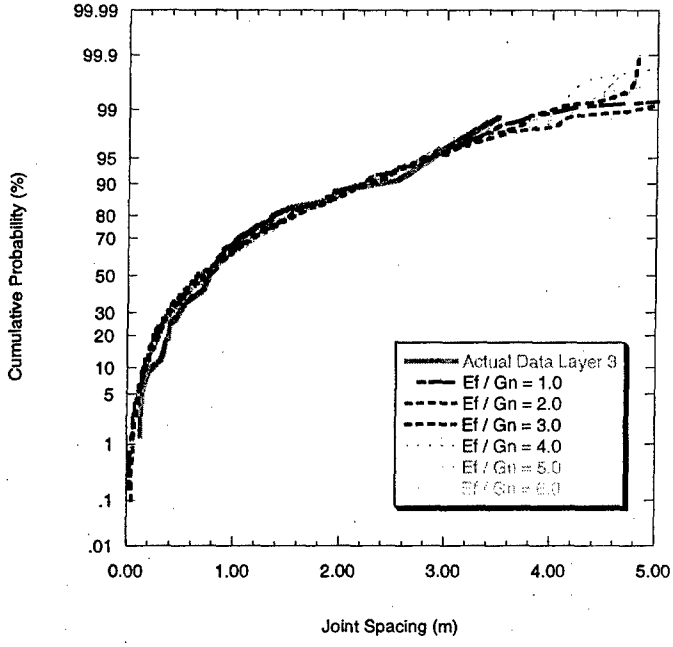


Figure 394 - Comparison between actual and simulated joint spacing CDFs for layer 3. The bounding layer thickness is 0.03 m.

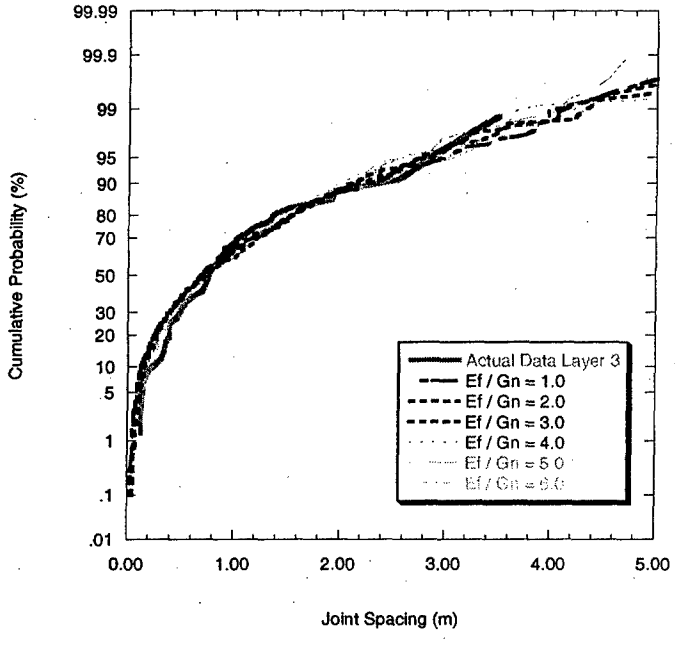


Figure 395 - Comparison between actual and simulated joint spacing CDFs for layer 3. The bounding layer thickness is 0.05 m.

Correlated Strength Model

In a correlated strength model, the strength at some location is related to the strength at an adjacent location. Recall that the relationship between the strength values at two adjacent locations is given by:

$$\ln\left(\frac{\sigma_{t_i}}{\mu_{\sigma_t}}\right) = \phi \ln\left(\frac{\sigma_{t_{i-1}}}{\mu_{\sigma_t}}\right) + \varepsilon_i$$

where σ_{t_i} is the tensile strength at location i, $\sigma_{t_{i-1}}$ is the tensile strength at the previous adjacent location (i-1), μ_{σ_t} is the mean tensile strength, ϕ is the correlation factor ($0 < \phi < 1$) and ε_i is a normal random variable with mean equal to zero and a standard deviation of σ_ε. As before, an estimate of the value of σ_ε is obtained from the natural logarithms of the tensile strength data. Specifically, it is assumed that $\sigma_\varepsilon = \sqrt{\sigma^2_{\ln \sigma_t}}$ (i.e., the standard deviation of the natural logarithms of the tensile strength). However, for this case, no tensile strength data exist. To overcome this, some parametric studies similar to those for the uncorrelated strength model can be performed. Again, due to the low joint intensities, it might be possible that some parameters do not significantly affect the simulated joint spacing distributions and can, therefore, be disregarded. First, consider the effect of tensile strength. The tensile strength data determine the value of μ_{σ_t} and provide an estimate of σ_ε. **Figure 396** shows how the tensile strength ratio influences the simulated joint spacing CDF. The three strength ratios represent three different values of μ_{σ_t} (i.e., 1.5, 3.0 and 4.0 MPa). The value of μ_{σ_t} does not seem to strongly affect the joint spacing CDF. **Figure 397** and **Figure 398** show the effect of σ_ε on the joint spacing distribution for low and high values of the correlation factor (0.1 and 0.8), respectively. In each case, the value of σ_ε does not appear to significantly affect the joint spacing CDF.

Figure 396 to **Figure 398** demonstrate that tensile strength is not an important factor when using the flaw model with correlated strength at low joint intensity. This information helps reduce the number of simulations that one needs to compare simulations to the field data using very limited information regarding the material properties of the rock. Similar observations are made regarding the $\frac{E_f}{G_n}$ ratio, bounding layer thickness (d), and the Poisson's ratios of the jointing and bounding layers. None of these significantly affect the simulated joint spacing CDFs.

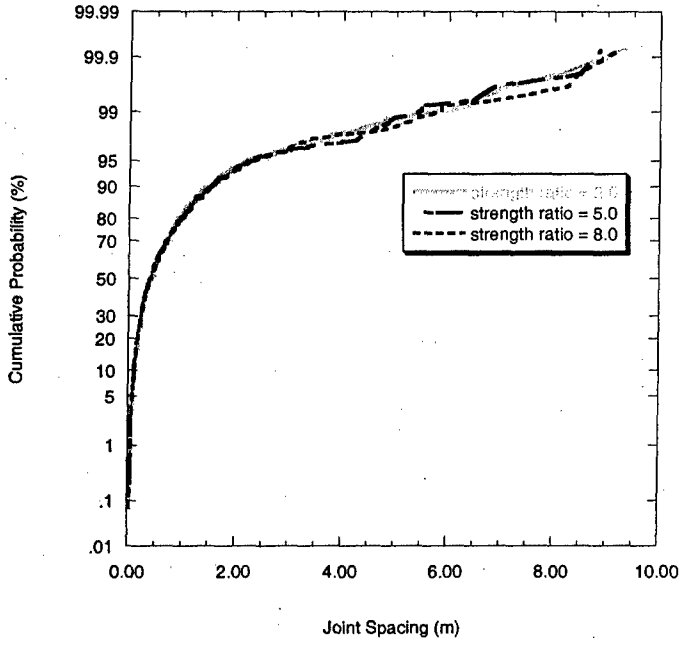


Figure 396 – Effect of the tensile strength ratio on the simulated joint spacing CDF.

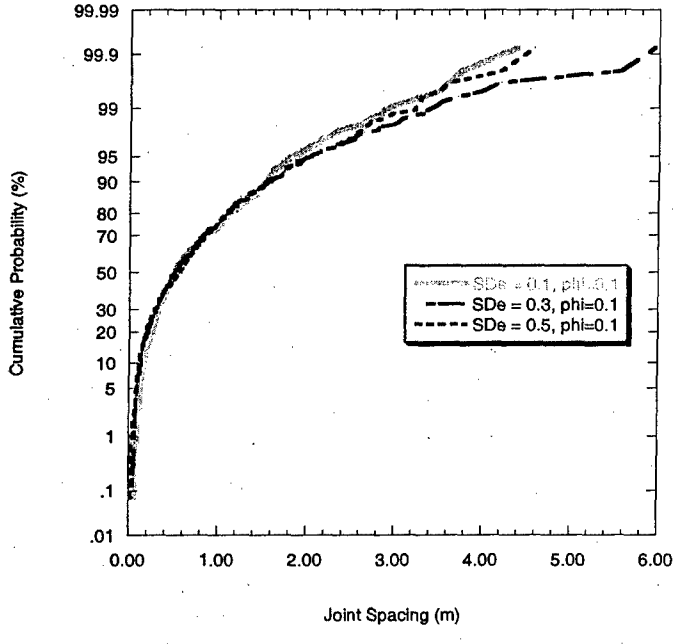


Figure 397 – Effect of σ_ε (SDe in figure) on the joint spacing CDF for $\phi = 0.1$.

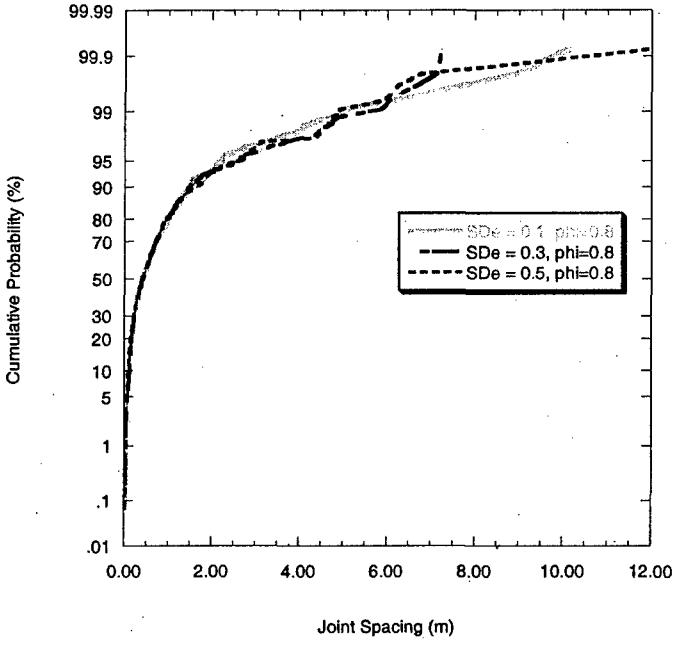


Figure 398 – Effect of σ_ε (SDe in figure) on the joint spacing CDF for $\phi = 0.8$.

Given the information about how certain parameters affect the resulting joint spacing distribution when using a correlated strength model, it was decided that the $\frac{E_f}{G_n}$ ratio, the bounding layer thickness (*d*), and the Poisson's ratios of the jointing and bounding layers remain fixed in the simulations. For each layer, two sets of simulations were generated. One set used a low value of σ_ε (= 0.1), and the other, a higher value (= 0.8) even though it was shown that σ_ε does not significantly affect the simulated joint spacing CDF. Within each set, the correlation factor (ϕ) is varied from 0.1 to 0.9.

Figure 399 and **Figure 400** show the comparisons between the actual and simulated joint spacing CDFs for layer 1. In **Figure 399**, $\sigma_\varepsilon = 0.1$ whereas in **Figure 400**, $\sigma_\varepsilon = 0.8$. There are slight differences between the CDFs curves for the two sets of simulations. However, there is no considerable difference in the shapes of the CDFs. Visually, it appears that the flaw model with correlated strength yields joint spacing CDFs that are similar to the actual CDFs. However, K-S testing rejects H_0 at the 0.05 level in all cases in **Figure 399** and **Figure 400** except for $\phi = 0.1$ in **Figure 399**. This results from the large difference between the actual and simulated CDFs at joint spacing values < 1.0 m.

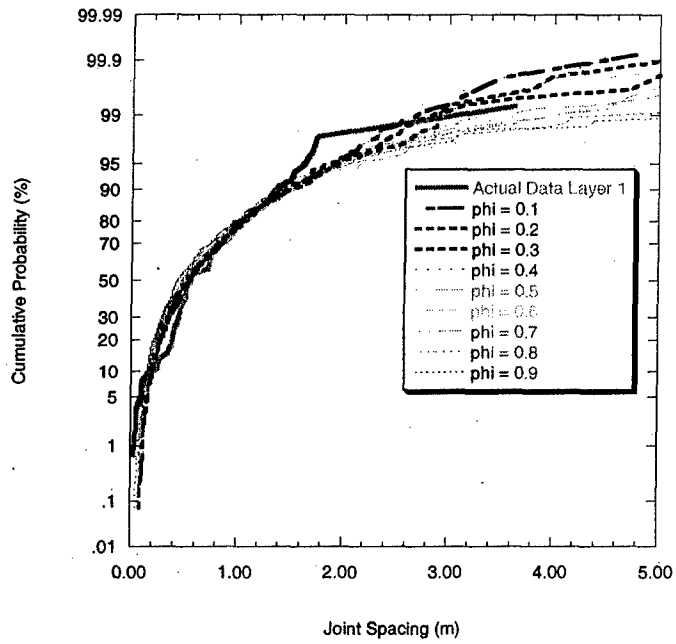


Figure 399 – Comparison between actual and simulated joint spacing CDFs for layer 1 using $\sigma_\varepsilon = 0.1$.

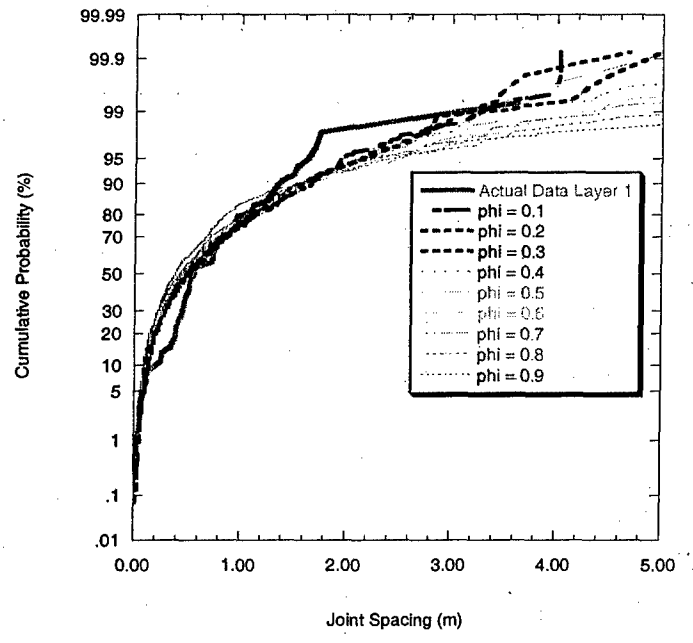


Figure 400 – Comparison between actual and simulated joint spacing CDFs for layer 1 using $\sigma_\varepsilon = 0.8$.

Figure 401 and **Figure 402** show the actual and simulated joint spacing CDFs for layer 2 using $\sigma_\varepsilon = 0.1$ and $\sigma_\varepsilon = 0.8$, respectively. The flaw model with a correlated strength model does not appear visually to yield joint spacing CDFs similar to the actual CDF for

layer 2. The simulations underestimate the frequency of the smaller spacings and overestimate that of the larger spacings. However, Kolmogorov-Smirnov testing accepts hypothesis H_0 in all cases in **Figure 401** and **Figure 402** except for $\phi = 0.1$ to 0.3 in **Figure 401**.

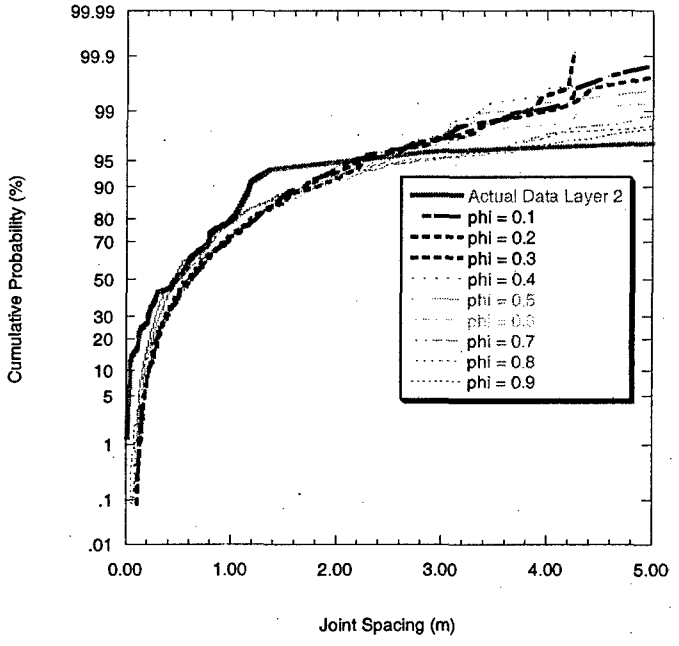


Figure 401 – Comparison between actual and simulated joint spacing CDFs for layer 2 using $\sigma_\varepsilon = 0.1$.

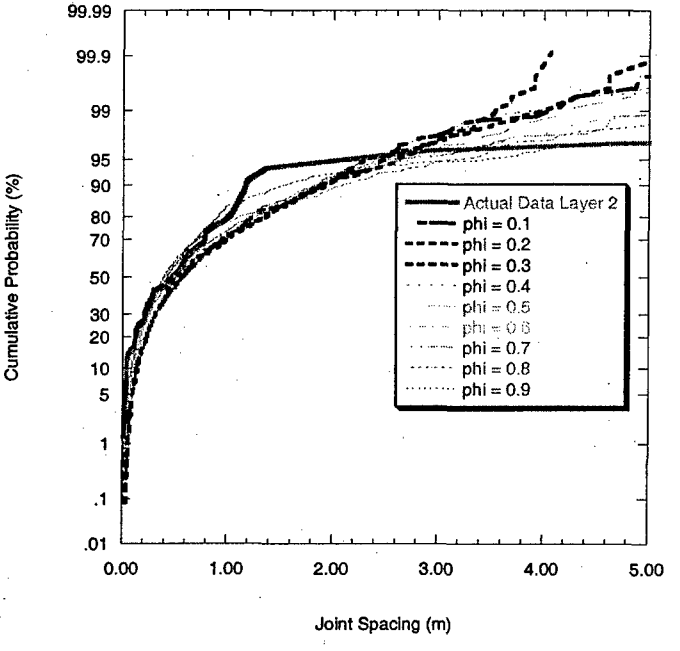


Figure 402 – Comparison between actual and simulated joint spacing CDFs for layer 2 using $\sigma_\varepsilon = 0.8$.

Figure 403 and **Figure 404** show the actual and simulated joint spacing CDFs for layer 3. The parameter σ_ε is equal to 0.1 in **Figure 403** and 0.8 in **Figure 404**. In both cases, the flaw model produces joint spacing CDFs similar to the actual CDF especially at low correlation factors. This observation is consistent with K-S testing where the hypothesis H_0 is accepted for all cases in **Figure 403** and **Figure 404** except for $\phi = 0.9$ in **Figure 403** and $\phi = 0.7$ to 0.9 in **Figure 404**.

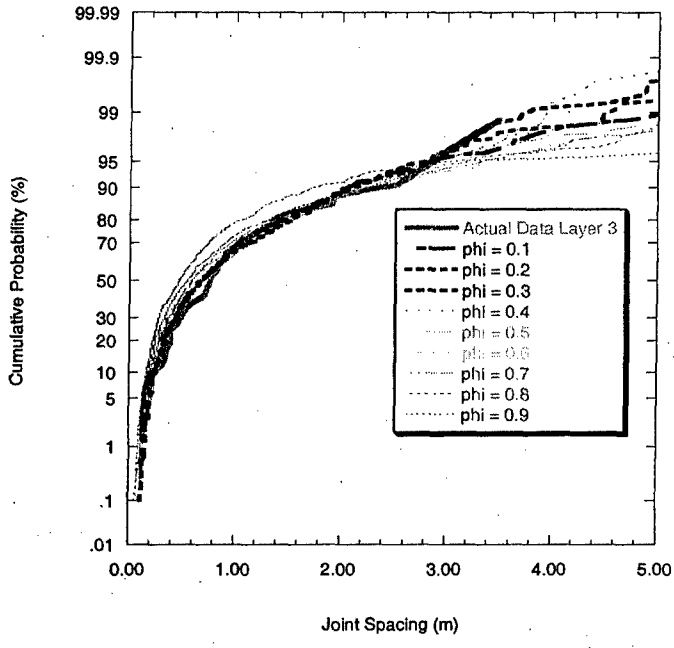


Figure 403 – Comparison between actual and simulated joint spacing CDFs for layer 3 using $\sigma_\varepsilon = 0.1$.

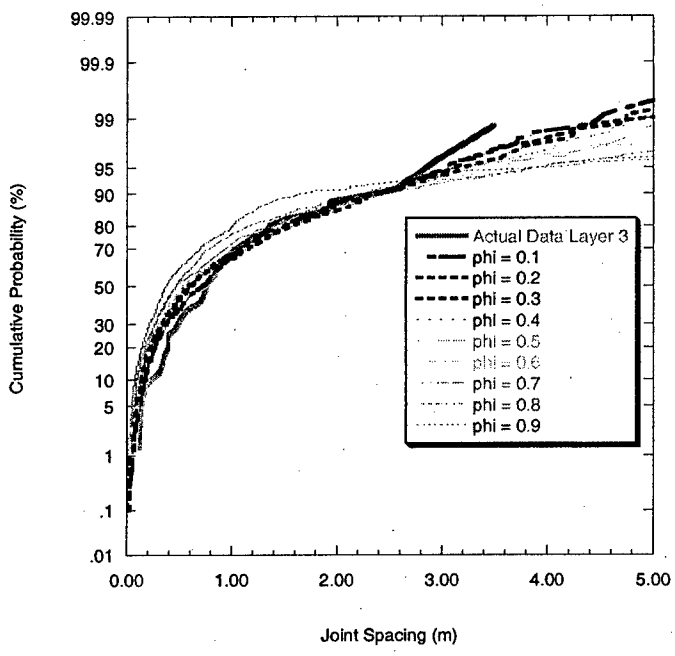


Figure 404 – Comparison between actual and simulated joint spacing CDFs for layer 3 using $\sigma_\varepsilon = 0.8$.

7.5.4.2 Rejection Procedure Results

Before proceeding with the simulations using the rejection procedure, a brief parametric study was performed to determine the effects of individual parameters on the resulting joint spacing CDFs. This was necessitated by the absence of material property data as well as the variation in bounding layer thickness along each individual scanline.

Figure 405 shows the effect of bounding layer thickness on the simulated joint spacing CDF for layer 1. It appears that varying the bounding layer thickness does not cause a large change in the resulting joint spacing CDF. **Figure 406** and **Figure 407** show the CDFs for the jointing layer and bounding layer Poisson's ratios, respectively. The deviations near the tails are magnified because of the vertical scale.

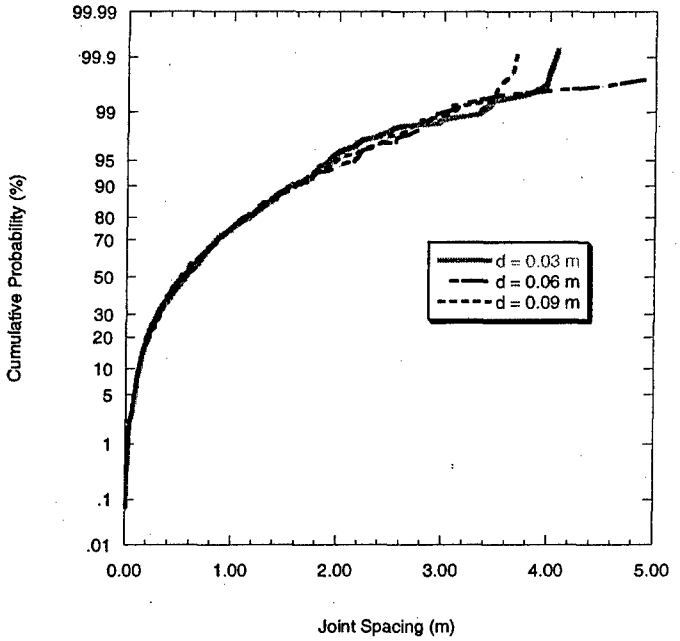


Figure 405 – Effect of the bounding layer thickness on the simulated joint spacing CDF for layer 1.

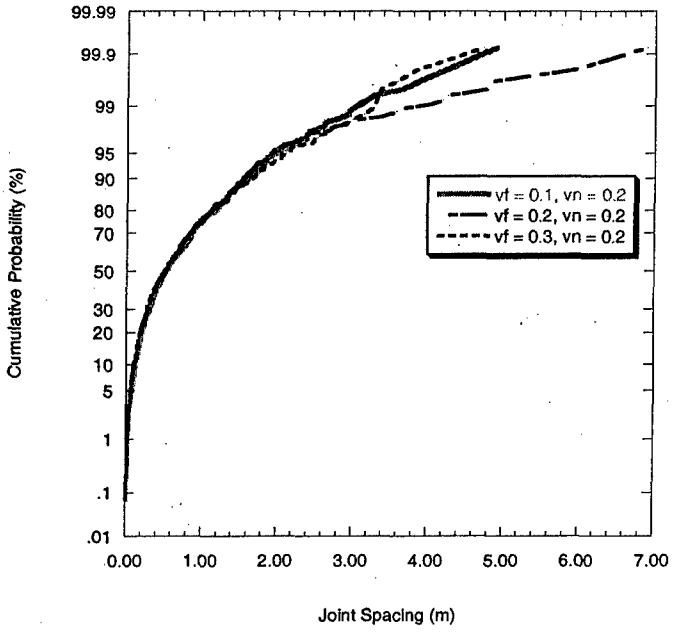


Figure 406 - Effect of the jointing layer Poisson's ratio on the simulated joint spacing CDF for layer 1.

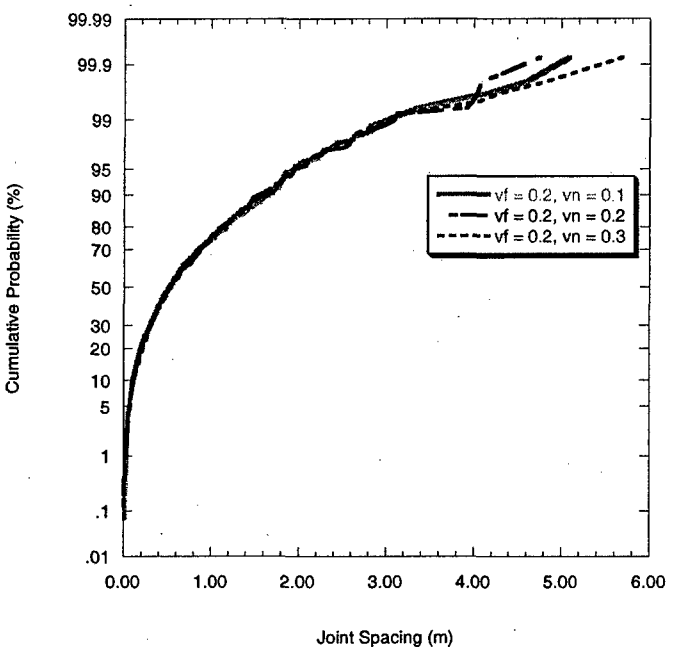


Figure 407 - Effect of the bounding layer Poisson's ratio on the simulated joint spacing CDF for layer 1.

Based on the results of this analysis, the number of parameters that need to be considered in the simulations can be reduced. Specifically, only the $\frac{E_f}{G_n}$ ratio is varied in the following simulations. So, only one set of simulations is needed for each layer.

Figure 408 shows the comparison between the actual and simulated joint spacing CDFs for layer 1. It appears that the rejection procedure produces joint spacing CDFs that are similar to the actual CDF for the range of $\frac{E_f}{G_n}$ values used. However, K-S testing indicates that the hypothesis (H_0) that the actual and simulated joint spacings come from the same probability distribution is rejected for all cases in **Figure 408**. Again, this is due to the large difference in the cumulative probability between the actual and simulated CDFs for spacing values < 1.0 m.

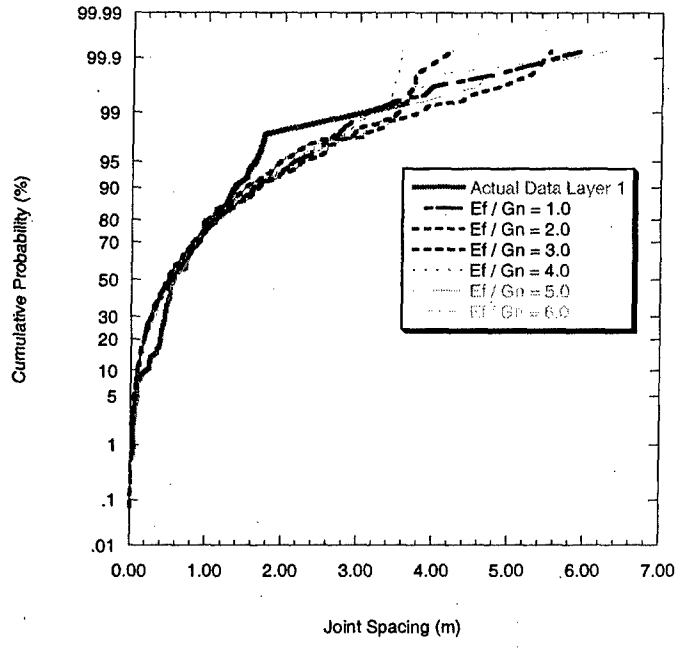


Figure 408 – Comparison between the actual and simulated joint spacing CDFs for layer 1 using the rejection procedure.

Figure 409 shows the actual and simulated joint spacing CDFs using the rejection procedure for layer 2. The simulated joint spacing CDFs in **Figure 409** do not appear to closely resemble the actual joint spacing CDF. However, K-S testing accepts H_0 for all cases in **Figure 409**.

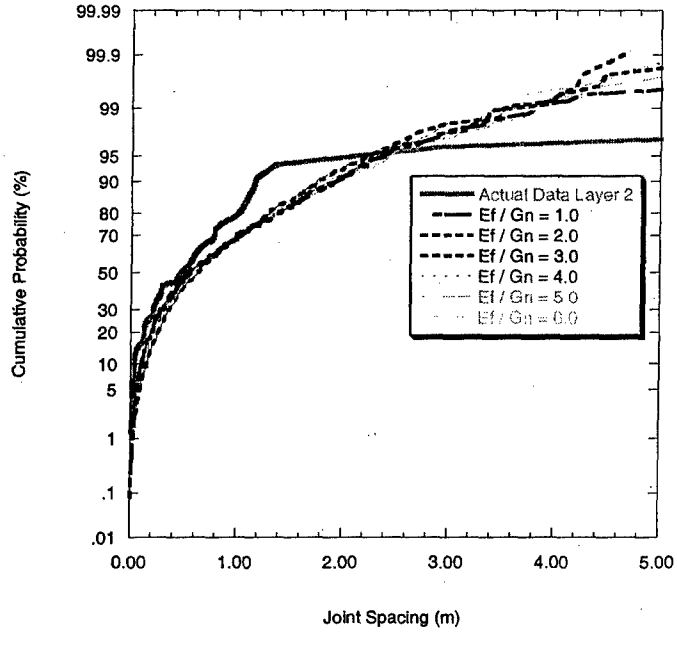


Figure 409 - Comparison between the actual and simulated joint spacing CDFs for layer 2 using the rejection procedure.

Figure 410 shows the simulated and actual joint spacing CDFs for layer 3. Visually, the simulated joint spacing CDFs appear to model the actual joint spacing well. In fact, K-S testing accepts H_0 for all cases in **Figure 410**.

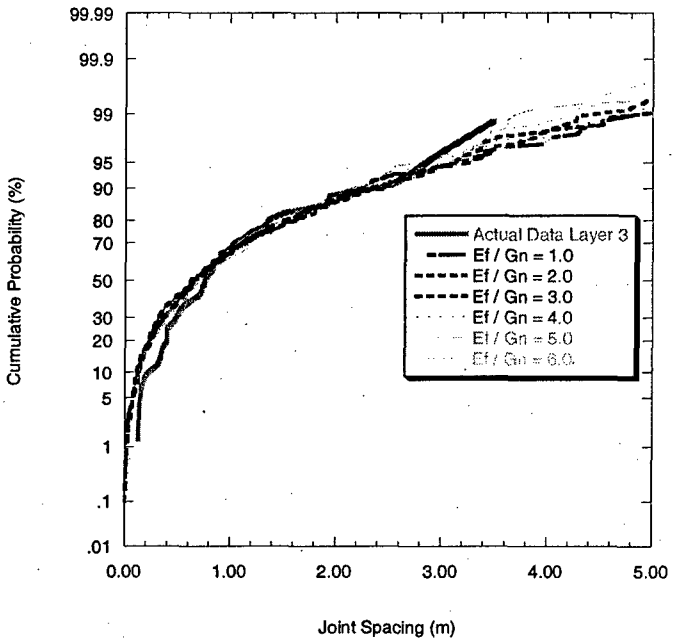


Figure 410 - Comparison between the actual and simulated joint spacing CDFs for layer 3 using the rejection procedure.

Based on a visual comparison, the rejection procedure models the joint spacing data from layer 1 and layer 3 better than it does for layer 2. However, statistical tests indicate that the rejection procedure simulates the joint spacing from layers 2 and 3 better than it does layer 1.

The results of the comparisons using the rejection procedure are consistent with those of the flaw model using either the uncorrelated or correlated strength model. In both flaw model variants, visual comparisons suggest that the joint spacing data from layers 1 and 3 are modeled better than those from layer 2. However, Kolmogorov-Smirnov testing shows that the flaw model (uncorrelated or correlated strength) actually performed better for layers 2 and 3 than for layer 1. In the case of layer 3, the Kolmogorov-Smirnov results and the visual comparison are consistent. However, for layers 1 and 2, it is somewhat difficult to accept the results of the Kolmogorov-Smirnov tests given the visual comparisons.

Table 24, **Table 25**, and **Table 26** show the visual comparison and Kolmogorov-Smirnov test results for each layer for the different models that were used. In the visual comparisons, the term "acceptable" is used if the simulated joint spacing probability distributions appear similar to the probability distribution of the actual joint spacing data. The tables show that for layer 1, visual comparison suggests that the flaw model and

rejection procedure provide acceptable results but the statistical comparison indicates otherwise. For layer 2, visual comparisons suggest that all models give unacceptable results whereas the statistical comparison indicates that the results are acceptable. For layer 3, both the visual and statistical comparisons indicate that the models yield joint spacing probability distributions similar to that of the data. Hence, based on the information presented in **Table 24**, **Table 25**, and **Table 26**, the visual and statistical comparisons often don't agree. Only in the case of layer 3 are the two methods of comparison consistent.

Table 24 – Results of visual and statistical comparisons for joint spacing data from the three layers using the flaw model with uncorrelated strength.

Flaw Model (Uncorrelated Strength)	Visual Comparison	Kolmogorov-Smirnov Tests (0.05 level)
Layer 1	acceptable	rejected in 10 out of 12 cases
Layer 2	not acceptable	accepted in 11 out of 12 cases
Layer 3	acceptable	accepted in 12 out of 12 cases

Table 25 – Results of visual and statistical comparisons for joint spacing data from the three layers using the flaw model with correlated strength.

Flaw Model (Correlated Strength)	Visual Comparison	Kolmogorov-Smirnov Tests (0.05 level)
Layer 1	acceptable	rejected in 17 out of 18 cases
Layer 2	not acceptable	accepted in 15 out of 18 cases
Layer 3	acceptable at low ϕ values	accepted in 14 out of 18 cases

Table 26 – Results of visual and statistical comparisons for joint spacing data from the three layers using the rejection procedure

Rejection Procedure	Visual Comparison	Kolmogorov-Smirnov Tests (0.05 level)
Layer 1	acceptable	rejected in 6 out of 6 cases
Layer 2	not acceptable	accepted in 6 out of 6 cases
Layer 3	acceptable	accepted in 6 out of 6 cases

The low joint intensities in the three layers allowed comparisons to be made despite limited information about the material properties of the sedimentary layers. Fortunately, parametric studies in this section (**7.5**) show that the joint spacing probability distribution is not strongly affected by material properties (e.g., the $\frac{E_f}{G_n}$ ratio) or bounding layer thickness at the relatively low joint intensities observed in this case. For both models,

this is an interesting yet expected result: in the flaw model, the $\frac{E_f}{G_n}$ ratio and the bounding layer thickness, d, both affect how quickly the tensile stress increases to the remote or far-field value with increasing distance from an existing joint. Similarly, $\frac{E_f}{G_n}$ and d also affect how quickly the probability density function increases with increasing distance from an existing joint in the rejection procedure. This rate of increase up to the maximum value of tensile stress or probability density controls how much of the segment is exposed to the maximum tensile stress or probability density (**Figure 411**). This in turn affects where new joints might form and consequently, the joint spacing probability distribution. This is critical at high joint intensities (i.e., short segments or narrow spacing) but not at low joint intensities (i.e., long segments or wide spacing) because if the spacings are particularly wide, much of the segment will be exposed to the maximum tensile stress or probability density regardless of $\frac{E_f}{G_n}$ and d. Thus, the effect of material properties and bounding layer thickness on the simulated joint spacing probability distribution is much less at low joint intensities than at high joint intensities.

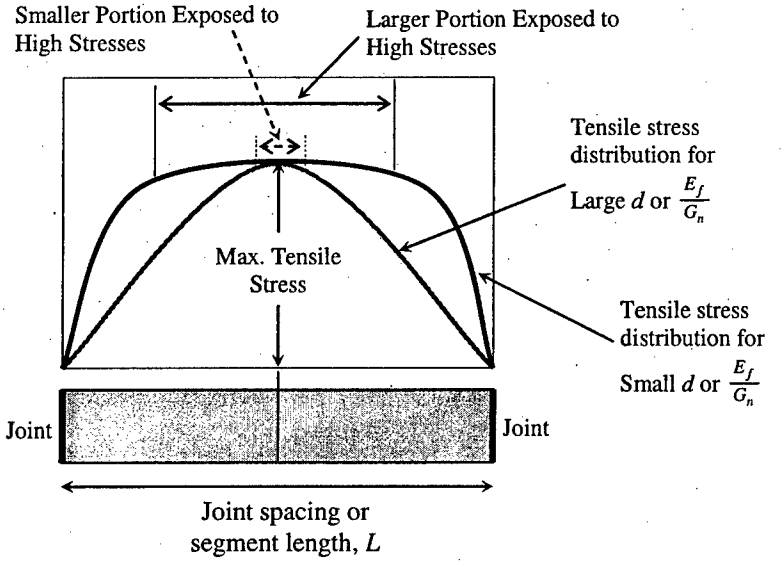


Figure 411 – Effect of $\frac{E_f}{G_n}$ ratio and bounding layer thickness, d, on the length of segment exposed to maximum tensile stress.

Overall, the flaw model and rejection procedure are inconsistent in modeling the joint spacing probability distribution in case 4. Even though joint intensities and lithologies in the three layers are similar, both models often give conflicting visual and statistical comparisons. This may be partly due to the differences in grain size among the different layers. Grain size, as noted earlier, can affect spacing. The subjective nature of the visual comparison and because the statistical comparisons are based on the maximum difference between the observed and simulated joint spacing CDFs (i.e., the Kolmogorov-

Smirnov statistic) also contribute to the discrepancy. There are a number of possible reasons for the inconsistencies that have to do with the assumptions that were made in **Table 23**:

1. The spacing of the set II joints may have been influenced by the existence of the set I joints. Even though set I joints are much more widely-spaced than the set II joints, they are often older than set II joints based on abutting relationships (Baudo, 2001). Also, set I and set II joints do not necessarily intersect at right angles (Engelder and Geiser, 1980; Baudo, 2001). Given the non-perpendicularity between set I and set II joints as well as their relative ages, it is highly likely that set I joints affected the stresses during the formation of set II joints (i.e., the presence of a set I joint may influence the spacing of set II joints that form near it). This most likely leads to an increase in the set II joint spacing near set I joints. The flaw model and rejection procedure cannot model the effect of the existing set I joints and thus may overestimate the frequency of the smaller spacings. This is probably what happened in the simulations for layers 1 and 3. However, it is unclear why the opposite is true for layer 2 where the simulations underestimate the frequency of smaller spacings.

2. The range in strike for set II joints is wide. In the simulations, the stresses in the jointing layer are calculated based on the assumption that existing joints are approximately parallel. Actual data indicate that this is not always the case. **Figure 412**, **Figure 413**, and **Figure 414** show histograms of strikes for set II joints in each layer. In layer 1, strikes range from about 020° to 070° but are mostly between 030° to 040° (**Figure 412**). In layer 2, the range of strikes is the same as in layer 1 but most of the joints strike 040° to 050° (**Figure 413**). In layer 3, strikes range from 030° to 080° with 070° the most common orientation (**Figure 414**). Baudo (2001) also noted that NNE-striking set II joints are generally older than ENE-striking set II joints. It is likely that the older NNE-striking set II joints had some effect on the spacing of the younger ENE-striking set II joints. During the formation of ENE-striking set II joints, the stress field near the NNE-striking joints would be different from those near the ENE-striking joints. This means that within joint set II, there may be spacing variations controlled by the orientation.

3. The joints mostly cut through multiple rock layers (Baudo, 2001). The assumption that all joints found in a specific layer initiated in that specific layer and later propagated into the bounding top and bottom layers may be inaccurate. If a joint were to propagate into a layer (say, into layer A) from another layer (layer B) where it initiated, the location of that joint should largely be controlled by the stresses in layer B rather than those in layer A. In the simulations that were run, it is essentially assumed that the locations of all the joints in a layer, say layer A, (including throughgoing joints) are controlled only by the stresses that were developed in that layer (A) during the jointing process. In reality, it is possible that a number of throughgoing joints observed in that layer (A) initiated in another layer (say B) and later propagated into layer A. The locations of those joints should have therefore been controlled by the stresses in layer B not by the stresses in layer A. Therefore,

the joint spacing probability distribution that is observed in layer A may be some combination of the joint patterns in layer A and B.

Given the results and the three items above, it appears that the conditions for using both the flaw model and rejection procedure were less than ideal in this case. This may explain the discrepancies between the actual and simulated joint spacing CDFs that were observed in the comparisons and also explain, to some extent, the inconsistencies between the visual and statistical comparisons.

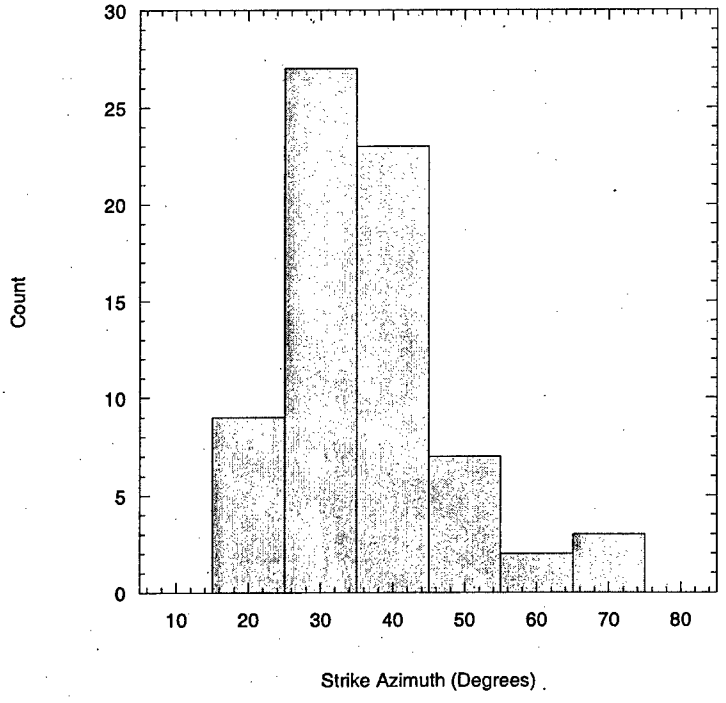


Figure 412 – Strike histogram for set II joints in layer 1.

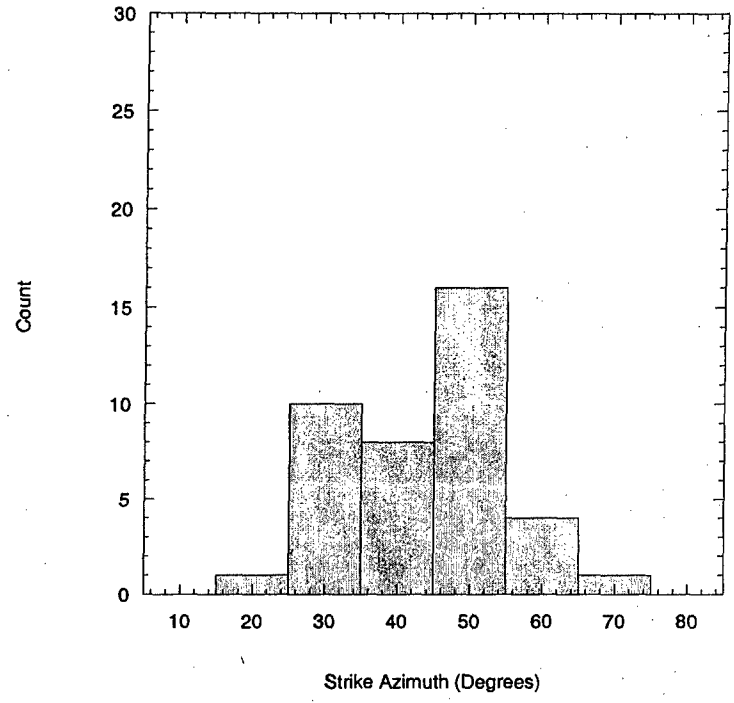


Figure 413 – Strike histogram for set II joints in layer 2.

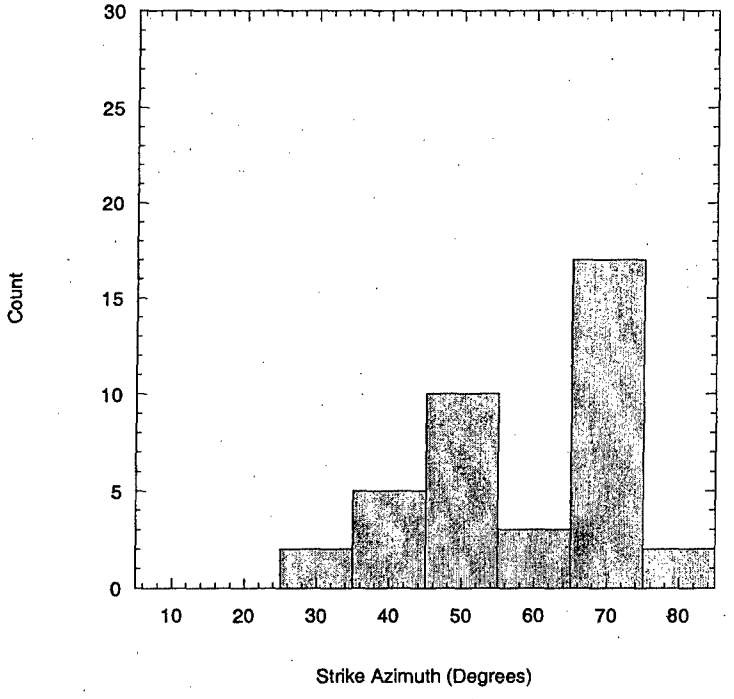


Figure 414 – Strike histogram for set II joints in layer 3.

8 Summary and Conclusions

Fracture characteristics (e.g., spacing, size, orientation) have often been observed to follow some form of probability distribution (e.g., Priest and Hudson, 1976; Huang and Angelier, 1989; Narr and Suppe, 1991; Rives et al., 1992). Ideally, one would like to model rock fracture patterns mechanically but this is a complex undertaking. As a consequence, geometric-probabilistic methods are usually employed to simulate the mechanics (e.g., Ivanova, 1998; Pascal et al., 1997; Josnin et al., 2002; Rabinovitch and Bahat, 1999; etc.). However, these probabilistic methods are based on observations on the actual fracture network geometry rather than the mechanisms behind its formation. Probabilistic fracture network models usually attempt to reflect the characteristics of a particular geologic setting by applying geometric modifications to an initial simulated fracture pattern (e.g., rotation and translation of fractures in Ivanova, 1998). As a result, the modeled fracture network characteristics resemble those of the actual fracture network but are not clearly linked to the mechanisms responsible for fracture formation. Therein lies the problem: probabilistic/geometric models use geologic settings mostly to define the target geometry rather than to describe the fracture formation mechanisms within the fracture model. In order to relate the modeled fracture network characteristics to a specific mechanism, it is therefore necessary that such mechanisms be incorporated in the model rather than simply provide a target geometry for the final result. Fracture models using a combination of mechanical and probabilistic concepts may be used to achieve this because full mechanical models may be impractical at this stage. This is so because there are various mechanisms that can cause fracturing in rocks and a single model that applies to all cases may therefore be impossible to formulate. As a consequence, a model must be built for each case in order to recognize the particular fracturing mechanism. Layer-perpendicular joints in sedimentary rock are considered here. This is done because sedimentary rock is most frequently found near the Earth's surface; also numerous studies and observations regarding fractures in sedimentary rock can be found in the literature.

Past Efforts - Field and Laboratory Observations, Analytical and Mechanical Models

The spacing of layer-perpendicular joints in sedimentary rock has been widely accepted to be linearly related to the layer thickness (e.g., Gross, 1993; Ruf et al., 1998; Narr and Lerche, 1984; Narr, 1991; etc.) although some researchers have also observed a non-linear relationship between spacing and layer thickness (e.g., Ladeira and Price, 1991; McQuillan, 1973). Joints in thicker layers tend to be more widely-spaced than those in thinner layers. Joint spacing has also often been observed to follow some probability distribution. Specifically, a log-normal joint spacing distribution has been widely observed (e.g., Becker and Gross, 1996; Narr and Suppe, 1991; Rives et al., 1992). Some have also used the Gamma distribution to describe field joint spacing (Huang and Angelier, 1989). Generally, field joint spacing distributions found in the literature are unimodal and skewed towards smaller spacings (i.e., positively skewed).

Laboratory experiments have also been performed to simulate the formation sequence of joints in layered sedimentary rock (e.g., Rives et al., 1992; Wu and Pollard, 1995). The

laboratory experiments described in the literature typically consisted of a brittle layer bonded onto a ductile layer and then subjected to extensional strain. Joints are formed on the brittle layer as the strain is increased. Rives et al. (1992) observed that the form of the joint spacing distribution changed as more joints are formed. At low strain or joint intensity, a shifted exponential probability distribution was observed. At intermediate strain or joint intensity, a log-normal probability distribution was observed while at high strain or joint intensity, a quasi-normal probability distribution of joint spacing was reached. Also, Rives et al. (1992) and Wu and Pollard (1995) observed that the joint density in the brittle layer ceased to change after some level of strain is reached. This phenomenon has often been called "joint saturation." Bai and Pollard (2000) used finite-element elastic analyses to define joint saturation in terms of a critical joint spacing-to-thickness ratio (or $\left(\frac{s}{t}\right)_{cr}$). According to Bai and Pollard (2000), below this critical ratio, no new joints can form between two existing joints because mostly compressive stresses rather than tensile stresses develop in the area between them. It must be noted, however, that the stresses at the interface remain tensile. Laboratory experiments by Bai and Pollard (2000) showed that only compressive stresses can be developed at the midpoint of the line connecting the midpoints of two joints when they are spaced closely enough.

Hobbs (1967) formulated a simplified model for the tensile stress distribution in the intact rock between two adjacent joints in a layer bounded by ductile un-jointed layers at the top and bottom all subjected to some far-field extensional strain. The basic principle for the calculation of tensile stress is that the forces in the intact rock between two adjacent joints balance the shear forces at the interface between the jointing and bounding layers. Hobbs' (1967) model has been used to explain the often observed linear relationship between joint spacing and layer thickness in sedimentary rock. Other researchers have used the same approach as Hobbs (1967) but also included the effect of the bounding layer thickness (e.g., Ji and Saruwatari, 1998). The effect of interface slippage on the tensile stress distribution has also been considered (Ji et al. (1998)). Finite-element methods (e.g., FRANC2D by Wawrzynek and Ingraffea, 1991; Bai and Pollard, 2000) have been used to calculate the stresses in the intact rock between joints since analytical solutions for this case do not yet exist.

Rives et al. (1992) attempted to numerically reproduce the joint spacing distribution forms that were observed in the laboratory experiments and in field data. Simple numerical processes were used to generate the locations of layer perpendicular joints. Examples of these numerical processes include midpoint bisection (i.e., placing new joints midway between the most widely-spaced pair of joints) and random placement (i.e., placing new joints in a randomly generated location along the layer). These have been found to be inadequate in modeling actual observed joint spacing distributions. Narr and Suppe (1991) used Hobbs' (1967) stress distribution model to produce joint spacing patterns in layered sedimentary rock. Their approach produced log-normal joint spacing probability distributions. Using their model, Narr and Suppe (1991) were also able to generate joint spacing probability distributions similar to what they had observed in the field. In a different approach, Rabinovitch and Bahat (1999) used a hazard function, $q(x)$, to determine the probability density function, $f(x)$, of the location of a new joint relative to a single existing joint.

New Models

Although Narr and Suppe's (1991) model was able to produce positively-skewed joint spacing distributions that resemble those observed in the field, it is still not entirely satisfactory. First, the use of Hobbs' (1967) model excludes the possible effect of the bounding layer thickness on the resulting joint spacing (e.g., Ladeira and Price, 1981). Second, they did not consider the possible effects of joint saturation mechanisms on the joint pattern (e.g., Ji et al., 1998; Bai and Pollard, 2000). Third, their comparisons were made only against a single set of data representing a single joint intensity. Joints in layered sedimentary rock can be found at various intensities (e.g., Becker and Gross, 1996; Saltzman, 2001; Baudo, 2001). Rabinovitch and Bahat's (1999) approach to deriving the probability density function of the new joint location relative to an existing one is an unusual application of a hazard function. Their approach is also not satisfactory. Hazard functions are typically used for uni-directional random variables such as time (e.g., in "time to failure" problems). As a consequence, the resulting probability density function, $f(x)$, is one-sided in that it only considers x - values in one direction from the existing joint. This problem can be solved when generating the location of the first new joint by assigning a 50-50 chance that the new joint forms to the left or right of the existing joint. Beyond the first new joint, this solution no longer applies because $f(x)$ is no longer valid (i.e., there is more than one existing joint). In other words, $f(x)$ should be updated to reflect the presence of the new joint and each one that is formed thereafter.

New Models - Flaw Model

Given the shortcomings of existing models, two new models are proposed. The first model (called the flaw model) utilizes a comparison between the tensile stress and the tensile strength along the sedimentary rock layer in order to determine new joint locations. It is similar to the model by Narr and Suppe (1991). A new joint is added at a location where the tensile stress exceeds the tensile strength. This model is composed of two parts: the tensile stress distribution submodel and the jointing layer strength submodel.

The tensile stress distribution in the jointing layer depends on the material properties of the layers (i.e., the jointing and bounding layers) as well as the locations of existing joints. The tensile stress distribution therefore changes with the addition of new joints. To include the effect of the bounding layer thickness, the tensile stress distribution submodel formulated by Ji et al. (1998) is used.

The strength submodel, on the other hand, is used to define the tensile strength along the jointing layer using some probability distribution. At random points along the layer, "flaws" are introduced. Each flaw is assigned a value of tensile strength according to some probability distribution. As a result of these flaws, the jointing layer has non-uniform tensile strength. The non-uniformity of the jointing layer tensile strength can be controlled by varying the number of flaws. The tensile strength submodel can either be uncorrelated or correlated. In an uncorrelated strength submodel, the tensile strength at one location is independent of the tensile strength at an adjacent location. In the correlated strength submodel, there is dependence between the tensile strength values at

adjacent locations. Each new joint is added at a location where the tensile stress exceeds the tensile strength.

In order to include the effects of joint saturation, the model checks individual spacing values against a critical spacing-to-thickness ratio (Bai and Pollard, 2000) before new joints are added. Interface slippage (Ji et al., 1998) is also considered as a saturation mechanism in this model. Interface slip occurs when the interface shear strength is reached. Since the tensile stress in the jointing layer is proportional to the interface shear stress in the tensile stress distribution submodel (i.e., Ji et al., 1998), limiting the interface shear stress imposes a limit to the tensile stresses that can be developed in the jointing layer. Limiting the tensile stresses in the layer stops the jointing process if they cannot exceed the tensile strength.

New Models – Rejection Procedure

This second new model determines the location (x) of each new joint in the jointing layer using its probability density function, $f(x)$. Intuitively, $f(x)$ should be a function of both the local tensile stress and tensile strength (i.e., $f(x) = g(\sigma_{local}, \sigma_t)$). The local tensile stress varies along the length of the jointing layer and also depends on the applied strain (ε) so that $\sigma_{local} = \sigma(x, \varepsilon)$. The function $\sigma(x, \varepsilon)$ also changes with the addition of new joints. The tensile strength can also be assumed to vary along the layer so that $\sigma_t = \sigma_t(x)$. The exact form of $f(x) = g(\sigma_{local}, \sigma_t)$ is difficult to obtain. As a simplification, it is assumed that $f(x) \propto \frac{\sigma_{local}}{\sigma_{farfield}}$. The expression for $\frac{\sigma_{local}}{\sigma_{farfield}}$ is given by a simplified tensile stress distribution model (e.g., Ji et al., 1998). Tensile stress distribution models indicate that higher stresses are developed in longer segments than in shorter ones. Therefore, $f(x) \propto \frac{\sigma_{local}}{\sigma_{farfield}}$ simply means that a new joint is more likely to form in a longer segment than in a shorter one. After the formation of each new joint, $\frac{\sigma_{local}}{\sigma_{farfield}}$ is updated to reflect changes in segment geometry. To generate random values of x from $f(x)$, a rejection procedure is employed. The rejection procedure is a simple way of generating random values from a probability density function. In the rejection procedure, a preliminary joint location is first generated assuming that one is equally likely to form at each point in the layer (i.e., using a uniform distribution). The ratio between $\frac{\sigma_{local}}{\sigma_{farfield}}$ at that location and $\left(\frac{\sigma_{local}}{\sigma_{farfield}}\right)_{\max}$ for the entire layer is calculated (the proportionality constant in $f(x) \propto \frac{\sigma_{local}}{\sigma_{farfield}}$ need not be calculated since it cancels out in this step). A random number between zero and 1.0 is generated using a uniform distribution. If the ratio exceeds this number, the preliminary location is accepted and a joint forms. The function $\frac{\sigma_{local}}{\sigma_{farfield}}$ is then updated. Otherwise, the preliminary location is rejected and the process is repeated. The compressive stress saturation mechanism is included by simply letting $f(x) = 0$ inside segments shorter than the critical joint spacing, $t \cdot \left(\frac{s}{t}\right)_{cr}$.

Parametric Studies

Parametric studies were conducted for the two proposed models. The effects on the mean joint spacing-layer thickness relationship and on the probability distribution of joint spacing were investigated. The mean joint spacing-layer thickness relationship is taken at saturation while the joint spacing distribution changes with joint intensity.

As a guide to understanding the effect of each parameter on the mean joint spacing-layer thickness relationship, one can look at how each parameter affects the tensile stresses and the overall tensile strength of the layer. The tensile stress is a link between the flaw model and rejection procedure. In the flaw model, certain model parameters may limit the tensile stresses or affect the shape of the tensile stress distribution. Other parameters control how the tensile strength varies in the layer and also describe the average tensile strength. In the rejection procedure the probability density of new joint locations, $f(x)$, is assumed to be directly proportional to tensile stress. Therefore, effects of the parameters that influence the tensile stress are the same in the flaw model and rejection procedure. For the mean joint spacing-layer thickness relationship at saturation, model parameters can be classified into these two groups:

1. Parameters that limit the tensile stress - If a parameter limits the tensile stress, the overall tensile strength may also affect the mean joint spacing-layer thickness relationship. For example, in the flaw model with interface slippage only, there is a limit to the tensile stress (triangular in **Figure 415**) that is controlled by the interface shear strength, τ_0. A joint can form if flaws sufficiently lower the tensile strength at some points (e.g., dashed curve in **Figure 415**). If there are no flaws, the limiting tensile stress distribution may not be high enough to form a new joint (e.g., **Figure 415**). In the flaw model with compressive stress mechanism only, it does not matter whether or not flaws exist because there is no limit to the tensile stress as long as the spacing is above critical (**Figure 416**). In **Figure 416**, a new joint can form with both tensile strength profiles (i.e., with or without flaws) but at different locations. When the spacing becomes below critical, compressive stresses develop inside the segment that may preclude further jointing. In the rejection procedure with compressive stress mechanism, the probability density of joint location, $f(x)$, is assumed to be directly proportional to the tensile stress so a similar behavior can be expected even though the tensile strength is not required. Interface slip is not considered in the rejection procedure. **Table 27** summarizes the effects of parameters that influence the maximum tensile stress and the overall tensile strength of the layer on the mean joint spacing-layer thickness relationship.

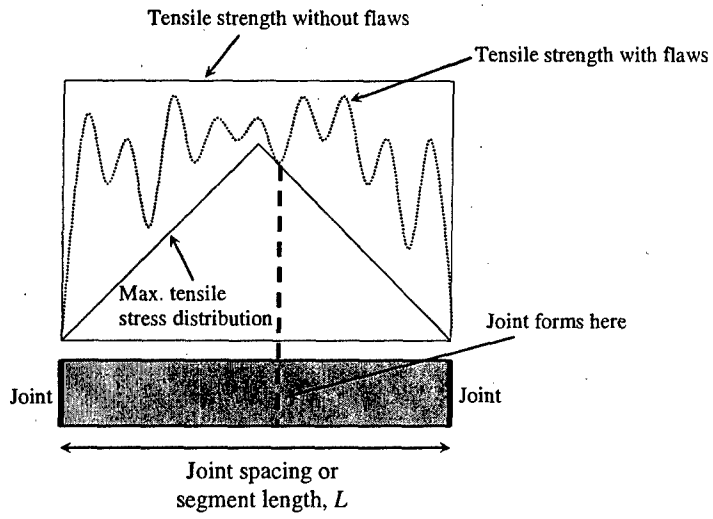


Figure 415 – Tensile stress vs. tensile strength for the interface slippage saturation mechanism for the case with and without flaws. New joint formation is only possible with the existence of flaws because there is a limit to the tensile stress that can be achieved.

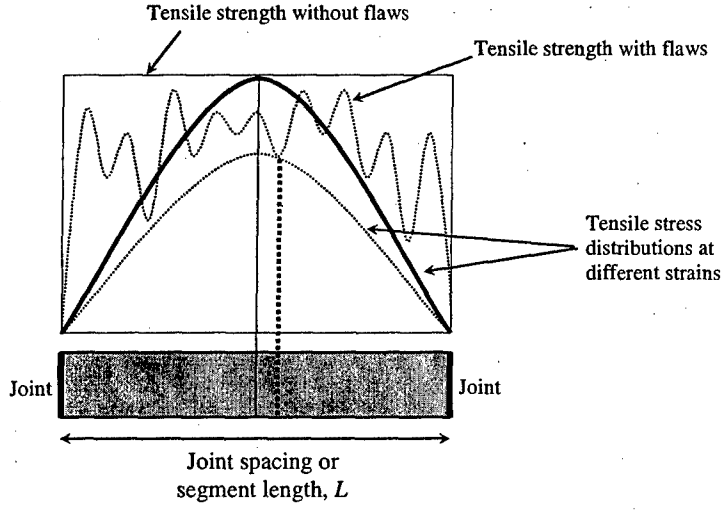


Figure 416 – Tensile stress vs. tensile strength for the compressive stress saturation mechanism for the case with and without flaws. The existing joints are spaced above the critical spacing. A new joint can form with or without the flaws (the two dropdown lines) because there is no limit to the tensile stress as long as the spacing is above critical.

Table 27 – Effects of parameters that limit tensile stress on the mean joint spacing-layer thickness relationship.

	Interface Slippage Mechanism	Compressive Stress Mechanism
Parameter that limits or affects the stress in the jointing layer	***Flaw Model***: τ_0 limits interface shear stress, in turn, limiting tensile stress in jointing layer. ***Rejection Procedure***: Interface slippage not considered.	***Flaw Model***: For segments where $\left(\frac{s}{t}\right) > \left(\frac{s}{t}\right)_{cr}$, tensile stress not limited. For segments where $\left(\frac{s}{t}\right) \leq \left(\frac{s}{t}\right)_{cr}$, stress is compressive (i.e., limited to negative values). ***Rejection Procedure***: For segments where $\left(\frac{s}{t}\right) > \left(\frac{s}{t}\right)_{cr}$, $f(x)$ is non-zero. For segments where $\left(\frac{s}{t}\right) \leq \left(\frac{s}{t}\right)_{cr}$, $f(x)$ is zero.
Is the overall tensile strength of the jointing layer a factor?	***Flaw Model***: Yes, if the overall tensile strength is low enough to be reached by the limited tensile stress, jointing will occur. If overall tensile strength high enough such that the limited tensile stress cannot reach it, jointing cannot occur. ***Rejection Procedure***: Interface slippage not considered. Tensile strength not specified.	***Flaw Model***: Not a factor for $\left(\frac{s}{t}\right) > \left(\frac{s}{t}\right)_{cr}$ because there is no limit to tensile stress so tensile strength can always be reached. Also not a factor for $\left(\frac{s}{t}\right) \leq \left(\frac{s}{t}\right)_{cr}$ because stresses are compressive. It does not matter what the tensile strength is since the stress is compressive so jointing will not occur. ***Rejection Procedure***: Tensile strength not specified. $f(x)$ relies on tensile stress alone.
Conclusion	***Flaw Model***: Two parameters strongly affect the mean joint spacing-layer thickness relationship: τ_0 and flaw density. Flaw density affects the overall tensile strength of the jointing layer. More flaws means that the layer has lower overall tensile strength. ***Rejection Procedure***: Interface slippage not considered.	***Flaw Model***: Although the tensile stress that can be developed is unlimited for segments with $\left(\frac{s}{t}\right) > \left(\frac{s}{t}\right)_{cr}$, the stress is limited to compressive values for $\left(\frac{s}{t}\right) \leq \left(\frac{s}{t}\right)_{cr}$. Therefore, $\left(\frac{s}{t}\right)_{cr}$ itself affects the mean joint spacing-layer thickness relationship because it dictates the smallest spacing where jointing can still occur. ***Rejection Procedure***: $\left(\frac{s}{t}\right)_{cr}$ affects the mean joint spacing-layer thickness relationship because it dictates the smallest spacing for which $f(x)$ is non-zero (i.e., jointing still possible).
Effect on mean joint spacing for a given jointing layer thickness	***Flaw Model***: Mean joint spacing increases with decreasing τ_0. Mean joint spacing increases with decreasing flaw density (i.e., increasing overall tensile strength). ***Rejection Procedure***: Interface slippage not considered.	***Flaw Model***: Mean joint spacing increases as $\left(\frac{s}{t}\right)_{cr}$ increases. ***Rejection Procedure***: Mean joint spacing increases as $\left(\frac{s}{t}\right)_{cr}$ increases. Note that $\left(\frac{s}{t}\right)_{cr}$ depends on material properties and overburden (see Bai and Pollard, 2000).

2. Parameters that affect the rate at which the tensile stress reaches its maximum value with distance from a joint (i.e., "stress recovery") – This effect is more important for the compressive stress saturation mechanism than for the interface slippage mechanism where the interface shear strength (τ_0) is the major factor especially in the latter part of the jointing process when slip starts to occur. In the flaw model with compressive stress mechanism, the shape of the tensile stress distribution is influenced mostly by the $\frac{E_f}{G_n}$ ratio and the non-jointing layer thickness, d (e.g., **Figure 417**). In **Figure 417**, a large or small portion of the segment may be exposed to the highest tensile stresses depending on $\frac{E_f}{G_n}$ and d. This affects the lengths of the smaller segments into which it is divided and, consequently, how many more divisions beyond that are possible. For example, a segment whose length is twice that of the critical spacing (i.e., $2 \cdot t \cdot \left(\frac{s}{t}\right)_{cr}$) will likely be divided into two segments that have approximately critical lengths (i.e., $t \cdot \left(\frac{s}{t}\right)_{cr}$) if the maximum tensile stress is reached only at the midpoint and further jointing cannot occur. However, if the maximum tensile stress were present over some length in the segment, the segment may be divided into one that is below critical (say, $0.5 \cdot t \cdot \left(\frac{s}{t}\right)_{cr}$) and another that is above critical ($1.5 \cdot t \cdot \left(\frac{s}{t}\right)_{cr}$). In this case, jointing continues until the above-critical segment ($1.5 \cdot t \cdot \left(\frac{s}{t}\right)_{cr}$) is divided into smaller below-critical segments. As a result, the final mean joint spacing is smaller because more joints are formed. In the rejection procedure with compressive stress mechanism, the same behavior can be expected because the probability density $f(x)$ is directly proportional to the tensile stress. **Table 28** summarizes the effects of these parameters on the final mean joint spacing for both the flaw model and rejection procedure.

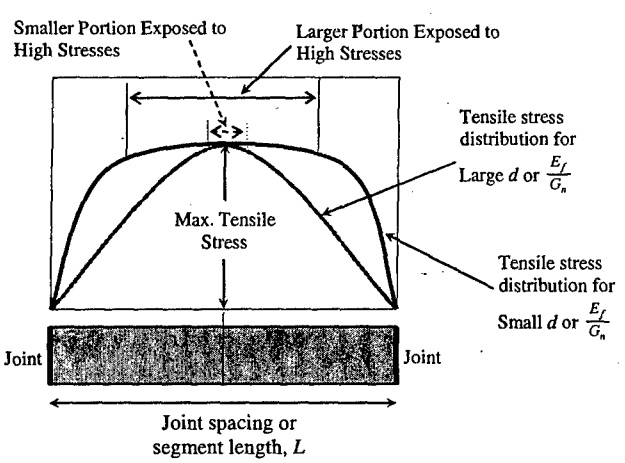


Figure 417 – Shape of the tensile stress distribution for different values of $\frac{E_f}{G_n}$ or d values.

Table 28 – Effect of $\frac{E_f}{G_n}$ and d on the mean joint spacing when using the compressive stress saturation mechanism in both the flaw model and rejection procedure. f – flaw model. r – rejection procedure.

Value of $\frac{E_f}{G_n}$ or non-jointing layer thickness d	Stress Recovery with Distance from Joints Forming the Segment	Portion of Segment Exposed to Highest Tensile Stresses (f) or Probability Density (r)	Possible Locations of New Joints	Rate at which critical spacing is reached and final mean spacing for a given jointing layer thickness
Small	Fast	Long	Many	Slow rate, small final mean spacing
Large	Slow	Short	Few	Fast rate, large final mean spacing

Similar to what was done for the mean joint spacing-layer thickness relationship, a guide is also outlined for understanding the effect of each parameter on the joint spacing distribution regardless of whether or not saturation mechanisms are implemented. In this case, the parameter effects can be classified into two groups based on how they affect the shape of the tensile stress distribution or the tensile strength profile:

1. Parameters that affect the rate at which the tensile stress reaches its maximum value with distance from a joint (i.e., "stress recovery") – The shape of the tensile stress distribution not only affects the number of possible divisions before reaching the critical spacing, it also affects the joint spacing distribution. If a larger portion of a segment is exposed to the highest stresses, there are more possible locations for a new joint than when a smaller portion of a segment is exposed to the highest stresses (see **Figure 417**). As a result, the variance of spacing would be larger in the former than in the latter. Two parameters affect the shape of the tensile stress distribution: the $\frac{E_f}{G_n}$ ratio and the non-jointing layer thickness d. **Table 29** provides a summary of the effects of these two parameters on the joint spacing distribution, specifically on the joint spacing variance.

Table 29 – Effect of $\frac{E_f}{G_n}$ and d on joint spacing distribution in the flaw model and rejection procedure. f – flaw model. r – rejection procedure.

Value of $\frac{E_f}{G_n}$ or non-jointing layer thickness d	Stress Recovery with Distance from Joints Forming the Segment	Portion of Segment Exposed to Highest Tensile Stresses (f) or Probability Density (r)	Possible Locations of New Joints	Effect on Joint Spacing Distribution
Small	Fast	Long	Many	High Spacing Variance
Large	Slow	Short	Few	Low Spacing Variance

2. Parameters that affect the variation of tensile strength along the layer – This applies only to the flaw model because the rejection procedure does not use tensile strength to generate joint locations. Along with the tensile stress distribution, the tensile strength variation determines where new joints form. The tensile strength variation depends on whether uncorrelated strength or correlated strength is used. The use of correlated strength leads to a tensile strength profile with clear sections of strength and weakness compared to when uncorrelated strength is used. If there are clear sections of weakness, it is likely that new joints will form inside these sections leaving stronger sections largely un-jointed. This leads to a larger variance in spacing. For the correlated strength submodel, three parameters affect the tensile strength variation: the correlation factor (ϕ), the mean tensile strength (μ_{σ_i}), and the variance of the random variable ε_i (σ_ε). In an uncorrelated strength submodel, the strength at a point is independent of the strength at adjacent points and there are no clear sections of strength and weakness. In this case, it is found that the ratio between maximum and minimum tensile strength affects the joint spacing distribution. If the tensile strength ratio is small, the layer will be close to having uniform tensile strength and new joints are likely to form near the midpoints of segments. This leads to a smaller spacing variance than when the tensile strength ratio is large and new joints are also likely to form away from a segment midpoint. **Table 30** and **Table 31** show summaries of parameter effects for the uncorrelated and correlated strength submodels on the joint spacing distribution, respectively.

Table 30 – Effect of ratio of maximum to minimum tensile strength on joint spacing distribution in the flaw model with uncorrelated strength.

Value of max/min tensile strength ratio	Range of Tensile Strength	Uniformity of Tensile Strength	Possible Locations of New Joints	Effect on Joint Spacing Distribution
Small	Narrow	Close to uniform	Likely Near Segment Midpoint	Lower Spacing Variance
Large	Wide	Non-uniform	More Scattered within Segment	Higher Spacing Variance

Table 31 – Effects of correlated strength parameters* on joint spacing distribution in the flaw model. * - varying one, keeping others constant.

Value* of ϕ, μ_{σ_i} or σ_ε	Sections of Strength and Weakness	Range of Tensile Strength	Possible Locations of New Joints	Effect on Joint Spacing Distribution
Small	Not Well-Defined	Narrow	Less Concentrated in Particular Sections	Lower Spacing Variance
Large	Well-Defined	Wide	Concentrated in Sections of Weakness	Higher Spacing Variance

Comparisons with Actual Field Data

In addition to the parametric studies, the two proposed models were used to simulate joint spacing patterns that were compared to actual joint spacing data. Four different cases with varying joint intensities were considered. Comparisons between the actual and simulated joint spacing distributions were made using Kolmogorov-Smirnov statistical tests and visual assessments of the joint spacing cumulative probability curves.

Case 1: Becker and Gross, 1996

Becker and Gross (1996) gathered joint spacing data from a single flat-lying limestone/dolostone layer in the Gerofit Formation in Israel. The limestone/dolostone jointing layer is approximately of uniform thickness (18 ± 1.2 cm) and bounded by marlstone layers (Becker and Gross, 1996) approximately 5 cm thick. Measurements were made along a scanline approximately 190 m long. The vertical joint set strikes ~293° and is parallel to the maximum compressive stress direction associated with the Syrian Arc Stress field (SAS) (Eyal et al. (2001)). Eyal et al. (2001) also found that the ~293°-striking joint set is the first formed joint set in the layer considered by Becker and Gross (1996). No material properties were measured by Becker and Gross (1996) for both the jointing and non-jointing layers but Saltzman (2001) measured Young's moduli and tensile strength in limestone/dolostone layers in the same formation but in a different area. Along the scanline, Becker and Gross (1996) noted the existence of four fault zones and four joint zones that extend beyond the thickness of the limestone/dolostone layer. The joints in most of these zones could not be measured properly by the authors because of intense weathering. However, they were able to measure the joint spacing near one of the fault zones. A moving average plot by Becker and Gross (1996) revealed that mean joint spacing is lower in the middle section of the scanline than in the ends. Based on this plot, Becker and Gross (1996) divided the scanline into four sections: I, II III, and IV. The joint zones and fault zones are located inside sections II and III. **Table 32** shows the statistics of the spacing in each section. Chi-squared tests indicate that only the joint spacing data from sections I and IV may be described by log-normal probability distributions.

Table 32 – Summary of joint spacing statistics from data by Becker and Gross (1996)

	Section I	Section II	Section III	Section IV
Number of Spacing Data	110	237	271	94
Mean Spacing (cm)	23.66	13.82	14.40	20.67
Standard Deviation (cm)	14.96	7.76	9.31	12.85
Mean Spacing / Layer Thickness	1.31	0.77	0.80	1.15

The Young's modulus ranges from about 30 GPa to 80 GPa (Saltzman, 2001) with most of the test samples having Young's moduli that are around 50 GPa. This value is used in the model simulations. As for the $\frac{E_f}{G_n}$ ratio, the material properties of the marlstone are needed. Available data from the literature indicate that marlstone can have a Young's modulus typically between about 21.0 and 25.0 GPa. For Poisson's ratios between about 0.15 and 0.25, this leads to shear modulus values between 8.0 and 11.0 GPa. Given that the Young's modulus of the limstone/dolostone layer is assumed to be 50 GPa, this leads to $\frac{E_f}{G_n}$ values that range from about 4.5 to about 6.25. In the simulations, it is assumed that $\frac{E_f}{G_n}$ ranges from about 3.0 to 6.0. Saltzman (2001) also performed tensile strength tests on the limestone/dolostone samples from the four layers. The tensile strength values of intact samples range from about 4.0 MPa to 10.0 MPa (Saltzman, 2001) and appear to follow an approximately uniform probability distribution. **Table 33** and **Table 34** show the values of simulation parameters. The parameter combinations represent the different cases that are simulated.

Table 33 – Parameter values for uncorrelated strength submodel in flaw model. The same values are used in the rejection procedure except for the tensile strength ranges.

Parameter	Simulation Values
Jointing Layer Thickness (t)	0.18 m
Non-Jointing Layer Thickness (d)	0.05 m
$\frac{E_f}{G_n}$ ratio	3.0 to 6.0
E_f	50 GPa
Tensile Strength Ranges	4.0-10.0 MPa, 2.0-12.0 MPa, very wide

Table 34 – Parameter values for correlated strength submodel.

Parameter	Simulation Values
Jointing Layer Thickness (t)	0.18 m
Non-Jointing Layer Thickness (d)	0.05 m
$\frac{E_f}{G_n}$ ratio	3.0
E_f	50 GPa
Correlation Factor, ϕ	0.70-0.95
Mean Tensile Strength, μ_{σ_t}	7.0 MPa
σ_ε	0.2, 0.5

Table 35 below shows the comparison results for the two proposed models. The flaw model results are separated into the uncorrelated and correlated strength submodels.

Table 35 – Summary of results for the case of Becker and Gross, 1996.

	Flaw Model Uncorrelated Strength		Flaw Model Correlated Strength		Rejection Procedure	
Section	**K-S at 0.05 level**	**Visual**	**K-S at 0.05 level**	**Visual**	**K-S at 0.05 level**	**Visual**
I	Accepted in most cases. Rejected when narrowest tensile strength range used (i.e., 4-10 MPa).	Fit is good for different tensile strength ranges used.	Rejected in most cases.	Fit does not appear to be good. Simulated CDF differs much in curvature to the actual.	Accepted in all cases.	Fit is good.
II	Rejected in most cases.	Fit is not good.	Rejected in all cases	Fit is not good.	Accepted in all cases.	Fit is good.
III	Rejected in all cases.	Fit is not good.	Rejected in all cases.	Fit is not good.	Accepted in all cases.	Fit is good.
IV	Accepted for wider tensile strength range (e.g., 2-12 MPa and wider). Rejected for narrowest tensile strength range (i.e., 4-10 MPa).	Good fit for wider tensile strength range (e.g., 2-12 MPa and wider). Fit is not good for narrowest tensile strength range (i.e., 4-10 MPa).	Rejected in most cases.	Fit does not appear to be good. Simulated CDF differs much in curvature to the actual.	Accepted in all cases.	Fit is good.

Overall, the flaw model with uncorrelated strength is able to simulate the joint spacing CDF for sections I and IV more effectively than in sections II and III. Sections II and III are more densely jointed than sections I and IV. In fact, the mean spacing values for sections II and III (~0.14 m and ~0.144, respectively) lie inside the calculated saturation mean spacing range of 0.094 m to 0.151 m for this case. This indicates the possibility that sections II and III may be jointed beyond saturation. Additional jointing may have occurred beyond saturation and such a process is beyond the scope of the flaw model.

The flaw model with correlated strength does not appear to model the joint spacing in any of the sections well. In sections I and IV, the shape of the simulated joint spacing cumulative distribution curves are much different from the actual. As for sections II and III, it was hoped that the correlated strength model would help produce the smaller spacing values that could not be produced with the uncorrelated strength model. However, the use of a correlated strength model could not eliminate this discrepancy.

Although the rejection procedure appears to work better than the flaw model in terms of the joint spacing CDF for all four sections, one must be cautious because the rejection procedure is not a mechanical model. In fact, one characteristic of the rejection procedure is that it assigns a non-zero probability that a joint occurs very near an existing joint. In the flaw model, it is virtually impossible for a new joint very near an existing one. As a result, the rejection procedure allows very closely-spaced joints which are almost impossible in the flaw model. The rejection procedure performs better in sections II and III than the flaw model. It also performs very well in sections I and IV. Based on the results for this case, it seems that the rejection procedure is reliable in the same joint intensity range as the flaw model and it is apparently able to reproduce the joint spacing CDFs at higher joint intensity (sections II and III).

Case 2: Saltzman, 2001

Saltzman (2001) investigated layer-confined vertical joints in limestone/dolostone layers bounded by marlstone layers in the Gerofit formation at Nahal Nekarot in southern Israel. In Saltzman's (2001) study, joint spacing measurements were taken from a single joint set striking ~165° or ~345° found in four limestone/dolostone layers with thickness ranging from 12.0 cm (0.12 m) to 52.0 cm (0.52 m). Note that Becker and Gross (1996) measured the ~293° joint set in a different layer nearby. The ~165° striking joint set is the primary or first-formed joint set in these four layers (Saltzman, 2001). Eyal et al. (2001) found that the ~165° or ~345° joint set was formed under the Dead Sea Transform stress field (DSS). Saltzman (2001) observed much higher joint intensities in this set compared to those observed by Becker and Gross (1996) in the ~293° set. Chi-Squared goodness-of-fit tests indicate that the four joint spacing datasets in Saltzman (2001) may be described by log-normal probability distributions. Also, despite the very high joint intensities observed here, none of the joint spacing data exhibit a quasi-normal distribution as Rives et al. (1992) observed in their laboratory experiments at high joint intensities.

Table 36 – Summary of spacing statistics from data by Saltzman (2001)

	Layer 1 (GN1)	Layer 2 (GN2)	Layer 3 (GN3)	Layer 4 (GN4)
Number of Spacing Data	30	59	49	62
Mean Spacing (cm)	13.96	10.38	8.64	5.91
Standard Deviation (cm)	6.67	4.48	3.44	2.91
Layer Thickness (cm)	52	12	37	30
Mean Spacing / Layer Thickness	0.27	0.87	0.23	0.20

Saltzman (2001) studied essentially the same type of rocks as Becker and Gross (1996): jointed limestone/dolostone bounded by un-jointed marlstone layers. Some of the material property values used in the case study for Becker and Gross' (1996) data come from laboratory tests by Saltzman (2001). Important information used in the simulations is shown in **Table 37** and **Table 38**.

Table 37 - Parameter values for uncorrelated strength submodel in flaw model. The same values are used in the rejection procedure except for the tensile strength ranges.

Parameter	Simulation Values
Jointing Layer Thickness (t)	0.52 m (layer 1), 0.12 m (layer 2), 0.37 m (layer 3), 0.30 m (layer 4)
Non-Jointing Layer Thickness (d)	0.05 m
$\frac{E_f}{G_n}$ ratio	3.0 to 6.0
E_f	50 GPa
Tensile Strength Ranges	4.0-10.0 MPa, 2.0-12.0 MPa, very wide

Table 38 - Parameter values for correlated strength submodel.

Parameter	Simulation Values
Jointing Layer Thickness (t)	0.52 m (layer 1), 0.12 m (layer 2), 0.37 m (layer 3), 0.30 m (layer 4)
Non-Jointing Layer Thickness (d)	0.05 m
$\frac{E_f}{G_n}$ ratio	3.0
E_f	50 GPa
Correlation Factor, ϕ	0.10-0.90
Mean Tensile Strength, μ_{σ_t}	7.0 MPa
σ_ε	0.2

Preliminary simulations show that the compressive stress saturation mechanism prevents the flaw model and rejection procedure from reaching the joint intensities observed in layer 1, 3, and 4. For this reason, simulations were performed without the saturation mechanism for these layers. For layer 2, no such problem was encountered. For the joint intensity observed in layer 2, there is not much difference between the joint spacing distributions if the saturation mechanism is used and those when it is not. **Table 39** shows the results of the comparisons when no saturation is used in layers 1, 3, and 4.

Table 39 – Summary of comparison results for the joint spacing data in Saltzman (2001). ♠ - without saturation mechanism. * - with saturation mechanism.

	Flaw Model Uncorrelated Strength		Flaw Model Correlated Strength		Rejection Procedure	
Layer	**K-S at 0.05 level**	**Visual**	**K-S at 0.05 level**	**Visual**	**K-S at 0.05 level**	**Visual**
1 (GN1) ♠	Accepted in all cases.	Fit is better for wider tensile strength range. Frequencies of smaller spacings underestimated.	Accepted in all cases.	Fit is not good. Frequencies of smaller spacings are always underestimated.	Accepted in all cases.	Fit is good but frequencies of smaller spacings are overestimated.
2 (GN2) *	Accepted in all cases.	Fit is good in all cases.	Accepted in all cases.	Fit is good in most cases.	Accepted in all cases.	Fit is good but frequencies of smaller spacings are overestimated.
3 (GN3) ♠	Accepted in all cases.	Fit is good in all cases but slight overestimation of frequencies of larger spacing when widest tensile strength range is used.	Accepted in all cases.	Fit is not that good. Frequencies of smaller spacings underestimated.	Accepted in all cases except $\frac{E_f}{G_n}$=6.0.	Fit is not good.
4 (GN4) ♠	Accepted in all but one case.	Fit is good for most cases but improvement is apparent as tensile strength range is increased.	Rejected in all cases.	Fit is not good. Frequencies of smaller spacings grossly underestimated	Accepted in all cases except $\frac{E_f}{G_n}$=6.0.	Fit is good.

The flaw model with saturation was found incapable of simulating the joint spacing CDF for the very high joint intensities observed in the data by Saltzman (2001). For the only case where the joint intensity was not too high (i.e., layer 2, GN2), it provided a good agreement between the actual and simulated joint spacing CDFs. In the other cases where the joint intensities are very high, the flaw model without saturation mechanisms is able to produce joint spacing CDFs that resemble the actual joint spacing CDFs. This means that the saturation mechanism proposed by Bai and Pollard (2000) may not always be applicable.

For the flaw model with correlated strength, a good fit both visually and by hypothesis testing is achieved only for layer 2 where the joint intensity is lowest. For layers 1 and 3, the visual and hypothesis testing results do not agree. For layer 4, the visual and

statistical assessments agree that the model does not work well. Overall, the flaw model with correlated strength performs poorly at very high joint intensity.

Overall, the rejection procedure is able to produce joint spacing CDFs that agree with the actual data based on hypothesis testing (i.e., K-S statistic) although in some cases, visual comparisons do not support K-S hypothesis testing results. Also, the saturation mechanism prevents the rejection procedure from attaining the actual joint intensity in all cases except layer 2 (GN2) where the joint intensity is lowest. In the layers with higher joint intensity (layers 1, 3, and 4), the saturation mechanism was not used so that the target joint intensity could be attained.

Case 3: Gross et al., 1997

Gross et al. (1997) studied joints in six chalk layers (17 cm to 63 cm thick) interbedded with chert (about 7 cm thick in the area, Bahat, 1988) located near Beer Sheva, Israel. The layers belong to the lower Eocene Mor Formation and have been exposed by a road cut (Gross et al., 1997). The layers have been slightly folded but are still essentially flat-lying (Bahat, 1988). Two sets of vertically-dipping joints are observed in the area: cross-fold joints (326°) and strike joints (055°). Cross-fold joints generally strike the perpendicular to the fold axis in the area while strike joints are oriented parallel to the fold axis. Gross et al. (1997) measured spacings between the 055° joints. A normal fault zone older than the 055° set that strikes 292° and dips 45°N is also observed on the exposure. Gross et al. (1997) noted that the fault does not appear to affect the orientations of the 055° joint set, even those that are near the fault. Interestingly, Gross et al. (1997) noted that the joint intensity in one of the layers (specifically, layer 4) changes drastically from one side of the fault to the other. This coincides with their observation that the measured slip across the fault zone is lower in the vicinity of that layer. **Table 40** shows the spacing statistics from each of the six chalk layers. Note the change in joint intensity across the fault in layer 4. The joint intensity north of the fault is higher than that south of the fault. **Table 40** also indicates the larger dataset to which each smaller dataset is assigned based on the normalized mean spacing.

Table 40 – Summary of spacing statistics for the data by Gross et al. (1997).

Layer (combined dataset) (thickness, cm)	Number of spacing data	Normalized mean spacing (mean spacing/layer thickness)	Normalized median spacing (median spacing/layer thickness)
1 (A)(26,29)	27	1.11	1.10
2 (B)(43,46)	47	0.76	0.76
3 (A)(22,17)	43	1.17	1.18
4 North of Fault (none)(62.5)	33	0.45	0.45
4 South of Fault (B)(62.5)	23	0.70	0.67
4 Combined (Neither A nor B)(62.5,62.5)	56	0.56	0.52
5 (A)(19.5,17.4)	68	1.13	1.06
7* (B)(60,60)	71	0.75	0.75

Due to the small number of spacing data in each layer, data from different layers were combined to form two larger datasets (A and B) according to the normalized mean spacing values (i.e., mean spacing divided by layer thickness) of each layer. **Table 41** shows the statistics of datasets A and B.

Table 41 – Summary of spacing statistics for datasets A and B.

Combined dataset	Number of spacing data	Normalized mean spacing	Normalized median Spacing	Skewness of normalized data	Standard deviation of normalized data
A	138	1.12	1.09	2.27	0.51
B	141	0.74	0.74	0.84	0.29

Chi-square goodness-of-fit tests indicate that dataset A can be described by a log-normal probability distribution. Chi-square goodness-of-fit tests reject the hypotheses that dataset B can be described by either a log-normal or a normal probability distribution.

No material properties were measured in this case but typical values of chert shear modulus found in literature range from 31.0 to 33.0 GPa (e.g., Gross et al., 1995). The Young's modulus of chalk reported in the literature ranges from about 2.0 GPa to 20.0 GPa. This translates to $\frac{E_f}{G_n}$ ratios from 0.06 to 0.65; a range of values that is not surprising because intact chert is generally much stiffer than chalk. In the simulations, $\frac{E_f}{G_n}$ ratios from 0.05 to 1.05 are used for the assumption that the chert layers are intact.

For the case where the chert layers are brecciated (i.e., heavily fractured) the $\frac{E_f}{G_n}$ is allowed to vary from 2.0 to 10.0. Available tensile strength data on Lower Eocene Mor chalks in the area (Palchik and Hatzor, 2004) indicate a range between about 3.0 MPa to 9.0 MPa.

In the simulations involving intact chert (i.e., $\frac{E_f}{G_n}$ ratios from 0.05 to 1.05), the joint spacing distributions do not resemble the actual joint spacing distributions unless large values of non-jointing layer thickness are used (i.e., > 0.2 m). Such non-jointing layer thickness values are unrealistic. Simulations with brecciated chert (i.e., $\frac{E_f}{G_n}$ ratios greater than unity) were also performed. **Table 42** and **Table 43** show the corresponding simulation parameter values for both the flaw model and rejection procedure. **Table 44** shows a summary of comparison results.

Table 42 - Parameter values for uncorrelated strength submodel in flaw model. The same values are used in the rejection procedure except for the tensile strength range. Note that $\frac{E_f}{G_n}$ >1.0 (i.e., chert is brecciated).

Parameter	Simulation Values
Jointing Layer Thickness (t)	1.0 for both A and B (due to normalization)
Non-Jointing Layer Thickness (d)	0.05 and 0.10 m
$\frac{E_f}{G_n}$ ratio	2.0 to 10.0
E_f	15 GPa
Tensile Strength Ranges	3.0-9.0 MPa

Table 43 - Parameter values for correlated strength submodel.

Parameter	Simulation Values
Jointing Layer Thickness (t)	1.0 for both A and B (due to normalization)
Non-Jointing Layer Thickness (d)	0.10 m
$\frac{E_f}{G_n}$ ratio	2.0, 6.0, 10.0
E_f	15 GPa
Correlation Factor, ϕ	0.2-0.9
Mean Tensile Strength, μ_{σ_t}	6.0 MPa
σ_ε	0.37

Table 44 - Summary of comparison results for the data by Gross et al. (1997).

	Flaw Model Uncorrelated Strength		Flaw Model Correlated Strength		Rejection Procedure	
Dataset	**K-S at 0.05 level**	**Visual**	**K-S at 0.05 level**	**Visual**	**K-S at 0.05 level**	**Visual**
A (chert fractured)	Accepted in cases where $\frac{E_f}{G_n}$>4.0.	Frequencies of smaller spacings often overestimated.	Rejected in cases where $\frac{E_f}{G_n}$=2.0 and for larger ϕ values for $\frac{E_f}{G_n}$=6.0 and 10.0	Fit not good. Frequencies of smaller spacings overestimated.	Rejected in all cases.	Fit not good. Frequencies of smaller spacings grossly overestimated.
B (chert fractured)	Accepted in all cases.	Frequencies of smaller spacings often overestimated.	Accepted in cases where $\frac{E_f}{G_n}$=6.0 and 10.0. Accepted in most cases for $\frac{E_f}{G_n}$=2.0.	Fit is better when $\frac{E_f}{G_n}$=6.0 and 10.0. For $\frac{E_f}{G_n}$=2.0, frequencies of smaller spacings overestimated.	Rejected in most cases.	Fit not good. Frequencies of smaller spacings grossly overestimated.

The flaw model with uncorrelated strength simulates the actual joint spacing CDFs at different levels of success depending on whether or not the bounding chert layers are intact. If the bounding chert layers are assumed to be intact, the $\frac{E_f}{G_n}$ ratios should be less than 1.0 because chert is generally stiffer than the chalk layer. If the bounding chert layers are considered brecciated (as was observed by Gross et al., 1997), their overall stiffness would decrease and $\frac{E_f}{G_n}$ ratios greater than 1.0 may be possible. If the bounding chert layers are considered intact (i.e., $\frac{E_f}{G_n}$<1.0), the flaw model with uncorrelated strength does not perform well. On the other hand, when the chert bounding layers are considered fractured (i.e., $\frac{E_f}{G_n}$>1.0), the flaw model with uncorrelated strength yields joint spacing CDFs that are close to the actual joint spacing CDFs. When correlated strength is used in the flaw model, a good fit between the simulated and actual joint spacing CDFs is achieved when the chert bounding layers are considered fractured.

The rejection procedure does not appear to be effective in producing joint spacing CDFs that are similar to those of the actual joint spacing data. Statistical tests confirm this observation and the hypothesis that the actual and simulated joint spacing data come from

the same probability distribution is rejected in most cases. Visual comparisons are consistent with the statistical test results.

Case 4: Baudo, 2001

Baudo (2001) gathered joint spacing data from the sandstones and shales of the Catskill Delta Complex in Southwestern New York State. Joint spacing measurements were made along numerous scanlines (totaling a length of 4 km) that trace the path of the Cattaraugus Creek. While the sandstone beds can be massive (~2 m thick), most of the individual layers are less than 0.5 m thick (Engelder and Geiser, 1980). Although the study area is located within the Appalachian Plateau, folds with limbs dipping less than 2° can be found (Baudo, 2001).

Major joint sets in the Appalachian Plateau have been classified roughly into two groups (e.g., Engelder and Geiser, 1980) depending on their orientation with respect to the general trend of the folds in the area: cross-fold joints (set I) and strike joints (set II). Set I joints generally strike NW while the set II joints are generally oriented NE and both sets dip approximately vertically (Baudo, 2001). Set I joints are generally spaced more widely than set II joints. A third joint set (set III) that is geometrically unrelated to the fold orientations in the area is also present (Engelder and Geiser, 1980; Engelder, 1985). In the southwestern region of the Appalachian Plateau in New York State, set III joints cannot be clearly distinguished from set II joints (Engelder and Geiser, 1980).

Because not all scanline segments contain abundant spacing data, only three scanline segments where set II joints are abundant were considered. Set I joints also intersect these three scanlines but are much too widely spaced to comprise data sets that have a significant number of joints. Since the three scanline segments intersect three different jointing layers, the datasets are referred to as layer 1, layer 2 and layer 3 datasets.

Table 45 shows the different lithologies intersected by the three scanline segments. A single scanline segment often intersects more than one layer. However, along each scanline segment, there is one layer that is intersected more often than the other layers. For example, scanline 1 intersects mostly a sandstone and a siltstone layer (Baudo, 2001 combined this into a single "sandstone + siltsone" layer). Scanline 2 intersects mostly a fine sandstone layer as does scanline 3. As a result, layer 1 is considered to be a sandstone/siltstone layer that is 0.09 m thick. Layers 2 and 3 are considered as fine sandstone layers that are 0.10 m thick.

Table 45 – Summary of layer lithologies and thicknesses for the data by Baudo (2001).

Scanline (orientation)	Jointing Layer Lithologies	Jointing Layer Thickness	Top Bounding Layer	Top Bounding Layer Thickness	Bottom Bounding Layer	Bottom Bounding Layer Thickness
Scanline 1 (277°)	sandstone, siltstone, shaly siltstone, interbedded siltstone and shale, interbedded sandstone and siltstone	sandstone and siltstone have a combined thickness of 0.09 m, thickness for other lithologies not indicated	sandstone, shale, shaly siltstone, silty shale	sandstone layer is from 0.03 to 0.10 m thick, others are between 0.01 and 0.05 m thick	sandstone, shale, interbedded siltstone and shale, shaly siltstone, siltstone	sandstone layer is from 0.03 to 0.10 m thick, others are between 0.02 and 0.06 m thick
Scanline 2 (290°)	fine sandstone, silty shale, shaly siltstone, siltstone	fine sandstone is 0.10 m thick, silty shale is < 0.01 m thick, thickness for others not indicated	fine sandstone, silty shale	fine sandstone layer is from 0.03 to 0.10 m thick, silty shale is 0.005 m thick at some point	fine sandstone, silty shale	fine sandstone layer is 0.03 m thick, thickness for others not indicated
Scanline 3 (111°)	silty shale, fine sandstone, siltstone, interbedded siltstone and shale, interbedded sandstone and siltstone	fine sandstone is 0.10 m thick, others are between 0.01 to 0.05 m thick	silty shale, siltstone, fine sandstone	fine sandstone is 0.03 m, thickness for others not indicated	fine sandstone	fine sandstone layer is 0.05 m in some parts

The top and bottom bounding layers noted by Baudo (2001) also change along each scanline. However, a "representative" top and bottom bounding layer can be chosen based on what layers persist most along the length of the jointing layer. For example, for scanline 1, sandstone layers bound the jointing layer for most of its length. For scanlines 2 and 3, the representative top and bottom bounding layers are found to be fine sandstone.

Using the scanline orientation, the scanline spacing data are corrected to obtain the perpendicular spacing between joints of the same set. From here on, the term "spacing data" refers to the corrected spacing data. The spacing data come from relatively thin layers. Layer 1 is roughly 0.09 m (9 cm) thick while layers 2 and 3 are about 0.10 m (10 cm) thick. Meanwhile, joint spacings are large compared to the layer thicknesses. For

example, set II joints in layer 1 have a mean spacing of 0.72 m. This results in a mean spacing-to-thickness ratio of 8.0. Similarly, layers 2 and 3 have mean spacing-to-thickness ratios of 8.3 and 9.9, respectively. These ratios are much larger than those considered in the three previous cases. Given such large ratios, it should be safe to say that the layers being considered here are below joint saturation.

Table 46 shows some important assumptions that were made in the simulations. These assumptions were necessary because the joints in Baudo (2001) are not the first-formed joints and normally cut across multiple layers.

Table 46 – Important field observations and corresponding assumptions for the case of Baudo (2001).

Field Observations	Model Implications
Joints are typically not confined to a single layer (i.e., joint height is greater than the jointing layer thickness).	This violates the assumption that the joints are layer-confined in the derivation of the stress distribution within the jointing layer. However, it is assumed that the joints are initially layer-confined when they are formed. As the strain increased, it is accommodated by propagation into the adjacent layers rather than the addition of new joints.
Cross-fold joints (set I) and strike joints (set II) are both found in the area. Observations indicate that set I joints are older than set II joints (Engelder, 1985; Baudo, 2001). Set I joints are much more widely-spaced than set II joints. Data used in comparisons are from set II.	Set II joints are not first-formed joints and may be influenced by existing set I joints. Set I and set II joints are not necessarily perpendicular in the study area (Engelder and Geiser, 1980; Baudo, 2001). However, set I joints are so widely spaced that many set II joints could be found in the area between two adjacent set I joints. It is assumed that in that area, the set II joints are only influenced by the existence of other set II joints (i.e., set I joints are essentially remote).

A Chi-square goodness-of-fit test accepts the hypothesis that joint spacing from layer 1 can be described by a log-normal probability distribution at the 0.05 level. Chi-squared goodness-of-fit tests reject the hypotheses that an exponential or a log-normal probability distribution can be used to describe the joint spacing data for layer 2. A Chi-squared goodness-of-fit test accepts the hypothesis that a log-normal distribution can be used to describe the joint spacing data from layer 3 at the 0.05 level.

Unlike the previous cases (i.e., Becker and Gross, 1996; Saltzman, 2001; Gross et al., 1997), no material properties have been measured for the layers studied by Baudo (2001). However, because of the relatively low joint intensities, it is found from additional parametric studies that the effects of certain parameters on the joint spacing CDF are not significant in the flaw model and rejection procedure. For the flaw model, it is found that changes in the ratio between the maximum and minimum tensile strength and the bounding layer thickness do not have a significant effect on the joint spacing CDF (**Figure 418**). If a correlated strength model is used in the flaw model, it is found that the

effect of changes in tensile strength ratio on joint spacing CDF is not significant. Also, changes in the parameters μ_{σ_t} and σ_ε which determine the mean tensile strength and control the variance of tensile strength in the correlated strength model, respectively, do not appear to have a significant effect on the joint spacing CDF at low joint intensity. For the rejection procedure, it is also found that changes in the bounding layer thickness do not have a significant effect on the joint spacing CDF. Also, the saturation mechanism does not significantly affect the resulting joint spacing CDF for both approaches at these low joint intensities. These observations mean that the exact values of model parameters need not be known to make a comparison. Also, the number of simulations that are needed to consider the uncertainty in the model parameters is greatly reduced. **Table 47** and **Table 48** show summaries of input parameter values for both the flaw model and rejection procedure. **Table 49** presents the comparison results.

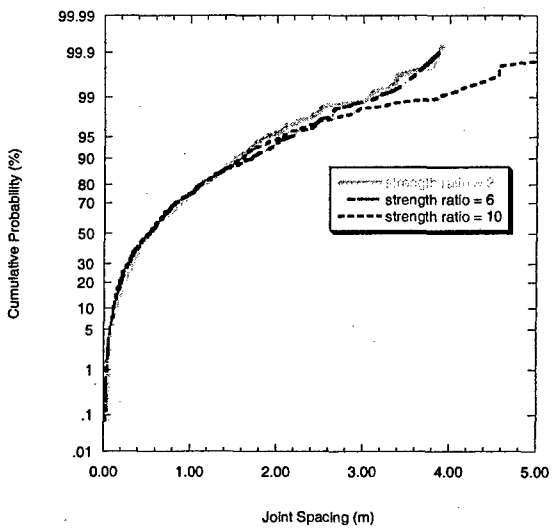


Figure 418 – Illustration of the (insignificant) effect of the tensile strength ratio in the flaw model with uncorrelated strength on the joint spacing CDF. Tensile strength ratio is the maximum tensile strength divided by the minimum tensile strength.

Table 47 - Parameter values for uncorrelated strength submodel in flaw model. The same values are used in the rejection procedure.

Parameter	Simulation Values
Jointing Layer Thickness (t)	0.09 m (layer 1), 0.10 m (layer 2 and 3)
Non-Jointing Layer Thickness (d)	0.03 and 0.10 m
$\frac{E_f}{G_n}$ ratio	1.0 to 6.0

Table 48 - Parameter values for correlated strength submodel.

Parameter	Simulation Values
Jointing Layer Thickness (t)	0.09 m (layer 1), 0.10 m (layer 2 and 3)
Non-Jointing Layer Thickness (d)	0.03 m and 0.10 m
$\frac{E_f}{G_n}$ ratio	4.0
Correlation Factor, ϕ	0.10-0.90
σ_ε	0.10 and 0.80

Table 49 – Summary of comparison results for the data by Baudo (2001).

	Flaw Model Uncorrelated Strength		Flaw Model Correlated Strength		Rejection Procedure	
Layer	**K-S at 0.05 level**	**Visual**	**K-S at 0.05 level**	**Visual**	**K-S at 0.05 level**	**Visual**
1	Rejected in most cases.	Fit is not good. Large discrepancies in frequencies for spacings <1.0 m.	Rejected in all but one case.	Fit appears good but large discrepancy in frequencies for spacings <1.0 m.	Rejected in all cases.	Fit appears good but large discrepancy in frequencies for spacings <1.0 m.
2	Accepted in all but one case.	Fit is not good. Frequencies of spacing smaller than 2.5 m underestimated.	Accepted in all but three cases.	Fit is not good. Frequencies of spacings <2.5 m are mostly underestimated.	Accepted in all cases.	Fit is not good. Frequencies of spacings <2.5 m are mostly underestimated.
3	Accepted in all cases.	Fit is good.	Accepted in most cases except for high correlation factors.	Fit appears good at low correlation factors but worsens as it increases.	Accepted in all cases.	Fit appears good but still some discrepancies at smaller spacings.

Overall, the flaw model and rejection procedure are not always consistent in modeling the joint spacing probability distribution in this case. Even though the joint intensities and the lithologies in the three layers are similar, both models often give conflicting visual and statistical comparisons. This is partly due to the subjective nature of the visual comparison and partly because the statistical comparisons are based on the maximum difference between the observed and simulated joint spacing CDFs (i.e., the Kolmogorov-Smirnov statistic). There are a number of possible reasons for the inconsistencies that have to do with the assumptions that were made:

4. The non-perpendicularity between set I and set II joints (Engelder and Geiser, 1980; Baudo, 2001) as well as their relative ages mean that set I joints may have affected

the stresses during the formation of set II joints. This most likely leads to an increase in the set II joint spacing near set I joints and consequently to a different joint spacing distribution that would result if set II joints are the first-formed joints.

5. The strike orientations for the set II joints in each layer take on a wide range of values. In the models, the stresses in the jointing layer are calculated based on the assumption that existing joints are approximately parallel. This is not entirely the case in Baudo's (2001) data. In layer 1, the strike ranges from about 020° to 070° but most strike 030° to 040°. In layer 2, the range of strike orientations is the same as in layer 1 but most of the joints strike 040° to 050°. In layer 3, the strike orientations range from 030° to 080° with most striking about 070°.

6. The joints mostly cut through multiple rock layers (Baudo, 2001). The assumption was made that all joints found in a specific layer initiated in that specific layer and later propagated into the bounding top and bottom layers may be inaccurate.

Given the results and the three items above, it can be said that the conditions for using both the flaw model and rejection procedure were less than ideal in this case. This may explain the discrepancies between the actual and simulated joint spacing CDFs that were observed in the comparisons and also explain, to some extent, the inconsistencies between the visual and statistical comparisons.

Conclusions

Based on all the information presented, the following conclusions can be made:

1. The flaw model and rejection procedure produce linear spacing-thickness relationships such as those often observed in the field.

2. The relationship between spacing and layer thickness depends on layer geometry (non-jointing layer thickness) and material properties ($\frac{E_f}{G_n}$ ratio) in the flaw model and rejection procedure. In the flaw model, it also depends on tensile strength.

3. In the flaw model, the joint spacing distribution depends on layer geometry (non-jointing layer thickness) and material properties ($\frac{E_f}{G_n}$ ratio) which all affect the shape of the tensile stress distribution. The joint spacing distribution also depends on how tensile strength varies along the jointing layer. Tensile strength variation depends on the type of tensile strength submodel (uncorrelated or correlated) and the flaw density.

4. In the rejection procedure, the joint spacing distribution depends on layer geometry (non-jointing layer thickness) and material properties ($\frac{E_f}{G_n}$ ratio) which all determine the shape of the probability density function of joint location, $f(x)$. Note that in the rejection procedure, $f(x)$ is based on the tensile stress distribution.

5. Non-uniform tensile strength leads to more realistic joint spacing distributions in the flaw model. Tensile strength uniformity/non-uniformity can be controlled by specifying the number of flaws.

6. The flaw model (with or without saturation) produces joint spacing distributions that are exponential at low joint intensity, log-normal at intermediate joint intensity, and quasi-normal at high joint intensity.

7. The rejection procedure produces joint spacing distributions that are exponential at low joint intensity, log-normal at intermediate and high joint intensities when no saturation mechanism is present. If saturation is implemented, the spacing distribution appears quasi-normal at high joint intensity.

8. The flaw model with uncorrelated strength is able to produce joint spacing distributions that better compare with actual data than those produced using correlated strength.

9. The rejection procedure is able to produce realistic joint spacing distributions in some cases but especially for higher joint intensities (e.g., Becker and Gross, 1996 for sections II and III; Saltzman, 2001 for layers 1, 3, and 4).

10. The compressive stress saturation mechanism may not be applicable to all cases of layer-perpendicular joints in sedimentary rock (i.e., joint spacings closer than those predicted by the saturation mechanism do occur in reality; e.g., Saltzman's, 2001 data).

11. The models do not perform particularly well if the joint strike varies considerably (see case for Baudo, 2001).

12. The models do not perform well if joints are through-going (i.e., cuts through multiple layers; see case for Becker and Gross, 1996 and Baudo, 2001).

9 References

Adda-Bedia M. and M. Ben Amar, 2001, Fracture spacing in layered materials: Physical Review Letters, v. 86, No. 25, p. 5703-5706.

Bahat D., 1988, Early single-layer and late multi-layer joints in the Lower Eocene chalks near Beer Sheva, Israel: Annales Tectonicæ, v. 2, No. 1, p. 3-11.

Bahat D., 1999, Single-layer burial joints vs single-layer uplift joints in Eocene chalk from the Beer Sheva syncline in Israel: Journal of Structural Geology, v. 21, No. 3, p. 293-303.

Bai, T.X. and D.D. Pollard, 2000, Fracture spacing in layered rocks: a new explanation based on the stress transition: Journal of Structural Geology, v. 22, No. 1, p. 43-57.

Baudo, A., 1-D Fractal, Geostatistical and Abutting Analyses of Fractures along a 4 km Scanline, M.S. Thesis, The State University of New York at Buffalo, 2001.

Becker, A. and M.R. Gross, 1996, Mechanism for Joint Saturation in Mechanically Layered Rocks: an Example from Southern Israel: Tectonophysics, v. 257, p. 223-237.

Cox, H.L., 1952, The Elasticity and Strength of Paper and other Fibrous Materials: British Journal of Applied Physics, 3, p. 72-79.

Engelder, T., 1985, Loading Paths to Joint Propagation During a Tectonic Cycle – An Example from the Appalachian Plateau, USA: Journal of Structural Geology, v. 7, No. 3-4, p. 459-476.

Engelder, T. and P. Geiser, 1980, On the Use of Regional Joint Sets as Trajectories of Paleostress Fields During the Development of the Appalachian Plateau, New York: Journal of Geophysical Research, v. 85, No. NB11, p. 6319-6341.

Engelder, T., M.R. Gross and P. Pinkerton, 1997, An Analysis of Joint Development in Thick Sandstone Beds of the Elk Basin Anticline, Montana-Wyoming in: Fractured Reservoirs: Characterization and Modeling Guidebook. Rock Mountain Association of Geologists.

Eyal, Y., M.R. Gross, T. Engelder and A. Becker, 2001, Joint Development During Fluctuation of Regional Stress Field in Southern Israel: Journal of Structural Geology, v. 23, p. 279-296.

Gross, M.R., 1993, The Origin and Spacing of Cross Joints: Examples from the Monterey Formation, Santa Barbara Coastline, California: Journal of Structural Geology, v. 15, No. 6, p. 737-751.

Gross, M.R., D. Bahat and A. Becker, 1997, Relations between Jointing and Faulting Based on Fracture-Spacing Ratios and Fault-Slip Profiles: A New Method to Estimate Strain in Layered Rocks: Geology, v. 25, No. 10, p. 887-890.

Gross, M.R., M.P. Fischer, T. Engelder and R.J. Greenfield, 1995, Factors controlling joint spacing in interbedded sedimentary rocks: integrating numerical models with field observations from the Monterey Formation, USA. In: M.S. Ameen (Editor), Fractography: Fracture Topography as a Tool in Fracture Mechanics and Stress Analysis. Geological Society of London Special Publication, 92, p. 215-233.

Harris, J.F., G.L. Taylor and J.L. Walper, 1960, Relation of Deformational Fractures in Sedimentary Rocks to Regional and Local Structure: AAPG Bulletin, v. 44, No. 12, p. 1853-1873.

Hobbs, D.W., 1967, The Formation of Tension Joints in Sedimentary Rocks: An Explanation: Geological Magazine, v. 104, No. 6, p. 550-556.

Hogg, R.V. and E.A. Tanis, Probability and statistical inference, 6th ed., 2001, Prentice Hall.

Huang, Q. and J. Angelier, 1989, Fracture Spacing and its Relation to Bed Thickness: Geological Magazine, v. 126, No. 4, p. 355-362.

Ivanova, V.M., Geologic and stochastic modeling of fracture systems in rocks. PhD Thesis, Massachusetts Institute of Technology, 1998.

Ji, S.C. and K. Saruwatari, 1998, A Revised Model for the Relationship between Joint Spacing and Layer Thickness: Journal of Structural Geology, v. 20, No. 11, p. 1495-1508.

Ji S.C., Z.M. Zhu and Z.C. Wang, 1998, Relationship between joint spacing and bed thickness in sedimentary rocks: effects of interbed slip: Geological Magazine, v. 135, No. 5, p. 637-655.

Josnin J.Y., H. Jourde, P. Fenart, et al., 2002, A three-dimensional model to simulate joint networks in layered rocks: Canadian Journal of Earth Sciences, v. 39, No. 10, p. 1443-1455.

Kottegoda, N.T. and R. Rosso, Statistics, probability, and reliability for civil and environmental engineers, 1997, McGraw-Hill.

Ladeira, F.L. and N.J. Price, 1981, Relationship between Fracture Spacing and Bed Thickness: Journal of Structural Geology, v. 3, No. 2, p. 179-183.

McQuillan, H., 1973, Small-scale Fracture Density in Asmari Formation of Southwest Iran and its Relation to Bed Thickness and Structural Setting: AAPG Bulletin, v. 57, No. 12, p. 2367-2385.

Narr, W., 1991, Fracture Density in the Deep Subsurface – Techniques with Application to Point Arguello Oil-Field: AAPG Bulletin – American Association of Petroleum Geologists, v. 75, No. 8, p. 1300-1323.

Narr, W., 1996, Estimating Average Fracture Spacing in Subsurface Rock: AAPG Bulletin, v. 80, No. 10, p. 1565-1586.

Narr, W. and I. Lerche, 1984, A Method for Estimating Subsurface Fracture Density in Core: AAPG Bulletin, v. 68, No. 5, p. 637-648.

Narr, W. and J. Suppe, 1991, Joint Spacing in Sedimentary Rocks: Journal of Structural Geology, v. 13, No. 9, p. 1037-1048.

Palchik V. and Y.H. Hatzor, 2004, The influence of porosity on tensile and compressive strength of porous chalks: Rock Mechanics and Rock Engineering, v. 37, No. 4, p. 331-341.

Pascal, C., J. Angelier, M.C. Cacas and P.L. Hancock, 1997, Distribution of joints: Probabilistic Modelling and Case Study near Cardiff (Wales, UK): Journal of Structural Geology, v. 19, No. 10, p. 1273-1284.

Priest S.D. and J.A. Hudson, 1976, Discontinuity Spacings in Rock: International Journal of Rock Mechanics and Mining Sciences, v. 13, No. 5, p. 135-148.

Priest S.D. and J.A. Hudson, 1981, Estimation of Discontinuity Spacing and Trace Length using Scanline Surveys: International Journal of Rock Mechanics and Mining Sciences, v. 18, No. 3, p. 183-197.

Rabinovitch A. and D. Bahat, 1999, Model of joint spacing distribution based on shadow compliance: Journal of Geophysical Research-Solid Earth, v. 104, No. B3, p. 4877-4886.

Rives T., M. Razack, J.P. Petit, et al., 1992, Joint Spacing - Analog and Numerical Simulations: Journal of Structural Geology, v. 14, No. 8-9, p. 925-937.

Ruf, J.C., K.A. Rust and T. Engelder, 1998, Investigating the Effect of Mechanical Discontinuities on Joint Spacing: Tectonophysics, v. 295, p. 245-257.

Saltzman, B., Possible Correlation between Mechanical Layer's Joint Spacing and its Rock Mechanical Properties, M.S. Thesis, Ben Gurion University of the Negev, 2001.

Timoshenko, S.P. and J.N. Goodier, Theory of Elasticity, 3rd ed., McGraw-Hill, 1970.

Wawrzynek P.A., A.R. Ingraffea, 1987, Iinteractive Finite-Element Analysis of Fracture Processes - An Integrated Approach: Theoretical and Applied Fracture Mechanics, v. 8, No. 2, p. 137-150.

Wu, H. and D. Pollard, 1995, An Experimental Study of the Relationship between Joint Spacing and Layer Thickness: Journal of Structural Geology, v. 17, No. 6, p. 887-905.

10 Appendix

10.1 Flaw Model Code

```
#include <math.h>
#include <stdio.h>
#include <fstream.h>
#include <stdlib.h>
#include <sys/types.h>
#include <time.h>

//RANDOM NUMBER GENERATOR STUFF FOR THE STRENGTH CORRELATIONS
#include "\Important_Folder\Research
2\Random_Number_Generator_Stuff\randomc.h"                    // define
classes for random number generators
#include "\Important_Folder\Research
2\Random_Number_Generator_Stuff\userintf.cpp"                 // define
system specific user interface
// define which random number generator to base random library on:
#include "\Important_Folder\Research
2\Random_Number_Generator_Stuff\mersenne.cpp"                 // members
of class TRandomMersenne
#define RANDOM_GENERATOR TRandomMersenne
#include "\Important_Folder\Research
2\Random_Number_Generator_Stuff\stocc.h"                      // define
random library classes
#include "\Important_Folder\Research
2\Random_Number_Generator_Stuff\stoc1.cpp"                    // random
library source code

//declare some global functions
double get_random_number(int);
double get_normal_number(int);
double get_random_number01();

//declare some global variables
int random_number_taken=0;
int normal_number_taken=0;

/*class strength
{
public:
double end1;
double end2;
static double width;
double strength_value;
strength* next_strength;
static int number_of_strength_segments;
static strength* starting_strength_segment;

strength()
{
end1=0;
end2=0;
strength_value=0;
next_strength=0;
```

```
number_of_strength_segments++;
};

strength(double end1, double strength_value)
{
this->end1=end1;
this->end2=end1+width;
this->strength_value=strength_value;
this->next_strength=0;
number_of_strength_segments++;
};

~strength()
{
number_of_strength_segments--;
};

};*/

class flaw
{
public:
double location;
double strength;
flaw* next_flaw;
static int number_of_flaws;
static flaw* starting_flaw;

//write restart file
void flaw::write_restart_file()
{
ofstream outfile("Flaw_Restart.xls");
outfile<<number_of_flaws<<endl;
flaw* cur=starting_flaw;
for(int i=0;i<number_of_flaws;i++)
{
outfile<<cur->location<<"\t"<<cur->strength<<endl;
cur=cur->next_flaw;
}
outfile.close();
return;
};


flaw()
{
location=0;
strength=0;
next_flaw=0;
number_of_flaws++;
};

flaw(double l,double s)
{
location=l;
strength=s;
next_flaw=0;
```

```
number_of_flaws++;
};

~flaw()
{
number_of_flaws--;
};

//!!use the starting flaw to call this function!!
//note that the first generated flaw is the starting flaw
//the first generated flaw may no longer  be the starting flaw as new
flaws are generated
void flaw::insert_new_flaw(double new_flaw_loc, double new_flaw_str)
{
flaw* cur_flaw=this;

if(new_flaw_loc>=cur_flaw->location)
{
if(cur_flaw->next_flaw==0)
{
cur_flaw->next_flaw=new flaw(new_flaw_loc,new_flaw_str);
//cur_flaw->next_flaw->previous_flaw=cur_flaw;
return;
}

if(new_flaw_loc>cur_flaw->next_flaw->location)
cur_flaw->next_flaw->insert_new_flaw(new_flaw_loc,new_flaw_str);

if(new_flaw_loc<=cur_flaw->next_flaw->location)
{
flaw* temp=new flaw(new_flaw_loc,new_flaw_str);
temp->next_flaw=cur_flaw->next_flaw;
//cur_flaw->next_flaw->previous_flaw=temp;
//temp->previous_flaw=cur_flaw;
cur_flaw->next_flaw=temp;
return;
}

}

if(new_flaw_loc<cur_flaw->location)
{
flaw* temp=new flaw(new_flaw_loc,new_flaw_str);
temp->next_flaw=cur_flaw;
//temp->previous_flaw=cur_flaw->previous_flaw;
//cur_flaw->previous_flaw=temp;
flaw::starting_flaw=temp;
return;
}
};

};

class segment
{
public:
double end1;
```

```
double end2;
double segment_length;
double min_strain;
double slippage_strain;
double joint_location;

segment* next_segment;
static double layer_length;
static double layer_thickness;
static double non_jointing_layer_thickness;
static double max_length;
static double min_length;
static double shadow_length;
static double limit_spacing;
static double E_over_Gn;
static double E_of_layer;
static double Tau;
static double epsilon1;
static double base_strength;
static double beta;
static int number_of_segments;
//static int target_number_of_segments;
static segment* longest_segment;
static segment* starting_segment;

static double non_jointing_layer_Poisson_ratio;
static double jointing_layer_Poisson_ratio;
static double parameter_D;
static double critical_spacing_thickness_ratio;
static double overburden;

//default constructor
segment()
{
end1=0;
end2=0;
segment_length=0;
min_strain=0;
slippage_strain=0;
joint_location=0;
next_segment=0;
number_of_segments++;
};

//another constructor
segment(double e1, double e2)
{
end1=e1;
end2=e2;
segment_length=end2-end1;
min_strain=0;
slippage_strain=0;
joint_location=0;
next_segment=0;
number_of_segments++;
};
```

```
//default destructor
~segment() {number_of_segments--;};

//function to update the length of the segment after the addition of a
new joint
void segment::update_length()
{
this->segment_length=end2-end1;
return;
};

//function to insert a new segment into an existing segment
//loc is the distance from end1 of the starting segment to joint
location
void segment::insert_new_segment(double loc)
{
if (loc<=this->end1 || loc>=this->end2) return;

segment* temp=new segment(loc,this->end2);
temp->next_segment=this->next_segment;
this->next_segment=temp;
this->end2=temp->end1;
this->update_length();
starting_segment->set_max_spacing();
return;
};

//write the spacing data to file
//use the ONLY head segment to call this function
void segment::write_spacing_to_file()
{
segment* cur=this;
ofstream out("Spacing.xls",ios::app);
out<<"SPACING BREAK"<<endl;
for(int j=0; j<number_of_segments; j++)
{
out<<cur->segment_length<<endl;
cur=cur->next_segment;
}
out.close();
return;
};

//writes the joint pattern to be displayed in sigmaplot
void segment::write_joint_pattern_to_file()
{
ofstream out("Pattern.txt");
double x_coord=0;
double y_coord=0;

out<<x_coord<<"\t"<<y_coord<<endl;
y_coord+=segment::layer_thickness;
out<<x_coord<<"\t"<<y_coord<<endl;

segment* cur=this;
for(int i=0;i<segment::number_of_segments;i++)
{
```

```
x_coord+=cur->segment_length;
out<<x_coord<<"\t"<<y_coord<<endl;
if(y_coord==segment::layer_thickness) y_coord-
=segment::layer_thickness;
else y_coord+=segment::layer_thickness;
out<<x_coord<<"\t"<<y_coord<<endl;
cur=cur->next_segment;
}
out.close();
};

//write the joint locations to file
//use ONLY the head segment to call this function
void segment::write_joint_locations_to_file()
{
segment* cur=this;
ofstream out("Joints.txt");
for(int j=0; j<number_of_segments; j++)
{
out<<cur->end1<<endl;
if (cur->next_segment=0) out<<cur->end2;
cur=cur->next_segment;
}
out.close();
return;
};

//writes the moving average to a file
//calculates the moving average at n segment intervals.
//segments used in calculation overlap unlike the first moving average
function
void write_moving_average_data_to_file_overlap(int n)
{
segment* cur_starting_segment=starting_segment;
segment* cur=0;
double x_coord=0;
double moving_average=0;
ofstream out("Moving_Ave_1.txt");

for(int k=0;k<n-1;k++)
{
moving_average+=cur_starting_segment->segment_length;
x_coord=moving_average/2;//midpoint of the total segment considered so
far
out<<x_coord<<"\t"<<moving_average/(k+1)<<endl;
cur_starting_segment=cur_starting_segment->next_segment;
}

cur_starting_segment=starting_segment;//restart from the first segment

for(int i=0;i<number_of_segments;i++)
{
cur=cur_starting_segment;
int indicator=0;
moving_average=0;
x_coord=cur_starting_segment->end1;
for(int j=0;j<n;j++)
```

```
{
indicator++;
moving_average+=cur->segment_length;
if(cur->next_segment==0 || indicator==n)
{
j=n-1;//force loop to finish
x_coord+=moving_average/2;//at this point moving average is just the
sum of n segments from current starting seg.
moving_average=moving_average/indicator;
out<<x_coord<<"\t"<<moving_average<<endl;
}
cur=cur->next_segment;
}
cur_starting_segment=cur_starting_segment->next_segment;
}
out.close();
return;

};

//function to get the maximum spacing
//use only the HEAD segment to call this function
//also sets the longest_segment pointer to the location of the longest
segment
void segment::set_max_spacing()
{
double smax=starting_segment->segment_length;
segment* cur=starting_segment;
for(int i=0; i<number_of_segments; i++)
{
if(cur->segment_length>smax)
{
smax=cur->segment_length;
longest_segment=cur;
}
cur=cur->next_segment;
}
max_length=smax;
return;
};

//function to get the minimum spacing
//use only the HEAD segment to call this function
void segment::set_min_spacing()
{
double smin=starting_segment->segment_length;
segment* cur=starting_segment;
for(int i=0; i<number_of_segments; i++)
{
if(cur->segment_length<smin) smin=cur->segment_length;
cur=cur->next_segment;
}
min_length=smin;
return;
};

//function to get the total segment length
```

```
double segment::get_total_segment_length()
{
double sum=0;
segment* cur=this;
for(int i=0; i<number_of_segments; i++)
{
sum+=cur->segment_length;
cur=cur->next_segment;
}
return sum;
};

//function to get the mean length
double segment::get_mean_length()
{
return segment::layer_length/segment::number_of_segments;
};

//function to get the standard deviation of all segment lengths
double segment::get_standard_deviation()
{
double sum=0;
double mean_segment_length=starting_segment-
>get_total_segment_length()/number_of_segments;
//cout<<"\nMean segment length = "<<mean_segment_length<<"\n";
segment* cur=this;//called by the head segment
for (int i=0; i<number_of_segments; i++)
{
sum+=((cur->segment_length-mean_segment_length)*(cur->segment_length-
mean_segment_length));
cur=cur->next_segment;
}
return sqrt(sum/(number_of_segments-1));
};

//function to calculate skewness
double segment::get_skewness()
{
double skewness=0;
double mean_segment_length=starting_segment-
>get_total_segment_length()/number_of_segments;
double stdev=this->get_standard_deviation();
segment* cur=this;
for (int i=0;i<number_of_segments; i++)
{
skewness+=((cur->segment_length-mean_segment_length)/stdev)*((cur-
>segment_length-mean_segment_length)/stdev)*((cur->segment_length-
mean_segment_length)/stdev);
cur=cur->next_segment;
}
return skewness*(number_of_segments)/((number_of_segments-
1)*(number_of_segments-2));
};

/*************************************************************************
*****************/
```

```
/*************************************************************************
*****************/
//function to calculate the strain that brings about jointing
double segment::calc_strain(flaw* f,double dist_from_mdpt)
{
double strain=0;
double
Beta=sqrt(8*segment::E_of_layer*(1/segment::E_over_Gn)/(segment::E_of_l
ayer*segment::layer_thickness*segment::non_jointing_layer_thickness));
double arg_numer=Beta*dist_from_mdpt;
double arg_denom=Beta*(segment_length/2);
if(fabs(arg_numer)>710.475 && fabs(arg_denom)>710.475)
{
//if(dist_from_mdpt<0) dist_from_mdpt=(-1)*dist_from_mdpt;
double new_x=(segment_length/2)-fabs(dist_from_mdpt);
strain=(f->strength/segment::E_of_layer)/(1-exp(-Beta*new_x));
}
else
{
double cosh_numer=cosh(arg_numer);
double cosh_denom=cosh(arg_denom);
strain=(f->strength/segment::E_of_layer)/(1-(cosh_numer/cosh_denom));
}

//check strain against slippage strain, there are three conditions
here, remember??
//on the triangle (easy), below the triangle (a bit hard), above the
triangle & at the tip (return strain=0 here)
if(strain>this->slippage_strain)//IMPORTANT TO CALCULATE SLIPPAGE
STRAIN BEFORE THIS!!!!!
{
double
stress_at_flaw_due_to_slippage=(2*Tau/layer_thickness)*(segment_length/
2-fabs(dist_from_mdpt));
if(dist_from_mdpt==0)
{
if(f->strength<stress_at_flaw_due_to_slippage)//can joint at flaw
strain=calc_strain_beyond_slippage(f,dist_from_mdpt);
if(f->strength>=stress_at_flaw_due_to_slippage)//cannot joint at flaw
strain=0;
}
if(dist_from_mdpt!=0)
{
if(f->strength<=stress_at_flaw_due_to_slippage)//can joint at flaw
location
strain=calc_strain_beyond_slippage(f,dist_from_mdpt);
if(f->strength>stress_at_flaw_due_to_slippage)//cannot joint
strain=0;
}
}
return strain;
};

/*************************************************************************
*****************/
/*************************************************************************
*****************/
```

```
//function that calculates the strain at which slippage starts
//this is the upper limit to the strain required to joint a segment
//no new joints may form for a specific layer if the required strain
exceeds this strain
void segment::calc_slippage_strain()
{
double
Beta=sqrt(8*segment::E_of_layer*(1/segment::E_over_Gn)/(segment::E_of_l
ayer*segment::layer_thickness*segment::non_jointing_layer_thickness));
double arg=Beta*(segment_length/2);
slippage_strain=(Tau/(E_of_layer*layer_thickness))*(2/Beta)*(1/tanh(arg
));
return;
};

/**************************************************************************
*****************/
/**************************************************************************
*****************/
//calculates the strain beyond slippage
double segment::calc_strain_beyond_slippage(flaw* f,double
dist_from_mdpt)
{
double sl=get_root_Ls(f,dist_from_mdpt,0,20,0);//Ls from Newton's
method

double max_Ls=2*(segment_length/2-fabs(dist_from_mdpt));
double f_sl=slippage_function(f,dist_from_mdpt,sl);

double f_sl_1=0;
double slip_length=0;

if(sl<max_Ls && sl>=0 && fabs(f_sl)<=1e-6) slip_length=sl;//Ls from
Newton's method is satisfactory

if(sl>max_Ls || sl<0 || fabs(f_sl)>1e-6)
{
//cout<<"tangent solution is wrong! L= "<<segment_length<<" Ls=
"<<sl<<" max Ls= "<<max_Ls<<endl;
double sl_1=get_root_Ls_1(f,dist_from_mdpt,0,max_Ls,0,40);//Ls from
bisection method

f_sl_1=slippage_function(f,dist_from_mdpt,sl_1);
if(sl_1>max_Ls || sl_1<0 || fabs(f_sl_1)>1e-6)
{
cout<<"bisection solution is wrong! L= "<<segment_length<<" Ls=
"<<sl_1<<" max Ls= "<<max_Ls<<" f_sl_1= "<<f_sl_1<<endl;
ofstream out_error("Errors.txt",ios::app);
out_error<<"tangent solution: L= "<<segment_length<<"max Ls=
"<<max_Ls<<" Ls= "<<sl<<" f(sl)= "<<f_sl<<
" bisection solution: Ls= "<<sl_1<<" f(sl_1)= "<<f_sl_1<<endl;
out_error.close();
}
if(sl_1<max_Ls && sl_1>=0)
{
slip_length=sl_1;
```

```
if(fabs(f_sl_1)>1e-6) cout<<"function value for bisection solution
="<<f_sl_1<<endl;
}
}

double
Beta=sqrt(8*segment::E_of_layer*(1/segment::E_over_Gn)/(segment::E_of_l
ayer*segment::layer_thickness*segment::non_jointing_layer_thickness));
double t1=Tau/(E_of_layer*segment::layer_thickness);
double t2=2/Beta;
double t3=Beta*(segment_length-slip_length)/2;
double t4=tanh(t3);
double slip_strain=t1*(slip_length+t2/t4);

if(slip_strain<0)
{
ofstream out("Slip_Strains.txt",ios::app);
out<<slip_strain<<"\t"<<segment_length<<"\t"<<f-
>strength<<"\t"<<dist_from_mdpt<<endl;
out.close();
}

return slip_strain;
};

/*************************************************************************
*****************/
/*************************************************************************
*****************/
//calculates the slippage length using Newton's method
double segment::get_root_Ls(flaw* f,double dist_from_mdpt,int
number_iter,int nmax,double Ls_trial)//newton's method
{
number_iter++;

double f_trial=slippage_function(f,dist_from_mdpt,Ls_trial);
double
f_prime_trial=slippage_function_slope(f,dist_from_mdpt,Ls_trial);
double new_Ls=-(f_trial/f_prime_trial)+Ls_trial;
if(fabs(f_trial/f_prime_trial)<1e-9 || number_iter>=nmax) return
new_Ls;
else return get_root_Ls(f,dist_from_mdpt,number_iter,nmax,new_Ls);
};

/*************************************************************************
*****************/
/*************************************************************************
*****************/
//calculates the slippage length using the bisection method
double get_root_Ls_1(flaw* f,double dist_from_mdpt,double left,double
right,int number_iter,int nmax)//bisection method
{
number_iter++;
double estimate=0.5*(left+right);

double f_left=slippage_function(f,dist_from_mdpt,left);
double f_right=slippage_function(f,dist_from_mdpt,right);
```

```
double f_estimate=slippage_function(f,dist_from_mdpt,estimate);

//cout<<f_left<<"\t"<<f_right<<endl;

if(fabs(f_estimate)<1e-12 || number_iter>=nmax) return estimate;
if(f_left*f_estimate<0 && f_right*f_estimate>0) return
get_root_Ls_1(f,dist_from_mdpt,left,estimate,number_iter,nmax);
if(f_left*f_estimate>0 && f_right*f_estimate<0) return
get_root_Ls_1(f,dist_from_mdpt,estimate,right,number_iter,nmax);
cout<<"final escape valve! returning estimate ->"<<estimate<<endl;
return estimate;
};

/*************************************************************************
*****************/
/*************************************************************************
*****************/
//slippage function
double segment::slippage_function(flaw* f,double dist_from_mdpt,double
Ls)
{
double
Beta=sqrt(8/(E_over_Gn*layer_thickness*non_jointing_layer_thickness));
double num_arg=Beta*dist_from_mdpt;
double L_minus_Ls_over_two=0.5*(segment_length-Ls);
double denom_arg=Beta*L_minus_Ls_over_two;

if(fabs(num_arg)>710.475 && fabs(denom_arg)>710.475)
{
//if(dist_from_mdpt<0) dist_from_mdpt=(-1)*(dist_from_mdpt);
double x_from_end=(segment_length/2)-fabs(dist_from_mdpt);
return slippage_function_approximate(f,x_from_end,Ls);
}

double cosh_num=cosh(num_arg);
double cosh_denom=cosh(denom_arg);
double cosh_ratio=cosh_num/cosh_denom;
double two_over_Beta=2/Beta;
double Tau_over_t=Tau/layer_thickness;
double t1=Tau_over_t*Ls;
double t2=Tau_over_t/E_of_layer;
double tanh_expression=tanh(denom_arg);
double answer=(f->strength-t1*cosh_ratio)/(E_of_layer*(1-cosh_ratio))-
t2*(Ls+two_over_Beta/tanh_expression);
return answer;
};

/*************************************************************************
*****************/
/*************************************************************************
*****************/
double segment::slippage_function_approximate(flaw* f,double
dist_from_end,double Ls)
{
double
Beta=sqrt(8/(E_over_Gn*layer_thickness*non_jointing_layer_thickness));
double Beta_Ls_over_two=Beta*Ls/2;
```

```
double Beta_x_prime=Beta*dist_from_end;
double arg=Beta_Ls_over_two-Beta_x_prime;
double exp_arg=exp(arg);
double Tau_over_t=Tau/layer_thickness;
double t1=Tau_over_t*Ls;
double t2=Tau_over_t/E_of_layer;
double two_over_Beta=2/Beta;
double answer=(f->strength-t1*exp_arg)/(E_of_layer*(1-exp_arg))-
t2*(Ls+two_over_Beta);
return answer;
};

/*************************************************************************
*****************/
/*************************************************************************
*****************/
double segment::slippage_function_slope(flaw* f,double
dist_from_mdpt,double Ls)
{
double t2 = 0.10e1 / layer_thickness;
double t4 = sqrt(0.2e1);
double t5 = 0.10e1 / E_of_layer;
double t10 = sqrt((E_of_layer/E_over_Gn) * t5 * t2 /
non_jointing_layer_thickness);
double t11 = t4 * t10;
double t11_a=0.2e1 * t11 * dist_from_mdpt;//beta*x
double t14 = cosh(0.2e1 * t11 * dist_from_mdpt);//cosh(beta*x)
double t16 = t11 * (segment_length - Ls);//beta*(L-Ls)/2

if(fabs(t11_a)>710.475 && fabs(t16)>710.475)
{
//if(dist_from_mdpt<0) dist_from_mdpt=(-1)*(dist_from_mdpt);
double x_from_end=(segment_length/2)-fabs(dist_from_mdpt);
return slippage_function_slope_approximate(f,x_from_end,Ls);
};

double t17 = cosh(t16);//cosh(beta*(L-Ls)/2)
double t18 = 0.10e1 / t17;
double t19 = t14 * t18;
double t21 = Tau * Ls;
double t22 = t2 * t14;
double t24 = t17 * t17;
double t26 = sinh(t16);
double t28 = 0.10e1 / t24 * t26 * t11;
double t32 = 0.1e1 - t19;
double t39 = t32 * t32;
double t45 = tanh(t16);
double t46 = t45 * t45;
double t53 = (-Tau * t2 * t19 - t21 * t22 * t28) * t5 / t32 + (f-
>strength - t21 * t22 * t18) * t5 / t39 * t14 * t28 - Tau * t5 * t2 *
(0.1e1 + 0.10e1 / t46 * (0.1e1 - t46));
return t53;
};

/*************************************************************************
*****************/
```

```
/*************************************************************************
*****************/
double segment::slippage_function_slope_approximate(flaw* f,double
dist_from_end,double Ls)
{
double t1 = sqrt(0.2e1);
double t2 = 0.10e1 / E_of_layer;
double t4 = 0.10e1 / layer_thickness;
double t8 = sqrt((E_of_layer/E_over_Gn) * t2 * t4 /
non_jointing_layer_thickness);
double t9 = t1 * t8;
double t10 = t9 * Ls;
double t11 = exp(t10);
double t12 = t11 * Tau;
double t19 = exp(0.2e1 * t9 * dist_from_end);
double t25 = pow(-t19 + t11, 0.2e1);
double t28 = (-t12 * t10 + t12 + t9 * t11 * f->strength *
layer_thickness - Tau * t19) * t19 * t2 * t4 / t25;
return t28;
};

/*************************************************************************
*****************/
/*************************************************************************
*****************/
//function to calculate beta, note that there is only one value for
beta for the entire layer
void segment::calc_beta()
{
beta=sqrt(8*segment::E_of_layer*(1/segment::E_over_Gn)/(segment::E_of_l
ayer*segment::layer_thickness*segment::non_jointing_layer_thickness));
return;
};

/*************************************************************************
*****************/
/*************************************************************************
*****************/
//function to check for midpoint fracturing
void segment::check_for_midpoint_fracturing()
{
double
Beta=sqrt(8*segment::E_of_layer*(1/segment::E_over_Gn)/(segment::E_of_l
ayer*segment::layer_thickness*segment::non_jointing_layer_thickness));
double arg=Beta*this->segment_length/2;
double temp_strain=(segment::base_strength/this->E_of_layer)/(1-
(1/cosh(arg)));
double location_temp=0.5*(end1+end2);

if(temp_strain>this->slippage_strain)//slippage has occurred, need
different calculations
{
double max_stress=Tau*segment_length/layer_thickness;//max stress
possible at midpoint. i.e. at full slippage
if(base_strength>=max_stress)//can't joint
temp_strain=0;
if(base_strength<max_stress)//can joint
```

```
{
flaw* temp_flaw=new flaw(location_temp,base_strength);
temp_strain=calc_strain_beyond_slippage(temp_flaw,0);
delete temp_flaw;
temp_flaw=0;
}
}
if(temp_strain!=0)
enter_strain_and_location(temp_strain,location_temp);
return;
};
/*************************************************************************
*****************/
/*************************************************************************
*****************/

//calculate the distance from segment midpoint to flaw
double calc_distance(double loc)
{
return ((0.5*(end1+end2))-loc);
};

//function to find the minimun strains for jointing of each segment
/*void segment::assign_min_strains(flaw* f)
{
double distance=0;
double strain=0;

if(f->location<=end1)
{
if(f->next_flaw!=0) assign_min_strains(f->next_flaw);
if(f->next_flaw==0)
{
check_for_midpoint_fracturing();//what about the next segments??
return;
}
}
if(f->location>end1)
{
if(f->location<end2)
{
distance=calc_distance(f->location);
strain=calc_strain(f,distance);
enter_strain_and_location(strain,f->location);
if(f->next_flaw!=0) assign_min_strains(f->next_flaw);
if(f->next_flaw==0)
{
check_for_midpoint_fracturing();//what about the next segments??
return;
}
}
if(f->location==end2)
{
check_for_midpoint_fracturing();
if(next_segment!=0 && f->next_flaw!=0) next_segment-
>assign_min_strains(f->next_flaw);
```

```
if(next_segment!=0 && f->next_flaw==0) next_segment-
>check_for_midpoint_fracturing();
if(next_segment==0 && f->next_flaw==0) return;
if(next_segment==0 && f->next_flaw!=0) return;//this should not
happen!!!

}
if(f->location>end2)
{
check_for_midpoint_fracturing();
if(next_segment!=0) next_segment->assign_min_strains(f);
if(next_segment==0) return;
}
}
};*/

//function for assigning the minimum strains for the segments
void segment::assign_min_strains(flaw* f)
{
double distance=0;
double strain=0;

if(f->location<=end1)
{
if(f->next_flaw!=0) assign_min_strains(f->next_flaw);
if(f->next_flaw==0) return;
}
if(f->location>end1)
{
if(f->location<end2)
{
distance=calc_distance(f->location);
strain=calc_strain(f,distance);
//ofstream out_strains("Strains.txt",ios::app);
//out_strains<<strain<<endl;
//out_strains.close();
if(strain!=0)
enter_strain_and_location(strain,f->location);
if(f->next_flaw!=0) assign_min_strains(f->next_flaw);
if(f->next_flaw==0) return;
}
if(f->location==end2)
{
if(next_segment!=0 && f->next_flaw!=0) next_segment-
>assign_min_strains(f->next_flaw);
if(next_segment==0 || f->next_flaw==0) return;

}
if(f->location>end2)
{
if(next_segment!=0) next_segment->assign_min_strains(f);
if(next_segment==0) return;
}
}
};
```

```
//update the minimum strain and joint location for the joints that have
been formed recently
//basically the same as assign_min_strains but calculates min strains
and joint locations
//for a newly jointed segment
void segment::update_min_strain_and_location(flaw* f)
{
double distance=0;
double strain=0;

if(f->location<=end1)
{
if(f->next_flaw!=0) update_min_strain_and_location(f->next_flaw);
if(f->next_flaw==0) return;
}
if(f->location>end1)
{
if(f->location<end2)
{
distance=calc_distance(f->location);
strain=calc_strain(f,distance);
if(strain!=0)
enter_strain_and_location(strain,f->location);
if(f->next_flaw!=0) update_min_strain_and_location(f->next_flaw);
if(f->next_flaw==0) return;
}
if(f->location>=end2)
{
return;
}
}
};

//function to place the new joints and update the min_strains and joint
locations of the new segments
//CHANGE THIS!!!!
void segment::place_new_joint_and_update_new_segments(flaw* f)
{
segment* target_segment=0;
segment* cur_segment=starting_segment;
double temp_strain=starting_segment->min_strain;
for(int i=0;i<number_of_segments;i++)
{
if(temp_strain!=0)
{
if(cur_segment->min_strain!=0)
{
if(cur_segment->min_strain<=temp_strain && cur_segment-
>segment_length/segment::layer_thickness>segment::critical_spacing_thic
kness_ratio)
{
target_segment=cur_segment;
temp_strain=cur_segment->min_strain;
}
}
}
if(temp_strain==0)
```

```
{
if(cur_segment->min_strain!=0 && cur_segment-
>segment_length/segment::layer_thickness>segment::critical_spacing_thic
kness_ratio)
{
target_segment=cur_segment;
temp_strain=cur_segment->min_strain;
}
}
cur_segment=cur_segment->next_segment;
}
if(target_segment!=0)
{
target_segment->insert_new_segment(target_segment->joint_location);
//ofstream outfile("Stats.txt",ios::app);
//outfile<<target_segment-
>min_strain<<"\t"<<segment::layer_length/segment::number_of_segments<<"
\t"<<starting_segment-
>get_standard_deviation()<<"\t"<<starting_segment-
>get_skewness()<<endl;
//outfile.close();
target_segment->reset_strain_and_location();
target_segment->next_segment->reset_strain_and_location();
target_segment->calc_slippage_strain();
target_segment->next_segment->calc_slippage_strain();
target_segment->check_for_midpoint_fracturing();
target_segment->next_segment->check_for_midpoint_fracturing();
target_segment->update_min_strain_and_location(f);
target_segment->next_segment->update_min_strain_and_location(f);

};
return;
};

//function to place the new joints and update the min_strains and joint
locations of the new segments without saturation
//CHANGE THIS!!!!
void segment::place_new_joint_and_update_new_segments_no_sat(flaw* f)
{
segment* target_segment=0;
segment* cur_segment=starting_segment;
double temp_strain=starting_segment->min_strain;
for(int i=0;i<number_of_segments;i++)
{
if(temp_strain!=0)
{
if(cur_segment->min_strain!=0)
{
if(cur_segment->min_strain<=temp_strain /*&& cur_segment-
>segment_length/segment::layer_thickness>segment::critical_spacing_thic
kness_ratio*/)
{
target_segment=cur_segment;
temp_strain=cur_segment->min_strain;
}
}
}
```

```
if(temp_strain==0)
{
if(cur_segment->min_strain!=0 /*&& cur_segment-
>segment_length/segment::layer_thickness>segment::critical_spacing_thic
kness_ratio*/)
{
target_segment=cur_segment;
temp_strain=cur_segment->min_strain;
}
}
cur_segment=cur_segment->next_segment;
}
if(target_segment!=0)
{
target_segment->insert_new_segment(target_segment->joint_location);
//ofstream outfile("Stats.txt",ios::app);
//outfile<<target_segment-
>min_strain<<"\t"<<segment::layer_length/segment::number_of_segments<<"
\t"<<starting_segment-
>get_standard_deviation()<<"\t"<<starting_segment-
>get_skewness()<<endl;
//outfile.close();
target_segment->reset_strain_and_location();
target_segment->next_segment->reset_strain_and_location();
target_segment->calc_slippage_strain();
target_segment->next_segment->calc_slippage_strain();
target_segment->check_for_midpoint_fracturing();
target_segment->next_segment->check_for_midpoint_fracturing();
target_segment->update_min_strain_and_location(f);
target_segment->next_segment->update_min_strain_and_location(f);

};
return;
};

//random bisection of a segment in the layer
void segment::halve_segment_using_random_bisection()
{
double new_joint_loc=get_random_number01()*segment::layer_length;
segment* temp=starting_segment;
segment* target_segment=0;

for(int i=0; i<segment::number_of_segments;i++)
{
if(new_joint_loc>=temp->end1 && new_joint_loc<temp->end2)
{
target_segment=temp;
break;//get out of loop when target segment is found
}

temp=temp->next_segment;
}

target_segment->insert_new_segment(new_joint_loc);
return;
};
```

```
//update the min_strain and joint_location
void segment::enter_strain_and_location(double s,double l)
{
//cout<<s<<endl;
if(min_strain==0)
{
min_strain=s;
joint_location=l;
return;
}
if(min_strain>0)
{
if(s<min_strain)
{
min_strain=s;
joint_location=l;
return;
}
}
return;
};

void segment::calc_parameter_D()
{
parameter_D=((1-
2*jointing_layer_Poisson_ratio)*(1+jointing_layer_Poisson_ratio)-(1-
2*non_jointing_layer_Poisson_ratio)*(1+non_jointing_layer_Poisson_ratio
))/((1-jointing_layer_Poisson_ratio*jointing_layer_Poisson_ratio)+(1-
non_jointing_layer_Poisson_ratio*non_jointing_layer_Poisson_ratio));
return;
};

void segment::calc_critical_spacing_thickness_ratio()
{
calc_parameter_D();
double beta_1=(0.976-0.302*parameter_D-
0.129*parameter_D*parameter_D+0.117*parameter_D*parameter_D*parameter_D
)/0.976;
double
alpha_1=segment::E_over_Gn/(2*(1+segment::non_jointing_layer_Poisson_ra
tio));
double gamma_1=(0.976+1.118e-4*overburden-7.562e-
8*overburden*overburden+2.806e-
9*overburden*overburden*overburden)/0.976;
segment::critical_spacing_thickness_ratio=beta_1*gamma_1*(0.792+0.328*(
1-exp(-0.824*pow(alpha_1-0.0025,0.824))));
return;
};

//calculate the distance for case 1
/*double segment::calc_distance_case_one(strength* s,double& loc)
{
loc=0.5*(s->end2+end1);
return (0.5*(end1+end2)-loc);
};

//calculate the distance for case 2
```

```
double segment::calc_distance_case_two(strength* s,double& loc)
{
loc=0.5*(s->end1+s->end2);
return (0.5*(end1+end2)-loc);
};

//calculate the distance for case 3
double segment::calc_distance_case_three(strength* s,double& loc)
{
loc=0.5*(s->end1+end2);
return (0.5*(end1+end2)-loc);
};*/

double segment::check_saturation()
{
double sum=0;
segment* cur_seg=segment::starting_segment;
for(int i=0;i<segment::number_of_segments;i++)
{
sum+=cur_seg->min_strain;
cur_seg=cur_seg->next_segment;
}
return sum;
};

void segment::write_strains_to_file()
{
ofstream outfile("Strains.txt");
segment* temp=starting_segment;
for(int i=0;i<number_of_segments;i++)
{
outfile<<temp->end1<<"\t"<<temp->end2<<"\t"<<temp->min_strain<<endl;
temp=temp->next_segment;
}
outfile.close();
return;
};

//write restart file
void segment::write_restart_file()
{
starting_segment->set_max_spacing();
starting_segment->set_min_spacing();
ofstream outfile("Segment_Restart.txt");
outfile<<layer_thickness<<"\t"<<non_jointing_layer_thickness<<"\t"<<max
_length<<"\t"<<min_length<<endl;
outfile<<E_over_Gn<<"\t"<<E_of_layer<<"\t"<<Tau<<"\t"<<base_strength<<"
\t"<<number_of_segments<<endl;
segment* cur=starting_segment;
for(int i=0;i<number_of_segments;i++)
{
outfile<<cur->end1<<"\t"<<cur->end2<<"\t"<<cur-
>segment_length<<"\t"<<cur->min_strain<<"\t"<<cur-
>slippage_strain<<"\t"<<cur->joint_location<<endl;
cur=cur->next_segment;
}
outfile.close();
```

```
return;
};

//function for writing the histograms
void write_histogram()
{
segment::starting_segment->set_max_spacing();
segment::starting_segment->set_min_spacing();
return;
};

void segment::reset_strain_and_location()
{
this->min_strain=0;
this->joint_location=0;
return;
};

};//END OF SEGMENT CLASS

//initialize the static variables
int segment::number_of_segments=0;
//int segment::target_number_of_segments=0;
double segment::layer_length=0;
double segment::max_length=0;
double segment::E_over_Gn=0;
double segment::shadow_length=0;//Determined by the layer thickness and
the E/Gn ratio via Hobbs 1967
double segment::min_length=segment::layer_length;
double segment::layer_thickness=0;
double segment::non_jointing_layer_thickness=0;
double segment::limit_spacing=0.012;
double segment::epsilon1=0;
double segment::E_of_layer=0;
double segment::Tau=0;
double segment::base_strength=0;
double segment::beta=0;
double segment::non_jointing_layer_Poisson_ratio=0;
double segment::jointing_layer_Poisson_ratio=0;
double segment::critical_spacing_thickness_ratio=0;
double segment::overburden=0;
double segment::parameter_D=0;
segment* segment::longest_segment=0;
segment* segment::starting_segment=0;

//double strength::width=0;
//int strength::number_of_strength_segments=0;
//strength* strength::starting_strength_segment=0;

int flaw::number_of_flaws=0;
flaw* flaw::starting_flaw=0;

/*************************************************************/
int main()
{
srand(time(NULL));
//char res;
```

```
//cout<<"Restart? (y/n) ->";
//cin>>res;
segment* head_segment=0;
flaw* head_flaw=0;
//cout<<time(NULL)<<endl;

//if(res=='n' || res=='N')
//{
//INPUT STAGE
ifstream infile("Input73.txt");

double layer_length_increment=0;
cout<<"Entering layer length and increment->";
infile>>segment::layer_length>>layer_length_increment;
cout<<segment::layer_length<<" , "<<layer_length_increment<<endl;

double layer_thickness_increment=0;
double layer_thickness_initial_value=0;
cout<<"Entering layer thickness ->";
infile>>segment::layer_thickness>>layer_thickness_increment;
cout<<segment::layer_thickness<<" , "<<layer_thickness_increment<<endl;
layer_thickness_initial_value=segment::layer_thickness;

double E_over_Gn_increment=0;
double temp_E_over_Gn_initial_value=0;
cout<<"Entering E/Gn ratio ->";
infile>>segment::E_over_Gn>>E_over_Gn_increment;
cout<<segment::E_over_Gn<<" , "<<E_over_Gn_increment<<endl;
temp_E_over_Gn_initial_value=segment::E_over_Gn;

double E_of_layer_increment=0;
cout<<"Entering Young's modulus (MPa) ->";
infile>>segment::E_of_layer>>E_of_layer_increment;
cout<<segment::E_of_layer<<" , "<<E_of_layer_increment<<endl;

double minimum_strength=0;
double minimum_strength_increment=0;
cout<<"Entering minimum strength (MPa) ->";
infile>>minimum_strength>>minimum_strength_increment;
cout<<minimum_strength<<" , "<<minimum_strength_increment<<endl;

double maximum_strength=0;
double maximum_strength_increment=0;
cout<<"Entering maximum strength (MPa) ->";
infile>>maximum_strength>>maximum_strength_increment;
segment::base_strength=maximum_strength;//MUST CHANGE THIS???
cout<<maximum_strength<<" , "<<maximum_strength_increment<<endl;
double maximum_strength_initial=maximum_strength;

int target_number_of_flaws=0;
int increment_number_of_flaws=0;
int temp_target_number_of_flaws=0;
cout<<"Entering number of flaws and increment ->";
infile>>target_number_of_flaws>>increment_number_of_flaws;
cout<<target_number_of_flaws<<" , "<<increment_number_of_flaws<<endl;
temp_target_number_of_flaws=target_number_of_flaws;
```

```
int additional_joints=0;
int additional_joints_increment=0;
cout<<"Entering number of additional joints ->";
infile>>additional_joints>>additional_joints_increment;
cout<<additional_joints<<" , "<<additional_joints_increment<<endl;

double non_jointing_layer_thickness_increment=0;
double temp_non_jointing_layer_thickness=0;
cout<<"Entering non-jointing layer thickness ->";
infile>>segment::non_jointing_layer_thickness>>non_jointing_layer_thick
ness_increment;
cout<<segment::non_jointing_layer_thickness<<" ,
"<<non_jointing_layer_thickness_increment<<endl;
temp_non_jointing_layer_thickness=segment::non_jointing_layer_thickness
;

double Tau_increment=0;
cout<<"Entering interface strength (MPa) ->";
infile>>segment::Tau>>Tau_increment;
cout<<segment::Tau<<" , "<<Tau_increment<<endl;

double jointing_layer_Poisson_ratio_increment=0;
cout<<"Entering jointing layer Poisson's ratio ->";
infile>>segment::jointing_layer_Poisson_ratio>>jointing_layer_Poisson_r
atio_increment;
cout<<segment::jointing_layer_Poisson_ratio<<" ,
"<<jointing_layer_Poisson_ratio_increment<<endl;
double
jointing_layer_Poisson_ratio_initial=segment::jointing_layer_Poisson_ra
tio;

double non_jointing_layer_Poisson_ratio_increment=0;
cout<<"Entering non-jointing layer Poisson's ratio ->";
infile>>segment::non_jointing_layer_Poisson_ratio>>non_jointing_layer_P
oisson_ratio_increment;
cout<<segment::non_jointing_layer_Poisson_ratio<<" ,
"<<non_jointing_layer_Poisson_ratio_increment<<endl;
double
non_jointing_layer_Poisson_ratio_initial=segment::non_jointing_layer_Po
isson_ratio;

double overburden_stress_increment=0;
cout<<"Entering overburden stress ->";
infile>>segment::overburden>>overburden_stress_increment;
cout<<segment::overburden<<" , "<<overburden_stress_increment<<endl;

double actual_skewness=0;
cout<<"Entering actual skewness ->";
infile>>actual_skewness;
cout<<actual_skewness<<endl;

double actual_SD=0;
cout<<"Entering actual SD ->";
infile>>actual_SD;
cout<<actual_SD<<endl;

double phi=0;//correlation factor
```

```
double phi_increment=0;
double initial_phi=0;
cout<<"Entering correlation factor, phi, and increment ->";
infile>>phi>>phi_increment;
cout<<phi<<" , "<<phi_increment<<endl;
initial_phi=phi;

double epsilon_SD=0;
double epsilon_SD_increment=0;
double epsilon_mean=0;
double epsilon_mean_increment=0;
double initial_epsilon_mean=0;
double initial_epsilon_SD=0;
cout<<"Entering epsilon mean, SD and their increments ->";
infile>>epsilon_mean>>epsilon_SD>>epsilon_mean_increment>>epsilon_SD_in
crement;
cout<<epsilon_mean<<" , "<<epsilon_SD<<" , "<<epsilon_mean_increment<<"
, "<<epsilon_SD_increment<<endl;
initial_epsilon_mean=epsilon_mean;
initial_epsilon_SD=epsilon_SD;

double random_bisection_start=1.0;
double random_bisection_start_increment=0.0;
cout<<"Entering fraction of intensity when random bisection starts ->";
infile>>random_bisection_start>>random_bisection_start_increment;
cout<<random_bisection_start<<" ,
"<<random_bisection_start_increment<<endl;
double random_bisection_start_initial=random_bisection_start;

//double crit_s_to_t=1.0;
//double crit_s_to_t_increment=0.0;
//cout<<"Entering critical spacing to thickness ratio and increment -
>";
//infile>>crit_s_to_t>>crit_s_to_t_increment;
//cout<<crit_s_to_t<<"\t"<<crit_s_to_t_increment<<endl;
//double crit_s_to_t_initial=crit_s_to_t;
//segment::critical_spacing_thickness_ratio=crit_s_to_t;

int total_number_of_simulations=1;

int number_of_cycles_flaws=1;
cout<<"Enter number of flaw densities ->";
cin>>number_of_cycles_flaws;
cout<<number_of_cycles_flaws<<endl;

total_number_of_simulations*=number_of_cycles_flaws;

int number_of_cycles=1;
cout<<"Enter number of Ef/Gn values ->";
cin>>number_of_cycles;
cout<<number_of_cycles<<endl;

total_number_of_simulations*=number_of_cycles;

int number_of_cycles_2=1;
cout<<"Enter number of non-jointing thickness values ->";
cin>>number_of_cycles_2;
```

```
cout<<number_of_cycles_2<<endl;

total_number_of_simulations*=number_of_cycles_2;

int number_of_cycles_phi=1;
cout<<"Enter number of phi values ->";
cin>>number_of_cycles_phi;
cout<<number_of_cycles_phi<<endl;

total_number_of_simulations*=number_of_cycles_phi;

int number_of_cycles_epsilon_SD=1;
cout<<"Enter number of epsilon_SD values ->";
cin>>number_of_cycles_epsilon_SD;
cout<<number_of_cycles_epsilon_SD<<endl;

total_number_of_simulations*=number_of_cycles_epsilon_SD;

int number_of_cycles_4=1;
cout<<"Enter number of maximum strength values ->";
cin>>number_of_cycles_4;
cout<<number_of_cycles_4<<endl;

total_number_of_simulations*=number_of_cycles_4;

int number_of_cycles_5=1;
cout<<"Enter number of jointing layer Poisson's ratios ->";
cin>>number_of_cycles_5;
cout<<number_of_cycles_5<<endl;

total_number_of_simulations*=number_of_cycles_5;

int number_of_cycles_6=1;
cout<<"Enter number of non-jointing layer Poisson's ratios ->";
cin>>number_of_cycles_6;
cout<<number_of_cycles_6<<endl;

total_number_of_simulations*=number_of_cycles_6;

char saturation='y';
cout<<"Apply saturation mechanism? (y/n) ";
cin>>saturation;
cout<<saturation<<endl;

char spacing_output='n';
cout<<"Spacing output? (y/n) ";
cin>>spacing_output;
cout<<spacing_output<<endl;
if(spacing_output=='Y' || spacing_output=='y')
{
ofstream outprepare("Spacing.xls");//clears the contents of file
outprepare.close();
}

char with_correlation='n';
cout<<"With strength correlation? (y/n) ";
cin>>with_correlation;
```

```
cout<<with_correlation<<endl;

char second_jointing_stage='n';
cout<<"Second jointing stage? (y/n) ";
cin>>second_jointing_stage;
cout<<second_jointing_stage<<endl;

char random_bisection='n';
cout<<"Random bisection if joint intensity is not reached? (y/n) ";
cin>>random_bisection;
cout<<random_bisection<<endl;

int number_of_cycles_3=1;
cout<<"Enter number of simulations per combination ->";
cin>>number_of_cycles_3;
cout<<number_of_cycles_3<<endl;

total_number_of_simulations*=number_of_cycles_3;

cout<<"\nThere will be "<<total_number_of_simulations<<"
simulations"<<endl;

infile.close();
//END OF INPUT STAGE

//FLAW FILE
/*ofstream out_flaw("Flaws.txt");
flaw* cur_flaw_pointer=flaw::starting_flaw;
for(int flaw_i=0;flaw_i<head_flaw->number_of_flaws;flaw_i++)
{
out_flaw<<cur_flaw_pointer->location<<"\t"<<cur_flaw_pointer-
>strength<<endl;
cur_flaw_pointer=cur_flaw_pointer->next_flaw;
};
out_flaw.close();*/
//END OF FLAW FILE CREATION

//ofstream out_prep("Stats_Distribution.txt");
//out_prep<<"SD\tSkewness"<<endl;
//out_prep.close();

ofstream out_2a("Skewness_and_SD_vs_E_over_Gn.xls");
out_2a<<"E/G\td\tMeanSkewness\tMeanSD\t%WithinSkewness\t%WithinSD\t%Wit
hinBoth\tMMean\tMNflaws\tPhi\te_SD\tcrit-s-t\tmax-
strength\tvf\tvn\tD"<<endl;
out_2a.close();

double sum_of_skewness=0;
double sum_of_SD=0;
double sum_of_mean=0;

int sum_of_flaws=0;

int number_within_mean_skewness=0;
int number_within_mean_SD=0;
int number_within_both_skewness_and_SD=0;
```

```
for (int jk0=0;jk0<number_of_cycles_flaws;jk0++)//for number of flaws
{
for(int jk1=0;jk1<number_of_cycles;jk1++)//for E_over_Gn
{
for(int jk2=0;jk2<number_of_cycles_2;jk2++)//for non-jointing layer
thickness
{
for(int jk4=0;jk4<number_of_cycles_phi;jk4++)//for correlation factor
phi
{
for(int jk5=0;jk5<number_of_cycles_epsilon_SD;jk5++)//for epsilon_SD
{
for(int jk6=0;jk6<number_of_cycles_4;jk6++)//for maximum strength
{
for(int jk7=0;jk7<number_of_cycles_5;jk7++)//for jointing layer
Poisson's ratios
{
for(int jk8=0;jk8<number_of_cycles_6;jk8++)//for non-jointing layer
Poisson's ratios
{
for(int jk3=0;jk3<number_of_cycles_3;jk3++)//within one combination of
values
{
//CREATE FLAWS
//determine flaw locations first
if(with_correlation=='y' || with_correlation=='Y')
{
head_flaw=new flaw(get_random_number01()*segment::layer_length,0);
flaw::starting_flaw=head_flaw;
for(int i=0;i<target_number_of_flaws-1;i++)
{
flaw::starting_flaw-
>insert_new_flaw(get_random_number01()*segment::layer_length,0);
}
head_flaw=flaw::starting_flaw;

//now assign flaw strengths considering correlations.  go from left to
right.
flaw* current_flaw=flaw::starting_flaw->next_flaw;
flaw* previous_flaw=flaw::starting_flaw;
StochasticLib1 sto(time(NULL));//the normal variate comes from here
//assign strength to first flaw only
//flaw::starting_flaw-
>strength=minimum_strength+get_random_number01()*(maximum_strength-
minimum_strength);
double mean_tensile_strength=(maximum_strength+minimum_strength)/2;
flaw::starting_flaw-
>strength=mean_tensile_strength*exp(sto.Normal(epsilon_mean,epsilon_SD)
);

double current_strength=0;
//assign strengths to the rest of the flaws
for(int flaw_num=0;flaw_num<flaw::number_of_flaws-1;flaw_num++)
{
```

```
current_strength=mean_tensile_strength*exp(phi*log(previous_flaw-
>strength/mean_tensile_strength)+sto.Normal(epsilon_mean,epsilon_SD));/
/correlation model
//Normal takes mean and SD as arguments
//if(current_strength>0)
//    current_flaw->strength=current_strength;
//if(current_strength<=0)
//    current_flaw->strength=0.00001;//lower bound on strength, can't
be negative
current_flaw->strength=current_strength;
previous_flaw=current_flaw;
current_flaw=current_flaw->next_flaw;
}
}

if(with_correlation=='n' || with_correlation=='N')
{
head_flaw=new flaw(get_random_number01()*segment::layer_length,
minimum_strength+get_random_number01()*(maximum_strength-
minimum_strength));
flaw::starting_flaw=head_flaw;
for(int i=0;i<target_number_of_flaws-1;i++)
{
flaw::starting_flaw-
>insert_new_flaw(get_random_number01()*segment::layer_length,
minimum_strength+get_random_number01()*(maximum_strength-
minimum_strength));
}
head_flaw=flaw::starting_flaw;
}

//head_flaw->write_restart_file();//check flaw data
//head_flaw=new flaw(164.08081054688,20.0192);
//flaw::starting_flaw=head_flaw;
//head_flaw->next_flaw=new flaw(256.95190429688,20.0284);
//END OF FLAW CREATION

//minimum_strength+get_random_number01()*(maximum_strength-
minimum_strength)

//CREATE JOINTING LAYER AND FIND INITIAL JOINTING STRAIN
head_segment=new segment(0,segment::layer_length);
segment::starting_segment=head_segment;
//cout<<"Initial slippage strain - un-initialized ->"<<head_segment-
>slippage_strain<<endl;
head_segment->calc_beta();
head_segment->calc_critical_spacing_thickness_ratio();
head_segment->calc_slippage_strain();
head_segment->check_for_midpoint_fracturing();
head_segment->assign_min_strains(head_flaw);
//cout<<"Initial minimum strain -> "<<head_segment->min_strain<<endl;
//cout<<"Initial slippage strain -> "<<head_segment-
>slippage_strain<<endl;
/*if(head_segment->min_strain>=head_segment->slippage_strain)
{
cout<<"Program Terminated: Minimum required strain exceeds initial
slippage strain, jointing cannot occur."<<endl;
```

```
return 0;
};*/
//END OF JOINTING LAYER CREATION AND FINDING INITIAL JOINTING STRAIN

//PREPARE STATS.TXT
//ofstream outfile("Stats.txt");
//outfile<<"strain\tspacing\tSD\tskewness\n";
//outfile.close();
//END OF STATS.TXT PREPARATION

//NEW JOINT FORMATION
//cout<<(int)(random_bisection_start*additional_joints)<<endl;
//cout<<(int)((1-random_bisection_start)*additional_joints)<<endl;
if(saturation=='Y' || saturation=='y')
{
if(second_jointing_stage=='n' || second_jointing_stage=='N')
{
for(int kl=0;kl<additional_joints;kl++)
head_segment->place_new_joint_and_update_new_segments(head_flaw);
}
if(second_jointing_stage=='y' || second_jointing_stage=='Y')
{
for(int kl=0;kl<(int)(random_bisection_start*additional_joints);kl++)
head_segment->place_new_joint_and_update_new_segments(head_flaw);
}
}

if(saturation=='N' || saturation=='n')
{
if(second_jointing_stage=='n' || second_jointing_stage=='N')
{
for(int klm=0;klm<additional_joints;klm++)
head_segment-
>place_new_joint_and_update_new_segments_no_sat(head_flaw);
}

if(second_jointing_stage=='y' || second_jointing_stage=='Y')
{
for(int
klm=0;klm<(int)(random_bisection_start*additional_joints);klm++)
head_segment-
>place_new_joint_and_update_new_segments_no_sat(head_flaw);
}
}

//cout<<segment::number_of_segments<<endl;

if(second_jointing_stage=='y' || second_jointing_stage=='Y')
{
for(int kln=0;kln<(int)((1-
random_bisection_start)*additional_joints);kln++)
head_segment->halve_segment_using_random_bisection();//Note that
strains are not updated here anymore!!!!
}

if(random_bisection=='y' || random_bisection=='Y')
{
```

```
int number_of_joints_needed=additional_joints-head_segment-
>number_of_segments;
if(number_of_joints_needed>0)
{
for(int
extra_joints=0;extra_joints<number_of_joints_needed;extra_joints++)
head_segment->halve_segment_using_random_bisection();//Note that
strains are no longer updated here!
}
}

//cout<<segment::number_of_segments<<endl;
//END OF NEW JOINT FORMATION
//};
/*
if(res=='y' || res=='Y')
{
ifstream in_seg("Segment_Restart.txt");
//outfile<<layer_thickness<<"\t"<<non_jointing_layer_thickness<<"\t"<<m
ax_length<<"\t"<<min_length<<endl;
//outfile<<E_over_Gn<<"\t"<<E_of_layer<<"\t"<<Tau<<"\t"<<base_strength<
<"\t"<<number_of_segments<<endl;
//outfile<<cur->end1<<"\t"<<cur->end2<<"\t"<<cur-
>segment_length<<"\t"<<cur->min_strain<<"\t"<<cur-
>slippage_strain<<"\t"<<cur->joint_location<<endl;
in_seg>>segment::layer_thickness>>segment::non_jointing_layer_thickness
>>segment::max_length>>segment::min_length;
in_seg>>segment::E_over_Gn>>segment::E_of_layer>>segment::Tau>>segment:
:base_strength>>segment::number_of_segments;
double e1=0,e2=0,s_l=0,min_s=0,slip_s=0,j_l=0;
in_seg>>e1>>e2>>s_l>>min_s>>slip_s>>j_l;
head_segment=new segment(e1,e2);
//head_segment->segment_length=s_l;
head_segment->min_strain=min_s;
head_segment->slippage_strain=slip_s;
head_segment->joint_location=j_l;
segment::starting_segment=head_segment;
segment* cur_seg=head_segment;

for(int j=0;j<segment::number_of_segments-1;j++)
{
in_seg>>e1>>e2>>s_l>>min_s>>slip_s>>j_l;
cur_seg->next_segment=new segment(e1,e2);
//cur_seg->next_segment->segment_length=s_l;
cur_seg->next_segment->min_strain=min_s;
cur_seg->next_segment->slippage_strain=slip_s;
cur_seg->next_segment->joint_location=j_l;
cur_seg=cur_seg->next_segment;
}
in_seg.close();

ifstream in_flaw("Flaw_Restart.txt");
in_flaw>>flaw::number_of_flaws;
//outfile<<cur->location<<"\t"<<cur->strength<<endl;
double loc=0,str=0;
in_flaw>>loc>>str;
head_flaw=new flaw(loc,str);
```

```
flaw::starting_flaw=head_flaw;
flaw* cur_flaw=head_flaw;

for(int k=0;k<flaw::number_of_flaws-1;k++)
{
in_flaw>>loc>>str;
cur_flaw->next_flaw=new flaw(loc,str);
cur_flaw=cur_flaw->next_flaw;
}
in_flaw.close();

int add_seg=0;
cout<<"Enter additional number of segments ->";
cin>>add_seg;

for(int m=0;m<add_seg;m++)
head_segment->place_new_joint_and_update_new_segments(head_flaw);
};
*/
//WRITE OUTPUT TO FILES
//cout<<"There are "<<head_segment->number_of_segments<<" spacing
values."<<endl;
//cout<<head_segment->check_saturation()<<endl;
//cout<<"done!"<<endl;
//ofstream out_1("Stats_Distribution.txt",ios::app);
//out_1<<head_segment->get_standard_deviation()<<
//     "\t"<<head_segment->get_skewness()<<endl;
//out_1.close();
//head_segment->write_strains_to_file();
if(spacing_output=='Y' || spacing_output=='y')
{
head_segment->write_spacing_to_file();
}
//head_segment->write_joint_pattern_to_file();
//head_segment->write_moving_average_data_to_file_overlap(7);
//head_segment->write_restart_file();
//head_flaw->write_restart_file();
//END OF WRITE OUTPUT TO FILES

double temp_skewness=head_segment->get_skewness();
double temp_SD=head_segment->get_standard_deviation();

sum_of_skewness+=temp_skewness;
sum_of_SD+=temp_SD;
sum_of_mean+=segment::layer_length/segment::number_of_segments;

sum_of_flaws+=flaw::number_of_flaws;

if(fabs(actual_skewness-temp_skewness)/actual_skewness<=0.1 &&
fabs(actual_SD-temp_SD)/actual_SD<=0.1)
number_within_both_skewness_and_SD++;//within 10% of actual skewness
and SD
if(fabs(actual_skewness-temp_skewness)/actual_skewness<=0.1)
number_within_mean_skewness++;//within 10% of actual skewness
if(fabs(actual_SD-temp_SD)/actual_SD<=0.1)
number_within_mean_SD++;//within 10% of actual SD
```

```
//DELETE SEGMENTS
segment* cur_seg=head_segment;
segment* cur_next_seg=head_segment->next_segment;
int segment_population=segment::number_of_segments;//because
segment::number_of_segments changes every time one is deleted
for(int del_n=0;del_n<segment_population;del_n++)
{
if(cur_seg!=0) delete cur_seg;
cur_seg=cur_next_seg;
if(cur_next_seg!=0) cur_next_seg=cur_next_seg->next_segment;
};
//cout<<"There are now "<<segment::number_of_segments<<"
segments."<<endl;
//END of DELETE SEGMENTS

//DELETE FLAWS
flaw* cur_flaw=head_flaw;
flaw* cur_next_flaw=head_flaw->next_flaw;
int flaw_population=flaw::number_of_flaws;
for(int del_f=0;del_f<flaw_population;del_f++)
{
if(cur_flaw!=0) delete cur_flaw;
cur_flaw=cur_next_flaw;
if(cur_next_flaw!=0) cur_next_flaw=cur_next_flaw->next_flaw;
};
//cout<<"There are now "<<flaw::number_of_flaws<<" flaws."<<endl;
//END of DELETE FLAWS

//ADD INCREMENTS TO PARAMETERS

//segment::layer_thickness+=layer_thickness_increment;

//END OF ADD INCREMENTS TO PARAMETERS
}
ofstream out_2("Skewness_and_SD_vs_E_over_Gn.xls",ios::app);
out_2<<segment::E_over_Gn<<"\t"<<segment::non_jointing_layer_thickness<
<"\t"<<sum_of_skewness/number_of_cycles_3<<
"\t"<<sum_of_SD/number_of_cycles_3<<
"\t"<<(double) number_within_mean_skewness/number_of_cycles_3<<
"\t"<<(double) number_within_mean_SD/number_of_cycles_3<<
"\t"<<(double) number_within_both_skewness_and_SD/number_of_cycles_3<<
"\t"<<sum_of_mean/number_of_cycles_3<<"\t"<<sum_of_flaws/number_of_cycl
es_3<<
"\t"<<phi<<"\t"<<epsilon_SD<<"\t"<<segment::critical_spacing_thickness_
ratio<<
"\t"<<maximum_strength<<"\t"<<segment::jointing_layer_Poisson_ratio<<
"\t"<<segment::non_jointing_layer_Poisson_ratio<<"\t"<<segment::paramet
er_D<<endl;

out_2.close();
number_within_mean_skewness=0;
number_within_mean_SD=0;
number_within_both_skewness_and_SD=0;
sum_of_skewness=0;
sum_of_SD=0;
sum_of_mean=0;
sum_of_flaws=0;
```

```
segment::non_jointing_layer_Poisson_ratio+=non_jointing_layer_Poisson_r
atio_increment;
}
segment::jointing_layer_Poisson_ratio+=jointing_layer_Poisson_ratio_inc
rement;
segment::non_jointing_layer_Poisson_ratio=non_jointing_layer_Poisson_ra
tio_initial;
}
maximum_strength+=maximum_strength_increment;
segment::base_strength=maximum_strength;
segment::jointing_layer_Poisson_ratio=jointing_layer_Poisson_ratio_init
ial;
}
epsilon_SD+=epsilon_SD_increment;
maximum_strength=maximum_strength_initial;
segment::base_strength=maximum_strength;
}
phi+=phi_increment;
epsilon_SD=initial_epsilon_SD;
}
//segment::layer_length+=layer_length_increment;
//segment::E_over_Gn+=E_over_Gn_increment;
//segment::Tau+=Tau_increment;
//segment::E_of_layer+=E_of_layer_increment;
//minimum_strength+=minimum_strength_increment;
//maximum_strength+=maximum_strength_increment;
//segment::base_strength=maximum_strength;
//additional_joints+=additional_joints_increment;
//if(segment::non_jointing_layer_thickness==0.05)
segment::non_jointing_layer_thickness=0.14;
segment::non_jointing_layer_thickness+=non_jointing_layer_thickness_inc
rement;
phi=initial_phi;
//segment::jointing_layer_Poisson_ratio+=jointing_layer_Poisson_ratio_i
ncrement;
//segment::non_jointing_layer_Poisson_ratio+=non_jointing_layer_Poisson
_ratio_increment;
//RESET LAYER THICKNESS
//segment::layer_thickness=layer_thickness_initial_value;
}
segment::E_over_Gn+=E_over_Gn_increment;
segment::non_jointing_layer_thickness=temp_non_jointing_layer_thickness
;
}
target_number_of_flaws+=increment_number_of_flaws;
segment::E_over_Gn=temp_E_over_Gn_initial_value;
}

//cout<<time(NULL)<<endl;
//system("PAUSE");
return 0;
};//END OF MAIN()
/*************************************************************/

//global function to get random number
//gets the jth number from the file Random.txt
```

```
double get_random_number(int j)
{
double rn=0;
ifstream in("Random.txt");
for (int i=0; i<j; i++)
in>>rn;
in.close();
random_number_taken++;
//cout<<rn<<endl;
return rn;
};

//global function to get normal random number
//gets the jth number from the file Random_Normal.txt
double get_normal_number(int j)
{
double rn=0;
ifstream in("Random_Normal.txt");
for (int i=0; i<j; i++)
in>>rn;
in.close();
normal_number_taken++;
//cout<<rn<<endl;
return rn;
};

double get_random_number01()
{
return ((double) rand()/ (double) (RAND_MAX+1));
};
```

10.2 Rejection Procedure Code

```
#include <math.h>
#include <stdio.h>
#include <fstream.h>
#include <stdlib.h>
#include <sys/types.h>
#include <time.h>

//declare some global functions
double get_random_number(int);
double get_normal_number(int);
double get_random_number01();

//declare some global variables
int random_number_taken=0;
int normal_number_taken=0;

class flaw
{
public:

double flaw_location;
double percent_strength;//percent of the tensile strength remaining due
to the flaw
flaw* next_flaw;
//flaw* previous_flaw;
static double min_percent_strength;//min strength the flaw can reduce
the section to
static int number_of_flaws;
static int target_number_of_flaws;
static flaw* starting_flaw;
//int mark;

//default constructor
flaw()
{
flaw_location=0;
percent_strength=0;
next_flaw=0;
//previous_flaw=0;
//mark=0;
number_of_flaws++;
};

//another constructor
flaw(double location, double percent_str)
{
flaw_location=location;
percent_strength=percent_str;
next_flaw=0;
//previous_flaw=0;
//mark=0;
number_of_flaws++;
};
```

```
//destructor
~flaw() {number_of_flaws--;};

//!!use the starting flaw to call this function!!
//note that the first generated flaw is the starting flaw
//the first generated flaw may no longer  be the starting flaw as new
flaws are generated
void flaw::insert_new_flaw(double new_flaw_loc, double new_flaw_str)
{
flaw* cur_flaw=this;

if(new_flaw_loc>=cur_flaw->flaw_location)
{
if(cur_flaw->next_flaw==0)
{
cur_flaw->next_flaw=new flaw(new_flaw_loc,new_flaw_str);
//cur_flaw->next_flaw->previous_flaw=cur_flaw;
return;
}

if(new_flaw_loc>cur_flaw->next_flaw->flaw_location)
cur_flaw->next_flaw->insert_new_flaw(new_flaw_loc,new_flaw_str);

if(new_flaw_loc<=cur_flaw->next_flaw->flaw_location)
{
flaw* temp=new flaw(new_flaw_loc,new_flaw_str);
temp->next_flaw=cur_flaw->next_flaw;
//cur_flaw->next_flaw->previous_flaw=temp;
//temp->previous_flaw=cur_flaw;
cur_flaw->next_flaw=temp;
return;
}

}

if(new_flaw_loc<cur_flaw->flaw_location)
{
flaw* temp=new flaw(new_flaw_loc,new_flaw_str);
temp->next_flaw=cur_flaw;
//temp->previous_flaw=cur_flaw->previous_flaw;
//cur_flaw->previous_flaw=temp;
flaw::starting_flaw=temp;
return;
}
};

};//END OF FLAW CLASS

class segment
{
public:
double end1;
double end2;
double segment_length;
segment* next_segment;
static double layer_length;
static double layer_thickness;
```

```
static double non_jointing_layer_thickness;
static double max_length;
static double min_length;
static double shadow_length;
static double limit_spacing;
static double E_over_Gn;
static double E_of_layer;
static double epsilon1;
static double valid_total_jointing_length;
static double critical_spacing_thickness_ratio;
static int number_of_segments;
static int target_number_of_segments;
static segment* longest_segment;
static segment* starting_segment;

static double non_jointing_layer_Poisson_ratio;
static double jointing_layer_Poisson_ratio;
static double parameter_D;
static double overburden;
static double beta;

//default constructor
segment()
{
end1=0;
end2=0;
segment_length=0;
next_segment=0;
number_of_segments++;
};

//another constructor
segment(double e1, double e2)
{
end1=e1;
end2=e2;
segment_length=end2-end1;
next_segment=0;
number_of_segments++;
};

//default destructor
~segment() {number_of_segments--;};

//function that divides all segments into smaller ones
//max spacing after this function is called will be <=2*shadow_length
//min spacing after this function is called will be >=shadow_length
//this function is recursive and stops only when all the segments
//are shorter than twice the shadow_length
//USE THE HEAD SEGMENT TO CALL THIS FUNCTION!!!
void segment::divide_all_segments()
{
//cout<<".";
if(this->segment_length<=2*shadow_length && this->next_segment==0)
return;
if(this->segment_length>2*shadow_length)
{
```

```
double rn=0;
rn=get_random_number(random_number_taken+1);
rn*=(this->segment_length-2*shadow_length);
segment* temp=0;
temp=new segment(this->end1+shadow_length+rn, this->end2);
temp->next_segment=this->next_segment;
this->next_segment=temp;
this->end2=this->next_segment->end1;//update the ends of the original
segment
this->update_length();
this->divide_all_segments();
}
if(this->segment_length<=2*shadow_length && this->next_segment!=0)
this->next_segment->divide_all_segments();
};

//function to calculate the stress at some location within a segment
double segment::calculate_stress_ratio(double dist_from_mdpt)
{
double ratio=0;
double
Beta=sqrt(8*segment::E_of_layer*(1/segment::E_over_Gn)/(segment::E_of_l
ayer*segment::layer_thickness*segment::non_jointing_layer_thickness));
double arg_numer=Beta*dist_from_mdpt;
double arg_denom=Beta*(segment_length/2);
if(fabs(arg_numer)>710.475 && fabs(arg_denom)>710.475)
{
if(dist_from_mdpt<0) dist_from_mdpt=(-1)*dist_from_mdpt;
double new_x=(segment_length/2)-dist_from_mdpt;
ratio=(1-exp(-Beta*new_x));
return ratio;
}
double cosh_numer=cosh(arg_numer);
double cosh_denom=cosh(arg_denom);
ratio=(1-(cosh_numer/cosh_denom));
return ratio;

/*double denom=cosh((segment_length/layer_thickness)/sqrt(E_over_Gn));
double numer=cosh(2*(loc/layer_thickness)/sqrt(E_over_Gn));
//note that loc is with respect to the segment midpoint

double ratio=1-(numer/denom);
return ratio;
*/
};

//LambertW function
double segment::LambertW(const double z)
{
int i;
const double eps=4.0e-16, em1=0.3678794411714423215955237701614608;
double p,e,t,w;
//if (dbgW) fprintf(stderr,"LambertW: z=%g\n",z);
/*if (z<-em1 || isinf(z) || isnan(z)) {
fprintf(stderr,"LambertW: bad argument %g, exiting.\n",z); exit(1);
}*/
if (0.0==z) return 0.0;
```

```
if (z<-em1+1e-4) { // series near -em1 in sqrt(q)
double q=z+em1,r=sqrt(q),q2=q*q,q3=q2*q;
return
-1.0
+2.331643981597124203363536062168*r
-1.812187885639363490240191647568*q
+1.936631114492359755363277457668*r*q
-2.353551201881614516821543561516*q2
+3.066858901050631912893148922704*r*q2
-4.175335600258177138854984177460*q3
+5.858023729874774148815053846119*r*q3
-8.401032217523977370984161688514*q3*q;  // error approx 1e-16
}
/* initial approx for iteration... */
if (z<1.0) { /* series near 0 */
p=sqrt(2.0*(2.718281828459045235360287471352662 5*z+1.0));
w=-1.0+p*(1.0+p*(-
0.333333333333333333333+p*0.152777777777777777777777));
}
else
w=log(z); /* asymptotic */
if (z>3.0) w-=log(w); /* useful? */
for (i=0; i<10; i++) { /* Halley iteration */
e=exp(w);
t=w*e-z;
p=w+1.0;
t/=e*p-0.5*(p+1.0)*t/p;
w-=t;
if (fabs(t)<eps*(1.0+fabs(w))) return w; /* rel-abs error */
}
/* should never get here */
//  fprintf(stderr,"LambertW: No convergence at z=%g, exiting.\n",z);
//  exit(1);
};

//get_root_L function,
double segment::get_root_L(double const cumulative, double const
lambda,
double const d,double const Gm, double const Ef)
{
//if(cumulative>0.9999) return get_root_L(0.9999,lambda,d,Gm,Ef);
double const_a=-2*log(1-cumulative)+d*lambda*sqrt(Ef/Gm);
double Lambert_arg=-exp(-(const_a/(d*lambda*sqrt(Ef/Gm))));
double LambertW_result=LambertW(Lambert_arg);
double const_b=d*lambda*sqrt(Ef/Gm)*LambertW_result;
double return_arg=(const_b+const_a)/(2*lambda);
return (const_b+const_a)/(2*lambda);
};

//function to insert a new segment into an existing segment
//loc is the distance from end1 of the starting segment to joint
location
void segment::insert_new_segment(double loc)
{
if (loc<=this->end1 || loc>=this->end2) return;

segment* temp=new segment(loc,this->end2);
```

```
//layer_length-=temp->segment_length;//there should be no additional
length
temp->next_segment=this->next_segment;
this->next_segment=temp;
this->end2=temp->end1;
this->update_length();
if(longest_segment==this) starting_segment->set_max_spacing();//update
the longest segment

if(this-
>segment_length/segment::layer_thickness<=segment::critical_spacing_thi
ckness_ratio)
segment::valid_total_jointing_length-=this->segment_length;
if(this->next_segment-
>segment_length/segment::layer_thickness<=segment::critical_spacing_thi
ckness_ratio)
segment::valid_total_jointing_length-=this->next_segment-
>segment_length;

return;
};

void segment::calc_parameter_D()
{
parameter_D=((1-
2*jointing_layer_Poisson_ratio)*(1+jointing_layer_Poisson_ratio)-(1-
2*non_jointing_layer_Poisson_ratio)*(1+non_jointing_layer_Poisson_ratio
))/((1-jointing_layer_Poisson_ratio*jointing_layer_Poisson_ratio)+(1-
non_jointing_layer_Poisson_ratio*non_jointing_layer_Poisson_ratio));
return;
};

void segment::calc_critical_spacing_thickness_ratio()
{
calc_parameter_D();
double beta_1=(0.976-0.302*parameter_D-
0.129*parameter_D*parameter_D+0.117*parameter_D*parameter_D*parameter_D
)/0.976;
double
alpha_1=segment::E_over_Gn/(2*(1+segment::non_jointing_layer_Poisson_ra
tio));
double gamma_1=(0.976+1.118e-4*overburden-7.562e-
8*overburden*overburden+2.806e-
9*overburden*overburden*overburden)/0.976;
segment::critical_spacing_thickness_ratio=beta_1*gamma_1*(0.792+0.328*(
1-exp(-0.824*pow(alpha_1-0.0025,0.824))));
return;
};

//function to calculate beta, note that there is only one value for
beta for the entire layer
void segment::calc_beta()
{
beta=sqrt(8*segment::E_of_layer*(1/segment::E_over_Gn)/(segment::E_of_l
ayer*segment::layer_thickness*segment::non_jointing_layer_thickness));
return;
};
```

```
//function that inserts new segments based on a rejection procedure
void segment::halve_segment_using_rejection()
{
double
new_joint_loc=get_random_number01()*segment::valid_total_jointing_lengt
h;//based on the valid lengths only!!!
segment* temp=starting_segment;
segment* target_segment=0;
double sum_of_valid_lengths=0;
double sum_of_invalid_lengths=0;

for(int i_loc=0; i_loc<number_of_segments; i_loc++)
{
if(temp-
>segment_length/segment::layer_thickness<=segment::critical_spacing_thi
ckness_ratio)
sum_of_invalid_lengths+=temp->segment_length;
if(temp-
>segment_length/segment::layer_thickness>segment::critical_spacing_thic
kness_ratio)
sum_of_valid_lengths+=temp->segment_length;

if(sum_of_valid_lengths>=new_joint_loc)//remember that new_joint_loc at
this point is based on the total valid length only!!
{
target_segment=temp;
break;//get out of the 'for' loop once target segment is found
}//inside of these brackets is executed ONLY when a valid segment is
found!!!

temp=temp->next_segment;
}

//now add the sum_of_invalid_lengths to new_joint_loc so that we can
start at end1 of the starting segment!!!
new_joint_loc+=sum_of_invalid_lengths;
//new_joint_loc is NOW the distance from end1 of the starting segment
to the prospective new joint location in a VALID SEGMENT

//NEXT STEPS:
//1.  calculate the stress ratio at new_joint_loc
if(target_segment==0) cout<<segment::valid_total_jointing_length<<" ,
"<<new_joint_loc<<endl;


//if(target_segment!=0)
//{
double loc_within_segment=0.5*(target_segment->end1+target_segment-
>end2)-new_joint_loc;
double stress_ratio_at_new_jt_loc=target_segment-
>calculate_stress_ratio(loc_within_segment);

//2.  calculate the maximum stress at the midpoint of the longest
segment

double max_stress_ratio=longest_segment->calculate_stress_ratio(0);
```

```
//3.  divide the result in 1 by the result in 2

double probability_1=stress_ratio_at_new_jt_loc/max_stress_ratio;

//4.  compare with a random number generated by get_random_number01()

double probability_2=get_random_number01();

//5.  keep if ratio of stress is greater, discard if lower (call
function again)

if(probability_1>=probability_2)
{
target_segment->insert_new_segment(new_joint_loc);
return;
}

if(probability_1<probability_2)
starting_segment->halve_segment_using_rejection();
//}
}

//random bisection of a segment in the layer
void segment::halve_segment_using_random_bisection()
{
double new_joint_loc=get_random_number01()*segment::layer_length;
segment* temp=starting_segment;
segment* target_segment=0;

for(int i=0; i<segment::number_of_segments;i++)
{
if(new_joint_loc>=temp->end1 && new_joint_loc<temp->end2)
{
target_segment=temp;
break;//get out of loop when target segment is found
}

temp=temp->next_segment;
}

target_segment->insert_new_segment(new_joint_loc);
return;
};

//function to update the length of the segment after the addition of a
new joint
void segment::update_length()
{
this->segment_length=end2-end1;
return;
};

//function to determine the fraction of spacing values below critical
double segment::get_fraction_below_critical_spacing(double crit_ratio)
{
int num_below_crit=0;
```

```
segment* cur_seg=segment::starting_segment;
for(int i=0;i<segment::number_of_segments;i++)
{
if(cur_seg->segment_length/segment::layer_thickness<crit_ratio)
num_below_crit++;
cur_seg=cur_seg->next_segment;
}
return (double) (num_below_crit/segment::number_of_segments);
};

//write the spacing data to file
//use the ONLY head segment to call this function
void segment::write_spacing_to_file()
{
segment* cur=this;
ofstream out("Spacing.xls",ios::app);
out<<"SPACING BREAK"<<endl;
for(int j=0; j<number_of_segments; j++)
{
out<<cur->segment_length<<endl;
cur=cur->next_segment;
}
out.close();
return;
};

//writes the joint pattern to be displayed in sigmaplot
void segment::write_joint_pattern_to_file()
{
ofstream out("Pattern.txt");
double x_coord=0;
double y_coord=0;

out<<x_coord<<"\t"<<y_coord<<endl;
y_coord+=segment::layer_thickness;
out<<x_coord<<"\t"<<y_coord<<endl;

segment* cur=this;
for(int i=0;i<segment::number_of_segments;i++)
{
x_coord+=cur->segment_length;
out<<x_coord<<"\t"<<y_coord<<endl;
if(y_coord==segment::layer_thickness) y_coord-
=segment::layer_thickness;
else y_coord+=segment::layer_thickness;
out<<x_coord<<"\t"<<y_coord<<endl;
cur=cur->next_segment;
}
out.close();
};

//write the joint locations to file
//use ONLY the head segment to call this function
void segment::write_joint_locations_to_file()
{
segment* cur=this;
ofstream out("Joints.txt");
```

```
for(int j=0; j<number_of_segments; j++)
{
out<<cur->end1<<endl;
if (cur->next_segment=0) out<<cur->end2;
cur=cur->next_segment;
}
out.close();
return;
};

//writes the moving average to a file
//calculates the moving average at n segment intervals.
//segments used in calculation overlap unlike the first moving average
function
void write_moving_average_data_to_file_overlap(int n)
{
segment* cur_starting_segment=starting_segment;
segment* cur=0;
double x_coord=0;
double moving_average=0;
ofstream out("Moving_Ave_1.txt");

for(int k=0;k<n-1;k++)
{
moving_average+=cur_starting_segment->segment_length;
x_coord=moving_average/2;//midpoint of the total segment considered so
far
out<<x_coord<<"\t"<<moving_average/(k+1)<<endl;
cur_starting_segment=cur_starting_segment->next_segment;
}

cur_starting_segment=starting_segment;//restart from the first segment

for(int i=0;i<number_of_segments;i++)
{
cur=cur_starting_segment;
int indicator=0;
moving_average=0;
x_coord=cur_starting_segment->end1;
for(int j=0;j<n;j++)
{
indicator++;
moving_average+=cur->segment_length;
if(cur->next_segment==0 || indicator==n)
{
j=n-1;//force loop to finish
x_coord+=moving_average/2;//at this point moving average is just the
sum of n segments from current starting seg.
moving_average=moving_average/indicator;
out<<x_coord<<"\t"<<moving_average<<endl;
}
cur=cur->next_segment;
}
cur_starting_segment=cur_starting_segment->next_segment;
}
out.close();
return;
```

```
};

//function to get the maximum spacing
//use only the HEAD segment to call this function
//also sets the longest_segment pointer to the location of the longest
segment
void segment::set_max_spacing()
{
double smax=0;
segment* cur=this;
for(int i=0; i<number_of_segments; i++)
{
if(cur->segment_length>smax)
{
smax=cur->segment_length;
longest_segment=cur;
}
cur=cur->next_segment;
}
max_length=smax;
return;
};

//function to get the minimum spacing
//use only the HEAD segment to call this function
void segment::set_min_spacing()
{
double smin=layer_length;
segment* cur=this;
for(int i=0; i<number_of_segments; i++)
{
if(cur->segment_length<smin) smin=cur->segment_length;
cur=cur->next_segment;
}
min_length=smin;
return;
};

//function to get the total segment length
double segment::get_total_segment_length()
{
double sum=0;
segment* cur=this;
for(int i=0; i<number_of_segments; i++)
{
sum+=cur->segment_length;
cur=cur->next_segment;
}
return sum;
};

//function to get the mean length
double segment::get_mean_length()
{
return segment::layer_length/segment::number_of_segments;
};
```

```
//function to get the standard deviation of all segment lengths
double segment::get_standard_deviation()
{
double sum=0;
double mean_segment_length=starting_segment-
>get_total_segment_length()/number_of_segments;
//cout<<"\nMean segment length = "<<mean_segment_length<<"\n";
segment* cur=this;//called by the head segment
for (int i=0; i<number_of_segments; i++)
{
sum+=((cur->segment_length-mean_segment_length)*(cur->segment_length-
mean_segment_length));
cur=cur->next_segment;
}
return sqrt(sum/(number_of_segments-1));
};

//function to calculate skewness
double segment::get_skewness()
{
double skewness=0;
double mean_segment_length=starting_segment-
>get_total_segment_length()/number_of_segments;
double stdev=this->get_standard_deviation();
segment* cur=this;
for (int i=0;i<number_of_segments; i++)
{
skewness+=((cur->segment_length-mean_segment_length)/stdev)*((cur-
>segment_length-mean_segment_length)/stdev)*((cur->segment_length-
mean_segment_length)/stdev);
cur=cur->next_segment;
}
return skewness*(number_of_segments)/((number_of_segments-
1)*(number_of_segments-2));
};

//calculates the kurtosis of the simulated spacing data
double segment::get_kurtosis(double standard_dev)
{
double kurtosis=0;
double average=segment::layer_length/segment::number_of_segments;
segment* cur_seg=segment::starting_segment;
for(int i=0;i<segment::number_of_segments;i++)
{
kurtosis+=pow(((cur_seg->segment_length-average)/standard_dev),4);
cur_seg=cur_seg->next_segment;
}
int n_minus_1=segment::number_of_segments-1;
int n_minus_2=n_minus_1-1;
int n_minus_3=n_minus_2-1;
int n_plus_1=segment::number_of_segments+1;
double factor_1=(double)
(segment::number_of_segments*n_plus_1/(n_minus_1*n_minus_2*n_minus_3));
double factor_2=(double) (3*n_minus_1*n_minus_1/(n_minus_2*n_minus_3));
return (factor_1*kurtosis-factor_2);
};
```

```
};//END OF SEGMENT CLASS

//initialize the static variables
int segment::number_of_segments=0;
int segment::target_number_of_segments=0;
double segment::layer_length=0;
double segment::max_length=0;
double segment::E_over_Gn=0;
double segment::shadow_length=0;//Determined by the layer thickness and
the E/Gn ratio via Hobbs 1967
double segment::min_length=segment::layer_length;
double segment::layer_thickness=0;
double segment::non_jointing_layer_thickness=0;
double segment::limit_spacing=0.012;
double segment::epsilon1=0;
double segment::E_of_layer=0;
double segment::valid_total_jointing_length=0;
double segment::critical_spacing_thickness_ratio=0;

double segment::beta=0;
double segment::non_jointing_layer_Poisson_ratio=0;
double segment::jointing_layer_Poisson_ratio=0;
double segment::parameter_D=0;
double segment::overburden=0;

segment* segment::longest_segment=0;
segment* segment::starting_segment=0;

int flaw::target_number_of_flaws=0;
int flaw::number_of_flaws=0;
double flaw::min_percent_strength=0;
flaw* flaw::starting_flaw=0;

/*************************************************************/
int main()
{
srand(time(NULL));

//INPUT STAGE
int section_number=0;
/*ifstream infile;
cout<<"Enter Gerofit section (1 to 4) ->";
cin>>section_number;
if(section_number==1) infile.open("Input69_I.txt");
if(section_number==2) infile.open("Input69_II.txt");
if(section_number==3) infile.open("Input69_III.txt");
if(section_number==4) infile.open("Input69_IV.txt");
if(section_number<1 || section_number>4)
{
cout<<"Not a valid section, program ending...."<<endl;
return 0;
}*/

ifstream infile("Input74.txt");
double input_lambda=0;
cout<<"Entering lambda ->";
```

```
infile>>input_lambda;
cout<<input_lambda<<endl;

double layer_thickness_increment=0;
cout<<"Entering layer thickness and increment -> ";
infile>>segment::layer_thickness>>layer_thickness_increment;
cout<<segment::layer_thickness<<" , "<<layer_thickness_increment<<endl;
double layer_thickness_initial=segment::layer_thickness;

double non_jointing_layer_thickness_increment=0;
cout<<"Entering non-jointing layer thickness and increment -> ";
infile>>segment::non_jointing_layer_thickness>>non_jointing_layer_thick
ness_increment;
cout<<segment::non_jointing_layer_thickness<<" ,
"<<non_jointing_layer_thickness_increment<<endl;
double
non_jointing_layer_thickness_initial=segment::non_jointing_layer_thickn
ess;

double target_length=0;
cout<<"Entering target layer length -> ";
infile>>target_length;
cout<<target_length<<endl;
segment::layer_length=target_length;

double E_over_Gn_increment=0;
cout<<"Entering E/Gn ratio and increment -> ";
infile>>segment::E_over_Gn>>E_over_Gn_increment;
cout<<segment::E_over_Gn<<" , "<<E_over_Gn_increment<<endl;

cout<<"Entering Young's modulus (MPa)";
infile>>segment::E_of_layer;
cout<<segment::E_of_layer<<endl;

double target_mean_spacing=0;
cout<<"Entering target mean spacing: ";
infile>>target_mean_spacing;
cout<<target_mean_spacing<<endl;

double target_skewness=0;
cout<<"Entering target skewness: ";
infile>>target_skewness;
cout<<target_skewness<<endl;

double target_SD=0;
cout<<"Entering target SD: ";
infile>>target_SD;
cout<<target_SD<<endl;

int number_of_additional_joints=0;
cout<<"Entering number of joints ->";
infile>>number_of_additional_joints;
cout<<number_of_additional_joints<<endl;

double jointing_layer_Poisson_ratio_initial=0;
double jointing_layer_Poisson_ratio_increment=0;
cout<<"Entering jointing layer Poisson's ratio and increment ->";
```

```
infile>>segment::jointing_layer_Poisson_ratio>>jointing_layer_Poisson_r
atio_increment;
cout<<segment::jointing_layer_Poisson_ratio<<" ,
"<<jointing_layer_Poisson_ratio_increment<<endl;
jointing_layer_Poisson_ratio_initial=segment::jointing_layer_Poisson_ra
tio;

double non_jointing_layer_Poisson_ratio_initial=0;
double non_jointing_layer_Poisson_ratio_increment=0;
cout<<"Entering non-jointing layer Poisson's ratio and increment ->";
infile>>segment::non_jointing_layer_Poisson_ratio>>non_jointing_layer_P
oisson_ratio_increment;
cout<<segment::non_jointing_layer_Poisson_ratio<<" ,
"<<non_jointing_layer_Poisson_ratio_increment<<endl;
non_jointing_layer_Poisson_ratio_initial=segment::non_jointing_layer_Po
isson_ratio;

//double critical_spacing_to_thickness_ratio_increment=0;
//cout<<"Entering critical spacing to thickness ratio ->";
//infile>>segment::critical_spacing_thickness_ratio>>critical_spacing_t
o_thickness_ratio_increment;
//cout<<segment::critical_spacing_thickness_ratio<<" ,
"<<critical_spacing_to_thickness_ratio_increment<<endl;
//double
critical_spacing_to_thickness_ratio_initial=segment::critical_spacing_t
hickness_ratio;

infile.close();

int number_of_cycles=1;
cout<<"Enter number of simulations for each parameter value: ";
cin>>number_of_cycles;
cout<<number_of_cycles<<endl;

int number_of_cycles_2=1;
cout<<"Enter number of E/G values: ";
cin>>number_of_cycles_2;
cout<<number_of_cycles_2<<endl;

int number_of_cycles_3=1;
cout<<"Enter number of non-jointing thickness values: ";
cin>>number_of_cycles_3;
cout<<number_of_cycles_3<<endl;

//int number_of_cycles_4=1;
//cout<<"Enter number of spacing to thickness ratios: ";
//cin>>number_of_cycles_4;
//cout<<number_of_cycles_4<<endl;

int number_of_cycles_5=1;
cout<<"Enter number of layer thickness values: ";
cin>>number_of_cycles_5;
cout<<number_of_cycles_5<<endl;

int number_of_cycles_6=1;
cout<<"Enter number of jointing layer Poisson's ratio values: ";
cin>>number_of_cycles_6;
```

```
cout<<number_of_cycles_6<<endl;

int number_of_cycles_7=1;
cout<<"Entering number of non-jointing layer Poisson's ratio values: ";
cin>>number_of_cycles_7;
cout<<number_of_cycles_7<<endl;

cout<<"There will be
"<<number_of_cycles*number_of_cycles_2*number_of_cycles_3*number_of_cyc
les_5*number_of_cycles_6*number_of_cycles_7<<" cycles."<<endl;
//END OF INPUT STAGE

ofstream out_2a("Skewness_and_SD_vs_E_over_Gn.xls");
out_2a<<"E/G\tMeanSkewness\tMeanSD\t%WithinSkewness\t%WithinSD\t%Within
Both\tminSD\tmaxSD\tminSk\tmaxSk\t%BelowCrit\td\tcrit_s_to_t\tMMean\tt\
tD\tvf\tvn\tBeta"<<endl;
out_2a.close();

double sum_of_skewness=0;
double sum_of_SD=0;
double sum_of_mean=0;
double min_skewness=0;
double max_skewness=0;
double min_SD=0;
double max_SD=0;
double sum_of_frac_below_critical_spacing=0;

int number_within_mean_skewness=0;
int number_within_mean_SD=0;
int number_within_both=0;

for(int i=0;i<number_of_cycles_2;i++)//for E/G values
{
for(int jk3=0;jk3<number_of_cycles_3;jk3++)//for non-jointing layer
thickness values
{
//for(int jk4=0;jk4<number_of_cycles_4;jk4++)//for critical spacing to
thickness ratios
//{
for(int jk5=0;jk5<number_of_cycles_5;jk5++)//for layer thickness values
{
for(int jk6=0;jk6<number_of_cycles_6;jk6++)//for jointing layer
Poisson's ratios
{
for(int jk7=0;jk7<number_of_cycles_7;jk7++)//for non-jointing layer
Poisson's ratios
{
for(int j=0;j<number_of_cycles;j++)
{
segment* head=0;
head=new segment(0,target_length);
segment::starting_segment=head;
head->calc_beta();
head->calc_critical_spacing_thickness_ratio();
//segment::critical_spacing_thickness_ratio=1.0;//direct assignment,
not calculated from properties.  trial!!
```

```
if(target_length/segment::layer_thickness>segment::critical_spacing_thi
ckness_ratio)
segment::valid_total_jointing_length=target_length;

/*double first_length=head-
>get_root_L(get_random_number01(),input_lambda,segment::layer_thickness
,
(1/segment::E_over_Gn)*segment::E_of_layer,segment::E_of_layer);
head=new segment(0,first_length);
segment::starting_segment=head;
double length_sum=first_length;
segment *last_segment=head;*/

/*while(length_sum<target_length)//adds new segments until target layer
length is reached
{
segment* temp=0;
double new_length=temp-
>get_root_L(get_random_number01(),input_lambda,segment::layer_thickness
,
(1/segment::E_over_Gn)*segment::E_of_layer,segment::E_of_layer);
temp=new segment(last_segment->end2,last_segment->end2+new_length);
last_segment->next_segment=temp;
last_segment=temp;
length_sum+=new_length;
}*/

//cout<<"layer length: "<<segment::layer_length<<endl;
//cout<<"starting_segment: "<<segment::starting_segment<<endl;
//cout<<"head: "<<head<<endl;

//ofstream outdata("Stats.txt");
//outdata<<"lambda: "<<input_lambda<<endl;
//outdata<<"layer thickness: "<<segment::layer_thickness<<endl;
//outdata<<"Ef/Gm ratio: "<<segment::E_over_Gn<<endl;
//outdata<<"Ef: "<<segment::E_of_layer<<" MPa"<<endl;
//outdata<<"Number\tSt. Dev.\tSkewness"<<endl;
//outdata<<segment::number_of_segments<<"\t"<<head-
>get_standard_deviation()<<"\t"<<head->get_skewness()<<endl;

//cout<<"total segment length: "<<head-
>get_total_segment_length()<<endl;
//cout<<length_sum<<endl;
//cout<<"number of segments: "<<head->number_of_segments<<endl;

//cout<<"skewness: "<<head->get_skewness()<<endl;
//cout<<"standard deviation: "<<head->get_standard_deviation()<<endl;

head->set_max_spacing();
head->set_min_spacing();

//cout<<"longest segment after setting: "<<head->longest_segment-
>segment_length<<endl;

for(int
num_joints=0;num_joints<number_of_additional_joints;num_joints++)
{
```

```
if(segment::valid_total_jointing_length>1e-6)//valid total length
threshold
head->halve_segment_using_rejection();
if(segment::valid_total_jointing_length<=1e-6)
break;
}

//while(head-
>get_mean_length()/segment::layer_thickness>segment::critical_spacing_t
hickness_ratio
//    && head->layer_length/head-
>number_of_segments>target_mean_spacing /*&&
//    head-
>max_length/segment::layer_thickness>segment::critical_spacing_thicknes
s_ratio*/)
//{
//    head->halve_segment_using_rejection();
//}

//Will this ever reach the random bisection process?????  What is the
suitable criterion??
//max spacing>critical spacing or mean spacing>critical spacing???

/*while(head->layer_length/head-
>number_of_segments>target_mean_spacing)
{
//cout<<".";
head->halve_segment_using_random_bisection();
}*/

//cout<<head->get_mean_length()<<endl;

/*if(infill_indicator)
{
for(int i=0; i<number_of_cycles;i++)
{
for (int j=0; j<segments_per_cycle; j++) head-
>halve_segment_using_rejection();
outdata<<segment::number_of_segments<<"\t"<<head-
>get_standard_deviation()<<"\t"<<head->get_skewness()<<endl;
};
}

outdata.close();
*/

//cout<<"total segment length: "<<head-
>get_total_segment_length()<<endl;
//cout<<"number of segments: "<<head->number_of_segments<<endl;

//cout<<"skewness: "<<head->get_skewness()<<endl;
//cout<<"standard deviation: "<<head->get_standard_deviation()<<endl;

//WRITE FINAL DATA TO FILE
//head->set_max_spacing();
//head->set_min_spacing();
//cout<<head->longest_segment->segment_length<<endl;
```

```
//cout<<head->get_total_segment_length();
head->write_spacing_to_file();
//head->write_joint_pattern_to_file();
//head->write_moving_average_data_to_file_overlap(3);
//ofstream out("Segment_Stats.txt", ios::app);
//out<<head->number_of_segments<<"\t"<<head->layer_length/head-
>number_of_segments<<"\t"<<head->min_length<<"\t"<<head-
>max_length<<"\t"<<head->get_standard_deviation()<<"\t"<<head-
>get_skewness()<<endl;
//out.close();


double temp_skewness=head->get_skewness();
double temp_SD=head->get_standard_deviation();
//double temp_frac_below_critical_spacing=head-
>get_fraction_below_critical_spacing(segment::critical_spacing_thicknes
s_ratio);
//double temp_kurtosis=head->get_kurtosis(temp_SD);

//if(min_skewness!=0) if(temp_skewness<min_skewness)
min_skewness=temp_skewness;
//if(min_skewness==0) min_skewness=temp_skewness;

//if(max_skewness!=0) if(temp_skewness>max_skewness)
max_skewness=temp_skewness;
//if(max_skewness==0) max_skewness=temp_skewness;

//if(min_SD!=0) if(temp_SD<min_SD) min_SD=temp_SD;
//if(min_SD==0) min_SD=temp_SD;

//if(max_SD!=0) if(temp_SD>max_SD) max_SD=temp_SD;
//if(max_SD==0) max_SD=temp_SD;

sum_of_skewness+=temp_skewness;
sum_of_SD+=temp_SD;
sum_of_mean+=segment::layer_length/segment::number_of_segments;
//sum_of_frac_below_critical_spacing+=temp_frac_below_critical_spacing;

if(fabs(target_skewness-temp_skewness)/target_skewness<=0.1)
number_within_mean_skewness++;//within 10% of actual skewness
if(fabs(target_SD-temp_SD)/target_SD<=0.1)
number_within_mean_SD++;//within 10% of actual SD
if(fabs(target_skewness-temp_skewness)/target_skewness<=0.1 &&
fabs(target_SD-temp_SD)/target_SD<=0.1) number_within_both++;

//DELETE SEGMENTS
segment* cur_seg=head;
segment* cur_next_seg=head->next_segment;
int segment_population=segment::number_of_segments;//because
segment::number_of_segments changes every time one is deleted
for(int del_n=0;del_n<segment_population;del_n++)
{
if(cur_seg!=0) delete cur_seg;
cur_seg=cur_next_seg;
if(cur_next_seg!=0) cur_next_seg=cur_next_seg->next_segment;
};
```

```
//cout<<"There are now "<<segment::number_of_segments<<"
segments."<<endl;
//END of DELETE SEGMENTS
}
ofstream out_2("Skewness_and_SD_vs_E_over_Gn.xls",ios::app);
out_2<<segment::E_over_Gn<<"\t"<<sum_of_skewness/number_of_cycles<<
"\t"<<sum_of_SD/number_of_cycles<<
"\t"<<(double) number_within_mean_skewness/number_of_cycles<<
"\t"<<(double) number_within_mean_SD/number_of_cycles<<
"\t"<<(double) number_within_both/number_of_cycles<<
"\t"<<min_SD<<"\t"<<max_SD<<"\t"<<min_skewness<<"\t"<<max_skewness<<
"\t"<<sum_of_frac_below_critical_spacing/number_of_cycles<<
"\t"<<segment::non_jointing_layer_thickness<<"\t"<<segment::critical_sp
acing_thickness_ratio<<
"\t"<<sum_of_mean/number_of_cycles<<"\t"<<segment::layer_thickness<<"\t
"<<segment::parameter_D<<
"\t"<<segment::jointing_layer_Poisson_ratio<<"\t"<<segment::non_jointin
g_layer_Poisson_ratio<<
"\t"<<segment::beta<<endl;
out_2.close();
number_within_mean_skewness=0;
number_within_mean_SD=0;
number_within_both=0;
sum_of_skewness=0;
sum_of_SD=0;
sum_of_mean=0;
sum_of_frac_below_critical_spacing=0;

min_skewness=0;
max_skewness=0;
min_SD=0;
max_SD=0;

segment::non_jointing_layer_Poisson_ratio+=non_jointing_layer_Poisson_r
atio_increment;
}
segment::jointing_layer_Poisson_ratio+=jointing_layer_Poisson_ratio_inc
rement;
segment::non_jointing_layer_Poisson_ratio=non_jointing_layer_Poisson_ra
tio_initial;
}
segment::layer_thickness+=layer_thickness_increment;
segment::jointing_layer_Poisson_ratio=jointing_layer_Poisson_ratio_init
ial;
}
segment::non_jointing_layer_thickness+=non_jointing_layer_thickness_inc
rement;
segment::layer_thickness=layer_thickness_initial;
}
segment::E_over_Gn+=E_over_Gn_increment;
segment::non_jointing_layer_thickness=non_jointing_layer_thickness_init
ial;
};

cout<<"\nDONE!!\n";
//END OF WRITING FINAL DATA TO FILE
```

```
//system("PAUSE");
return 0;
};//END OF MAIN()
/*****************************************************************/

//global function to get random number
//gets the jth number from the file Random.txt
double get_random_number(int j)
{
double rn=0;
ifstream in("Random.txt");
for (int i=0; i<j; i++)
in>>rn;
in.close();
random_number_taken++;
//cout<<rn<<endl;
return rn;
};

//global function to get normal random number
//gets the jth number from the file Random_Normal.txt
double get_normal_number(int j)
{
double rn=0;
ifstream in("Random_Normal.txt");
for (int i=0; i<j; i++)
in>>rn;
in.close();
normal_number_taken++;
//cout<<rn<<endl;
return rn;
};

double get_random_number01()
{
return ((double) rand()/ (double) (RAND_MAX+1));
};
```